

Catalytic Membrane Reactors for e-chemicals production & processing

Citation for published version (APA):

Richard, S. P. (2025). *Catalytic Membrane Reactors for e-chemicals production & processing*. [Phd Thesis 1 (Research TU/e / Graduation TU/e), Chemical Engineering and Chemistry]. Eindhoven University of Technology.

Document status and date:

Published: 20/03/2025

Document Version:

Publisher's PDF, also known as Version of Record (includes final page, issue and volume numbers)

Please check the document version of this publication:

- A submitted manuscript is the version of the article upon submission and before peer-review. There can be important differences between the submitted version and the official published version of record. People interested in the research are advised to contact the author for the final version of the publication, or visit the DOI to the publisher's website.
- The final author version and the galley proof are versions of the publication after peer review.
- The final published version features the final layout of the paper including the volume, issue and page numbers.

[Link to publication](#)

General rights

Copyright and moral rights for the publications made accessible in the public portal are retained by the authors and/or other copyright owners and it is a condition of accessing publications that users recognise and abide by the legal requirements associated with these rights.

- Users may download and print one copy of any publication from the public portal for the purpose of private study or research.
- You may not further distribute the material or use it for any profit-making activity or commercial gain
- You may freely distribute the URL identifying the publication in the public portal.

If the publication is distributed under the terms of Article 25fa of the Dutch Copyright Act, indicated by the "Taverne" license above, please follow below link for the End User Agreement:

www.tue.nl/taverne

Take down policy

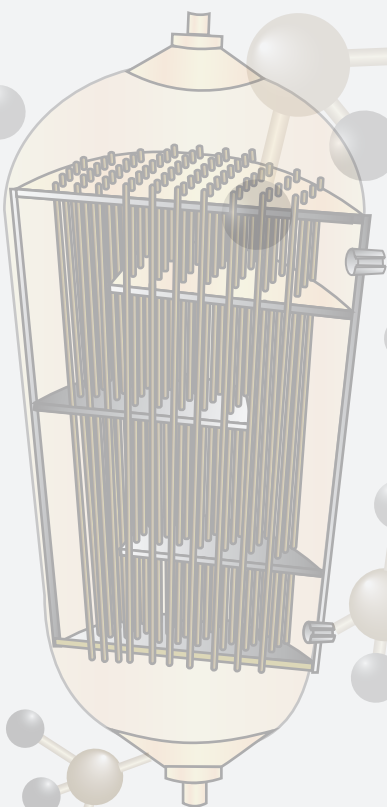
If you believe that this document breaches copyright please contact us at:

openaccess@tue.nl

providing details and we will investigate your claim.

Catalytic Membrane Reactors

for e-chemicals production & processing



Simon Richard

Catalytic Membrane Reactors for e-chemicals production & processing

PROEFSCHRIFT

ter verkrijging van de graad van doctor aan de Technische Universiteit Eindhoven, op gezag van de rector magnificus prof. Silvia Lenaerts, voor een commissie aangewezen door het College voor Promoties, in het openbaar te verdedigen op dinsdag 20 maart 2025 om 11:00 uur

door

Simon Pierre RICHARD

geboren te Rueil-Malmaison, Frankrijk

Dit proefschrift is goedgekeurd door de promotoren en de samenstelling van de promotiecommissie is als volgt:

Voorzitter:	prof.dr. E. Rebrov
1 st promotor:	prof.dr. F. Gallucci
2 nd promotor:	prof.dr.ir. J. van der Schaaf
leden:	dr. S. Soheil Mansouri (Danmarks Tekniske Universitet)
	dr. V.S. Spallina (University of Manchester)
	prof.dr.ir. M. van Sint Annaland
Advisors	dr. M.F. Neira d'Angelo
	dr. P. Olivier (Engie Lab Crigen)

Het onderzoek of ontwerp dat in dit proefschrift wordt beschreven is uitgevoerd in overeenstemming met de TU/e Gedragscode Wetenschapsbeoefening.

Part of this research described in this thesis has been part of the European project AMBHER. This project has received funding from the European Union's Horizon 2020 research and innovation program under grant agreement No 101058565 (*Ambher* project). Funded by the European Union. Views and opinions expressed are however those of the author(s) only and do not necessarily reflect those of the European Union. Neither the European Union nor the granting authority can be held responsible for them.



**Funded by
the European Union**

Copyright © 2025 by Simon Richard, Eindhoven, The Netherlands.

All rights reserved. No part of the material protected by this copyright notice may be reproduced or utilized in any form or by any means, electronic or mechanical, including photocopying, recording or by any information storage and retrieval system, without the prior permission of the author.

ISBN: 978-90-386-6321-0

Summary

Synthetic chemicals produced from green hydrogen and captured carbon dioxide for methanol and methane, or nitrogen for ammonia, can address renewable energy intermittency issues and provide fossil-free resources for hard-to-electrify sectors like transportation and distributed power generation. However, these reaction systems are typically limited by thermodynamic equilibrium, which constrains reactant conversion under relevant process conditions. Membrane reactors (MRs) have established as a significant contribution in process intensification allowing overcoming these limitations through the combination of reaction and product separation in a single device. In their most basic configuration, a MR involves a tubular vessel with vertically inserted membranes surrounded by a catalyst-packed bed. Reactants enter from the bottom and move upward, with the product collected inside the membrane as permeate, while other chemical components form the retentate. This thesis explores the use of the MR technology in the Power-to-X context from various perspectives, including process synthesis, techno-economic analysis and the potential of additive manufacturing to enhance the basic MR configuration along with experimental testing of the technology.

Chapter 1 begins with a general introduction to the topic, emphasizing the pressing need to limit CO₂ emissions and the importance of Power-to-X (PtX) technologies in addressing this challenge. It then introduces membrane reactor systems, highlighting their potential in sustainable chemical processes. Additionally, the chapter provides an overview of 3D-printed catalytic supports as well as a discussion on the modeling approaches used to study & optimize these systems.

Chapter 2 provides an in depth state-of-the-art in membrane reactors for hydrogen and e-chemical production. Most studies report improved conversion rates depending on reactor operating conditions. Future directions include stronger integration of functionalities such as structured catalysts, enhanced thermal management, and more selective membranes. While some process-level insights indicate higher performance, there remains limited knowledge on the benefits of integrating membrane reactors into several e-fuel synthesis pathways.

Chapter 3 & 4 discuss the use of MRs for power generation applications first in combination with proton exchange membrane (PEM) fuel cells and then to improve ammonia combustion in large combined cycle gas turbines (CCGTs). An economic comparison is made between small-scale PEM fuel cell gensets using membrane reactors for methanol, ammonia, and methane. Methane emerges as the most cost-effective fuel, while ammonia offers the highest efficiency (Chap. 3). At the large scale for CCGT, it has been found that CMR systems can achieve better performance than the traditional concept. However, their adoption is hindered by the scarcity of palladium and ruthenium, making this approach currently impractical (Chap. 4).

Chapter 5, 6 & 7 explore the potential of 3D printed Periodic Open Cell Structures (POCS) to improve the basic configurations of MRs. First, Chap. 6. provides a fundamental investigation into the thermohydraulic performance of POCS reactors. Using computational fluid dynamic (CFD) simulations and experiments, Kelvin, Body Centered Cubic (BCC), and gyroid lattice structures were 3D-printed, characterized, and analyzed. The gyroid lattice showed optimal performance at

low velocities, while the BCC lattice performed better at higher velocities. Afterward, Chap. 6 examines how external mass transfer rates in POCS reactors affect ammonia synthesis, both independently and with selective membranes. Chap. 7 extends this to ammonia cracking, emphasizing the role of POCS baffles in improving hydrogen permeation through palladium-based membranes.

Chapter 8 evaluates the cost and efficiency of power-to-ammonia processes under uniform assumptions, highlighting the advantages of innovative pathways, including MRs and solid oxide electrolysis cell (SOEC) integrations.

Contents

Summary	v
Contents	vii
List of Abbreviations.....	x
Chapter 1 Introduction.....	1
1.1. Power-to-X	1
1.2. E-molecules properties	2
1.3. E-fuel Production and Processing.....	4
1.4. Membrane reactors	14
1.5. Structured catalyst	15
1.6. Modelling membrane reactors	17
1.7. Objectives and scope	18
1.8. References	19
Chapter 2 Membrane reactors technologies for e-fuel processing & production: a review	26
2.1. Introduction	28
2.2. Performance Indicators generally used.....	30
2.3. Membrane reactors design.....	31
2.4. Lab scale performance.....	43
2.5. Process environments	54
2.6. Conclusion.....	57
2.7. References	58
Chapter 3 PEM gensets using membrane reactors technologies: an economic comparison among different e-fuels	68
3.1. Introduction	68
3.2. Materials and Methods	70
3.3. Results and discussions	82
3.4. Conclusions	98
3.5. References	99
Appendix A.	106
Chapter 4 Techno-economic analysis of ammonia cracking for large scale power generation...	112
4.1. Introduction	113

4.2. Material and Methods.....	116
4.3. Results and discussion.....	126
4.4. Conclusions	136
4.5. References	137
Appendix B.	143
Chapter 5 Comparison of thermo-hydraulic performance among different 3D printed Periodic Open Cellular Structures.....	150
5.1. Introduction	151
5.2. Experimental	152
5.3. Numerical investigation.....	154
5.4. Result and discussion	157
5.5. Conclusions	168
5.6. References	169
Appendix C	171
Chapter 6 Ammonia synthesis using POCS membrane reactor: influence of cell types.....	177
6.1. Introduction	178
6.2. Experimental set up.....	179
6.3. Numerical investigation.....	183
6.4. Results.....	187
6.5. Conclusion.....	194
6.6. References	195
Appendix D	197
Chapter 7 Ammonia cracking using membrane reactors: towards the utilization of POCS to improve external mass transfer.....	199
7.1. Introduction	200
7.2. Experimental set-up.....	201
7.3. Numerical investigation.....	204
7.4. Results.....	208
7.5. Conclusion.....	215
7.6. References	216
Appendix E.....	218
Chapter 8 Power-to-ammonia synthesis process using membrane reactors: Techno-economic study	223

8.1. Introduction	224
8.2. Material and Method	225
8.3. Results and discussion	234
8.4. Conclusion.....	243
8.5. References	244
Appendix F.....	248
Conclusion and Outlooks	259
Conclusion.....	259
Outlooks	261
Appendix G: Energy and power densities	266
Research Outputs.....	273
Peer-reviewed publications	273
Oral presentations.....	273
Acknowledgments.....	274
Curriculum Vitae.....	275

List of Abbreviations

0D 1D 2D 3D	0 to 3 Dimensional
AC	Alternating Current
ACM	Aspen Custom Modeler™
AEC	Alkaline Electrolysis Cell
AM	Additive Manufacturing
ASU	Air Separation Unit
BEC	Bare Erected Cost
BET	Brauner-Emmett-Teller
BBM	Bubbling Bed Model
BCC	Body-Centered Cubic cell
BOP	Balance Of Plant
CAD	Computer-Aided Design
CAPEX	Capital Expenditure
CCF	Capital Charge Factor
CCU	Carbon Capture and utilisation
CCGT	Combined Cycle Gas Turbine
CEPCI	Chemical Engineering Plant Index Cost
CFD	Computational fluid dynamic
CPC	Concentration Polarization Coefficient
GDC	Gadolinium Doped Ceria
CMSM	Carbon Molecular Sieve Membrane
CP	Concentration Polarization
CPC	Concentration Polarization Coefficient
CSC	Cathode-Supported Cells
DAC	Direct Air Capture
DC	Direct Current
DNS	Direct Numerical Simulation
DME	Dimethyl ether
ESC	Electrolyte-Supported Cell
FBMR	Fluidized Bed Membrane Reactors
FC	Fuel Cell
FP	Fuel Processor
FT	Fischer Tropsch
FTD	Fischer Tropsch Diesel
FTR	Fire Tubular Reactor
Genset	Generator Set
GHG	Greenhouse gas
GHSV	Gas hourly Space Velocity
GT	Gas Turbine

HEX	Heat Exchanger
HRF	Hydrogen Recovery Factor
HRGS	Heat Recovery Steam Generators
IC	Indirect Costs
ICE	Internal Combustion Engine
IEA	International Energy Agency
ICE	Internal Combustion Engine
IMO	International Maritime Organization
KC	Kelvin Cell
KPIs	Key performance Indicators
LCOH	Levelized Cost Of Hydrogen, €/kgH ₂
LCOA	Levelized Cost Of Ammonia, €/kgNH ₃
LCOE	Levelized Cost Of Electricity, €/MWh
LHV	Lower Heating Value
LSCF	Lanthanum Strontium Cobalt Ferrite
MAPE	Mean Absolute Percentage Error
MR	Membrane Reactor
OPEX	Operation expenditure, €/year
O&M	Operation and Maintenance costs, €
OCF	Open-Cell Foam
OEM	Original Equipment Manufacturer
NTP	Non Thermal plasma
PCMR	Proton Conducting Membrane Reactor
PEMFC	Polymer Electrolyte Membrane Fuel Cells
POCS	Periodic Open Cell Structures
PBR	Packed Bed Reactor
PBMR	Packed Bed Membrane Reactor
PSA	Pressure Swing Adsorption
PSE	Process System Engineering
PSS	Porous Stainless Steel
PtX	Power-to-X
RF	Recovery Factor
RMSE	Root Mean Square Error
RWGS	Reverse Water Gas Shift
SEM	Scanning Electron Microscopy
SCR	Steam to Carbon Ratio
SEM	Scanning Electron Microscopy
SLM	Selective Laser Melting
SMA	Specific Membrane Area
SR	Steam Reforming
SSA	Specific Surface Area
SW	Sweep gas ratio

SWOT	Strengths, Weaknesses, Opportunities, Threats
T	Temperature
TEC	Total equipment cost, €
TGA	Thermogravimetric Analysis
TIC	Total Installation Cost, €
TPC	Total Plant Cost, €
TPMS	Triply Periodic Minimal Surface
TR	Traditional Reactor
TRL	Technology Readiness Level
P	Pressure
WGS	Water Gas Shift
WSV	Weight Space Velocity
YSZ	Yttria Stabilized Zirconia

Chapter 1 | Introduction

1.1. Power-to-X

Today, the global average surface temperature is approximately 1.2 °C above pre-industrial levels, leading to heatwaves and other extreme weather events, while greenhouse gas emissions have yet to peak [1]. Achieving carbon neutrality by 2050 necessitates a drastic reduction in emissions and a shift from fossil fuels to renewable energy. Leading the way, countries like Greece, the Netherlands, Spain, Denmark, and Germany already generate over 40% of their electricity from renewables and are expected to exceed 50% by 2028. According to the International Energy Agency (IEA), renewables could account for 44% of global electricity by 2040 and nearly 90% by 2050 under the Net Zero scenario [2]. As renewable energy continues to expand, energy storage technologies will play a crucial role in ensuring grid stability and maximizing the effective use of these resources. Emerging solutions such as "power-to-liquid" and "power-to-gas" are considered to address the intermittency of renewable energy by converting surplus renewable energy into synthetic molecules (also called e-molecules). Green hydrogen, produced through water electrolysis, is the simplest option and a building block in the synthesis of other Power-to-X molecules. As of 2023, the global installed electrolyzer capacity stands at ~1.4 GW, with projections rising to 230 GW by 2030 or even 520 GW including early-stage projects [1,3]. However, this ambitious growth trajectory faces several challenges, such as high production costs, supply chain bottlenecks, and uncertainties in demand and regulatory frameworks [4-5]. Furthermore, hydrogen's low volumetric energy density and risks of leakage and corrosion complicate its direct use [6-8]. Hydrogen-derived molecules present a promising solution, offering practical options for storage and transport while utilizing existing infrastructure. These e-molecules play a pivotal role in decarbonizing hard-to-abate sectors by replacing fossil-based fuels and serving as sustainable alternatives to traditional fossil-derived molecules in industries such as chemicals, agriculture, and manufacturing. Key examples of hard-to-abate sectors include heavy-load vehicles, stationary power generators (e.g. backup power [9], off-grid projects [10], residential [11] and mobile [12] applications) or maritime shipping, which alone contributes ~3% of global greenhouse gas (GHG) emissions [13] and releases harmful pollutants like sulphur oxides (SO_x), nitrogen oxides (NO_x), and particulate matter (PM) [14-15]. Ammonia and methanol, traditionally produced from fossil fuels, are prime examples of products that could be replaced by their green hydrogen-based counterparts. Ammonia, with over 180 million tons produced annually, primarily supports agriculture as nitrogen-based fertilizers (85–90%), essential for nearly half of global food production [16-18], and is also used in dyes and explosives. Methanol, with annual production nearing 90 million metric tons, serves as a fuel, a chemical feedstock, and a precursor for compounds like formaldehyde and methyl tert-butyl ether (MTBE). The conventional production of these chemicals is associated with substantial CO₂ emissions per ton, primarily due to the reliance on hydrogen from natural gas reforming: 3.2 tCO₂/t for jet fuel, 2.4 tCO₂/t for ammonia, and 2.1 tCO₂/t for methanol. In comparison, cement and steel emit 0.6 tCO₂/t and 1.4 tCO₂/t, respectively, with 30% of steel now produced using low-emission electric arc furnaces powered by renewable electricity and scrap steel. While cement and steel production volumes far exceed those of hydrogen-derived chemicals, the

chemical process industry remains a major contributor to global CO₂ emissions [19]. **Figure 1-1** illustrates this, reporting sectoral CO₂ emissions and emphasizing the contributions from transport, electricity, and industry.

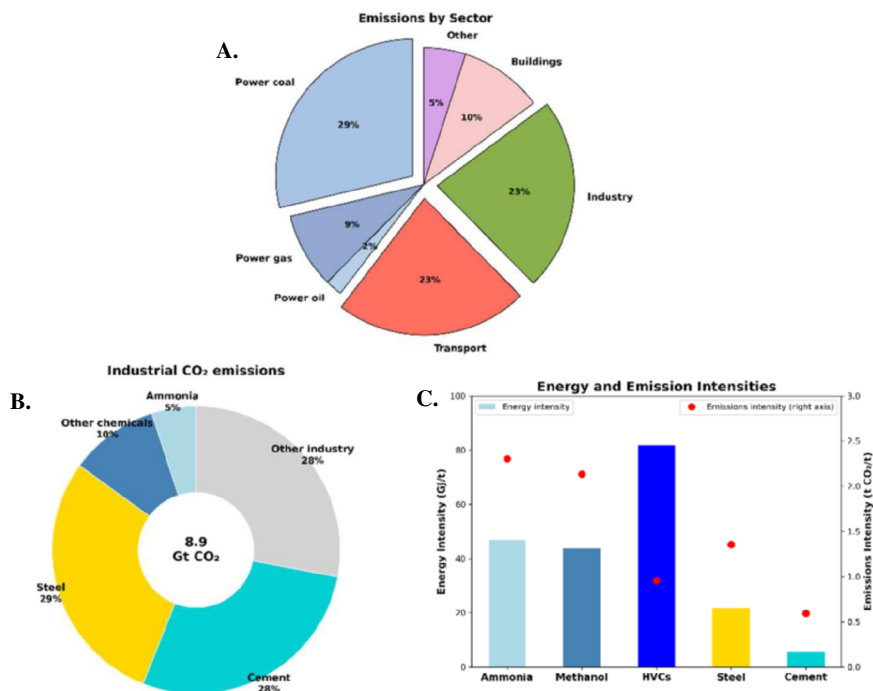


Figure 1-1: Reproduced from IEA reports [19-20]: (A) Breakdown of CO₂ emissions by sector [20] total CO₂ emission of 36.8 t in 2022 and 37.4 t in 2023 (B) Energy demand associated to the Industry sector emissions in 2020 [19] (C) Energy intensity and carbon intensity associated to steel, cement, ammonia and other chemicals production [19]

1.2. E-molecules properties

E-molecules vary significantly in their energy density, hydrogen content, handling requirements, costs & combustion characteristics, costs, and emissions, making their careful evaluation essential for specific applications. The following discussion briefly highlights key aspects [21]. From a storage perspective, **Figure 1-2** compares their volumetric (kWh/L) and gravimetric (kWh/kg) energy densities, considering the impact of storage equipment while **Table 1-1** lists approximative energy densities ratios between stored fuels and diesel, the benchmark. Diesel, with high energy density (8.3 kWh/kg and 8.2 kWh/L), retains most of its intrinsic energy due to minimal storage requirements, making it ideal for long-range and high-demand applications. Hydrogen, despite its high gravimetric energy density as a pure fuel (33 kWh/kg), is limited by heavy and bulky storage systems. For example, liquefied hydrogen requires cryogenic storage at -253 °C, reducing

its volumetric energy density to ~ 1.3 kWh/L (~ 6.8 times smaller than diesel) and gravimetric energy density to ~ 1.5 kWh/kg (~ 4.1 times smaller than diesel). Methanol and, to a lesser extent, ammonia are easier to store but still fall short of diesel. Methanol achieves ~ 4 kWh/kg and ~ 3.8 kWh/L, roughly half of diesel's energy density. Ammonia, requiring cryogenic storage at -33 °C and corrosion-resistant tanks, has an effective energy density of ~ 3.6 kWh/kg and ~ 2.7 kWh/L, about three times smaller than diesel. Compared to lithium-ion batteries, diesel and methanol offer significantly higher energy densities, while hydrogen, compressed or liquefied, provides only modest improvements [22]. While not the focus of this work, it is relevant to note that lithium-ion batteries currently achieve up to 0.140 kWh/kg and 0.200 kWh/L at the pack level, with projected targets of 0.235 kWh/kg and 0.500 kWh/L to support long-range mobility [106]. Recent advancements include for example Tesla Model 3 (2017) reaching 236 Wh/kg and 673 Wh/L (cell level) offering a driving range of 490 - 630 km or CATL's commercial battery packs reaching 0.175 kWh/kg and 0.305 kWh/L with R&D claims of reaching 0.330 kWh/kg [107]. These energy density factors are critical to consider in the decision-making phase for space-constrained applications like shipping or some genset markets (e.g., data centers or cold ironing). In addition, easier storage conditions often translate to lower costs. For instance, storing ammonia requires only 2.45 kWh/kg compared to 11.82 kWh/kg for compressed hydrogen, making it $\sim 80\%$ more energy-efficient [23] and 26 - 30 times cheaper [24]. From the perspective of compatibility with existing infrastructure, certain e-molecules, such as e-methane, e-kerosene, e-diesel, and e-gasoline, can be seamlessly integrated into current infrastructure and conventional combustion systems as drop-in e-fuels. In contrast, e-molecules like e-ammonia and e-methanol, which primarily function as commodity chemicals, require modifications to distribution networks, bunkering systems, and combustion devices. Additionally, they may involve partial or complete hydrogen recovery, via ammonia decomposition or methanol reforming, to address flammability concerns or to generate high-purity hydrogen for applications like Proton Exchange Membrane (PEM) fuel cells. Liquid ammonia has a density of approximately 123 kg_{H₂}/m³, while methanol has density of 99 kg_{H₂}/m³, which are well above other advanced hydrogen storage systems like metal hydrides (25 kg_{H₂}/m³), liquefied hydrogen (71 kg_{H₂}/m³), compressed hydrogen at 700 bar (42.2 kg_{H₂}/m³) or formic acid (53 kg_{H₂}/m³) [25]. From a safety perspective, adopting drop-in fuels like ammonia and methanol presents significant challenges that require thorough evaluation and proactive mitigation strategies. Methanol's flammability and toxicity necessitate robust safety measures, such as inert gas systems and emergency protocols, as outlined in International Maritime Organization (IMO) standards (MSC.1/Circ.1621). Ammonia, while less flammable, poses severe toxicity risks, with US EPA Acute Exposure Guideline Levels (AEGLs) indicating life-threatening concentrations at 2700 ppm for 10 minutes and 390 ppm for 8 hours, far exceeding its odor detection range of 5 to 50 ppm. Research, including Hu et al. (2024) [26], highlights ammonia's toxicity as a primary hazard in marine applications, stressing the need for early-warning systems, water curtains (capable of dissolving large volumes of ammonia gas), effective ventilation, and safe upwind escape routes.

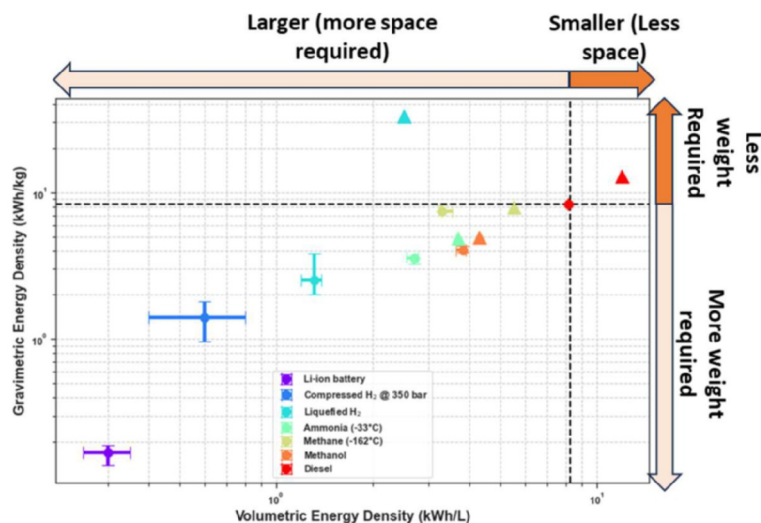


Figure 1-2: Energy densities of various energy carriers. Triangle markers represent pure fuels, while dot markers indicate approximative effective energy densities considering storage. [24, 27-31].

Table 1-1: Rough energy densities ratio between stored diesel and other storage medium

	Gravimetric	Volumetric
Li-ion battery	48.8	27.3
Compressed H₂ (350 bar)	5.9	16.4
Liquefied H₂ (-253 °C)	4.1	6.8
Ammonia (-33 °C)	2.6	3.5
Liquefied Methane (-162 °C)	1.1	2.4
Methanol	2.1	2.2
Diesel	1	1

1.3. E-fuel Production and Processing

For e-molecules to be effective, their synthesis, utilization, and potential reconversion to hydrogen, whether for use in PEM fuel cells or as a booster in combustion, should be seamlessly integrated into an efficient value chain (see **Figure 1-3**). This section provides a summary of the key steps in this value chain, including the electrolysis, fuel synthesis, and the recovery of hydrogen for end-use applications.

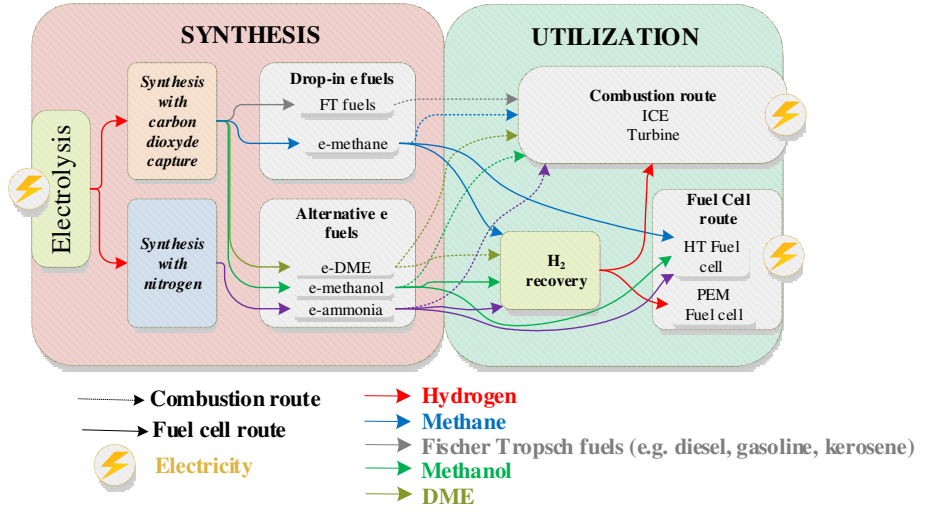


Figure 1-3: Illustration of the e-fuel value chain from production to utilization including a recovery step for on-site production when required.

1.3.1. Electrolysis

Power-to-X technologies begin with renewable hydrogen production through electrolysis, using renewable electricity to split water into hydrogen and oxygen. Various electrolysis technologies are being developed, with low-temperature processes like Alkaline Electrolysis Cells (AEC) and Proton Exchange Membrane (PEM) cells being the most common [32]. While AECs dominate the market, PEM cells are valued for their flexibility, though they rely on costly materials like iridium and platinum. Solid Oxide Electrolysis Cells (SOEC), operating at higher temperatures, offer advantages in heat integration and co-electrolysis, where both water and CO₂ are converted to produce syngas in one step [33]. **Table 1-2** summarizes the main characteristics of each primary type of electrolysis technology, highlighting differences in materials (e.g., electrolytes, electrodes, bipolar plates), operating conditions (e.g., temperature, current density), and reaction mechanisms. These distinctions result in unique attributes for each technology, such as power density, lifespan, and fuel flexibility, making them suitable for specific applications. The Second Law of Thermodynamics as per Eq. 1.1 offers great insights into the energy efficiency of water electrolysis processes, by delineating energy requirements and setting theoretical efficiency limits. The total energy requirement (ΔH) consisting of electrical energy (ΔG) and thermal energy ($T\Delta S$). As shown in **Figure 1-4**, the energy contributions shift with temperature. At lower temperatures, the process is dominated by electrical energy demand (ΔG), while at higher temperatures, the thermal energy contribution ($T\Delta S$) increases, reducing the demand for electrical energy and encouraging the use of heat in an energy-efficient manner. For example, the ratio of ΔG to ΔH decreases from 93% at 373 K to 70% at 1273 K, indicating enhanced thermal-to-hydrogen energy conversion efficiency at elevated temperatures. This principle is particularly advantageous in high-temperature electrolysis processes, such as SOECs, where external thermal energy significantly enhances overall system

efficiency. SOECs are particularly well-suited for scenarios where a high-temperature heat source is available, as this can be utilized for water evaporation, further improving efficiency. The Nernst potential (E), as described by Eq. 1.2, is directly tied to the thermodynamic driving force of the reaction ($-\Delta G$), normalized by the amount of charge (nF) involved in the process. (n is the number of moles of electrons transferred per mole of reaction & F is the Faraday constant, representing the charge of one mole of electrons). It represents the equilibrium voltage for an electrochemical reaction, under ideal conditions. As temperature increases, the Nernst potential decreases, indicating a reduced equilibrium voltage requirement for the reaction to occur reflecting a reduced energy requirement for the process and thereby theoretically enhancing the efficiency of hydrogen production. However, real-world systems deviate from this ideal behavior due to irreversibilities, including ohmic losses, activation and concentration overpotentials. These irreversibilities generate entropy and reduce the overall efficiency of the system. Advanced materials and optimized designs are therefore key levers to minimizing these losses and moving closer to the theoretical efficiency dictated by the Nernst potential.

$$\Delta H = \Delta G + T\Delta S \text{ Eq. 1.1}$$

$$E = -\frac{\Delta G}{nF} \text{ Eq. 1.2}$$

Beyond thermodynamic efficiency, system efficiency serves as a practical performance metric by accounting for real-world losses, including compression, electrical heating, and auxiliary power consumption & AC–DC conversion. It is defined as the ratio of the lower heating value of hydrogen (LHV_{H_2}) (33.3 kWh/kg H_2) to the system's specific energy consumption, as described by Eq. 1.3. Based on reported SOEC energy consumption values in **Table 1-2**, system efficiencies can be calculated as ~84% for 40 kWh/kg H_2 (with steam at 150 °C) and ~70% for 48 kWh/kg H_2 (without steam).

$$\eta = \frac{\text{LHV}_{\text{H}_2}}{\text{Specific Energy Consumption}} \text{ Eq. 1.3}$$

SOECs offer significant thermodynamic and kinetic advantages, making them a promising technology for hydrogen and syngas production. However, their widespread adoption is limited by challenges in achieving long-term stack durability. Common degradation mechanisms include nickel depletion in fuel electrodes, strontium migration in oxygen electrodes, and microstructural changes in zirconia electrolytes, such as the formation of small pores along grain boundaries [34, 35]. Recent durability studies at the stack level, summarized in **Table 1-3**, suggest progress toward meeting the Clean Hydrogen Joint Undertaking's 2030 target of reducing degradation rates to 0.5% per 1000 hours [36]. For instance, stack-level tests of electrolyte-supported cell-based stacks over >1000 hours reported varying degradation rates, with some studies observing values between 0.5% and 1.3% per 1000 hours. Other long-term studies prefer to measure degradation using the increase in area-specific resistance (ASR) over time, reporting values of 12–18 $\text{m}\Omega\cdot\text{cm}^2$ per 1000 hours [34, 35, 42, 45–48]. SOEC technology is now starting to be demonstrated at multi-MW scale in Europe (MultiPLHY project with Sunfire technology) or in the USA (4 MW system from Bloom Energy installed at NASA) [48].

Table 1-2: Summary of the main technical characteristics for the three main typical types of electrolysis technologies [37-41]

	AEC	PEM	SOEC
Anode reaction	$2OH^- \rightarrow H_2O + \frac{1}{2}O_2 + 2e^-$	$H_2O \rightarrow 2H^+ + \frac{1}{2}O_2 + 2e^-$	$O^{2-} \rightarrow \frac{1}{2}O_2 + 2e^-$
Cathode reaction	$2H_2O + 2e^- \rightarrow H_2 + 2OH^-$	$2H_2O + 2e^- \rightarrow H_2 + 2OH^-$	$H_2O + 2e^- \rightarrow H_2 + O^{2-}$
Charge carrier	HO^-	H^+	O^{2-}
Reactant	Liquid water	Liquid water	Water vapor
Anode catalyst	Ni, Ni-Mo alloys	Iridium oxide	LSM/YSZ or LSCF/GDC electrode supported [42]
Cathode catalyst	Ni, Ni-Mo alloys	Platinum	Ni/YSZ
Electrolyte	20-40 wt% KOH	PSFA membrane	YSZ
Hydrogen purity [%]	99.5–99.9998%	99.9–99.9999%	99.9% [39]
Temperature [°C]	60-80	50-80 [39]	650-900 [42]
Pressure [bar]	1-30 bar [41]	1-50 bar [38] <70 bar [39,41]	1 bar
Nominal Current density [A cm⁻²]	0.2-0.4 [39-40]	0.6-2 [38]	0.3-1 [39] 0.3-2 [40]
Maturity	Mature	Commercial	Demonstration
Stack specific consumption* kWh/Nm³ <small>*Nominal condition</small>	4.2-5.9	4.2-5.5	NA
System specific consumption kWh/Nm³	4.5-6.6	4.2-6.6	~4.32 without steam ~3.6 with steam at 150 °C
Cold start time (min)	<60	<20	<60
Lifetime of stack (hr)	<90000 [38]	50000–80000 [38]	20000 [38]
Capital cost stack	USD 270/kW _{BEC} [40]	USD 400/kW _{BEC} [40]	>USD 2000/kW _{BEC} [40]

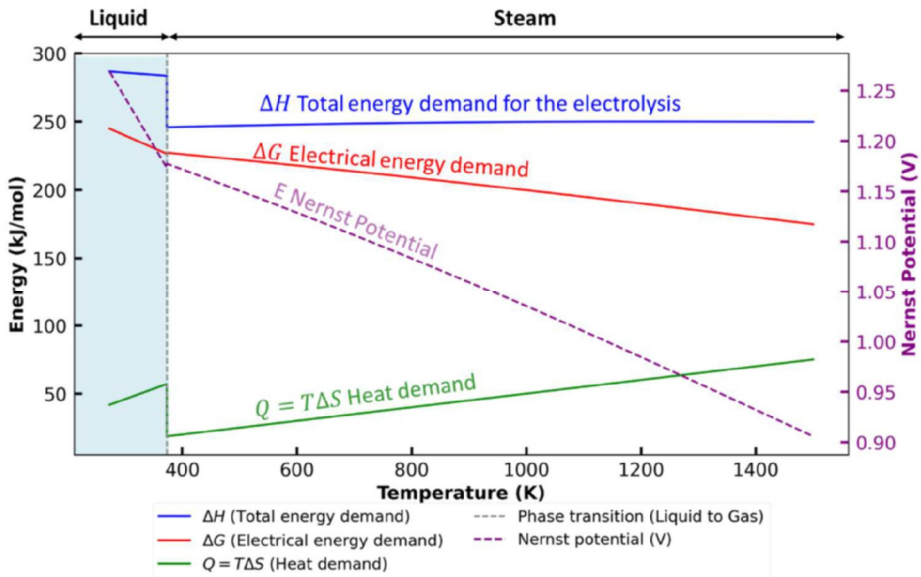


Figure 1-4: Energy demand for water and steam electrolysis $H_2O \rightarrow H_2 + \frac{1}{2}O_2$ with Thermodynamic properties derived using Kirchhoff's equations and data from [43]. Note: slight adjustments (<10%) to ΔS and ΔH were made to ensure continuity in the Nernst potential (A similar plot can be found in [44]).

Table 1-3: Examples of recent long-term durability tests at the stack level in SOEC systems

Author	Steam / CO ₂ electrolysis/ reversible	ESC / CSC ¹	Test Durations (h)	Number of cells and cell area	Fuel electrode gas composition	Operation		Degradation rates ²			
						Current density [A cm ⁻²]	RU	Temp. (°C)	(% U kh ⁻¹)	(K·kh ⁻¹)	(mΩ·cm ² ·kh ⁻¹)
Rinaldi et al. (2017)[34]	Steam	ESC	10700	6 NA cm ²	90% H ₂ O & 10% H ₂	0.6 - 0.5	51%	710-730	>0.5	NA	NA
Riegraph et al. (2024) [45]	Steam	SolidPOWER™ ESC Fraunhofer IKTS™	3400	10 127 cm ²	80% H ₂ O & 20% H ₂	0.6	75%	816	-0.33 improvement	NA	NA
Riegraph et al. (2024) [46]	Steam Reversible 137 cycles	ESC Fraunhofer IKTS™	3300	10 127 cm ²	80% H ₂ O & 20% H ₂ (SOEC) 80% H ₂ O & 20% H ₂ (SOFC)	0.6	75%	816	+0.58 (SOEC) -1.23 (SOFC)	NA	+10.8
Lang et al. (2020)[47]	Steam	ESC Sunfire™	3370	30 128 cm ²	80% H ₂ O, 9% H ₂ 11% H ₂	0.38-0.52	70%	820	0.5	3	+12
Lang et al. (2020)[47]	Steam Reversible 97 cycles	ESC Sunfire™	2500	30 128 cm ²	40% H ₂ , 60% N ₂ (SOFC); 80% H ₂ O 9% H ₂ , 11% N ₂ (SOEC)	0.180	70%	820 (SOEC) & 750 (SOFC)	+1.2 (SOEC) -3.1 (SOFC)	NA	+39
Aicart et al. (2024) [48]	Steam	ESC Sunfire™	9500	30 128 cm ²	90% H ₂ O & 10% H ₂	0.52	70%	780-850	NA	2.5	+12
Kamkeng et al. (2022) [35]	CO ₂ electrolysis	Lab stack Risø DTU	1000	2 80 cm ²	20% CO ₂ , 70% H ₂ O & 10% H ₂	1	NA	850	3.96	NA	NA
Agersted et al. (2017) [42]	CO ₂ electrolysis	Haldrup Topsoe™ ESC	6000	8 NA cm ²	45% CO ₂ , 45% H ₂ O & 10% H ₂	0.5	39% (H ₂ O and CO ₂)	750	1.4	NA	NA

¹ Electrolyte-Supported Cells (ESCs) use a thick electrolyte for mechanical support, are more robust and easier to manufacture but suffer from higher ohmic losses and lower performance. Cathode-Supported Cells (CSCs) rely on a porous cathode, enabling a thinner electrolyte which reduces resistance and enhances efficiency and power density.

² The rate of mΩ·cm²·kh⁻¹ reflects the increase in area-specific resistance (ASR) degradation over 1000 hours, indicating growing electrical resistance and reduced efficiency. The K·kh⁻¹ metric measures the rise in operating temperature needed to sustain performance, i.e. the degradation is compensated by gradually increasing stack temperature to sustain thermoneutral operation.

1.3.2. E-fuel production

Figure 1-5 outlines the key stages involved in e-fuel production, starting with renewable hydrogen generation via electrolysis. Regarding the synthesis steps, commercial-scale reactor technologies typically react CO₂ or CO with H₂ for carbon products and N₂ with H₂ for ammonia, but achieve low single-pass conversion despite operating under demanding conditions. Methanol synthesis uses typically copper catalysts at 200-300 °C and 50-100 bar, while ammonia synthesis typically relies on iron catalysts at 150-250 bar and 380-520 °C [49-51], with milder conditions achievable using ruthenium. Fischer-Tropsch (FT) synthesis occurs through two main processes: high-temperature FT (300-350 °C), using iron catalysts, which favors the production of shorter hydrocarbons like synthetic gasoline and low-molecular-weight olefins, and low-temperature FT (200-240 °C), utilizing iron or cobalt catalysts to produce longer hydrocarbon chains such as kerosene and diesel. FT typically operates at pressures ranging from 20 to 40 bar, with higher pressures favoring the production of longer hydrocarbons. However, direct CO₂ utilization, particularly in Fischer-Tropsch synthesis, remains challenging due to current catalyst limitations. Traditional systems are optimized for syngas feedstock (CO and H₂), not pure CO₂, which results in excessive water by-products that can inhibit reaction kinetics, accelerate catalyst deactivation and can lead to catalyst oxidation [52, 53]. A detailed discussion is unnecessary here, as these reactions will be thoroughly addressed in the next chapter's literature review.

A brief discussion on e-fuel production efficiencies and costs seems nonetheless required. Despite extensive literature on the topic, significant variability exists due to differing assumptions (e.g., CO₂ capture, electrolysis technology, subsidies), methodologies, system boundaries (e.g., inclusion of storage, transport, and infrastructure costs), and study types (e.g., broad-based studies vs. process systems engineering [PSE] analyses) [91–104]. **Figure 1-6** & **Figure 1-7** illustrate discrepancies in both absolute and relative values for production efficiencies and costs. In terms of cost rankings, broad-based studies generally identify e-diesel as the most expensive e-fuel, while the relative costs of e-methanol, e-ammonia, and e-methane depend on key assumptions—particularly CO₂ capture costs and whether transport and storage expenses are included. Dias et al. [71] indicate that if direct air capture (DAC) costs rise to 1000 €/ton CO₂ (compared to 30 €/ton CO₂ under their default scenario), hydrogen and ammonia become more cost-competitive than carbon-based e-fuels. The comparison between e-methanol and e-methane varies across studies. Under low CO₂ capture costs and when excluding storage and transport, e-methane is generally reported as less expensive than e-methanol [71, 99]. However, when factoring in storage and transport costs, Dias et al. [71] and Korberg et al. [91] find that e-methanol becomes more advantageous than e-methane. The relative ranking between these fuels also depends on CO₂ capture costs. Ueckert et al. [108] suggest that e-methane requires ~20% less CO₂ per unit of energy, making it slightly cheaper than e-methanol in high CO₂ cost scenarios (DAC), where its storage disadvantages are outweighed by reduced CO₂ requirements. Similarly, different cost rankings exist for e-methane and e-ammonia. For example, Bellotti et al. [99] consider ammonia more expensive than methane, while Horvath et al. [94] and Dias et al. [71] report similar costs under their default assumptions, and Korberg et al. [91] suggest the opposite. This study also indicates that, when infrastructure costs are considered, hydrogen becomes more expensive than e-methanol and e-ammonia due to higher costs associated

with fuel handling, storage, and bunkering in ports. It indicates that infrastructure costs are particularly significant for methane, accounting for 10–17% of the final fuel cost, while for liquid hydrogen (LH₂), these costs can reach up to 23%. Specialized PSE studies focusing on individual fuels, such as diesel [97, 100, 101], methanol [102-105], and ammonia [33, 96], also provide valuable insights but are difficult to compare due to differences in process designs and assumptions regarding CAPEX, OPEX, and infrastructure. Beyond cost factors, assessments must account for the technical maturity of production methods, as these significantly impact well-to-tank efficiency and total cost of ownership, key metrics for industries like shipping and genset markets aiming to decarbonize with these e-fuels. To enhance comparability across future studies, standardizing key variables, such as electricity prices, CAPEX/OPEX, and energy demands for electrolysis, direct air capture, and Fischer-Tropsch synthesis would be crucial. For context, **Figure 1-7** also presents the retail price range of fossil diesel from March 2021 to March 2024, as these data are more readily available than production costs. However, these figures should be interpreted with caution, as retail prices include taxes, distribution, marketing, and profit margins. In Europe, for example, taxes alone can account for 40–60% of the retail price, significantly inflating costs relative to production⁺. Finally, it is important to highlight that some of the lower cost estimates reported in the literature appear optimistic, as they incorporate anticipated reductions in electrolyzer costs and renewable electricity prices, making e-fuels potentially competitive with their fossil fuel counterparts. Ueckert et al. [108] project a lower bound of ~10 €/GJ for hydrogen and ~15 €/GJ for e-methanol under their 2050 scenario. Similarly, IEA (2024) [21] estimates that by 2030, e-methanol could cost ~35 €/GJ and e-ammonia ~30 €/GJ, making them comparable with the upper range of fossil diesel prices.

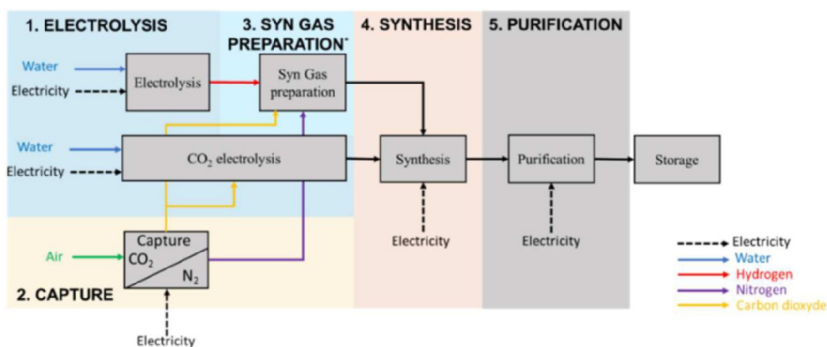


Figure 1-5: Master flow diagram of an e-fuel production plan featuring the main process steps.

⁺ The government taxes were consulted from this website: <https://www.fuel-prices.eu/government-fuel-taxes-diesel/> illustrating that taxes can constitute a substantial portion of diesel fuel prices in Europe, often ranging from 40% to 60% of the retail price, thereby significantly inflating the cost relative to production.

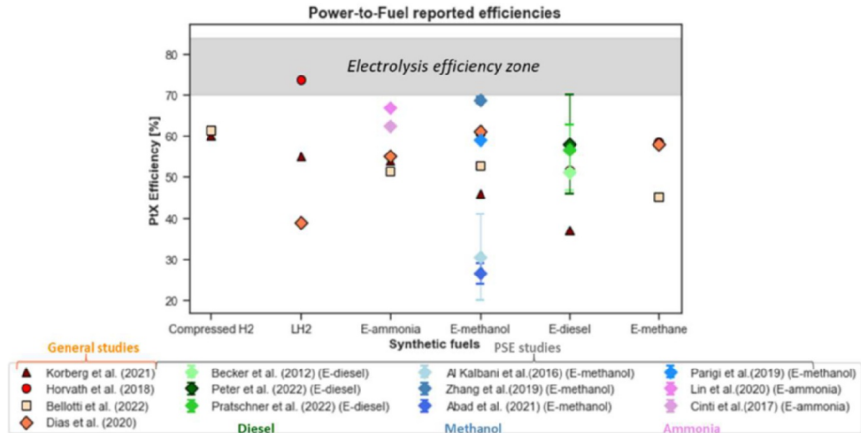


Figure 1-6: Literature analysis of PtX efficiencies from generalized studies and process system engineering studies. General studies using fuel price as an input [91, 99, 31, 94], and specific studies on diesel [100, 97, 101], methanol [102, 103, 104, 105], and ammonia [96, 33].

Note that Cinti et al. (2017), Zhang et al. (2019), and Peter et al. (2022) considered SOEC technologies in their analyses. The electrolysis efficiency zone (in grey) is depicted between approximately 70% (without steam) and 84% (with steam at 150 °C) calculated from SOEC specific consumptions given in **Table 1-2**.

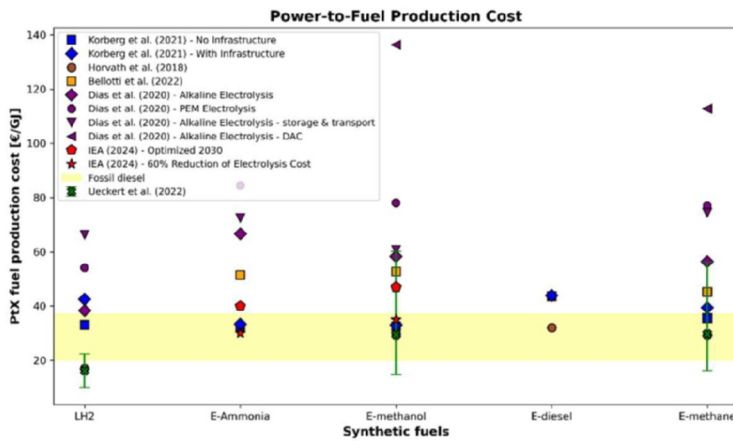


Figure 1-7: Levelized cost of PtX production comparing different fuel options from [91, 99, 31, 21, 94, 108], with diesel fuel retail prices shown for reference, showing its fluctuation range from March 2021 to March 2024*. Main assumptions: Dias et al. (2020) [71] (electrolysis: PEM 2100 €/kW & alkaline 1100 €/kW, electricity cost: 50 €/MWh, CO₂ capture: 30 €/ton or

* Diesel retails prices taken from:

https://www.eia.gov/dnav/pet/hist/LeafHandler.ashx?n=p&s=emd_epd2d_pte_nus_dpg&f=m

DAC: 1000 €/ton) - *Korberg et al. (2021) [91]* (electricity cost: 33 €/MWh, electrolysis: 600 €/kW, CO₂ capture: 400 €/ton) - *IEA (2024) [21]* (electrolysis: 800 €/kW, CO₂ capture: 30 €/ton) - *Ueckert et al. (2022) [108]* (H₂ cost: 80 €/MWh ~2.7 €/kg, CO₂ capture: 30 – 920 €/ton) - *Bellotti et al. (2022) [99]* (electricity cost: 50 €/MWh, electrolysis: 1000 €/kW, CO₂ capture: 15 €/ton)

1.3.3. H₂ recovery

For reconversion of these molecules to hydrogen, whether for use in PEM fuel cells, as a combustion booster, or to meet hydrogen demand (e.g. at ammonia terminals or refueling stations), an additional processing step is required. Similar to the synthesis process, traditional hydrogen recovery methods vary depending on the type of molecule. These techniques have evolved from methane steam reforming to methanol steam reforming- initially developed for high-energy-density military fuel cells [22] and more recently to ammonia cracking [54], as the use of these commodity chemicals as hydrogen carriers gains increasing recognition. Methane steam reforming operates at high temperatures (800 - 1000 °C) and typically utilizes nickel or more active alternatives like Ru, Rh, or Ir, followed by water-gas shift reactions and subsequent CO purification [55]. Methanol reforming occurs at lower temperatures (220 - 300 °C) with copper-based catalysts, often avoiding secondary shift reactions but still requiring CO purification [55]. The ammonia cracking process normally runs at temperatures exceeding 700 °C, to achieve complete conversion and frequently makes use of nickel as a catalyst. However, precious metal catalysts like rhodium, iridium, platinum, and especially ruthenium demonstrate better catalytic activity in this process [56-59]. For these different systems, purification step is commonly accomplished using Pressure Swing Adsorption (PSA), although cryogenic separation and ion-exchange zeolites are also viable alternatives [60]. However, the semi-continuous nature of traditional PSA and hence the need for multiple units reduces its overall economic efficiency. Therefore, a key opportunity for hydrogen recovery systems is to simplify balance-of-plant components, reducing costs [61] while also addressing space constraints in specific markets, such as cold ironing and onboard applications. Similarly, further discussion is unnecessary at this point, as these reactions will be thoroughly covered in the literature review in the next chapter, with the economic aspects explored in detail in **Chapter 3**.

1.3.4. Power-to-power efficiency

When e-molecules are used as fuel, it is important to acknowledge that power-to-power efficiency is low due to multiple conversion steps—electrolysis, fuel synthesis, storage, and reconversion to power. But efficiency isn't everything—for sectors where electrification isn't feasible, energy density and power density can matter just as much. A comparative analysis on different e-fuels for onboard applications in the thesis outlook (page 266) considering fuel use in PEM fuel cells (with reforming when needed) and internal combustion engines (ICEs), compared to battery-based direct electrification as the primary alternative. The results show that while e-diesel in ICEs has very low power-to-power efficiency (~0.14), its high energy density makes it one of the few viable options for long-haul applications. In contrast, batteries, despite their high efficiency (~0.81), have low energy density, limiting them to short, high-power applications (1–5 hours). Meanwhile, LH₂, ammonia, and liquefied methane, when used in PEM fuel cells with reforming,

provide a balance between efficiency and energy density, with efficiencies of ~ 0.27 for LH_2 and ~ 0.24 for ammonia, supporting operations up to 15 hours. Ultimately, e-fuels, as previously mentioned, are essential for decarbonizing hard-to-electrify sectors. The key challenge lies in improving the global efficiency to enhance competitiveness and facilitate their integration.

1.4. Membrane reactors

Advancing these processes, namely fuel synthesis and reverse hydrogen recovery, to operate under milder conditions aligns with the principles of Process Intensification (PI), a key strategy in modern chemical engineering aimed at enhancing efficiency, sustainability, and process compactness often through the integration of multiple unit operations or by employing novel reactor designs [109]. PI-driven approaches can extend equipment lifespan, reduce energy consumption, and enable scalable, flexible production systems. Membrane reactor (MR) technology exemplifies a PI-based solution by overcoming thermodynamic limitations of conventional processes through the integration of reaction and separation into a single unit. In a typical MR setup, reactants flow through a tubular vessel containing selective membranes within a catalyst-packed bed. These membranes selectively extract desired products (permeate) based on gradients in partial pressure, while retaining other components (retentate). This configuration generally allows MRs to surpass equilibrium constraints, achieving higher conversion rates at lower temperatures, reducing catalyst deactivation and side reactions, and significantly improving target-product yields-which may not be attained through catalyst development alone. Furthermore, highly selective membranes can minimize or even eliminate the need for downstream purification. As will be demonstrated in this thesis, membrane reactors (MRs) have been applied or are actively being explored in various processes, including hydrogen production and the synthesis of e-chemicals. A sketch of a packed bed membrane reactor is reported in **Figure 1-8**.

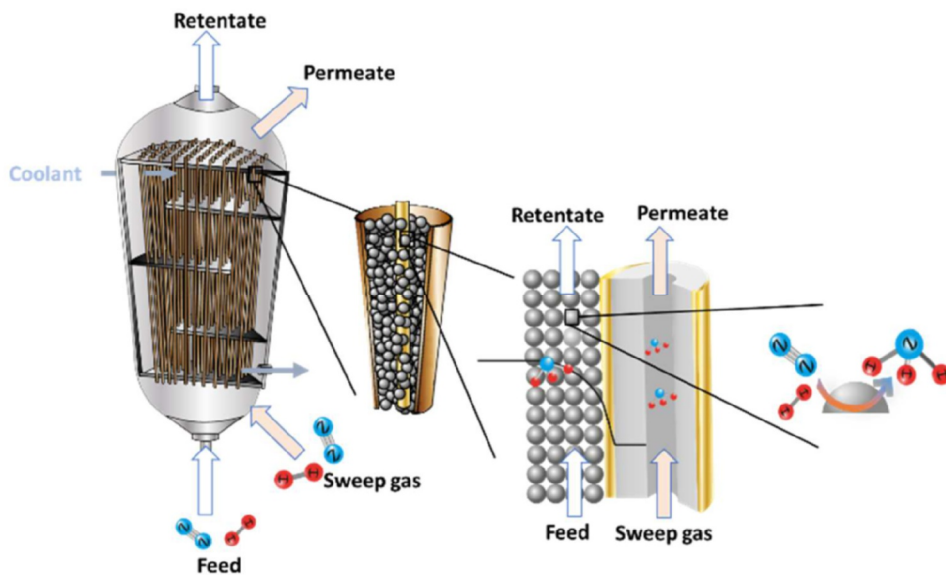


Figure 1-8: Schematic representation of multi-tubular packed bed membrane reactor. This type of reactor is often chosen for its ease of manufacturing, scalability from a single tube to multiple tubes and efficient heat exchange. Membrane reactor-concept represented for ammonia synthesis reaction [62]

1.5. Structured catalyst

The traditional packed bed configuration (as represented in **Figure 1-8**) while valued for its straightforward design and substantial catalyst loading capacity, faces several challenges, including flow channeling, inconsistent flow distribution, and limitations in mass and heat transfer. Moreover, these reactors often encounter significant pressure drops, which increase operational costs [63]. In the case of membrane reactors, the low thermal conductivity of packed catalyst beds can result in substantial temperature gradients, leading to degradation of both the catalyst and the membrane. Designing these reactors requires careful consideration of trade-offs: smaller catalyst pellets can improve catalyst utilization and heat transfer but also result in higher pressure drops. Balancing these factors adds complexity to achieving optimal designs. To address these challenges, alternative catalytic supports have been developed, offering greater design flexibility and enhanced control over fluid flow, species distribution, and heat transfer. For example, the nature-inspired honeycomb design presents advantages like a high surface-to-volume ratio, enabling efficient gas-to-solid mass and heat transfer rates, all while ensuring low pressure drops in a homogeneous structure [64-65]. Similarly, open-cell foams (OCF) [66] have been introduced, characterized by their tortuous solid matrix of interconnected open cells. The diverse solid ligaments within OCFs foster fluid mixing, leading to heightened fluid-solid transfer rates. Recently, there has been a surge in interest surrounding Periodic Open-Cell Structures (POCS) as a novel catalytic support [67].

These supports are defined by their structured network of consistently shaped, interconnected unit cells forming a three-dimensional framework. Combining the advantages of OCFs and honeycombs, POCS effectively manage both axial and radial heat transfer while maintaining a uniform structure with a reasonable pressure drop. Using additive manufacturing, also referred to as 3D printing, POCS could offer a new way to design catalytic supports tailored to specific needs [68-69]. A range of 3D printing methods have already been used to produce POCS with precision, including robocasting [70] selective electron beam melting (SEBM) [71], selective laser melting (SLM) [72-73], direct metal laser sintering (DMLS) and stereolithography [74]. The literature also presents a variety of unit cell types such as cubic [71,75,76], diamond [74-75, 77], octet [78] and triply periodic minimal surface (TPMS) [79-82]. Some examples of POCS printed by SLM for membrane reactor integration are reported in **Figure 1-9**. Advances in 3D printing have positioned POCS supports as a compelling alternative to traditional packed beds, offering significant advantages in heat and mass transfer, minimized temperature gradients, and hotspot prevention, all while maintaining low pressure drops. The design flexibility of 3D printing allows for localized optimization in critical areas of the reactor, such as the inlet or regions near the membrane. However, compared to packed beds, POCS have a reduced catalyst holdup due to their open structure, which can impact reaction rates that depend heavily on catalyst weight and the fluid-solid interfacial area (cf. **Figure 1-10**).



Figure 1-9: POCS Support for Ambher EU Project proof of concept, 3D-Printed by ENGIE Laborelec using Selective Laser Melting with Kelvin Cell design [83] (featuring gyroid and BCC lattices and holes for the membranes & thermocouple integration)

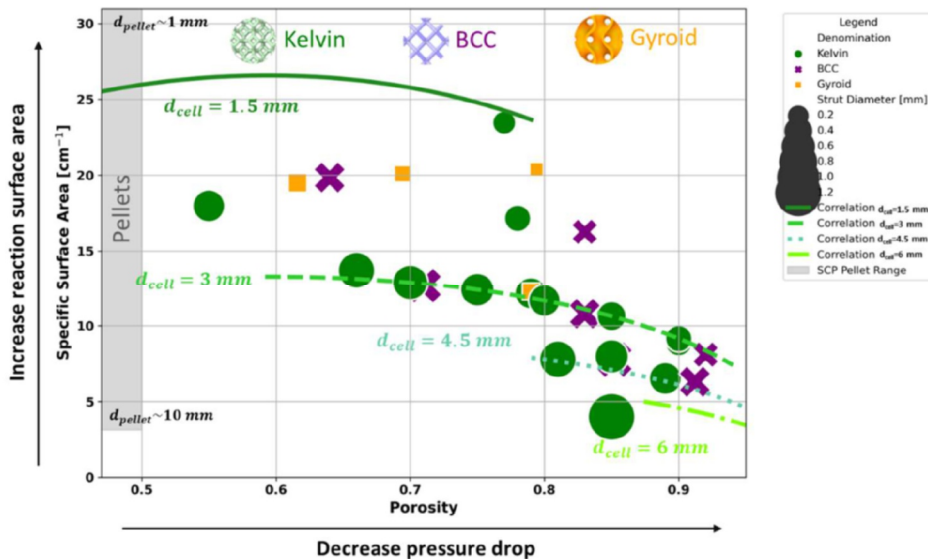


Figure 1-10: Specific surface area vs porosity of different POCS supports reported in the literature [84-85] together with the generalization of a correlation for the kelvin cell plotted for strut diameters from 0.3 to 0.9 mm and several cell diameters (d_{cell}) [86]. The pellet bed porosity and specific surface area were estimated assuming a simple cubic packing (SCP) i.e. void fraction of 0.48, pellet diameter $\in [1-10]$ mm

1.6. Modelling membrane reactors

Modeling membrane reactors (MRs) is indispensable for their developments, providing a comprehensive understanding of reactor behavior under various operating conditions. It supports key engineering tasks such as performance optimization, feedstock comparison, design modifications, and industrial scaling. Due to the multiscale nature of MR processes, modeling an entire reactor requires integrating phenomena at the microscale (e.g., membrane transport), mesoscale (e.g., external mass transfer limitations), and macroscale, including the surrounding process environment. (cf. **Figure 1-11**). At the microscale (\sim nm– μ m), pore-level processes such as Knudsen diffusion, surface reactions, and molecular interactions can dominate. These microscale phenomena are often parameterized into simplified expressions, which are validated experimentally and then incorporated into larger-scale models. For example, the intrinsic rates of reaction are often based on assumptions like the Langmuir-Hinshelwood or Eley-Rideal mechanisms.

The mesoscale (\sim 100 μ m–1 mm) focuses on localized transport phenomena within reactor internals. For mesoscale reactor modeling, the microscale simplified expressions are integrated with transport equations to account for non-idealities like concentration or temperature gradients or pressure drops. Computational Fluid Dynamics (CFD) tools play a critical role here [87-90], providing a robust framework for detailed reactor design and optimization. Moreover, CFD can generate empirical correlations, such as pressure drop or permeability, which simplify the modeling

of localized phenomena and can be incorporated into macroscale models. Compared to experimental methods that require specialized equipment for preparation and testing, numerical simulations are often faster and more cost-effective. These simulations also enable detailed analysis prior to reactor construction, allowing for the exploration of multiple configurations to identify the optimal design while providing understanding of how reactor geometry influences transport phenomena. At the macroscale (mm-dam), MR modeling focuses on system-wide behavior, integrating the reactor and its surrounding process environment, often referred to as the balance of plant (BOP). In this context, simplified models, such as 0D or 1D approaches, provide high-level insights into reactor performance while maintaining low computational demand. These models depend on inputs from smaller scales, such as concentration polarization losses or pressure drop correlations, to ensure accurate predictions.

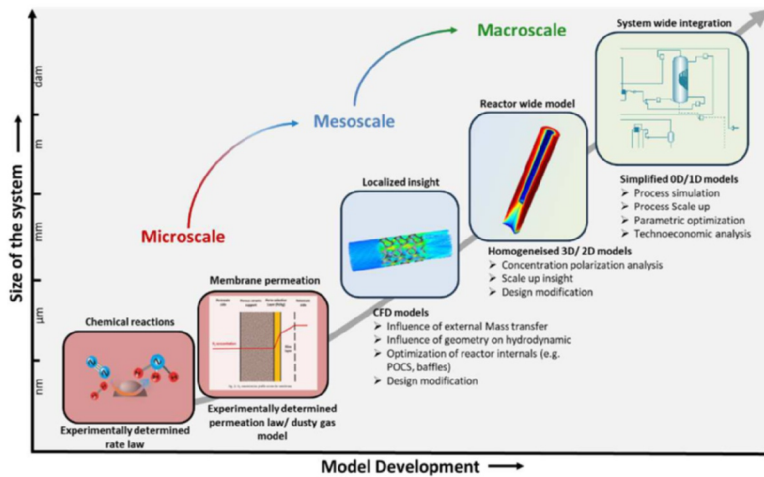


Figure 1-11: Multiscale modeling framework in (membrane) reactors. At the microscale, molecular simulation (e.g., Monte Carlo and molecular dynamics) can also provide atomistic insights, accelerate the design of new catalysts/membrane through computational screening.

1.7. Objectives and scope

This thesis investigates the application of membrane reactors in Power-to-X processes from two main perspectives: First, it explores the potential integration of 3D-printed catalyst structures with selective membranes as a means to enhance reactor performance. This approach is explored through experimental studies, supported by computational fluid dynamics modeling, to assess the impact of POCS design parameters and operational conditions on mass transfer and thermohydraulic behavior. Second, it evaluates the deployment of membrane reactors at the macroscale level in Power-to-X environments (e.g. choice of e-molecules or choice of process configurations). To achieve this, simplified 0D/1D phenomenological models are developed for key unit operations, such as membrane reactors, electrolysis, and fuel cells, and are implemented within

a process systems engineering (PSE) simulation tool. The thesis manuscript is structured according to the following plan:

Chapter 2 aims to provide a more thorough analysis of recent advancements in MR design and applications relevant to Power-to-X systems, focusing on the past decade. The goal is here to embrace a larger scope and concisely summarize the progress in membrane reactor and will allow the reader to gain a deep understanding of membrane reactor and help identify research gap. It provides a background on the topic and examines how membrane reactors have evolved in design and application to address key reaction engineering challenges.

Chapter 3 & 4 investigate the use of MRs in power generation applications. Chapter 3 examines their integration with proton exchange membrane (PEM) fuel cells, assessing the impact of fuel choice, methanol, ammonia, or methane, on the performance of the fuel processor and genset. Chapter 4 explores the advantages and challenges of using MRs compared to conventional Fired Tubular Reactors (FTRs) for ammonia cracking in large Combined Cycle Gas Turbine (CCGT) plants, emphasizing their potential to improve efficiency and overall performance.

Chapter 5, 6 & 7 investigate the potential of 3D-printed Periodic Open Cell Structures (POCS) to enhance the performance of membrane reactors. First, Chapter 5 investigates how the cell type- Kelvin, Body Centered Cubic (BCC), and gyroid lattice- impact the thermohydraulic behaviour of a POCS reactor. Then Chapter 6 examines how external mass transfer rates in POCS reactors affect ammonia synthesis, both independently and with selective membranes. Finally Chapter 7 extends this to ammonia cracking, emphasizing the role of POCS baffles in improving hydrogen permeation through palladium-based membranes.

Chapter 8 evaluates the cost and efficiency of power-to-ammonia process, highlighting the advantages of innovative pathways, including MRs and solid oxide electrolysis cell (SOEC) integrations.

Finally, the findings are summarized and an outlook is given.

1.8. References

- [1] IEA, World Energy Outlook 2023, (2024).
- [2] IEA, Renewables 2023 Analysis and forecast to 2028, (2024).
- [3] U. Remme, Global Hydrogen Review 2024, (2024).
- [4] G. Glenk, S. Reichelstein, Economics of converting renewable power-to-hydrogen, *Nat Energy* 4 (2019) 216–222. <https://doi.org/10.1038/s41560-019-0326-1>.
- [5] D. Tonelli, L. Rosa, P. Gabrielli, K. Caldeira, A. Parente, F. Contino, Global land and water limits to electrolytic hydrogen production using wind and solar resources, *Nat Commun* 14 (2023) 5532. <https://doi.org/10.1038/s41467-023-41107-x>.
- [6] Z. Wang, Y. Wang, S. Afshan, J. Hjalmarsson, A review of metallic tanks for H₂ storage with a view to application in future green shipping, *International Journal of Hydrogen Energy* 46 (2021) 6151–6179. <https://doi.org/10.1016/j.ijhydene.2020.11.168>.
- [7] H. Nazir, N. Muthuswamy, C. Louis, S. Jose, J. Prakash, M.E. Buan, C. Flox, S. Chavan, X. Shi, P. Kauranen, T. Kallio, G. Maia, K. Tammeveski, N. Lymperopoulos, E. Carcadea, E. Veziroglu, A. Iranzo, A.M. Kannan, Is the H₂ economy realizable in the foreseeable future?

- Part II: H₂ storage, transportation, and distribution, *International Journal of Hydrogen Energy* 45 (2020) 20693–20708. <https://doi.org/10.1016/j.ijhydene.2020.05.241>.
- [8] A. Hammad, I. Dincer, Analysis and assessment of an advanced hydrogen liquefaction system, *International Journal of Hydrogen Energy* 43 (2018) 1139–1151. <https://doi.org/10.1016/j.ijhydene.2017.10.158>.
 - [9] A.C. Riekstin, S. James, A. Kansal, No More Electrical Infrastructure: Towards Fuel Cell Powered Data Centers, (n.d.).
 - [10] W.J. Sembler, S. Kumar, D. Palmer, Fuel Cells as an Alternative to Cold Ironing, *Journal of Fuel Cell Science and Technology* 6 (2009) 031009. <https://doi.org/10.1115/1.3006305>.
 - [11] J.L. Viviente, J. Meléndez, D.A. Pacheco Tanaka, F. Gallucci, V. Spallina, G. Manzolini, S. Foresti, V. Palma, C. Ruocco, L. Roses, Advanced m-CHP fuel cell system based on a novel bio-ethanol fluidized bed membrane reformer, *International Journal of Hydrogen Energy* 42 (2017) 13970–13987. <https://doi.org/10.1016/j.ijhydene.2017.03.162>.
 - [12] I. Petreanu, M. Dragan, S. Laurentiu Badea, Fuel Cells: Alternative Energy Sources for Stationary, Mobile and Automotive Applications, in: P. Vizureanu (Ed.), *Thermodynamics and Energy Engineering*, IntechOpen, 2020. <https://doi.org/10.5772/intechopen.93032>.
 - [13] Methanex, Methanol as a Marine Fuel, (n.d.). <https://www.methanex.com/about-methanol/marine-fuel/>.
 - [14] M. Perčić, N. Vladimir, A. Fan, Techno-economic assessment of alternative marine fuels for inland shipping in Croatia, *Renewable and Sustainable Energy Reviews* 148 (2021) 111363. <https://doi.org/10.1016/j.rser.2021.111363>.
 - [15] M. Sofiev, J.J. Winebrake, L. Johansson, E.W. Carr, M. Prank, J. Soares, J. Vira, R. Kouznetsov, J.-P. Jalkanen, J.J. Corbett, Cleaner fuels for ships provide public health benefits with climate tradeoffs, *Nat Commun* 9 (2018) 406. <https://doi.org/10.1038/s41467-017-02774-9>.
 - [16] IRENA, *Innovation Outlook: Renewable Ammonia*, (2022).
 - [17] L. Wang, M. Xia, H. Wang, K. Huang, C. Qian, C.T. Maravelias, G.A. Ozin, Greening Ammonia toward the Solar Ammonia Refinery, *Joule* 2 (2018) 1055–1074. <https://doi.org/10.1016/j.joule.2018.04.017>.
 - [18] H. Ritchie, How many people does synthetic fertilizer feed?, (2017). <https://ourworldindata.org/how-many-people-does-synthetic-fertilizer-feed> (accessed June 25, 2023).
 - [19] International Energy Agency, Ammonia Technology Roadmap: Towards more sustainable nitrogen fertiliser production, OECD, 2021. <https://doi.org/10.1787/f6daa4a0-en>.
 - [20] IEA, The role of CCUS in low-carbon power systems, (2020).
 - [21] IEA, The Role of E-fuels in Decarbonising Transport, (2024).
 - [22] R. Palo, J.D. Holladay, R.T. Rozmiarek, Development of a soldier-portable fuel cell power system Part I: A bread-board methanol fuel processor, *Fuel and Energy Abstracts* 44 (2003) 225. [https://doi.org/10.1016/S0140-6701\(03\)82901-6](https://doi.org/10.1016/S0140-6701(03)82901-6).
 - [23] C. Quintero-Masselski, J.-F. Portha, L. Falk, Conception and optimization of an ammonia synthesis superstructure for energy storage, *Chemical Engineering Research and Design* 177 (2022) 826–842. <https://doi.org/10.1016/j.cherd.2021.11.039>.
 - [24] A. Valera-Medina, F. Amer-Hatem, A.K. Azad, I.C. Dedoussi, M. de Joannon, R.X. Fernandes, P. Glarborg, H. Hashemi, X. He, S. Mashruk, J. McGowan, C. Mounaim-Rouselle, A. Ortiz-Prado, A. Ortiz-Valera, I. Rossetti, B. Shu, M. Yehia, H. Xiao, M. Costa, Review on Ammonia as a Potential Fuel: From Synthesis to Economics, *Energy Fuels* 35 (2021) 6964–7029. <https://doi.org/10.1021/acs.energyfuels.0c03685>.
 - [25] J. Eppinger, K.-W. Huang, Formic Acid as a Hydrogen Energy Carrier, *ACS Energy Lett.* 2 (2017) 188–195. <https://doi.org/10.1021/acsenergylett.6b00574>.
 - [26] L. Hu, J. Niu, W. Wu, Z. Zhao, M. Du, L. Chen, Q. Zheng, H. Cao, Quantitative analysis of toxicity risks in the operation of ammonia-fueled tugboats, *Ocean Engineering* 310 (2024) 118759. <https://doi.org/10.1016/j.oceaneng.2024.118759>.

- [27] B. Stolz, M. Held, G. Georges, K. Boulouchos, Techno-economic analysis of renewable fuels for ships carrying bulk cargo in Europe, *Nat Energy* 7 (2022) 203–212. <https://doi.org/10.1038/s41560-021-00957-9>.
- [28] L. van Biert, M. Godjevac, K. Visser, P.V. Aravind, A review of fuel cell systems for maritime applications, *Journal of Power Sources* 327 (2016) 345–364. <https://doi.org/10.1016/j.jpowsour.2016.07.007>.
- [29] A. Valera-Medina, H. Xiao, M. Owen-Jones, W.I.F. David, P.J. Bowen, Ammonia for power, *Progress in Energy and Combustion Science* 69 (2018) 63–102. <https://doi.org/10.1016/j.pecs.2018.07.001>.
- [30] Y. Zhao, B.P. Setzler, J. Wang, J. Nash, T. Wang, B. Xu, Y. Yan, An Efficient Direct Ammonia Fuel Cell for Affordable Carbon-Neutral Transportation, *Joule* 3 (2019) 2472–2484. <https://doi.org/10.1016/j.joule.2019.07.005>.
- [31] V. Dias, M. Pochet, F. Contino, H. Jeanmart, Energy and Economic Costs of Chemical Storage, *Front. Mech. Eng.* 6 (2020) 21. <https://doi.org/10.3389/fmech.2020.00021>.
- [32] O. Schmidt, A. Gambhir, I. Staffell, A. Hawkes, J. Nelson, S. Few, Future cost and performance of water electrolysis: An expert elicitation study, *International Journal of Hydrogen Energy* 42 (2017) 30470–30492. <https://doi.org/10.1016/j.ijhydene.2017.10.045>.
- [33] G. Cinti, D. Frattini, E. Jannelli, U. Desideri, G. Bidini, Coupling Solid Oxide Electrolyser (SOE) and ammonia production plant, *Applied Energy* 192 (2017) 466–476. <https://doi.org/10.1016/j.apenergy.2016.09.026>.
- [34] G. Rinaldi, S. Diethelm, E. Oveisi, P. Burdet, J. Van herle, D. Montinaro, Q. Fu, A. Brisse, Post-test Analysis on a Solid Oxide Cell stack Operated for 10,700 Hours in Steam Electrolysis Mode, *Fuel Cells* (2017) 541–549.
- [35] A.D.N. Kamkeng, M. Wang, Long-term performance prediction of solid oxide electrolysis cell (SOEC) for CO₂/H₂O co-electrolysis considering structural degradation through modelling and simulation, *Chemical Engineering Journal* 429 (2022) 132158. <https://doi.org/10.1016/j.cej.2021.132158>.
- [36] CHJU, Clean Hydrogen Joint Undertaking, Multi - Annual Work Plan 2021-2027, (2021).
- [37] K.H.R. Rouwenhorst, A.G.J. Van Der Ham, G. Mul, S.R.A. Kersten, Islanded ammonia power systems: Technology review & conceptual process design, *Renewable and Sustainable Energy Reviews* 114 (2019) 109339. <https://doi.org/10.1016/j.rser.2019.109339>.
- [38] F. Gambou, D. Guilbert, M. Zasadzinski, H. Rafaralaly, A Comprehensive Survey of Alkaline Electrolyzer Modeling: Electrical Domain and Specific Electrolyte Conductivity, *Energies* 15 (2022) 3452. <https://doi.org/10.3390/en15093452>.
- [39] S. Shiva Kumar, H. Lim, An overview of water electrolysis technologies for green hydrogen production, *Energy Reports* 8 (2022) 13793–13813. <https://doi.org/10.1016/j.egyr.2022.10.127>.
- [40] O. Schmidt, A. Gambhir, I. Staffell, A. Hawkes, J. Nelson, S. Few, Future cost and performance of water electrolysis: An expert elicitation study, *International Journal of Hydrogen Energy* 42 (2017) 30470–30492. <https://doi.org/10.1016/j.ijhydene.2017.10.045>.
- [41] M. Chatenet, B.G. Pollet, D.R. Dekel, F. Dionigi, J. Deseure, P. Millet, R.D. Braatz, M.Z. Bazant, M. Eikerling, I. Staffell, P. Balcombe, Y. Shao-Horn, H. Schäfer, Water electrolysis: from textbook knowledge to the latest scientific strategies and industrial developments, *Chem. Soc. Rev.* 51 (2022) 4583–4762. <https://doi.org/10.1039/D0CS01079K>.
- [42] K. Agersted, M. Chen, P. Blennow, R. Küngas, V. Hendriksen, Long-term operation of a solid oxide cell stack for co- electrolysis of steam and CO₂, (n.d.).
- [43] Y.A. çengel, M.A. Boles, *Thermodynamics: An engineering approach*, 8th ed., McGraw-Hill, n.d.
- [44] L. Mingyi, Y. Bo, X. Jingming, C. Jing, Thermodynamic analysis of the efficiency of high-temperature steam electrolysis system for hydrogen production, *Journal of Power Sources* 177 (2008) 493–499. <https://doi.org/10.1016/j.jpowsour.2007.11.019>.
- [45] M. Riegraf, P. Szabo, M. Lang, R. Costa, S. Rothe, S. Megel, M. Kusnezoff, Electrochemical Analysis of an Electrolyte-Supported Solid Oxide Cell-Based MK35x Stack during Long-

- Term Electrolysis Operation, *J. Electrochem. Soc.* 171 (2024) 054504. <https://doi.org/10.1149/1945-7111/ad417f>.
- [46] M. Riegraf, P. Szabo, M. Lang, R. Costa, S. Rothe, S. Megel, M. Kusnezoff, Reversible Long-Term Operation of a MK35x Electrolyte-Supported Solid Oxide Cell-Based Stack, *J. Electrochem. Soc.* 171 (2024) 104505. <https://doi.org/10.1149/1945-7111/ad8036>.
- [47] M. Lang, S. Raab, M.S. Lemcke, C. Bohn, M. Physik, Long-term behavior of a solid oxide electrolyzer (SOEC) Stack, *Fuel Cells* (2020) 690–700.
- [48] J. Aicart, L. Tallobre, A. Surrey, B. Gervasoni, C. Geipel, H. Fontaine, S. Desousanobre, J. Mougin, Lifespan evaluation of two 30-cell electrolyte-supported stacks for hydrogen production by high temperature electrolysis, *International Journal of Hydrogen Energy* 60 (2024) 531–539. <https://doi.org/10.1016/j.ijhydene.2024.02.239>.
- [49] K.H.R. Rouwenhorst, A.G.J. Van Der Ham, G. Mul, S.R.A. Kersten, Islanded ammonia power systems: Technology review & conceptual process design, *Renewable and Sustainable Energy Reviews* 114 (2019) 109339. <https://doi.org/10.1016/j.rser.2019.109339>.
- [50] H. Liu, Ammonia synthesis catalyst 100 years: Practice, enlightenment and challenge, *Chinese Journal of Catalysis* 35 (2014) 1619–1640. [https://doi.org/10.1016/S1872-2067\(14\)60118-2](https://doi.org/10.1016/S1872-2067(14)60118-2).
- [51] M. Aziz, A.T. Wijayanta, A.B.D. Nandiyanto, Ammonia as Effective Hydrogen Storage: A Review on Production, Storage and Utilization, *Energies* 13 (2020) 3062. <https://doi.org/10.3390/en13123062>.
- [52] T. Chompupun, S. Limtrakul, T. Vatanatham, C. Kanhari, P.A. Ramachandran, Experiments, modeling and scaling-up of membrane reactors for hydrogen production via steam methane reforming, *Chemical Engineering and Processing - Process Intensification* 134 (2018) 124–140. <https://doi.org/10.1016/j.cep.2018.10.007>.
- [53] R.L. Espinoza, E. Du Toit, J. Santamaria, M. Menendez, J. Coronas, S. Irusta, Use of membranes in fischer-tropsch reactors, in: *Studies in Surface Science and Catalysis*, Elsevier, 2000: pp. 389–394. [https://doi.org/10.1016/S0167-2991\(00\)80988-X](https://doi.org/10.1016/S0167-2991(00)80988-X).
- [54] V. Cechetto, L. Di Felice, J.A. Medrano, C. Makhloufi, J. Zuniga, F. Gallucci, H₂ production via ammonia decomposition in a catalytic membrane reactor, *Fuel Processing Technology* 216 (2021) 106772. <https://doi.org/10.1016/j.fuproc.2021.106772>.
- [55] N. de Nooijer, F. Gallucci, E. Pellizzari, J. Melendez, D.A. Pacheco Tanaka, G. Manzolini, M. van Sint Annaland, On concentration polarisation in a fluidized bed membrane reactor for biogas steam reforming: Modelling and experimental validation, *Chemical Engineering Journal* 348 (2018) 232–243. <https://doi.org/10.1016/j.cej.2018.04.205>.
- [56] K.E. Lamb, M.D. Dolan, D.F. Kennedy, Ammonia for hydrogen storage; A review of catalytic ammonia decomposition and hydrogen separation and purification, *International Journal of Hydrogen Energy* 44 (2019) 3580–3593. <https://doi.org/10.1016/j.ijhydene.2018.12.024>.
- [57] I. Lucentini, X. Garcia, X. Vendrell, J. Llorca, Review of the Decomposition of Ammonia to Generate Hydrogen, *Ind. Eng. Chem. Res.* 60 (2021) 18560–18611. <https://doi.org/10.1021/acs.iecr.1c00843>.
- [58] M. Asif, S. Sidra Bibi, S. Ahmed, M. Irshad, M. Shakir Hussain, H. Zeb, M. Kashif Khan, J. Kim, Recent advances in green hydrogen production, storage and commercial-scale use via catalytic ammonia cracking, *Chemical Engineering Journal* 473 (2023) 145381. <https://doi.org/10.1016/j.cej.2023.145381>.
- [59] C. Chen, K. Wu, H. Ren, C. Zhou, Y. Luo, L. Lin, C. Au, L. Jiang, Ru-Based Catalysts for Ammonia Decomposition: A Mini-Review, *Energy Fuels* 35 (2021) 11693–11706. <https://doi.org/10.1021/acs.energyfuels.1c01261>.
- [60] V. Cechetto, L. Di Felice, F. Gallucci, Advances and Perspectives of H₂ Production from NH₃ Decomposition in Membrane Reactors, *Energy Fuels* 37 (2023) 10775–10798. <https://doi.org/10.1021/acs.energyfuels.3c00760>.
- [61] G. Di Marcoberardino, S. Foresti, M. Binotti, G. Manzolini, Potentiality of a biogas membrane reformer for decentralized hydrogen production, *Chemical Engineering and*

- Processing - Process Intensification 129 (2018) 131–141. <https://doi.org/10.1016/j.cep.2018.04.023>.
- [62] S. Richard, V. Verde, N. Kezibri, C. Makhloufi, A. Saker, I. Gargiulo, F. Gallucci, Power-to-ammonia synthesis process with membrane reactors: Techno-economic study, *International Journal of Hydrogen Energy* 73 (2024) 462–474. <https://doi.org/10.1016/j.ijhydene.2024.06.041>.
- [63] F. Kapteijn, J.A. Moulijn, Structured catalysts and reactors – Perspectives for demanding applications, *Catalysis Today* 383 (2022) 5–14. <https://doi.org/10.1016/j.cattod.2020.09.026>.
- [64] H.J. Venvik, J. Yang, Catalysis in microstructured reactors: Short review on small-scale syngas production and further conversion into methanol, DME and Fischer-Tropsch products, *Catalysis Today* 285 (2017) 135–146. <https://doi.org/10.1016/j.cattod.2017.02.014>.
- [65] L.C. Almeida, O. Sanz, D. Merino, G. Arzamendi, L.M. Gandía, M. Montes, Kinetic analysis and microstructured reactors modeling for the Fischer–Tropsch synthesis over a Co–Re/Al₂O₃ catalyst, *Catalysis Today* 215 (2013) 103–111. <https://doi.org/10.1016/j.cattod.2013.04.021>.
- [66] M. Bracconi, M. Ambrosetti, O. Okafor, V. Sans, X. Zhang, X. Ou, C.P. Da Fonte, X. Fan, M. Maestri, G. Groppi, E. Tronconi, Investigation of pressure drop in 3D replicated open-cell foams: Coupling CFD with experimental data on additively manufactured foams, *Chemical Engineering Journal* 377 (2019) 120123. <https://doi.org/10.1016/j.cej.2018.10.060>.
- [67] M. Iwaniszyn, Periodic Open Cellular Structures (POCS) as Catalyst Supports—A Review, *Energies* 15 (2022) 7703. <https://doi.org/10.3390/en15207703>.
- [68] C. Parra-Cabrera, C. Achille, S. Kuhn, R. Ameloot, 3D printing in chemical engineering and catalytic technology: structured catalysts, mixers and reactors, *Chem. Soc. Rev.* 47 (2018) 209–230. <https://doi.org/10.1039/C7CS00631D>.
- [69] Y. Zhang, Additive Manufacturing of Metallic Materials: A Review, *Journal of Materials Engineering and Performance* (n.d.) 13.
- [70] S. Danaci, Optimisation et integration de catalyseurs structurés pour la conversion de CO₂ en methane, Université Grenoble Alpes, 2017.
- [71] M. Klumpp, A. Inayat, J. Schwerdtfeger, C. Körner, R.F. Singer, H. Freund, W. Schwieger, Periodic open cellular structures with ideal cubic cell geometry: Effect of porosity and cell orientation on pressure drop behavior, *Chemical Engineering Journal* 242 (2014) 364–378. <https://doi.org/10.1016/j.cej.2013.12.060>.
- [72] Z. Li, Y. Nie, B. Liu, Z. Kuai, M. Zhao, F. Liu, Mechanical properties of AlSi10Mg lattice structures fabricated by selective laser melting, *Materials & Design* 192 (2020) 108709. <https://doi.org/10.1016/j.matdes.2020.108709>.
- [73] C. Yan, L. Hao, A. Hussein, D. Raymont, Evaluations of cellular lattice structures manufactured using selective laser melting, *International Journal of Machine Tools and Manufacture* 62 (2012) 32–38. <https://doi.org/10.1016/j.ijmachtools.2012.06.002>.
- [74] R. Balzarotti, A. Bisaccia, M.C. Tripi, M. Ambrosetti, G. Groppi, E. Tronconi, Production and characterization of copper periodic open cellular structures made by 3D printing-replica technique, *Journal of Advanced Manufacturing and Processing*, 2 (2020). <https://doi.org/10.1002/amp2.10068>.
- [75] Horneber, T, Thermo-fluid dynamic characterization and technical optimization of structured open-cell metal foam by means of numerical simulation, Friedrich Alexander Universität Erlangen Nürnberg, 2015.
- [76] S. Meinicke, K. Dubil, T. Wetzel, B. Dietrich, Characterization of heat transfer in consolidated, highly porous media using a hybrid-scale CFD approach, *International Journal of Heat and Mass Transfer* 149 (2020) 119201. <https://doi.org/10.1016/j.ijheatmasstransfer.2019.119201>.
- [77] M. Lämmermann, G. Horak, W. Schwieger, H. Freund, Periodic open cellular structures (POCS) for intensification of multiphase reactors: Liquid holdup and two-phase pressure drop, *Chemical Engineering and Processing - Process Intensification* 126 (2018) 178–189. <https://doi.org/10.1016/j.cep.2018.02.027>.

- [78] A. Chaudhari, P. Ekade, S. Krishnan, Experimental investigation of heat transfer and fluid flow in octet-truss lattice geometry, *International Journal of Thermal Sciences* 143 (2019) 64–75. <https://doi.org/10.1016/j.ijthermalsci.2019.05.003>.
- [79] F.M. Baena-Moreno, M. González-Castaño, J.C. Navarro de Miguel, K.U.M. Miah, R. Ossenbrink, J.A. Odriozola, H. Arellano-García, Stepping toward Efficient Microreactors for CO₂ Methanation: 3D-Printed Gyroid Geometry, *ACS Sustainable Chem. Eng.* 9 (2021) 8198–8206. <https://doi.org/10.1021/acssuschemeng.1c01980>.
- [80] Z. Cheng, R. Xu, P.-X. Jiang, Morphology, flow and heat transfer in triply periodic minimal surface based porous structures, *International Journal of Heat and Mass Transfer* 170 (2021) 120902. <https://doi.org/10.1016/j.ijheatmasstransfer.2021.120902>.
- [81] Z. Ahmed Qureshi, S. Addin Burhan Al-Omari, E. Elnajjar, O. Al-Ketan, R. Abu Al-Rub, Architected lattices embedded with phase change materials for thermal management of high-power electronics: A numerical study, *Applied Thermal Engineering* 219 (2023) 119420. <https://doi.org/10.1016/j.applthermaleng.2022.119420>.
- [82] Z.A. Qureshi, S. Addin Burhan Al-Omari, E. Elnajjar, O. Al-Ketan, R.A. Al-Rub, On the effect of porosity and functional grading of 3D printable triply periodic minimal surface (TPMS) based architected lattices embedded with a phase change material, *International Journal of Heat and Mass Transfer* 183 (2022) 122111. <https://doi.org/10.1016/j.ijheatmasstransfer.2021.122111>.
- [83] AMBHER, (n.d.). <https://www.ambherproject.eu/> (accessed September 1, 2024).
- [84] C. Ferroni, F.S. Franchi, M. Ambrosetti, M. Bracconi, M. Maestri, E. Tronconi, Numerical and experimental investigation of pressure drop in Periodic Open Cellular Structures for intensification of catalytic processes, (n.d.) 23.
- [85] S. Richard, D. Tasso, M. Rajana, A. Saker, A. Ramirez Santos, C. Makhloufi, N. Meynet, B. Hary, S. Nardone, G. Marino, M. Thomas, C. Italiano, A. Vita, F. Gallucci, Comparison of thermo-hydraulic performance among different 3D printed periodic open cellular structures, *Chemical Engineering Journal* 492 (2024) 152005. <https://doi.org/10.1016/j.cej.2024.152005>.
- [86] C. Ferroni, M. Bracconi, M. Ambrosetti, M. Maestri, G. Groppi, E. Tronconi, A fundamental investigation of gas/solid heat and mass transfer in structured catalysts based on Periodic Open Cellular Structures (POCS), (n.d.) 20.
- [87] R.J.W. Voncken, I. Roghair, M. van Sint Annaland, A numerical study on concentration polarization in 3D cylindrical fluidized beds with vertically immersed membranes, *Chemical Engineering Science* 205 (2019) 299–318. <https://doi.org/10.1016/j.ces.2019.05.010>.
- [88] R. Ma, B. Castro-Dominguez, A.G. Dixon, Y.H. Ma, Scalability of multitube membrane modules for hydrogen separation: Technical considerations, issues and solutions, *Journal of Membrane Science* 564 (2018) 887–896. <https://doi.org/10.1016/j.memsci.2018.08.003>.
- [89] H. Choi, S.H. Kim, J. Bae, S.P.R. Katikaneni, A. Jamal, A. Harale, S.N. Paglieri, J.H. Lee, CFD analysis and scale up of a baffled membrane reactor for hydrogen production by steam methane reforming, *Computers & Chemical Engineering* 165 (2022) 107912. <https://doi.org/10.1016/j.compchemeng.2022.107912>.
- [90] A. Caravella, L. Melone, Y. Sun, A. Brunetti, E. Drioli, G. Barbieri, Concentration polarization distribution along Pd-based membrane reactors: A modelling approach applied to Water-Gas Shift, *International Journal of Hydrogen Energy* 41 (2016) 2660–2670. <https://doi.org/10.1016/j.ijhydene.2015.12.141>.
- [91] A.D. Korberg, S. Brynolf, M. Grahn, I.R. Skov, Techno-economic assessment of advanced fuels and propulsion systems in future fossil-free ships, *Renewable and Sustainable Energy Reviews* 142 (2021) 110861. <https://doi.org/10.1016/j.rser.2021.110861>.
- [92] A. Sánchez, E.C. Blanco, M. Martín, Comparative assessment of methanol and ammonia: Green fuels vs. hydrogen carriers in fuel cell power generation, *Applied Energy* 374 (2024) 124009. <https://doi.org/10.1016/j.apenergy.2024.124009>.
- [93] L. Kistner, A. Bensmann, C. Minke, R. Hanke-Rauschenbach, Comprehensive techno-economic assessment of power technologies and synthetic fuels under discussion for ship

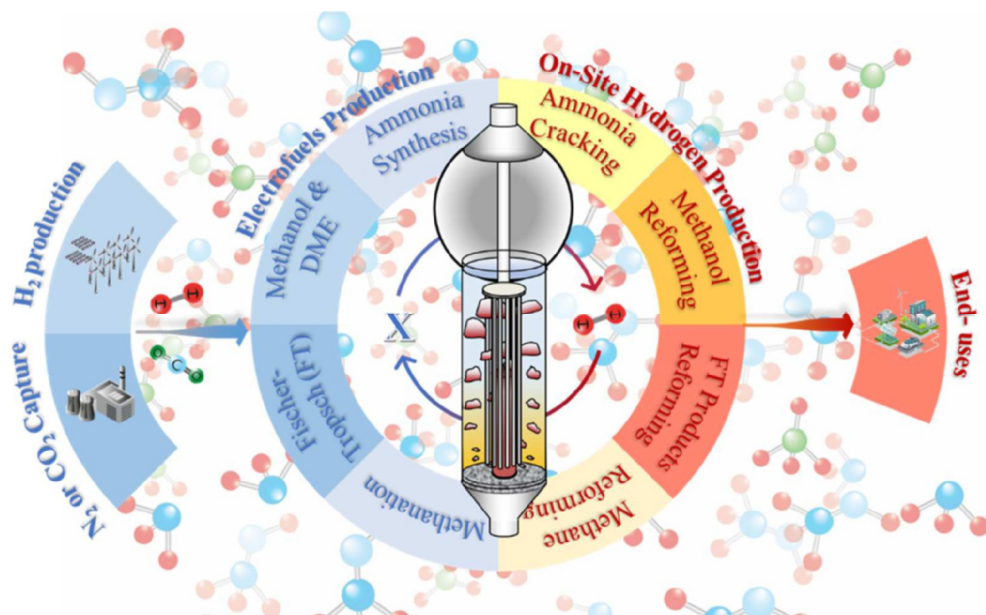
- applications, *Renewable and Sustainable Energy Reviews* 183 (2023) 113459. <https://doi.org/10.1016/j.rser.2023.113459>.
- [94] S. Horvath, M. Fasihi, C. Breyer, Techno-economic analysis of a decarbonized shipping sector: Technology suggestions for a fleet in 2030 and 2040, *Energy Conversion and Management* 164 (2018) 230–241. <https://doi.org/10.1016/j.enconman.2018.02.098>.
- [95] S. Brynolf, M. Taljegard, M. Grahn, J. Hansson, Electrofuels for the transport sector: A review of production costs, *Renewable and Sustainable Energy Reviews* 81 (2018) 1887–1905. <https://doi.org/10.1016/j.rser.2017.05.288>.
- [96] B. Lin, T. Wiesner, M. Malmali, Performance of a Small-Scale Haber Process: A Techno-Economic Analysis, *ACS Sustainable Chem. Eng.* 8 (2020) 15517–15531. <https://doi.org/10.1021/acssuschemeng.0c04313>.
- [97] R. Peters, N. Wegener, R.C. Samsun, F. Schorn, J. Riese, M. Grünwald, D. Stolten, A Techno-Economic Assessment of Fischer–Tropsch Fuels Based on Syngas from Co-Electrolysis, *Processes* 10 (2022) 699. <https://doi.org/10.3390/pr10040699>.
- [98] C. Arnaiz del Pozo, S. Cloete, Á. Jiménez Álvaro, Techno-economic assessment of long-term methanol production from natural gas and renewables, *Energy Conversion and Management* 266 (2022) 115785. <https://doi.org/10.1016/j.enconman.2022.115785>.
- [99] D. Bellotti, M. Rivarolo, L. Magistri, A comparative techno-economic and sensitivity analysis of Power-to-X processes from different energy sources, *Energy Conversion and Management* 260 (2022) 115565. <https://doi.org/10.1016/j.enconman.2022.115565>.
- [100] W.L. Becker, R.J. Braun, M. Penev, M. Melaina, Production of Fischer–Tropsch liquid fuels from high temperature solid oxide co-electrolysis units, *Energy* 47 (2012) 99–115. <https://doi.org/10.1016/j.energy.2012.08.047>.
- [101] S. Pratschner, M. Hammerschmid, F.J. Müller, S. Müller, F. Winter, Simulation of a Pilot Scale Power-to-Liquid Plant Producing Synthetic Fuel and Wax by Combining Fischer–Tropsch Synthesis and SOEC, *Energies* 15 (2022) 4134. <https://doi.org/10.3390/en15114134>.
- [102] H. Al-Kalbani, J. Xuan, S. García, H. Wang, Comparative energetic assessment of methanol production from CO₂: Chemical versus electrochemical process, *Applied Energy* 165 (2016) 1–13. <https://doi.org/10.1016/j.apenergy.2015.12.027>.
- [103] H. Zhang, L. Wang, J. Van herle, F. Maréchal, U. Desideri, Techno-Economic Optimization of CO₂-to-Methanol with Solid-Oxide Electrolyzer, *Energies* 12 (2019) 3742. <https://doi.org/10.3390/en12193742>.
- [104] D. Abad, F. Vega, B. Navarrete, A. Delgado, E. Nieto, Modeling and simulation of an integrated power-to-methanol approach via high temperature electrolysis and partial oxy-combustion technology, *International Journal of Hydrogen Energy* 46 (2021) 34128–34147. <https://doi.org/10.1016/j.ijhydene.2021.04.029>.
- [105] D. Parigi, E. Giglio, A. Soto, M. Santarelli, Power-to-fuels through carbon dioxide Re-Utilization and high-temperature electrolysis: A technical and economical comparison between synthetic methanol and methane, *Journal of Cleaner Production* 226 (2019) 679–691. <https://doi.org/10.1016/j.jclepro.2019.04.087>.
- [106] R. Schmuck, R. Wagner, G. Hörpel, T. Placke, M. Winter, Performance and cost of materials for lithium-based rechargeable automotive batteries, *Nat Energy* 3 (2018) 267–278. <https://doi.org/10.1038/s41560-018-0107-2>.
- [107] CATL, 2025. Commercial EV Solution. [online] Available at: <https://www.catl.com/en/solution/commercialEV/> [Accessed 11 Feb. 2025].
- [108] F. Ueckerdt, C. Bauer, A. Dirnaichner, J. Everall, R. Sacchi, G. Luderer, Potential and risks of hydrogen-based e-fuels in climate change mitigation, *Nat. Clim. Chang.* 11 (2021) 384–393. <https://doi.org/10.1038/s41558-021-01032-7>.
- [109] A. I. Stankiewicz & J. A. Moulijn (2000). Process Intensification: Transforming Chemical Engineering. *Chemical Engineering Progress*, 96(1), (2000) 22–34

Chapter 2 | Membrane reactors technologies for e-fuel processing & production: a review

Abstract

This chapter* aims to provide a comprehensive analysis of recent advancements in MR (membrane reactor) design and applications relevant to Power-to-X systems, focusing on the past decade. Using a top-down approach, the study begins with an evaluation of shared design attributes such as main membrane materials, heat management, and catalyst configurations, followed by a comparison of several laboratory-scale demonstrations and their performance in various process environments. Advanced integration in membrane reactors were highlighted, including additive manufacturing for optimizing porosity and shape, addressing heat and mass transfer challenges. Combined with electric heating, these innovations could result in compact, flexible technologies ideal for the Power-to-X framework. Laboratory studies have demonstrated significant conversion enhancements, including up to ~250% in methanol synthesis, ~200% in DME synthesis, ~30% in methanol reforming (with a large specific membrane area), ~30% in ammonia decomposition, and ~175% in methane reforming, as well as the potential to eliminate side reactions, such as those in Fischer-Tropsch synthesis. However, differences in membrane properties, catalyst behavior, and operating conditions complicate direct comparison across different studies. Despite similar temperature and pressure, variations in specific membrane area, space velocity, and driving forces are the main factors causing performance differences. These differences are discussed in more detail in this review.

* This review chapter is based on the following paper: S. Richard, P. Olivier, M. Jegoux, C. Makhloufi, F. Gallucci, Membrane reactors technologies for e-fuel processing & production: Review, Submitted to Int. J. Hydrogen Energy



2.1. Introduction

As noted in **Chapter 1** (page 14), MRs can offer a promising solution to the limitations of conventional processes by combining reaction and separation in a single unit. This integration enables MRs to overcome equilibrium constraints, achieving superior (or similar) performance under similar (or milder) operating conditions. This approach also reduces catalyst deactivation and side reactions, significantly enhancing target-product yields, achievements often unattainable through catalyst development alone. Additionally, the use of highly selective membranes can minimize or even eliminate the need for downstream purification. Alternatively, membranes can serve as reactant distributors, allowing for precise dosing along the reactor axis, or as contactors, facilitating the selective removal of products through interaction with a solvent. MRs have been applied, or are currently being explored, in a variety of processes, including hydrogen production and the synthesis of e-chemicals. As shown in **Figure 2-1**, certain applications, such as ammonia decomposition, have gained popularity, while others, like methanol reforming, have attracted only modest interest. Meanwhile, processes like ammonia synthesis remain rarely mentioned in the literature. In terms of development trajectory, these reactors follow a similar path. Early laboratory-scale studies typically focus on minimizing mass and heat transfer limitations to address kinetic and thermodynamic constraints. As development progresses towards industrial applications, optimizing heat and mass transfer becomes crucial. This requires refining catalyst configurations, heat management strategies, and developing membranes that are thermally, chemically, and mechanically stable under process conditions. These considerations open numerous design possibilities (cf. **Figure 2-3**) and hold significant potential for advancing Power-to-X processes, particularly in the creation of compact and dynamic systems.

Although more than 30 reviews (e.g., [1-5]) have examined membrane reactors from various angles, none have specifically addressed their potential within the Power-to-X framework. A thorough review on this subject seems essential to consolidate the state of the art across different applications, assess MR performance from a comparative perspective, and clearly highlight the research gaps and technological challenges that must be addressed to make membrane reactors a viable industrial solution. This chapter aims to offer a comprehensive overview of the evolving design and key applications of membrane reactors in Power-to-X processes, highlighting their role in addressing common reaction engineering challenges over the past decade. Adopting a top-down approach, the chapter begins with an assessment of shared design features, including membrane materials, heat management, and catalyst configurations, and then compares several laboratory-scale demonstrations and their performance in various process environments.

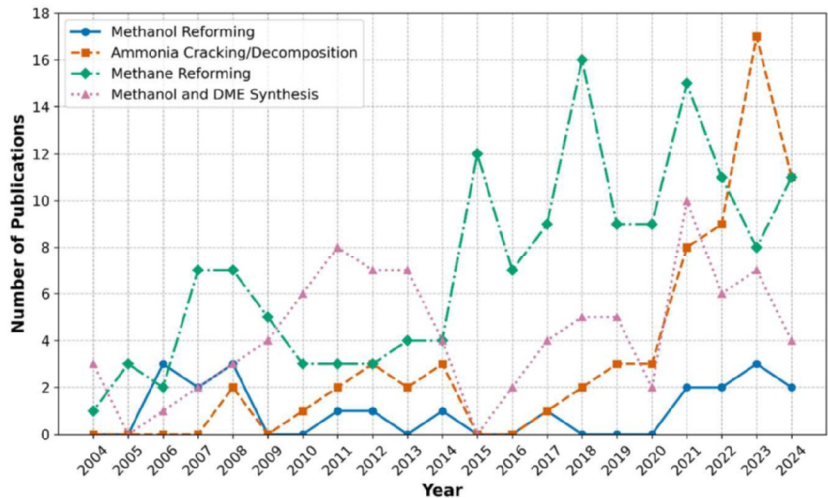


Figure 2-1: Annual publication trends on various membrane reactor applications obtained by a Scopus search of 'Membrane Reactor' and relevant keywords (cf. legend) in research and review articles (accessed on 5/08/2024)

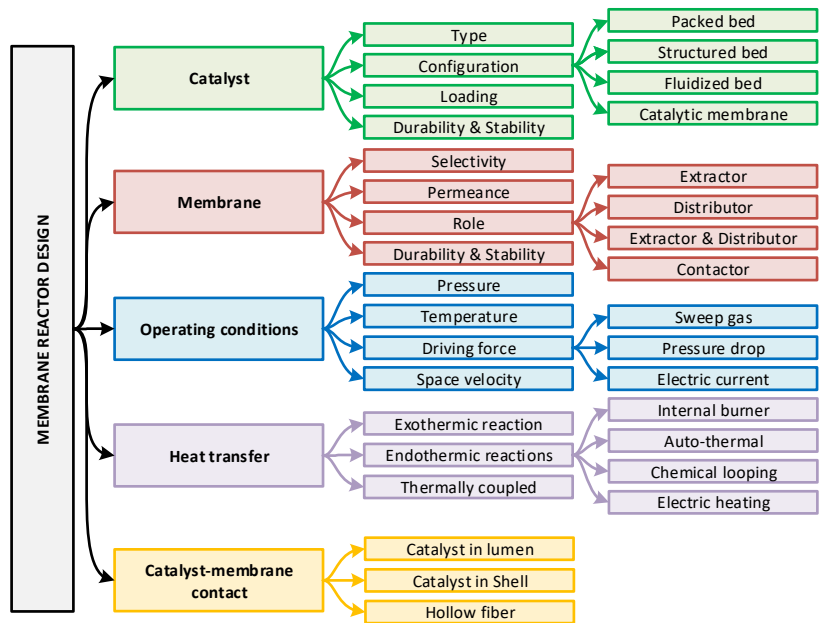


Figure 2-2: Membrane reactor key design elements

2.2. Performance Indicators generally used

To compare experimental results, several key performance indicators (KPIs) are used to assess membrane performance, including permeance (K_i), permeability (Pe_i), and selectivity ($\alpha_{i/j}$) as defined per Eq. 2.1-2.3. Permeance represents the species flux across the membrane (J_i) per unit pressure difference ΔP_i , while permeability is the permeance normalized by membrane thickness (t_m). Selectivity is the ratio of the permeance of one gas to another under the same conditions.

$$K_i = \frac{J_i}{\Delta P_i} \quad \text{Eq. 2.1}$$

$$Pe_i = \frac{K_i}{t_m} \quad \text{Eq. 2.2}$$

$$\alpha_{i/j} = \frac{K_i}{K_j} \quad \text{Eq. 2.3}$$

In evaluating membrane reactor performance, key performance indicators (KPIs) include feedstock conversion (X_i), product yield (Y_i), and the recovery factor (RF). Conversion, as defined in Eq. 2.4, measures the percentage of reactants transformed into products, while product yield (Eq. 2.5) is the ratio of the desired product's molar flow rate to that of the limiting reactant (or all reactants), reflecting the efficiency of converting reactants into the desired product. The recovery factor quantifies the amount of pure compound successfully separated by the membrane. However, the definition of these KPIs can vary across studies; for instance, the hydrogen recovery factor (HRF) can be calculated based on either the maximum possible hydrogen production at full conversion or the actual conversion achieved, as outlined in Eq. 2.6 and Eq. 2.7 [6-8]. Another important KPI is the enhanced conversion in the membrane reactor (MR) compared to a traditional reactor (TR), where TR refers to a conventional reactor without a membrane, as defined by Eq. 2.8. Additionally, specific membrane area (SMA) - the membrane surface area per unit mass of catalyst - and gas hourly space velocity (GHSV), which normalizes the flow rate at standard conditions by either reactor volume or catalyst mass, are critical parameters. These factors play a significant role in reactor efficiency, influencing both conversion rates and scalability.

$$X_{\text{reactant}} = \frac{F_{\text{reactant,in}}^{\text{Ret}} - F_{\text{reactant,out}}^{\text{Ret}}}{F_{\text{reactant,in}}^{\text{Ret}}} \cdot 100 \quad \text{Eq. 2.4}$$

$$Y_i = \frac{(F_{i,\text{out}}^{\text{Ret}} + F_{i,\text{out}}^{\text{Perm}})}{F_{\text{reactant,in}}^{\text{Ret}}} \cdot 100 \quad \text{Eq. 2.5}$$

$$HRF_{\text{fuel}}^{\text{stoichiometric}} = \frac{F_{H_2}^{\text{Perm}}}{\delta_{\text{fuel}} \cdot F_{\text{fuel,in}}^{\text{Ret}}} \cdot 100 \quad \text{where } \left\{ \delta_{CH_3OH} = 3; \delta_{CH_4} = 4; \delta_{NH_3} = \frac{3}{2} \right\} \quad \text{Eq. 2.6}$$

$$HRF_{\text{fuel}} = \frac{F_{H_2}^{\text{Perm}}}{F_{H_2}^{\text{Perm}} + F_{H_2}^{\text{Ret}}} \cdot 100 \quad \text{Eq. 2.7}$$

$$\text{Improvement (\%)} = \frac{X_{MR} - X_{TR}}{X_{MR}} \cdot 100 \quad \text{Eq. 2.8}$$

2.3. Membrane reactors design

This section evaluates the shared attributes commonly encountered in MR design, beginning with catalyst configurations (e.g., packed bed, fluidized bed, structured bed), followed by an analysis of the main membrane materials (e.g., H₂-selective membranes or water-selective membranes), the permeation driving force, and a discussion on heat management.

2.3.1. Catalyst configuration

2.3.1.1. Packed-bed

Membrane reactors can be designed with various catalyst configurations, with the packed bed being the most common and often the first to be tested due to its simplicity. However, packed bed membrane reactors (PBMRs) face industrial challenges such as flow channeling, pressure drops, and poor heat and mass transfer, which can negatively impact permeation efficiency. These challenges are particularly pronounced in high-flux membranes, where mass transfer limitations, known as concentration polarization, arise from the buildup of species in the retentate, leading to reduced membrane performance (cf. section “2.3.3. Permeation reduction”). Additionally, the low thermal conductivity of packed beds can create temperature gradients due to reaction exo- or endothermicity, accelerating catalyst degradation, increasing byproduct formation, and posing safety risks (e.g. thermal runaway). These issues may also reduce membrane flux and stability. Traditional industrial solutions for managing reaction heat include quench reactors, which inject fresh feed gas to regulate temperature, and mostly externally cooled multi-tubular reactor, such as the Lurgi™ design developed in 1970s for methanol synthesis (now part of Air Liquide™ since 2007 [9]). Dieterich et al. (2022) [10] in their review highlighted alternative advanced designs focused on efficient temperature control, low pressure drop, and scalability. Examples include Linde™'s Variobar process with coil-wound heat exchangers, Toyo™'s Multi-Stage Radial Flow reactor with bayonet tubes for minimal pressure drop, Mitsubishi™'s "Superconverter" integrating gas cooling and steam raising, and Methanol Casale™'s Isothermal Methanol Converter with hollow plates for precise temperature management. Reducing radial temperature gradients can also be achieved by using smaller tube diameters, though this often leads to an increased number of tubes and higher overall investment costs. Other strategies involve reducing catalytic activity by diluting the catalyst bed or increasing the gas inlet velocity to enhance convective heat transfer. However, these adjustments may necessitate the use of longer reactor tubes to ensure sufficient residence time for the reaction, which can, in turn, result in higher pressure drops [11]. Balancing these factors is essential to ensure efficient heat management without compromising reactor performance. To further address the limitations of packed bed reactors, researchers have explored innovative designs such as fluidized bed membrane reactors (FBMRs) and structured reactors. These alternatives are particularly suited for highly energetic processes like methane reforming and propane dehydrogenation [12, 13]. Some of these concepts are illustrated in **Figure 2-3** compared in **Table 2-1** and discussed hereafter.

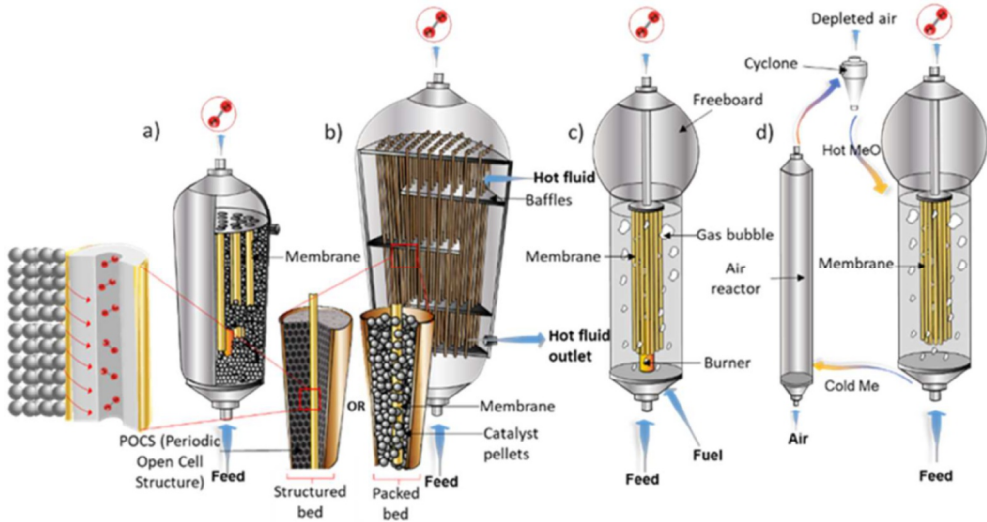


Figure 2-3: Examples of membrane reactor concepts for hydrogen production: (a) Conventional packed bed reactor (b) Multi-tubular membrane reactor (packed or structured bed) (c) Fluidized bed reactor (d) Chemical looping

Table 2-1: Relative comparison of three different catalyst configurations (+++ ↔ Good / ++ ↔ Medium / + ↔ Bad performance with respect to the criteria)

Criteria	Packed bed	Fluidized bed	Periodic Open Cell Structure (POCS)
Low Pressure drop	+	++	++/+++
High radial heat transfer and mass transfer	+ / ++	+++	++/+++
Scale up ease	+++	+	++
Membrane preservation (e.g. prevent erosion)	++	+	+++
Low manufacturing cost	+++	+	++
Catalyst loading	+++	++	+
Changing/recycling the catalyst	+++	++	+
Design freedom	+	+	+++

2.3.1.2. Structured-bed

Cellular structures, such as open-cell foams (OCF), present a promising solution to address heat and mass transport limitations in catalytic reactors. These novel fixed-bed supports, made from conductive metals like AlSi10Mg (120 W/m/K), IN718 (11.4 W/m/K), and Ti6Al4V (6.7 W/m/K), enhance overall heat transfer through thermal conduction and promote high radial mixing due to their tortuous fluid paths, all while maintaining reasonable pressure drops and short contact times [14]. Yan et al. (2022) [15] demonstrated that silicon carbide (SiC) OCF reactors, combined with palladium membranes and Ru-based catalysts, can outperform packed beds, particularly at higher temperatures, by improving radial mass transfer and achieving greater gas flow rates. Additionally, Periodic Open-Cell Structures (POCS) have emerged as innovative catalytic supports with

interconnected cells in various shapes (e.g., cubic [17-19], diamond [18, 20-21], octet [22] and triply periodic minimal surface (TPMS) [23-26].), forming highly regular three-dimensional structures. These supports combine the advantages of OCF by enhancing both axial and radial gas-solid transfer rates while maintaining a consistent and uniform framework.

3D printing offers a promising approach for fabricating POCS, with the added benefits of reducing material waste and improving energy efficiency compared to traditional subtractive manufacturing methods [27]. Techniques such as robocasting [28], selective electron beam melting (SEBM) [17], selective laser melting (SLM) [11, 29-30], direct metal laser sintering (DMLS), and stereolithography [20] have already been employed to produce highly reproducible POCS. For example, lattice structures with struts as fine as 0.5–0.6 mm can be achieved, while ceramic stereolithography allows for even greater precision, producing structures with dimensions as small as 0.2 mm [31]. While predominantly investigated in thermohydraulic studies (e.g. heat transfer [14, 24, 32-33] and pressure drop [24,33]), POCS are also beginning to demonstrate promising success in reactive processes affected by external heat and mass transfer limitations. These include methanation [23,28], methanol synthesis [34], Fischer Tropsch [35], methane reforming [36-37] or methanol reforming [38], ammonia cracking [39] CO oxidation [20,40] methanol oxidation [11] and ammonia synthesis (cf. **Figure 2-4.A**). The superior conductive heat transfer properties of POCS were utilized for isothermal kinetic measurements at elevated temperatures, particularly under low flow rates due to superior conductive heat transfer compared to a packed bed [11]. This allows for safer operation in harsher environments, such as higher wall temperatures and increased catalyst loadings, while also potentially reducing catalyst deactivation through improved temperature control. However, at high flow rates, packed beds perform better due to increased convective heat transfer, though at the expense of higher pressure drops [14]. Additionally, wall coupling is crucial, as even a small contact area (10-20%) significantly enhances heat transport, as demonstrated by Busse et al. (2018) [14] (cf. **Figure 2-4.C**). 3D printing offers design flexibility to optimize transport properties in key reactor areas, such as membranes and inlets, through advanced designs like optimized lattice orientations, new cell shapes, or porosity gradients (cf. **Figure 2-4.D**).

Despite the promising benefits of POCS, converting them into active catalytic supports poses significant challenges. With a few exceptions, so called self-catalytic POCS [38,41], the structures reported so far are typically not catalytically active. The development of uniform catalytic layers on the POCS support, which remain active and stable under the reaction's operational conditions, is a crucial aspect of this technology. A variety of activation techniques have been employed [42] involves investigated depositing catalytically active phases on metallic supports, including chemical vapor deposition (e.g. Ti–6Al–4V diamond lattice [43]), solution combustion synthesis [36,44], and washcoating (e.g. iron based OCF [45], copper based diamond cell [46] or aluminium based cubic cell [40]), each aimed at anchoring a catalytically active phases onto the POCS. These methods involve a series of additional stages after the printing process that can increase the cost of this type of structure investigated. For instance, the washcoating method, one of the most common methods, involves multiple steps: including preparing and controlling powder materials, dispersing them in a solvent, adjusting the slurry's viscosity, applying the slurry through dip and spin coating to achieve a homogeneously thick active material layer, followed by drying or

calcination, and repeating the process until the desired loading is achieved. The SCS method seems to be promising in terms of time reduction, it takes the advantage of an exothermic, very quick and self-sustaining chemical reaction between metal/oxides precursors and an organic fuel (i.e., urea), resulting in the synthesis of nanocrystalline oxide powders over the surface of structured supports, however, it is more suitable for activating ceramic-based supports. These methods are particularly beneficial for mass transfer-limited processes, as they can lead to higher specific activity per catalyst mass compared to conventional packed beds. However, in kinetically limited processes, the lower catalyst loading may necessitate reactor oversizing. A potential solution could involve combining POCS supports with catalyst particles, as proposed by Politecnico di Milano, by packing the cavities with catalyst pellets. However, this approach may compromise the pressure drop advantage typically provided by POCS [47].

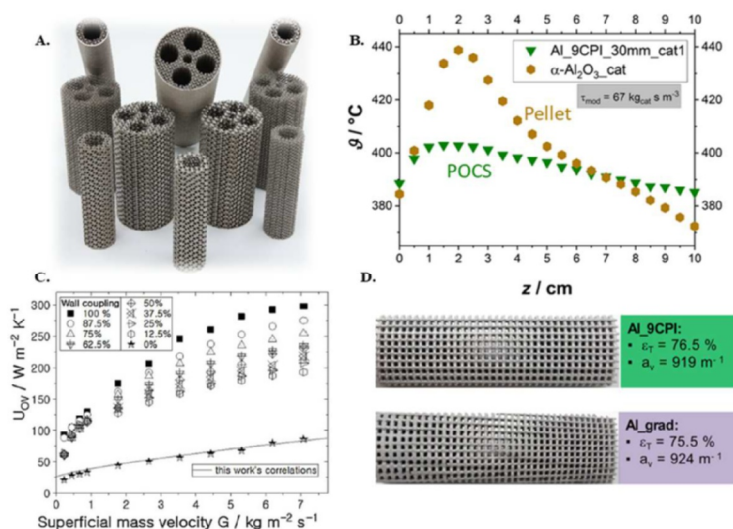


Figure 2-4: (A) POCS Support for Ambher EU Project proof of concept, 3D-Printed by ENGIE Laborelec using Selective Laser Melting [48] (B) Temperature profile comparison: conventional reactor randomly packed beds of egg-shell catalyst vs. POCS Reactor made of AlSi10Mg under similar catalytic loading [11] (C) Overall heat transfer coefficient U_{ov} vs. superficial mass velocity G with varying wall couplings [14]. (D) POCS with increasing porosity from inlet to outlet, as shown in the plot on the right. Both structures offer the same overall specific surface area and porosity [11]

2.3.1.3. Fluidized-bed

In Fluidized Bed Membrane Reactors (FBMRs), membranes are immersed in a catalytic bed that operates under bubbling to turbulent fluidization regimes, as shown in **Figure 2-3.c**. One of the key advantages of fluidized beds is their low pressure drop and uniform temperature profile, achieved through the internal circulation of solids. The integration of membranes in a fluidized bed

has been shown to create a synergistic effect, improving fluidization behavior by compartmentalizing the bed, reducing axial back-mixing, and decreasing average bubble size through enhanced bubble breakage. This leads to improved mass transfer between bubbles and the emulsion phase [49]. Despite these benefits, FBMRs face challenges like erosion of catalysts and membranes from particle movement. Additionally, membrane extractive flux can create densified zones near the membrane, negatively impacting hydrogen extraction and recovery. Voncken et al. (2019) [50] provided numerical insights, showing that 500 μm particles help minimize densified zones, whereas 250 μm particles significantly increase emulsion phase density near the membrane, reducing local hydrogen flux. FBMRs are generally considered promising for scaling up membrane reactor applications, especially in endothermic processes like methane reforming [51], where precise temperature control is key to optimizing hydrogen production and membrane longevity. Adris et al. (1997) [52] were among the first to demonstrate hydrogen removal in FBMRs for steam methane reforming using palladium membranes. Since then, extensive research has been conducted through both experimental studies and modeling efforts.

2.3.1.4. Catalytic membrane

Catalytic membranes offer an alternative approach, directly integrating the catalyst into the membrane support, where it serves both as nucleation sites for membrane deposition and as active sites for chemical reactions. This close membrane-catalyst proximity minimizes transport limitations, enabling high performance even with minimal catalyst loading. Additionally, this configuration shields delicate membranes from abrasion by catalyst particles, a common issue in packed bed reactors. Mechanical damage, such as scratching, is also reduced since the membrane is not directly exposed to external surfaces, enhancing its durability and practicality [53-54]. This design offers a promising solution for improving durability and performance in membrane reactors. The challenge of low catalyst loading, similar to that faced by structured supports, can be addressed by packing catalyst particles at the interface of the catalytic membrane, as demonstrated in **Figure 2-5** for ammonia cracking applications.

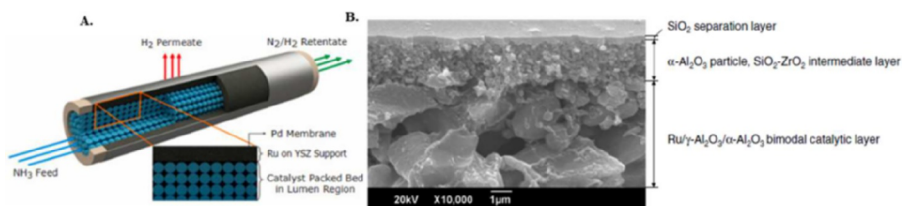


Figure 2-5: (A) Sketch of the catalytic membrane reported proposed by Sitar et al. [54] for ammonia decomposition application (the authors also added catalyst in the lumen of the membrane) (B) SEM of the catalytic membrane reactor proposed by Li et al. [55]

2.3.2. Membrane choices

2.3.2.1. Hydrogen selective membrane

➤ Palladium membranes

Dense palladium-based membranes are widely considered the most effective for hydrogen production in membrane reactors due to their excellent permeability and selectivity as shown in **Figure 2-6.A** palladium membrane reactors often function as extractors in hydrogen production processes such as methanol reforming, methane reforming, ammonia decomposition, and propane dehydrogenation. Additionally, although less commonly demonstrated experimentally, they can serve as distributors for controlled hydrogen introduction along the reactor axis in e-fuel synthesis pathways, including ammonia synthesis [56] and Fischer-Tropsch synthesis [57-58]. Their performance is highly dependent on factors such as temperature, transmembrane pressure, and membrane thickness. To improve the long-term performance and high-temperature stability of palladium membranes, ongoing research focuses on different alloying and advancements in support materials. Alloying palladium with metals such as silver, yttrium, gold, and copper has been shown to reduce embrittlement below 300 °C and mitigate the poisoning effects of contaminants like H₂S and CO [57,59]. Supported membranes on porous structures, such as ceramics and porous stainless steel (PSS), are favored for their high mechanical strength, ability to withstand high pressure differentials, and the capability to support thin palladium layers. Metallic supports, while robust and capable of reducing sealing struggles, face challenges in matching the deposition-ready nature of ceramic supports counterparts, often requiring an inter-metallic diffusion barrier between the support and the Pd-based layer [60] (**Figure 2-6.B**). The use of very thin Pd-based membranes increases hydrogen permeability and reduces material costs, but this comes at the expense of selectivity. Thinner membranes are more prone to defects, which can allow small contaminants like CO or NH₃ to pass through (**Figure 2-6.C**). These problems associated to defects can be exacerbated under high pressure differentials; for example, Anzelmo et al. (2017) [8] observed a drop in selectivity from near-infinite at 100 kPa to values of 9000 and 40000 at 200 kPa, attributed to membrane defects. Several long-term tests have demonstrated stable performance over 600-1000 hours of operation [61], nonetheless performance declines are still commonly observed especially at temperatures above 550 °C (**Figure 2-6.D**).

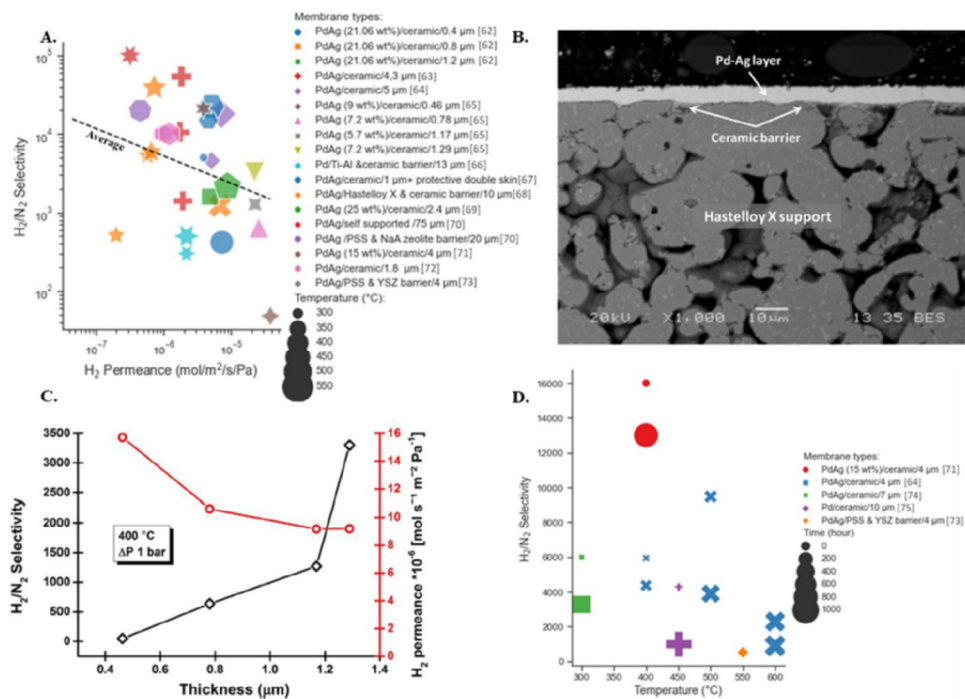


Figure 2-6: (A) Example of ideal H₂-N₂ Selectivity vs H₂ Permeability for various Pd-based membranes collected at around 1 bar transmembrane pressure [62-73] (B) Ideal selectivity vs permeance at different membrane thickness taken from Melendez et al. (2017) [65] (C) H₂/N₂ selectivity obtained during long-term stability tests conducted across various temperature [64,71, 73, 74-75] (D) SEM of a Pd-Ag membrane supported on ceramic coated Hastelloy X porous tube [60]

➤ Non palladium membranes

To remove hydrogen, non-palladium membranes such as silica [7, 55], zeolite [72] and carbon molecular sieve membranes (CMSMs) [76-77] have emerged as cost-effective alternatives to palladium membranes (cf. **Figure 2-7.A**), each with unique advantages and limitations. These membranes typically separate hydrogen through size exclusion, which often results in lower selectivity compared to dense inorganic palladium membranes (cf. **Figure 2-7.B & C**). Although these membranes can achieve higher H₂ recovery in some cases, additional purification steps are usually required to meet the high purity standards necessary for fuel cell applications. CMSMs, produced through the pyrolysis of polymer precursors, offer high separation factors and mechanical stability, with permeance values comparable or higher to those of zeolite. These membranes have shown promise in gas separation and membrane reactor applications, sometimes even surpassing the Robeson line for polymeric membranes and approaching the lower selectivity range of palladium membranes. Additionally, new materials like graphene and other two-dimensional (2D) atomically

thin structures are gaining attention due to their minimal thickness, high mechanical strength, chemical stability, and the ability to create selective nanoscale pores within their unique layered lattices [78]. Wu et al. (2024) [79] reported that MXene (titanium carbide, $\text{Ti}_3\text{C}_2\text{TX}$) exhibited performance comparable to zeolite membranes in ammonia cracking applications. **Table 2-2** presents several examples of non-palladium hydrogen-selective membranes tested in reaction environments.

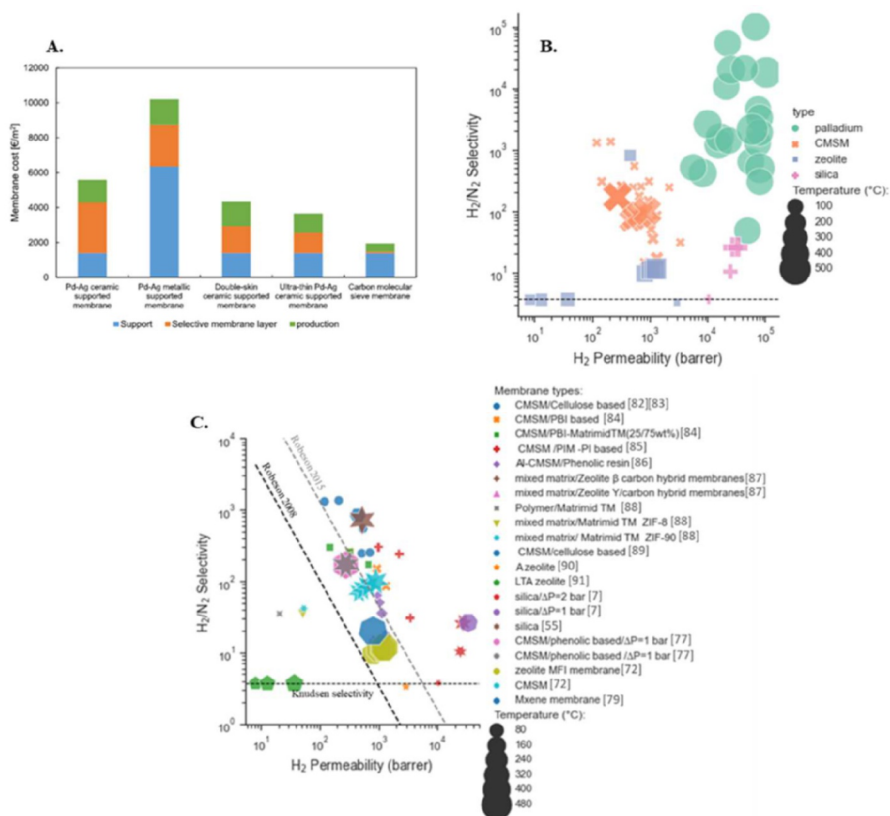


Figure 2-7: (A) Cost breakdown of various membrane types [80] (B) Comparison of ideal H_2 – N_2 selectivity versus H_2 permeability for palladium-based and other membranes, including CMSM and polymeric membranes (C) Performance details of non-palladium membranes, highlighting the 2008 and 2015 Robeson upper bound limits [81]. Note: for membranes without a specified thickness in the source article, a thickness of 1 μm was assumed for permeability calculations. Araújo et al. (2024) [82] Rodrigues et al. (2019) [83] Hosseini et al. (2009) [84] Ogieglo et al. (2019) [85] Llosa Tanco et al. (2021) [86] Li et al. (2015) [87] Moral et al. (2024) [88] Lei et al. (2021) [89] Gallucci et al. (2004) [90] Rodriguez-Vega et al. (2021) [91] Ghasemzadeh et al. (2015) [7] Li et al. (2013) [55] Cechetto et al. (2024) [77] Jiang et al. (2021) [72] Wu et al. (2024) [79]

Table 2-2: Example of separation performance of non-palladium membranes tested for hydrogen production in membrane reactors

Authors	Membrane material	Single or gas mixture tests	Temp. (°C)	Pressure gradient (bar)	Thickness (µm)	Permeance $mol\ m^{-2}\ s^{-1}\ Pa^{-1}$	Selectivity				Reaction
							H ₂ /CO ₂	H ₂ /CH ₄	H ₂ /N ₂	H ₂ /NH ₃	
Ghasenzadeh et al. (2015) [71]	Silica supported on Al ₂ O ₃ tubes	Single gas	200	1	10	$9.5 * 10^{-7}$	19.9	-	26.2	-	Methanol reforming
Ghasenzadeh et al. (2015) [71]	Silica supported on Al ₂ O ₃ tubes	Single gas	200	2	10	$11.7 * 10^{-7}$	22.2	-	29.5	-	Methanol reforming
Briceño et al. (2012) [76]	CMSM using Polyimide as precursor pyrolysed 650 °C	Single gas	25	2	-	-	2.5	-	5.5	-	Methanol reforming
Seshimo et al. (2021) [98]	Silica supported on Al ₂ O ₃ tubes	Single gas	300	-	-	$1.3 * 10^{-6}$	-	-	10	-	Methylcyclohexane dehydrogenation
Jiang et al. (2021) [72]	Zeolite MFI	Mixture 5%NH ₃ /71%H ₂ /24% N ₂	300	-	8	$3.59 * 10^{-8}$			9.7	3.29	Ammonia cracking
Jiang et al. (2021) [72]	Zeolite MFI	Mixture 5%NH ₃ /71%H ₂ /24% N ₂	450	-	8	$5.58 * 10^{-8}$			11.78	4.9	Ammonia cracking
Jiang et al. (2021) [72]	CMSM	Mixture 5%NH ₃ /71%H ₂ /24% N ₂	350	-	8	$5.58 * 10^{-8}$			11.78	4.9	Ammonia cracking
Cechetto et al. (2024) [77]	CMSM on Al ₂ O ₃ tube	Single gas	400	1		$9.8 * 10^{-8}$	-	-	165	16	Ammonia cracking
Cechetto et al. (2024) [77]	CMSM on Al ₂ O ₃ tube	Single gas	450	1	<1	$1 * 10^{-7}$	-	-	169	16	Ammonia cracking

2.3.2.2. Hydrophilic membranes

To tackle water accumulation in CO/CO₂ hydrogenation, which can limit reaction equilibrium and deactivate catalysts, water-selective membranes have been proposed. However, developing these membranes is challenging due to the need to selectively extract water (kinetic diameter of ~2.6 Å) from small gases like H₂ (~2.9 Å) under the harsh conditions typical of e-chemical processes, which often exceed 200 °C and 20 bar. Owing to their high thermal stability, inorganic materials like zeolites [92-93] or CMSM [94] as shown in **Table 2-3**, have been tested in reaction environments. This selectivity can arise from pore blocking by condensed H₂O in the micropores, which prevents other gases from penetrating. However, at elevated temperatures, the hydrophilicity diminishes, reducing the pore-blocking effect and consequently the selectivity towards H₂O [94]. While polymeric membranes are typically unsuitable for high-temperature applications due to challenges like plasticization and swelling, certain types, such as polyimide membranes, have demonstrated promising selectivity ($\alpha_{H_2O/H_2} = 200$ at 300 °C) [95], albeit with moderate durability due to operation at temperature close from their glass transition temperature. Their ease of processing and ability to form hollow fiber membranes with high surface-area-to-volume ratios make them worth further investigation for applications requiring high permeation rates per unit reactor volume. In a follow up study from the same group, Hyeon et al. (2023) [96] developed a thermally rearranged polybenzoxazole membrane that demonstrated high H₂O selectivity up to 440 °C, offering a promising solution for water extraction in extreme conditions.

Table 2-3: Examples of recent water-selective membrane performance tested in reaction environments

Author	Material	Single or gas mixture tests	Temp (°C)	Pressure gradient (bar)	Thick-ness (µm)	H ₂ O Permeance $mol\ m^{-2}\ s^{-1}\ Pa^{-1}$	Selectivity					Reaction
							H ₂ O/CO ₂	H ₂ O/CO	H ₂ O/H ₂	H ₂ O/MeOH	H ₂ O/DME	
Li et al. (2020) [97]	Na+ gated micro channel (zeolite)	mixture	200	21	3	4.86×10^{-7}	786	112	128	49	-	Methanol synthesis
Li et al. (2020) [97]	Na+ gated micro channel (zeolite)	mixture	250	21	3	1.85×10^{-7}	373	87	92	41	-	Methanol synthesis
Seshimo et al. (2021) [98]	Si- rich LTA zeolite	Mixture 10/90 wt%	200	-	-	1.5×10^{-6}	-	-	-	2000	-	Methanol synthesis
Poto et al. (2023) [99]	boehmite-phenolic resin (CMSM)	Single Gas	200	-	34	1.39×10^{-6}	2.37	3.99	2.06	2.39	-	DME synthesis
Ateka et al. (2021) [92]	LTA zeolite	Mixture	275	-	-	7.9×10^{-8}	0.56	2.39	1	1.62	8	DME synthesis
Sakai et al. (2022) [100]	ZSM-5 membrane (zeolite)	Single Gas	250	-	1	3.89×10^{-7}	-	-	2.24	-	-	RWGS
Sakai et al. (2022) [100]	ZSM-5 membrane (zeolite)	Single Gas	350	-	1	3.58×10^{-7}	-	-	1.35	-	-	RWGS

Hyeon et al. (2023) [96]	Polybenzoxazole membrane	Single gas	250	2	48	7.91×10^{-7}	133	528	44	-	-	RWGS & FT
Hyeon et al. (2023) [96]	Polybenzoxazole membrane	Single gas	400	2	48	1.74×10^{-6}	224	488	60	-	-	RWGS & FT

2.3.3. Permeation reduction

When designing membrane reactors, it is also important to address potential permeation reduction to avoid underestimating the required membrane surface area. This reduction can mainly be caused by two factors: concentration polarization and competitive adsorption involving species such as H_2S or CO .

In concentration polarization, non-permeable species accumulate near the membrane, forming a boundary layer that reduces permeate flux **Figure 2-8.A** shows this effect in palladium membranes, where significant permeation reduction is observed, with polarization becoming more pronounced under conditions of low hydrogen content but also high driving force, and reduced space velocity. While this issue is well-documented in high flux palladium membranes, its impact on porous, less selective membranes is less clear. For example, Cechetto et al. (2024) [77] reported no noticeable concentration polarization effect on a CMSM membrane with a H_2/N_2 selectivity of 165, possibly due to the small specific membrane area (SMA) used in their study. Methods for mitigating the impact of concentration polarization have often been proposed through numerical simulations, focusing on strategies such as: (i) increasing convective forces and (ii) designing baffles to enhance radial mass transfer, which is typically lacking in catalytic packed bed reactors [101]. During the scale-up of multi-tube membrane reactors, concentration polarization can also intensify due to overlapping zones from adjacent membranes, reducing recovery. Voncken et al. (2019) [50] highlighted this in a fluidized bed reactor (cf. **Figure 2-8.B**) study using a Euler-Euler approach with 500 μm particles under bubbling fluidization. The effect was found more pronounced when membrane spacing was below 2 cm.

Regarding permeation reduction due to competitive adsorption, **Figure 2-8.C** illustrates the impact of CO on hydrogen flux, showing a steep initial decline in flux with just 5% CO , followed by a more gradual reduction as CO concentration increases. Studies have shown that CO significantly hinders hydrogen permeation in Pd-based membranes, especially at lower temperatures or higher CO concentrations [57,65,102]. In CO -rich environments (up to 30%) and at temperatures around 250 $^{\circ}C$, hydrogen flux can decrease by more than 70% [57].

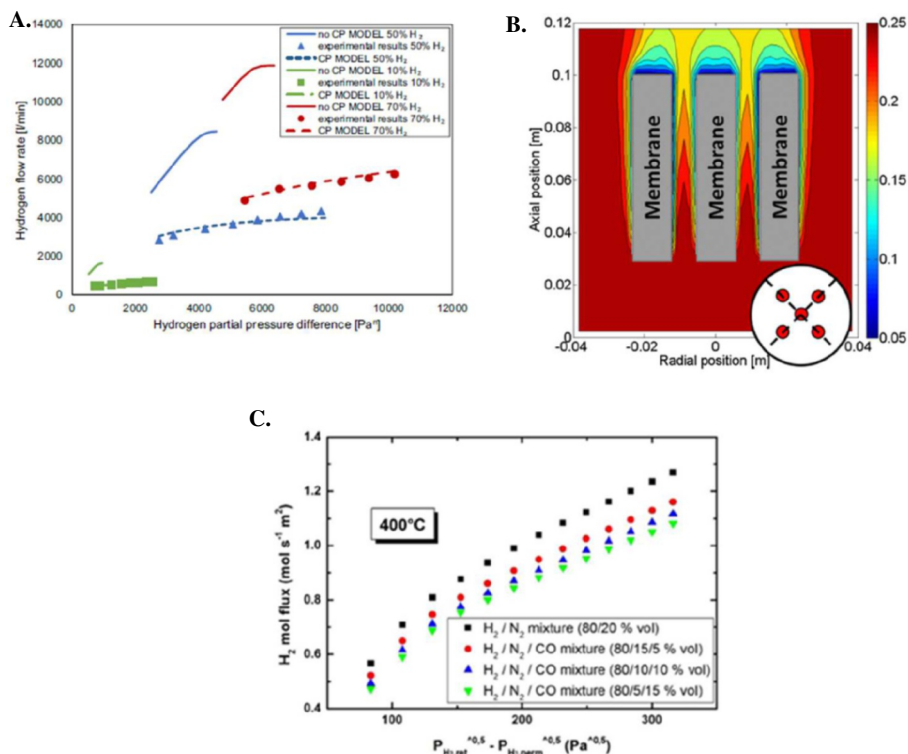


Figure 2-8: (A) Comparison of hydrogen flow rates obtained from experimental data on Pd membrane and modeled results for mixtures with different hydrogen inlet contents; solid line represents the ideal case, while the dotted line accounts for mass transfer limitations at 400 °C [103] (B) Averaged hydrogen mole fractions with an inter membrane distance of 1.75 cm simulated on a fluidized bed membrane reactor [50] (C) H₂ flux through a Pd-Ag membrane with varying CO concentrations (5% to 15%) at 400 °C as a function of H₂ partial pressure difference [65]

2.3.4. Membrane-catalyst contact

It is worth noting that the catalyst can be placed either inside the membrane tube (lumen) [74,91] or on the shell side, with the permeate collected on the opposite side of the membrane. The latter configuration provides greater flexibility in adjusting the membrane area relative to bed volume and is often preferred for scale-up applications [51]. An alternative method to increase membrane area is the use of hollow fiber membranes [6,96,104].

2.3.5. Permeation driving forces

The choice of driving force in membrane reactors is crucial and must suit the specific membrane. A pressure gradient, achieved by either applying a vacuum or using a sweep gas, is commonly used. For selective membranes like palladium, a simple pressure drop is often sufficient.

However, for porous membranes, a sweep gas is preferred as it helps retain reactants, operates at lower pressure gradients, dilutes permeated species, and assists with thermal management [99]. For example, using reactants as a sweep gas in methanol steam reforming enhances performance and reduces CO production, while a similar approach in methanol synthesis helps retain H₂. This approach, sometimes combined with a pressure drop, can significantly enhance the efficiency of a membrane reactor. The recovery efficiency depends on the sweep gas flow configuration, with counter-current flow generally outperforming co-current flow. However, at high sweep gas flow rates, the performance differences between the two configurations have been reported as negligible [62].

2.3.6. Heat management

Effective heat management is essential in membrane reactors to avoid temperature gradients that can damage catalysts and membranes. Common strategies include catalyst dilution, high flow rates, and external cooling, which help mitigate hotspots and minimize conversion losses. Additionally, membranes can contribute to heat management by evenly distributing reactants along the reactor axis, promoting a uniform temperature profile. The introduction of a sweep gas further supports a homogeneous temperature distribution. For endothermic reaction direct combustion within the catalytic bed, using a burner with heat provided by immersed tubes carrying hot flue gases, is a viable option. Alternatively, autothermal reforming, where air or oxygen is fed directly into the reactor, has proven effective, especially in fluidized bed reactors to avoid hot spots, as demonstrated in methane reforming [105]. Another approach is chemical looping (cf. **Figure 2-3.e**), where a membrane reactor with a solid oxygen carrier acts as a catalyst [106]. The carrier is regenerated in an air reactor for continuous use in a fluidized bed catalyst configuration, offering an innovative method for managing heat and reaction efficiency. Thermally coupling exothermic and endothermic reactions is another effective strategy. For example, Pati et al. (2020) [107] successfully coupled propane dehydrogenation with CO₂ hydrogenation in a membrane reactor. When green electricity is available, emerging methods like electricity-driven heating, such as Joule, induction, and microwave heating, could offer significant potential for dynamic operation. By supplying energy directly to the catalyst through close contact with the heat source, these methods offer precise control over the reaction front, making them particularly suitable for systems that demand exact thermal management. Electrification also brings additional benefits, including eliminating the need for a furnace, reducing reactor volume, lowering CO₂ and NO_x emissions, and minimizing waste heat streams. A review by Zheng et al. (2024) [108] identified Joule heating as particularly promising, noting that the knowledge from furnace heating can be directly applied to Joule-heated catalytic reactors. Plasma-assisted reactors, with or without catalysts, are also emerging as promising methods for efficient heat transfer [109-111].

2.4. Lab scale performance

This section reviews laboratory-scale applications of membrane reactors for various e-chemical reactions and hydrogen production, as summarized in **Table 2-4**. Equilibrium conversions

are plotted in **Figure 2-9**. From a thermodynamic perspective, hydrogen production processes are endothermic and require high temperatures for significant conversion, whereas exothermic e-chemical production typically benefits from lower temperatures. Methanol and DME synthesis are exceptions, as they involve both exothermic and endothermic reactions, leading to non-monotonic CO_2 equilibrium conversion. At lower temperatures, the exothermic reactions are favored, while at higher temperatures, the endothermic reverse water-gas shift (RWGS) reaction becomes more dominant due to the presence of H_2O , H_2 , and CO . In the case of methanation, the highly exothermic nature of the CO and CO_2 hydrogenation reactions masks the effect of the RWGS. The significant heat release from methane formation dominates the reaction equilibrium, suppressing the influence of RWGS even under conditions where it might otherwise become relevant. Pressure also plays a critical role in these reactions. For hydrogen production, higher pressures tend to reduce conversion, as the reaction produces more moles of product, leading to volume expansion (Le Châtelier principle). On the other hand, higher pressures generally improve conversion in e-chemical synthesis, where reactions benefit from the compression effect. Although membrane reactors can offer an elegant, integrated solution by combining reaction and separation into a single unit, this approach is not always superior to using separate reactors and separation units, where each process step can be optimized independently. In membrane reactors, the integration of catalyst and membrane requires careful optimization of reactor geometry and operating conditions to balance conversion, which may be limited either by thermodynamics or catalytic performance, and the permeation rate of species, as illustrated in **Figure 2-10** highlighting two limiting regimes. In a conversion-limited regime, the system's performance is dictated by the catalyst's efficiency or the thermodynamic equilibrium. Here, the production of reactants is insufficient relative to their extraction by the membrane, and the membrane's influence on the overall system behavior is minimal (e.g., due to insufficient membrane area or excessively high GHSV). Conversely, in a permeation-limited regime, the membrane's permeance becomes the bottleneck. The membrane's removal capacity surpasses the rate of reactant production, which can lead to uneconomical operation (e.g., due to excessive membrane area or very low GHSV). Achieving the right balance between reaction and permeation is thus critical for optimal system performance.

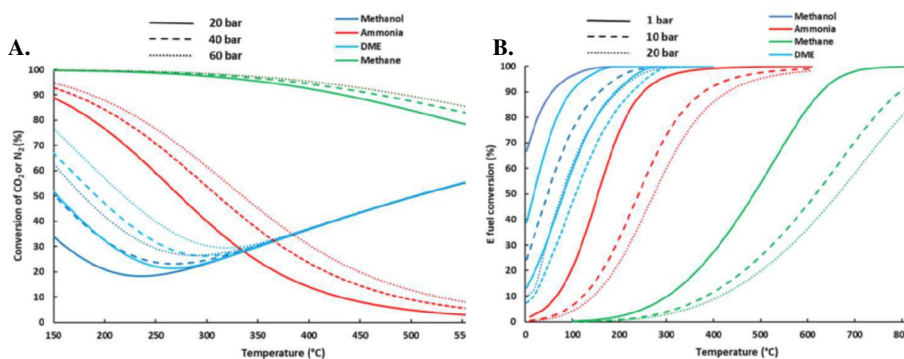


Figure 2-9: Equilibrium conversion as a function of temperature and pressure obtained using Aspen PlusTM & Peng Robinson equation of state: (A) Synthesis reactions ($\text{H}_2/\text{CO}_2=3$ for

methanol & DME synthesis, $H_2/CO_2 = 4$ for methane synthesis and $H_2/N_2=3$ for ammonia synthesis) (B) Steam reforming / decomposition reactions (SCR=1 and 3 for methanol and methane respectively)

Table 2-4: Reactions where membrane reactors are considered beneficial in power-to-x applications

	Synthesis	Reforming/ Cracking
Methanol	$CO_2 + 3H_2 \rightleftharpoons CH_3OH + H_2O \Delta H_r^\circ = -49.5 \frac{kJ}{mol}$ <i>CO₂ hydrogenation</i> $H_2 + CO_2 \rightleftharpoons CO + H_2O \Delta H_r^\circ = 41.2 \frac{kJ}{mol}$ <i>RWGS</i> $CO + 2H_2 \rightleftharpoons CH_3OH \Delta H_r^\circ = -90.5 \frac{kJ}{mol}$ <i>CO hydrogenation</i>	$CH_3OH + H_2O \rightleftharpoons CO_2 + 3H_2 \Delta H_r^\circ = 49.5 \frac{kJ}{mol}$ <i>Steam Reforming</i> $CO + H_2O \rightleftharpoons H_2 + CO_2 \Delta H_r^\circ = -41.2 \frac{kJ}{mol}$ <i>WGS</i> $CH_3OH \rightleftharpoons CO + 2H_2 \Delta H_r^\circ = 91 \frac{kJ}{mol}$ <i>Methanol decomposition</i>
DME	$CO_2 + 3H_2 \rightleftharpoons CH_3OH + H_2O \Delta H_r^\circ = -49.5 \frac{kJ}{mol}$ <i>CO₂ hydrogenation</i> $H_2 + CO_2 \rightleftharpoons CO + H_2O \Delta H_r^\circ = 41.2 \frac{kJ}{mol}$ <i>RWGS</i> $CO + 2H_2 \rightleftharpoons CH_3OH \Delta H_r^\circ = -90.5 \frac{kJ}{mol}$ <i>CO hydrogenation</i> $2CH_3OH \rightleftharpoons CH_3OCH_3 + H_2O \Delta H_r^\circ = -23.4 \frac{kJ}{mol}$ <i>Methanol dehydration</i>	Not considered in this review as DME is more likely to be used directly rather than as a hydrogen carrier.
Ammonia	$N_2 + 3H_2 \rightleftharpoons 2NH_3 \Delta H_r^\circ = -45.92 \frac{kJ}{mol}$ This reaction is not included in this review as, to our knowledge, only a single research study addresses ammonia synthesis using a membrane reactor (distributor role) [56]	$NH_3 \rightleftharpoons \frac{1}{2}N_2 + \frac{3}{2}H_2 \Delta H_r^\circ = 45.92 \frac{kJ}{mol}$
Methane	$CO_2 + 4H_2 \rightleftharpoons CH_4 + 2H_2O \Delta H_r^\circ = -165 \frac{kJ}{mol}$ <i>CO₂ hydrogenation</i> $H_2 + CO_2 \rightleftharpoons CO + H_2O \Delta H_r^\circ = 41.2 \frac{kJ}{mol}$ <i>RWGS</i> $CO + 2H_2 \rightleftharpoons CH_4 + H_2O \Delta H_r^\circ = -206 \frac{kJ}{mol}$ <i>CO hydrogenation</i> Not considered in this review, as the thermodynamic conversion is already high under such conditions and is very rarely studied in the literature for membrane reactors.	$CH_4 + H_2O \rightleftharpoons 3H_2 + CO \Delta H_r^\circ = 206 \frac{kJ}{mol}$ <i>Steam Reforming</i> $CO + H_2O \rightleftharpoons H_2 + CO_2 \Delta H_r^\circ = -41.2 \frac{kJ}{mol}$ <i>WGS</i>
FT	$H_2 + CO_2 \rightleftharpoons CO + H_2O \Delta H_r^\circ = 41.2 \frac{kJ}{mol}$ <i>RWGS</i> $CO + 2H_2 \rightleftharpoons (-CH_2-)_n + H_2O \Delta H_r^\circ \approx -195 \frac{kJ}{mol}$	Not considered in this review. FT fuels (e.g. diesel or gasoline) are meant to be used for combustion applications. Alternatively it can be useful to crack some derived product (e.g. propane) [13].

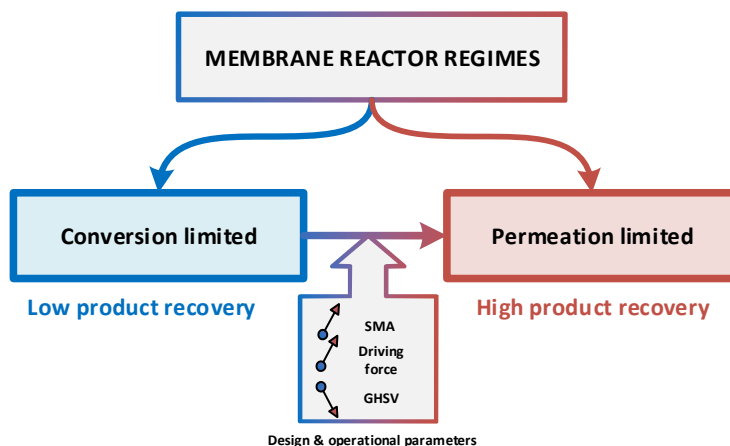


Figure 2-10: Membrane reactor regimes

2.4.1. E-Chemical production

2.4.1.1. Methanol synthesis

Traditional methanol synthesis relies on Cu-based catalysts like Cu/ZnO/Al₂O₃, but their effectiveness decreases when pure CO₂ is used as the sole carbon source. To overcome this challenge, researchers have explored alternative Cu-based formulations with various oxide supports and promoters, such as ZrO₂, CeO₂, Fe₂O₃, SiO₂, and TiO₂ [91,104]. Pioneering work by Struis et al. (1996) [112] firstly introduced the application of membrane reactors to improve methanol conversion, conducting experiments with a lithiated Nafion™ membrane at 200 °C. Building on this, more thermally resistant membranes, such as zeolites (e.g. NaA [53], A [54], LTA [55]) have been developed, focusing on removing either methanol [55] or water [53] from the reaction environment thus alleviating thermodynamic limitations. **Figure 2-11** highlights some of the recent progress in this area. Notably, Li et al. (2020) [97] developed a sodium ion-gated water-conduction nanochannel membrane using NaA zeolite crystals, achieving a more than 200% improvement in yield and conversion by removing 95% of water in situ, resulting in very high-purity methanol at 95.9 wt%. The performance of this membrane, with high selectivities of H₂O over H₂, CO, and methanol (H₂O/H₂ = 190, H₂O/CO = 170, H₂O/MeOH = 80), significantly contributed to these results. Similarly, Seshimo et al. (2021) [113] achieved substantial conversion increases and methanol purity of around 95% by targeting methanol separation with a zeolite membrane, boasting an impressive H₂O/MeOH selectivity of approximately 2000. Li and Tsotsis et al. (2019) [114] proposed a novel approach using tetra ethylene glycol dimethyl ether as a sweep gas, selectively absorbing methanol while preventing the passage of permanent gases. Although this method showed more modest conversion gains, it holds potential with improved design, particularly regarding membrane area per bed volume and sweep flow rate

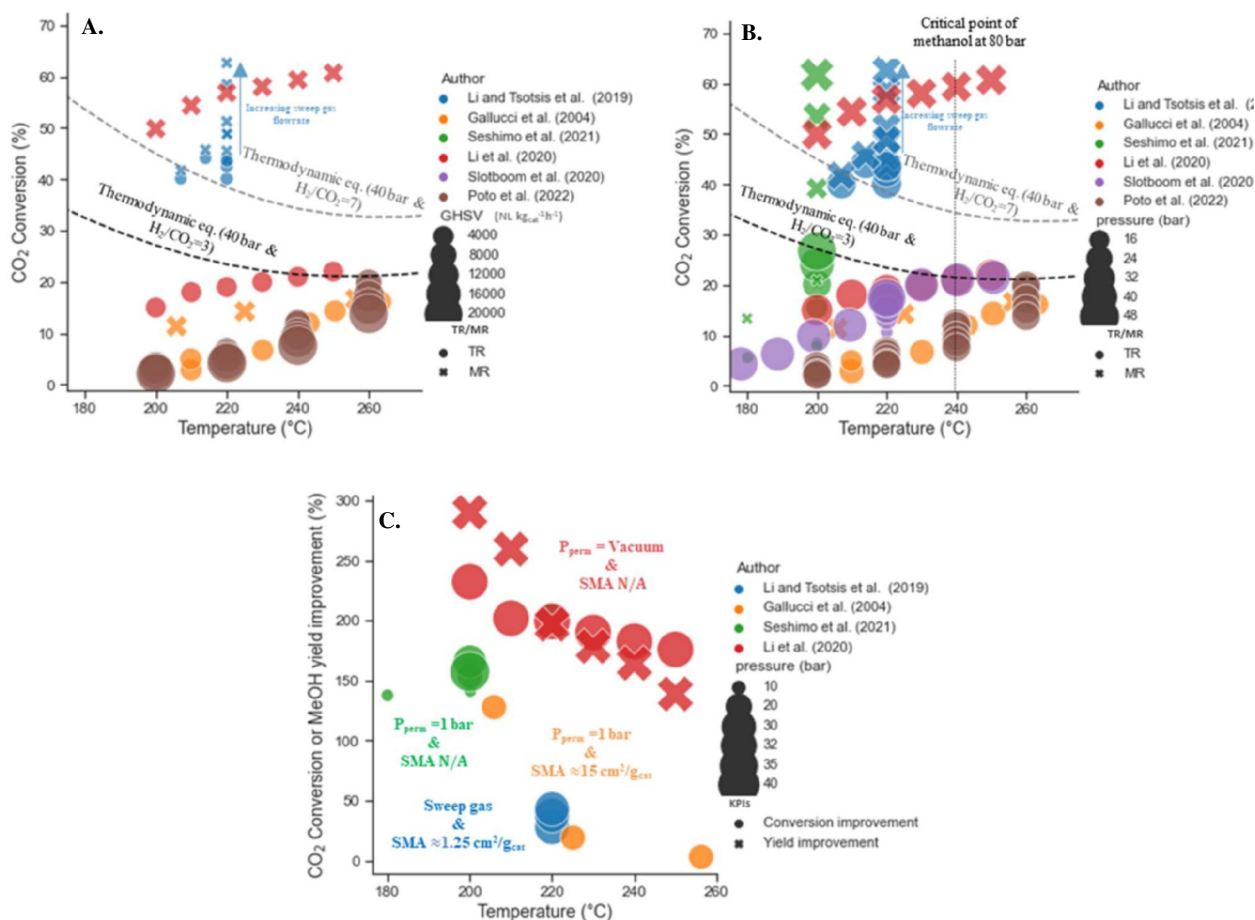


Figure 2-11: Literature data about methanol synthesis (A) Effect of temperature and GHSV on CO₂ conversion for both MRs (cross symbols) and TRs (circle symbols) (B) Effect of temperature and pressure on catalytic CO₂ conversion for both MRs (cross symbols) and TRs (circle symbols) (C) CO₂ conversion (circle symbols) & Methanol yield improvement (cross symbols) as a function of temperature and pressure [90, 97, 113-116].

2.4.1.2. DME synthesis

Dimethyl ether (DME) is traditionally produced via an indirect process involving methanol dehydration. However, integrating methanol synthesis and dehydration into a single reactor using a bifunctional catalyst with selective membranes may offer a more efficient and streamlined process with significantly improved conversion rates. Typically, this bifunctional catalyst combines a methanol synthesis catalyst with an acid catalyst for methanol dehydration, such as γ -Al₂O₃ or zeolites like HZSM-5, FER, and MOR [104]. Several studies have explored one-step

DME synthesis in membrane reactors, with their findings summarized in **Figure 2-12**. Rodriguez-Vega et al. (2021) [91] were among the first to demonstrate the potential of in-situ water removal to enhance DME synthesis by integrating a hydrophilic LTA membrane with a Si/Al ratio of 1 and using a CuO-ZnO-ZrO₂/SAPO-11 catalyst. However, due to high operating temperatures and the aforementioned challenges, the performance improvement they achieved was modest. Notably, Dong et al. (2022) [104] achieved a 2-3 fold increase in conversion and a sixfold increase in DME yield at 300 °C by using a system that combined selective NaA zeolite membranes with bifunctional Cu-ZnO-ZrO₂-Al₂O₃/HZSM-5 catalysts. The NaA zeolite membrane exhibited high selectivity for H₂O over CO₂, H₂, CO, and methanol (with selectivities of 551, 190, 170, and 80, respectively, under 21 bar at 250 °C). In contrast, Poto et al. (2023) [99] employed a carbon molecular sieve membrane with much lower selectivity (H₂O/CO₂, H₂O/H₂, H₂O/CO, and H₂O/MeOH selectivities of 2.37, 2.06, 3.99, and 2.39, respectively, at 200 °C). They observed a similar enhancement in conversion but a significantly lower increase in DME yield (67%). Above 200 °C, the DME yield became negligible and was actually worse than in a traditional reactor at 300 °C, due to the intensified reverse water-gas shift (RWGS) reaction under these conditions, which led to a CO yield 2.7 times higher than that of a traditional packed-bed reactor at 260 °C. This effect was not reported by Dong et al. (2022), possibly because they used a fivefold higher proportion of acid catalyst. The authors also observed that even a slight positive pressure differential caused nearly all the gas to permeate from the reaction zone to the permeation zone, leading to lower performance compared to the traditional reactor. This highlights the need for careful tuning of the driving force for the specific membrane used.

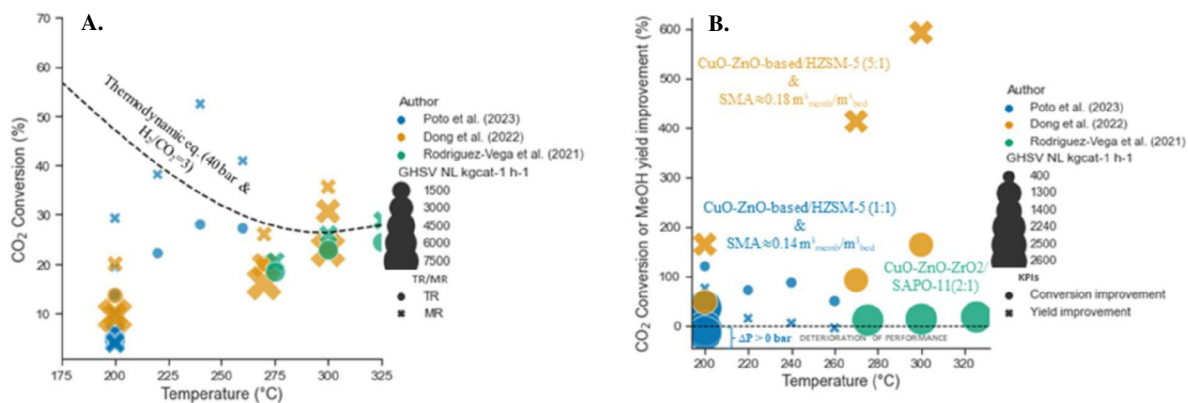


Figure 2-12: Literature data on DME synthesis (A) Effect of temperature and GHSV on CO₂ conversion for both MRs (cross symbols) and TRs (circle symbols) (B) CO₂ conversion (circle symbols) & Methanol yield improvement (cross symbols)-as a function of temperature and GHSV. These results are reported for identical stoichiometric proportion of H₂/CO₂=3 and operating pressure of ~40 bar [91, 99, 104]

2.4.1.3. Fischer Tropsch and Reverse water gas shift

The Fischer-Tropsch (FT) process predominantly utilizes iron (Fe), cobalt (Co), and ruthenium (Ru) catalysts, with Ru being the most active [117]. For CO₂ conversion, FT synthesis often involves a multi-step system where CO₂ is first converted to syngas via the Reverse Water Gas Shift (RWGS) reaction, followed by the FT process. Membrane reactor configurations have shown potential in integrating these steps, as summarized in **Table 2-5**. Regarding FT, membrane reactors, particularly in a distributor configuration, have demonstrated precise control over the H₂/CO ratio along the reactor, improving selectivity toward longer-chain hydrocarbons. However, Liuzzi et al. (2016) [58] reported a decrease in conversion and H₂ permeation due to membrane deactivation caused by adsorbed CO species and pore blockage from wax formation (C₂₀+). These challenges could be mitigated by employing alternative H₂-selective membrane types (cf. section 2.3.2). Escorihuela et al. (2021) [57] for instance, demonstrated that a Cu protective membrane layer effectively mitigated these issues, maintaining stable conversion rates. Additionally, the removal of water vapor during the reaction using hydrophilic membranes has been studied extensively [118]. Hyeon et al. (2023) [96] demonstrated that using a polybenzoxazole membrane integrated with an Fe catalyst suppressed side reactions by removing produced H₂O. This significantly improved hydrocarbon selectivity, reducing CO₂ production by the WGS reaction from 47.9% to 15.1%. Several studies have demonstrated that integrating water-selective membranes in the RWGS process can shift the equilibrium favorably [95-96,100]. While the RWGS reaction is essential for CO₂ conversion, direct one-step FT synthesis is also gaining attention [119-121] and could be an area where membrane reactor have a role to play.

Table 2-5: Recent studies related to FT and RWGS with membrane reactors

Reaction	Author	Membrane role	Membrane & support	Catalyst	Driving force	Operating conditions	Conversion / Yield	Selectivity
FT	Escorihuela et al. (2021) [57]	Distributor	Cu-protective layer (0.5 -1 μm) deposited onto the Pd-based 100 μm -Self supported	Bifunctional CoRu/Al ₂ O ₃ -β zeolite	Pressure gradient ΔP=19-23 bar & N ₂ sweep gas	T= 250 °C P=20 bar H ₂ /CO= 2 SV=29300 NL kg _{cat} ⁻¹ h ⁻¹	At H ₂ /CO =2: $X_{CO}^{MR} \approx 30\%$ $X_{CO}^{TR} \approx 41\%$	At H ₂ /CO =2: $frac_{C_6-C_{12}}^{MR} \approx 50\%$ $frac_{C_6-C_{12}}^{TR} \approx 46\%$
FT	Liuzzi et al. (2016) [58]	Distributor	PdAg 13–15% of Ag (ceramic) 3.2 μm	B doped Ru/TiO ₂ (3 wt% Ru; B:Ru 1:1 at),	Pressure gradient ΔP=2 bar & He sweep gas	T= 280 °C P=10 bar H ₂ /CO= 2 SV=7500 NL kg _{cat} ⁻¹ h ⁻¹	At H ₂ /CO =1: $X_{CO}^{MR} \approx 39\%$ (initial) $X_{CO}^{MR} \approx 15\%$ (at 15 hour) $X_{CO}^{TR} \approx 10\%$ At H ₂ /CO =2: $X_{CO}^{TR} \approx 40\%$	At H ₂ /CO =1: $frac_{C_{10}^{+}}^{MR} \approx 49\%$ At H ₂ /CO =2: $frac_{C_{10}^{+}}^{TR} \approx 17\%$
FT	Hyeon et al. (2023) [96]	Extractor	Polybenzoxazole membrane	K ₄ Fe ₁₀₀ Cu ₆ Al ₁₆ catalyst with SiC	Sweep gas of same composition as feed SW=1	T= 320 °C P=1 bar H ₂ /CO= 2 SV=1800 NL kg _{cat} ⁻¹ h ⁻¹	-	-
RWGS	Lee et al. (2021) [95]	Extractor	Polyimide	Cu/ZnO/Al ₂ O ₃	Sweep gas of same composition as feed SW=1-8	T= 200-250 °C P=1 bar H ₂ /CO ₂ =1 SV=225 NL kg _{cat} ⁻¹ h ⁻¹	$X_{CO_2}^{MR} \approx 28\%$ $X_{CO_2}^{TR} \approx 24\%$	-

RWGS	Sakai et al. (2022) [100]	Extractor	Hydrophilic ZSM-5 membrane	Cu/ZnO/Al ₂ O ₃	Sweep gas of same composition as feed	T= 242-336 °C P=1 bar H ₂ /CO ₂ =1/3	$Y_{CO}^{MR} \approx 24\%$ $Y_{CO}^{TR} \approx 21\%$	-
RWGS	Hyeon et al. (2023) [96]	Extractor	Polybenzoxazole membrane	CuO/ZnO/Al ₂ O ₃ catalyst (ShiftMax210, Clariant)	H ₂ /CO ₂ stream was used as the sweep gas SW=1	T= 200-250 °C P=1 bar H ₂ /CO ₂ =1 SV=225 NL kg _{cat} ⁻¹ h ⁻¹	$X_{CO_2}^{MR} \approx 32\%$ $X_{CO_2}^{TR} \approx 20\%$	-

2.4.2. Hydrogen restitution

In the context of hydrogen production through cracking and steam reforming of various feedstocks, the process becomes increasingly thermodynamically limited as it transitions from methanol reforming to ammonia cracking, and finally to methane reforming under typical process conditions. Palladium-based membranes perform exceptionally well at higher temperatures, however, their effectiveness diminishes in low-temperature reactions like methanol reforming. This is due to a mismatch between the optimal operating conditions of the reaction and those of the membrane. In such cases, the change in conversion is less pronounced, particularly for reactions approaching complete conversion, as shown in **Figure 2-13**, leading to reduced hydrogen recovery. As an alternative to palladium membranes, porous membranes have been proposed (cf. section 2.3.2) While these membranes are relevant for Internal Combustion Engines (ICE), they may require additional downstream purification, particularly for applications in Proton Exchange Membrane Fuel Cells (PEMFCs). For PEMFCs, it is critical that the anode feed gas contains carbon monoxide (CO) at concentrations below 10 ppm and ammonia levels below 0.1 ppm to prevent poisoning of the platinum-based anode catalyst. This section compares results obtained from three dehydrogenation systems-methanol, methane, and ammonia reforming-while highlighting the impact of specific operating conditions and reactor designs (cf. **Figure 2-14**).

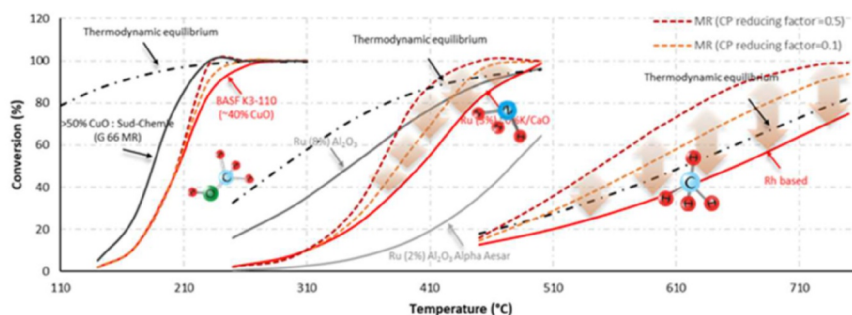
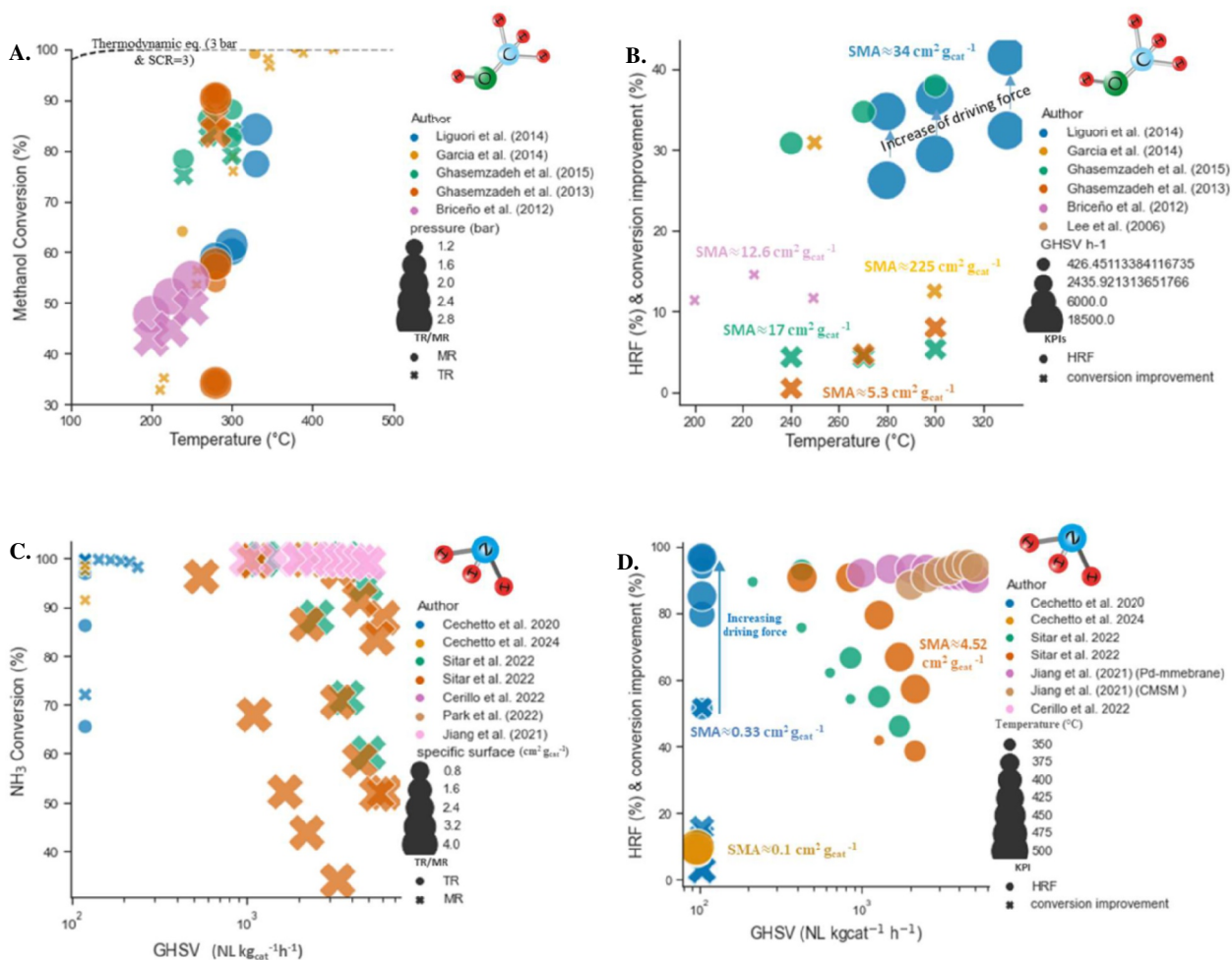


Figure 2-13: Comparison of TR and MR at 10 bar with the same space velocity and specific membrane area: Methanol reforming (SCR=1) [122, 123], Ammonia cracking [124, 125], Methane reforming (SCR=3) [126], modelled developed in [127], thermodynamic equilibriums plotted using the Peng-Robinson Equation of State using Aspen PlusTM software. The MR curves are plotted for two permeations reducing factors accounting for concentration polarization limitations

Methanol reforming typically utilizes Cu-based catalysts similar to those used in methanol synthesis. Briceño et al. (2012) [76] employed a carbon molecular sieve membrane (CMSM) with a modest H_2 -to- N_2 selectivity of 5.5 at 25 °C and a permeance of approximately 10^{-7} mol/m²/Pa/s, achieving hydrogen purities between 83.1% and 87.3% on the permeate side, with a maximum conversion improvement of 15%. Ghasemzadeh et al. (2015) [7] used a more efficient microporous silica membrane, offering a hydrogen-to-nitrogen selectivity of 26 at 25 °C and a permeance of 10^{-6} mol/m²/Pa/s, resulting in a modest enhancement of around 5%, likely due to higher space velocity and lower pressure drop across the membrane, with hydrogen recovery reaching 38% at 300 °C. García-García et al. (2014) [6], using a Pd-based membrane with a hydrogen-to-argon selectivity exceeding 5000, reported up to 34% higher conversion at 250 °C compared to conventional reactors, with hydrogen recovery of 50%. Liguori et al. [74], while not directly comparing with traditional reactors, achieved an 85% methanol conversion and produced highly pure hydrogen with a CO content below 10 ppm. This was accomplished using the highest space velocity among the reviewed studies and a membrane area per unit mass of catalyst of 34 cm²/g.

Ammonia cracking in membrane reactors typically uses ruthenium-based catalysts [128], though cobalt and nickel catalysts have also been explored [79]. The increase in NH_3 conversion can be attributed to shifts in thermodynamic equilibrium due to selective H_2 separation, or alternatively, to a kinetic enhancement effect. The removal of H_2 through the membrane walls reduces its inhibitory effect on the forward kinetics of NH_3 decomposition, thereby improving conversion. Cechetto et al. (2021) [128] achieved notable performance using a double-skin palladium membrane, with a maximum 50% enhancement compared to a conventional reactor and 93% hydrogen recovery under vacuum conditions, using a very low space velocity and a small specific membrane area of approximately 0.33 cm²/g_{cat}. They observed a gradual improvement in purity with increasing GHSV, reaching between 99.978% and 99.989%. However, in a subsequent study, the same authors used a carbon molecular sieve membrane under similar operating conditions and catalyst but achieved a much lower hydrogen recovery, with a maximum of 9.8%. This reduction in performance could be attributed to the even lower SMA of approximately 0.1 cm²/g_{cat} [77]. Jiang et al. (2021) [72] compared three types of membranes: modified MFI zeolite, carbon molecular sieve, and Pd/Ag. At 400 °C, the CMSM exhibited a permeance of $2.5 \cdot 10^{-7}$ mol/m²/Pa/s, while the palladium membrane showed four times higher permeance. The H_2/N_2 selectivity ranged from 90 to nearly infinite between the different membranes. Their tests, conducted with a significantly higher SMA of approximately 4.5 cm²/g_{cat}, showed no substantial drop in performance with increasing GHSV. NH_3 conversion exceeded 99%, with H_2 recovery over 90% under pressurized NH_3 feed at 7 bar. In terms of purity, the corresponding average H_2 and NH_3 concentrations in the permeate for the modified MFI membrane, CMS membrane, and Pd/Ag membrane were 87.5% and 4.1%, 97.2% and 1.2%, and 100% and less than 10 ppb, respectively.



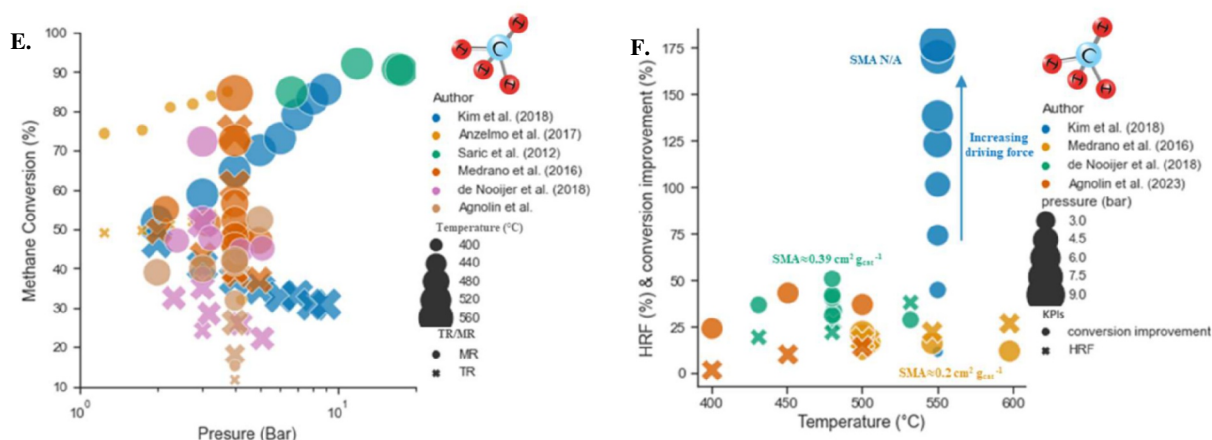


Figure 2-14: Focus on the impact of operating conditions & design aspects for 3 dehydrogenation systems: A-B Methanol reforming C-D Ammonia cracking E-F Methane reforming

Methane reforming with membrane reactors has shown high activity with noble metals like Rh, Ru, Pt, and Pd, with Rhodium (Rh) generally offering the best performance. Kim et al. (2018) [73] investigated a Pd-supported PSS membrane reactor using a commercial Ru-based catalyst. Their study demonstrated that increasing the pressure difference significantly improved methane conversion, achieving up to 82% at a 9 bar pressure difference, although this reduced the equilibrium conversion. Hydrogen purity remained consistently between 92.4% and 97%. Sarić et al. (2012) [129] explored a supported alumina Pd membrane coupled with a nickel-based catalyst at pressures up to 26 bar. They observed a maximum methane conversion of 92% at 12 bar, beyond which conversion decreased due to thermodynamic limitations. The reactor maintained stable performance for nearly 1100 hours, though hydrogen purity was lower (80-92%), likely due to defects, leaks, and impurities from high pressure. Other studies reported more modest conversion at lower pressure conditions, where the performance improvement with increasing pressure is less apparent. For example, De Nooijer et al. (2018) [12] used a ceramic-supported palladium membrane in a fluidized bed, achieving a 50% maximum conversion increase, with hydrogen purity ranging from 97.34% to 99.88%. Agnolin et al. (2024) [102] integrated a Pd membrane on porous Hastelloy-X, ensuring 99.3% hydrogen purity at 500 °C and 4 bar, with a 43% conversion enhancement. They observed a maximum conversion enhancement of 43%. Anzelmo et al. (2017) [8] utilized a Pd/PSS membrane in a nickel bed, varying reaction pressures modestly between 150 and 300 kPa. Despite the lower pressures, they achieved an 84% methane conversion and 82% hydrogen recovery, comparable to studies at higher pressures. The Pd/PSS membrane reactor operated for over 700 hours, achieving nearly 100% hydrogen purity. Notably, compared to other applications, particularly methanol reforming, a much smaller membrane area is needed to achieve an increase in conversion.

2.5. Process environments

2.5.1. Hydrogen restitution

As mentioned in the introduction, the processing of methane, methanol, and ammonia (illustrated in **Figure 2-15**) involves multiple stages, each with unique requirements, particularly in terms of heat management. These multi-step processes can significantly impact the system's power density and response times, emphasizing the need to simplify fuel processors and balance-of-plant components to reduce costs. The integration of membrane reactor technology into these processes offers several benefits, including improved performance at lower temperatures compared to conventional methods, reduced or eliminated need for downstream separation, and minimized space requirements, a critical advantage in space-constrained applications. Different process architectures can be tailored to the specific environment. Systems can be electrically heated where green electricity is available, such as in hydrogen refueling scenarios, or they may require a catalytic burner for reactor heating, as in onboard PEM fuel cell engines or genset markets. In such environments, a fraction of the hydrogen produced can be used to meet the energy demands of the entire process, for instance, by utilizing the hydrogen that is not recovered in the permeate. Thermodynamically, ammonia decomposition requires around 15-20% of the hydrogen's calorific value. Therefore, with H₂ recoveries of approximately 80-85%, the energy content of the retentate is sufficient to satisfy the endothermic requirements for NH₃ decomposition [61]. The heat required to sustain hydrogen production could also be supplied by external sources such as gas turbines, high-temperature fuel cells exhausts. Additionally, when high-purity hydrogen is needed, such as for low temperature fuel cell applications, it may be necessary to remove impurities like NH₃ or CO. These impurities can result from membrane defects, sealing issues, or the use of less selective membranes. For instance, Sitar et al. (2022) [54] demonstrated that zeolite clinoptilolite is an effective adsorbent for reducing ammonia in the permeate stream to the ppb levels required by PEMFCs. From a system efficiency perspective, several sources, primarily process systems engineering studies and some commercial claims, have reported relevant values. Since the permeate is typically produced at low pressures, mechanical compression may be required for storage, depending on the application. For instance, fuel cells may require pressures up to 10 bar, vehicles up to 350 bar, and hydrogen storage systems up to 700 bar. **Figure 2-16** illustrates the impact of H₂ delivery pressure on system efficiency across various feedstocks. In terms of absolute values, the technical results are generally consistent. For instance, for biogas reforming, Ongis et al. (2025) [142] obtained achieves an efficiency of 62.7%, which aligns closely with the 66.1% reported by Di Marcoberardino et al. (2018) [143] for a similar system. Comparisons between membrane reactor (MR) systems and traditional reactors (TR) with downstream purification methods, such as pressure swing adsorption (PSA), show that MRs generally offer superior performance. For example, latter in this thesis (**Chapter 4**) it will be demonstrated that integrating a membrane reactor for ammonia cracking improved efficiency by over 25%, while Di Marcoberardino et al. (2018) [143] found that a membrane reactor increased biogas reforming efficiency by more than 20 percentage points compared to TR systems. Across various feedstocks, it will be seen in **Chapter 3** for hydrogen production at 1 bar, methanol reforming systems exhibit the lowest efficiency (57%), followed by methane (77%), while ammonia reforming achieves the highest efficiency at 92%. However, it is important to note that methanol's

lower reforming temperatures present several advantages, including reduced heat losses, an aspect often underestimated in process simulations, along with decreased insulation requirements and simplified thermal management for the integrated system [130]. Cerrillo et al. (2021) [61] observed, in the context of ammonia cracking, a significant variation in the required energy as a function of the permeate pressure of H_2 , revealing that the efficiency drop is less pronounced when the permeate pressure increases. In scenarios where green electricity is available, electrochemical separation and compression using proton-conducting ceramic membranes, alongside electrical heating technologies, hold promise for further process intensification and improvements in energy efficiency.

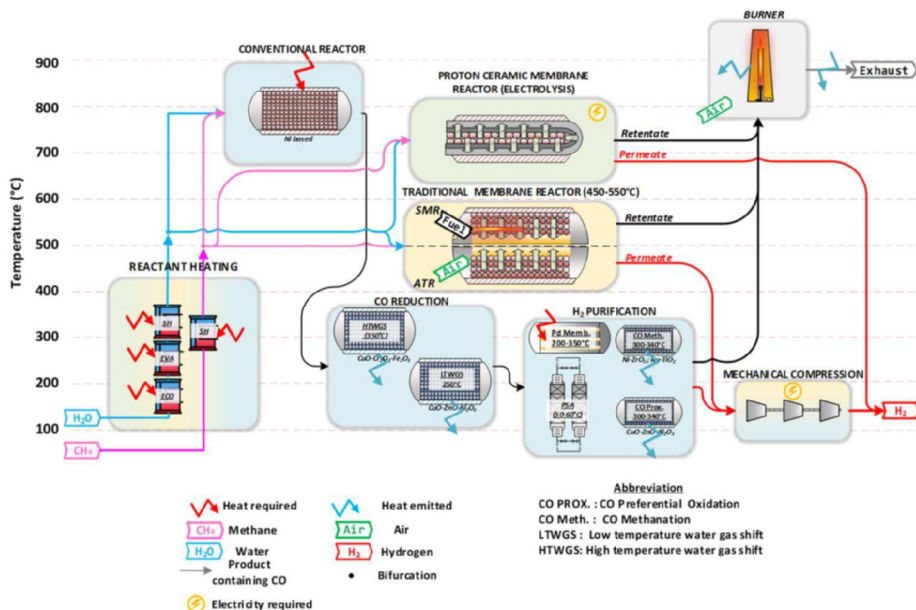


Figure 2-15: Overview of fuel processing steps with indication of their operational temperature taking as example methane reforming to produce pure hydrogen. The presence of a burner is really dependent on the operating conditions / process whether electric heating is implemented is deployed or not

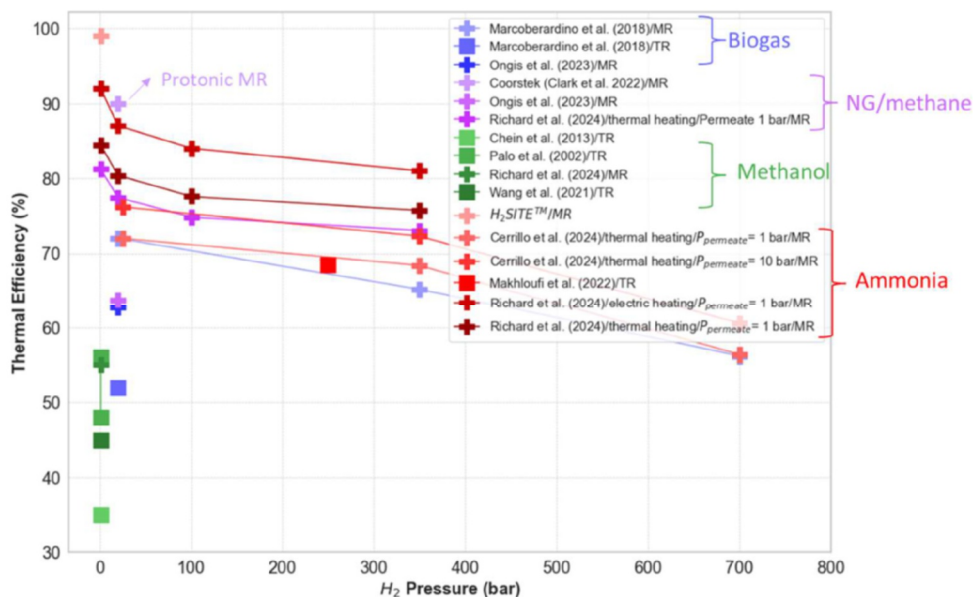


Figure 2-16: H_2 production efficiencies reported from various sources as a function of hydrogen delivery pressure e.g. fuel cells (up to 10 bar), vehicles (up to 350 bar), and hydrogen storage (up to 700 bar). Note: these overall efficiencies are dependent on process assumptions (e.g. compressor efficiencies, compression ratios, process layout considered etc.) [61,127, 131-135]- Square symbols refers to TRs and cross symbols refers to MRs

2.5.2. Fuel production

Efficiency gains from implementing membrane reactors in e-fuel production have been modest, with limited studies addressing process-level impacts. For example, Dietrich et al. [136] reported a ~3% increase in energetic efficiency for methanol synthesis compared to traditional reactors (excluding the balance of plant). Similarly, Richard et al. [137] observed an 8% performance improvement in ammonia synthesis using membrane reactors. Hamed et al. [138] demonstrated significant utility savings in membrane-based DME synthesis: 1.5% in power, 44.5% in heating, and 69.4% in refrigerants, but did not account for the global efficiency loss from additional hydrogen sweep gas, which could offset power savings. The oxidative coupling of methane (OCM) could presents a promising addition to Power-to-X (PtX) strategies, utilizing low-cost methane and electrolysis by-product oxygen to produce high-value chemicals like ethylene, a key polymer precursor [139]. OCM faces challenges such as competing reactions and hotspot formation in conventional reactors, limiting ethylene yields to ~15% [140]. Membrane reactors can address these issues [141] by gradually supplying oxygen, enhancing selectivity, reducing overoxidation, and improving heat management. Studies suggest that integrating membranes into OCM reactors can boost performance and reduce energy use by 25–30% compared to naphtha steam cracking, positioning OCM as a competitive alternative for sustainable chemical production [139]

2.6. Conclusion

This chapter aimed to provide a comprehensive overview of the evolving design and applications of membrane reactors in addressing key reaction engineering challenges in the framework of Power-to-X such as equilibrium limitations, catalyst deactivation, and process simplifications. By employing a top-down approach, the study highlighted critical research gaps and technological challenges that must be overcome to make membrane reactors a viable solution for industrial applications.

- The shared attributes commonly encountered in membrane reactor (MR) design, ranging from catalyst configurations to membrane material were analyzed. The potential for advanced integration in membrane reactor technology was highlighted, with for example additive manufacturing enabling precise modifications to reactor parameters such as porosity and shape, addressing current heat and mass transfer challenges as well as very detailed structure optimization. Combined with electric heating, these innovations could result in compact and flexible technologies well-suited for the Power-to-X framework. Future research should focus on developing robust and cost-effective and scalable membranes with high temperature and chemical resistance to expand their applicability.
- Laboratory studies often show improved conversion in membrane reactors under specific conditions, but comparing results across studies is difficult due to complex interactions between the membrane, catalyst, and operating parameters. Despite similar temperature and pressure conditions, performance variations are mainly influenced by factors like membrane area, space velocity, and driving force. Care should be taken when comparing experimental results together. Conversion enhancements observed in the literature include up to 250% for methanol synthesis, ~200% for DME synthesis, ~30% for methanol reforming (with a large specific membrane area), ~30% for ammonia decomposition, and up to ~175% for methane reforming. However, palladium membranes may not be ideal for processes like methanol reforming and Fischer-Tropsch synthesis due to incompatible reaction conditions and membrane performance. Polymeric membranes type commonly judged unsuitable because they have a low temperature resistance are now employed in a few studies with promising results in process environments. Future laboratory-scale research could also benefit from exploring reaction systems that have received limited attention, such as ammonia synthesis or direct Fischer-Tropsch synthesis, to further expand the scope of membrane reactor applications.
- At the process scale, while some studies address fuel processing in membrane reactors, data on e-chemical production remains limited compared to their laboratory demonstrations and requires further investigation. Comparisons between membrane reactor (MR) systems and traditional reactors (TR) with downstream purification, such as pressure swing adsorption (PSA), indicate that MRs have the potential to outperform TRs by over 20%. Among feedstocks, hydrogen production from ammonia is the most efficient, followed by methane and methanol reforming. These efficiencies are influenced by factors such as process layout, heating method (thermal vs. electric), permeate pressure,

and H₂ delivery pressure. Regarding techno-economic results, a few studies suggest that MRs have the potential to outperform TRs by approximately 10%. However, further system-level research is needed, particularly for e-chemical production, to benchmark membrane reactors against traditional systems and explore innovative reactor configurations. Additionally, in scenarios where green electricity is available, a detailed comparison of the performance of protonic membrane reactors versus palladium membrane reactors would be particularly insightful.

2.7. References

- [1] F. Gallucci, E. Fernandez, P. Corengia, M. van Sint Annaland, Recent advances on membranes and membrane reactors for hydrogen production, *Chemical Engineering Science* 92 (2013) 40–66. <https://doi.org/10.1016/j.ces.2013.01.008>.
- [2] S. Hafeez, S.M. Al-Salem, G. Manos, A. Constantinou, Fuel production using membrane reactors: a review, *Environ Chem Lett* 18 (2020) 1477–1490. <https://doi.org/10.1007/s10311-020-01024-7>.
- [3] S.M. Jokar, A. Farokhnia, M. Tavakolian, M. Pejman, P. Parvasi, J. Javanmardi, F. Zare, M.C. Gonçalves, A. Basile, The recent areas of applicability of palladium based membrane technologies for hydrogen production from methane and natural gas: A review, *International Journal of Hydrogen Energy* 48 (2023) 6451–6476. <https://doi.org/10.1016/j.ijhydene.2022.05.296>.
- [4] V. Cechetto, L. Di Felice, F. Gallucci, Advances and Perspectives of H₂ Production from NH₃ Decomposition in Membrane Reactors, *Energy Fuels* 37 (2023) 10775–10798. <https://doi.org/10.1021/acs.energyfuels.3c00760>.
- [5] O. Jazani, J. Bennett, S. Liguori, Carbon-low, renewable hydrogen production from methanol steam reforming in membrane reactors – a review, *Chemical Engineering and Processing - Process Intensification* (2023) 109382. <https://doi.org/10.1016/j.cep.2023.109382>.
- [6] F.R. García-García, S.C. Tsang, K. Li, Hollow fibre based reactors for an enhanced H₂ production by methanol steam reforming, *Journal of Membrane Science* 455 (2014) 92–102. <https://doi.org/10.1016/j.memsci.2013.12.070>.
- [7] K. Ghasemzadeh, A. Aghaeinejad-Meybodi, M.J. Vaezi, A. Gholizadeh, M.A. Abdi, A.A. Babaluo, M. Haghighi, A. Basile, Hydrogen production via silica membrane reactor during the methanol steam reforming process: experimental study, *RSC Adv.* 5 (2015) 95823–95832. <https://doi.org/10.1039/C5RA14002A>.
- [8] B. Anzelmo, J. Wilcox, S. Liguori, Natural gas steam reforming reaction at low temperature and pressure conditions for hydrogen production via Pd/PSS membrane reactor, *Journal of Membrane Science* 522 (2017) 343–350. <https://doi.org/10.1016/j.memsci.2016.09.029>.
- [9] Air Liquide, Acquisition of the firm Lurgi, (2007). <https://www.airliquide.com/group/press-releases-news/2007-04-17/acquisition-firm-lurgi> (accessed November 16, 2024).
- [10] V. Dieterich, A. Buttler, A. Hanel, H. Spliethoff, S. Fendt, Power-to-liquid *via* synthesis of methanol, DME or Fischer–Tropsch-fuels: a review, *Energy Environ. Sci.* 13 (2020) 3207–3252. <https://doi.org/10.1039/D0EE01187H>.
- [11] C. Busse, H. Freund, W. Schwieger, Periodic open cellular structures (POCS) as catalyst support for intensified heat transport in the partial oxidation of methanol to formaldehyde, *Chemical Engineering Journal* 489 (2024) 151139. <https://doi.org/10.1016/j.cej.2024.151139>.
- [12] N. de Nooijer, F. Gallucci, E. Pellizzari, J. Melendez, D.A. Pacheco Tanaka, G. Manzolini, M. van Sint Annaland, On concentration polarisation in a fluidized bed membrane reactor for

- biogas steam reforming: Modelling and experimental validation, *Chemical Engineering Journal* 348 (2018) 232–243. <https://doi.org/10.1016/j.cej.2018.04.205>.
- [13] C. Brenicio, L. Di Felice, F. Gallucci, Fluidized Bed Membrane Reactor for the Direct Dehydrogenation of Propane: Proof of Concept, *Membranes* 12 (2022) 1211. <https://doi.org/10.3390/membranes12121211>.
- [14] C. Busse, H. Freund, W. Schwieger, Intensification of heat transfer in catalytic reactors by additively manufactured periodic open cellular structures (POCS), *Chemical Engineering and Processing - Process Intensification* 124 (2018) 199–214. <https://doi.org/10.1016/j.cep.2018.01.023>.
- [15] P. Yan, Foam structured membrane reactor for distributed hydrogen production, *Journal of Membrane Science* (2022).
- [16] R. Dittmeyer, T. Boeltken, P. Piermartini, M. Selinsek, M. Loewert, F. Dallmann, H. Kreuder, M. Cholewa, A. Wunsch, M. Belimov, S. Farsi, P. Pfeifer, Micro and micro membrane reactors for advanced applications in chemical energy conversion, *Current Opinion in Chemical Engineering* 17 (2017) 108–125. <https://doi.org/10.1016/j.coche.2017.08.001>.
- [17] M. Klumpp, A. Inayat, J. Schwerdtfeger, C. Körner, R.F. Singer, H. Freund, W. Schwieger, Periodic open cellular structures with ideal cubic cell geometry: Effect of porosity and cell orientation on pressure drop behavior, *Chemical Engineering Journal* 242 (2014) 364–378. <https://doi.org/10.1016/j.cej.2013.12.060>.
- [18] Horneber, T, Thermo-fluid dynamic characterization and technical optimization of structured open-cell metl foam by means of numerical simulation, Friedrich Alexander Universitat Erlangen Nurnberg, 2015.
- [19] S. Meinicke, K. Dubil, T. Wetzels, B. Dietrich, Characterization of heat transfer in consolidated, highly porous media using a hybrid-scale CFD approach, *International Journal of Heat and Mass Transfer* 149 (2020) 119201. <https://doi.org/10.1016/j.ijheatmasstransfer.2019.119201>.
- [20] R. Balzarotti, A. Bisaccia, M.C. Tripi, M. Ambrosetti, G. Groppi, E. Tronconi, Production and characterization of copper periodic open cellular structures made by 3D printing-replica technique, *Jnl Adv Manuf & Process* 2 (2020). <https://doi.org/10.1002/amp2.10068>.
- [21] M. Lämmermann, G. Horak, W. Schwieger, H. Freund, Periodic open cellular structures (POCS) for intensification of multiphase reactors: Liquid holdup and two-phase pressure drop, *Chemical Engineering and Processing - Process Intensification* 126 (2018) 178–189. <https://doi.org/10.1016/j.cep.2018.02.027>.
- [22] A. Chaudhari, P. Ekade, S. Krishnan, Experimental investigation of heat transfer and fluid flow in octet-truss lattice geometry, *International Journal of Thermal Sciences* 143 (2019) 64–75. <https://doi.org/10.1016/j.ijthermalsci.2019.05.003>.
- [23] F.M. Baena-Moreno, M. González-Castaño, J.C. Navarro de Miguel, K.U.M. Miah, R. Ossenbrink, J.A. Odriozola, H. Arellano-García, Stepping toward Efficient Microreactors for CO₂ Methanation: 3D-Printed Gyroid Geometry, *ACS Sustainable Chem. Eng.* 9 (2021) 8198–8206. <https://doi.org/10.1021/acssuschemeng.1c01980>.
- [24] Z. Cheng, R. Xu, P.-X. Jiang, Morphology, flow and heat transfer in triply periodic minimal surface based porous structures, *International Journal of Heat and Mass Transfer* 170 (2021) 120902. <https://doi.org/10.1016/j.ijheatmasstransfer.2021.120902>.
- [25] A. Ahmed Qureshi, S. Addin Burhan Al-Omari, E. Elnajjar, O. Al-Ketan, R. Abu Al-Rub, Architected lattices embedded with phase change materials for thermal management of high-power electronics: A numerical study, *Applied Thermal Engineering* 219 (2023) 119420. <https://doi.org/10.1016/j.applthermaleng.2022.119420>.
- [26] Z.A. Qureshi, S. Addin Burhan Al-Omari, E. Elnajjar, O. Al-Ketan, R.A. Al-Rub, On the effect of porosity and functional grading of 3D printable triply periodic minimal surface (TPMS) based architected lattices embedded with a phase change material, *International Journal of Heat and Mass Transfer* 183 (2022) 122111. <https://doi.org/10.1016/j.ijheatmasstransfer.2021.122111>.

- [27] A. Jandyal, I. Chaturvedi, I. Wazir, A. Raina, M.I. Ul Haq, 3D printing – A review of processes, materials and applications in industry 4.0, *Sustainable Operations and Computers* 3 (2022) 33–42. <https://doi.org/10.1016/J.SUSOC.2021.09.004>.
- [28] S. Danaci, *Optimisation et integration de catalyseurs structurés pour la conversion de CO₂ en methane*, Université Grenoble Alpes, 2017.
- [29] Z. Li, Y. Nie, B. Liu, Z. Kuai, M. Zhao, F. Liu, Mechanical properties of AlSi10Mg lattice structures fabricated by selective laser melting, *Materials & Design* 192 (2020) 108709. <https://doi.org/10.1016/j.matdes.2020.108709>.
- [30] C. Yan, L. Hao, A. Hussein, D. Raymont, Evaluations of cellular lattice structures manufactured using selective laser melting, *International Journal of Machine Tools and Manufacture* 62 (2012) 32–38. <https://doi.org/10.1016/j.ijmachtools.2012.06.002>.
- [31] O. Santoliquido, G. Bianchi, P. Dimopoulos Eggenschwiler, A. Ortona, Additive manufacturing of periodic ceramic substrates for automotive catalyst supports, *Int. J. Appl. Ceram. Technol.* 14 (2017) 1164–1173. <https://doi.org/10.1111/ijac.12745>.
- [32] I. Kaur, P. Singh, Flow and Thermal Transport Through Unit Cell Topologies of Cubic and Octahedron Families, *International Journal of Heat and Mass Transfer* 158 (2020) 119784. <https://doi.org/10.1016/j.ijheatmasstransfer.2020.119784>.
- [33] C. Ferroni, F.S. Franchi, M. Ambrosetti, M. Bracconi, G. Groppi, M. Maestri, E. Tronconi, Numerical and Experimental Investigation of Pressure Drop in Periodic Open Cellular Structures for Intensification of Catalytic Processes, *ACS Eng. Au* (2022) acsengineeringau.1c00034. <https://doi.org/10.1021/acsengineeringau.1c00034>.
- [34] A. Montebelli, C.G. Visconti, G. Groppi, E. Tronconi, C. Ferreira, S. Kohler, Enabling small-scale methanol synthesis reactors through the adoption of highly conductive structured catalysts, *Catalysis Today* 215 (2013) 176–185. <https://doi.org/10.1016/j.cattod.2013.02.020>.
- [35] D. Merino, O. Sanz, M. Montes, Effect of the thermal conductivity and catalyst layer thickness on the Fischer-Tropsch synthesis selectivity using structured catalysts, *Chemical Engineering Journal* 327 (2017) 1033–1042. <https://doi.org/10.1016/j.cej.2017.07.003>.
- [36] C. Italiano, M.A. Ashraf, L. Pino, C.W.M. Quintero, S. Specchia, A. Vita, Rh/CeO₂ Thin Catalytic Layer Deposition on Alumina Foams: Catalytic Performance and Controlling Regimes in Biogas Reforming Processes, *Catalysts* 8 (2018) 448. <https://doi.org/10.3390/catal8100448>.
- [37] J.J. Bolívar Caballero, T. Han, R. Svanberg, I.N. Zaini, H. Yang, R. Gond, P. Cao, T. Lewin, P.G. Jönsson, W. Yang, Advanced application of a geometry-enhanced 3D-printed catalytic reformer for syngas production, *Energy Conversion and Management* 287 (2023) 117071. <https://doi.org/10.1016/j.enconman.2023.117071>.
- [38] C. Li, S. Yuan, X. Yao, X. Yu, B. Li, S.-T. Tu, Structured nanoporous copper catalysts prepared by laser powder bed fusion and dealloying for on-board methanol steam reforming, *Fuel* 347 (2023) 128367. <https://doi.org/10.1016/j.fuel.2023.128367>.
- [39] I. Lucentini, G. García Colli, C. Luzi, I. Serrano, L. Soler, N.J. Divins, O.M. Martínez, J. Llorca, Modelling and simulation of catalytic ammonia decomposition over Ni-Ru deposited on 3D-printed CeO₂, *Chemical Engineering Journal* 427 (2022) 131756. <https://doi.org/10.1016/j.cej.2021.131756>.
- [40] R. Balzarotti, M. Ambrosetti, M. Arnesano, A. Anglani, G. Groppi, E. Tronconi, Periodic open cellular structures (POCS) as enhanced catalyst supports: Optimization of the coating procedure and analysis of mass transport, *Applied Catalysis B: Environmental* 283 (2021) 119651. <https://doi.org/10.1016/j.apcatb.2020.119651>.
- [41] Q. Wei, H. Li, G. Liu, Y. He, Y. Wang, Y.E. Tan, D. Wang, X. Peng, G. Yang, N. Tsubaki, Metal 3D printing technology for functional integration of catalytic system, *Nat Commun* 11 (2020) 4098. <https://doi.org/10.1038/s41467-020-17941-8>.
- [42] P.H. Ho, M. Ambrosetti, G. Groppi, E. Tronconi, R. Palkovits, G. Fornasari, A. Vaccari, P. Benito, Structured Catalysts-Based on Open-Cell Metallic Foams for Energy and Environmental Applications, in: *Studies in Surface Science and Catalysis*, Elsevier, 2019: pp. 303–327. <https://doi.org/10.1016/B978-0-444-64127-4.00015-X>.

- [43] T. Knorr, P. Heinel, J. Schwerdtfeger, C. Körner, R.F. Singer, B.J.M. Etzold, Process specific catalyst supports—Selective electron beam melted cellular metal structures coated with microporous carbon, *Chemical Engineering Journal* 181–182 (2012) 725–733. <https://doi.org/10.1016/j.cej.2011.10.009>.
- [44] A. Vita, C. Italiano, C. Fabiano, L. Pino, M. Laganà, V. Recupero, Hydrogen-rich gas production by steam reforming of n-dodecane, *Applied Catalysis B: Environmental* 199 (2016) 350–360. <https://doi.org/10.1016/j.apcatb.2016.06.042>.
- [45] R. Balzarotti, C. Cristiani, L.F. Francis, Spin coating deposition on complex geometry substrates: Influence of operative parameters, *Surface and Coatings Technology* 330 (2017) 1–9. <https://doi.org/10.1016/j.surfcoat.2017.09.077>.
- [46] R. Balzarotti, A. Beretta, G. Groppi, E. Tronconi, A comparison between washcoated and packed copper foams for the intensification of methane steam reforming, *React. Chem. Eng.* 4 (2019) 1387–1392. <https://doi.org/10.1039/C9RE00125E>.
- [47] M. Ambrosetti, M. Bracconi, M. Maestri, G. Groppi, E. Tronconi, Packed foams for the intensification of catalytic processes: assessment of packing efficiency and pressure drop using a combined experimental and numerical approach, *Chemical Engineering Journal* 382 (2020) 122801. <https://doi.org/10.1016/j.cej.2019.122801>.
- [48] AMBHER, (n.d.). <https://www.ambherproject.eu/> (accessed September 1, 2024).
- [49] S.A.R.K. Deshmukh, S. Heinrich, L. Mörl, M. Van Sint Annaland, J.A.M. Kuipers, Membrane assisted fluidized bed reactors: Potentials and hurdles, *Chemical Engineering Science* 62 (2007) 416–436. <https://doi.org/10.1016/j.ces.2006.08.062>.
- [50] R.J.W. Voncken, I. Roghair, M. van Sint Annaland, A numerical study on concentration polarization in 3D cylindrical fluidized beds with vertically immersed membranes, *Chemical Engineering Science* 205 (2019) 299–318. <https://doi.org/10.1016/j.ces.2019.05.010>.
- [51] MACBETH, (n.d.). <https://www.macbeth-project.eu/> (accessed February 3, 2023).
- [52] A.M. Adris, C.J. Lim, J.R. Grace, The fluidized-bed membrane reactor for steam methane reforming: model verification and parametric study, *Chemical Engineering Science* 52 (1997) 1609–1622. [https://doi.org/10.1016/S0009-2509\(96\)00511-8](https://doi.org/10.1016/S0009-2509(96)00511-8).
- [53] T. Maneerung, K. Hidajat, S. Kawi, Triple-layer catalytic hollow fiber membrane reactor for hydrogen production, *Journal of Membrane Science* 514 (2016) 1–14. <https://doi.org/10.1016/j.memsci.2016.03.034>.
- [54] R. Sitar, J. Shah, Z. Zhang, H. Wikoff, J.D. Way, C.A. Wolden, Compact ammonia reforming at low temperature using catalytic membrane reactors, *Journal of Membrane Science* 644 (2022) 120147. <https://doi.org/10.1016/j.memsci.2021.120147>.
- [55] G. Li, M. Kanezashi, T. Tsuru, Highly enhanced ammonia decomposition in a bimodal catalytic membrane reactor for CO -free hydrogen production, *Catalysis Communications* 15 (2011) 60–63. <https://doi.org/10.1016/j.catcom.2011.08.011>.
- [56] T.F. Fuerst, S.T.B. Lundin, Z. Zhang, S. Liguori, J.D. Way, C.A. Wolden, Dense Metallic Membrane Reactor Synthesis of Ammonia at Moderate Conditions and Low Cost, *NH₃ Fuel Conference* (2017) 25.
- [57] S. Escorihuela, F. Toldra-Reig, S. Escolástico, R. Murciano, A. Martínez, J.M. Serra, Copper surface-alloying of H₂-permeable Pd-based membrane for integration in Fischer–Tropsch synthesis reactors, *Journal of Membrane Science* 619 (2021) 118516. <https://doi.org/10.1016/j.memsci.2020.118516>.
- [58] D. Liuzzi, F.J. Pérez-Alonso, J.L.G. Fierro, S. Rojas, F.L. Van Wijk, I. Roghair, M.V.S. Annaland, E. Fernandez, J.L. Viviente, D.A.P. Tanaka, Catalytic membrane reactor for the production of biofuels, *Catalysis Today* 268 (2016) 37–45. <https://doi.org/10.1016/j.cattod.2015.11.014>.
- [59] A.M. Tarditi, C. Imhoff, F. Braun, J.B. Miller, A.J. Gellman, L. Cornaglia, PdCuAu ternary alloy membranes: Hydrogen permeation properties in the presence of H₂S, *Journal of Membrane Science* 479 (2015) 246–255. <https://doi.org/10.1016/j.memsci.2014.12.030>.
- [60] J.A. Medrano, E. Fernandez, J. Melendez, M. Parco, D.A.P. Tanaka, M. Van Sint Annaland, F. Gallucci, Pd-based metallic supported membranes: High-temperature stability and

- fluidized bed reactor testing, *International Journal of Hydrogen Energy* 41 (2016) 8706–8718. <https://doi.org/10.1016/j.ijhydene.2015.10.094>.
- [61] J.L. Cerrillo, N. Morlanés, S.R. Kulkarni, N. Realpe, A. Ramírez, S.P. Katikaneni, S.N. Paglieri, K. Lee, A. Harale, B. Solami, A. Jamal, S. Mani Sarathy, P. Castaño, J. Gascon, High purity, self-sustained, pressurized hydrogen production from ammonia in a catalytic membrane reactor, *Chemical Engineering Journal* (2021) 134310. <https://doi.org/10.1016/j.cej.2021.134310>.
- [62] T. Maneerung, K. Hidajat, S. Kawi, Ultra-thin (<1 μm) internally-coated Pd–Ag alloy hollow fiber membrane with superior thermal stability and durability for high temperature H₂ separation, *Journal of Membrane Science* 452 (2014) 127–142. <https://doi.org/10.1016/j.memsci.2013.10.040>.
- [63] W.J.R. Ververs, M. Ongis, A. Arratibel, L. Di Felice, F. Gallucci, On the modeling of external mass transfer phenomena in Pd-based membrane separations, *International Journal of Hydrogen Energy* 71 (2024) 1121–1133. <https://doi.org/10.1016/j.ijhydene.2024.04.337>.
- [64] N. de Nooijer, A. Arratibel Plazaola, J. Meléndez Rey, E. Fernandez, D. Pacheco Tanaka, M. Sint Annaland, F. Gallucci, Long-Term Stability of Thin-Film Pd-Based Supported Membranes, *Processes* 7 (2019) 106. <https://doi.org/10.3390/pr7020106>.
- [65] J. Melendez, E. Fernandez, F. Gallucci, M. Van Sint Annaland, P.L. Arias, D.A. Pacheco Tanaka, Preparation and characterization of ceramic supported ultra-thin (~1 μm) Pd–Ag membranes, *Journal of Membrane Science* 528 (2017) 12–23. <https://doi.org/10.1016/j.memsci.2017.01.011>.
- [66] D. Zhang, J. Zhao, P. Yang, Y. Chen, Y. Fan, Preparation of High Stability Pd/Ceramic/Ti–Al Alloy Composite Membranes by Electroless Plating, *Front. Chem.* 8 (2020) 202. <https://doi.org/10.3389/fchem.2020.00202>.
- [67] A. Arratibel, A. Pacheco Tanaka, M. van Sint Annaland, F. Gallucci, On the use of double-skinned membranes to prevent chemical interaction between membranes and catalysts, *International Journal of Hydrogen Energy* (2019) S0360319919340765. <https://doi.org/10.1016/j.ijhydene.2019.10.203>.
- [68] S. Agnolin, Development of metallic supported Pd-based membranes for H₂ separation, (n.d.).
- [69] G. Zeng, L. Shi, Y. Liu, Y. Zhang, Y. Sun, A simple approach to uniform PdAg alloy membranes: Comparative study of conventional and silver concentration-controlled co-plating, *International Journal of Hydrogen Energy* 39 (2014) 4427–4436. <https://doi.org/10.1016/j.ijhydene.2014.01.022>.
- [70] B. Faroldi, M.L. Bosko, J. Múnera, E. Lombardo, L. Cornaglia, Comparison of Ru/La₂O₃CO₃ performance in two different membrane reactors for hydrogen production, *Catalysis Today* 213 (2013) 135–144. <https://doi.org/10.1016/j.cattod.2013.02.024>.
- [71] A. Helmi, E. Fernandez, J. Melendez, D. Pacheco Tanaka, F. Gallucci, M. van Sint Annaland, Fluidized Bed Membrane Reactors for Ultra-Pure H₂ Production—A Step forward towards Commercialization, *Molecules* 21 (2016) 376. <https://doi.org/10.3390/molecules21030376>.
- [72] J. Jiang, Q. Dong, K. McCullough, J. Lauterbach, S. Li, M. Yu, Novel hollow fiber membrane reactor for high purity H₂ generation from thermal catalytic NH₃ decomposition, *Journal of Membrane Science* 629 (2021) 119281. <https://doi.org/10.1016/j.memsci.2021.119281>.
- [73] C.-H. Kim, J.-Y. Han, S. Kim, B. Lee, H. Lim, K.-Y. Lee, S.-K. Ryi, Hydrogen production by steam methane reforming in a membrane reactor equipped with a Pd composite membrane deposited on a porous stainless steel, *International Journal of Hydrogen Energy* 43 (2018) 7684–7692. <https://doi.org/10.1016/j.ijhydene.2017.11.176>.
- [74] S. Liguori, A. Iulianelli, F. Dalena, V. Piemonte, Y. Huang, A. Basile, Methanol steam reforming in an Al₂O₃ supported thin Pd-layer membrane reactor over Cu/ZnO/Al₂O₃ catalyst, *International Journal of Hydrogen Energy* 39 (2014) 18702–18710. <https://doi.org/10.1016/j.ijhydene.2013.11.113>.

- [75] A. Iulianelli, S. Liguori, Y. Huang, A. Basile, Model biogas steam reforming in a thin Pd-supported membrane reactor to generate clean hydrogen for fuel cells, *Journal of Power Sources* 273 (2015) 25–32. <https://doi.org/10.1016/j.jpowsour.2014.09.058>.
- [76] K. Briceño, A. Iulianelli, D. Montané, R. Garcia-Valls, A. Basile, Carbon molecular sieve membranes supported on non-modified ceramic tubes for hydrogen separation in membrane reactors, *International Journal of Hydrogen Energy* 37 (2012) 13536–13544. <https://doi.org/10.1016/j.ijhydene.2012.06.069>.
- [77] V. Cechetto, G. Anello, A. Rahimalimamaghani, F. Gallucci, Carbon Molecular Sieve Membrane Reactors for Ammonia Cracking, *Processes* 12 (2024) 1168. <https://doi.org/10.3390/pr12061168>.
- [78] H.B. Park, J. Kamcev, L.M. Robeson, M. Elimelech, B.D. Freeman, Maximizing the right stuff: The trade-off between membrane permeability and selectivity, *Science* 356 (2017) eaab0530. <https://doi.org/10.1126/science.aab0530>.
- [79] C. Wu, Y. Jin, Y. Fan, N.H. Wong, J. Sunarso, N. Yang, Membrane reactor supported by MXene (Ti₃C₂TX) for hydrogen production by ammonia decomposition, (2023).
- [80] M. Nordio, S.A. Wassie, M. Van Sint Annaland, D.A. Pacheco Tanaka, J.L. Viviente Sole, F. Gallucci, Techno-economic evaluation on a hybrid technology for low hydrogen concentration separation and purification from natural gas grid, *International Journal of Hydrogen Energy* 46 (2021) 23417–23435. <https://doi.org/10.1016/j.ijhydene.2020.05.009>.
- [81] R. Swaidan, B. Ghanem, I. Pinnau, Fine-Tuned Intrinsically Ultramicroporous Polymers Redefine the Permeability/Selectivity Upper Bounds of Membrane-Based Air and Hydrogen Separations, *ACS Macro Lett.* 4 (2015) 947–951. <https://doi.org/10.1021/acsmacrolett.5b00512>.
- [82] T. Araújo, G. Bernardo, A. Mendes, High-performance hydrogen separation using cellulose-based carbon molecular sieve membranes, *Journal of Membrane Science* 693 (2024) 122337. <https://doi.org/10.1016/j.memsci.2023.122337>.
- [83] S.C. Rodrigues, M. Andrade, J. Moffat, F.D. Magalhães, A. Mendes, Preparation of carbon molecular sieve membranes from an optimized ionic liquid-regenerated cellulose precursor, *Journal of Membrane Science* 572 (2019) 390–400. <https://doi.org/10.1016/j.memsci.2018.11.027>.
- [84] S.S. Hosseini, T.S. Chung, Carbon membranes from blends of PBI and polyimides for N₂/CH₄ and CO₂/CH₄ separation and hydrogen purification, *Journal of Membrane Science* 328 (2009) 174–185. <https://doi.org/10.1016/j.memsci.2008.12.005>.
- [85] W. Ogieglo, T. Puspasari, X. Ma, I. Pinnau, Sub-100 nm carbon molecular sieve membranes from a polymer of intrinsic microporosity precursor: Physical aging and near-equilibrium gas separation properties, *Journal of Membrane Science* 597 (2020) 117752. <https://doi.org/10.1016/j.memsci.2019.117752>.
- [86] M.A. Llosa Tanco, J.A. Medrano, V. Cechetto, F. Gallucci, D.A. Pacheco Tanaka, Hydrogen permeation studies of composite supported alumina-carbon molecular sieves membranes: Separation of diluted hydrogen from mixtures with methane, *International Journal of Hydrogen Energy* 46 (2021) 19758–19767. <https://doi.org/10.1016/j.ijhydene.2020.05.088>.
- [87] L. Li, C. Wang, N. Wang, Y. Cao, T. Wang, The preparation and gas separation properties of zeolite/carbon hybrid membranes, *J Mater Sci* 50 (2015) 2561–2570. <https://doi.org/10.1007/s10853-015-8819-1>.
- [88] G. Moral, A. Ortiz, D. Gorri, I. Ortiz, Hydrogen recovery from industrial waste streams using Matrimid®/ZIF mixed matrix membranes, *International Journal of Hydrogen Energy* 51 (2024) 210–224. <https://doi.org/10.1016/j.ijhydene.2023.03.368>.
- [89] L. Lei, F. Pan, A. Lindbräthen, X. Zhang, M. Hillestad, Y. Nie, L. Bai, X. He, M.D. Guiver, Carbon hollow fiber membranes for a molecular sieve with precise-cutoff ultramicropores for superior hydrogen separation, *Nat Commun* 12 (2021) 268. <https://doi.org/10.1038/s41467-020-20628-9>.

- [90] F. Gallucci, L. Paturzo, A. Basile, An experimental study of CO₂ hydrogenation into methanol involving a zeolite membrane reactor, *Chemical Engineering and Processing: Process Intensification* 43 (2004) 1029–1036. <https://doi.org/10.1016/j.ccep.2003.10.005>.
- [91] P. Rodriguez-Vega, A. Ateka, I. Kumakiri, H. Vicente, J. Ereña, A.T. Aguayo, J. Bilbao, Experimental implementation of a catalytic membrane reactor for the direct synthesis of DME from H₂+CO/CO₂, *Chemical Engineering Science* 234 (2021) 116396. <https://doi.org/10.1016/j.ces.2020.116396>.
- [92] A. Ateka, P. Rodriguez-Vega, T. Cordero-Lanzac, J. Bilbao, A.T. Aguayo, Model validation of a packed bed LTA membrane reactor for the direct synthesis of DME from CO/CO₂, *Chemical Engineering Journal* 408 (2021) 127356. <https://doi.org/10.1016/j.cej.2020.127356>.
- [93] N. Wang, Y. Liu, A. Huang, J. Caro, Hydrophilic SOD and LTA membranes for membrane-supported methanol, dimethylether and dimethylcarbonate synthesis, *Microporous and Mesoporous Materials* 207 (2015) 33–38. <https://doi.org/10.1016/j.micromeso.2014.12.028>.
- [94] S. Poto, J.G.H. Endepoel, M.A. Llosa-Tanco, D.A. Pacheco-Tanaka, F. Gallucci, M.F. Neira d'Angelo, Vapor/gas separation through carbon molecular sieve membranes: Experimental and theoretical investigation, *International Journal of Hydrogen Energy* 47 (2022) 11385–11401. <https://doi.org/10.1016/j.ijhydene.2021.10.155>.
- [95] J. Lee, H.-G. Park, M.-H. Hyeon, B.-G. Kim, S.K. Kim, S.-Y. Moon, Low-temperature CO₂ hydrogenation overcoming equilibrium limitations with polyimide hollow fiber membrane reactor, *Chemical Engineering Journal* 403 (2021) 126457. <https://doi.org/10.1016/j.cej.2020.126457>.
- [96] M.-H. Hyeon, H.-G. Park, J. Lee, C.-I. Kong, E.-Y. Kim, J.H. Kim, S.-Y. Moon, S.K. Kim, Equilibrium shift, poisoning prevention, and selectivity enhancement in catalysis via dehydration of polymeric membranes, *Nat Commun* 14 (2023) 1673. <https://doi.org/10.1038/s41467-023-37298-y>.
- [97] H. Li, C. Qiu, S. Ren, Q. Dong, S. Zhang, F. Zhou, X. Liang, J. Wang, S. Li, M. Yu, Na⁺-gated water-conducting nanochannels for boosting CO₂ conversion to liquid fuels, *Science* 367 (2020) 667–671. <https://doi.org/10.1126/science.aaz6053>.
- [98] M. Seshimo, H. Urai, K. Sasa, H. Nishino, Y. Yamaguchi, R. Nishida, S. Nakao, Bench-Scale Membrane Reactor for Methylcyclohexane Dehydrogenation Using Silica Membrane Module, *Membranes* 11 (2021) 326. <https://doi.org/10.3390/membranes11050326>.
- [99] S. Poto, M.A. Llosa Tanco, D.A. Pacheco Tanaka, M.F. Neira d'Angelo, F. Gallucci, Experimental investigation of a packed bed membrane reactor for the direct conversion of CO₂ to dimethyl ether, *Journal of CO₂ Utilization* 72 (2023) 102513. <https://doi.org/10.1016/j.jcou.2023.102513>.
- [100] M. Sakai, K. Tanaka, M. Matsukata, An Experimental Study of a Zeolite Membrane Reactor for Reverse Water Gas Shift, *Membranes* 12 (2022) 1272. <https://doi.org/10.3390/membranes12121272>.
- [101] H. Choi, S.H. Kim, J. Bae, S.P.R. Katikaneni, A. Jamal, A. Harale, S.N. Paglieri, J.H. Lee, CFD analysis and scale up of a baffled membrane reactor for hydrogen production by steam methane reforming, *Computers & Chemical Engineering* 165 (2022) 107912. <https://doi.org/10.1016/j.compchemeng.2022.107912>.
- [102] S. Agnolin, L. Di Felice, A.P. Tanaka, M.L. Tanco, W.J.R. Ververs, F. Gallucci, Intensification of Hydrogen Production: Pd–Ag Membrane on Tailored Hastelloy-X Filter for Membrane-Assisted Steam Methane Reforming, *Processes* 12 (2023) 40. <https://doi.org/10.3390/pr12010040>.
- [103] M. Nordio, J. Melendez, M. van Sint Annaland, D.A. Pacheco Tanaka, M. Llosa Tanco, F. Gallucci, Comparison between carbon molecular sieve and Pd–Ag membranes in H₂–CH₄ separation at high pressure, *International Journal of Hydrogen Energy* 45 (2020) 28876–28892. <https://doi.org/10.1016/j.ijhydene.2020.07.191>.
- [104] Q. Dong, W.L. Xu, X. Fan, H. Li, N. Klinghoffer, T. Pyrzynski, H.S. Meyer, X. Liang, M. Yu, S. Li, Prototype Catalytic Membrane Reactor for Dimethyl Ether Synthesis via CO₂

- Hydrogenation, *Ind. Eng. Chem. Res.* 61 (2022) 14656–14663. <https://doi.org/10.1021/acs.iecr.2c02851>.
- [105] A. Arratibel, D.A. Pacheco Tanaka, M. van Sint Annaland, F. Gallucci, Membrane reactors for autothermal reforming of methane, methanol, and ethanol, in: *Membrane Reactors for Energy Applications and Basic Chemical Production*, Elsevier, 2015: pp. 61–98. <https://doi.org/10.1016/B978-1-78242-223-5.00003-0>.
- [106] J.A. Medrano, I. Potdar, J. Melendez, V. Spallina, D.A. Pacheco-Tanaka, M. van Sint Annaland, F. Gallucci, The membrane-assisted chemical looping reforming concept for efficient H₂ production with inherent CO₂ capture: Experimental demonstration and model validation, *Applied Energy* 215 (2018) 75–86. <https://doi.org/10.1016/j.apenergy.2018.01.087>.
- [107] S. Pati, J. Ashok, N. Dewangan, T. Chen, S. Kawi, Ultra-thin (~1 μm) Pd–Cu membrane reactor for coupling CO₂ hydrogenation and propane dehydrogenation applications, *Journal of Membrane Science* 595 (2020) 117496. <https://doi.org/10.1016/j.memsci.2019.117496>.
- [108] L. Zheng, M. Ambrosetti, E. Tronconi, Joule-Heated Catalytic Reactors toward Decarbonization and Process Intensification: A Review, *ACS Eng. Au* 4 (2024) 4–21. <https://doi.org/10.1021/acsengineeringau.3c00045>.
- [109] S. Renda, M. Cortese, G. Iervolino, M. Martino, E. Meloni, V. Palma, Electrically driven SiC-based structured catalysts for intensified reforming processes, *Catalysis Today* 383 (2022) 31–43. <https://doi.org/10.1016/j.cattod.2020.11.020>.
- [110] Y. Hayakawa, S. Kambara, T. Miura, Hydrogen production from ammonia by the plasma membrane reactor, *International Journal of Hydrogen Energy* 45 (2020) 32082–32088. <https://doi.org/10.1016/j.ijhydene.2020.08.178>.
- [111] Z. Liu, W. Zhou, Y. Xie, F. Liu, Z. Fang, G. Zhang, W. Jin, Highly effective CO₂ splitting in a plasma-assisted membrane reactor, *Journal of Membrane Science* 685 (2023) 121981. <https://doi.org/10.1016/j.memsci.2023.121981>.
- [112] R.P.W.J. Struis, S. Stucki, M. Wiedorn, A membrane reactor for methanol synthesis, *Journal of Membrane Science* 113 (1996) 93–100. [https://doi.org/10.1016/0376-7388\(95\)00222-7](https://doi.org/10.1016/0376-7388(95)00222-7).
- [113] M. Seshimo, B. Liu, H.R. Lee, K. Yogo, Y. Yamaguchi, N. Shigaki, Y. Mogi, H. Kita, S. Nakao, Membrane Reactor for Methanol Synthesis Using Si-Rich LTA Zeolite Membrane, *Membranes* 11 (2021) 505. <https://doi.org/10.3390/membranes11070505>.
- [114] Z. Li, T.T. Tsotsis, Methanol synthesis in a high-pressure membrane reactor with liquid sweep, *Journal of Membrane Science* 570–571 (2019) 103–111. <https://doi.org/10.1016/j.memsci.2018.09.071>.
- [115] Y. Slotboom, M.J. Bos, J. Pieper, V. Vrieswijk, B. Likozar, S.R.A. Kersten, D.W.F. Brilman, Critical assessment of steady-state kinetic models for the synthesis of methanol over an industrial Cu/ZnO/Al₂O₃ catalyst, *Chemical Engineering Journal* 389 (2020) 124181. <https://doi.org/10.1016/j.cej.2020.124181>.
- [116] S. Poto, D. Vico van Berkel, F. Gallucci, M. Fernanda Neira d'Angelo, Kinetic modelling of the methanol synthesis from CO₂ and H₂ over a CuO/CeO₂/ZrO₂ catalyst: The role of CO₂ and CO hydrogenation, *Chemical Engineering Journal* 435 (2022) 134946. <https://doi.org/10.1016/j.cej.2022.134946>.
- [117] H. Jahangiri, J. Bennett, P. Mahjoubi, K. Wilson, S. Gu, A review of advanced catalyst development for Fischer–Tropsch synthesis of hydrocarbons from biomass derived syn-gas, *Catal. Sci. Technol.* 4 (2014) 2210–2229. <https://doi.org/10.1039/C4CY00327F>.
- [118] R.L. Espinoza, E. Du Toit, J. Santamaria, M. Menendez, J. Coronas, S. Irusta, Use of membranes in fischer-tropsch reactors, in: *Studies in Surface Science and Catalysis*, Elsevier, 2000: pp. 389–394. [https://doi.org/10.1016/S0167-2991\(00\)80988-X](https://doi.org/10.1016/S0167-2991(00)80988-X).
- [119] M. Tavares, G. Westphalen, J.M. Araujo Ribeiro De Almeida, P.N. Romano, E.F. Sousa-Aguiar, Modified fischer-tropsch synthesis: A review of highly selective catalysts for yielding olefins and higher hydrocarbons, *Front. Nanotechnol.* 4 (2022) 978358. <https://doi.org/10.3389/fnano.2022.978358>.

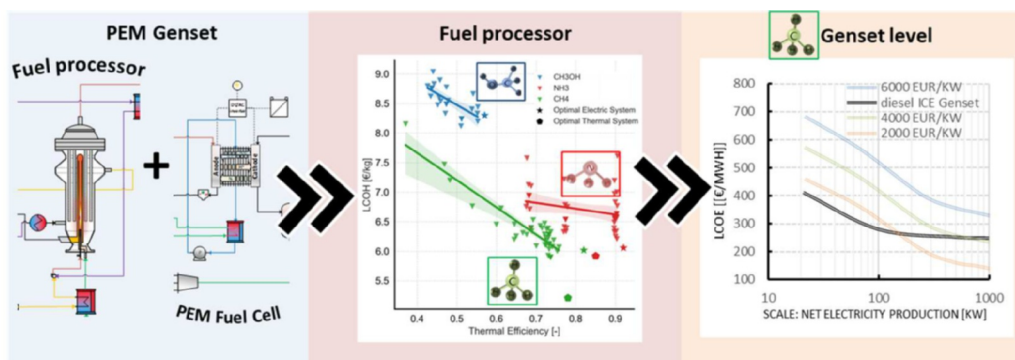
- [120] J. Zhang, S. Lu, X. Su, S. Fan, Q. Ma, T. Zhao, Selective formation of light olefins from CO₂ hydrogenation over Fe–Zn–K catalysts, *Journal of CO₂ Utilization* 12 (2015) 95–100. <https://doi.org/10.1016/j.jcou.2015.05.004>.
- [121] R. Murciano, J.M. Serra, A. Martínez, Direct hydrogenation of CO₂ to aromatics via Fischer-Tropsch route over tandem K-Fe/Al₂O₃+H-ZSM-5 catalysts: Influence of zeolite properties, *Catalysis Today* 427 (2024) 114404. <https://doi.org/10.1016/j.cattod.2023.114404>.
- [122] B.A. Peppley, J.C. Amphlett, L.M. Kearns, R.F. Mann, Methanol–steam reforming on Cu/ZnO/Al₂O₃. Part 1: the reaction network, *Applied Catalysis A: General* 179 (1999) 21–29. [https://doi.org/10.1016/S0926-860X\(98\)00298-1](https://doi.org/10.1016/S0926-860X(98)00298-1).
- [123] H. Purnama, T. Ressler, R.E. Jentoft, H. Soerijanto, R. Schlögl, R. Schomäcker, CO formation/selectivity for steam reforming of methanol with a commercial CuO/ZnO/Al₂O₃ catalyst, *Applied Catalysis A: General* 259 (2004) 83–94. <https://doi.org/10.1016/j.apcata.2003.09.013>.
- [124] S. Sayas, N. Morlanés, S.P. Katikaneni, A. Harale, B. Solami, J. Gascon, High pressure ammonia decomposition on Ru–K/CaO catalysts, *Catal. Sci. Technol.* 10 (2020) 5027–5035. <https://doi.org/10.1039/D0CY00686F>.
- [125] A. Di Carlo, L. Vecchione, Z. Del Prete, Ammonia decomposition over commercial Ru/Al₂O₃ catalyst: An experimental evaluation at different operative pressures and temperatures, *International Journal of Hydrogen Energy* 39 (2014) 808–814. <https://doi.org/10.1016/j.ijhydene.2013.10.110>.
- [126] N. de Nooijer, F. Gallucci, E. Pellizzari, J. Melendez, D.A. Pacheco Tanaka, G. Manzolini, M. van Sint Annaland, On concentration polarisation in a fluidized bed membrane reactor for biogas steam reforming: Modelling and experimental validation, *Chemical Engineering Journal* 348 (2018) 232–243. <https://doi.org/10.1016/j.cej.2018.04.205>.
- [127] S. Richard, A. Ramirez Santos, F. Gallucci, PEM gensets using membrane reactors technologies: An economic comparison among different e-fuels, *International Journal of Hydrogen Energy* (2023) S0360319923032913. <https://doi.org/10.1016/j.ijhydene.2023.06.312>.
- [128] V. Cechetto, L. Di Felice, J.A. Medrano, C. Makhloufi, J. Zuniga, F. Gallucci, H₂ production via ammonia decomposition in a catalytic membrane reactor, *Fuel Processing Technology* 216 (2021) 106772. <https://doi.org/10.1016/j.fuproc.2021.106772>.
- [129] M. Sarić, Y.C. Van Delft, R. Sumbharaju, D.F. Meyer, A. De Groot, Steam reforming of methane in a bench-scale membrane reactor at realistic working conditions, *Catalysis Today* 193 (2012) 74–80. <https://doi.org/10.1016/j.cattod.2012.04.009>.
- [130] R. Palo, J.D. Holladay, R.T. Rozmiarek, Development of a soldier-portable fuel cell power system Part I: A bread-board methanol fuel processor, *Fuel and Energy Abstracts* 44 (2003) 225. [https://doi.org/10.1016/S0140-6701\(03\)82901-6](https://doi.org/10.1016/S0140-6701(03)82901-6).
- [131] C. Makhloufi, Large-scale decomposition of green ammonia for pure hydrogen production, (2021) 11.
- [132] M. Ongis, G. Di Marcoberardino, G. Manzolini, F. Gallucci, M. Binotti, Membrane reactors for green hydrogen production from biogas and biomethane: A techno-economic assessment, *International Journal of Hydrogen Energy* (2023) S0360319923005700. <https://doi.org/10.1016/j.ijhydene.2023.01.310>.
- [133] G. Marcoberardino, D. Vitali, F. Spinelli, M. Binotti, G. Manzolini, Green Hydrogen Production from Raw Biogas: A Techno-Economic Investigation of Conventional Processes Using Pressure Swing Adsorption Unit, *Processes* 6 (2018) 19. <https://doi.org/10.3390/pr6030019>.
- [134] D. Clark, H. Malerød-Fjeld, M. Budd, I. Yuste-Tirados, D. Beeaff, S. Aamodt, K. Nguyen, L. Ansaloni, T. Peters, P.K. Vestre, D.K. Pappas, M.I. Valls, S. Remiro-Buenamañana, T. Norby, T.S. Bjørheim, J.M. Serra, C. Kjølseth, Single-step hydrogen production from NH₃, CH₄, and biogas in stacked proton ceramic reactors, *Science* 376 (2022) 390–393. <https://doi.org/10.1126/science.abj3951>.
- [135] H2SITE, (n.d.). <https://h2site.eu/> (accessed September 20, 2024).

- [136] V. Dieterich, N. Wein, H. Spliethoff, S. Fendt, Performance Requirements of Membrane Reactors for the Application in Renewable Methanol Synthesis: A Techno-Economic Assessment, *Advanced Sustainable Systems* 6 (2022) 2200254. <https://doi.org/10.1002/adsu.202200254>.
- [137] S. Richard, V. Verde, N. Kezibri, C. Makhloufi, A. Saker, I. Gargiulo, F. Gallucci, Power-to-ammonia synthesis process with membrane reactors: Techno-economic study, *International Journal of Hydrogen Energy* 73 (2024) 462–474. <https://doi.org/10.1016/j.ijhydene.2024.06.041>.
- [138] H. Hamed, T. Brinkmann, Valorization of CO₂ to DME using a membrane reactor: A theoretical comparative assessment from the equipment to flowsheet level, *Chemical Engineering Journal Advances* 10 (2022) 100249. <https://doi.org/10.1016/j.cej.2022.100249>.
- [139] A. Cruellas, J.J. Bakker, M. Van Sint Annaland, J.A. Medrano, F. Gallucci, Techno-economic analysis of oxidative coupling of methane: Current state of the art and future perspectives, *Energy Conversion and Management* 198 (2019) 111789. <https://doi.org/10.1016/j.enconman.2019.111789>.
- [140] A. Cruellas, J. Heezius, V. Spallina, M. van Sint Annaland, J.A. Medrano, F. Gallucci, Oxidative Coupling of Methane in Membrane Reactors; A Techno-Economic Assessment, *Processes* 8 (2020) 274. <https://doi.org/10.3390/pr8030274>.
- [141] S. Lei, A. Wang, J. Xue, H. Wang, Catalytic ceramic oxygen ionic conducting membrane reactors for ethylene production, *React. Chem. Eng.* 6 (2021) 1327–1341. <https://doi.org/10.1039/D1RE00136A>.
- [142] Ongis M, Baiguini M, Di Marcobertardino G, Gallucci F, Binotti M. Techno-economic analysis for the design of membrane reactors in a small-scale biogas-to-hydrogen plant. *International Journal of Hydrogen Energy* 2025;101:887–903. <https://doi.org/10.1016/j.ijhydene.2024.12.245>.
- [143] G. Di Marcobertardino, S. Foresti, M. Binotti, G. Manzolini, Potentiality of a biogas membrane reformer for decentralized hydrogen production, *Chemical Engineering and Processing - Process Intensification* 129 (2018) 131–141. <https://doi.org/10.1016/j.cep.2018.04.023>.
- [144] M. Ongis, M. Baiguini, G. Di Marcobertardino, F. Gallucci, M. Binotti, Techno-economic analysis for the design of membrane reactors in a small-scale biogas-to-hydrogen plant, *International Journal of Hydrogen Energy* 101 (2025) 887–903. <https://doi.org/10.1016/j.ijhydene.2024.12.245>.

Chapter 3 | PEM gensets using membrane reactor technologies: an economic comparison among different e-fuels

Abstract

The aim of this chapter* is to compare, from an economic viewpoint, the performance of small-scale PEM fuel cell gensets (based on 3 Nedstack™ stacks in series, representing a maximum gross power of 40 kWe) that integrate a membrane reactor for three different e-fuels: methanol, ammonia, and methane. To achieve this objective, computer-aided process simulation is deployed to optimize the operational conditions (flow rate, temperature, pressure, and vacuum) and design (number of membranes) based on Aspen Plus™ software. The efficiency maximization resulted in a decreasing levelized cost of hydrogen (LCOH) from 8.29 €/kg_{H2} in the methanol system to 6.12 €/kg_{H2} in the ammonia system and ultimately to 5.43 €/kg_{H2} in the methane system, with associated thermal efficiencies of 0.57, 0.92, and 0.77, respectively, at the fuel processor level. At the genset level, the reduction was from 1400 €/MWh in the electric methanol system to 848 €/MWh and 665 €/MWh in the electric and thermal ammonia systems, and finally to 627 €/MWh in the methane system, with corresponding electric efficiencies ranging from 25% to 38%. From an economic point of view only, methane would be the preferred fuel option while ammonia would be the best option from the efficiency point of view. The wide exploitation of these systems is still hindered by high costs compared to traditional ICE engine. A comprehensive cost analysis was performed for the full system with the objective to understand cost drivers and to guide future component development.



* This chapter is based on the following paper: S. Richard, A. Ramirez Santos, F. Gallucci, PEM gensets using membrane reactor technologies: an economic comparison among different e-fuels Int. J. Hydrogen Energy vol. 50 part A, pp. 433-457, 2024.

3.1. Introduction

Chapter 2 highlighted the advantages of palladium-based membrane reactors (MRs) for hydrogen recovery, offering significant conversion enhancements, up to ~30% for methanol reforming, ~30% for ammonia decomposition, and ~175% for methane reforming, while reducing or eliminating the need for downstream hydrogen separation. This hydrogen is particularly well-suited for fuel cells, valued for their silent operation, high efficiency, and direct conversion of chemical energy into electricity [1]. Fuel cells are extensively considered to decarbonize "hard-to-abate" applications, including backup power, off-grid projects, residential use, and mobile systems [2-5]. Among fuel cell types, Polymer Electrolyte Membrane Fuel Cells (PEMFCs) stand out due to their low operating temperature (60–70 °C), quick start-up, high power density, long lifespan, and commercial viability. While PEMFCs rely on high-purity hydrogen, posing storage and distribution challenges, membrane reactors could support their deployment by enabling efficient on-site hydrogen production [7-11].

A full techno-economic analysis helps evaluating the commercial viability of the systems. In this context, several studies have been conducted for various reaction systems. For example, Byun et al. (2020) [12] investigated methanol steam reforming and found that the membrane reactor resulted in a cost reduction of 15% at small scale (H_2 production capacities of 30 Nm^3/hr) and a 10% reduction at a larger scale (H_2 production capacity of 700 Nm^3/hr). Similarly, Lim et al. (2022) [13] reported an 11% cost reduction in favor of the membrane reactor for ammonia cracking at 300 kg H_2 per day and a 14% reduction at 900 kg_{H_2} per day. Furthermore, Kim et al. (2019) [14] achieved a cost saving of around 23% in the membrane reactor for methanol reforming. In addition, Di Marcoberardino et al. (2018) [15] investigated the potential of biogas reforming in a membrane reactor and reported a 20% increase in system efficiency compared to the conventional system. These findings demonstrate the potential economic and efficiency benefits of using membrane reactors for certain reaction systems. Numerous studies have explored the potential efficiencies gained from integrating membrane reactors with PEM fuel cell systems. For instance, Roses et al. (2011) [16] carried out a study on a 2kW natural gas micro Combined Heat and Power (CHP) system. They reached an efficiency of 34% utilizing conventional fuel processing methods, but when a membrane reactor was integrated into the system, the efficiency improved significantly, climbing to 43%. Similarly, as part of the FLUIDCELL EU. project [17], Foresti et al. (2015) [18] studied a 5kW ethanol micro CHP system and achieved a net electric efficiency of around 40%. Building on the same process, Viviente et al. (2017) [4] achieved electric efficiencies ranging between 38% to 41%. In the FERRET EU project, Di Marcoberardino et al. (2017) [19] researched a 5 kW micro CHP system based on natural gas. They examined various natural gas compositions and membrane reactor setups, including the application of a sweep gas or vacuum, to augment the permeation driving force. Their findings illustrated that the use of a sweep gas resulted in a higher efficiency, reaching up to 41.1%. In a subsequent investigation, the same author [20] undertook a comparative analysis between the current membrane reactor-based system and traditional fuel processors for hydrogen production. They also assessed a simpler conventional fuel processor paired with a high-temperature PEM fuel cell. The study revealed that the membrane reactor-based system showed superior performance, attaining the highest electric efficiency (42.7%) among all the configurations

examined. These studies demonstrate how integrating membrane reactors with PEM fuel cells can enhance system efficiency (up to 7-10% higher than conventional FPs [21-22])). These systems have already achieved competitive operational efficiency, comparable to diesel ICE engines (15-35% range [18,23]).

While numerous theoretical studies have examined the integration of membrane reactors with PEM fuel cells or have exclusively focused on the fuel processing capabilities of the membrane reactor, there exists a gap in comprehensive process-level research that takes into account the impact of fuel choice on system performance. This consideration is particularly relevant given the potential role E-fuels can play in decarbonizing various generator set markets. Additionally, prior studies (e.g. [4,16,18]) have often oversimplified the membrane reactor model by using a series of equilibrium reactors and intermediate separators, thereby neglecting key phenomena like concentration polarization or bubble emulsion mass transfer in the case of fluidized bed reactors. These factors are crucial in accurately estimating parameters like hydrogen concentration, membrane area, and the heat duty of the system. Consequently, this study aims to assess the feasibility of using methane, ammonia, and methanol as potential e-fuels for a PEM genset integrated with a membrane reactor. The evaluation will primarily focus on the performance analysis of these fuels under standardized assumptions.

3.2. Materials and Methods

The computer-aided process design package Aspen One™. (v.11) is the main tool used in this work. Its capabilities include an accurate description of physical properties, rigorous models for unit operations and numerical techniques for solving large systems of algebraic and differential equation. To model reactors and stacks, Aspen Customized Modeler™ (ACM) is utilized, enabling straightforward integration with the Aspen Plus™ architecture as a customized component. This software has embedded methods to retrieve thermodynamic properties and employs a coding syntax similar to Visual Basic. In all simulations, the Peng-Robinson cubic equation of state [24] is selected to evaluate the thermodynamic properties of all substances which is consistent with other similar studies [25-26].

3.2.1 Plant Layout and general assumptions

The focus of the investigation involves the production of hydrogen from methane, ammonia, and methanol using a membrane reactor, which is then utilized in a PEMFC to generate electricity. The fuel processors are specifically designed for a small-scale PEMFC consisting of three stacks (Nedstacks™ FCS 13XXL), with a maximum gross power output of 40 kW_e, which is suitable for various entry level market applications. **Figure 3-1** illustrates the system layouts for the three feedstocks. Each layout is divided into two sections: the "PEMFC" section, which comprises the fuel cell stack and all necessary control and power conditioning equipment, and the "Fuel Processor" section denoted FP, which consists of the membrane reactors used for hydrogen production and their respective balance of plant. In membrane reactors, the reactants are introduced from the bottom and move upwards as the reaction takes place. The hydrogen produced in the

membrane's inner section is referred to as "permeate" while the chemical constituents that ascend without crossing through the membranes form the "retentate". In the FP section, the reactants (water and either methanol or methane as shown in **Figure 3-1.a** and **1.b**, respectively, in one case, and ammonia presented in **1.c** in the other) are pressurized and pre-heated through a series of heat exchangers for evaporation and superheating before entering the membrane reactors. To enhance hydrogen permeation, vacuum is utilized (steam may also be used as an alternative sweep gas especially in dead-end fuel cell configurations to increase both permeation enhancement and hydrogen stream humidification). Employing vacuum also benefits reactor construction by minimizing welded joints, leading to lower reactor costs and higher reliability. However, there is a risk of infiltrations occurring in the plant section below atmospheric pressure. The permeate flow rate is subsequently cooled down to 60 °C and directed to the PEMFC anode, while the retentate is throttled and combusted to support the reactant preheating and endothermic reaction. In order to sustain the endothermic reactions, extra fuel is burned with the introduction of air to attain a molar basis O₂ content of 5% in the combustion gases. The endothermic reaction is supported by indirect heat transfer from a high-temperature furnace situated within the reactor. An alternative option for the NH₃ system is shown in **Figure 3-2**, which utilizes an electric furnace. This approach offers several advantages, especially in terms of eliminating uncertainties associated with burning a variable mixture of ammonia and hydrogen. In addition, this configuration allows for separate temperature control of the reactor, enabling operation under a wide range of thermal conditions. Nevertheless, to guarantee complete oxidation of unconverted fuel and H₂ in the retentate, a second external burner is still necessary, while the exhaust energy can be used for reactant pre-heating. Another drawback of this setup is the loss of net electricity production from the genset's standpoint. To achieve a consistent temperature during transient operation, an electrical heater (EI-1) is also installed at the reactor inlet in all genset configurations. This ensures that the temperature is raised to the level required for the reaction to occur. In the "PEMFC" section, filtered air humidified by the cathode off-gas and pure hydrogen are supplied to the stack. In the proposed configuration, a humidifier is placed in conjunction with cathode inlet and exhaust, where it utilizes the water produced by the chemical reaction inside the fuel cells to humidify inlet air. The inlet air is optimally humidified after passing through the humidifier. The relative humidity of air entering the cathode is arbitrarily set to 95% in the simulations. On the anode side, the hydrogen is humidified by means of water crossover through cell membrane and recirculation of the anode exhaust into the inlet stream, thereby abandoning a need for a separate humidifier. The anode exhaust's unused hydrogen is returned to the feed stream via a recirculation blower (Blower-4) that compensates for the pressure drop in the anode loop. This recirculation loop allows for the complete utilization of hydrogen, with the exception of any losses due to nitrogen build-up purging, which are not considered. To ensure proper operation, the fuel cell stack must be kept at a consistent operating temperature of approximately 60 °C [27]. This is achieved by transferring the heat generated by the chemical reaction, ohmic resistance, and mass transport overpotential to a circulating liquid coolant within the stack. The coolant, which is water, is then actively cooled by passing through an air-cooled radiator. Despite the low temperature of the excess heat generated, which makes it challenging to integrate it usefully with the FP upstream, it still plays a crucial role in cooling the permeate hydrogen (HEX-2) before it enters the vacuum pump. To prevent water droplets from entering the

stack and causing flooding, a water knockout and drain are incorporated into the recirculation loop. The water produced during the PEMFC reaction can be repurposed in the methanol or methane fuel processing. Finally, the DC current drawn from the stack is delivered to external devices such as a DC/DC converter, DC/AC inverters. A battery is also required to cover for system start up or abrupt load change. **Table 3-1** recaps the general process assumptions mainly taken from Di Marcoberardino et al. (2019) [15] and Ongis et al. (2023) [26]. The turbomachines (compressors, pumps, and steam turbines) were simulated with the assumption of isentropic and mechanical efficiency to determine the thermodynamic conditions of the outlet. The counter-current shell and tube heat exchangers were modeled using a shortcut method based on design parameters and various design specifications were established to meet the desired constraints, such as the set values of hydrogen production, steam-carbon ratio or oxygen molar fraction in the dry flue gases or the PEMFC anode and cathode stoichiometry. In particular, the feedstock flow rate is adjusted to generate the desired quantity of pure hydrogen, while the steam flow rate is established to maintain a fixed steam-to-carbon ratio at the reactor inlet, thereby avoiding carbon deposition on the catalyst or membrane surface. Empirical evidence [28-29] suggest that steam-to-carbon ratio of 3 and 1 are adequate for the methane and methanol systems, respectively.

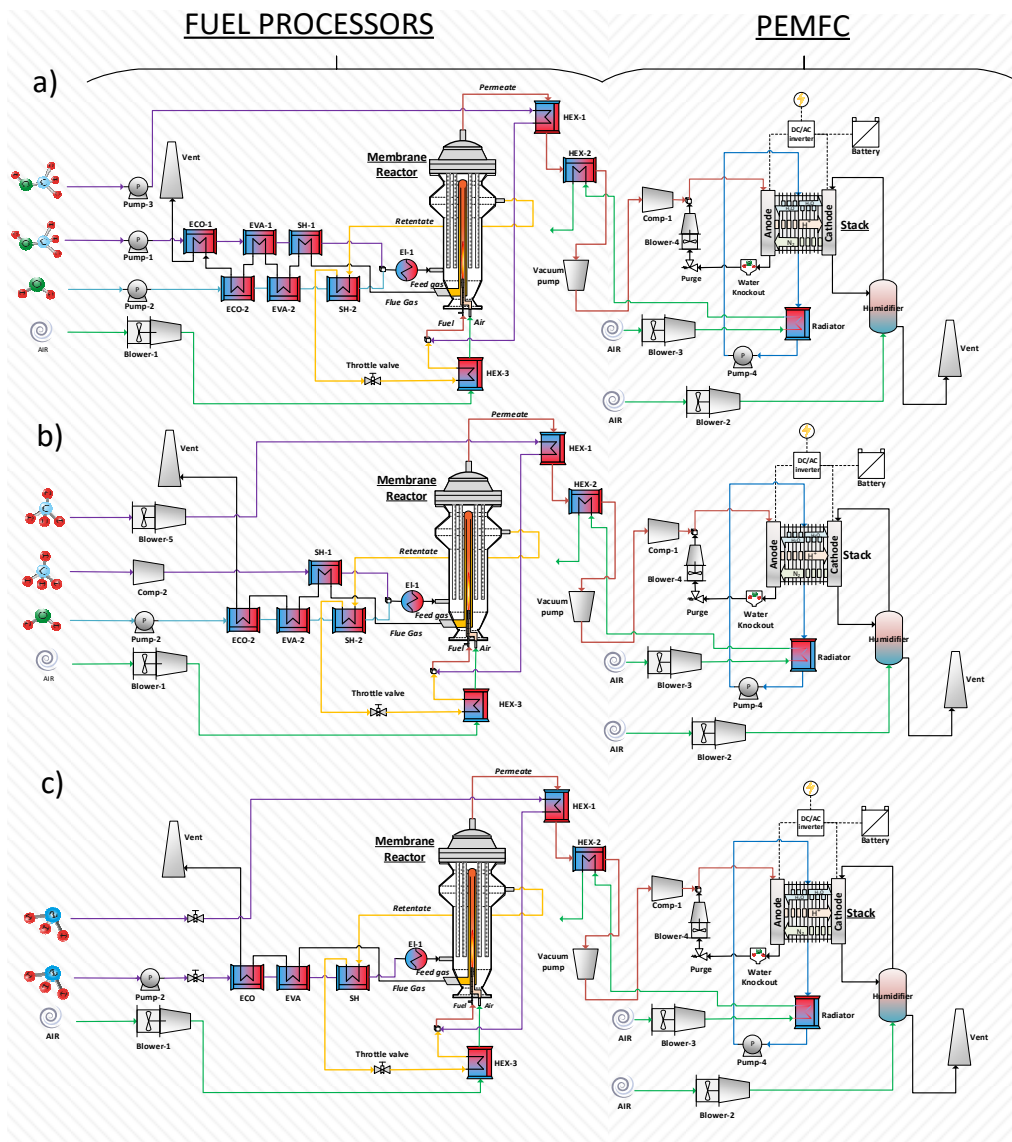


Figure 3-1: Schematic depiction of genset systems showcasing variation in the fuel processing steps: (a) methane steam reforming (b) ammonia cracking (c) methanol steam reforming (Note: While not explicitly shown in the sketch, an additional purification step should be incorporated in the permeate line before the PEMFC as an extra precaution [30])

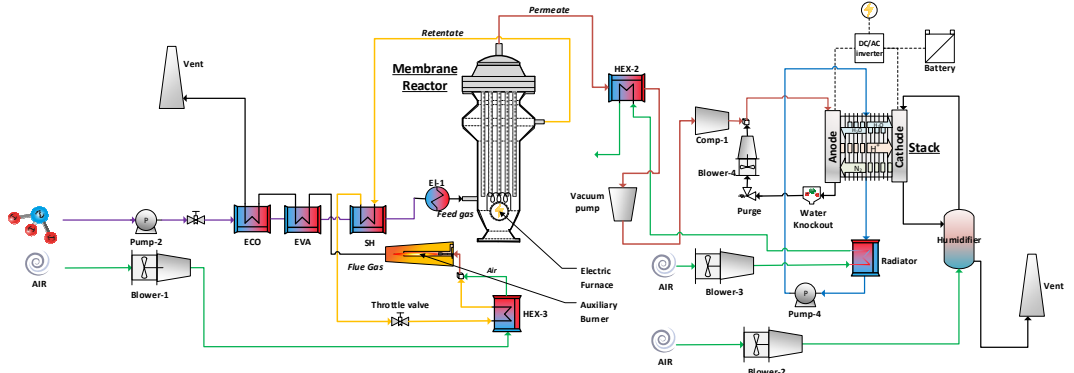


Figure 3-2: Electric furnace system also proposed (presented here for the ammonia system)

Table 3-1: Main assumptions and design parameters assumed in the base case scenario.

Parameters	Unit	Value
Referenced fuel processor operating conditions		
Hydrogen production	kmol/hr	0.83
Reactor temperature (CH ₃ OH /NH ₃ / CH ₄ cases)	°C	240/430/500
Reactor inlet temperature (CH ₃ OH /NH ₃ / CH ₄ cases)	°C	240/430/500
Pressure reaction side	Bar	10
Permeate pressure	Bar	0.5
Steam to carbon ratio (CH ₄ & CH ₃ OH case)	-	3 & 1
Heat exchangers		
Pressure drop in gas water HEX (%)	Bar	1
Design Minimum ΔT in exchanger gas/liquid	°C	15
Minimum ΔT in exchanger gas/gas	°C	30
Heat transfer coefficient gas/gas	W/m ² /K	60
Heat transfer coefficient gas/liquid	W/m ² /K	70
Pump and compressors		
Pump isentropic efficiency/mechanical efficiency	%	70/90
Compressor/fan/blower isentropic efficiency	%	70/85
Vacuum pump isentropic efficiency/mechanical efficiency	%	70/85
Vacuum pump discharge pressure	bar	1.2
Fuel cell power conditioning		
DC stack/DC booster converter efficiency η_{DC-AC}	%	97.8
DCbooster/AC230 @ 50Hz inverter η_{DC-DC}	%	96.8
Other		
Maximum outlet temperature	°C	150
Ambient temperature	°C	20
Total heat loss	kW	1

3.2.2. PEMFC modelling

The PEMFC stack model used is described thanks to a 0D lumped model developed by Hosseinzadeh and Rokni (2013) [31] and improved by Rabbani et al. (2013) [32]. The model incorporates the governing equations for cell electrochemical potential, polarization overpotentials, heat transfer, water and nitrogen diffusion across the membrane which are reported in **Appendix**

A1. The following hypothesis were considered: 1) There are no concentration losses since the system is not operated at maximum current density; 2) The anode side doesn't contribute to the activation loss [33] given that low temperature fuel cells exhibit high activation polarization at low current densities; 3) The stack temperature is equal to the coolant temperature at the outlet; and 4) the stack maintains a constant thermal heat capacity. The characteristics of the commercially available Nedstack™ FCS 13XXL [27] were replicated in this study. This stack contains 96 cells with a total estimated area to 200 cm². To ensure optimal stack lifespan and efficiency, the stack manufacturer recommends the following operating conditions: a temperature around 60 °C and a pressure range of 1.1-2.2 bar. The stack can produce up to 13.6 kW at 230 A. However, it's common practice to operate stacks at partial loads between 0.6 to 0.8 V (a trade-off between stack power, efficiency, and lifetime).

Table 3-2: List of PEM fuel cell system specifications at nominal conditions

Parameters	Unit	Value
Inlet temperature	°C	60
Coolant temperature	°C	50
Relative humidity	%	80
Max Pressure anode	mbarg	250
Max Pressure cathode	mbarg	200
Anode stoichiometry	-	1.25
Cathode stoichiometry	-	2
ΔP anode cathode	mbar	50
Stack current	A	150
Single Cell voltage	V	0.71
Current density j	$\frac{A}{cm^2}$	0.6
Power density	$\frac{W}{cm^2}$	0.43
Pressure drop per stack (anode, cathode, coolant)	bar	0.1/0.3/0.1

3.2.3. Reactors modelling

In accordance with current practices, a fluidized bed reactor (FBMR) [15] is chosen for methane reforming reaction, while packed bed reactors (PBMR) [34] are employed for methanol and ammonia reforming. Both FBMR and PBMR are modeled using 1D (i.e. discretized along the vertical length) homogeneous models developed in Aspen Custom Modelers (ACM). These models assume steady-state conditions, kinetic control regimes (i.e. no internal or external mass transfer limitation), plug flow regimes and negligible pressure drop in the permeation side. The ordinary differential equations are integrated with a Euler method in ACM. For the sake of brevity, the governing equations and empirical correlations used in these models are provided in the **Appendix A2**. A conventional membrane reactor configuration is adopted where the catalyst is packed (or fluidized for the FBMR) on the shell side while the permeation stream is collected on the opposite side of the membrane. The FBMR model is a modification of the Bubbling Bed Model (BBM) proposed by Kunii and Levenspiel (1968) [35] (the BBM is a well-known model in the chemical and petrochemical industry to design and optimize fluidized bed reactor). Essentially, this model

describes the fluidization process by considering two phases: the emulsion and the bubble phase. The gas phase is introduced into the reactor at a superficial gas velocity (u_0) above the minimum fluidization velocity (u_{mf}) and forms a bubble phase with fraction (f_b) with a characteristic bubble diameter (d_b) at any axial position. The remaining gas moves upwards in the emulsion phase at the emulsion velocity (u_e) and the gas is exchanged with the gas in the bubble phase (K_{be}). The model assumes that bubbles are free of particles and a fraction travelling behind it (defined as wake) is responsible of the movement of the solids. Finally, it is assumed that the presence of catalyst particles in the freeboard region does not cause any additional conversion (i.e. there is no entrainment of particle near the bed surface). Material balances are performed in both the emulsion and bubble phases to calculate the variation in moles of all components due to chemical reactions (only in the emulsion phase) and membrane permeation (from both phases), as well as transfer coefficients between the two phases due to differences in component concentrations. The adaptation of the formalism to membrane reactors has been demonstrated several time [36-38]. The selective extraction of hydrogen in the model is described by Sieverts' law [39] with permeation parameters coming from the experimental analysis of Fernandez et al. (2015) [40] (pre-exponential factor k_0 , apparent activation energy E_a an exponential factor n) listed in **Table 3-3**. When describing hydrogen extraction from a mixture through a highly selective and permeable membrane, experimental findings indicate that Sieverts' law alone is insufficient [41-42] for predicting the transmembrane flux due to a phenomena known as "concentration polarization". To accurately describe the membrane permeation it is necessary to determine the concentration at the membrane surface [43-44]. In this study, the Sieverts' law underwent an adjustment through the utilization of a reducing factor derived from a homogeneous Computational Fluid Dynamics (CFD) model, which is outlined briefly in **Appendix A3**. However, it is worth noting that potential permeance inhibitions caused by other factors, such as CO (or other species) adsorption [45] or the formation of coke [46], have not been considered. Additionally, any possible mass transfer limitations in the membrane support have been neglected. In both PBM and FBM, the membranes are positioned 1 cm away from the inlet region, where significant temperature gradients are present [47]. The assumption is also made that all membranes have the same level of performance and that their selectivity towards hydrogen is infinite. Moreover, the presence of membranes in a fluidized bed is well-known to have a significant impact on the hydrodynamics of the FBM preventing bubble coalescence and promoting bubble splitting [48-49]. To account for this in phenomenological models an arbitrary restriction is usually placed on the maximum bubble diameter [38]. In this study an arbitrary maximum bubble fraction equivalent to one-fourth of the bed diameter has been adopted in this study based on the observation of CFD analysis [48]. Apart from that the fluidized bed hydrodynamic correlations are substantially the same as those presented in other similar works [26] [15]. Finally, precisely accounting for reaction kinetics is critical when modeling catalytic reactors under diverse configurations and conditions, as it can have a significant impact on equipment size and cost. This study employs kinetic rates from literature, namely Sayas et al. (2020) [50] for ammonia cracking, Peppley et al. (1999) [51] for methanol reforming, and Marra et al. (2014) [52] for methane reforming. The reaction schemes are recapped in **Chapter 2** (page 43) and additional information concerning the kinetic model equations and parameters utilized are provided in **Appendix A4**. **Table 3-3** summarizes the main assumptions considered.

Table 3-3: Membrane reactor modelling choices

Parameters	Unit	Value
Numerical method	-	Euler method
Discretization number of point for each reactor	-	150
Membrane OD	m	0.014
Membrane thickness	μm	4
Length	m	1
Membranes volumetric coverage	m	0.1
Start position of the membranes	m	0.1
Catalyst particle diameter (FBMR)	μm	180
Number of membranes (CH_4 ; NH_3 ; CH_3OH)	-	34, 40, 22
Pre exponential factor of hydrogen permeability k_0	$\text{mol m}^{-2}\text{s}^{-1}\text{bar}^{0.5}$	$4.57 * 10^{-8}$
Apparent activation energy for hydrogen permeability E_a	kJ kmol^{-1}	9.23
Bed porosity β	-	0.4
n	-	0.5
Density (Al_2O_3 ; CaO)	kg m^{-3}	3950; 3350
Catalyst density (CH_4 ; NH_3 ; CH_3OH)	$\text{kg m}_{\text{bed}}^{-3}$	1580 & 1340 & 1300
H_2 selectivity over other gases	-	Infinite

3.2.4. Economic assumptions

A preliminary techno economic assessment is conducted at the plant level to compare the cost of the genset systems. Following recommended methodology adopted in the literature [53-56] the total plant cost (TPC) is calculated as per Eq. 3.1. with a bottom-up approach breaking down the power plant into the basic components or equipment, and then adding installation costs (TIC), indirect costs (IC) and owner's and contingencies costs (C&OC). Those values can vary among studies ranging from 0.65 [26, 57] to 0.8 [53, 58] regarding the TIC whilst IC is typically taken 0.14 [26, 53] and C&OC around 0.15 [58].

$$TPC = (\sum_i C_i) * (1 + \%_{TIC}) * (1 + \%_{IC}) * (1 + \%_{c\&oc}) \quad \text{Eq. 3.1}$$

The component costs, obtained from several correlations adapted from Turton et al. (2018) [59] and vendor quotes are scaled (Eq. 3.2) and actualized with the Chemical Engineering Plant Index Cost (CEPCI) index for considering price fluctuations like inflation, deflation. (cf. **Table 3-4**). For this analysis, an index of 596.2 was used to adjust to the 2020 period. The reactor vessel and pump costs are specifically calculated using a correlation from Turton et al. (2018) [59] and incorporating a correction factor for stainless steel material, which is necessary for ammonia due to its corrosive nature but not as critical for the other two feedstocks (methanol and methane) examined in this study. The other cost correlations used are consistent with the study of Ongis et al. 2023 [60]

$$C_i = C_{i,0} \left(\frac{S_i}{S_{i,0}} \right)^f \quad \text{Eq. 3.2}$$

Table 3-4: Cost assumption for plant component cost calculated using a scaling law method [26]

Component	Scaling parameters	$S_{i,0}$	$C_{i,0}$ (k€)	f	Year cost	CEPCI
-----------	--------------------	-----------	----------------	-----	-----------	-------

Compressor	Power [kW]	5	3.3	0.82	2006	499.6
Vacuum Pump	Electric Power [kW]	10	9.82	0.44	2001	394.3
Furnace	Duty [kW]	5.6	5000	0.67	2020	596.2
Air compressor	Power [kW]	680	3420	0.67	2009	521.9

The TPC is converted in an annual operating cost using the Capital Charge Factor (CCF) as described in Eq. 3.3 as a function of the discount rate i and the plant lifetime n .

$$CCF = \sum_{j=1}^N \frac{1}{(1+i)^j} = \frac{i \times (1+i)^n}{(1+i)^n - 1} \quad \text{Eq. 3.3}$$

Subsequently, the final cost of hydrogen (LCOH) and cost of electricity (LCOE) were estimated following the established formula defined in Eq. 3.4 and Eq. 3.5. These two metrics are composed of the annualized TPC and the Operations and Maintenance fixed $C_{O\&M,fix}$, and variables $C_{O\&M,var}$ which are determined by the expenses associated with consumables such as catalysts, reactants, water, and membranes, as well as maintenance, insurance, and labor costs, divided by the plant's productivity (i.e., hydrogen or electricity output).

$$LCOH \left[\frac{\text{€}}{\text{kg}_{H_2}} \right] = \frac{(TPC[\text{€}] \times CCF[\%/year]) + C_{O\&M,fix}[\text{€}/year] + (C_{O\&M,var} \left[\frac{\text{€}}{year} \right] \times h_{eq})}{Production\ capacity \left[\frac{\text{kg}_{H_2}}{year} \right] \times h_{eq} \left[\frac{h}{year} \right]} \quad \text{Eq. 3.4}$$

$$LCOE \left[\frac{\text{€}}{\text{MWh}} \right] = \frac{(TPC[\text{€}] \times CCF[\%/year]) + C_{O\&M,fix}[\text{€}/year] + (C_{O\&M,var} \left[\frac{\text{€}}{year} \right] \times h_{eq})}{Production\ capacity \left[\frac{\text{MWh}}{year} \right] \times h_{eq} \left[\frac{h}{year} \right]} \quad \text{Eq. 3.5}$$

Table 3-5 presents the key assumptions utilized for estimating the levelized costs in the base case scenario, with some of these assumptions being briefly discussed below. Labor costs, especially at a small scale, have a substantial impact on the final cost. In literature regarding similar systems, these costs have been estimated to range from 16 k€/year [14] up to 60 k€/year [15, 58], with several studies considering halfway points of around 30 k€/year [13, 26]. In this study, a labor cost of 20 k€/y was assumed. The literature often reports vastly different costs for catalysts, typically calculated by material cost per weight, leading to a significant discrepancy. For instance, Yoshida et al. (2021) [61] estimated the cost of Ru/C catalyst at around 295 €/kg, while Makhloufi et al. (2021) [62] used a cost of 22.3 €/kg and concluded that the impact of this factor on the final cost was negligible. To arrive at a compromise, this study adopts a common catalyst cost of 143 €/kg [63] and assumes a lifespan of 5 years for all catalysts. Similarly, there exists a significant discrepancy in reported prices of e-fuels, as depicted in **Figure 3-3**. The wide range of estimates presented in research papers are generally attributed to differences in technological, energy source, and cost parameters. In this study, the baseline scenario assumes that renewable fuels are priced competitively with current market rates, with methanol, ammonia, and methane priced at 60 €, 57 €, and 35 € per MWh, respectively. Although this assumption is optimistic in terms of e-fuel costs, it enables a more dependable comparison among them, rather than relying on arbitrary values from the literature. Furthermore, some sources predict that e-fuels would become cost-competitive with fossil fuels when electricity prices drop below 20 €/MWh [64]. Preliminary forecasts also suggest that green ammonia will be more affordable due to the high cost of direct air capture of CO₂, which

aligns with the considered history of fossil fuel prices [65] (cf. **Figure 3-4**). Moreover, Power-to-X processes are still in their developmental stage, and substantial advancements are predicted in the years ahead. For instance, a decline in the cost of power generation units is projected and a significant improvement in the electrolyzer's performance is expected, resulting from greater energy efficiency and reduced operating costs. The cost of Pd membranes, including the recycling of both Pd-Ag waste and membranes can be estimated to range from 2000 to 5000 €/m², according to the FluidCell Eu. Project [66]. The membrane lifetime for Pd-Ag membranes at temperatures ≤ 425 °C was previously estimated to be 3 years, but it is expected to increase to 5 years, as targeted by the Macbeth Eu. Project [67]. The baseline scenario for this study assumes a membrane cost of 6000 euro/m², with a recovery factor of 0.8 considered to account for the recycling process. The installed cost of a PEMFC system has been extensively researched, with the JU H₂ report [68] providing estimates of 6000 €/kWe, 2500 €/kWe, and 1900 €/kWe for productivity levels of 5 kWe, 50 kWe, and 500 kWe, respectively. Additionally, the Grasshopper Eu. Project [69] aims to achieve a cost of 1500 €/kWe at a megawatt scale. For this study, a reference cost of 6000 €/kWe has been assumed, which is consistent with vendor quotes consulted for similar scale systems as the one considered. It is further assumed that this cost covers the installed system, including the BoP (Balance of Plant) and battery expenses. Some of these parameters were subjected to a sensitivity analysis to evaluate their impact on the final cost. It is assumed that the lifespan of the stack is distinct from that of the MEA. The stack is constructed with durable components that allow for an estimated lifespan of 25 years, while the MEA is projected to endure for 20000 hours.

Table 3-5: Base case economic assumptions

O&M Fixed Cost	
Maintenance cost	0.02*TPC [15]
Insurance	0.025*TPC [15]
Labour cost	20k€/year (1person)
O&M Variable	
E fuel (Methanol-Ammonia-Methane) €/MWh	60-57-35
Electricity cost	85 €/MWh
Storage CH ₄ @ 200 bar/ NH ₃ /CH ₃ OH (€/kg _{fuel})	0.69 [70]/0.9 [70]/0.1 [71]&[70]
Stack lifetime	20000 hr
Catalyst cost	143 €/kg [63]
Catalyst lifetime	5 years[57]
Pd Membrane cost recovery	80%
Membrane lifetime	5 years [72]
Demineralized water	6 €/m ³ [73]
Carbon tax	-
General Assumptions	
CCF	0.0953
Plant availability heq	0.65
Discount factor	8%
Operating lifetime	25 years
Conversion €/§	0.92
Component cost	
Pd Membrane price	6000 €/m ²

PEMFC cost	6000 €/kWe
Share of the stack on PEMFC cost	57% [74]
Share of the MEA on the stack cost (assuming only this portion of the stack is changed)	55% [74]
TPC calculation	
% TIC	80 [53]
% IC	14 [53]
% $c\&oC$	16 [53]

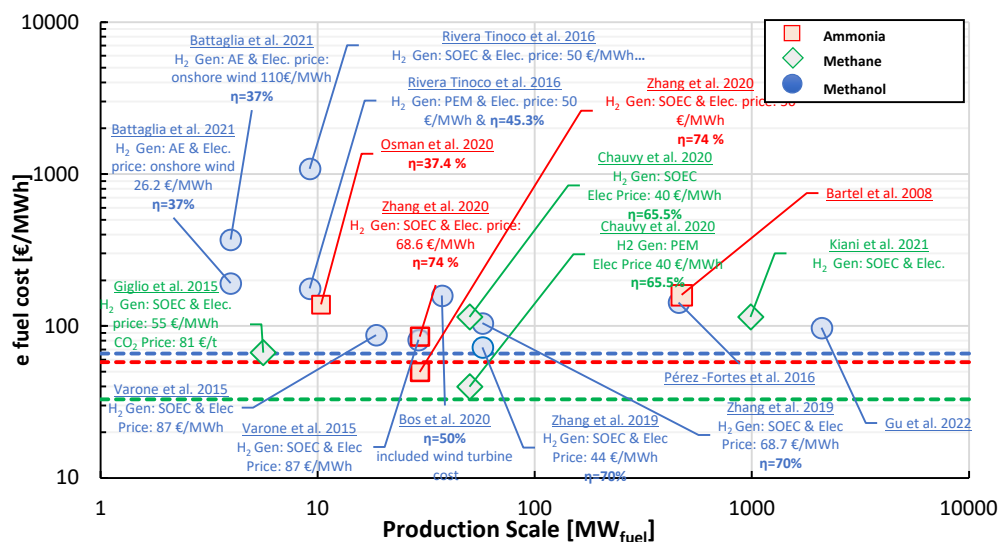


Figure 3-3: Recent techno-economic studies on e-fuels synthesis: a review of literature (blue= Methanol [75-78] red= Ammonia [79-80] green=Methane [81-83]). The dashed lines correspond to the approximative average market price between Sept. 2018 and Oct. 2022. (Reference: NG [84]; CH₃OH [85]; NH₃ [86])

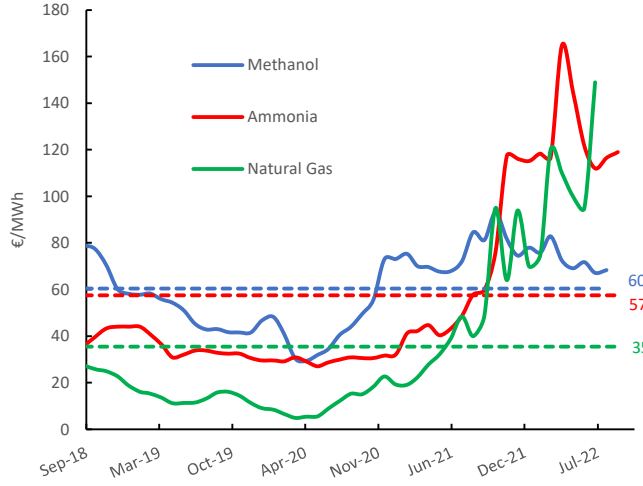


Figure 3-4: Price of fossil fuels between Sept. 2018 and Oct. 2022. (Source NG [84]; CH₃OH [85]; NH₃ [86]). The dashed lines represent the average cost over the specified period.

3.2.5. Performance indicators

Apart from economic indicators, various metrics are also employed to assess the performance and make comparisons between the different feedstocks under varying operating conditions. Two indicators from the perspective of the reactor are feedstock conversion X_{fuel} and hydrogen recovery factors HRF_{fuel} as defined in **Chapter 2**, page 30. The latter pertains to the overall amount of pure H₂ separated by the membrane, relative to the total H₂ fed into the reactor (based on the stoichiometry of the reaction). These metrics anyhow do not take into account heat integration and auxiliaries' consumption of the overall plant. At the fuel processor level, an intermediate hydrogen thermal efficiency denoted η_{FP} is defined in Eq. 3.6. This efficiency represents the ratio of the energy output associated with the produced hydrogen, excluding the electricity consumption from the system BOP, to the total thermal input power.

$$\eta_{FP} = \frac{F_{H_2} LHV_{H_2} - P_{aux}}{F_{fuel} LHV_{fuel}} \quad \text{Eq. 3.6}$$

P_{aux} is the sum of the electric consumptions of the system auxiliaries (i.e. compressors, pumps, control system). Finally, at the genset level, the electric efficiency is calculated in term of the net AC power output over fuel feed as per equation 3.7:

$$\eta_{AC_{tot}} = \frac{P_{net,AC}}{F_{fuel} LHV_{fuel}} = \frac{P_{gross,DC} \eta_{DC/DC} \eta_{DC/AC} - P_{aux}}{F_{fuel} LHV_{fuel}} \quad \text{Eq. 3.7}$$

Where $P_{gross,DC}$ refers to the fuel cell gross power DC power output, $\eta_{DC/DC}$ to the converter efficiency and $\eta_{DC/AC}$ to the inverter efficiency. Finally, Eq. 3.6 and Eq. 3.7 utilize the symbol LHV_{fuel} to denote the lower heating value of the fuels which are assumed to be 19.9 MJ/kg, 11.5 MJ/kg, 55.5 MJ/kg and 120 MJ/kg for methanol, ammonia, methane and hydrogen respectively.

3.3. Results and discussions

3.3.1. Model validations

The modeling of catalytic reactors is heavily reliant on the accurate consideration of reaction kinetics, which can have a substantial impact on equipment size and cost. **Figure 3-5** exhibits the validation results for the three cases, demonstrating a satisfactory fit within a 20% error margin. The models of the reactors align well with experimental data, indicating the correct incorporation of kinetics rates obtained from literature, namely Sayas et al. (2020) [50] for ammonia cracking, Peppley et al. (1999) [51] for methanol reforming, and Marra et al. (2014) [52] (The details of the kinetic models used are reported in **Appendix A4**).

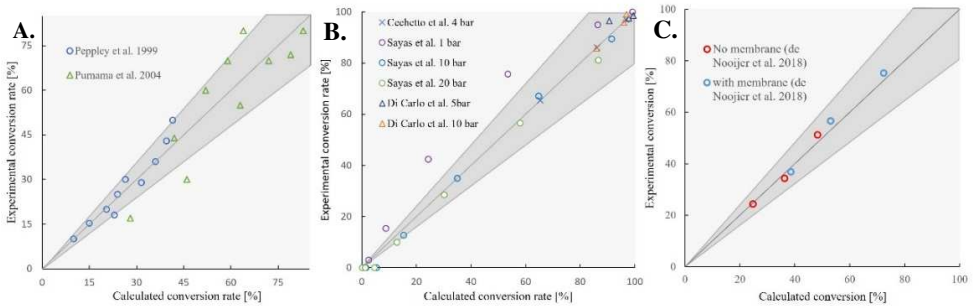


Figure 3-5: Results of kinetic laws validations with experimental data retrieved from (A) Methanol reforming: Purnama et al. (2004) [87] & Peppley et al. (1999) [51, 29]; (B) Ammonia cracking: Sayas et al. (2020) [50]; (C) Methane reforming : De Nooijer et al. (2018) [44] (for the latter case the membrane results were validated using a reducing factor of 0.6).

As mentioned in section 3.2.2, the parameters of the stack model were adjusted for the NedstackTM FCS 13XXL [27] stack, with the reaction speed in the anode side k_a and the two constants in the ionic resistance C_1 & C_2 and membrane thickness t_m being the parameters that were adjusted during the calibration process. The aim was to fit these parameters so that the theoretical polarization curve matches the commercial polarization curve and stack efficiencies based on the beginning-of-life stack performance given on the product data sheet [27]. **Table 3-6** displays the fitted parameter values, and **Figure 3-6.A** illustrates the polarization curve obtained from these parameters, which is compared to the commercial data, demonstrating a satisfactory level of agreement. From these data, the electric efficiency of the PEMFC system is assessed and plotted in **Figure 3-6.B**. It can be observed that as more current is drawn from the fuel cell, the voltage decreases due to its electrical resistance. Increasing the current density results in higher power generation by the stack, but also leads to increased power consumption by the auxiliary components, causing a reduction in efficiency. At extremely low current densities, the system efficiency decreases due to the high parasite loss in the BOP. To prevent excessive wear (membrane drying out), it is generally

recommended to maintain cell voltages below 800 mV and avoid operating at currents below 30 A, including open circuit voltage. Throughout the rest of this study, each stack is operated at 150 A.

Table 3-6: Parameters value taken for the calibration of the model against data given on the Nedstack™ stack selected

Phenomena	Parameters	Range	Value
Ohmic overpotential	C_1	[100 – 300]	300
	C_2	[5 – 100]	40.4
Activation overpotential	Reaction rate coefficient k_c	[0.1 – 1]	2.98
	Symmetry factor β	[0.1 – 1]	0.5
Concentration overpotential	Maximum current density I_{Max}	[0.1 – 3]	0.63
Membrane	Thickness t_m [mm]	[0.1 – 0.3]	0.1

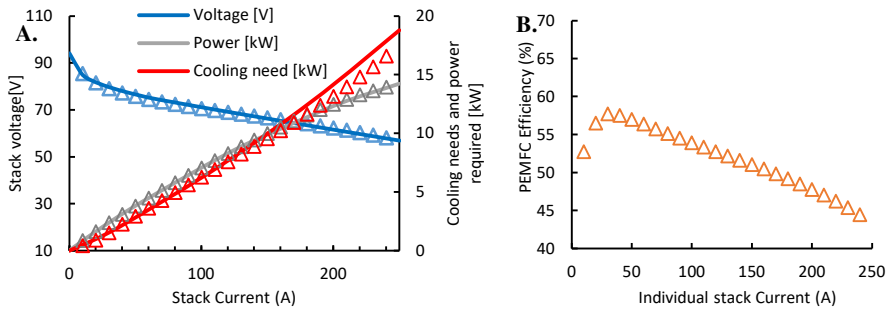


Figure 3-6: (A) Comparison of Nedstack™ operational data and calculated polarization curve from the model (condition coolant inlet temperature 57 °C and $\Delta T = 10$ °C a relative humidity of 85% at cathode and anode side taken from the technical specification of the Nedstack™ system [27] (B) PEMFC system efficiency obtained.

3.3.2. Sensitivity study at the fuel processor level

As mentioned in section 3.2.1, a base-case have been defined considering heuristic values for reactor parameters and operating conditions. However, to ensure proper design of the reactor, it's important to understand how operating conditions (such as reactor temperature, pressure, and permeate-side pressure) affect the global performance of these fuel processors. A sensitivity study is conducted at the fuel processor level by varying the reactor pressure, temperature, and permeate pressure above and below the baseline value at a fixed membrane area while adjusting only the feedstock flowrate to achieve the required hydrogen productivity. Each parameter is altered one at a time while keeping all other parameters constant at their base case values. The results, which are presented in **Figure 3-7** in term of reactant conversion, LCOH, HRF and thermal efficiency, yield several key observations. In this investigation regarding the fuel processor, it is assumed that the delivery pressure of hydrogen is 1 bar, and the cost of electricity is 85 €/MWh.

- 1) Looking at the effect of retentate pressure, It is evident that the effect of increasing pressure differs according to the system under consideration. While in certain cases, increasing pressure from 5 to 10 bar may result in a higher conversion rate (as seen in methane or methanol systems), it may also lead to a lower conversion rate (as observed in ammonia systems). In the first two systems, this phenomenon can be explained by the increase in the difference in square root partial pressure of hydrogen between the lumen side and the shell side resulting in a greater driving force exceeding the decrease in equilibrium conversion at higher pressure. However, in the case of the ammonia system, the shift effect seems insufficient to overcome the thermodynamic limitations. This latter point is sometimes emphasized in experimental studies at lab scale in which it is not always possible to work at high pressure [34, 44] in which a pressure increase has often a minor impact on reactant conversion. Upon further increasing the pressure from 10 to 15 bar, all three systems manage to surpass their thermodynamic limitations. However, despite this commonality, they still exhibit distinct behaviors. Increasing the pressure in the ammonia system was discovered to enhance the conversion rate, efficiency, and LCOH. Conversely, in the methanol system, thermal efficiency appears to level off at high pressure, while in the methane system, thermal efficiency decreases as pressure increases. The observed variations in efficiency in response to the increased pressure can be explained by the energy requirements associated with pressurizing the reactants. These demands are higher for the methane system, as compared to the other two systems that are pressurized in a liquid state. It is noteworthy that pump duties are usually insignificant in comparison to other plant consumptions (cf. **Figure 3-8**). Regarding the LCOH, it exhibits an inverse correlation with system efficiency as anticipated due to reduced feedstock expenses. Finally, the reduction in HRF observed in the methane systems is attributed due to an over-extraction of hydrogen relative to its production. This imbalance is in fact a result of an excessively large membrane surface area in relation to the desired productivity. As a last consideration, in addition to other performance indicators, the purity of hydrogen must also be carefully considered when evaluating the potential of such systems operating at higher retentate pressures. Recent studies have revealed that as pressure increases, the purity may decline because of a higher concentration of impurities in the permeate. [30] [88].
- 2) When examining the impact of permeate pressure, it is preferable to use lower values to promote permeation from the HRF point of view. However, lower permeate pressure values result in increased electricity consumption and higher costs for the vacuum pump. It is important to note that the effect of this parameter varies for each system. For instance, while the methanol and methane system seems to reach a tradeoff permeate pressure within the investigated range, the ammonia system is unaffected by lower permeate pressure values. Furthermore, it should be noted that conditions that impede permeation, such as low pressure and high vacuum pressure, require a higher reactant flow to achieve the desired productivity. This leads to an increase in the GHSV (gas hourly space velocity) and a reduction in conversion, resulting in significant losses of CH_4 and H_2 in the retentate and ultimately decreasing efficiency.

- 3) In term of reactor temperature, while an increase generally has a positive impact on reactor performance (efficiency and LCOH), as it enhances membrane permeability and improves kinetic and equilibrium conversion, the methanol system appears to be an exception to this trend. Although an increase in temperature results in higher conversion, it does not lead to a reduction in LCOH under these conditions. One possible reason for this is that the methanol system requires the most energy at the pre-heating stage, as shown in **Figure 3-8**, and therefore, higher temperatures are not always beneficial from a system perspective. Finally, as a side note it is also noteworthy to report that temperature affects the hydrogen purity. De Nooijer et al. (2018) [44] reported the highest purity at the highest temperature in their study.

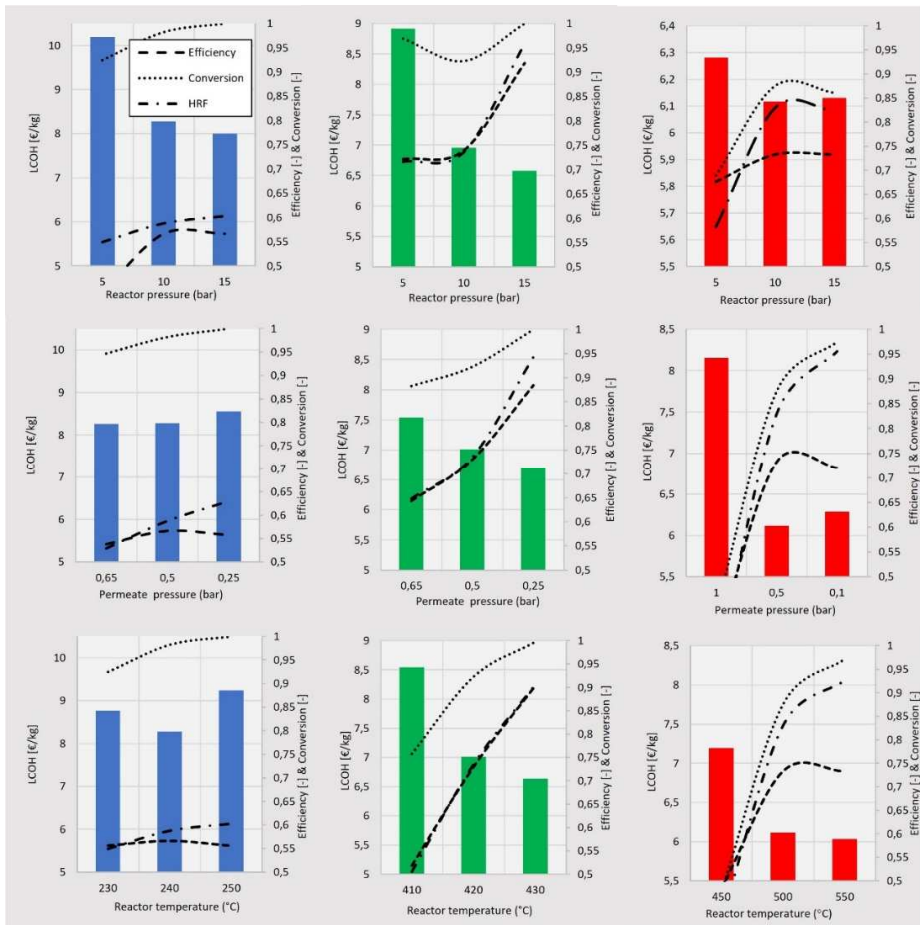


Figure 3-7: Sensitivity analysis on three main variable: reactor pressure, permeate pressure and temperature for methanol (in blue) ammonia (green) and methane (red) the baseline corresponding to the bar in the middle. The dotted line refers to the conversion, the dashed line refers to the

efficiency and the hybrid dash-dotted line refers to the HRF (The reactant flowrates are regulated to reach the required productivity at each operating conditions).

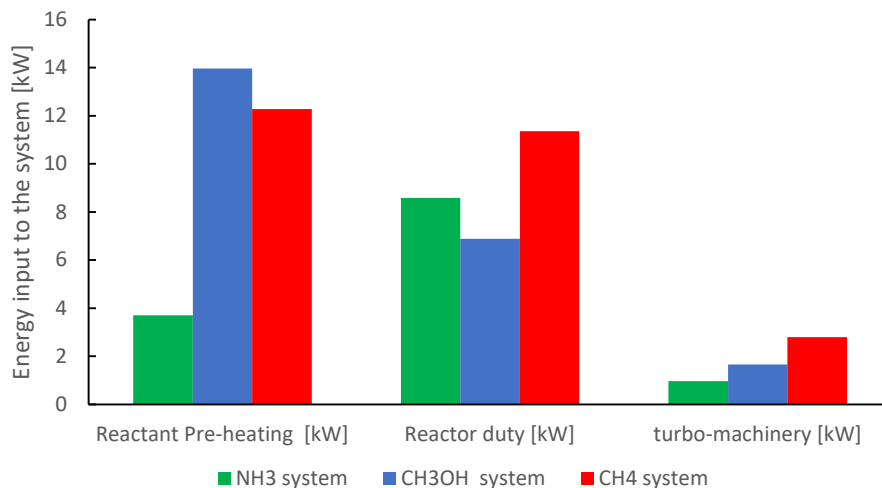


Figure 3-8: Main location of energy demand for each FP: NH₃ system (red) CH₃OH system (blue) and CH₄ system (green)

Another parameter to be investigated is the SCR (Steam-to-Carbon ratio), defined as the ratio between steam and methane molar flows in the feed. The effect of SCR on the methane system is reported in **Figure 3-9**. Increasing the water content leads to higher methane conversion at the reactor level, but this comes at the cost of an increased requirement for thermal power for steam production at the system level. The range of operating conditions investigated shows that a trade-off value can be found that minimizes the LCOH. For the methanol system, a detailed analysis (cf. **Figure 3-10**) is conducted at the reactor level to study the impact of SCR in relation to reactant flowrate and permeate pressure. It shows that at low flowrate and high permeate pressure, a higher SCR results in a lower HRF due to the lower reactant concentration decreasing the permeation driving force. Conversely, at low permeate pressure and high flowrate, a higher SCR leads to a higher HRF because the higher conversions resulting from higher SCR promote a higher driving force.

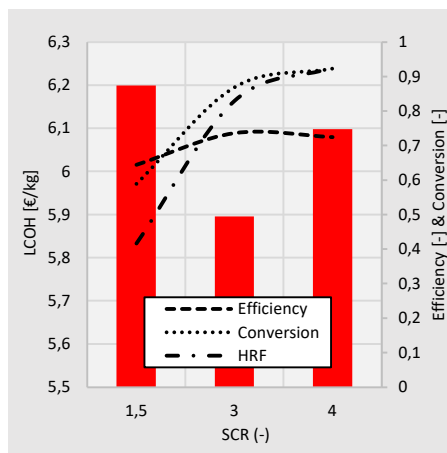


Figure 3-9: Impact of the SCR on the methane FP system around the base case. The dotted line refers to the conversion, the dashed line refers to the efficiency and the hybrid dash-dotted line refers to the HRF. (The reactant flowrates are regulated to reach the required productivity at each operating conditions)

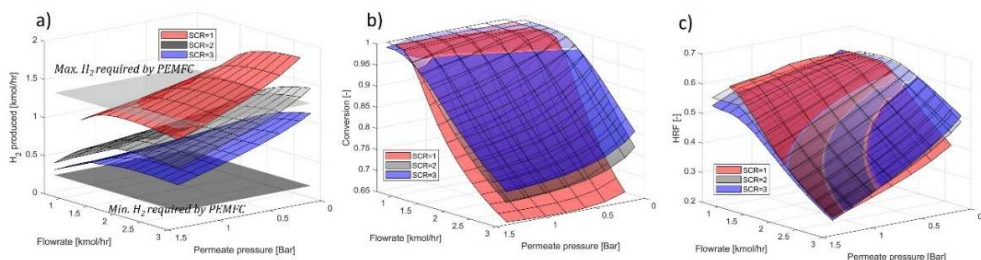


Figure 3-10: Detailed sensitivity analysis on SCR effect at the reactor level on the methanol system (a) hydrogen produced (b) Conversion and (c) HRF

This section highlights that the techno-economic considerations of hydrogen production from e-fuels are system-specific. To achieve efficient hydrogen production, it is generally necessary to strike a balance between insufficient and excessive membrane surface while taking into account the potential collateral effects that are inherent in each fuel processor system. 1) Insufficient membrane surface area can result in suboptimal hydrogen production due to reduced residence time in the reactor, which in turn restricts membrane flux and lowers the reactant conversion. This can also lead to significant hydrogen losses and wasted exhaust energy as a result of high temperatures in the exhaust, which directly impacts the overall efficiency of the system. 2) When the membrane surface area in the reactor is excessive, it may cause hydrogen to be extracted more rapidly than its production rate. While this could be advantageous for the reactor, it also lowers the hydrogen concentration within the reactor, thereby reducing the driving force for permeation. This may necessitate the use of additional utilities, such as fuel or electricity, to preheat the reactants and

maintain the endothermic reaction. In addition, the extra cost of the membrane required for the larger surface area could lead to negative economic consequences. 3) Finally, several trade-offs were observed depending on the operating conditions (SCR, permeate pressure and retentate pressure). To obtain a wider performance map of each system, a more comprehensive range of sensitivity analyses was carried out for each fuel processor illustrated in **Figure 3-11**. Based on the results, the NH_3 system demonstrates superior efficiency compared to the other systems, while the CH_4 system is found to be the most cost-effective option, albeit only slightly ahead of the NH_3 system. Notably, the methanol system lags significantly behind in terms of both economic and efficiency performance at the operating conditions studied.

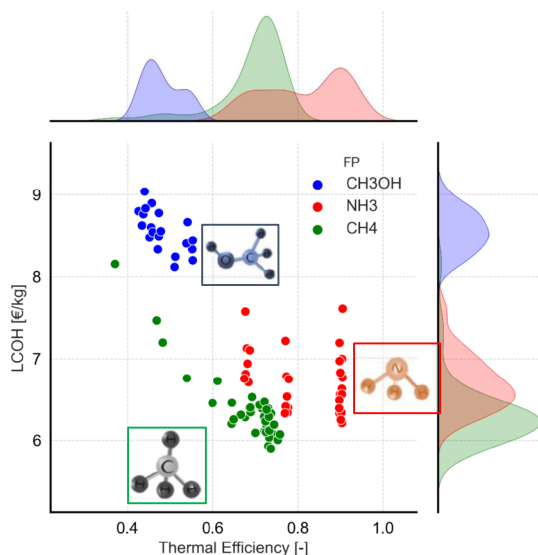


Figure 3-11: Result of an extended sensitivity analysis on the three FPs: NH_3 system (green) CH_3OH system (blue) and CH_4 system (red) with fixed H_2 productivity of 0.84 kmol/h

3.3.3. Optimization of the different systems

In order to facilitate a fair comparison between the three systems, the Aspen Plus software's SQRP (Successive Quadratic Programming) was utilized to optimize the parameters of the flowsheet structure. This optimization process involved fine-tuning the operating conditions, such as permeate pressure, reactor inlet pressure, flow rate, and temperature, as well as sizing parameters, including membrane area, for a total of five parameters. The primary goal was to maximize the fuel processor efficiency η_{th} , while still satisfying specific constraints, such as the addition of air to the burner to attain an O_2 content of 5% (on a molar basis), maintaining the required hydrogen productivity (i.e. 0.84 kmol/hr), and ensuring that the fluidized bed reactor remains in the "bubbling bed regime" with a u/u_{mf} ratio between 2 and 10. In addition, different setups were investigated such as electrical heating, thermal heating, and methane storage conditions. **Table 3-7** provides a summary of the results and associated operating conditions. At the fuel processor level,

the ammonia system achieves the highest maximum efficiency of 0.92, followed by the methane system with 0.82, and the methanol system with the lowest maximum efficiency of 0.57. The LCOH exhibits a declining trend from 8.3 €/kg-H₂ in the methanol system to 6.06 €/kg-H₂ and 6.02 €/kg-H₂ in the ammonia and methane systems, respectively. In contrast, when considering a thermal furnace, the methane system achieves the lowest cost of 5.21 €/kg-H₂ among all the cases considered, albeit with a slightly lower efficiency compared to its electric case counterpart. **Figure 3-12** shows that the reductions in LCOH correspond to fuel cost shares of 32% and 29% for the methanol and ammonia systems, respectively, when electrically heated, which decrease to 24% and 16%, respectively, for the methane system when thermally heated. The CAPEX shares range between 16% and 21% of the LCOH, depending on the system considered. Specifically, the methanol system has the highest CAPEX compared to the other systems due to the greater number of membranes and associated reactor volume and heat exchangers required to achieve the required productivity. In terms of the TPC composition (see **Figure 3-13**), the two primary expenses for each system in order of importance are related to the heat exchanger and membranes (in the ammonia system) heat exchangers and reactor vessel (in the methanol system), and heat exchanger and furnace (in the methane system) which aligns with the primary location of heat inputs for the latter two feedstocks. The methanol system is somewhat negatively affected by this situation, as reducing the membrane surface and associated reactor volume also leads to a higher heat exchanger area due to increased fuel requirements which is not an ideal situation. To emphasize the difference between the various configurations (electric vs thermal) and feedstock options, **Figure 3-14** provides a comparative view of the "best efficiency" points at the FP level in relation to the sensitivity analysis conducted in the previous paragraph. It can be observed that the highest efficiencies are located near the minimum number of membranes for the thermally heated system, whereas this is not the case for the electrically heated system. The reason for this is that in the latter configuration, the retentate flow only guarantees the thermal balance of the system. Therefore, in those conditions, the conversion is required to be slightly tempered to enable sufficient heating. Overall, the fuel processor level analysis confirms that the ammonia system is the most efficient, while the methane system seems to be the most cost-effective, although depending on the configuration, it can yield costs that are close to the ammonia system based on the considered assumptions.

This trend in hydrogen cost is reflected in the LCOE at the GENSET level as shown in **Figure 3-15**, with a reduction from 865 €/MWh in the electric methanol system to 673 €/MWh and 849 €/MWh in the electric and thermal ammonia systems, and finally to 654 €/MWh in the methane system with corresponding efficiencies ranging from 25% to 38%, as presented in **Table 3-7**. These efficiencies are competitive with ICE engines (i.e. efficiency in the range of 15-35% [23]) indicating the technological relevance of these systems. Compared to other studies on similar systems, the efficiency identified here is slightly lower than that reported by Marcoberardino et al. (2017) [26], who calculated an electric efficiency of 42%. However, their assessment was based on an assumed fuel cell efficiency of 62%. With the assumptions made, these systems however do not compare favorably to diesel ICE in terms of cost.

The PEMFC's cost dominates the economic performance, being twice as expensive as the FP for the ammonia system and almost 1.5 times as costly for the methane system. Finally, although the system

is designed for eco-friendly fuels, it's essential to acknowledge that fossil fuels remain a potential alternative. Hence, it's necessary to evaluate the greenhouse gas emissions potential within the system boundary. The ammonia systems are entirely carbon-free, but they still emit greenhouse gases in the form of nitrous oxide (NO_x), such as NO , NO_2 , and N_2O , due to NH_3 combustion in the furnace. The GWP (Global Warming Potential) of NO_x is estimated at 298 [89] [13]. According to this study (cf. **Table 3-7**), the methanol system has the highest greenhouse gas emissions, followed by the CH_4 system. Conversely, the ammonia genset emissions are insignificant. It is important to highlight that these systems can lead to higher emissions, particularly during transient operation. Roughly, a diesel engine typically emits 0.6-1.0 kgCO_2/kWh of electricity produced, which is comparable in magnitude to the CH_4 and CH_3OH systems. Therefore, only the NH_3 system outperforms the diesel genset from an environmental impact standpoint.

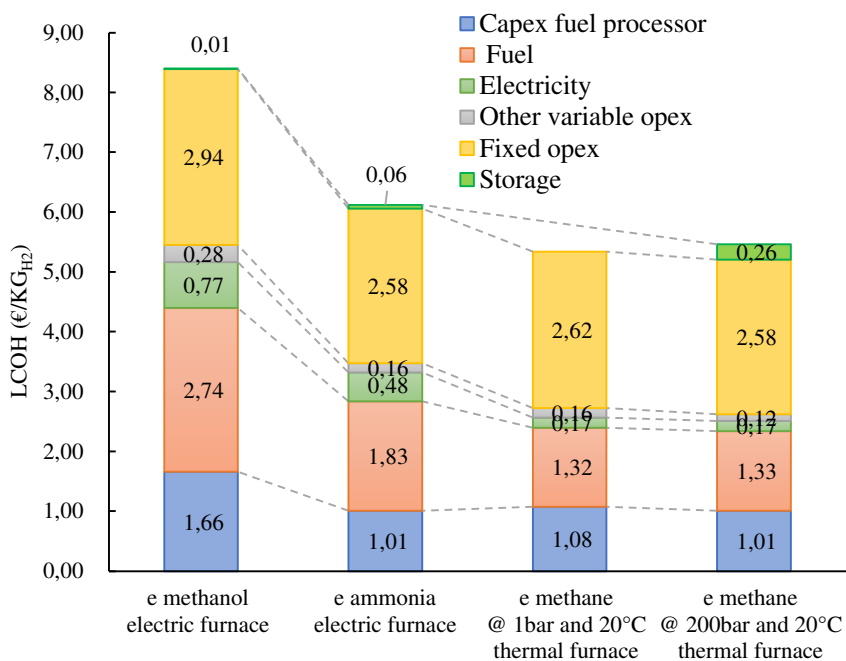


Figure 3-12: LCOH breakdown (assuming an electricity cost 85 €/MWh & a discharged pressure of H_2 of 1 bar, no storage cost for the e CH_4 at 1 bar).

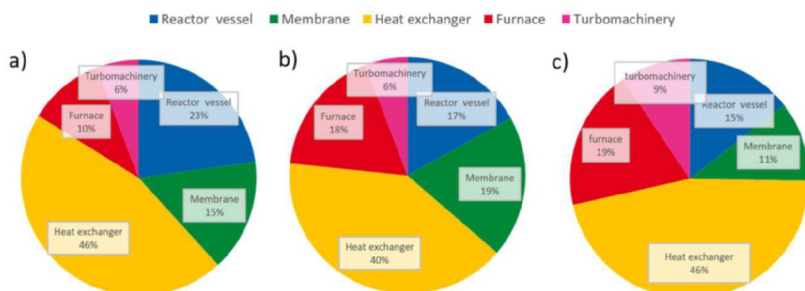


Figure 3-13: TPC composition at the fuel processor level of the (a) methanol (electric furnace) FP, (b) ammonia (electric furnace) FP and (c) methane (thermal furnace) FP at the maximum efficiency point obtained.

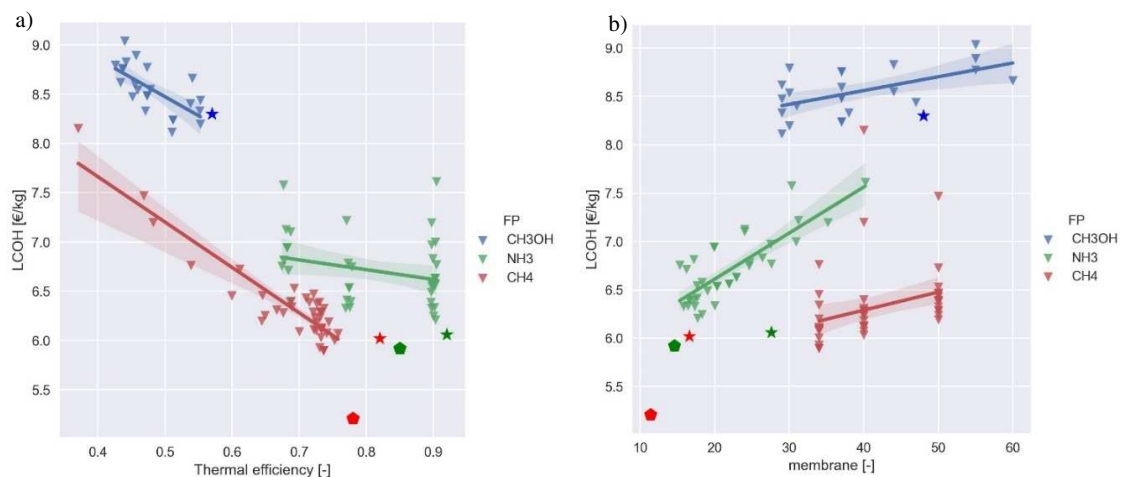


Figure 3-14: Comparing maximum efficiency points for electric and thermal furnace systems (represented by star and pentagon symbols, respectively) in relation to the sensitivity analysis in Section 3.3.2 (a) LCOH vs thermal efficiency; (b) LCOH vs number of membranes required

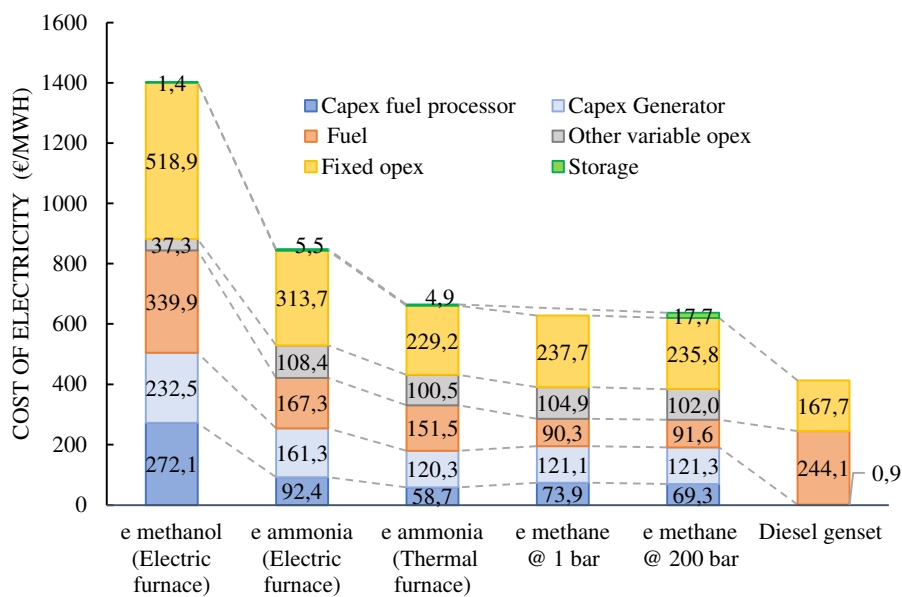


Figure 3-15: LCOE breakdown for the systems considered (assuming the PEM system supplies for the BOP of the fuel processor).

Table 3-7: Summary of the optimal operating conditions, optimized for maximum efficiency in different systems (constraints H_2 productivity of 0.84 kmol/hr, exhaust temperature $<150\text{ }^\circ\text{C}$, 5% O_2 excess in the flue gas)

		CASE 1: CH_4 System			CASE 2: NH_3 system		CASE 3: CH_3OH System
		Electric heating e- CH_4 at 1 bar	Thermal heating e- CH_4 at 1 bar	Thermal heating e- CH_4 at 200 bar	Thermal heating	Electric heating	Electric heating
Parameters	Reactor Temperature ($^\circ\text{C}$) * \in [450-550] Case 1 * \in [400-460] Case 2 * \in [200-260] Case 3	550	550	550	457	400	218
	Pressure \in [5-23] bar	19.1	7.27	20(fixed)	11.52	12	15.4
	Vacuum pressure \in [0.1-1] bar	0.526	0.258	0.169	0.189	0.7	0.242
	E-fuel flowrate [kmol/hr] * \in [0.05-1] Case 1 * \in [0.1-2] Case 2 * \in [0.58-3] Case 3	0.227	0.230	0.222	0.576	0.580	0.434
	Number of membranes \in [10-70]	16.6	11.5	11.5	14.6	27.6	48.8
Results	Exhaust temperature ($^\circ\text{C}$) $<150\text{ }^\circ\text{C}$ (inequality constraint)	106	60.7	71.9	79.4	21	26.2
	Thermal efficiency η_{th}	0.82	0.79	0.78	0.85	0.92	0.57
	Reactor conversion	0.955	0.953	0.961	0.999	0.996	0.963
	LCOH [$\text{€}/\text{kgH}_2$] (Considering an electricity price of 85 $\text{€}/\text{MWh}$ and a H_2 delivery pressure of 1bar)	6.02	5.21	5.47	5.92	6.06	8.30
	Electrical efficiency $\eta_{AC_{tot}}$	0.201	0.356	0.358	0.395	0.358	0.223
	Associated LCOE [$\text{€}/\text{MWh}$] (PEMFC provide for FP auxiliary consumption)	1343	627	637	665	848	1401
	Electricity production [kW]	10.3	24.4	25.1	23.2	17.7	12.7
	Emissions [$\text{kgGHG}/\text{kgH}_2$]	5.97	7.92	8.09	4.48E-3	1.12E-3	11.9

3.3.4. Sensitivity analysis on economic parameters

To highlight the dependence on some of the main assumptions, a sensitivity study is conducted on the primary parameters that affect the system cost (cf. **Figure 3-16**). For the sake of brevity, only a few of these parameters are being discussed, namely fuel cost, carbon tax, and plant

availability. Regarding the fuel cost, It is important to bear in mind that the study relies on the market price of e-fuels, however, recent estimates indicate that the cost of green fuels could range from being equivalent to fossil fuels to being ten times more expensive. In terms of the analysis, it reveals that a 50% hike in fuel costs results in a 16% increase in the LCOH of the methanol system, a 13% increase in the ammonia system, and a 12% increase in the methane system. The analysis also takes into account plant availability, which is assumed to be 0.65 in the base case and relatively low. The availability of the plant depends on the intended market, such as prime power genset or backup power genset. Increasing the availability by 50% results in a decrease of 23%, 19%, and 17% in the methane, ammonia, and methanol systems, respectively. In the base case, no carbon tax is considered, If fossil fuels are used, a carbon tax needs to be factored into the techno economic analysis, revealing that the ammonia system becomes more economically advantageous than the methane system at carbon tax rates above 85 €/tCO₂. Currently, the carbon tax policy is however not uniformly adopted, and its magnitude is dependent on the laws of individual nations. For example, in European countries that have already implemented a carbon tax, the range can fluctuate from 116.33 €/tCO₂ for Sweden to as low as 0.07 €/tCO₂ for Poland, with an average being 24 €/tCO₂. Nonetheless, as regulations on CO₂ emissions become stricter for achieving "Net-Zero by 2050" and carbon tax policies are gradually implemented worldwide, the carbon tax is expected to increase in the future.

To explore the potential for expanding the genset system into various markets, an economic analysis was conducted, including the possibility of scaling up to the megawatt level. Scaling up can be accomplished through increasing the reactor size or numbering up units, each with its own challenges. Membrane fragility and leakage make numbering up units a preferable approach, but the control and monitoring of individual units in parallel can be problematic, leading to increased capital costs. To address these challenges, a combination of modular and scaling up strategies was considered. Furthermore, promising results were obtained from the investigation of metallic supports for the development of thin Pd-based membranes, which could help alleviate these challenges and enable scale-up [90]. As a result, achieving the scale-up plan presented in **Figure 3-17** may be a possible option in the future. It is shown that the system at around 1 MW reaches an LCOE of 419 €/MWh with the baseline assumption (i.e. roughly increasing the productivity by 5 decreases the cost by almost 2.6) with a CAPEX strongly dominated by the PEMFC systems.

Anticipated full industrialization, mass production, and government subsidies for energy savings are however expected to drive down the cost of PEMFC. According to estimates from the JU H₂ [68] report indicate that electricity production levels of 5kWe, 50kWe, and 500kWe could be as low as 6000 €/kWe, 2500 €/kWe, and 1900 €/kWe, respectively. Furthermore, the Grasshopper Eu. Project [69] is working towards achieving cost of 1,500 €/kWe at a megawatt scale. In **Figure 3-18**, the economic viability of the composite GENSET proposed in this study is evaluated by assessing the influence of the PEMFC cost and comparing it with a diesel ICE engine. If the cost of PEMFC can be reduced from the base case of 6000 €/kWe to an achievable target of 2000 €/kWe, the electricity generated by the proposed system has the potential to be cost-competitive with that generated by a diesel ICE engine at an electricity production level of 150 kW.

In conclusion, techno-economic evaluations are useful for comparing various processes, but the values obtained may not be exact. Caution should be exercised when examining and interpreting costs derived from specific studies as they may differ depending on various assumptions or cost correlations. Nonetheless, it is still interesting to compare these costs with those found in previous literature, which indicates that the LCOH costs obtained in this study are generally in line with those reported in other scientific literature

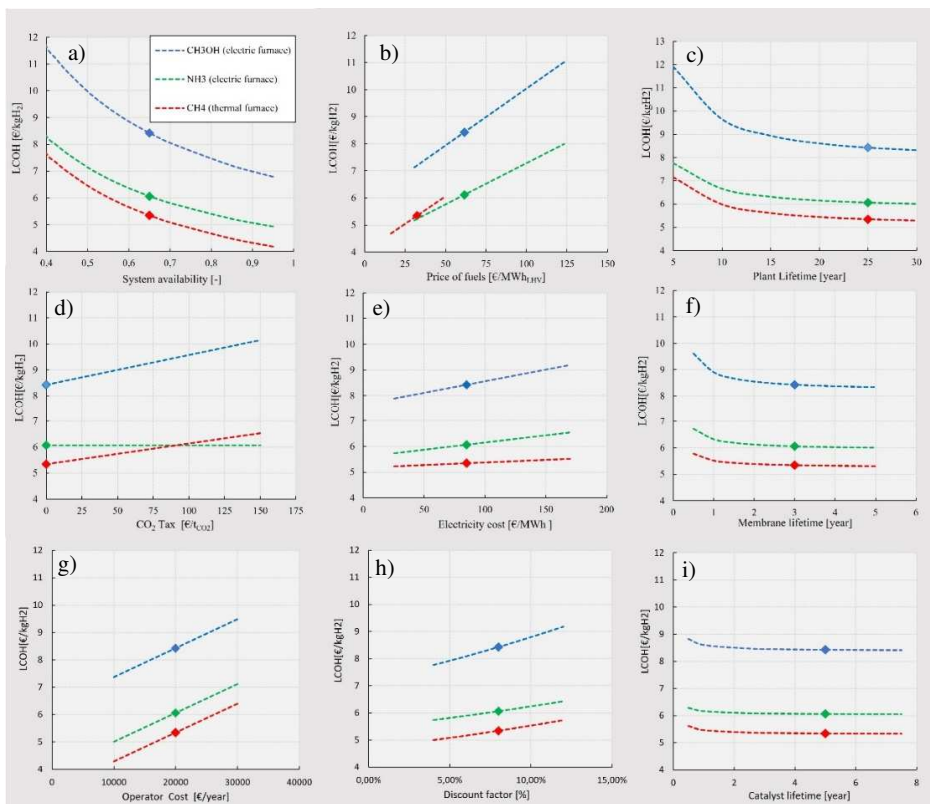


Figure 3-16: LCOH sensitivity towards the main economic variables for each FP, the dots represent the base case. (a) system availability; (b) Price of fuel; (c) Plant Lifetime; (d) CO₂ tax; (e) Electricity cost; (f) Membrane lifetime; (g) Operator cost; (h) Discount factor; (i) Catalyst lifetime.

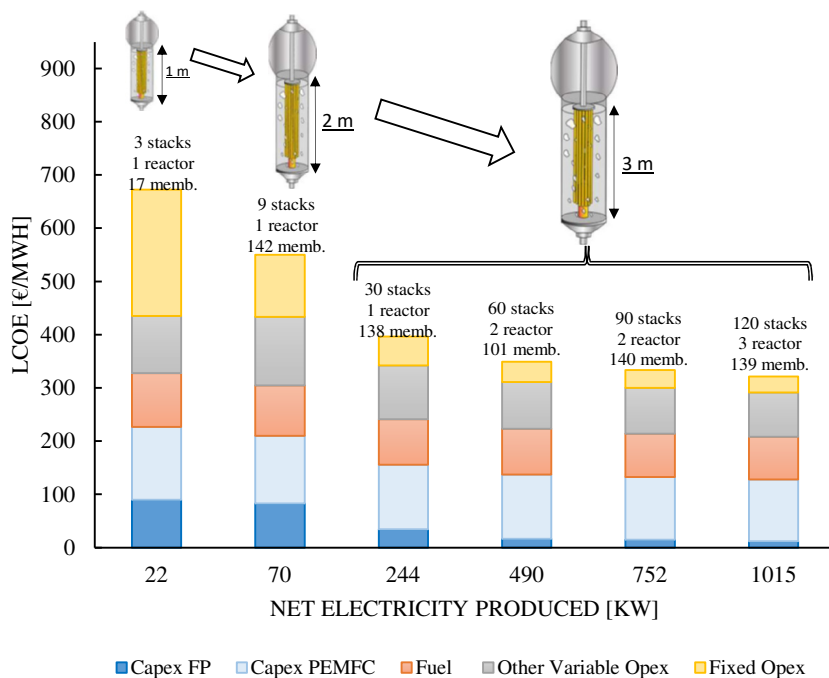


Figure 3-17: Scale up of the CH₄ PEM Genset system up to a capacity of ~ 1MW. 3 sized of reactor were selected and numbered up when a membrane number in the system was superior to 200. A fixed labor cost of 20000 €/ year (i.e. ~1 person) is assumed. The conditions taken are a reactor temperature of 525 °C a vacuum pressure of 0.25 and reaction pressure of 20 bar, a SCR=3 while the number of membranes and the feedstock flowrate are varied aiming at maximizing the efficiency

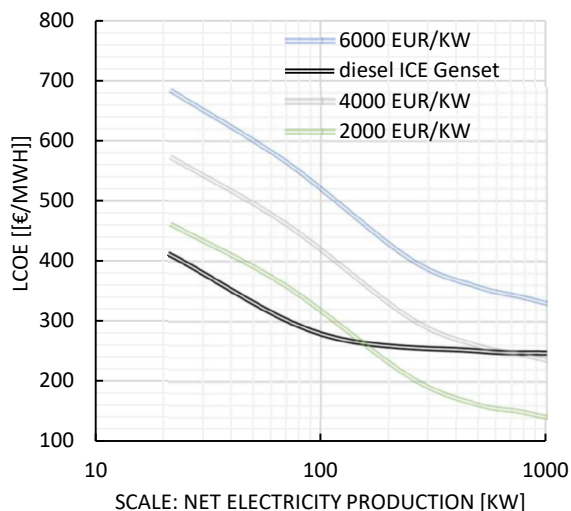


Figure 3-18: Comparison of the CH₄ PEM Genset with a diesel ICE engine. The cost correlation for the ICE engine is taken from Turton et al. (2018) [59] & A constant labor cost of 20 k€/ year is assumed to take care/operate the system for the whole production range

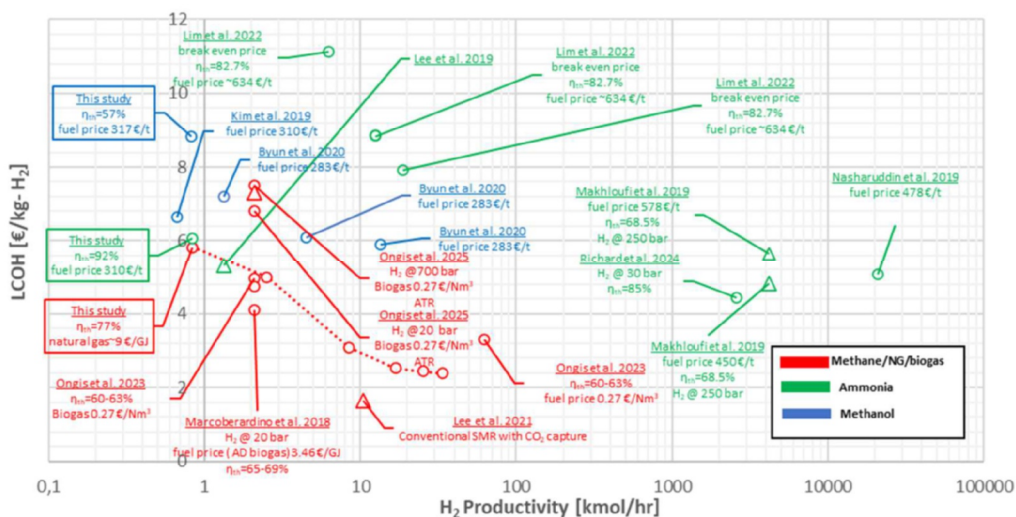


Figure 3-19: Overview of some hydrogen production costs from various literature sources. Dot markers represent membrane reactor (MR) systems, while triangle markers indicate traditional reactor (TR) systems. Differences in system boundaries, such as H₂ delivery pressure, and economic methodologies make the results indicative rather than directly comparable. Refer to the original sources for comprehensive details.

3.4. Conclusions

The objective of this chapter was to carry out an initial techno-economic evaluation of PEMFC genset systems that integrate membrane reactors as fuel processors, utilizing various feedstocks such as methane, ammonia, and methanol for storing significant amounts of renewable energy in the power-to-X framework. To accomplish this objective, the study employed a computer-based process simulation approach utilizing Aspen PlusTM software and utilized a two-steps optimization method. Initially, a sensitivity analysis was conducted to examine the influence of different operating conditions, such as reactor temperature, pressure, and permeate-side pressure on the overall efficiency of the fuel processors. Subsequently, a parameter optimization was performed to facilitate a fair comparison of the three feedstocks hydrogen and screen quickly through the variety of combination which can arise (electrical or thermal furnace, storage conditions of the methane). Finally, a sensitivity analysis was conducted on economic parameters to determine what could be realistically achieved in the near future and to address the significant uncertainties associated with certain economic variables.

- According to the sensitivity analysis conducted on operating conditions, the techno-economic aspects of hydrogen production from e-fuels are dependent on the system being used. Achieving optimal hydrogen production conditions requires balancing the membrane surface area while considering the specific trade-offs associated with each system based on its operating conditions, such as permeate pressure, retentate pressure, reactor temperature, and steam to carbon ratio. The study focused on discussing the impact of these individual parameters. Furthermore, the results show that the NH₃ system has superior efficiency from the FP perspective compared to other systems. On the other hand, the CH₄ system is the most cost-effective option, slightly ahead of the NH₃ system. It is worth noting that the methanol system appears to have lower economic and efficiency performance under the studied operating conditions.
- In terms of optimization, the study showed a decreasing levelized cost of hydrogen (LCOH) from 8.3 €/kg_{H2} in the methanol system to 6.21 €/kg_{H2} in the ammonia system and ultimately to 5.43 €/kg_{H2} in the methane system, with associated thermal efficiencies of 0.57, 0.92, and 0.77, respectively, at the fuel processor level. At the genset level, the reduction was from 1400 €/MWh in the electric methanol system to 848 €/MWh and 665 €/MWh in the electric and thermal ammonia systems, and finally to 627 €/MWh in the methane system, with corresponding electric efficiencies ranging from 25% to 39% provides a comparative view of the "best efficiency" points at the FP level in relation to the sensitivity analysis conducted in the previous paragraph. It can be observed that the highest efficiencies are located near the minimum number of membranes for the thermally heated system, whereas this is not the case for the electrically heated system. The study found that, while the systems were competitive with ICE engines from an efficiency point of view, they did not compare favorably to diesel ICE engines in terms of cost. This highlights the dependency of the optimization on the considered process architecture.

- Lastly, sensitivity analyses were carried out to highlight the reliance on certain key assumptions. Most notably, results showed that if the cost of PEMFC can be lowered to less than 2000 €/kW, the system could become economically competitive at the 150 kW, making it feasible for industrial application in the near future (provided that E-fuels can compete with fossil fuels, which is a key assumption of this study). In parallel, the ongoing advancements in technological maturity of membrane reactors, which are being promoted through various scale-up projects and EU initiatives, would play a crucial role in achieving economic competitiveness at the genset level.

While this research's findings align with established scientific literature, it's important to recognize the variety of uncertainties at play, such as reaction kinetics, feedstock costs, equipment expenses, and the selection of materials. These factors, along with any associated approximations, can profoundly impact the results of the study. For instance, revising the assumption that the same material (stainless steel) is used for each system could potentially reduce the observed economic disparity with the methanol system. Future research could reassess these elements, perhaps adjusting based on the actual equipment purchase costs. In addition, to offer a fairer comparison between methanol and ammonia, it would be beneficial to conduct future research exploring the effects of matching the methanol reforming temperature to that of the ammonia system. This would necessitate replacing the copper catalyst and discovering a new kinetic model, given that the current model in this study is only valid up to 260 °C. As a final perspective, it might be beneficial to expand the comparative study to encompass other types of generator systems, such as SOFCs (Solid Oxide Fuel Cells), and turbines. This could enrich a decision-making tool, aiding in identifying the technology with the greatest potential for specific applications.

3.5. References

- [1] V. Cigolotti, M. Genovese, P. Fragiaco, Comprehensive Review on Fuel Cell Technology for Stationary Applications as Sustainable and Efficient Poly-Generation Energy Systems, *Energies* 14 (2021) 4963. <https://doi.org/10.3390/en14164963>.
- [2] A.C. Riekstin, S. James, A. Kansal, No More Electrical Infrastructure: Towards Fuel Cell Powered Data Centers, (n.d.).
- [3] W.J. Sembler, S. Kumar, D. Palmer, Fuel Cells as an Alternative to Cold Ironing, *Journal of Fuel Cell Science and Technology* 6 (2009) 031009. <https://doi.org/10.1115/1.3006305>.
- [4] J.L. Viviente, J. Meléndez, D.A. Pacheco Tanaka, F. Gallucci, V. Spallina, G. Manzolini, S. Foresti, V. Palma, C. Ruocco, L. Roses, Advanced m-CHP fuel cell system based on a novel bio-ethanol fluidized bed membrane reformer, *International Journal of Hydrogen Energy* 42 (2017) 13970–13987. <https://doi.org/10.1016/j.ijhydene.2017.03.162>.
- [5] I. Petreanu, M. Dragan, S. Laurentiu Badea, Fuel Cells: Alternative Energy Sources for Stationary, Mobile and Automotive Applications, in: P. Vizureanu (Ed.), *Thermodynamics and Energy Engineering*, IntechOpen, 2020. <https://doi.org/10.5772/intechopen.93032>.
- [6] W.R.W. Daud, R.E. Rosli, E.H. Majlan, S.A.A. Hamid, R. Mohamed, T. Husaini, PEM fuel cell system control: A review, *Renewable Energy* 113 (2017) 620–638. <https://doi.org/10.1016/j.renene.2017.06.027>.

- [7] X. Yang, S. Wang, Y. He, Review of catalytic reforming for hydrogen production in a membrane-assisted fluidized bed reactor, *Renewable and Sustainable Energy Reviews* 154 (2022) 111832. <https://doi.org/10.1016/j.rser.2021.111832>.
- [8] E. Fernandez, A. Helmi, J.A. Medrano, K. Coenen, A. Arratibel, J. Melendez, N.C.A. de Nooijer, V. Spallina, J.L. Viviente, J. Zuñiga, M. van Sint Annaland, D.A. Pacheco Tanaka, F. Gallucci, Palladium based membranes and membrane reactors for hydrogen production and purification: An overview of research activities at Tecnalia and TU/e, *International Journal of Hydrogen Energy* 42 (2017) 13763–13776. <https://doi.org/10.1016/j.ijhydene.2017.03.067>.
- [9] D. Alique, D. Martinez-Diaz, R. Sanz, J. Calles, Review of Supported Pd-Based Membranes Preparation by Electroless Plating for Ultra-Pure Hydrogen Production, *Membranes* 8 (2018) 5. <https://doi.org/10.3390/membranes8010005>.
- [10] F. Gallucci, J.A. Medrano, J. Melendez, M. Van Sint Annaland, D.A. Pacheco Tanaka, Advances on High temperature Pd based membranes and membrane reactors for Hydrogen purification and production, *Journal of Membrane Science and Research* 3 (2017) 142–156.
- [11] A. Helmi, F. Gallucci, Latest Developments in Membrane (Bio)Reactors, *Processes* 8 (2020) 1239. <https://doi.org/10.3390/pr8101239>.
- [12] M. Byun, B. Lee, H. Lee, S. Jung, H. Ji, H. Lim, Techno-economic and environmental assessment of methanol steam reforming for H₂ production at various scales, *International Journal of Hydrogen Energy* 45 (2020) 24146–24158. <https://doi.org/10.1016/j.ijhydene.2020.06.097>.
- [13] D. Lim, A. Lee, A. Kim, J. Haider, H. Mikulčić, B. Brigljević, H. Lim, A 4E feasibility analysis of an on-site, ammonia sourced, hydrogen refueling station, *Journal of Cleaner Production* 363 (2022) 132356. <https://doi.org/10.1016/j.jclepro.2022.132356>.
- [14] S. Kim, S.-W. Yun, B. Lee, J. Heo, K. Kim, Y.-T. Kim, H. Lim, Steam reforming of methanol for ultra-pure H₂ production in a membrane reactor: Techno-economic analysis, *International Journal of Hydrogen Energy* 44 (2019) 2330–2339. <https://doi.org/10.1016/j.ijhydene.2018.08.087>.
- [15] G. Di Marcoberardino, S. Foresti, M. Binotti, G. Manzolini, Potentiality of a biogas membrane reformer for decentralized hydrogen production, *Chemical Engineering and Processing - Process Intensification* 129 (2018) 131–141. <https://doi.org/10.1016/j.ccep.2018.04.023>.
- [16] L. Roses, F. Gallucci, G. Manzolini, S. Campanari, M. van Sint Annaland, Comparison between fixed bed and fluidized bed membrane reactor configurations for PEM based micro-cogeneration systems, *Chemical Engineering Journal* 171 (2011) 1415–1427. <https://doi.org/10.1016/j.cej.2011.05.061>.
- [17] J.L. Viviente, FluidCell : Advanced m-CHP fuel cell system based on a novel bioethanol fluidized bed membrane reformer, 2018.
- [18] S. Foresti, G. Manzolini, Performances of a micro-CHP system fed with bio-ethanol based on fluidized bed membrane reactor and PEM fuel cells, *International Journal of Hydrogen Energy* 41 (2016) 9004–9021. <https://doi.org/10.1016/j.ijhydene.2016.03.210>.
- [19] G. Di Marcoberardino, G. Manzolini, Investigation of a 5 kW micro-CHP PEM fuel cell based system integrated with membrane reactor under diverse EU natural gas quality, *International Journal of Hydrogen Energy* 42 (2017) 13988–14002. <https://doi.org/10.1016/j.ijhydene.2017.02.016>.
- [20] G.D. Marcoberardino, A Techno-economic comparison of micro-cogeneration systems based on polymer electrolyte membrane fuel cell for residential applications, *Applied Energy* (2019) 14.
- [21] I. Rossetti, M. Compagnoni, M. Torli, Process simulation and optimization of H₂ production from ethanol steam reforming and its use in fuel cells. 2. Process analysis and optimization, *Chemical Engineering Journal* 281 (2015) 1036–1044. <https://doi.org/10.1016/j.cej.2015.08.045>.

- [22] M. Benito, R. Padilla, J.L. Sanz, L. Daza, Thermodynamic analysis and performance of a 1kW bioethanol processor for a PEMFC operation, *Journal of Power Sources* 169 (2007) 123–130. <https://doi.org/10.1016/j.jpowsour.2007.02.001>.
- [23] A. Stiel, M. Skyllas-Kazacos, Feasibility Study of Energy Storage Systems in Wind/Diesel Applications Using the HOMER Model, *Applied Sciences* 2 (2012) 726–737. <https://doi.org/10.3390/app2040726>.
- [24] D.-Y. Peng, D.B. Robinson, A New Two-Constant Equation of State, *Ind. Eng. Chem. Fund.* 15 (1976) 59–64. <https://doi.org/10.1021/i160057a011>.
- [25] R. Nasharuddin, M. Zhu, Z. Zhang, D. Zhang, A technoeconomic analysis of centralised and distributed processes of ammonia dissociation to hydrogen for fuel cell vehicle applications, *International Journal of Hydrogen Energy* 44 (2019) 14445–14455. <https://doi.org/10.1016/j.ijhydene.2019.03.274>.
- [26] M. Ongis, G. Di Marcoberardino, G. Manzolini, F. Gallucci, M. Binotti, Membrane reactors for green hydrogen production from biogas and biomethane: A techno-economic assessment, *International Journal of Hydrogen Energy* (2023) S0360319923005700. <https://doi.org/10.1016/j.ijhydene.2023.01.310>.
- [27] Nedstack, Product Data sheet Nedstack FCS 13-XXL PEM Fuel Cell Stack, (2019).
- [28] Y.-S. Seo, A. Shirley, S.T. Kolaczowski, Evaluation of thermodynamically favourable operating conditions for production of hydrogen in three different reforming technologies, *Journal of Power Sources* 108 (2002) 213–225. [https://doi.org/10.1016/S0378-7753\(02\)00027-7](https://doi.org/10.1016/S0378-7753(02)00027-7).
- [29] B.A. Peppley, J.C. Amphlett, L.M. Kearns, R.F. Mann, Methanol–steam reforming on Cu/ZnO/Al₂O₃. Part 1: the reaction network, *Applied Catalysis A: General* 179 (1999) 21–29. [https://doi.org/10.1016/S0926-860X\(98\)00298-1](https://doi.org/10.1016/S0926-860X(98)00298-1).
- [30] V. Cechetto, L. Di Felice, R. Gutierrez Martinez, A. Arratibel Plazaola, F. Gallucci, Ultra-pure hydrogen production via ammonia decomposition in a catalytic membrane reactor, *International Journal of Hydrogen Energy* 47 (2022) 21220–21230. <https://doi.org/10.1016/j.ijhydene.2022.04.240>.
- [31] E. Hosseinzadeh, M. Rokni, Development and Validation of a Simple Analytical Model of the Proton Exchange Membrane Fuel Cell (PEMFC) in a Fork-Lift Truck Power System, *International Journal of Green Energy* 10 (2013) 523–543. <https://doi.org/10.1080/15435075.2012.678525>.
- [32] H. Lee, I. Jung, G. Roh, Y. Na, H. Kang, Comparative Analysis of On-Board Methane and Methanol Reforming Systems Combined with HT-PEM Fuel Cell and CO₂ Capture/Liquefaction System for Hydrogen Fueled Ship Application, *Energies* 13 (2020) 224. <https://doi.org/10.3390/en13010224>.
- [33] V.A. Danilov, M.O. Tade, An alternative way of estimating anodic and cathodic transfer coefficients from PEMFC polarization curves, *Chemical Engineering Journal* 156 (2010) 496–499. <https://doi.org/10.1016/j.cej.2009.09.022>.
- [34] V. Cechetto, L. Di Felice, J.A. Medrano, C. Makhloufi, J. Zuniga, F. Gallucci, H₂ production via ammonia decomposition in a catalytic membrane reactor, *Fuel Processing Technology* 216 (2021) 106772. <https://doi.org/10.1016/j.fuproc.2021.106772>.
- [35] D. Kunii, O. Levenspiel, Bubbling Fluidized Beds, in: *Fluidization Engineering*, Elsevier, 1991: pp. 137–164. <https://doi.org/10.1016/B978-0-08-050664-7.50012-3>.
- [36] V. Spallina, D. Pandolfo, A. Battistella, M.C. Romano, M. Van Sint Annaland, F. Gallucci, Techno-economic assessment of membrane assisted fluidized bed reactors for pure H₂ production with CO₂ capture, *Energy Conversion and Management* 120 (2016) 257–273. <https://doi.org/10.1016/j.enconman.2016.04.073>.
- [37] I. Iliuta, R. Tahoces, G.S. Patience, S. Riffart, F. Luck, Chemical-looping combustion process: Kinetics and mathematical modeling, *AIChE Journal* 56 (2010) 17.
- [38] S. Foresti, G. Di Marcoberardino, G. Manzolini, N. De Nooijer, F. Gallucci, M. van Sint Annaland, A comprehensive model of a fluidized bed membrane reactor for small-scale

- hydrogen production, *Chemical Engineering and Processing - Process Intensification* 127 (2018) 136–144. <https://doi.org/10.1016/j.cep.2018.01.018>.
- [39] F. Gallucci, M. van Sint Annaland, J.A.M. Kuipers, Chapter 10. Modeling of Membrane Reactors for Hydrogen Production and Purification, in: 2011: pp. 1–39. <https://doi.org/10.1039/9781849733489-00001>.
- [40] E. Fernandez, A. Helmi, K. Coenen, J. Melendez, J.L. Viviente, D.A. Pacheco Tanaka, M. van Sint Annaland, F. Gallucci, Development of thin Pd–Ag supported membranes for fluidized bed membrane reactors including WGS related gases, *International Journal of Hydrogen Energy* 40 (2015) 3506–3519. <https://doi.org/10.1016/j.ijhydene.2014.08.074>.
- [41] W.-H. Chen, M.-H. Hsia, Y.-L. Lin, Y.-H. Chi, C.-C. Yang, Hydrogen permeation and recovery from H₂–N₂ gas mixtures by Pd membranes with high permeance, *International Journal of Hydrogen Energy* 38 (2013) 14730–14742. <https://doi.org/10.1016/j.ijhydene.2013.08.086>.
- [42] A. Helmi, R.J.W. Voncken, A.J. Rajmakers, I. Roghair, F. Gallucci, M. van Sint Annaland, On concentration polarization in fluidized bed membrane reactors, *Chemical Engineering Journal* 332 (2018) 464–478. <https://doi.org/10.1016/j.cej.2017.09.045>.
- [43] M. Nordio, S. Soresi, G. Manzolini, J. Melendez, M. Van Sint Annaland, D.A. Pacheco Tanaka, F. Gallucci, Effect of sweep gas on hydrogen permeation of supported Pd membranes: Experimental and modeling, *International Journal of Hydrogen Energy* 44 (2019) 4228–4239. <https://doi.org/10.1016/j.ijhydene.2018.12.137>.
- [44] N. de Nooijer, F. Gallucci, E. Pellizzari, J. Melendez, D.A. Pacheco Tanaka, G. Manzolini, M. van Sint Annaland, On concentration polarisation in a fluidized bed membrane reactor for biogas steam reforming: Modelling and experimental validation, *Chemical Engineering Journal* 348 (2018) 232–243. <https://doi.org/10.1016/j.cej.2018.04.205>.
- [45] M.A. Murmura, M. Sheintuch, Permeance inhibition of Pd-based membranes by competitive adsorption of CO: Membrane size effects and first principles predictions, *Chemical Engineering Journal* 347 (2018) 301–312. <https://doi.org/10.1016/j.cej.2018.04.072>.
- [46] C. Brencio, F.W.A. Fontein, J.A. Medrano, L. Di Felice, A. Arratibel, F. Gallucci, Pd-based membranes performance under hydrocarbon exposure for propane dehydrogenation processes: Experimental and modeling, *International Journal of Hydrogen Energy* (2021) S036031992103874X. <https://doi.org/10.1016/j.ijhydene.2021.09.252>.
- [47] C.S. Patil, M. van Sint Annaland, J.A.M. Kuipers, Fluidised bed membrane reactor for ultrapure hydrogen production via methane steam reforming: Experimental demonstration and model validation, *Chemical Engineering Science* 62 (2007) 2989–3007. <https://doi.org/10.1016/j.ces.2007.02.022>.
- [48] V. Verma, T. Li, J.-F. Dietiker, W.A. Rogers, Hydrodynamics of gas–solids flow in a bubbling fluidized bed with immersed vertical U-tube banks, *Chemical Engineering Journal* 287 (2016) 727–743. <https://doi.org/10.1016/j.cej.2015.11.049>.
- [49] R.J.W. Voncken, I. Roghair, M. van Sint Annaland, A numerical study on concentration polarization in 3D cylindrical fluidized beds with vertically immersed membranes, *Chemical Engineering Science* 205 (2019) 299–318. <https://doi.org/10.1016/j.ces.2019.05.010>.
- [50] S. Sayas, N. Morlanés, S.P. Katikaneni, A. Harale, B. Solami, J. Gascon, High pressure ammonia decomposition on Ru–K/CaO catalysts, *Catal. Sci. Technol.* 10 (2020) 5027–5035. <https://doi.org/10.1039/D0CY00686F>.
- [51] B.A. Peppley, J.C. Amphlett, L.M. Kearns, R.F. Mann, Methanol–steam reforming on Cu/ZnO/Al₂O₃ catalysts. Part 2. A comprehensive kinetic model, *Applied Catalysis A: General* 179 (1999) 31–49. [https://doi.org/10.1016/S0926-860X\(98\)00299-3](https://doi.org/10.1016/S0926-860X(98)00299-3).
- [52] L. Marra, P.F. Wolbers, F. Gallucci, M. van S. Annaland, Development of a RhZrO₂ catalyst for low temperature autothermal reforming of methane in membrane reactors, *Catalysis Today* 236 (2014) 23–33. <https://doi.org/10.1016/j.cattod.2013.10.069>.

- [53] V. Spallina, D. Pandolfo, A. Battistella, M.C. Romano, M. Van Sint Annaland, F. Gallucci, Techno-economic assessment of membrane assisted fluidized bed reactors for pure H₂ production with CO₂ capture, *Energy Conversion and Management* 120 (2016) 257–273. <https://doi.org/10.1016/j.enconman.2016.04.073>.
- [54] J.A. Medrano, M.A. Llosa-Tanco, V. Cechetto, D.A. Pacheco-Tanaka, F. Gallucci, Upgrading biogas with novel composite carbon molecular sieve (CCMS) membranes: Experimental and techno-economic assessment, *Chemical Engineering Journal* 394 (2020) 124957. <https://doi.org/10.1016/j.cej.2020.124957>.
- [55] G. Manzolini, E. Macchi, M. Gazzani, CO₂ capture in natural gas combined cycle with SEWGS. Part B: Economic assessment, *International Journal of Greenhouse Gas Control* 12 (2013) 502–509. <https://doi.org/10.1016/j.ijggc.2012.06.021>.
- [56] K. Gerdes, W. Summers, J. Wimer, *Quality Guidelines for Energy System Studies: Cost Estimation Methodology for NETL Assessments of Power Plant Performance*, 2011. <https://doi.org/10.2172/1513278>.
- [57] G. Di Marcoberardino, S. Foresti, M. Binotti, G. Manzolini, Potentiality of a biogas membrane reformer for decentralized hydrogen production, *Chemical Engineering and Processing - Process Intensification* 129 (2018) 131–141. <https://doi.org/10.1016/j.ccep.2018.04.023>.
- [58] Gioele Marcoberardino, Dario Vitali, Francesco Spinelli, Marco Binotti, Giampaolo Manzolini, Green Hydrogen Production from Raw Biogas: A Techno-Economic Investigation of Conventional Processes Using Pressure Swing Adsorption Unit, *Processes* 6 (2018) 19. <https://doi.org/10.3390/pr6030019>.
- [59] R. Turton, ed., *Analysis, synthesis, and design of chemical processes*, 5th edition, Prentice Hall, Boston, 2018.
- [60] M. Ongis, G. Di Marcoberardino, M. Baiguini, F. Gallucci, M. Binotti, Optimization of Small-Scale Hydrogen Production with Membrane Reactors, *Membranes* 13 (2023) 331. <https://doi.org/10.3390/membranes13030331>.
- [61] M. Yoshida, T. Ogawa, Y. Imamura, K.N. Ishihara, Economies of scale in ammonia synthesis loops embedded with iron- and ruthenium-based catalysts, *International Journal of Hydrogen Energy* 46 (2021) 28840–28854. <https://doi.org/10.1016/j.ijhydene.2020.12.081>.
- [62] C. Makhoulfi, Large-scale decomposition of green ammonia for pure hydrogen production, (2021) 11.
- [63] T.A. Atspha, T. Yoon, B.-H. Yoo, C.-J. Lee, Techno-Economic and Environmental Analysis for Direct Catalytic Conversion of CO₂ to Methanol and Liquid/High-Calorie-SNG Fuels, *Catalysts* 11 (2021) 687. <https://doi.org/10.3390/catal11060687>.
- [64] A. Valentini, Green shift to create 1 billion tonne ‘green ammonia’ market?, (2020) 6.
- [65] Z. Cesaro, M. Ives, R. Nayak-Luke, M. Mason, R. Bañares-Alcántara, Ammonia to power: Forecasting the levelized cost of electricity from green ammonia in large-scale power plants, *Applied Energy* 282 (2021) 116009. <https://doi.org/10.1016/j.apenergy.2020.116009>.
- [66] Fluid Cell Project, (n.d.). <https://www.fluidcell.eu/> (accessed April 3, 2023).
- [67] MACBETH, (n.d.). <https://www.macbeth-project.eu/> (accessed February 3, 2023).
- [68] CHJU, Clean Hydrogen Joint Undertaking, Multi - Annual Work Plan 2021-2027, (2021).
- [69] Grasshopper Eu. Project, (n.d.). <https://www.grasshopperproject.eu/> (accessed April 12, 2023).
- [70] D. Bellotti, M. Rivarolo, L. Magistri, A comparative techno-economic and sensitivity analysis of Power-to-X processes from different energy sources, *Energy Conversion and Management* 260 (2022) 115565. <https://doi.org/10.1016/j.enconman.2022.115565>.
- [71] V. Dias, M. Pochet, F. Contino, H. Jeanmart, Energy and Economic Costs of Chemical Storage, *Front. Mech. Eng.* 6 (2020) 21. <https://doi.org/10.3389/fmech.2020.00021>.
- [72] M. Nordio, S.A. Wassie, M. Van Sint Annaland, D.A. Pacheco Tanaka, J.L. Viviente Sole, F. Gallucci, Techno-economic evaluation on a hybrid technology for low hydrogen

- concentration separation and purification from natural gas grid, *International Journal of Hydrogen Energy* 46 (2021) 23417–23435. <https://doi.org/10.1016/j.ijhydene.2020.05.009>.
- [73] G. Manzolini, E. Sanchez Fernandez, S. Rezvani, E. Macchi, E.L.V. Goetheer, T.J.H. Vlugt, Economic assessment of novel amine based CO₂ capture technologies integrated in power plants based on European Benchmarking Task Force methodology, *Applied Energy* 138 (2015) 546–558. <https://doi.org/10.1016/j.apenergy.2014.04.066>.
- [74] S. Wang, S.P. Jiang, Prospects of fuel cell technologies, *National Science Review* 4 (2017) 163–166. <https://doi.org/10.1093/nsr/nww099>.
- [75] R. Rivera-Tinoco, M. Farran, C. Bouallou, F. Auprêtre, S. Valentin, P. Millet, J.R. Ngameni, Investigation of power-to-methanol processes coupling electrolytic hydrogen production and catalytic CO₂ reduction, *International Journal of Hydrogen Energy* 41 (2016) 4546–4559. <https://doi.org/10.1016/j.ijhydene.2016.01.059>.
- [76] P. Battaglia, G. Buffo, D. Ferrero, M. Santarelli, A. Lanzini, Methanol synthesis through CO₂ capture and hydrogenation: Thermal integration, energy performance and techno-economic assessment, *Journal of CO₂ Utilization* 44 (2021) 101407. <https://doi.org/10.1016/j.jcou.2020.101407>.
- [77] A. Varone, M. Ferrari, Power-to-liquid and power-to-gas: An option for the German Energiewende, *Renewable and Sustainable Energy Reviews* 45 (2015) 207–218. <https://doi.org/10.1016/j.rser.2015.01.049>.
- [78] M.J. Bos, S.R.A. Kersten, D.W.F. Brilman, Wind power-to-methanol: Renewable methanol production using electricity, electrolysis of water and CO₂ air capture, *Applied Energy* 264 (2020) 114672. <https://doi.org/10.1016/j.apenergy.2020.114672>.
- [79] O. Osman, S. Sgouridis, A. Sleptchenko, Scaling the production of renewable ammonia: A techno-economic optimization applied in regions with high insolation, *Journal of Cleaner Production* 271 (2020) 121627. <https://doi.org/10.1016/j.jclepro.2020.121627>.
- [80] H. Zhang, L. Wang, J. Van herle, F. Maréchal, U. Desideri, Techno-economic comparison of green ammonia production processes, *Applied Energy* 259 (2020) 114135. <https://doi.org/10.1016/j.apenergy.2019.114135>.
- [81] R. Chauvy, L. Dubois, P. Lybaert, D. Thomas, G. De Weireld, Production of synthetic natural gas from industrial carbon dioxide, *Applied Energy* 260 (2020) 114249. <https://doi.org/10.1016/j.apenergy.2019.114249>.
- [82] E. Giglio, A. Lanzini, M. Santarelli, P. Leone, Synthetic natural gas via integrated high-temperature electrolysis and methanation: Part II—Economic analysis, *Journal of Energy Storage* 2 (2015) 64–79. <https://doi.org/10.1016/j.est.2015.06.004>.
- [83] A. Kiani, M. Lejeune, C. Li, J. Patel, P. Feron, Liquefied synthetic methane from ambient CO₂ and renewable H₂ - A technoeconomic study, *Journal of Natural Gas Science and Engineering* 94 (2021) 104079. <https://doi.org/10.1016/j.jngse.2021.104079>.
- [84] statista, Dutch TTF gas futures at the beginning of each week from January 4, 2021 to February 27, 2023, <https://www.Statista.Com/Statistics/1267202/Weekly-Dutch-Ttf-Gas-Futures/> (2023). <https://www.statista.com/statistics/1267202/weekly-dutch-ttf-gas-futures/>.
- [85] Methanol Institute, METHANOL PRICE AND SUPPLY/DEMAND, (2022). <https://www.methanol.org/methanol-price-supply-demand/>.
- [86] Trading economic, Urea Ammonium nitrate, (2023). <https://tradingeconomics.com/commodity/urea-ammonium>.
- [87] H. Purnama, T. Ressler, R.E. Jentoft, H. Soerijanto, R. Schlögl, R. Schomäcker, CO formation/selectivity for steam reforming of methanol with a commercial CuO/ZnO/Al₂O₃ catalyst, *Applied Catalysis A: General* 259 (2004) 83–94. <https://doi.org/10.1016/j.apcata.2003.09.013>.
- [88] A. Iulianelli, S. Liguori, Y. Huang, A. Basile, Model biogas steam reforming in a thin Pd-supported membrane reactor to generate clean hydrogen for fuel cells, *Journal of Power Sources* 273 (2015) 25–32. <https://doi.org/10.1016/j.jpowsour.2014.09.058>.

- [89] O. Kurata, N. Iki, T. Matsunuma, T. Inoue, T. Tsujimura, H. Furutani, H. Kobayashi, A. Hayakawa, Performances and emission characteristics of NH_3 -air and NH_3 CH_4 -air combustion gas-turbine power generations, *Proceedings of the Combustion Institute* 36 (2017) 3351–3359. <https://doi.org/10.1016/j.proci.2016.07.088>.
- [90] S. Agnolin, Surface roughness improvement of Hastelloy X tubular filters for H_2 selective supported Pd-Ag alloy membranes preparation, *International Journal of Hydrogen Energy* (2022) 13.
- [91] R.F. Mann, J.C. Amphlett, M.A.I. Hooper, H.M. Jensen, B.A. Peppley, P.R. Roberge, Development and application of a generalised steady-state electrochemical model for a PEM fuel cell, (2000) 8.
- [92] S. Mori, C.Y. Wen, Estimation of bubble diameter in gaseous fluidized beds, *AIChE J.* 21 (1975) 109–115. <https://doi.org/10.1002/aic.690210114>.
- [93] J.A. Medrano, I. Potdar, J. Melendez, V. Spallina, D.A. Pacheco-Tanaka, M. van Sint Annaland, F. Gallucci, The membrane-assisted chemical looping reforming concept for efficient H_2 production with inherent CO_2 capture: Experimental demonstration and model validation, *Applied Energy* 215 (2018) 75–86. <https://doi.org/10.1016/j.apenergy.2018.01.087>.
- [94] V. Spallina, G. Matturro, C. Ruocco, E. Meloni, V. Palma, E. Fernandez, J. Melendez, A.D. Pacheco Tanaka, J.L. Viviente Sole, M. van Sint Annaland, F. Gallucci, Direct route from ethanol to pure hydrogen through autothermal reforming in a membrane reactor: Experimental demonstration, reactor modelling and design, *Energy* 143 (2018) 666–681. <https://doi.org/10.1016/j.energy.2017.11.031>.
- [95] L. Marra, P.F. Wolbers, F. Gallucci, M. van S. Annaland, Development of a RhZrO_2 catalyst for low temperature autothermal reforming of methane in membrane reactors, *Catalysis Today* 236 (2014) 23–33. <https://doi.org/10.1016/j.cattod.2013.10.069>.
- [96] A. Di Carlo, L. Vecchione, Z. Del Prete, Ammonia decomposition over commercial $\text{Ru}/\text{Al}_2\text{O}_3$ catalyst: An experimental evaluation at different operative pressures and temperatures, *International Journal of Hydrogen Energy* 39 (2014) 808–814. <https://doi.org/10.1016/j.ijhydene.2013.10.110>.
- [97] Z. Zhang, S. Liguori, T.F. Fuerst, J.D. Way, C.A. Wolden, Efficient Ammonia Decomposition in a Catalytic Membrane Reactor To Enable Hydrogen Storage and Utilization, *ACS Sustainable Chem. Eng.* 7 (2019) 5975–5985. <https://doi.org/10.1021/acssuschemeng.8b06065>.
- [98] J. Zhu, S.S. Araya, X. Cui, S.L. Sahlin, S.K. Kær, Modeling and Design of a Multi-Tubular Packed-Bed Reactor for Methanol Steam Reforming over a $\text{Cu}/\text{ZnO}/\text{Al}_2\text{O}_3$ Catalyst, *Energies* 13 (2020) 610. <https://doi.org/10.3390/en13030610>.
- [99] F. Qureshi, F. Ahmad, M. Idrees, A.A. Khan, S. Zaidi, Simulation of methanol steam reforming process for the production of hydrogen, *Indian Chemical Engineer* 63 (2021) 99–116. <https://doi.org/10.1080/00194506.2019.1689186>.
- [100] F. Gallucci, L. Paturzo, A. Basile, Hydrogen Recovery from Methanol Steam Reforming in a Dense Membrane Reactor: Simulation Study, *Ind. Eng. Chem. Res.* 43 (2004) 2420–2432. <https://doi.org/10.1021/ie0304863>.
- [101] M.S. Herdem, M. Mundhwa, S. Farhad, F. Hamdullahpur, Multiphysics Modeling and Heat Distribution Study in a Catalytic Microchannel Methanol Steam Reformer, *Energy Fuels* 32 (2018) 7220–7234. <https://doi.org/10.1021/acs.energyfuels.8b01280>.
- [102] V. Gurau, A. Ogunleke, F. Strickland, Design of a methanol reformer for on-board production of hydrogen as fuel for a 3 kW High-Temperature Proton Exchange Membrane Fuel Cell power system, *International Journal of Hydrogen Energy* 45 (2020) 31745–31759. <https://doi.org/10.1016/j.ijhydene.2020.08.179>.
- [103] Y. Im, H. Muroyama, T. Matsui, K. Eguchi, Ammonia decomposition over nickel catalysts supported on alkaline earth metal aluminate for H_2 production, *International Journal of Hydrogen Energy* 45 (2020) 26979–26988. <https://doi.org/10.1016/j.ijhydene.2020.07.014>.

- [104] M. Ongis, M. Baiguini, G. Di Marcoverardino, F. Gallucci, M. Binotti, Techno-economic analysis for the design of membrane reactors in a small-scale biogas-to-hydrogen plant, *International Journal of Hydrogen Energy* 101 (2025) 887–903. <https://doi.org/10.1016/j.ijhydene.2024.12.245>

Appendix A.

A1. Constitutive equations for the PEMFC stack

Table A1: List of constitutive equations of the stack model similar to [32]

Average Cell Voltage	$V = E - \eta_{act} - \eta_{ohmic} - \eta_{conc}$	Eq. A1
Theoretical cell voltage (Nernst equation)	$E = E^0 + \frac{RT}{2F} \ln \left(P_{H_2} P_{O_2}^{\frac{1}{2}} \right)$	Eq. A2
Activation overpotential (Butler Volmer equation)	$\eta_{act} = \eta_{act,c} + \eta_{act,a} = \frac{RT}{\alpha_c F} \ln \left(\frac{i + i_{loss}}{i_{0,c}} \right) + \frac{RT}{\alpha_a F} \ln \left(\frac{i + i_{loss}}{i_{0,a}} \right)$ with $i_{0,a} = n F k_a \exp \left(\frac{(1-\beta) \cdot n F E}{RT} \right)$ & $i_{0,c} = n F k_a \exp \left(\frac{\beta \cdot n F E}{RT} \right)$ $\alpha_a = \beta \eta_{el,a}$ and $\alpha_a = (1-\beta) \eta_{el,c}$	Eq. A3
Ohmic overpotential	$\eta_{ohmic} = (r_{el} + r_{ion}) i$	Eq. A4
Ionic resistance in the cell [91]	$r_{ion} = \frac{C_1 \left[1 + 0.03i + 0.062 \left(\frac{T}{303} \right)^2 \times i^{2.5} \right]}{(\lambda_{mem} - 0.634 - 3i) \exp \left[C_2 \left(\frac{T - 303}{T} \right) \right]} \times t_m$	Eq. A5
Membrane water content	$\lambda_{memb} = \frac{\lambda_c - \lambda_a}{t_m} z + \lambda_a$ Where the water activity is expressed: $\lambda_{c\&a} = 0.043 + 17.18a_w - 39.85a_w^2 + 36a_w^3$ if $0 < a_w < 1$ $\lambda_{c\&a} = 14 + 1.4(a_w - 1)$ if $0 < a_w < 3$	Eq. A5
Net water transport through membrane	$J_{H_2O,drag} = J_{H_2O,drag} - J_{H_2O,back\ diff}$ $= 2 * n_{drag}^{sat} \times \frac{\lambda_{mem} \times i}{22 \times n_p F} - \frac{\rho_{dry}}{M_m} \times D_w \times \frac{d\lambda_{mem}}{dz}$	Eq. A5
Water diffusion coefficient	$D_w = 10^{-6} (2.563 - 0.33\lambda_{mem} + 0.0264\lambda_{mem}^2 - 0.000671\lambda_{mem}^3) \times \exp \left[2416 \left(\frac{1}{303} - \frac{1}{T} \right) \right]$	Eq. A6
Net Nitrogen cross over	$J_{N_2} = K_{N_2} \frac{P_{N_2,ca} - P_{N_2,an}}{t_m}$	Eq. A7
Nitrogen permeation coefficient	$K_{N_2} = 8(0.0295 + 1.21f_v - 1.93f_v^2) \times 10^{-11} \times \exp \left[\frac{E_{N_2}}{R} \left(\frac{1}{303} - \frac{1}{T} \right) \right]$ $f_v = \frac{\lambda_{mem} \times V_w}{V_{mem} + \lambda_{mem} \times V_w}$	Eq. A8
Material balance	$\dot{n}_{H_2,req} = \frac{I}{n_p F} S_{H_2}$	Eq. A9
Energy balance	$C_t \times \frac{dT}{dt} = \dot{E}_{in} - \dot{E}_{out} - \dot{E}_{el} - \dot{E}_{loss}$	Eq. A10

A2. Fluidized bed model

Table A2: Empirical correlations used in the FBMR model to describe the fluidized bed hydrodynamic and mass transfer similar to [26]

u_{mf}	$Ar = \left(\frac{1.75}{\varepsilon_{mf}^3 \phi_s} \right) Re_{p_{mf}}^2 + 150 \frac{(1 - \varepsilon_{mf})}{\varepsilon_{mf}^3 \phi_s^2} Re_{p_{mf}}$	Eq. A11
ε_{mf}	$\varepsilon_{mf} = (1 - \varepsilon_{packed}) Ar^{-0.029} \left(\frac{\rho_{gas}}{\rho_s} \right)^{0.021}$	Eq. A12

Initial bubble diameter $d_{b,0}$	$d_{b,0} = 0.376(u_0 - u_{mf})^2$	Eq. A13
Maximum bubble diameter	$d_{b,max} = \min(1.6374A_T(u_0 - u_{mf})^{0.4}; D_x)$ $D_x = \min(D_{reactor}; dist_{memb})$	Eq. A14
Average bubble diameter $d_{b,av}$[92]	$d_{b,av} = d_{b,max} - (d_{b,max} - d_{b,0})e^{-\frac{0.3H}{D_t}}$	Eq. A15
Bubble phase fraction f_b	$f_b = \frac{u_0 - u_{mf}}{u_{b,avg}}$ or $f_b = \frac{u_0 - u_{mf}}{u_{b,avg} + u_{mf}}$	Eq. A16
Wake parameter α $f_w = \alpha f_b$	0.15	Eq. A17
Cloud emulsion f_{ce}	$1 - f_w - f_b$	Eq. A18
Emulsion gas velocity	$u_e = \frac{u_0 - f_b u_b}{1 - f_b}$	Eq. A19

A3. Impact of concentration polarization

In this work, concentration polarization is modeled using a simple reducing factor, f_{cp} . This factor adjusts the ideal permeation flux based on the Richardson equation, as expressed in Eq. A20:

$$J_{H_2} = f_{cp} * \frac{Pe}{\delta} (p_{H_{2,ret}}^n - p_{H_{2,perm}}^n) \left[\frac{mol}{s \cdot m^2} \right] \quad \text{Eq. A20}$$

Such a factor is challenging to determine from the literature due to scattered data and its dependence on operating conditions (e.g., temperature, flow rate, and driving force) as well as reactor design parameters, such as the specific membrane area (cf. **Table A3**). To simplify the analysis, a brief sensitivity study was conducted using a homogeneous CFD model (see **Figure A1**) under conditions similar to those of this study. The goal was to evaluate the influence of parameters such as temperature and H_2 inlet fraction on the Concentration Polarization Coefficient (CPC) and H_2 flux in a packed bed reactor (see **Figure A2**). The CPC represents the ratio of the average H_2 concentration at the membrane surface to that at the wall. A CPC value of one indicates the presence of radial diffusion limitations, while lower values suggest more efficient radial diffusion. Additional details on the CPC are discussed in **Chapter 6** (page 198) of this thesis. The analysis suggests that concentration polarization in packed bed reactors for this study can be approximated with a reduction factor of 0.15 (see **Figure A3**). For fluidized bed reactors, a reduction factor of 0.6, derived from trusted literature sources [93], is applied.

Table A3: Example of CP reducing factor in literature .

	FBMR or PBMR	Exp/model	Membranes	Max Reducing factor
Chen et al. (2013) [41]	PBMR	Exp.	Pd-Ag	~0.0420
Helmi et al. (2018) [42]	FBMR	Both	Pd-Ag	~0.33
Medrano et al. (2018) [93]	FBMR	1D Model	Pd-Ag	0.6

Spallina et al. (2018) [94]	FBMR	Exp	Pd-Ag	~0.53
--------------------------------	------	-----	-------	-------

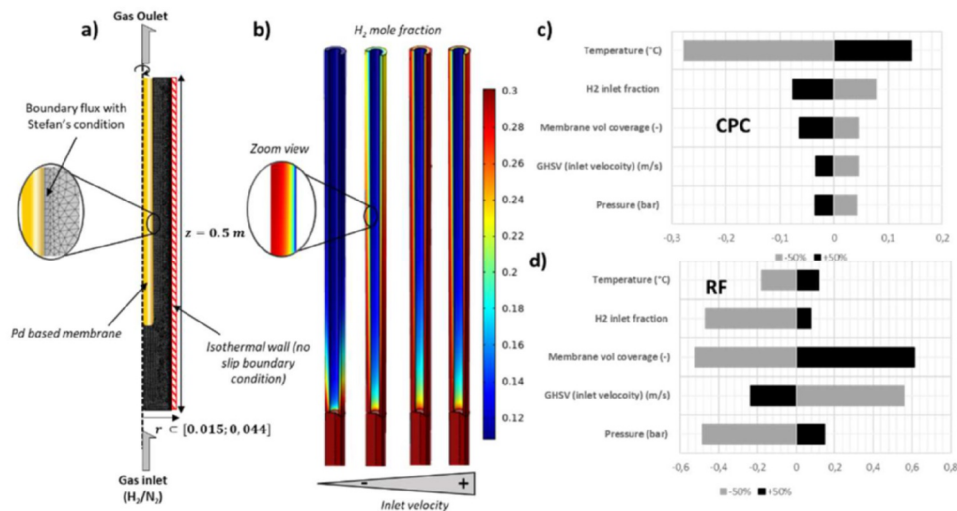
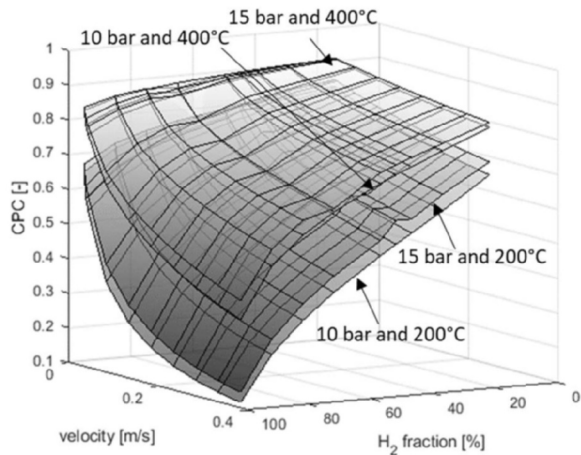


Figure A1: (a) Axisymmetric domain of the membrane module simulated with a zoom view of the mesh composed of a total of 33383 elements (no significant dependency on the mesh was found). (b) Molar fraction distribution of temperature and zoom view of the boundary layer (c)&(d) sensitivity study by applying -50% and +50% change in the baseline operating conditions for the polarization coefficient and the Recovery Factor.



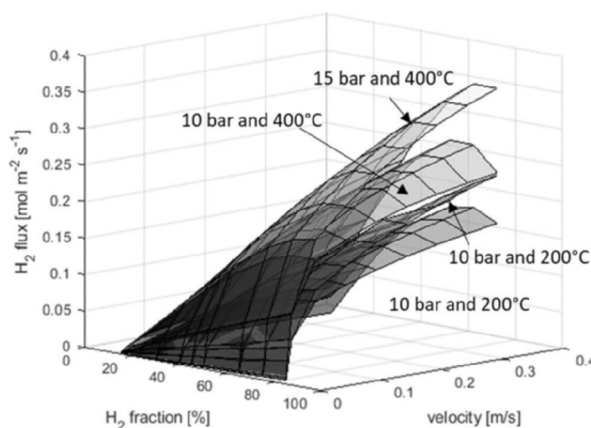


Figure A2: Visualization of the sensitivity sweep on the CPC (top), H₂ flux (bottom) at 200 °C and 400 °C and 10 and 15 bar using a bed diameter of 0.031 m

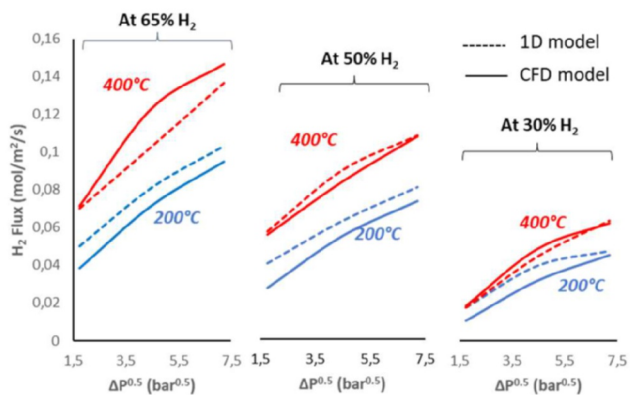


Figure A3: Comparison between CFD and 1D model assuming a 0.15 reducing factor which is then used this study. (in red 400 °C and in blue 200 °C).

A4. Kinetic rate laws & parameters

A4.1. Methane steam reforming

Table A4: Methane steam reforming kinetic rates laws from Marra et al. (2014) [95]

Reactions	Reaction rates
Methane reforming	$R_{SMR} = \frac{k_{SMR} \left(p_{CH_4} p_{H_2O} \frac{p_{H_2}^3 p_{CO}}{K_{SMR}^{eq}} \right)}{p_{H_2O}^{1.596}} \text{ Eq. A21}$

Water gas shift	$R_{WGS} = \frac{k_{WGS} \left(P_{CO} P_{H_2O} - \frac{P_{H_2} P_{CO_2}}{K_{WGS}^{eq}} \right)}{P_{H_2O}}$ Eq. A22
Kinetic constant formulation	$k_i = A_i e^{\left(-\frac{E_{act,i}}{RT} \right)}$ Eq. A23

Table A5: Methane steam reforming kinetic constants from Marra et al. (2014) [95] in Eq A23

$A_{SMR} (kmol \text{ bar}^{-0.404} kg_{cat}^{-1} h^{-1})$	$9.74 * 10^4$
$A_{WGS} (kmol \text{ bar}^{-0.5} kg_{cat}^{-1} h^{-1})$	$17.2 * 10^2$
$E_{act}^{SMR} \left(\frac{kJ}{mol} \right)$	$83.6 * 10^3$
$E_{act}^{WGS} \left(\frac{kJ}{mol} \right)$	$54.5 * 10^3$

A4.2. Ammonia decomposition

Regarding ammonia, the Temkin-Phyzev model (Eq. A24) has been accurately used in several other works to fit experimental conversion rate for both ammonia synthesis and decomposition reactions [62, 96, 97]. The kinetic law parameters were fitted for several Ruthenium (Ru)-based catalysts cited in the literature Hypermec 10010TM (8% Ru)[96] and Alfa AesarTM (2% Ru) [34] and a non-commercial catalyst based on Ru (3%)-K-CaO [50]. A nickel-based catalyst was also considered for reference [103]. Their values is reported in **Table A6**

$$R_{NH_3} = k_0 \exp \left(-\frac{E_{act}}{RT} \right) P_{NH_3}^{2*\beta} P_{H_2}^{-3*\beta} \quad \text{Eq.A24}$$

Table A6: Kinetic law parameters fitted using the Temkin-Pyzev (Eq. A24) Least square estimator & Nelder Mead Solver

	k_0 $\left[\frac{kmol}{m^3 hr \text{ bar}^{-\beta}} \right]$	E_0 $\left[\frac{kJ}{kmol} \right]$	β [–]
Cechetto et al. (2021) [34]	$4.09 * 10^{14}$	$1.87 * 10^5$	0.560
Sayas et al. (2020) [50]	$1.65 * 10^{14}$	$1.82 * 10^5$	0.584
Di Carlo et al. (2014) [96]	$4.09 * 10^{12}$	$1.49 * 10^5$	0.799
Im et al. (2020) [103]	$3.89 * 10^{14}$	$1.99 * 10^5$	0.477

A4.3. Methanol steam reforming

For methanol reforming, the Peppley reaction kinetic model was employed, a widely used approach (often used [98-102]). This model is based on Langmuir-Hinshelwood reaction rate expressions, which describe the kinetics of methanol steam reforming over a Cu/ZnO/Al₂O₃ catalyst. The key parameters of this model are summarized in **Table A7**.

$$R'_{SMR} = \frac{k_{SMR} * K_{CH_3O1} \left(\frac{P_{CH_3OH}}{P_{H_2}^{0.5}} \right) \left[1 - \frac{1}{K_{SMR}} \left(\frac{P_{H_2}^3 P_{CO_2}}{P_{CH_3OH} P_{H_2O}} \right) \right] CS_1^T CS_{1A}^T}{\left(1 + K_{CH_3O1} \left(\frac{P_{CH_3OH}}{P_{H_2}^{0.5}} \right) + K_{HCOO1} P_{CO_2} P_{H_2}^{0.5} + K_{OH1} \left(\frac{P_{H_2O}}{P_{H_2}^{0.5}} \right) \right) \left(1 + (K_{H1}^* P_{H_2})^{0.5} \right)}$$
 Eq. A25

$$R'_{WGS} = \frac{k_{WGS} * K_{OH1} P_{CO} \left(\frac{P_{H_2O}}{P_{H_2}^{0.5}} \right) \left[1 - \frac{1}{K_{WGS}} \left(\frac{P_{H_2} P_{CO_2}}{P_{CO} P_{H_2O}} \right) \right] (CS_1^T)^2}{\left(1 + K_{CH_3O1} \left(\frac{P_{CH_3OH}}{P_{H_2}^{0.5}} \right) + K_{HCOO1} P_{CO_2} P_{H_2}^{0.5} + K_{OH1} \left(\frac{P_{H_2O}}{P_{H_2}^{0.5}} \right) + K_{CO_21} P_{CO_2} \right)^2}$$
 Eq. A26

$$R'_{MD} = \frac{k_{MD} * K_{CH_3O2} \left(\frac{P_{CH_3OH}}{P_{H_2}^{0.5}} \right) \left[1 - \frac{1}{K_{MD}} \left(\frac{P_{H_2}^2 P_{CO}}{P_{CH_3OH}} \right) \right] CS_2^T CS_{2A}^T}{\left(1 + K_{CH_3O2} \left(\frac{P_{CH_3OH}}{P_{H_2}^{0.5}} \right) + K_{OH2} \left(\frac{P_{H_2O}}{P_{H_2}^{0.5}} \right) + K_{CO_22} P_{CO_2} \right) \left(1 + (K_{H2}^* P_{H_2})^{\frac{1}{2}} \right)}$$
 Eq. A27

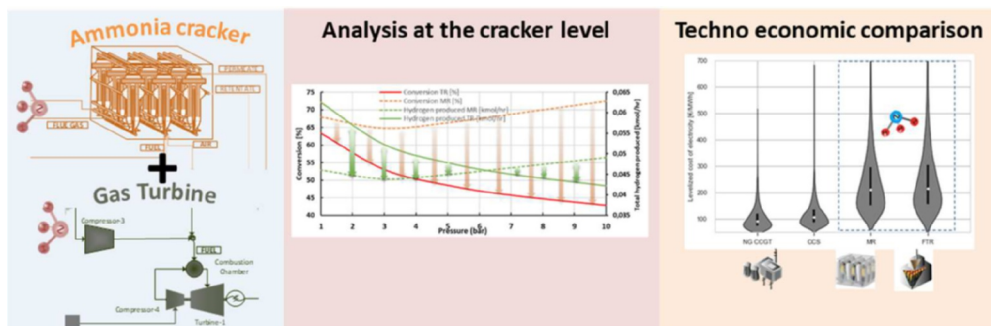
Table A7: Parameters for the kinetic equations of methanol reforming [29]

Equilibrium constant	ΔS [J mol ⁻¹ K ⁻¹]	ΔH [J mol ⁻¹]	Parameters	Values
$K_{CH_3O1} [bar^{-0.5}]$	-41.8	-2*10 ⁴	$k_{0SMR} [m^2 s^{-1} mol^{-1}]$	7.4 * 10 ¹⁴
$K_{HCOO1} [bar^{-1.5}]$	179.2	10 ⁵	$E_{actSMR} [J mol^{-1}]$	1.03 * 10 ⁵
$K_{OH1} [bar^{-0.5}]$	-44.5	-2*10 ⁴	$k_{0WGS} [m^2 s^{-1} mol^{-1}]$	5.9 * 10 ¹³
$K_{OH1} [bar^{-1.5}]$	-44.5	-2*10 ⁴	$E_{actWGS} [J mol^{-1}]$	8.7 * 10 ⁵
$K_{H1}^* [bar^{-1}]$	-100.8	-5*10 ⁴	$k_{0MD} [m^2 s^{-1} mol^{-1}]$	3.8 * 10 ²⁰
$K_{CH_3O2} [bar^{-0.5}]$	30.0	-2*10 ⁴	$E_{actMD} [J mol^{-1}]$	1.7*10 ⁵
$K_{OH2} [bar^{-0.5}]$	30.0	-2*10 ⁴	$CS_1^T \left[\frac{mol}{m^2} \right]$	7.5*10 ⁻⁶
$K_{H2} [bar^{-1}]$	-46.2	-5*10 ⁴	$CS_{1A}^T \left[\frac{mol}{m^2} \right]$	1.5*10 ⁻⁵
			$CS_2^T \left[\frac{mol}{m^2} \right]$	7.5*10 ⁻⁶
			$CS_{2A}^T \left[\frac{mol}{m^2} \right]$	1.5*10 ⁻⁵

Chapter 4 | Techno-economic analysis of ammonia cracking for large scale power generation

Abstract

The increased interest in leveraging green ammonia to mitigate carbon emissions in fertilizer production is paralleled by an expanding acknowledgment of its potential as a fuel for decarbonizing the electricity sector, particularly in high-efficiency gas turbine power plants. Co-firing ammonia with hydrogen presents a promising method for integrating ammonia into existing infrastructures. Within this context, the development of efficient technology for ammonia cracking presents a potential avenue for deploying ammonia in gas turbines. The objective of this chapter* is to conduct a preliminary techno-economic evaluation and uncertainty analysis of two cracking technologies namely a membrane reactor and a conventional FTR (Fired Tubular Reactor) for the co-firing of ammonia with hydrogen in a CCGT (Combined Cycle Gas Turbine) plant. The integration of a membrane reactor during the cracking stage demonstrates a remarkable improvement in the system's thermal efficiency, surpassing traditional approaches by over 25%. Additionally, it brings above 10% reduction in the levelized cost of hydrogen (LCOH), despite a higher initial capital expenditure (CAPEX). At the CCGT level, the discrepancy in levelized cost of electricity (LCOE) narrows, as it is strongly influenced by the cost of ammonia constituting 80% of the LCOE. Beyond LCOE, the widespread adoption of these systems also faces challenges due to material scarcity. Analysis reveals that revamping just 1 GWe of CCGT assets using membrane reactors would for example necessitate approximately 0.11% of the global palladium supply, and 10% of the global ruthenium production. Considering the limited availability of these resources, coupled with their high demand across multiple sectors and the possibility of external factors such as geopolitical tensions, this strategy seems unfeasible. To tap into this market, future research should prioritize the exploration of alternative membrane materials, such as carbon molecular sieves, and catalysts, like nickel.



*This chapter is based on the following paper: S. Richard, A. Ramirez Santos, P. Olivier, F. Gallucci, Techno-economic analysis of ammonia cracking for large scale power generation, Int. J. Hydrogen Energy vol. 71, pp. 571–587, 2024

4.1. Introduction

While **Chapter 4** explored the use of e-fuels for power generation with an emphasis on small-scale applications, utilizing PEM fuel cells, the present chapter shifts attention to the utilisation of ammonia in large-scale power generation. Specifically, it focuses on combined cycle gas turbines (CCGTs), which offer unmatched efficiency and flexibility at large scale. They have the potential to significantly contribute to a greener energy landscape while supporting the integration of variable renewable energy (VRE) sources [1]. This improvement plays a pivotal role in preventing carbon entrenchment and minimizing costly asset devaluation during the transition to a decarbonized grid [2]. The initial stages of this journey have been characterized by the incorporation of hydrogen blending in gas turbines, with gas turbine OEMs (original equipment manufacturers) recognizing the viability of incorporating up to 60 vol.% hydrogen in specific existing turbine types. According to a report by ETN Global (European Turbine Network)[1], some OEMs are now aiming to increase this ratio to 100 vol. % hydrogen. However, the widespread adoption of hydrogen as an energy carrier still faces substantial challenges, notably in the domains of transportation, storage, and the possibility of potential leaks [3-5].

In contrast, green ammonia has emerged as a remarkable zero-carbon alternative, primarily due to its dispatchability and relative ease of storage at high volumes [6]. Liquid ammonia offers several advantages, including a notably high hydrogen storage density, with a weight percentage of 17.8% by mass and a volume of 121 kg-H₂/m³. This exceeds the densities achieved by other advanced hydrogen storage systems or hydrogen-containing material, including metal hydrides (25 kg-H₂/m³), liquefied hydrogen (71 kg-H₂/m³) [7], compressed hydrogen at 700 bar (42.2 kg-H₂/m³) [7], methanol (99 kg-H₂/m³) [7], or formic acid (53 kg-H₂/m³) [8]. The increased hydrogen carrying capacity per unit volume of ammonia translates into a lower cost per unit of stored energy compared to alternative options [9-11]. For example, Zhao et al. (2019) [10] found that ammonia has the lowest global cost (including production, storage, and transportation) being 31% lower than compressed hydrogen. Dias et al. (2020) [11] indicated that storing hydrogen as a gas is costlier, with storage costs 46% higher than ammonia. The IEA [12] nuanced those finding by suggesting that hydrogen gas could be the best option for inland transport up to 3500 km, after which ammonia becomes more economical. Ammonia is also advantageous due to well-established standards, a long history of safety, and a storage and distribution infrastructure that has been in place for more than 75 years [13]. These numerous advantages have sparked a growing interest in utilizing ammonia as a carbon-free fuel for gas turbines, as evidenced by the increasing number of research papers dedicated to exploring this field, as depicted in **Figure 4-1**.

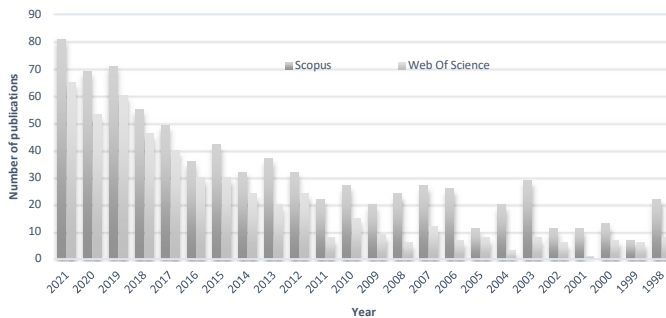


Figure 4-1: Number of scientific articles mentioning the key words “Turbine” and “Ammonia” in their abstract from Scopus and Web of Science

However, the combustion characteristics of ammonia differ significantly from those of traditional hydrocarbon and hydrogen fuels, posing certain challenges. One major concern is the relatively low flame speeds of ammonia-air mixtures, which are only one-fifth of those observed in methane-air mixtures at 298 K and 0.10 MPa [14–15]. Moreover, ammonia is a toxic substance, and the emission of unburned ammonia from gas turbines is undesirable. The presence of nitrogen oxides (NO_x), unburned species like NH₃, and trace amounts of hydrogen further complicate matters in this field. While direct combustion has been studied, it requires the development of new fuel delivery systems, modifications to gas turbine enclosures, and rethinking the design of NO_x treatments and combustors [1,13]. Numerous OEMs are currently involved in prototype development in this field. Notably, Mitsubishi Heavy Industries (MHI) which aims to create an industrial-scale turbine (50MW) by 2025–2030 [16]. In 2021, IHI partnered with GE (General Electric) to produce gas turbines with the goal of achieving 100% ammonia-based combustion by 2030 [17].

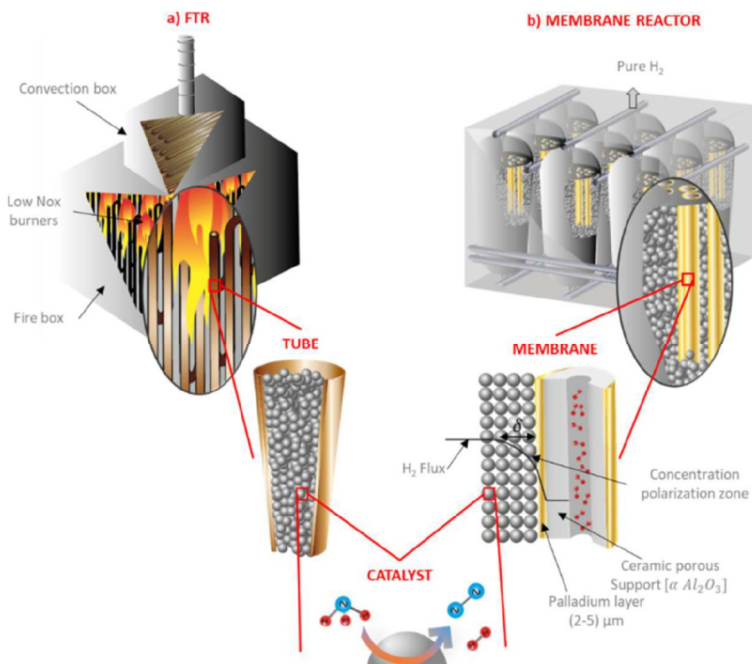
To overcome the challenge posed by the low burning velocity of ammonia and enable its use with existing industrial devices, alternative studies explore its use as a co-fuel, often in conjunction with hydrogen [18–19] or methane (although the latter emits carbon dioxide) [20]. Research as early as the 1960s [21] demonstrated that combining ammonia's slow flame with hydrogen's fast, hot flame can produce combustion properties comparable to methane in a gas turbine. A blend with 30% H₂ (vol. %) seems to have gained attention in this field but uncertainties still remain regarding safe, stable, and efficient operation while minimizing NO_x emissions. Numerous studies have been conducted on the combustion and emissions performance of ammonia/hydrogen blends [22–30]. For instance, Pugh et al. (2019) [24] highlighted the benefits of reactant humidification in reducing NO_x emissions and recommended a 70/30% NH₃/H₂ mix for optimal stability, mimicking the behavior of a premixed CH₄ flame. Hussein et al. (2019) [23] identified a 60/40% NH₃/H₂ ratio as ideal for minimizing unburned ammonia and achieving high flame temperatures, despite high NO emissions. Hu et al. (2024) [29] reached a parallel conclusion, noting optimal emissions of unburned NH₃, NO₂, and N₂O at stoichiometric conditions, with NO emissions decreasing under rich-burn conditions. Finally, Yan et al. (2023) [30] noted that a minimum of 20% hydrogen addition was necessary for effective operation, although it did not match

the combustion rates of gasoline or methane. They suggested that natural gas engines, with higher compression ratios, are better suited for ammonia-hydrogen use and recommended avoiding lean operation in spark ignition engines with ammonia.

Hydrogen enhances ammonia combustion as a carbon-neutral option by compensating for ammonia's lower reactivity and flame speed. Yet, retrofitting existing combined-cycle gas turbine (CCGT) assets with imported ammonia fuel requires on-site catalytic decomposition, presenting another challenge. While ammonia cracking has historically lacked commercial adoption, recent industrial announcements signal a shift, with plans for large-scale facilities to produce hydrogen from imported ammonia [31-33]. As already detailed in **Chapter 2 & 3**, this process typically involves high-temperature reactors operating above 700 °C, using nickel or precious metal catalysts like ruthenium, rhodium, and platinum for improved activity [34-36]. Hydrogen recovery is achieved via Pressure Swing Adsorption (PSA), cryogenic separation, or ion-exchange zeolites [37]. To address the challenges of high cracking temperatures and the separation of unreacted gases in traditional systems, researchers have investigated membrane reactors (MR) as a solution for efficient hydrogen recovery from ammonia [37-40, 42].

Several studies have also conducted economic analyses of this process, focusing on both traditional systems and, occasionally, membrane reactor systems. For instance, Lim et al. (2022) [43] discovered that the membrane reactor could lead to an 11% cost reduction at 300 kg_{H₂} per day and a 14% reduction at 900 kg_{H₂} per day, with an efficiency of 82.7% and 78.7%, respectively. Moreover, greenhouse gas emissions were reduced by approximately 17%, from 5.4 to 4.5 kgCO₂-eq/kg-H₂. Makhloufi et al. (2021) [44] designed a large-scale Ammonia-to-Hydrogen plant that operates at a thermal efficiency of 68.5% and produces 200 ton per day of pure hydrogen at 250 bar. The authors utilized a fire tubular reactor (FTR), a technology akin to traditional reformer technology seen in steam methane reforming, which involves vertical catalyst-filled tubes within a firebox, where radiant heat is transferred to the process tubes. The estimated LCOH (Levelized Cost Of Hydrogen) was about 4.82 €/kg with a base green ammonia cost of 450 €/ton. Nasharuddin et al. (2019) [45] estimated the levelized cost of H₂ to be 4.70 €/kg at a capacity of 1000 ton per day. They also noted that the cost of H₂ is closely linked to the feedstock price of NH₃, which varies between 3.00 and 6.28 €/kg when the NH₃ price is modified by ±75%. At the power plant level, Cesaro et al. (2021) [46] forecasted the price of electricity from green ammonia to be 167–197 \$/MWh at 25% power plant capacity factor.

Although there has been a recent increase in research conducted by many scholars on the subject of ammonia cracking and ammonia combustion, still a small number of papers have focused on the economic analysis aspect and even fewer are dedicated to ammonia cracking for power generation applications CCGTs. The present study aims at investigating from an economic viewpoint the potential to use large scale ammonia cracking facility to generate hydrogen from imported ammonia at the capacity required for a CCGT. The novelty of this study lies in the comprehensive modeling and techno-economic assessment of the membrane reactor technology specifically designed for this application. The study also includes a comparison with a more conventional process like the currently available SMR technology. (cf.

Figure 4-2).**Figure 4-2:** Sketch illustrating the two reactors under consideration in this study a) FTR and b) MR

4.2. Material and Methods

To achieve the objective, steady-state simulations were conducted in Aspen PlusTM v11. These simulations provided the required inputs for a techno-economic evaluation. The Peng Robinson equation of state was employed, and the NRTL (Non-Random Two-Liquid) method was utilized for the absorption section. As in **Chapter 3**, the membrane reactor was coded in Aspen Custom ModelerTM (ACM), allowing for seamless integration with Aspen PlusTM flowsheets as a custom component.

4.2.1. Layouts descriptions and general assumptions

This section outlines the process layouts depicted in **Figure 4-3**. The reference NGCC (Natural Gas Combined Cycle) power plant is representative of Amercoeur Power Plant located in Belgium utilizing a single large-scale gas turbine (GT) "F class" (General Electric 9FB) with a gross power output of approximately 310 MW. It also includes a heat recovery steam generator (HRSG) and a single steam turbine in a dual-shaft configuration, featuring two alternators for the steam turbine and gas turbine. The plant receives natural gas at 30 bar and 27 °C and has a net power output of 420 MW. The steam turbine comprises high-pressure (HP), intermediate-pressure (IP), and low-pressure

(LP) turbine, with extraction points for regenerative heating of feedwater and condensate. Additionally, this study considers a carbon dioxide recovery facility based on conventional ethanolamine absorption. This particular section is however not modeled and is solely considered from an efficiency & techno-economic perspective assuming that this process is at best 90-95% effective at capturing emissions as already reported [46] and that the amount of energy for regeneration of the solvent is assumed equal to 3.95 GJ/t CO₂ with steam at a pressure of 4.0 bar according to previous literature [47]. The CO₂ released in the stripper column is compressed in an intercooled compressor and, after reaching liquid phase liquefaction in the 80 bar aftercooler, pumped to the delivery pressure fixed at 110 bar.

Regarding the retrofits with ammonia, a mixture consisting of 30% hydrogen (H₂) by volume is adopted, which aligns with existing literature[15, 22-28]. In this scenario, the parameters set for the natural gas (NG) turbine are utilized, and a design specification is put in place to achieve the targeted fuel blend flow rate. This ensures that the power output matches that of its natural gas-based counterpart. This translates to a hydrogen need of 2600 kmol/hr at 30 bar. This assumption serves as a fundamental premise for this study. Furthermore, it is crucial to ensure that the temperature remains below 1400 °C to prevent any potential damage to the stainless-steel tubes. Further details on modeling both traditional and retrofitted combined-cycle gas turbine (CCGT) systems with hydrogen-ammonia blends in Aspen Plus are available in **Appendices B1** and **B2**.

To generate the necessary hydrogen amount for the blend, this study primarily evaluates two cracking technologies: a fire tubular reactor (FTR) and a membrane reactor (MR) process. The system layouts for these technologies can be viewed in **Figure 4-3**. These two processes are assumed decoupled (i.e. no heat integration) from the power production island which seems beneficial from the point of view of flexibility, and more realistic from the point of view of retrofitting existing assets. In adequation with current practice for large scale storage [48], ammonia is stored at 1 bar and -33 °C in insulated tanks in which the temperature is kept down by slow vaporization, and the ammonia vapor is continually compressed back to a liquid. It is also important to consider that ammonia poses safety and health risks and is corrosive, necessitating that storage containers be constructed or lined with resistant materials, such as stainless steel, which increases both the cost and complexity of storage solutions. However, with over a century of production experience, the technologies and standards for storing, transporting, safely handling, and industrially using ammonia are mature and well-established.

The FTR technology is based on conventional ‘reformer’ technology (vertical catalyst filled tubes in a firebox with radiant heat transfer to the process tubes) as employed in conventional steam methane reforming. The theoretical combustion study of ammonia with air is carried out by using Gibbs reactor model in Aspen Plus V.11. The ‘RPlug’ model is adopted to model the reactions tubes. In this work a parabolic distribution of the heat flux is assumed similar to the one outlined in Makhouloufi et al. (2021) [44] This distribution is generally influenced by variables difficult to simplify in a model, such as heat release rate, burner configuration, radiation properties, and the geometry of the heater. To retrieve any uncracked ammonia present in the gas, an absorption/desorption process has been designed based on the flow rate, pressure, and temperature of the process gas. In this process, water is utilized as the absorbent, taking advantage of ammonia's

high solubility in water. To regenerate the water, a stripping column is employed to evaporate the ammonia. The evaporated ammonia is subsequently cooled and pressurized, allowing it to be recycled back to the cracking step. Regarding purification, a cryogenic separation scenario is favored over the PSA scenario due to the inherent impracticality and safety complications of vast quantities of H_2 storage vessels in pressurized conditions of 200 bar. First the cracked gas is compressed to 240 bars in a 6-stage compressor with intermediate cooling, this is followed by a series of 3 fin plate heat exchangers used to decrease the temperature of the mixture. A Joule-Thomson valve is used to expand the gas mixture to near atmospheric pressure achieving temperature near $-230\text{ }^{\circ}\text{C}$ which enables a nearly complete liquefaction of nitrogen [44].

The solution involving the membrane reactor employs a modular design, comprising a series of interconnected units. Scaling up membrane reactors can be done by connecting membranes in series to create longer ones. However, this method faces difficulties with traditional ceramic supports, mainly due to potential seal leakage issues. Alternatively, metallic-supported membranes used in a modular setup are promising, providing an effective way to scale up membrane reactors. To ensure a steady inlet temperature, an electric heat exchanger is installed at the reactor's entrance. The retentate stream, which contains unconverted ammonia and unrecovered hydrogen, is throttled and used to provide the necessary heat for the endothermic cracking reaction. Additionally, ammonia is added as a fuel to ensure the energy balance is maintained when the energy from the retentate stream alone is insufficient to both supply heat to the reactor and pre-heat the reactant. The permeate exits the reactor at atmospheric pressure and is subsequently compressed to the delivery pressure necessary for the combined-cycle gas turbine (CCGT), which is 30 bar. It is then mixed with ammonia to achieve the desired blend composition. To optimize the process, various process parameters have been modified (e.g. temperature, pressure, feed flowrate...), as discussed in subsequent sections. It is important to mention that this study does not cover NO_x treatment, which would be essential for practical applications. Most of the assumptions related to the heat exchangers, reactor conditions, CO_2 process unit for compression and purification as well as steam cycle and turbomachines efficiencies are presented in **Table 4-1**.

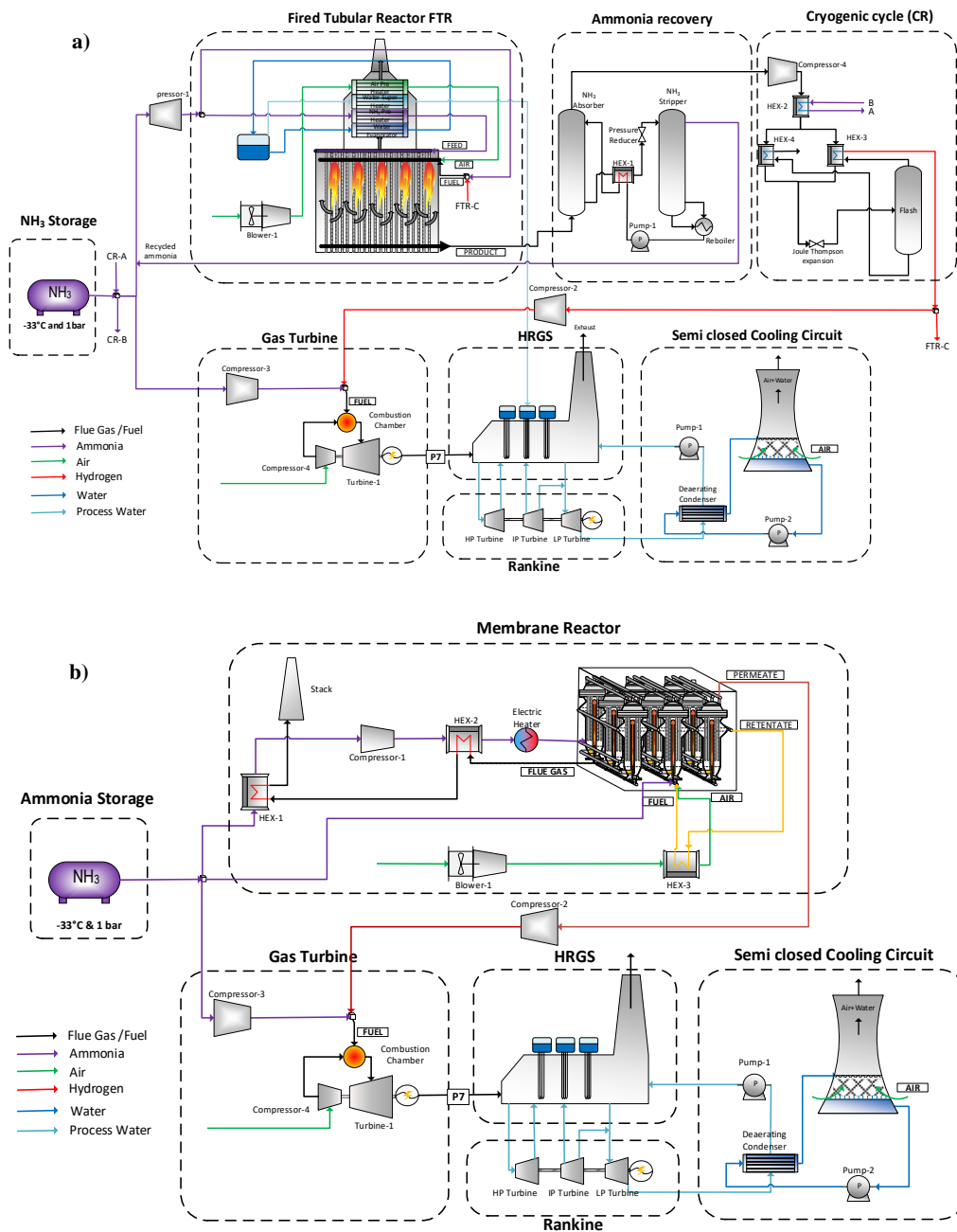


Figure 4-3: Process layouts: (a) FTR (b) MR

Table 4-1: Main assumptions

Parameters	Unit	Value
Reactors operating conditions		
Reactor inlet temperature	°C	400-460
Pressure reaction side	Bar	10-25
Permeate pressure	Bar	1
CCGT Gas turbine		
Gas turbine power gross power	MW	280
Turbine inlet temperature	°C	1360
Pressure ratio	[-]	18
Turbine isentropic efficiency	%	0.87
Compressor isentropic efficiency	%	0.85
NH ₃ -H ₂ blend composition	% (vol)	30
CCGT Steam cycle		
Steam evaporation pressure	bar	130, 28, 4
Condenser pressure	bar	0.0509
Pinch point ΔT (HP, IP, LP)	°C	50,30,10
Cooling water blowdown from ST condenser cooling tower	t/hr	109.9
Blowdown from HRSG drums	t/hr	2.9
CO₂ compression		
Final delivery pressure	bar	110
Compressor isentropic efficiency	%	85
Electrical and auxiliaries		
Driver efficiency	%	95
Generator efficiency	%	98.5
Mechanical efficiencies	%	99.6
Heat exchangers		
Minimum ΔT in exchanger gas-water	°C	15
Minimum ΔT in exchanger gas-gas	°C	30
Heat transfer coefficient gas/gas	W/m ² /K	60
Heat transfer coefficient gas/liquid	W/m ² /K	70
Pump and compressor		
Pump isentropic efficiency	%	70
Pump Motor mechanical efficiency	%	85
Compressor/fan/blower isentropic efficiency	%	70
Compressor/fan/blower motor mechanical efficiency	%	85
Natural Gas for the reference CCGT case		
Molar composition	%	CH ₄ 89.00, C ₂ H ₆ 7.00, C ₃ H ₈ 1.00, C ₄ H ₁₀ 0.11, CO ₂ 2.00, N ₂ 0.89
LHV	MJ/kg	46.482

4.2.2. Reactor and kinetic modelling

The membrane reactor model is described taking into account material and energy balance through linear differential equations. These equations are discretized along the axial length of the reactor. The model assumes steady-state conditions and negligible radial dispersion. To solve these equations, the Euler method implemented in ACM is utilized. To simulate the hydrogen flux across a Pd-based membrane, an equation based on the Richardson equation is used for each infinitesimal membrane element, as expressed in Eq. 4.1.

$$J_{H_2} = \frac{Pe}{\delta} \left(p_{H_{2,ret}}^n - p_{H_{2,perm}}^n \right) \left[\frac{mol}{s \cdot m^2} \right] \text{ Eq. 4.1}$$

Where P_e represents the permeability of the membrane, δ denotes the thickness of the membrane, $p_{H_2,ret}$ and $p_{H_2,perm}$ represent the hydrogen partial pressure on the retentate and permeate sides, respectively, and n represents the exponential factor that indicates the rate-limiting step of the mechanism by which hydrogen crosses the selective palladium layer. In the case of ideal conditions where there is thermodynamic equilibrium between the hydrogen atoms dissolved at the membrane surface and the hydrogen concentration in the gas phase, the pressure exponent n is equal to 0.5. In this scenario, Richardson equation (Eq 4.1) takes the form of Sieverts' law ($n=0.5$), suggesting that the diffusion of hydrogen atoms through the bulk of Pd is the limiting step in the hydrogen permeation mechanism. The membrane permeability P_e can be expressed using an Arrhenius-type correlation, as described in Eq. 4.2.

$$P_e = P_{e_{0,H_2}} e^{-\frac{E_a}{RT}} \quad \text{Eq. 4.2}$$

where $P_{e_{0,H_2}}$ represents the pre-exponential factor, E_a is the activation energy, R denotes the universal gas constant, and T represents the temperature. The permeation parameters utilized in the study are sourced from the literature, specifically the experiments conducted by Fernandez et al. (2015) [49], which closely align with parameters obtained from similar membranes [50-51] as presented in **Table 4-2**.

Table 4-2: Fitted parameter in the Sievert law of the most common Pd 0.85 Ag 0.25 on ceramic support (up to 3.5 mm). and fitted parameter in the Sieverts law

Reference	Thickness [μm]	Pre exponential factor [$\text{mol m}^{-1}\text{s}^{-1}\text{Pa}^{-0.5}$]	E_a [kJ/mol]
[51]	4.2	$1.76 * 10^{-8}$	7.1
[50]	5.2	$4.57 * 10^{-8}$	9.23
[49]	5	$6.93 * 10^8$	9.99

When describing hydrogen extraction from a mixture through a highly selective and permeable membrane, experimental findings indicate that Sieverts' law alone is insufficient [52-53] for predicting the transmembrane flux due to a phenomenon known as 'concentration polarization' (CP). To accurately describe the membrane permeation it is necessary to determine the concentration at the membrane surface [54-55]. In this work this phenomena is integrated into a so called 'CP factor' which is used as a multiplier in Sieverts' law. A CP factor of 0.15, determined through Computational Fluid Dynamics (CFD) simulation, is applied as determined in **Chapter 4**. However, other research suggests the potential for a higher contribution from concentration polarization [52]. Due to the very high selectivity of dense membranes, in the model it is assumed that only hydrogen crosses the membranes (so an infinite ideal selectivity), and then the permeate side is pure hydrogen. The effect of membrane ceramic support is neglected. For numerical simulations, the reaction rate is represented using Temkin-Pyzhev-like power laws, with details provided in the previous chapter.

Table 4-3: Membrane reactor specifications

Parameters	Unit	Value
Membrane outer diameter	m	0.014
Membrane length	m	2.7
Reactor diameter	m	0.7
Active height of the bed	m	3
Number of membranes per reactor	-	260
Membrane volumetric coverage	[-]	0.1
Start position of the membrane	m	0.3
Catalyst density	kg/m ³	980
Bed porosity β	-	0.4
CP Factor	-	0.15

4.2.3. Techno-economic model

A preliminary techno economic assessment is conducted to compare the different plants on the hydrogen production island and at the power plant level. In line with a methodology recommended in the literature [59-62] and described in **Chapter 3**, the Total Plant Cost (TPC) is calculated using a bottom-up approach as defined by Eq. 4.3.

$$TPC = (\sum_i C_i) * (1 + \%_{TIC}) * (1 + \%_{IC}) * (1 + \%_{c\&OC}) \quad \text{Eq. 4.3}$$

The costs associated with the hydrogen production island were determined using correlations adapted from Turton et al. (2018) [63] for stainless steel material, which was selected due to the corrosive nature of ammonia. The component costs for the power island were derived from literature sources as presented in **Table 4-4** and scaled using Eq. 4.4, where the reference size is denoted as $S_{i,0}$ and the reference cost is denoted as $C_{i,0}$.

$$C_i = C_{i,0} \left(\frac{S_i}{S_{i,0}} \right)^f \quad \text{Eq. 4.4}$$

The purchased cost derived from these correlations for the power island closely matches that obtained from a separate ThermoflowTM analysis with only an 8% difference observed. This consistency reinforces the validity and appropriateness of the chosen correlations. The component prices are then updated using the Chemical Engineering Plant Cost Index (CEPCI) method for considering price fluctuations like inflation, deflation. For this analysis, an index of 701 was used to adjust to the 2021 period.

Table 4-4: List of assumptions cost assumption for plant component cost calculated using a scaling law method [64]

Equipments	Scaling parameter	Ref capacity S_0	Ref erected cost C_0	Scale factor f	Cost year
Gas turbine, generator and auxiliaries.	Power net [MW]	272.12	49.4	0.3	2007
HRSG, ducting and stack.	U-S [MW/K]	12.9	32.6	0.67	2007

Steam turbine, generator and auxiliaries.	Power gross [MW]	200.0	33.7	0.67	2007
Cooling water system and BOP.	Heat rejected [MW]	470.0	49.6	0.67	2007
MEA CO₂ separation system.	CO ₂ captured [kg/s]	38.4	29.0	0.8	2007

The TPC is converted in an annualized operating cost using the Capital Charge Factor (CCF) as described in Eq. 4.5 as a function of the discount rate i and the plant lifetime n .

$$CCF = \sum_{j=1}^N \frac{1}{(1+i)^j} = \frac{i \times (1+i)^n}{(1+i)^n - 1} \quad \text{Eq. 4.5}$$

Subsequently, the final cost of hydrogen (LCOH) and cost of electricity (LCOE) were estimated following the acknowledge formula defined in Eq. 4.6 and Eq. 4.7. These two metrics are composed of the annualized TPC and the Operations and Maintenance fixed $C_{O\&M,fix}$, and variables $C_{O\&M,var}$ those two costs are represented by consumables (e.g. catalyst, reactant, water and membranes) and auxiliaries, maintenance, insurance and operators cost) divided by the plant productivity (viz. hydrogen or electricity production).

$$LCOH \left[\frac{\text{€}}{\text{kg}} \right] = \frac{(TPC[\text{€}] \times CCF[\%/year]) + C_{O\&M,fix}[\text{€}/year] + (C_{O\&M,var} \left[\frac{\text{€}}{year} \right] \times h_{eq})}{Production\ capacity \left[\frac{kg}{year} \right] \times h_{eq} \left[\frac{h}{year} \right]} \quad \text{Eq. 4.6}$$

$$LCOE \left[\frac{\text{€}}{MWh} \right] = \frac{(TPC[\text{€}] \times CCF[\%/year]) + C_{O\&M,fix}[\text{€}/year] + (C_{O\&M,var} \left[\frac{\text{€}}{year} \right] \times h_{eq})}{Production\ capacity \left[\frac{MWh}{year} \right] \times h_{eq} \left[\frac{h}{year} \right]} \quad \text{Eq. 4.7}$$

Economic estimations are inherently subjected to a wide range of uncertainties as detailed by Neveux et al. (2020) [65]. In this study three main sources of uncertainties are considered, associated namely to the type of estimation being performed, to the technological maturity of the process considered, (i.e., the level of understanding of the process) and lastly to the price of ammonia. The first two have a ripple effect on the production cost of the process This is because they influence the key elements involved in computing production costs, particularly CAPEX and in a lesser extent the OPEX, which are proportional to the various terms of the installation investment. A Monte Carlo sampling technique performing 10000 simulations per technology system is employed to propagate uncertainties in production costs. A log-normal distribution is used to represent each uncertainty distribution [65].

The uncertainties related to technology and preparation effort are already quantified by the AACE (Association for the Advancement of Cost Engineering) [65-66]. Concerning technological uncertainty, the Furnace Technology Reforming (FTR) has a higher Technology Readiness Level (TRL) than the MR. This is primarily because several commercial electric-based furnaces, albeit on a smaller scale, already exist and could potentially be upscaled. It is also worth mentioning that for example Topsoe have commercial offer of cracking unit as big as 500 ton per day of H₂ [67]. Furthermore, the FTR technology closely aligns with conventional natural gas reforming systems, which currently account for over 95% of the world's hydrogen production at scales exceeding 50,000

Nm³/hr [68]. The proven experience and successful implementation of this technology indicate a swift increase in TRL. Therefore, the ammonia FTR technology is assigned a virtual TRL of 7. On the contrary, membrane reactors currently stand at TRL 4-5. However, the ongoing European Project Arenha [69] is dedicated to advancing this technology to TRL 6, signaling progress in its development and bringing it closer to commercial readiness. **Figure 4-4** illustrates how both uncertainties are incorporated into the TPC calculation, including the addition of installation costs, indirect costs, and the costs for owner's contingencies taken in adequation with literature.

When considering feedstock uncertainty, current forecasts, based on existing technology and an average renewable electricity cost of 44 €/MWh [70], suggest that green ammonia would cost at least 578 €/ton in 2019. Nevertheless, with the continuous evolution of Power-to-Ammonia processes, substantial advancements are expected in the coming years. Projections indicate that by 2040, green ammonia could compete with fossil-based ammonia, with an estimated cost range of 210-215 €/ton if electricity prices fall below 20 €/MWh [46]. According to Fasihi et al. (2021) [71], estimated prices for renewable ammonia in 2030 range between 370-450 €/ton, and in 2050, between 285-350 €/ton. Cesaro et al. (2021) [46] estimated around 345 €/ton for ammonia by 2040. The literature provides a wide range of prices for renewable ammonia fuel, spanning from 210 to 1224 €/ton [72-74], highlighting the potential for lower prices to emerge by the 2040-2050 timeframe. **Figure 4-5** depicts a probability distribution outlining different scenarios. Values below the 25th percentile in the distribution signify an optimistic scenario where prices would be below the current market rate. Similarly, the price of natural gas is subject to significant fluctuations influenced by various factors, including supply and demand dynamics, geopolitical tensions, and environmental regulations. Recent trends indicate an increase in volatility within natural gas prices, and this volatility is expected to intensify in the future. The median value represents the average ammonia natural gas price observed during the current period (September 2018 to October 2022).

Table 4-5 presents the key assumptions utilized for estimating the levelized costs in the base case scenario these assumptions are less prohibitive than the other therefore no uncertainty is propagated. Some of these assumptions are briefly discussed below. In the literature, catalyst costs often vary widely, typically calculated based on material cost per weight, leading to substantial discrepancies. For instance, Yoshida et al. (2021) [75] estimated the cost of Ru/C catalyst at around 295 €/kg, while Makhloufi et al. (2021) [44] used a cost of 22.3 €/kg and concluded that the impact of this factor on the final cost was negligible. To arrive at a compromise, this study adopts a catalyst cost of 143 €/kg [76] and assumes a lifespan of 5 years. The cost of membranes, including the recycling of both Pd-Ag waste and membranes can be estimated to range from 2000 to 5000 €/m², [77] according to the FluidCell Eu. Project [78]. The membrane lifetime for Pd-Ag membranes at temperatures ≤ 425 °C was previously estimated to be 3 years, but it is expected to increase to 5 years, as targeted by the Macbeth Eu. Project [79]. The baseline scenario for this study assumes a membrane cost of 6000 €/m² [80], with a recovery factor of 0.8 considered to account for the recycling process. Another crucial assumption pertains to the capacity factor, where it is presumed that the plant operates at full load for a portion of the time and is inactive for the remainder, even though real-world plants often operate at partial load for certain periods. The assumed capacity factor in this context is 0.65. A carbon tax is also imposed on the natural gas combined cycle gas

turbine (NG CCGT). Examining European countries with an implemented carbon tax reveals a range of values, from 116 €/tonCO₂ in Sweden to as low as 0.07 €/tonCO₂ in Poland. For the purposes of this study, a carbon tax of 25 €/tonCO₂ is applied.

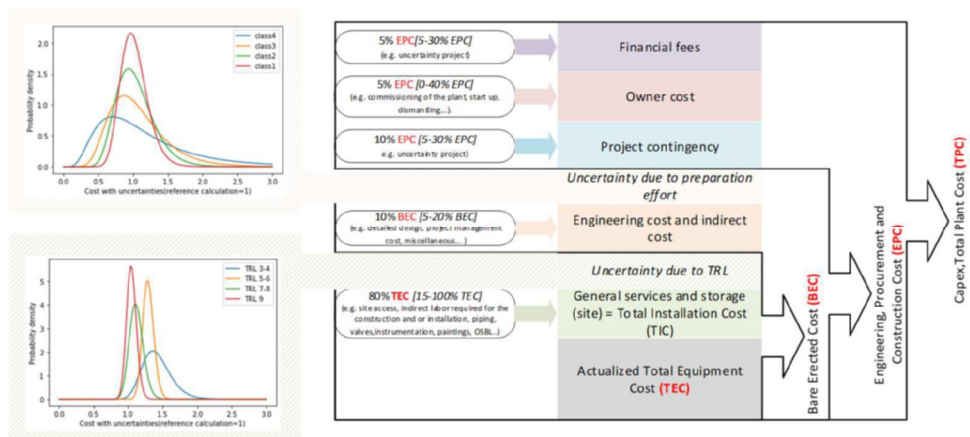


Figure 4-4: Determination of the TPC through a bottom up approach and uncertainty propagation on the TRL and Preparation effort as recommended by Neveux et al. (2020) [65]

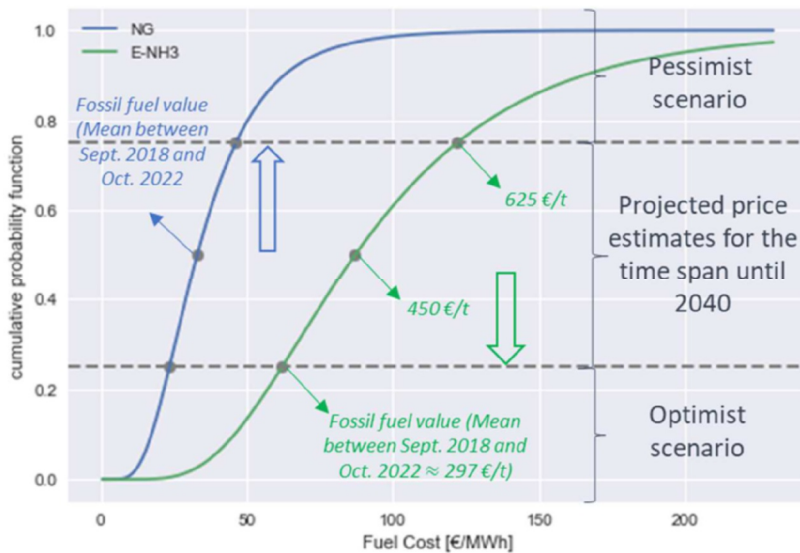


Figure 4-5: Cumulative fuel cost distribution for Natural Gas and E-NH₃; Future price projection trends are illustrated by arrows. (Optimistic scenario below 1st quartile, signifying potential for competitive costs with green ammonia or natural gas & Pessimistic scenario above 2nd Quartile).

Table 4-5: Main assumptions related to the techno-economic analysis

O&M Fixed Cost	
Maintenance cost	0.025*TPC[61]
Insurance	0.02*TPC [61]
Labor cost (no retrofit)	6M€ [61]
Labor cost (retrofit)	9M€ [61]
O&M Variable	
Ammonia cost (€/kg)	450 €/ton
Ammonia storage cost (€/kg)	0.9[81]
NG cost	9.15 €/GJ _{LHV}
Water cost	6€/m ³ [82]
Pd Membrane cost	6000 €/m ²
Electricity cost	60 €/MWh
Catalyst cost	143 €/kg
Membrane lifetime	3 years
Membrane cost recovery	0.5*Membrane Cost
Catalyst lifetime	5 years
Carbon tax (for NG CCGT)	25 €/t _{CO2}
General Assumptions	
Discount rate CCF	0.153
Plant Capacity factor	0.65
CEPCI	701 (2021 period)

4.2.4. Performance indicators

Beyond economic indicators, two indicators from the perspective of the reactor are NH_3 conversion X_{NH_3} and hydrogen recovery factors HRF as defined in **Chapter 2** (page 30). The latter pertains to the overall amount of pure H_2 separated by the membrane, relative to the total H_2 fed into the reactor (based on the stoichiometry of the reaction). These metrics anyhow do not consider heat integration and auxiliaries' consumption of the overall plant. At the fuel processor level, an intermediate hydrogen thermal efficiency denoted (η_{th}) is defined in Eq. 4.8 as the ratio of the energy output associated to the produced hydrogen by the total thermal input power discounting the electricity consumption.

$$\eta_{th} = \frac{F_{H_2} LHV_{H_2} - W_{aux}}{F_{NH_3} LHV_{NH_3}} \quad \text{Eq. 4.8}$$

W_{aux} is the sum of the electric consumptions of the system auxiliaries (i.e. compressors, pumps, control system) and $LHV_{H_2} = 120 \text{ MJ/kg}$ and $LHV_{NH_3} = 18 \text{ MJ/kg}$.

4.3. Results and discussion

This section starts with the validation of the reactor model and a discussion on existing catalyst performance. It is then followed by a sensitivity analysis that contrasts the Membrane Reactor (MR) with the Traditional Reactor (TR) at the reactor level before extending the comparison to the hydrogen production and CCGT levels, using a natural gas-fed plant as a reference.

4.3.1. Reactor model validation

The validation of the reactor model is already detailed in **Chapter 3** (page 110). **Figure 4-6** offers a direct comparison of reactant conversion for the mentioned catalyst under similar conditions ($P_{\text{ret}}=10$ bar, $W/F=2$ kg hr kmol⁻¹). Additionally, for the Ru (3%)-K-CaO catalyst, a membrane is integrated with assumed values of $P_{\text{perm}}=0.1$ bar and two different CP factors 0.2 and 0.5. This graph clearly illustrates that a higher loading of Ru results in greater conversion at a given temperature. Moreover, it shows that when the Ru (3%)-Ru-K-CaO catalyst is used as a membrane reactor (indicated as MR in the graph), it surpasses the performance of more heavily loaded catalysts under those conditions. Across the studied temperature range, this catalyst achieves an average conversion rate five times higher than the standard, less costly nickel-based catalyst. However, to attain complete conversion using this catalyst, extremely high temperatures (above 700 °C) are necessary.

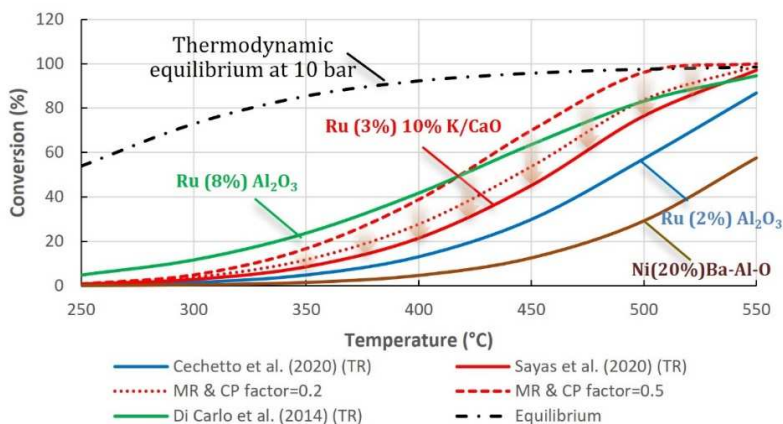


Figure 4-6: Conversion vs Temperature simulated on four catalysts. The conversion obtained with TR are represented by continuous line. The conversions obtained with MR for Sayas et al. (2020) [83]'s catalyst are represented with a dashed line considering two different concentration polarization reducing factors namely 0.2 and 0.5 ($P=10$ bar, $T=250-550$ °C, $W/F = 2$ kg hr kmol⁻¹, $P_{\text{perm}} = 0.1$ bar).

4.3.2. Sensitivity study at the reactor level

In this section, a sensitivity analysis is carried out comparing the performance of MR and TR reactors at the reactor level. Using the catalyst from Sayas et al. (2020) [85], which has been validated at higher pressures, the impact of Gas Hourly Spaced Velocity (GHSV) is explored at $T=425$ °C, $P_{\text{ret}}=10$ bar for the TR and considering $P_{\text{perm}}=0.1$ bar and a CP factor of 0.25 for the MR. **Figure 4-7a** shows that the ammonia conversion in the MR reach up to 87% higher conversion than the TR at GHSV=500 h⁻¹ and the gap reduced progressively with 15% at 4000 h⁻¹. Additionally, a

swap point becomes apparent, where the membrane reactor transitions from a regime in which it produces more hydrogen than the TR at low space velocities to the opposite scenario. **Figure 4-7.b** provides further insights into this situation. Firstly, it shows that HRF follows a similar trend as conversion, decreasing as GHSV increases. On the other hand, the recovered hydrogen flow rate, is found to increase with GHSV up to a maximum value at around 1000 h^{-1} , then decreases as GHSV continues to rise. This observed trend is consistent with findings from other studies in the literature, such as Sitar et al. (2022) [86], who also found that as temperature increases, the point of maximum recovery shifts towards higher GHSV values. Chen et al. (2023) [87] revealed a similar location as our study reaching a maximum recovered hydrogen flow at $\text{GHSV}=1100 \text{ h}^{-1}$ at $T=400^\circ\text{C}$. Finally, Cerrillo et al. (2021) [42] obtained also a similar maximum between 1260 and 1860 $\text{mL/g}_{\text{cat}}/\text{hr}$ which correspond to the space velocity range observed in this study. Clearly, membrane reactors demonstrate improved performance within a particular space velocity range when assessed on reactor-level criteria. When space velocities are high, the membrane faces challenges in permeating the produced hydrogen, which results in reduced H_2 recovery. It appears advantageous to operate at lower space velocities. Yet, it is important to highlight that this represents just one of many considerations. For instance, increasing the ammonia feed rate leads to a higher hydrogen purity in the emitted gas [37]. An additional sensitivity study examines the effect of pressure, as shown in **Figure 4-8**. The retentate side pressure is varied from 1 bar to 10 bar, while the permeate side pressure is maintained at 0.1 bar, and the W/F ratio is set to $5 \text{ kg hr kmol}^{-1}$. As often observed [56] [87], a pressurized feed benefits H_2 production in a membrane reactor, but it has a negative impact on the ammonia decomposition in the catalytic reaction. The increase in conversion is found notably 70% higher at 10 bar and 36% higher at 5 bar than the TR reactor. It is important to note that a pressure of at least 5-6 bar seems to be required for the MR to outperform the TR. This illustrates that the design of membrane reactors involves several conflicting trade-offs to consider.

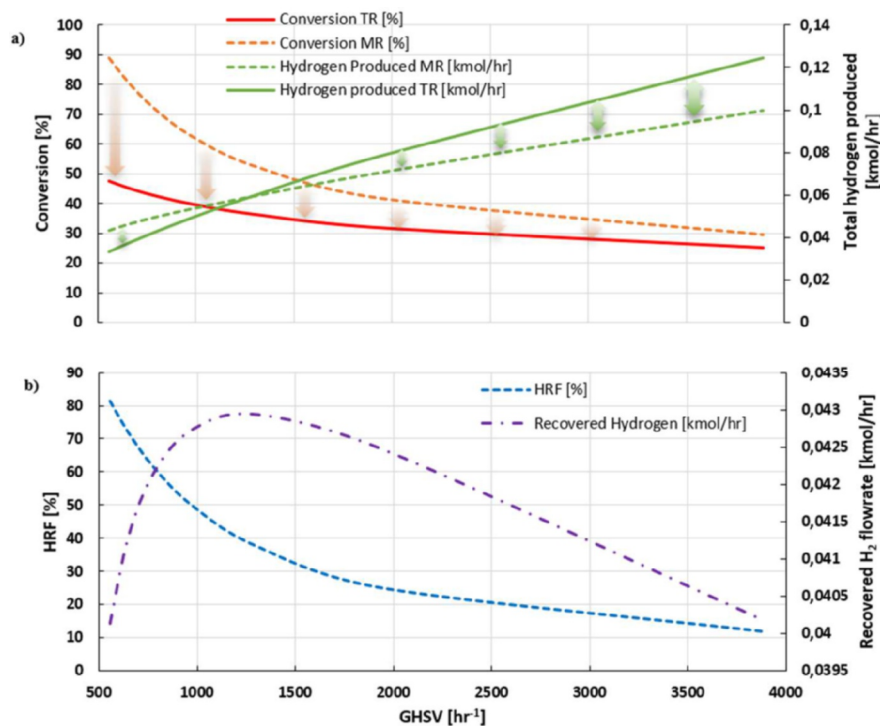


Figure 4-7: Effect of GHSV on the ammonia decomposition equipped Ru (3%) K-CaO catalyst [83] ($T=425\text{ }^{\circ}\text{C}$, $P_{\text{ret}}=10\text{ bar}$, $P_{\text{perm}}=0.1\text{ bar}$) (a) Conversion and Total hydrogen production for both TR and MR (b) HRF and Recovered hydrogen for the MR

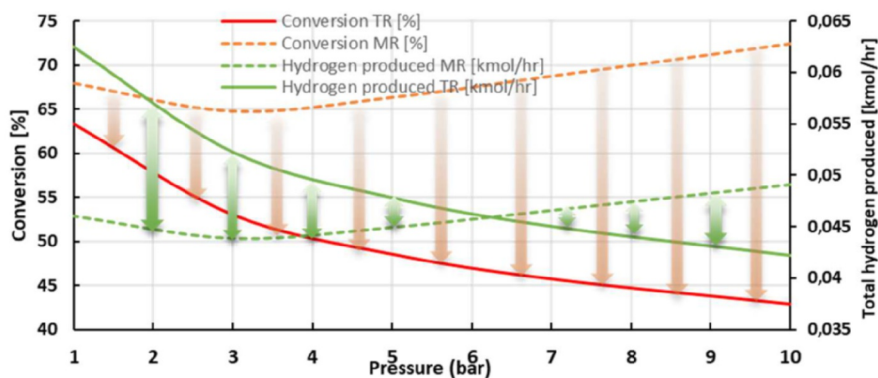


Figure 4-8: Effect of reaction pressure on the conversion and total hydrogen production for both TR and MR ($T=425\text{ }^{\circ}\text{C}$, $P_{\text{perm}}=0.1\text{ bar}$, $W/F=5\text{ kg hr kmol}^{-1}$)

4.3.3. Ammonia cracking system analysis

The economic purpose is clearly to identify the operating conditions and reactor geometries which minimize the LCOH. In order to detail the performance of the MR system, sensitivity studies are performed at designated ammonia flow rates while adjusting the number of reactors, thereby altering the Gas Hourly Space Velocity (GHSV), to maintain the necessary hydrogen production. The outcomes of this study are presented in **Figure 4-9**: **Figure 4-9.a** displays the cumulative effect of pressure and number of reactors (and therefore GHSV), while **Figure 4-9.b** illustrates the impact of temperature and GHSV on both thermal efficiency and cost. When considering the effect of pressure (cf. **Figure 4-9.a**) on the LCOH, it is generally observed that higher pressures have a positive impact. In general, higher pressures allows to reach the minimum at a lower number of membranes, which is preferred since membranes are a breakable component in the reactor. However, as the pressure is raised to even higher levels, its effect on the LCOH becomes less significant. On average, the most significant relative change in LCOH is observed when the pressure is raised from 10 to 15 bar, resulting in a mean LCOH reduction of almost 7%. In contrast, the LCOH only decreases by 2% when the pressure is raised to 20 and 25 bar. This observation can be put in relation with the number of reactors required which decrease by 25% between 10 to 15 bar and by 12% between 20 and 25 bar. While higher pressures privilege hydrogen permeation through the membrane, they do not favor the cracking reaction. Upon observing the thermal efficiency, it becomes evident that the influence of pressure is rather limited, leading to only a slight improvement in efficiency. This can be attributed to the reduction in reactor size and GHSV per reactor, which results in excess heat in the burner exhaust beyond what's needed for reactant pre-heating.

Regarding the effect of temperature (cf. **Figure 4-9.b**) ammonia decomposition is an endothermic process, so the conversion of ammonia into hydrogen and nitrogen is enhanced at elevated temperatures. However, temperatures above 500 °C can compromise Pd-based membrane stability, hence it is advisable to avoid such conditions [88]. Analysis within this study showed raising the temperature from 400 °C to 460 °C decreased the LCOH by 4.8% and reduced the number of reactors by 30%, with the most significant reductions and cost savings occurring between 400 °C and 430 °C.

Finally, to optimize the flowsheet structure's parameters conveniently, such as permeate pressure, reactor inlet pressure, flow rate, temperature, and the required number of reactors, the SQRP (Sequential Quadratic Programming) feature of Aspen Plus software is employed. This method proves highly beneficial to help select the appropriate design and operational parameters when the architecture is established. Results for the best design case are reported in **Table 4-6** together with the optimized parameters. The economic optimum appears to deviate slightly from the efficiency and membrane optima. However, considering the precision of equipment cost correlations, it is plausible to suggest that these optima may be somewhat conflated within the context of this process architecture.

As reported in **Figure 4-10**, the MR system outperforms the reference FTR system, with a 30% increase in thermal efficiency and a 15% drop in the Levelized Cost of Hydrogen (LCOH) to 4.45 €/kg_{H₂}. Meanwhile, the FTR system achieves a 68.5% thermal efficiency with an LCOH of 5.1 €/kg-

H₂, marginally above findings by Makhloufi et al. (2021) [44]. The discrepancy is partly due to the FTR's lower productivity in this study, about two-thirds of the original work. These LCOH figures are considerably above the Steam Methane Reforming (SMR) costs of 1.70 \$/kg_{H₂} to 2.09 \$/kg_{H₂}, largely due to the assumption of ammonia spot prices [89].

The cost breakdown shows the LCOH is largely driven by green ammonia prices, contributing to 70% of the MR system's LCOH and 65% of the FTR's. Due to its greater efficiency, the MR system uses less fuel and incurs lower operating expenses compared to the FTR system, yet it has the highest Total Purchased Equipment Cost (TPC). Significantly, 85% of the FTR system's TPC is allocated to cracking, purification, and compression. In addition, the results can be presented using violin plots, which provide a comprehensive visualization of statistical data, including the probability density of each system based on the technology and type of estimation, as well as the uncertainty in feedstock prices. **Figure 4-11**, emphasizes the significant impact of fuel cost on the LCOH, highlighting its key sensitivity in relation to technology and study type uncertainty. Additionally, further sensitivity studies, which are not part of the uncertainty analysis, are provided in **Appendices B4** and **B5**.

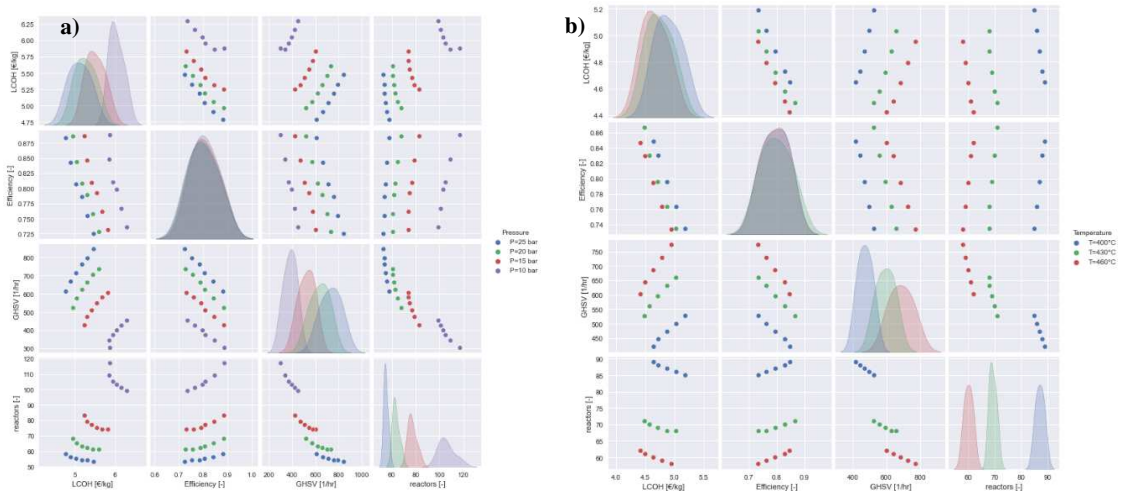


Figure 4-9: (a) Sensitivity study on the effect of pressure & GHSV on the thermal efficiency and LCOH (b) Sensitivity study on reactor temperature & GHSV on the LCOH. (the delivery pressure of hydrogen is assumed to be 30 bar).

Table 4-6: Summary of optimized conditions of the MR subjected to the following constraints H₂ productivity of 2600 kmol/hr at 30 bar

	Objective	Maximized Efficiency	Minimized LCOH	Minimized Number of reactors
Parameters	NH ₃ flowrate [kmol h ⁻¹] ∈ [1700-2700]	2067	2046	1922
	Reactor inlet pressure [bar] ∈ [10-20]	20	20	20
	Reactor temperature [°C] ∈ [400-460]	440.6	439.4	442
	Number of reactors [-] ∈ [55-120]	66.3	57.05	55
Results	GHSV [h ⁻¹]	585	570	653
	Thermal efficiency [-]	0.84	0.85	0.81
	LCOH [€/kgH ₂]	4.48	4.45	4.47
	NO _x emissions from the cracking step [kgNO _x /kgH ₂]	0.021	0.018	0.036

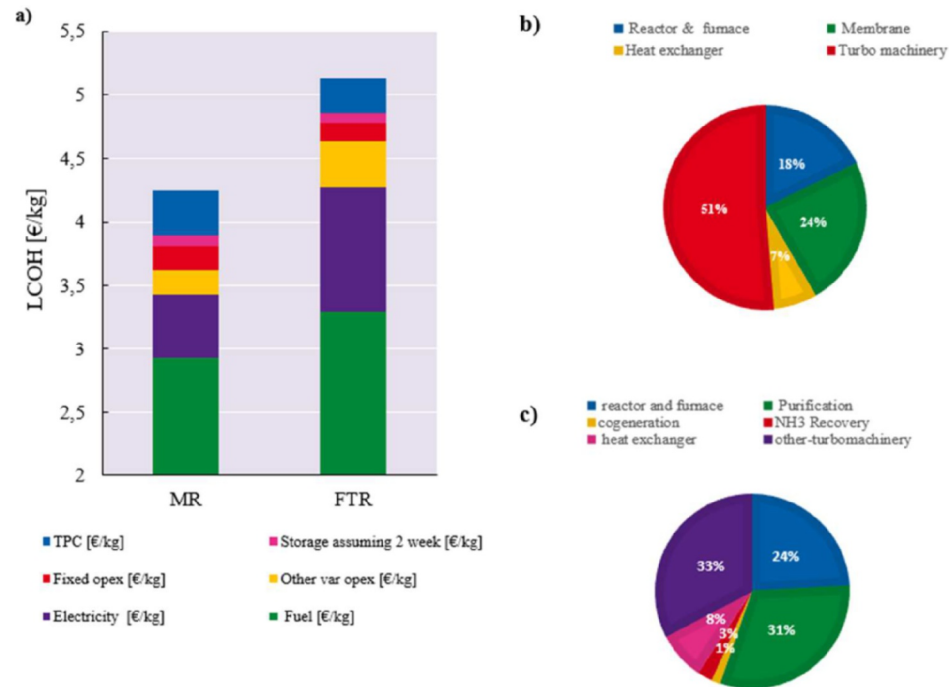


Figure 4-10: LCOH cost breakdown and TPC composition for the MR and FTR systems (a) LCOH cost breakdown, (b) TPC composition MR system and (c) TPC composition FTR system at the same hydrogen delivery pressure of 30 bar

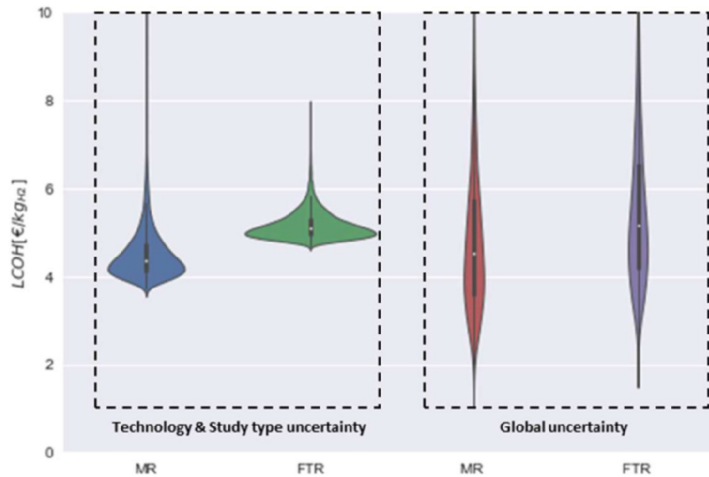
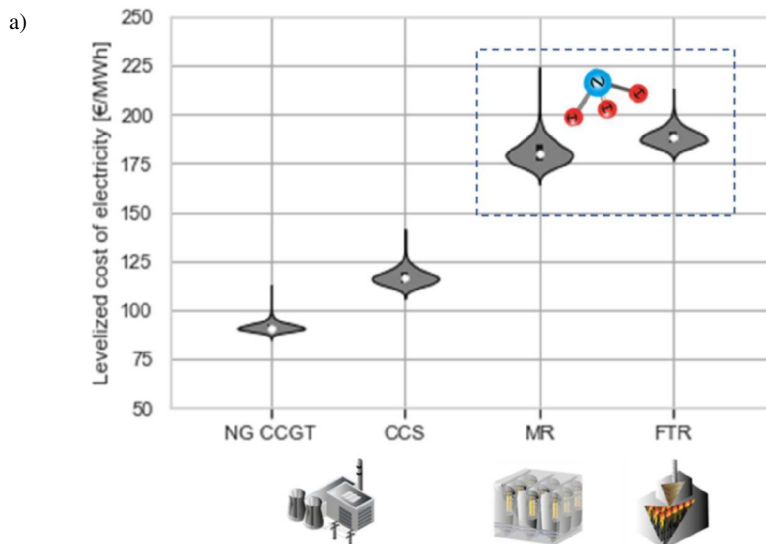


Figure 4-11: LCOH distribution comparing the technology uncertainty to the global uncertainty

4.3.4. Techno economic comparison at the CCGT level

In this section, the comparison extends to the level of the Combined Cycle Gas Turbine. **Figure 4-12.a** showcases the LCOE while considering uncertainties related to technology and preparation effort for both the retrofit solutions and the conventional natural gas Combined Cycle Gas Turbine. **Figure 4-12.b** represents the global effect of the uncertainties on the LCOE for each technology. At the median, ammonia contributes to approximately 80% of the Levelized Cost of Electricity, while natural gas accounts for around 60%. This indicates that ammonia has a significant impact on the overall LCOE. Therefore, variations in fuel prices can have a substantial influence on the LCOE, making it a critical factor to consider in cost analyses. When considering CAPEX, the FTR and CCS technologies demonstrate similar magnitudes, with values of around 20.6 €/MWh and 19.4 €/MWh, respectively. On the other hand, the MR has a slightly higher CAPEX, reaching approximately 26 €/MWh. In terms of the CAPEX share in the LCOE, this study finds that in the baseline scenario, the CCS technology accounts for 20% of the LCOE, while the FTR and MR technologies contribute 5% and 8%, respectively. This emphasizes the fact that fuel cost constitutes the major portion of the LCOE for these two technologies, overshadowing the influence of CAPEX on the overall cost. Therefore, when focusing on the lower range of fuel prices (below the lower quartile) that are more in line with projected prices for 2040-2050, the ammonia blend could be competitive with the reference NG CCGT under certain conditions. This finding aligns with the conclusions of Cesaro et al. (2021) [46]. Finally, besides considering the levelized cost of electricity, insights can be derived from the research conducted by Helmi et al. (2015) [90]. Their study investigates the required amount of palladium for a membrane reactor in an integrated gasification combined cycle unit for carbon capture. This study indicates that retrofitting the equivalent of 1 GWe facility would need approximately 10% of the global annual ruthenium production and around 0.11% of the global annual palladium production as detailed in **Table 4-7** and

Table 4-8. Thus, it's crucial to recognize the challenge posed by the scarcity of materials in adopting this technology. The constrained supply of these materials, coupled with their extensive demand for achieving net-zero goals and the possible implications of geopolitical tensions - particularly given the concentration of production in South Africa and Russia [91]- renders this approach impractical. This is especially true when considering that as of 2021, approximately 1.8 terawatts of natural gas turbines have already been installed worldwide [92]. **Appendix B6** provides details on the supply, demand, and recent price fluctuations of ruthenium and palladium. To tap into this market, future research should prioritize the exploration of alternative membrane materials, such as carbon molecular sieve, and catalysts, like nickel



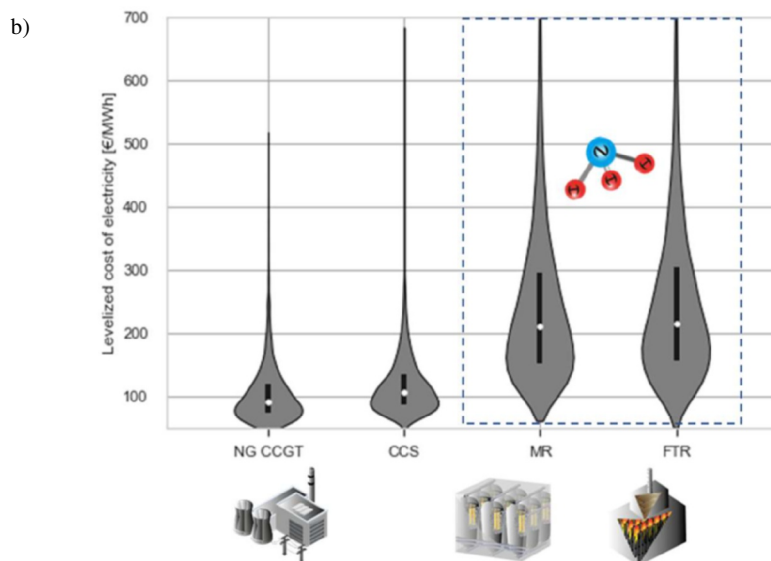


Figure 4-12: LCOE comparison using 65% power plant capacity factor (a) Technology and preparation effort uncertainties and (b) Total uncertainty (a carbon tax of 25 €/ton is assumed for the NG CCGT).

Table 4-7: Detail of the calculation to the mass of palladium required to retrofit 1GWe of CCGT asset (Total palladium supply in 2022:210 tons) [91]

Membrane length [m]	2.7
Membrane diameter [m]	0.014
Number of membranes [-]	210
Number of reactors [-]	64
Density of palladium [kg/m ³]	12000
Surface area of membrane per reactor [m ²]	24.93
Volume of palladium per reactor [m ³]	0.00012
Mass of palladium per reactor [kg]	1.49
Mass of palladium per reactor kg for 1 CCGT plant ~ 400MW [kg]	97.2
Mass of palladium for 1GWe [kg]	243.1
World Ruthenium production in 2022 [kg]	210000 [91]
As a percentage of the world palladium production [%]	~0.11%

Table 4-8: Detail of the calculation to the mass of Ruthenium required to retrofit 1GWe of CCGT asset (Global ruthenium is estimated at 27.8 tons [93])

Active volume of the bed (1 reactor) [m ³]	1.06
Catalyst type	Sayas et al. (2020) [85]
Bed density calculated [kg/m ³]	846

Number of reactors [-]	65
Mass of ruthenium per reactor [kg]	18.1
Mass of palladium per reactor kg for 1 CCGT plant ~ 400 MW [kg]	1174.4
Mass of ruthenium for 1GWe [kg]	2936.1
World Ruthenium production in 2020 [kg]	27800 [93]
As a percentage of the world Ruthenium production [%]	~10%

4.4. Conclusions

Incorporating ammonia into existing combined cycle gas turbine (CCGT) assets through co-firing with hydrogen in a specific blend holds promise as a viable strategy. However, the primary hurdle lies in advancing the development of efficient technology for ammonia cracking. To address this, this study conducted a preliminary techno-economic assessment of two cracking technologies taking into account uncertainties in feedstock costs, technology maturities, and preparation efforts for both cracking and CCGT. Special emphasis was placed on the detailed design of the membrane reactor plant.

- At the reactor level, a sensitivity study delved into the effects of various catalysts and operating conditions for both membrane and traditional reactors. Notably, increasing the Gas Hourly Space Velocity (GHSV) led to decreased ammonia conversion and H₂ recovery, pinpointing an optimal GHSV that maximizes H₂ recovery. From the hydrogen production criteria the membrane reactor emerges as a better system only in a very limited space velocity range.
- At the hydrogen production plant level, through various optimizations, the membrane reactor system demonstrated superior performance compared to the reference FTR (Fired Tubular Reactor) system. It exhibits a 30% increase in thermal efficiency and a 10% reduction in the levelized cost of hydrogen (LCOH), resulting in a LCOH of 4.45 €/kg_{H2}. On the other hand, the FTR system operates at a thermal efficiency of 68.5% and achieves a LCOH of 5.1 €/kg_{H2}. While the MR system benefits from a decreased fuel expense, its capital expenditure (CAPEX) is notably higher than that of the reference system. It is essential to remind that these results were derived based on specific process architectures and at a particular scale of hydrogen production.
- At the CCGT level, the difference in levelized cost of electricity (LCOE) becomes less pronounced, given the heavy influence of ammonia costs, which contribute to 80% of the LCOE. Beyond LCOE, material scarcity poses another hurdle for these systems' wider adoption. For instance, retrofitting just 1 GWe of CCGT assets with membrane reactors would demand about 0.11% of the global palladium and 10% of the global ruthenium production. Given these challenges, it is evident that exploring alternative materials is vital to truly harness the potential of retrofitting existing assets with ammonia-hydrogen blends.

4.5. References

- [1] ETN GLobal, ETN-R&D-Recommendation-Report-2021 Edition, (2021).
- [2] C.A. Hunter, Techno-economic analysis of long-duration energy storage and flexible power generation technologies to support high-variable renewable energy grids, (n.d.) 26.
- [3] Z. Wang, Y. Wang, S. Afshan, J. Hjalmarsson, A review of metallic tanks for H₂ storage with a view to application in future green shipping, *International Journal of Hydrogen Energy* 46 (2021) 6151–6179. <https://doi.org/10.1016/j.ijhydene.2020.11.168>.
- [4] H. Nazir, N. Muthuswamy, C. Louis, S. Jose, J. Prakash, M.E. Buan, C. Flox, S. Chavan, X. Shi, P. Kauranen, T. Kallio, G. Maia, K. Tammeveski, N. Lympieropoulos, E. Carcadea, E. Veziroglu, A. Iranzo, A.M. Kannan, Is the H₂ economy realizable in the foreseeable future? Part II: H₂ storage, transportation, and distribution, *International Journal of Hydrogen Energy* 45 (2020) 20693–20708. <https://doi.org/10.1016/j.ijhydene.2020.05.241>.
- [5] A. Hammad, I. Dincer, Analysis and assessment of an advanced hydrogen liquefaction system, *International Journal of Hydrogen Energy* 43 (2018) 1139–1151. <https://doi.org/10.1016/j.ijhydene.2017.10.158>.
- [6] N. Morlanés, S.P. Katikaneni, S.N. Paglieri, A. Harale, B. Solami, S.M. Sarathy, J. Gascon, A technological roadmap to the ammonia energy economy: Current state and missing technologies, *Chemical Engineering Journal* 408 (2021) 127310. <https://doi.org/10.1016/j.cej.2020.127310>.
- [7] M. Asif, S. Sidra Bibi, S. Ahmed, M. Irshad, M. Shakir Hussain, H. Zeb, M. Kashif Khan, J. Kim, Recent advances in green hydrogen production, storage and commercial-scale use via catalytic ammonia cracking, *Chemical Engineering Journal* 473 (2023) 145381. <https://doi.org/10.1016/j.cej.2023.145381>.
- [8] J. Eppinger, K.-W. Huang, Formic Acid as a Hydrogen Energy Carrier, *ACS Energy Lett.* 2 (2017) 188–195. <https://doi.org/10.1021/acsenergylett.6b00574>.
- [9] A. Valera-Medina, H. Xiao, M. Owen-Jones, W.I.F. David, P.J. Bowen, Ammonia for power, *Progress in Energy and Combustion Science* 69 (2018) 63–102. <https://doi.org/10.1016/j.pecs.2018.07.001>.
- [10] Y. Zhao, B.P. Setzler, J. Wang, J. Nash, T. Wang, B. Xu, Y. Yan, An Efficient Direct Ammonia Fuel Cell for Affordable Carbon-Neutral Transportation, *Joule* 3 (2019) 2472–2484. <https://doi.org/10.1016/j.joule.2019.07.005>.
- [11] V. Dias, M. Pochet, F. Contino, H. Jeanmart, Energy and Economic Costs of Chemical Storage, *Front. Mech. Eng.* 6 (2020) 21. <https://doi.org/10.3389/fmech.2020.00021>.
- [12] IEA, The Future of Hydrogen, (2019) 203.
- [13] A. Valera-Medina, F. Amer-Hatem, A.K. Azad, I.C. Dedoussi, M. de Joannon, R.X. Fernandes, P. Glarborg, H. Hashemi, X. He, S. Mashruk, J. McGowan, C. Mounaim-Rouselle, A. Ortiz-Prado, A. Ortiz-Valera, I. Rossetti, B. Shu, M. Yehia, H. Xiao, M. Costa, Review on Ammonia as a Potential Fuel: From Synthesis to Economics, *Energy Fuels* 35 (2021) 6964–7029. <https://doi.org/10.1021/acs.energyfuels.0c03685>.
- [14] E.C. Okafor, K.D.K.A. Somarathne, R. Ratthan, A. Hayakawa, T. Kudo, O. Kurata, N. Iki, T. Tsujimura, H. Furutani, H. Kobayashi, Control of NO_x and other emissions in micro gas turbine combustors fuelled with mixtures of methane and ammonia, *Combustion and Flame* 211 (2020) 406–416. <https://doi.org/10.1016/j.combustflame.2019.10.012>.
- [15] A. Ichikawa, A. Hayakawa, Y. Kitagawa, K.D. Kunkuma Amila Somarathne, T. Kudo, H. Kobayashi, Laminar burning velocity and Markstein length of ammonia/hydrogen/air premixed flames at elevated pressures, *International Journal of Hydrogen Energy* 40 (2015) 9570–9578. <https://doi.org/10.1016/j.ijhydene.2015.04.024>.
- [16] Mitsubishi, Mitsubishi Power Commences Development of World's First Ammonia-fired 40MW Class Gas Turbine System, (2021). <https://power.mhi.com/news/20210301.html>.

- [17] GE and IHI Sign Agreement to Develop Ammonia Fuels Roadmap across Asia, (2021). <https://www.ge.com/news/press-releases/ge-and-ihl-sign-agreement-to-develop-ammonia-fuels-roadmap-across-asia>.
- [18] K. Bioche, L. Briceux, A. Bertolino, A. Parente, J. Blondeau, Large Eddy Simulation of rich ammonia/hydrogen/air combustion in a gas turbine burner, *International Journal of Hydrogen Energy* 46 (2021) 39548–39562. <https://doi.org/10.1016/j.ijhydene.2021.09.164>.
- [19] Z. Li, S. Li, Kinetics modeling of NO_x emissions characteristics of a NH₃/H₂ fueled gas turbine combustor, *International Journal of Hydrogen Energy* 46 (2021) 4526–4537. <https://doi.org/10.1016/j.ijhydene.2020.11.024>.
- [20] O. Kurata, N. Iki, T. Matsunuma, T. Inoue, T. Tsujimura, H. Furutani, H. Kobayashi, A. Hayakawa, Performances and emission characteristics of NH₃–air and NH₃ CH₄–air combustion gas-turbine power generations, *Proceedings of the Combustion Institute* 36 (2017) 3351–3359. <https://doi.org/10.1016/j.proci.2016.07.088>.
- [21] F.J. Verkamp, M.C. Hardin, J.R. Williams, Ammonia combustion properties and performance in gas-turbine burners, *Symposium (International) on Combustion* 11 (1967) 985–992. [https://doi.org/10.1016/S0082-0784\(67\)80225-X](https://doi.org/10.1016/S0082-0784(67)80225-X).
- [22] A. Valera-Medina, R. Marsh, J. Runyon, D. Pugh, P. Beasley, T. Hughes, P. Bowen, Ammonia–methane combustion in tangential swirl burners for gas turbine power generation, *Applied Energy* 185 (2017) 1362–1371. <https://doi.org/10.1016/j.apenergy.2016.02.073>.
- [23] N.A. Hussein, A. Valera-Medina, A.S. Alsaegh, Ammonia- hydrogen combustion in a swirl burner with reduction of NO_x emissions, *Energy Procedia* 158 (2019) 2305–2310. <https://doi.org/10.1016/j.egypro.2019.01.265>.
- [24] D. Pugh, P. Bowen, A. Valera-Medina, A. Giles, J. Runyon, R. Marsh, Influence of steam addition and elevated ambient conditions on NO_x reduction in a staged premixed swirling NH₃/H₂ flame, *Proceedings of the Combustion Institute* 37 (2019) 5401–5409. <https://doi.org/10.1016/j.proci.2018.07.091>.
- [25] H. Xiao, A. Valera-Medina, P. Bowen, S. Dooley, 3D Simulation of Ammonia Combustion in a Lean Premixed Swirl Burner, *Energy Procedia* 142 (2017) 1294–1299. <https://doi.org/10.1016/j.egypro.2017.12.504>.
- [26] O. Kurata, Pure ammonia combustion micro gas turbine system, (2019).
- [27] J.H. Lee, J.H. Kim, J.H. Park, O.C. Kwon, Studies on properties of laminar premixed hydrogen-added ammonia/air flames for hydrogen production, *International Journal of Hydrogen Energy* 35 (2010) 1054–1064. <https://doi.org/10.1016/j.ijhydene.2009.11.071>.
- [28] C. Mounaïm-Rousselle, P. Bréquigny, C. Dumand, S. Houillé, Operating Limits for Ammonia Fuel Spark-Ignition Engine, *Energies* 14 (2021) 4141. <https://doi.org/10.3390/en14144141>.
- [29] X. Hu, J. Li, J. Pan, R. Zhang, H. Wei, G. Shu, On combustion and emission characteristics of ammonia/hydrogen engines: Emphasis on energy ratio and equivalence ratio, *Fuel* 365 (2024) 131183. <https://doi.org/10.1016/j.fuel.2024.131183>.
- [30] Y. Yan, Z. Liu, J. Liu, An Evaluation of the Conversion of Gasoline and Natural Gas Spark Ignition Engines to Ammonia/Hydrogen Operation From the Perspective of Laminar Flame Speed, *Journal of Energy Resources Technology* 145 (2023) 012302. <https://doi.org/10.1115/1.4054754>.
- [31] Port of Rotterdam, Large-Scale industrial ammonia cracking plant, 2023.
- [32] Air liquide, Air Liquide ouvre la voie à la conversion d’ammoniac en hydrogène avec une nouvelle technologie de craquage, (2023). <https://www.airliquide.com/fr/groupe/communiqués-presse-actualités/23-03-2023/air-liquide-ouvre-la-voie-la-conversion-dammoniac-en-hydrogene-avec-une-nouvelle-technologie-de>.
- [33] Agency for Natural Resources and Energy, Overview of Basic Hydrogen Strategy, (2023). https://www.meti.go.jp/shingikai/enecho/shoene_shinene/suiso_seisaku/pdf/20230606_4.pdf (accessed October 23, 2023).

- [34] K.E. Lamb, M.D. Dolan, D.F. Kennedy, Ammonia for hydrogen storage; A review of catalytic ammonia decomposition and hydrogen separation and purification, *International Journal of Hydrogen Energy* 44 (2019) 3580–3593. <https://doi.org/10.1016/j.ijhydene.2018.12.024>.
- [35] I. Lucentini, X. Garcia, X. Vendrell, J. Llorca, Review of the Decomposition of Ammonia to Generate Hydrogen, *Ind. Eng. Chem. Res.* 60 (2021) 18560–18611. <https://doi.org/10.1021/acs.iecr.1c00843>.
- [36] C. Chen, K. Wu, H. Ren, C. Zhou, Y. Luo, L. Lin, C. Au, L. Jiang, Ru-Based Catalysts for Ammonia Decomposition: A Mini-Review, *Energy Fuels* 35 (2021) 11693–11706. <https://doi.org/10.1021/acs.energyfuels.1c01261>.
- [37] V. Cechetto, L. Di Felice, F. Gallucci, Advances and Perspectives of H₂ Production from NH₃ Decomposition in Membrane Reactors, *Energy Fuels* 37 (2023) 10775–10798. <https://doi.org/10.1021/acs.energyfuels.3c00760>.
- [38] V. Cechetto, L. Di Felice, J.A. Medrano, C. Makhloufi, J. Zuniga, F. Gallucci, H₂ production via ammonia decomposition in a catalytic membrane reactor, *Fuel Processing Technology* 216 (2021) 106772. <https://doi.org/10.1016/j.fuproc.2021.106772>.
- [39] N. Itoh, Kinetic enhancement of ammonia decomposition as a chemical hydrogen carrier in palladium membrane reactor, *Catalysis Today* (2014) 7.
- [40] J. Liu, X. Ju, C. Tang, L. Liu, H. Li, P. Chen, High performance stainless-steel supported Pd membranes with a finger-like and gap structure and its application in NH₃ decomposition membrane reactor, *Chemical Engineering Journal* 388 (2020) 124245. <https://doi.org/10.1016/j.cej.2020.124245>.
- [41] Y. Park, J. Cha, H.-T. Oh, T. Lee, S.H. Lee, M.G. Park, H. Jeong, Y. Kim, H. Sohn, S.W. Nam, J. Han, C.W. Yoon, Y.S. Jo, A catalytic composite membrane reactor system for hydrogen production from ammonia using steam as a sweep gas, *Journal of Membrane Science* 614 (2020) 118483. <https://doi.org/10.1016/j.memsci.2020.118483>.
- [42] J.L. Cerrillo, N. Morlanés, S.R. Kulkarni, N. Realpe, A. Ramírez, S.P. Katikaneni, S.N. Paglieri, K. Lee, A. Harale, B. Solami, A. Jamal, S. Mani Sarathy, P. Castaño, J. Gascon, High purity, self-sustained, pressurized hydrogen production from ammonia in a catalytic membrane reactor, *Chemical Engineering Journal* (2021) 134310. <https://doi.org/10.1016/j.cej.2021.134310>.
- [43] D. Lim, A. Lee, A. Kim, J. Haider, H. Mikulčić, B. Brigljević, H. Lim, A 4E feasibility analysis of an on-site, ammonia sourced, hydrogen refueling station, *Journal of Cleaner Production* 363 (2022) 132356. <https://doi.org/10.1016/j.jclepro.2022.132356>.
- [44] C. Makhloufi, Large-scale decomposition of green ammonia for pure hydrogen production, (2021) 11.
- [45] R. Nasharuddin, M. Zhu, Z. Zhang, D. Zhang, A technoeconomic analysis of centralised and distributed processes of ammonia dissociation to hydrogen for fuel cell vehicle applications, *International Journal of Hydrogen Energy* 44 (2019) 14445–14455. <https://doi.org/10.1016/j.ijhydene.2019.03.274>.
- [46] Z. Cesaro, M. Ives, R. Nayak-Luke, M. Mason, R. Bañares-Alcántara, Ammonia to power: Forecasting the levelized cost of electricity from green ammonia in large-scale power plants, *Applied Energy* 282 (2021) 116009. <https://doi.org/10.1016/j.apenergy.2020.116009>.
- [47] G. Manzolini, E. Macchi, M. Binotti, M. Gazzani, Integration of SEWGS for carbon capture in Natural Gas Combined Cycle. Part B: Reference case comparison, *International Journal of Greenhouse Gas Control* 5 (2011) 214–225. <https://doi.org/10.1016/j.ijggc.2010.08.007>.
- [48] A. Klerke, C.H. Christensen, J.K. Nørskov, T. Vegge, Ammonia for hydrogen storage: challenges and opportunities, *J. Mater. Chem.* 18 (2008) 2304. <https://doi.org/10.1039/b720020j>.
- [49] E. Fernandez, A. Helmi, K. Coenen, J. Melendez, J.L. Viviente, D.A. Pacheco Tanaka, M. van Sint Annaland, F. Gallucci, Development of thin Pd–Ag supported membranes for fluidized bed membrane reactors including WGS related gases, *International Journal of Hydrogen Energy* 40 (2015) 3506–3519. <https://doi.org/10.1016/j.ijhydene.2014.08.074>.

- [50] N. de Nooijer, F. Gallucci, E. Pellizzari, J. Melendez, D.A. Pacheco Tanaka, G. Manzolini, M. van Sint Annaland, On concentration polarisation in a fluidized bed membrane reactor for biogas steam reforming: Modelling and experimental validation, *Chemical Engineering Journal* 348 (2018) 232–243. <https://doi.org/10.1016/j.cej.2018.04.205>.
- [51] A. Helmi, R.J.W. Voncken, A.J. Raijmakers, I. Roghair, F. Gallucci, M. van Sint Annaland, On concentration polarization in fluidized bed membrane reactors, *Chemical Engineering Journal* 332 (2018) 464–478. <https://doi.org/10.1016/j.cej.2017.09.045>.
- [52] W.-H. Chen, M.-H. Hsia, Y.-L. Lin, Y.-H. Chi, C.-C. Yang, Hydrogen permeation and recovery from H_2 - N_2 gas mixtures by Pd membranes with high permeance, *International Journal of Hydrogen Energy* 38 (2013) 14730–14742. <https://doi.org/10.1016/j.ijhydene.2013.08.086>.
- [53] A. Helmi, R.J.W. Voncken, A.J. Raijmakers, I. Roghair, F. Gallucci, M. van Sint Annaland, On concentration polarization in fluidized bed membrane reactors, *Chemical Engineering Journal* 332 (2018) 464–478. <https://doi.org/10.1016/j.cej.2017.09.045>.
- [54] M. Nordio, S. Soresi, G. Manzolini, J. Melendez, M. Van Sint Annaland, D.A. Pacheco Tanaka, F. Gallucci, Effect of sweep gas on hydrogen permeation of supported Pd membranes: Experimental and modeling, *International Journal of Hydrogen Energy* 44 (2019) 4228–4239. <https://doi.org/10.1016/j.ijhydene.2018.12.137>.
- [55] N. de Nooijer, F. Gallucci, E. Pellizzari, J. Melendez, D.A. Pacheco Tanaka, G. Manzolini, M. van Sint Annaland, On concentration polarisation in a fluidized bed membrane reactor for biogas steam reforming: Modelling and experimental validation, *Chemical Engineering Journal* 348 (2018) 232–243. <https://doi.org/10.1016/j.cej.2018.04.205>.
- [56] S. Richard, A. Ramirez Santos, F. Gallucci, PEM gensets using membrane reactors technologies: An economic comparison among different e-fuels, *International Journal of Hydrogen Energy* (2023) S0360319923032913. <https://doi.org/10.1016/j.ijhydene.2023.06.312>.
- [57] A. Di Carlo, L. Vecchione, Z. Del Prete, Ammonia decomposition over commercial Ru/Al_2O_3 catalyst: An experimental evaluation at different operative pressures and temperatures, *International Journal of Hydrogen Energy* 39 (2014) 808–814. <https://doi.org/10.1016/j.ijhydene.2013.10.110>.
- [58] S. Chiuta, R.C. Everson, R.C. Everson, H.W.J.P. Neomagus, H.W.J.P. Neomagus, D.G. Bessarabov, Ammonia Decomposition for Decentralized Hydrogen Production in Microchannel Reactors: Experiments and CFD Simulations, in: M. Sankir, N.D. Sankir (Eds.), *Hydrogen Production Technologies*, John Wiley & Sons, Inc., Hoboken, NJ, USA, 2017: pp. 77–111. <https://doi.org/10.1002/9781119283676.ch2>.
- [59] V. Spallina, D. Pandolfo, A. Battistella, M.C. Romano, M. Van Sint Annaland, F. Gallucci, Techno-economic assessment of membrane assisted fluidized bed reactors for pure H_2 production with CO_2 capture, *Energy Conversion and Management* 120 (2016) 257–273. <https://doi.org/10.1016/j.enconman.2016.04.073>.
- [60] J.A. Medrano, M.A. Llosa-Tanco, V. Cechetto, D.A. Pacheco-Tanaka, F. Gallucci, Upgrading biogas with novel composite carbon molecular sieve (CCMS) membranes: Experimental and techno-economic assessment, *Chemical Engineering Journal* 394 (2020) 124957. <https://doi.org/10.1016/j.cej.2020.124957>.
- [61] G. Manzolini, E. Macchi, M. Gazzani, CO_2 capture in natural gas combined cycle with SEWGS. Part B: Economic assessment, *International Journal of Greenhouse Gas Control* 12 (2013) 502–509. <https://doi.org/10.1016/j.ijggc.2012.06.021>.
- [62] K. Gerdes, W. Summers, J. Wimer, *Quality Guidelines for Energy System Studies: Cost Estimation Methodology for NETL Assessments of Power Plant Performance*, 2011. <https://doi.org/10.2172/1513278>.
- [63] R. Turton, ed., *Analysis, synthesis, and design of chemical processes*, 5th edition, Prentice Hall, Boston, 2018.
- [64] DOE/NETL, *Cost and Performance Baseline for Fossil Energy Plants*, 2007.

- [65] T. Neveux, O. Authier, Y.L. Moullec, Estimation technico-économique d'innovations technologiques en génie des procédés, (2020) 32.
- [66] AACE, 16R-90: Conducting Technical and Economic Evaluations - As Applied for the Process and Utility Industries, (1991) 11.
- [67] Haldor Topsoe A/S, Topsoes Ammonia cracking technology – Delivering green Hydrogen, (2021). <https://www.ammoniaenergy.org/wp-content/uploads/2021/11/Rasmus-Topsoe-NH3-cracking-AEA-2021.pdf> (accessed October 23, 2023).
- [68] S.T. Wismann, J.S. Engbæk, S.B. Vendelbo, F.B. Bendixen, W.L. Eriksen, K. Aasberg-Petersen, C. Frandsen, I. Chorkendorff, P.M. Mortensen, Electrified methane reforming: A compact approach to greener industrial hydrogen production, *Science* 364 (2019) 756–759. <https://doi.org/10.1126/science.aaw8775>.
- [69] Advanced materials and reactors for Energy storage through ammonia, (2023). <https://arenha.eu/> (accessed October 23, 2023).
- [70] A. Valentini, Green shift to create 1 billion tonne 'green ammonia' market?, (2020) 6.
- [71] M. Fasihi, R. Weiss, J. Savolainen, C. Breyer, Global potential of green ammonia based on hybrid PV-wind power plants, *Applied Energy* 294 (2021) 116170. <https://doi.org/10.1016/j.apenergy.2020.116170>.
- [72] Morgan, Techno-Economic Feasibility Study of Ammonia Plants Powered by Offshore Wind, (2021). <https://doi.org/10.7275/11KT-3F59>.
- [73] O. Osman, S. Sgouridis, A. Sleptchenko, Scaling the production of renewable ammonia: A techno-economic optimization applied in regions with high insolation, *Journal of Cleaner Production* 271 (2020) 121627. <https://doi.org/10.1016/j.jclepro.2020.121627>.
- [74] R.M. Nayak-Luke, C. Forbes, Z. Cesaro, R. Bañares-Alcántara, K.H.R. Rouwenhorst, Techno-Economic Aspects of Production, Storage and Distribution of Ammonia, in: *Techno-Economic Challenges of Green Ammonia as an Energy Vector*, Elsevier, 2021: pp. 191–207. <https://doi.org/10.1016/B978-0-12-820560-0.00008-4>.
- [75] M. Yoshida, T. Ogawa, Y. Imamura, K.N. Ishihara, Economies of scale in ammonia synthesis loops embedded with iron- and ruthenium-based catalysts, *International Journal of Hydrogen Energy* 46 (2021) 28840–28854. <https://doi.org/10.1016/j.ijhydene.2020.12.081>.
- [76] T.A. Atspha, T. Yoon, B.-H. Yoo, C.-J. Lee, Techno-Economic and Environmental Analysis for Direct Catalytic Conversion of CO₂ to Methanol and Liquid/High-Calorie-SNG Fuels, *Catalysts* 11 (2021) 687. <https://doi.org/10.3390/catal11060687>.
- [77] J.L. Viviente, FluidCell: Advanced m-CHP fuel cell system based on a novel bioethanol fluidized bed membrane reformer, 2018.
- [78] Fluid Cell Project, (n.d.). <https://www.fluidcell.eu/> (accessed April 3, 2023).
- [79] MACBETH, (n.d.). <https://www.macbeth-project.eu/> (accessed February 3, 2023).
- [80] M. Nordio, S.A. Wassie, M. Van Sint Annaland, D.A. Pacheco Tanaka, J.L. Viviente Sole, F. Gallucci, Techno-economic evaluation on a hybrid technology for low hydrogen concentration separation and purification from natural gas grid, *International Journal of Hydrogen Energy* 46 (2021) 23417–23435. <https://doi.org/10.1016/j.ijhydene.2020.05.009>.
- [81] D. Bellotti, M. Rivarolo, L. Magistri, A comparative techno-economic and sensitivity analysis of Power-to-X processes from different energy sources, *Energy Conversion and Management* 260 (2022) 115565. <https://doi.org/10.1016/j.enconman.2022.115565>.
- [82] G. Manzolini, E. Sanchez Fernandez, S. Rezvani, E. Macchi, E.L.V. Goetheer, T.J.H. Vlught, Economic assessment of novel amine based CO₂ capture technologies integrated in power plants based on European Benchmarking Task Force methodology, *Applied Energy* 138 (2015) 546–558. <https://doi.org/10.1016/j.apenergy.2014.04.066>.
- [83] S. Sayas, N. Morlanés, S.P. Katikaneni, A. Harale, B. Solami, J. Gascon, High pressure ammonia decomposition on Ru–K/CaO catalysts, *Catal. Sci. Technol.* 10 (2020) 5027–5035. <https://doi.org/10.1039/D0CY00686F>.
- [84] Y. Im, H. Muroyama, T. Matsui, K. Eguchi, Ammonia decomposition over nickel catalysts supported on alkaline earth metal aluminate for H₂ production, *International Journal of Hydrogen Energy* 45 (2020) 26979–26988. <https://doi.org/10.1016/j.ijhydene.2020.07.014>.

- [85] S. Sayas, N. Morlanés, S.P. Katikaneni, A. Harale, B. Solami, J. Gascon, High pressure ammonia decomposition on Ru–K/CaO catalysts, *Catal. Sci. Technol.* 10 (2020) 5027–5035. <https://doi.org/10.1039/D0CY00686F>.
- [86] R. Sitar, J. Shah, Z. Zhang, H. Wikoff, J.D. Way, C.A. Wolden, Compact ammonia reforming at low temperature using catalytic membrane reactors, *Journal of Membrane Science* 644 (2022) 120147. <https://doi.org/10.1016/j.memsci.2021.120147>.
- [87] W.-H. Chen, W.-S. Chou, R.-Y. Chein, A.T. Hoang, J.C. Juan, Multiple-objective optimization on ammonia decomposition using membrane reactor, *International Journal of Hydrogen Energy* (2023) S0360319923023339. <https://doi.org/10.1016/j.ijhydene.2023.05.081>.
- [88] H.W. Abu El Hawa, S.-T.B. Lundin, S.N. Paglieri, A. Harale, J. Douglas Way, The influence of heat treatment on the thermal stability of Pd composite membranes, *Journal of Membrane Science* 494 (2015) 113–120. <https://doi.org/10.1016/j.memsci.2015.07.021>.
- [89] S. Lee, H.S. Kim, J. Park, B.M. Kang, C.-H. Cho, H. Lim, W. Won, Scenario-Based Techno-Economic Analysis of Steam Methane Reforming Process for Hydrogen Production, *Applied Sciences* 11 (2021) 6021. <https://doi.org/10.3390/app11136021>.
- [90] A. Helmi, F. Gallucci, M. van Sint Annaland, Resource scarcity in palladium membrane applications for carbon capture in integrated gasification combined cycle units, *International Journal of Hydrogen Energy* 39 (2014) 10498–10506. <https://doi.org/10.1016/j.ijhydene.2014.05.009>.
- [91] Statista, Mine production of palladium worldwide in 2022, by country, (n.d.). <https://www.statista.com/statistics/273647/global-mine-production-of-palladium/> (accessed April 19, 2023).
- [92] IEA, The role of CCUS in low-carbon power systems, (2020).
- [93] Statista, Demand for ruthenium worldwide from 2010 to 2023, (n.d.). <https://www.statista.com/statistics/591965/demand-for-ruthenium-worldwide/> (accessed November 17, 2023).
- [94] A. Di Carlo, L. Vecchione, Z. Del Prete, Ammonia decomposition over commercial Ru/Al₂O₃ catalyst: An experimental evaluation at different operative pressures and temperatures, *International Journal of Hydrogen Energy* 39 (2014) 808–814. <https://doi.org/10.1016/j.ijhydene.2013.10.110>.
- [95] brgm, fiche criticité ruthenium, (2020).
- [96] Daily Metal Prices, (2024). <https://www.dailymetalprice.com/metalpricecharts.php?c=pd&u=oz&d=240> (accessed April 1, 2024).

Appendix B.

B1. Natural gas CCGT in Aspen plus

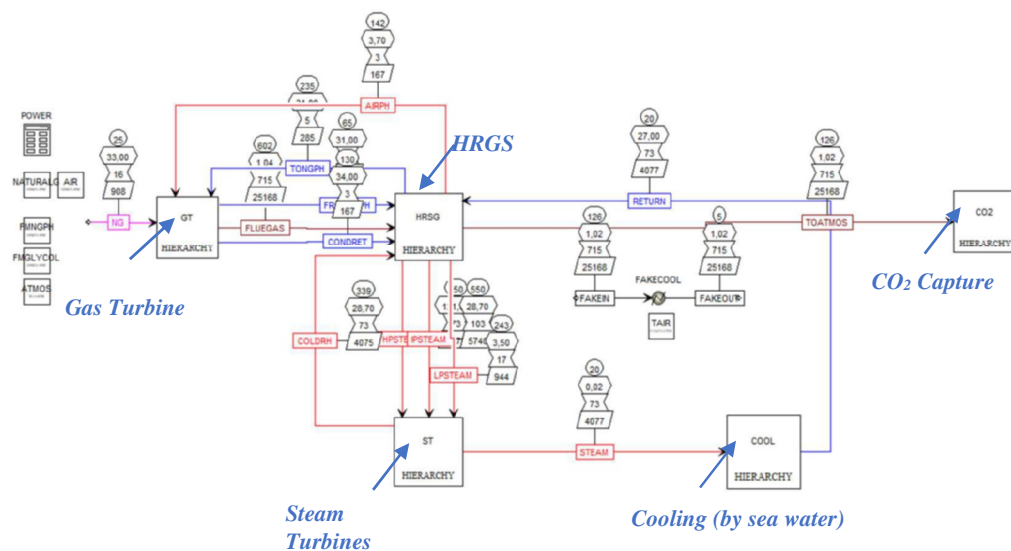
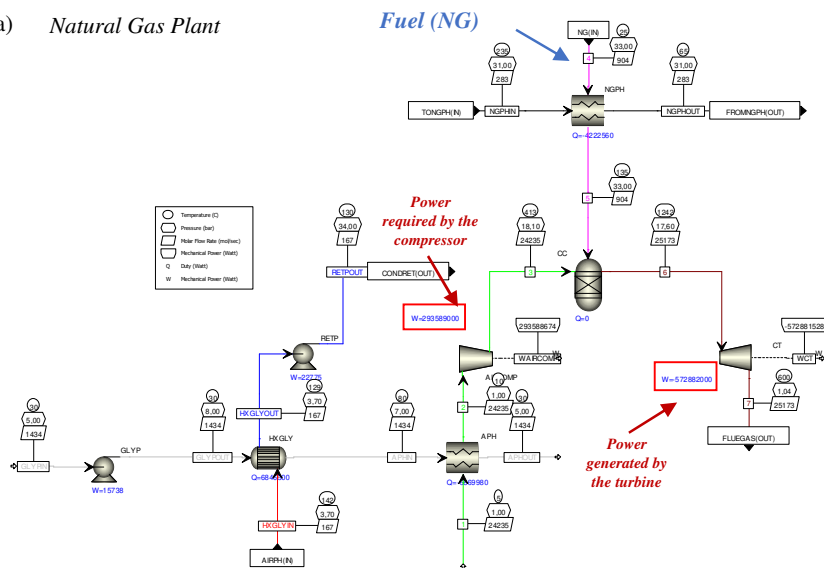


Figure B1: Flowsheet details from Aspen Plus highlighting the primary blocks of the reference natural gas power plant the main operating conditions

B2. NG GT and $\text{NH}_3\text{-H}_2$ GT: in Aspen plus

a) Natural Gas Plant



b) Ammonia-Hydrogen retrofit

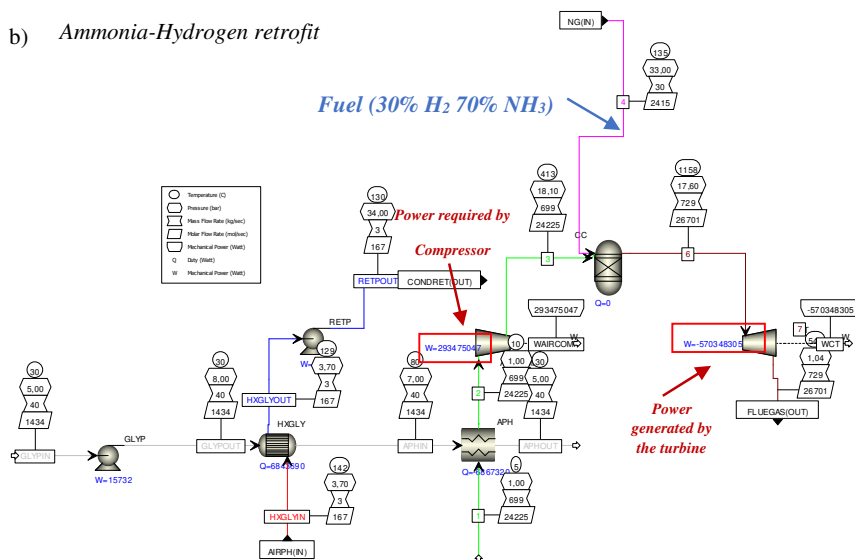


Figure B2: Flowsheet Configurations from Aspen Plus: a) Natural Gas Plant vs. b) Ammonia-Hydrogen Blend (30% H_2) with Comparable Power Outputs. To achieve this 2600 kmol/hr of H_2 at 30 bar is calculated.

B3. Ammonia cracking section

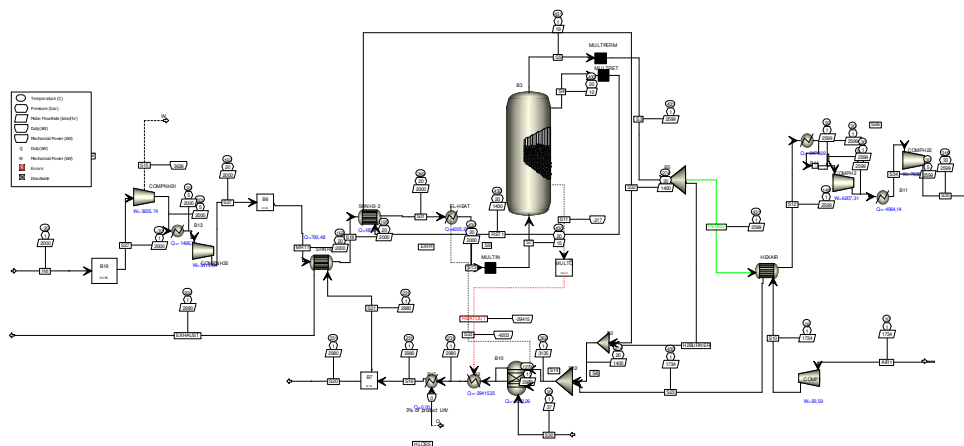


Figure B3: Flowsheet details from Aspen Plus highlighting the implementation of the cracking process considered in the study (MR process)

B4. Sensitivity analysis at the hydrogen production level

A dedicated sensitivity study, illustrated in **Figure B5**, focuses on the CP factor applied to Sieverts' law to account for concentration polarization, identified as one of the largest uncertainties in this analysis. The results reveal that a 50% reduction in the concentration polarization reduction factor, compared to the base case, leads to an 11% improvement, emphasizing the critical importance of accurately estimating this phenomenon. Additionally, a sensitivity analysis on techno-economic parameters—such as the discount factor, capacity factor, and membrane price, is presented in **Figure B6**.

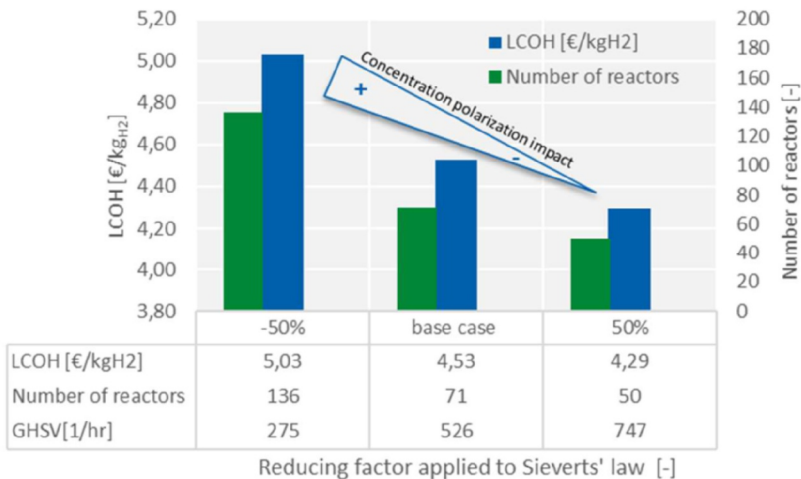


Figure B5: Effect of concentration polarization reducing factor on cracking economic on the base case

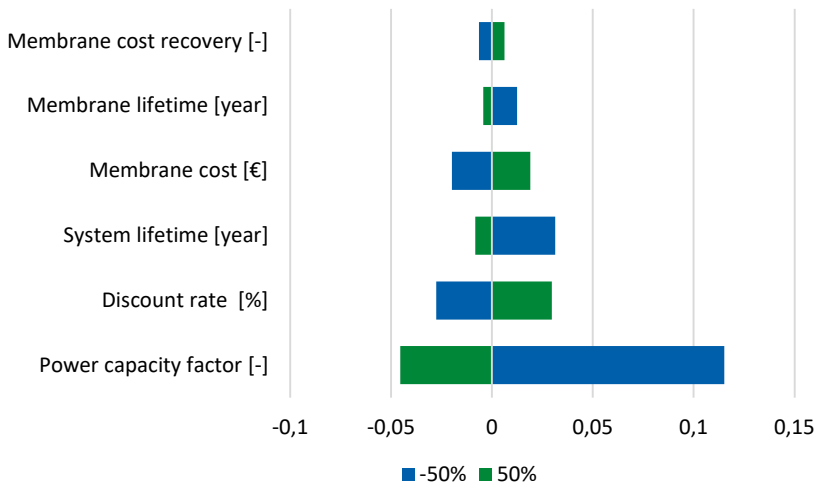


Figure B6: Sensitivity analysis on LCOH based on some parameters on the MR cracker compared to the base case

B5. Sensitivity analysis at the plant level

This emphasizes the fact that fuel cost constitutes the major portion of the LCOE for these two technologies, overshadowing the influence of CAPEX on the overall cost. Thus, when

considering the lower range of fuel prices (below the lower quartile), which aligns more closely with the potential prices in 2040-2050, the ammonia blend exhibits competitiveness within the plant described in this study. To further emphasize the significant cost dependency, a sensitivity analysis has been conducted, taking into account variations in fuel cost and the capacity factor. The results of this analysis are presented in **Figure B7** for capacity factor sensitivity and **Figure B8** for fuel cost sensitivity, demonstrating the impact of these variables on the overall cost and competitiveness of the ammonia blend which is coherent with the study of Cesaro et al. (2021) [46].

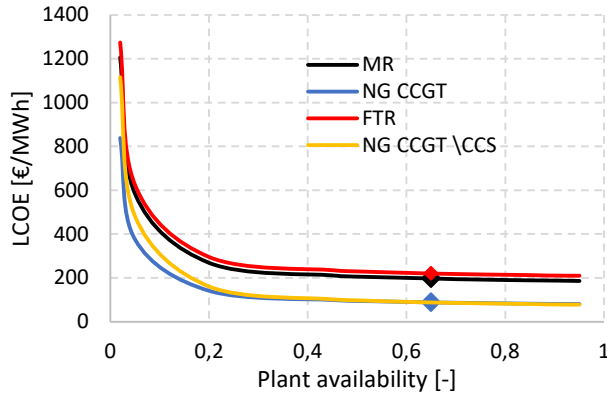


Figure B7: LCOE of CCGT systems considered in this study at a range of power plant capacity factors.

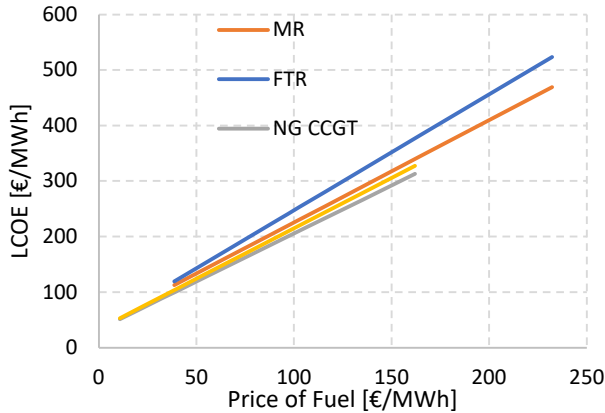


Figure B8: LCOE of CCGT systems at a range of fuel price.

B6. Palladium & Ruthenium ressource required to retrofit 1GWe of CCGT

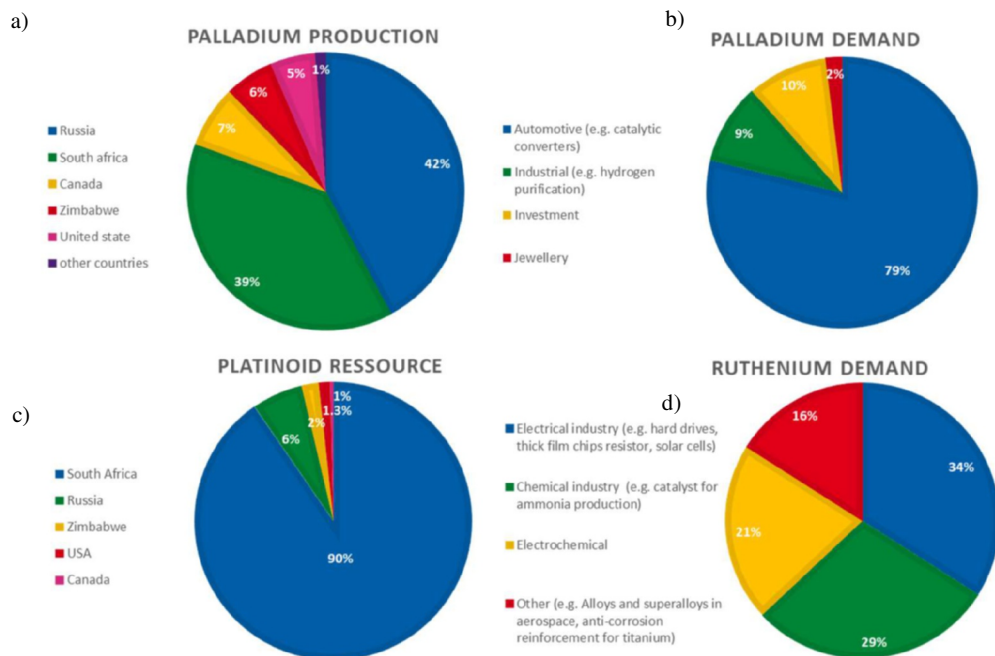


Figure B9: (a) Palladium supply by region (total palladium supply in 2022: 210 tons): Russia and South Africa together account for ~80% of global production [91] (b) Palladium demand by sectors: the primary use of palladium is in catalytic converters but it is also used in electronics, jewelry, medical device and fuel cells. (c) Platinoid estimated ressource location [95] (d) Ruthenium demand by sectors [95]

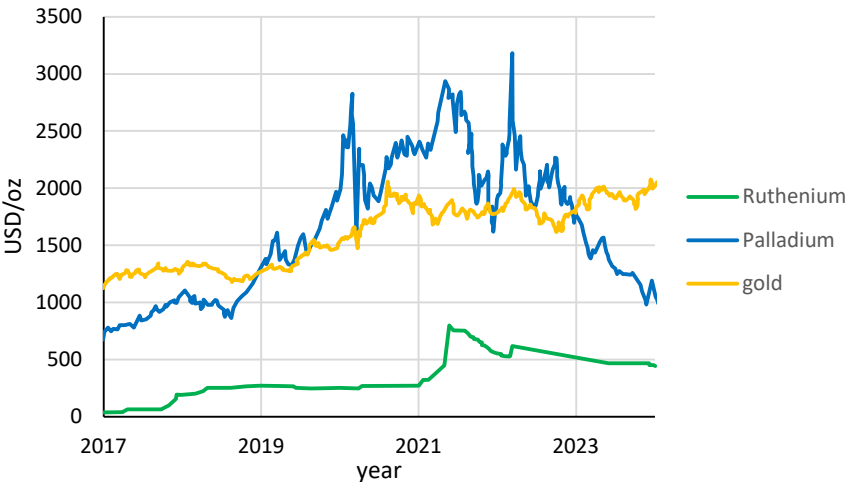
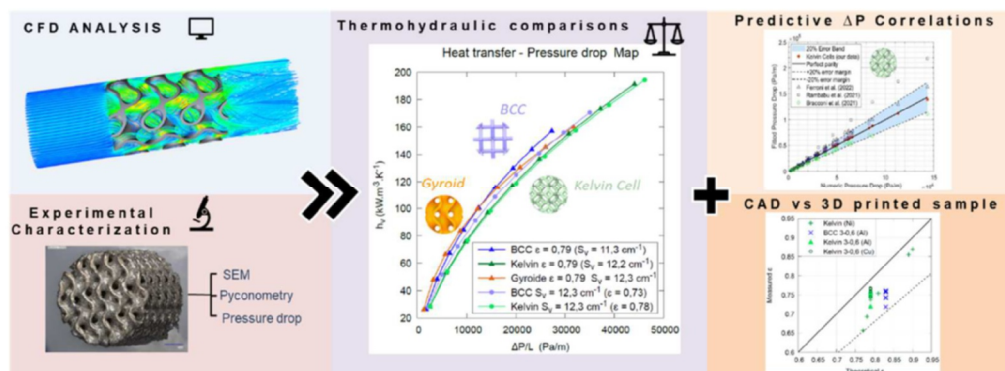


Figure B10: Spot price history (Ruthenium, Palladium and Gold) between 2017 and 2024 [96]

Chapter 5 | Comparison of thermo-hydraulic performance among different 3D printed Periodic Open Cellular Structures

Abstract

As additive manufacturing of periodic open cellular structures (POCS) is gaining interest in structured catalytic reactor research, this chapter* seeks to thermohydraulically compare the well-known Kelvin lattice structure with the lesser-researched BCC and gyroid lattice structures. Using a combined CFD (Computational Fluid Dynamic) and experimental approach, the selected POCS are fabricated through Laser Powder Bed Fusion (LPBF), characterized, and subsequently subjected to numerical analysis. From the manufacturability point of view, the 3D printed samples closely matched their CAD designs, showing a maximum porosity deviation of 15% below design values. A CFD model, validated through pressure drop experiment, was employed to compare the POCS designs on shared geometric attributes such as specific surface area and porosity. While all structures exhibited comparable performance in term of heat and momentum transfer, our findings suggest that the Gyroid lattice may provide the optimal balance between momentum and heat transfer rates in low-velocity region. Conversely, the BCC configuration may be more favourable at higher velocity. An Ergun-like correlation was also developed and validated for each lattice type, with a Mean Absolute Percentage Error (MAPE) below 10%. Our pressure drop results align quite well with existing literature correlations, showing a MAPE under 20%. Concerning heat transfer, the values forecasted in this research show a reasonable alignment with literature's results, though they tend to be on the lower spectrum.



* This chapter is based on the following paper: S. Richard, D. Tasso, M. Rajana, A. Saker, A. Ramirez Santos, C. Makhloufi, N. Meynet, B. Hary, S. Nardone, G. Marino, M. Thomas, C. Italiano, A. Vita, F. Gallucci, Comparison of thermo-hydraulic performance among different 3D printed periodic open cellular structures, Chemical Engineering Journal, vol. 47, no. 21, pp. 11385–11401, 2024

5.1. Introduction

To effectively design periodic open cellular structures (POCS) reactors, already introduced in **Chapter 1** (page 15) and **Chapter 2** (page 32), understanding transport phenomena is one of the important aspect. Previous research has often focused on heat transfer [1-5] and pressure drop [3-4], using Computational Fluid Dynamics (CFD) for analysis. These simulations generally allow for a systematic exploration of different topologies and the derivation of engineering correlations. For instance, Das et al. [6] employed Direct Numerical Simulation (DNS) to study the friction factor of a Kelvin lattice and, based on simulations across several topologies, formulated a correlation. Similarly, Rambabu et al. (2021) [7] employed RANS simulations to derive a pressure drop correlation for the same lattice structure. Some researchers compared these structures with alternative catalyst support [8] [8-10]. For instance, Lucci et al. (2017) [40] made a comparison between an OCF and a Kelvin cell lattice with similar porosity and surface area. They observed that the Kelvin cell generally had a better mass transfer - pressure drop trade off compared to its foam counterpart. In a similar vein, some researchers also contrasted different unit cells types [1, 11-14]. For example, Kaur et al. (2020) [1] explored the heat-transfer and pressure drop properties of four cell types and noted that the Octet structure outperformed the others in both pressure drop and Nusselt number. While numerous theoretical thermohydraulic studies are available, there is only a handful of experimental works on metallic POCS [2, 15-20]. For instance, Klump et al. (2014) [15] utilized the selective electron beam melting (SEBM) method to study Ti-based cubic cell geometries. Their research emphasized the distinct flow properties arising from different cell orientations. In contrast, Rebelo et al. (2018) [16] examined the design parameters of cubic cells, finding only minimal impact of angular orientation on pressure drop. They employed direct metal laser sintering (DMLS) for manufacturing and showcased cubic-cell foams 3D printed in aluminum. In an original approach Do et al. (2020) [18] delved into an interpenetrating POCS structure based on diamond geometry fabricated by fused deposition modeling. They introduced this design as adaptable, capable of adjusting flow characteristics to match process requirements. Chaudhari et al. (2019) [20] inspected the performance of the Octet-truss lattice structure made of AlSiMg alloy. They derived friction factor correlations for this specific sample. Busse et al. (2018) [2], conducted heat transfer experiments on SEBM printed cubic cells (Ti₆Al₄V, IN718) and formulated new heat transfer correlations. They demonstrated that enhancing the wall coupling between the POCS structure and the tube shell can notably increase the overall heat transfer coefficient. Specifically, a fully coupled structure displayed a heat transfer coefficient 3.5 times greater than a loosely structured counterpart.

Though there is obvious advancement in POCS thermohydraulic research, most studies focus on specific cell types, mainly Kelvin cells. There is a lack of comprehensive comparisons of various POCS designs, with many yet to be studied. Additionally, current literature sometimes presents conflicting findings, and even established POCS configurations have debated correlations. To address this, the present study aims at contrasting the thermohydraulic performance of three lattices: the popular Kelvin cell, and the lesser-studied BCC and gyroid lattice as represented in **Figure 5-1**. To achieve this aim, a holistic approach is employed, combining both CFD and experimental analyses. Within this framework, the selected POCS are printed using LPBF, comprehensively

characterized, and then analysed numerically. This approach enables the derivation of Ergun-like correlations for the precise description of pressure drop across the selected samples.

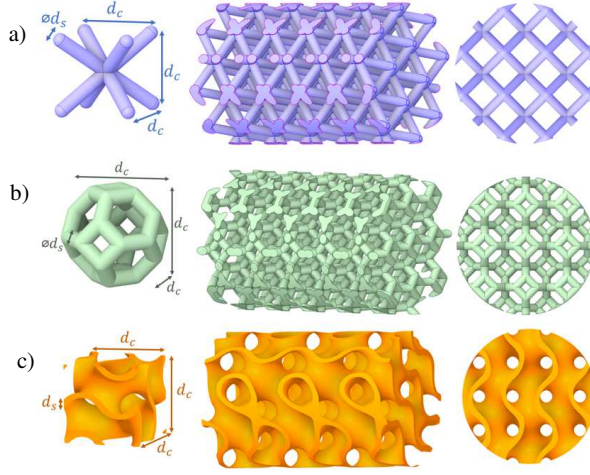


Figure 5-1: POCS structure investigated in this work (a) BCC (Top, purple) (b) Kelvin cell (Middle, green) (c) Gyroid (Bottom, orange); d_c represents the cell dimension and d_s indicates the thickness of the strut

5.2. Experimental

5.2.1. POCS Structure characteristics

POCS samples were produced using the LPBF (Laser Powder Bed Fusion) technique based on CAD designs, resulting in cylindrical models of 10 mm diameter and 15 mm height. These models represent three cell types: body-centered cubic, Kelvin, and gyroid, each with design variations to obtain different surface areas and porosities. The following feedstock materials were used for the printing: AlSi10Mg, IN625, and CuNi2SiCr. The first two materials were printed at ENGIE Laborelec using a SLM280 LPBF machine while the last material was printed and heat treated by Zare (under the BEAMIT group). AlSi10Mg is notable for its heat-transfer capabilities due to its high thermal conductivity but is suitable for processes requiring limited temperature (e.g. such as Fischer-Tropsch synthesis or methanol steam reforming). CuNi2SiCr also has high thermal conductivity and can withstand up to 500 °C, suitable for higher temperature processes (e.g. methane reforming with membrane reactors or ammonia cracking). On the other hand, IN625 material could stand out for Joule heating applications whilst remaining very suitable for high-temperature environments (at least up to 700 °C). **Table 5-1** summarizes the design parameters of the CAD models, including materials, strut diameter, cell length, porosity, and specific surface. The latter two properties are defined as per Eq. 5.1 & Eq. 5.2 respectively. A noteworthy observation pertains to the post-processing of the Kelvin 3-0.6 model in Al alloy and its counterpart in Cu alloy which

underwent a sand blasting procedure. All other configurations in AlSi10Mg and IN625 were preserved in their as-built state.

$$\epsilon = \frac{\text{Void volume}}{\text{Total volume}} = 1 - \frac{\text{Solid volume}}{\text{Total volume}} \quad \text{Eq. 5.1}$$

$$S_v = \frac{\text{Total POCS area}}{\text{Total volume}} \quad \text{Eq. 5.2}$$

Table 5-1: Geometrical features of the CAD design cell parameters printed. The porosity and specific surface area refer to the theoretical ones of the CAD. Structures denoted with a 'sb' superscript have been sandblasted; others are as-built

Cell type	Material	Cell length [mm]	Strut diameter [mm]	Theoretical Porosity %	Theoretical Specific surface area [cm ⁻¹]	Denomination
Kelvin	AlSi10Mg	3	0.6	0.79	12.16	Kelvin 3-0.6-Al ^{sb}
	CuNi2SiCr	3	0.6	0.79	12.16	Kelvin 3-0.6-Al ^{sb}
	IN625	3	0.6	0.79	12.16	Kelvin 3-0.6-Ni
	IN625	4	0.6	0.89	6.52	Kelvin 3-0.6-Ni
	IN625	3	0.8	0.66	13.70	Kelvin 3-0.6-Ni
	IN625	3	0.4	0.9	8.89	Kelvin 3-0.6-Ni
	IN625	1.5	0.3	0.77	23.46	Kelvin 3-0.6-Ni
	IN625	4	0.8	0.81	7.78	Kelvin 3-0.6-Ni
	IN625	2	0.4	0.78	17.15	Kelvin 3-0.6-Ni
BCC	IN625	2	0.6	0.55	17.97	Kelvin 3-0.6-Ni
	AlSi10Mg	3	0.6	0.83	10.79	BCC 3-0.6-Al
	IN625	2	0.4	0.83	16.26	BCC 3-0.6-Ni
	IN625	2	0.6	0.64	19.84	BCC 3-0.6-Ni
	IN625	3	0.4	0.92	8.09	BCC 3-0.6-Ni
	IN625	3	0.6	0.83	10.79	BCC 3-0.6-Ni
	IN625	3	0.8	0.71	12.68	BCC 3-0.6-Ni
	IN625	4	0.6	0.912	6.30	BCC 3-0.6-Ni
Gyroid	IN625	4	0.8	0.852	7.76	BCC 3-0.6-Ni
	IN625	3	0.2	0.794	20.4	Gyr 5-0.34-Ni
	IN625	3	0.3	0.694	20.1	Gyr 5-0.34-Ni
	IN625	3	0.4	0.616	19.5	Gyr 5-0.34-Ni
	IN625	5	0.34	0.79	12.3	Gyr 5-0.34-Ni

5.2.2. Geometrical characterization & pressure drop measurements

The samples were analysed using a Keyence VHX-7000 digital optical microscope. Detailed images of the POCS were taken with VHX-E20 (low magnification objective lens: 20 - 100 x) and VHX-E100 (medium magnification objective lens: 100 - 500 x) lenses. Measurements were made at various points on the struts and windows to identify any discrepancies from the CAD model. Further in-depth inspection was conducted with pycnometry and Scanning Electron Microscopy (SEM). A Multivolume Pycnometer 1305 (Micromeritics) was used to obtain true volume and relative densities/porosities of POCS (This device ensures a density calculation accuracy of ± 0.1 to 0.2% and a volume measurement accuracy of $\pm 0.2\%$). The sample chamber is initially pressurized with helium. The later expansion of this gas into a precisely measured volume induces a drop in

pressure. The sample's volume, density and the relative porosity can then be readily calculated based on the two pressure readings. SEM analyses were performed with a Philips XL-30 FEG operated at 5-20 kV. After characterization, the pressure drop of the samples was assessed using two different methods. In method "A", a U-tube manometer (internal diameter = 1cm, length = 13.5 cm) connected to a reactor containing the sample measured the pressure drop across various superficial velocities. N₂ at ambient temperature was introduced, and its flow rate was measured with a digital flowmeter (Agilent ADM 2000). The water height differential in the U-tube was converted to a pressure drop value using Stevin's law. For method "B", a micromanometer (DeltaOhm HD 2114.2, with an instrumental resolution of 0.005 mbar and an accuracy of $\pm 0.3\%$) was used, attached to the reactor housing the POCS. Similarly, N₂ was introduced at room temperature and its rate was determined by a different digital flowmeter (MesaLabs Defender 530+, volumetric accuracy : 0.75%, standardized accuracy: 1%) with velocities ranging from 0–10 m/s. **Table 5-2** summarizes the measurement techniques utilized throughout the experimental campaign. The pressure ports are located 6 cm from both the inlet and outlet of the sample (external diameter = 1 cm, length = 1.5 cm) positioned in the middle of the reactor tube. To mitigate the potential impact of the reactor setup, blank tests (without the structured support) have been carried out for each flow rate and sample used. These blank tests allow to isolate and subtract any interference arising from pressure loss attributable to the reactor setup and the positioning of pressure ports to ensure that the measured pressure drop accurately reflected the characteristics of the samples under investigation, independent of any external influences.

Table 5-2: Measurement techniques employed during the pressure drop experimental campaign

Sample	Measurements
BCC 3-0.6 (Al alloy)	1 series (A)
BCC 3-0.6 (Ni alloy)	1 series (B)
Kelvin 3-0.6 (Al alloy)	1 series (A)
Kelvin 3-0.6 (Cu alloy)	1 series (A)
Kelvin 3-0.6 (Ni alloy)	1 series (A)
Kelvin 3-0.8 (Ni alloy)	1 series (A)

5.3. Numerical investigation

5.3.1. CFD Modelling

To complement experimental data and gain deeper insights into POCS behavior under specific topologies, RANS (Reynolds-Averaged Navier-Stokes) simulations are deployed within Ansys Fluent (version 2023 R1). The simulations address both momentum and heat transfer aspects in two separate studies. **Figure 5-2** illustrates the computational domain, mirroring the experimental setup, and highlights the applied boundary conditions. Inlet velocities ranged between 1 and 9 m/s, while the outlet was maintained to atmospheric pressure. The exterior of the cylinder was set to a no-slip condition. Considering the intricate texture of the 3D-printed structure, a roughness

parameter with a constant of 0.5 and height of 0.1 mm was implemented at the surface of the POCS. Simulations were conducted with a cold, inert flow of nitrogen set at 293.15 K and 1 atm, replicating experimental conditions. In the heat transfer analysis, a conjugate heat transfer approach was employed, enabling a precise calculation of the POCS surface temperature. In this case, the inlet was assigned a temperature of 400 °C and the external surface of the cylinder had a temperature of 450°C. The POCS surface's temperature was then governed by heat fluxes and materials properties with Inconel's characteristics being the basis for this study. Additional insights into the physical settings are reported in **Appendix A**. From the numeric viewpoint, the chosen meshes comprise approximately 4.5 million cells for pressure drop simulations, and around 6 million for thermal simulations, encompassing both the fluid and solid domains. The simulations utilized a pressure-based solver in conjunction with the standard k- ϵ turbulence model also used in other similar study [21]. Gradient computations were handled using the Least Square Cell-Based discretization scheme, while the Second Order Upwind scheme was adopted for the discretization of transport properties, including momentum, energy, and turbulence variables. The "coupled" algorithm was chosen for pressure-velocity coupling, ensuring a stable and rapid convergence in this steady-state analysis. Convergence was deemed achieved when the residuals fell below 10^{-4} . A more comprehensive overview of the computational methods, encompassing domain, grid generation, mesh independence analysis and flow development analysis are presented in **Appendix B, C and D**

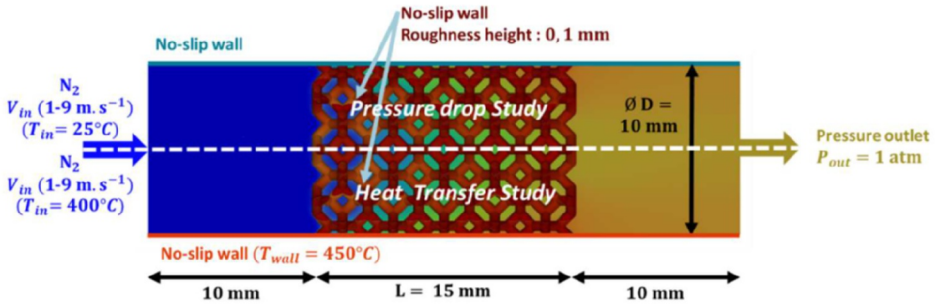


Figure 5-2: Implemented boundary conditions and physical setup applied during the pressure drop and heat transfer studies.

5.3.2. Performance indicators

The momentum and heat transfer performance are respectively assessed with two indicators namely the pressure drop across the sample and the volumetric heat transfer coefficient often adopted by researchers [22-23]. Pressure drop is defined as the difference between surface average pressure at inlet and outlet, divided by the sample length as per Eq. 5.3.

$$\frac{\Delta P}{L} = \frac{1}{L} \left(\frac{4}{\pi D^2} \iint p \, dS_{in} - \frac{4}{\pi D^2} \iint p \, dS_{out} \right) \quad \text{Eq. 5.3}$$

As expressed in Eq. 5.4, the volumetric heat coefficient denoted h_v is the product of the surface heat transfer coefficient h ($[W.m^{-2}.K^{-1}]$, defined in Eq. 5.5), and the specific surface area S_v ($[m^{-1}]$, defined in Eq. 5.2). This quantity is a relevant performance indicator, as it takes into account both the heat flux, and the contact surface allowed by POCS's geometry

$$h_v = S_v * h \quad \text{Eq. 5.4}$$

$$h = \frac{1}{S_{POCS}} \left(\sum_i \frac{\Phi(i)}{T_{solid(i)} - T_{ref}} \right) \quad \text{Eq. 5.5}$$

Where S_{POCS} is the total area of POCS surface. $\Phi(i)$ is the elementary power exchanged through each i cell's surface adjacent to the solid. $T_{solid(i)}$ is the temperature of each cell i on the solid surface. Within this study's framework, T_{ref} is provisionally defined as the inlet temperature. However, in section 5.4.3, it's adjusted to the volume-averaged fluid temperature (cf. Eq. 5.6), a reference that appears to be more universally accepted [24]. Subsequent comparisons are made with literature based on this adjusted reference.

$$T_{ref} = \frac{1}{V_f} \iiint T dV_f \quad \text{Eq. 5.6}$$

5.3.3. Engineering Correlations

Numerical findings provide the foundation for CFD-driven engineering correlations essential for reactor design. The pressure drop across a porous medium is influenced by its geometrical characteristics, the properties of the working fluid, and its velocity as per Eq. 5.7.

$$\frac{\Delta P}{L} = f(\epsilon, L_{char}, \rho, \mu, u) \quad \text{Eq. 5.7}$$

The Darcy-Forchheimer equation as presented in Eq. 5.8 is frequently employed in literature to model pressure drops across porous media and packed beds [25].

$$\frac{\Delta P}{L} = av + bv^2 \quad \text{Eq. 5.8}$$

This equation accounts for pressure drop in porous media by combining two terms: a viscous component, associated with fluid velocity and viscosity, and an inertial component, related to density and the square of the velocity. The Ergun equation is a standard method utilized by chemical engineers to determine pressure drop in packed beds, often integrated into simplified reactor models. Consistent with prior studies [26], our pressure drop data were regressed using an Ergun-like model, as shown in Eq. 5.9. In this model, A and B are the Ergun constants representing viscous and inertial terms, respectively. The superficial velocity term in the viscous term has been modified by adding an exponent C to better represent potential nonlinearities. Numerous definitions for characteristic lengths have been proposed, including specific surface area, cell size, and diverse diameters such as strut, hydraulic, or window, however a universal standard has yet to be established. For the scope of this study, the strut diameter is chosen for its relevance to catalyst support manufacturability and its straightforward application for engineers:

$$\frac{\Delta P}{L} = \frac{A(1-\epsilon)^C}{\epsilon^3} \frac{\mu v}{d_s^2} + \frac{B(1-\epsilon)}{\epsilon^3} \frac{\rho v^2}{d_s} \quad \text{Eq. 5.9}$$

In this study, MATLAB's `lsqcurvefit` function was utilized for nonlinear least-squares curve fitting [27]. This tool identifies parameter values by minimizing the squared differences between observed and predicted responses, using the Levenberg-Marquardt algorithm. The performance of the correlation was evaluated using the Mean Absolute Percentage Error (MAPE) and the Root Mean Squared Error (RMSE). MAPE provides a percentage-based insight into prediction errors, while RMSE measures the average magnitude of the error. The equations for MAPE and RMSE can be found in Eq. 5.10 & Eq. 5.11, with lower values suggesting a closer fit to the data.

$$MAPE = \frac{100}{N} \sum_{i=1}^N \left| \frac{y_{obs,i} - y_{fit,i}}{y_{obs,i}} \right| \quad \text{Eq. 5.10}$$

$$RMSE = \sqrt{\frac{1}{N} \sum_{i=1}^N (y_{obs,i} - y_{fit,i})^2} \quad \text{Eq. 5.11}$$

5.4. Result and discussion

5.4.1. Geometrical characterization

To ensure the accuracy of the 3D printing process, a geometric assessment of the printed replicas was carried out. **Figure 5-3** illustrates both the front and side perspectives of the sample using varying magnifications with a light microscope. The cell, strut and window diameters were additionally measured at different locations to evaluate the average morphological properties. In general, for the three lattice types, the measurements show that the cell size of the samples matches, on average, the cell size of the CAD while slight deviations can sometimes be noticed regarding strut diameter and window diameters. For example, slight strut thickening can be noticed in proximity of the node convergence. For further details **Figure 5-4** presents the SEM morphology of different cell surfaces, highlighting variations in textures based on the material used. The AlSi10Mg structure exhibits commonly observed features [28-29] such as partially melted Al alloy particles at the strut surface and a corrugated appearance due to the layer-by-layer additive manufacturing of the LPBF process. On the other hand, nickel and copper alloy samples exhibit a smoother surface. In case of Ni alloy, this could be due to optimized process parameter regarding the surface roughness and for the Cu alloy, it can directly be attributed to the sand-blasting process that removed the satellite particles from the surface. Finally, as observed in **Figure 5-5**, pycnometry experiments reveal that the porosity of the printed design is less than the one predicted by the CAD value file, with discrepancies reaching up to 15%. This is in line with deviation observed in the literature [3]. Such variations are particularly pronounced for the cell design with the finest details, like the Kelvin's square window at low porosity.

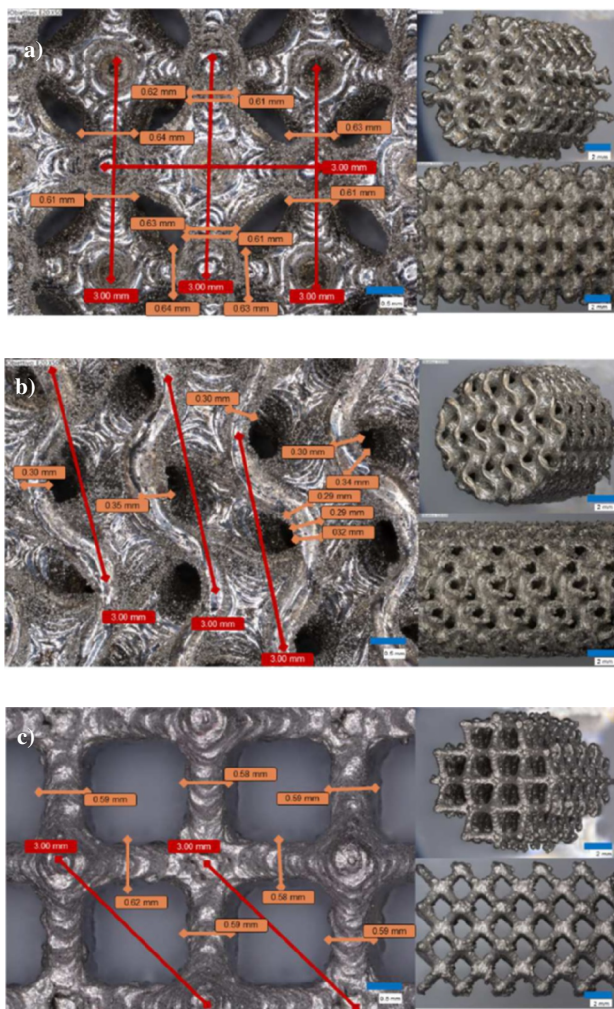


Figure 5-3: Macroscopic topography of the sample viewed by digital microscope a) Kelvin 3-0.6 (measurements: cells 3.0 mm; struts 0.63 mm) b) BCC 3-0.6 (measurements: cells 3.0 mm; struts 0.59 mm) c) Gyroid 3-0.3 (measurements: cells 3.03 mm; struts 0.32 mm). All structures presented in this figure are in Ni alloy.

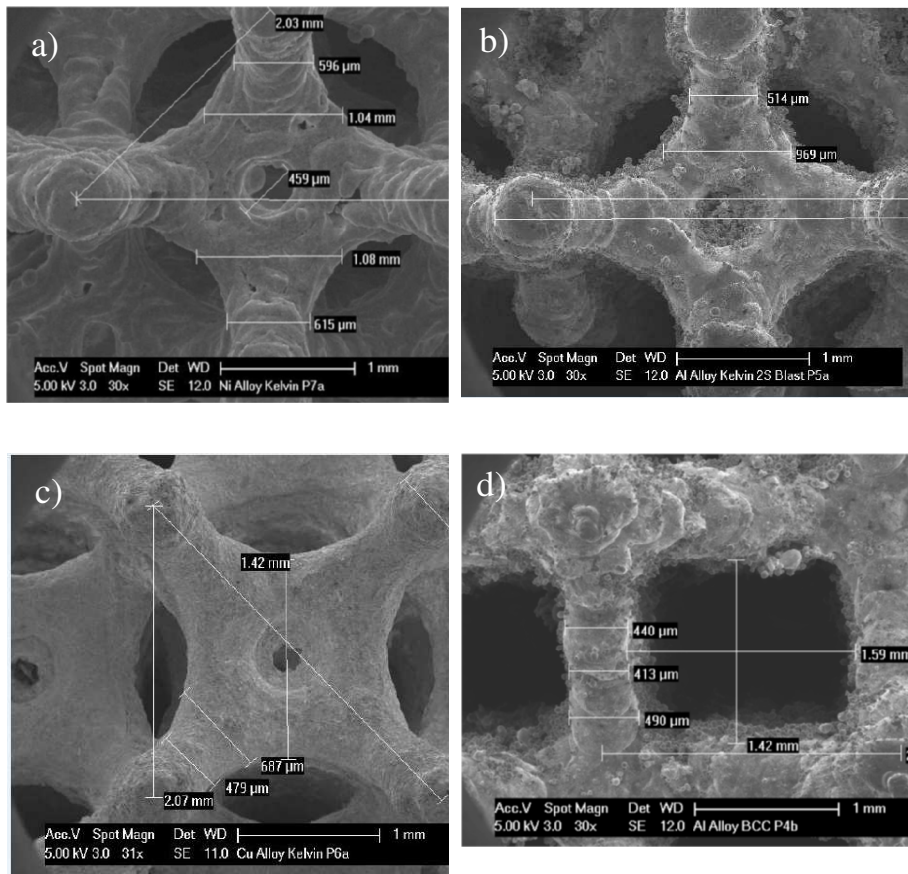


Figure 5-4: SEM images of strut surface of cellular structures after the post-processing: Scanning electron microscopy (SEM) micrograph at different magnification of three samples a) Kelvin 3-0.6 (Ni) b) Kelvin 3-0.6 (Al)^{sb} c) Kelvin 3-0.6 (Cu)^{sb} d) BCC 3-0.6 (Al alloy)

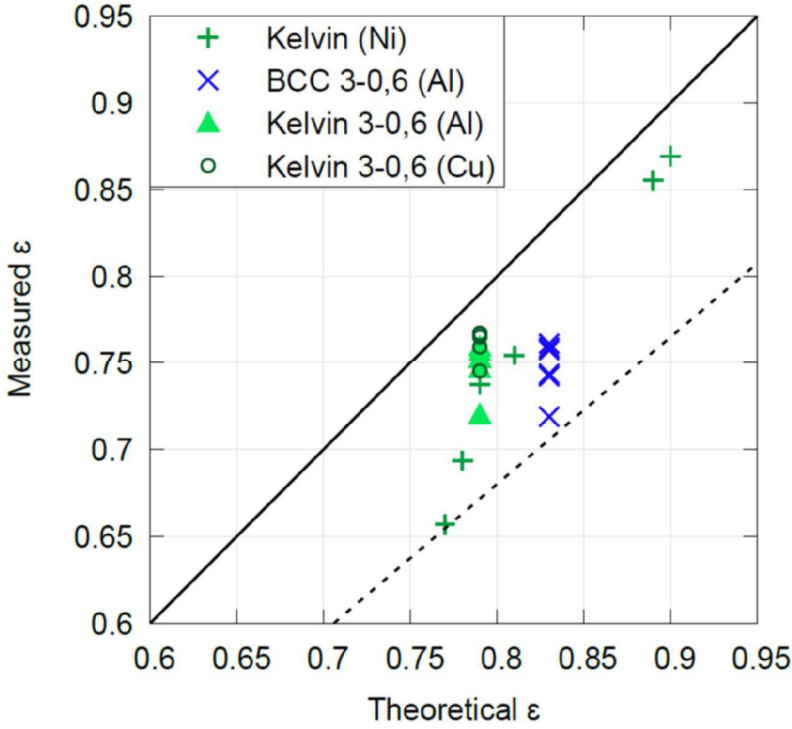


Figure 5-5: Experimental hydrodynamic porosity measured with pycnometry compared to the theoretical (CAD) porosity. The 15% error margin is indicated by the dashed line.

5.4.2. Pressure drop investigation

In this section, the outcomes of the CFD simulations are explored. First the accuracy of pressure drop predictions is verified against experimental results, and then the selected POCS designs are compared based on their specific surface area and porosity. **Figure 5-6** presents a comparison of pressure drop trends across velocities, contrasting experimental and simulation data for the chosen cell types. The shaded region for the BCC structure encompasses results from two experimental datasets: BCC 3-0.6 in both Al alloy and Ni alloy. In the case of the Kelvin cell 3-0.6, the shaded area includes readings from three different measurements: namely Al alloy, Cu alloy (both sandblasted), and Ni alloy. The shaded curve gives an average variability of 22 %, indicative of standard deviation across experiments. Such variations underline inherent differences across materials studied. Pressure drops obtained at high velocity ($\geq 5 \text{ m.s}^{-1}$) from CFD simulations align remarkably well within the experimental variability range. On the other hand, at slower velocities, there is an inclination towards over-predicting the pressure drop. This difference is especially notable for BCC 3-0.6, showing a deviation of up to 67% at 2 m.s^{-1} . Such variances may be rooted in turbulent flow modelling nuances, given the pronounced laminar tendencies at these speeds. Overall, a reasonable agreement is obtained between numerical and experimental data. To discern the cell type's influence on pressure drop, distinct structures, all maintaining a similar porosity ($\epsilon =$

0.79) and specific surface area ($S_v=12.3 \text{ cm}^{-1}$). The results are reported in **Figure 5-7**. Interestingly, the Kelvin structure consistently registered the most pronounced pressure drop, followed closely by the Gyroid (showing only a 3% differential at 9 m.s^{-1} with a constant porosity). Conversely, BCC showcased the least pressure drop, behind the Kelvin by 47% at 9 m.s^{-1} under similar porosity. Such distinctions can be attributed to the unique designs of the cells: as observed in **Figure 5-8**, the Kelvin structure, with its square openings oriented perpendicularly to the flow, creates flow constrictions that add considerable resistance, especially in the inertial regime. This design induces a more energy-intensive flow pattern within the matrix, amplifying energy dissipation, as supported by related studies [6,12]. Conversely, the gyroid lattice's streamlines depict a highly tortuous path also leading to increased friction and, thus, a higher pressure drop. Meanwhile, the BCC structure provides a relatively unimpeded flow. When evaluating solely on the basis of pressure drop, the BCC design is notably superior.

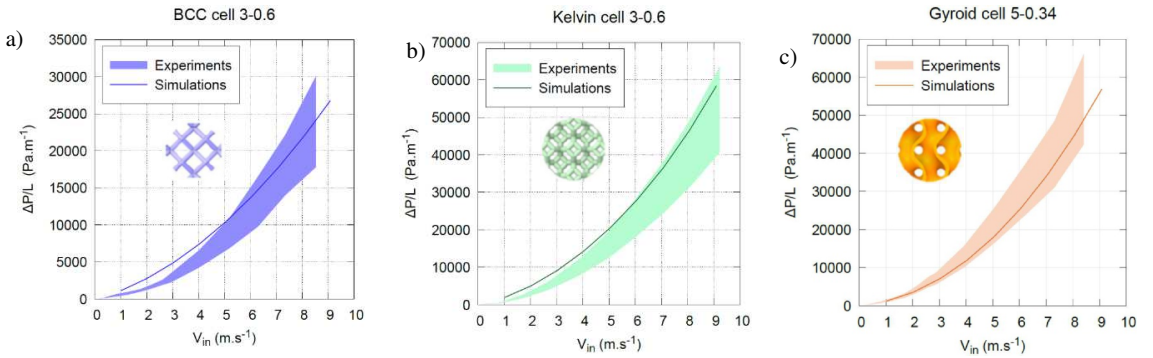


Figure 5-6: Experimental validation of our CFD settings (a) BCC (b) Kelvin (c) Gyroid

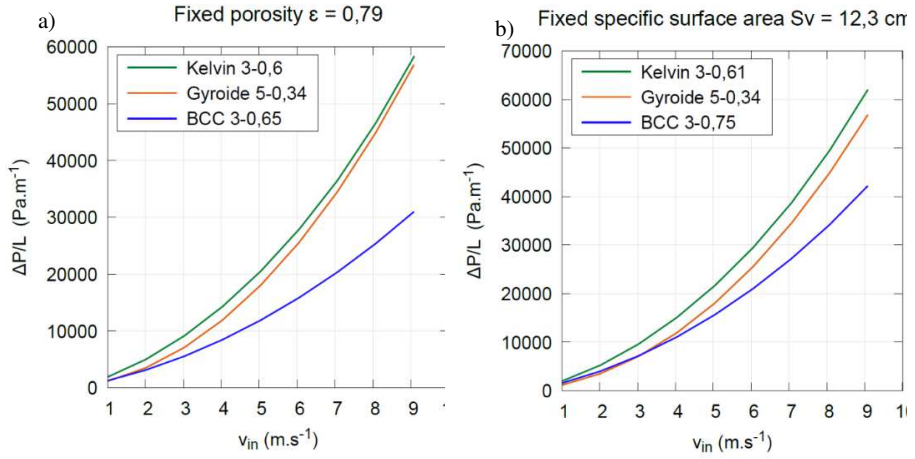


Figure 5-7: Pressure drop comparison on various structures, with fixed geometrical parameters (a) fixed porosity (b) fixed specific surface area (Reynolds number varies from 38 to 348 for Kelvin and BCC lattices, and from 22 to 254 for the Gyroid lattice)

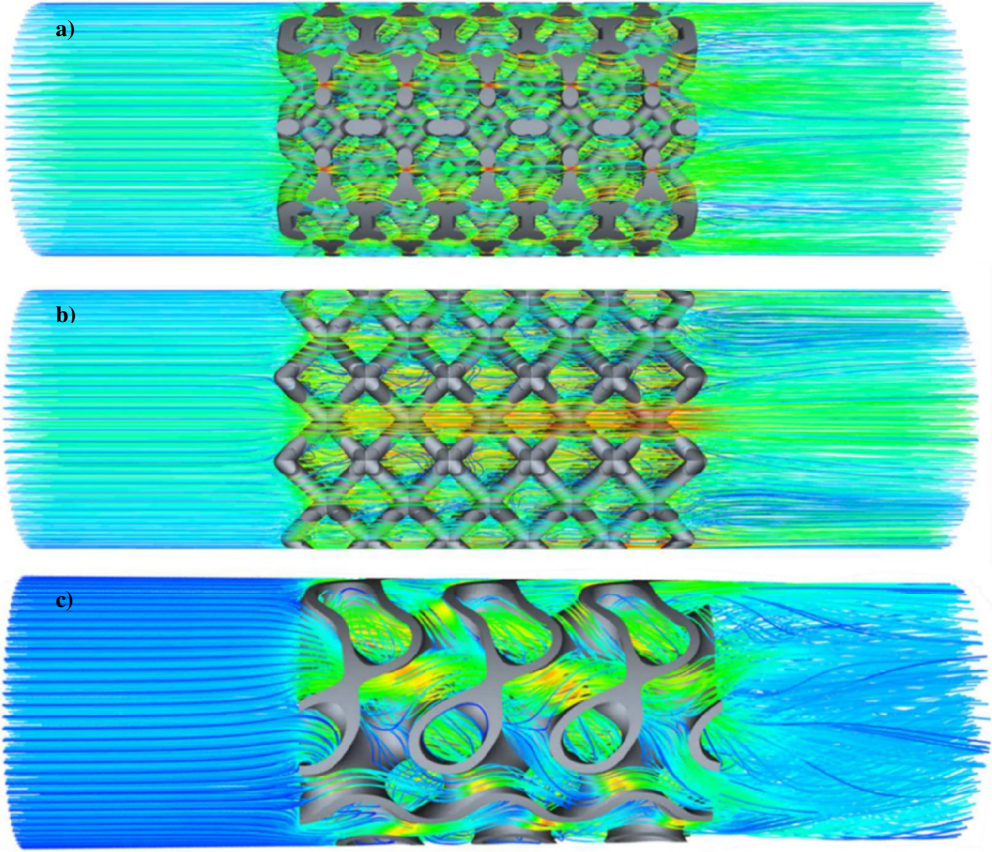


Figure 5-8: Streamline visualization across a) Kelvin b) BCC c) Gyroid lattices

5.4.3. Heat transfer investigation

While pressure drop is an important metric, it's just one piece of the puzzle. As many industrial applications involve significant heat transfer, it is essential to consider both pressure drop and heat transfer characteristics for a more holistic evaluation of the POCS. As stated in section 5.3.2. the volumetric heat transfer coefficient, denoted h_v (using the inlet temperature as the reference temperature) is the metric used to rank the structures. It can be seen in **Figure 5-9** that Kelvin cell consistently presents the highest value. At fixed specific surface area the BCC trails behind the Kelvin cell (18% deficit) but still surpasses the Gyroid structure by a margin of 6%. At fixed porosity, it is intriguing to note that the distinction between BCC and Gyroid is very light making

them almost analogous. Considering the aim to achieve the highest possible h_v , the Kelvin cell distinctly stands out as the best choice from the heat transfer viewpoint.

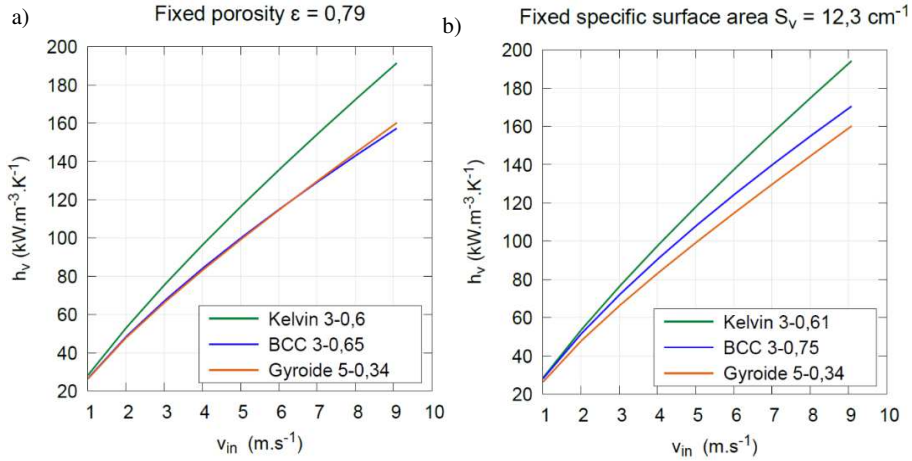


Figure 5-9: Volumetric heat transfer coefficient on various structures with fixed geometrical parameters (a) fixed porosity (b) fixed specific surface area

5.4.4. Trade off heat transfer-pressure drop

In evaluating optimal structural design, a balance between pressure drop and heat transfer is essential. Based on insights from prior sections, this section aims to identify the structure that offers minimal pressure drop while ensuring maximum volumetric heat transfer coefficient. A $h_v - \Delta P/L$ graph is therefore plotted on **Figure 5-10**. Although the performance between structures is fairly similar, a ranking can still be determined. When maintaining constant porosity, the Gyroid curve remains dominant until reaching a specific velocity, at which point the BCC becomes preferable. Yet, by extrapolating the current trends, the Kelvin cell could outperform the Gyroid when h_v exceeds $170 \text{ kW.m}^{-3}.\text{K}^{-1}$. In **Appendix C6** those results are also compared with packed bed performance obtained from correlations and several pellet diameter.

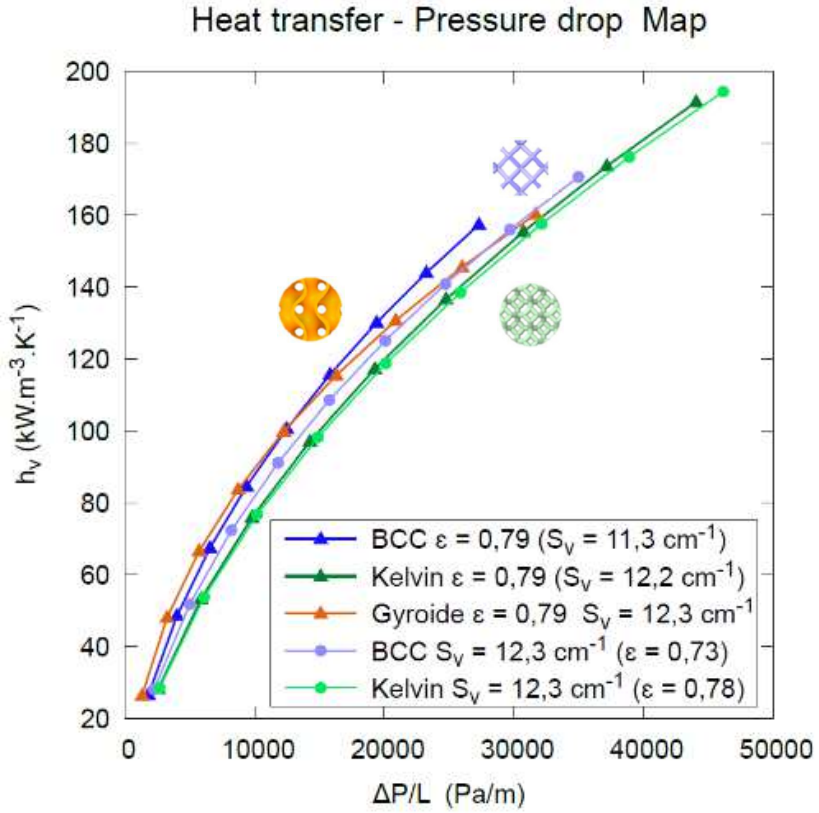


Figure 5-10: Heat transfer - pressure drop map

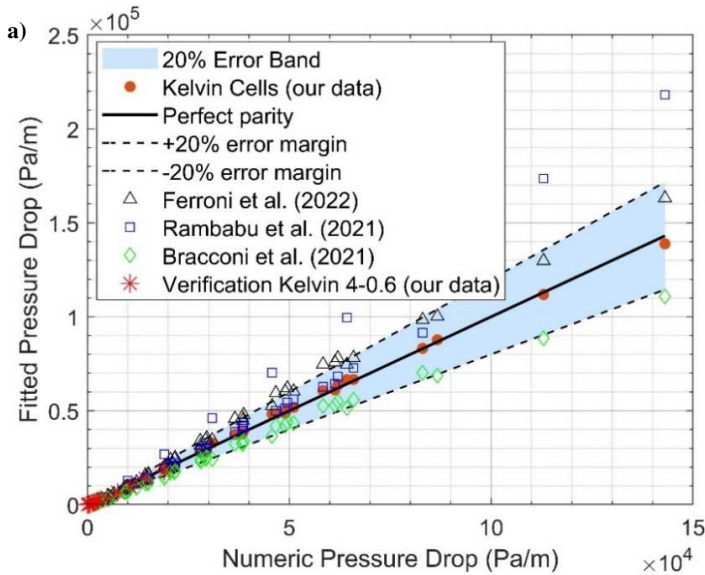
5.4.5. Engineering correlations & comparison with literature

An Ergun-type correlation, as detailed in Eq. 5.9 in section 5.3.3 is fitted to our CFD data to represent the pressure drop across our selected lattices. **Figure 5-11** presents the respective parity plots comparing the correlation predictions with the CFD simulation outcomes. Regression analysis constants, as well as the MAPE and RMSE values, are reported in **Table 5-3**. The results exhibit a good alignment, with a MAPE of less than 10%. For comparison with the literature, and given the absence of known existing correlations for the BCC and Gyroid lattices, our results are compared with established correlations obtained for the Kelvin cell lattice as display in **Figure 5-11.a**. The correlation of Ferroni et al. (2022) [3] is found to slightly overestimate our data with a MAPE of 18%, while Rambabu et al. (2021) [7] do so with a MAPE of 25%. Excluding data points with the lowest porosity value reduces the MAPE to 12%, implying that their correlation might not perform as well with lower porosities. The correlation of Bracconi et al. (2019) [26] derived from virtually generated OCF, yields a MAPE of 19.62%. On the whole, pressure drop results obtained in this study appear to be in quite good agreement with literature. Additionally, the simple correlations derived in this work, based on readily accessible parameters like strut size or gyroid thickness, could

assist in reactor design endeavors and also serve as a reference for comparison in subsequent research in this field. For the heat transfer analysis, comparisons of our results with established literature correlations are presented in **Figure 5-12**, utilizing the conventional heat transfer coefficient h . As explained in section 5.3.2, the heat transfer coefficient is recalculated using the volume-averaged fluid temperature as the reference, resulting in a higher value - a definition somewhat more adopted [6]. Nonetheless, there is a noticeable variation in heat transfer coefficient estimates. This variation could stem from several factors in numerical simulations: differing boundary conditions like constant wall heat flux versus constant wall temperature; the choice between conjugate heat transfer or a set thermal boundary in some research; the role of operating conditions and specific characteristics of the working fluid; and potential differences in methodologies for calculating the heat transfer coefficient across studies. Overall, the values predicted in this study align reasonably with literature data, albeit rather towards the lower end.

Table 5-3: Constants for the proposed pressure drop correlation as defined in Eq. 5.9 for the three lattices (presumed Reynolds validity range: $30 < Re_{ds} < 400$)

	Kelvin	BCC	Gyroid
Porosity validity interval	$0.66 < \epsilon < 0.8$	$0.72 < \epsilon < 0.92$	$0.7 < \epsilon < 0.8$
Fitted A	999.6348	83.5654	37260.0992
Fitted B	0.82099	0.26672	0.48628
Fitted C	3.4497	1.0837	9.818
RMSE (Pa/m)	1359.139	775.2997	1354.1546
MAPE (%)	9.0678	9.0718	6.5898



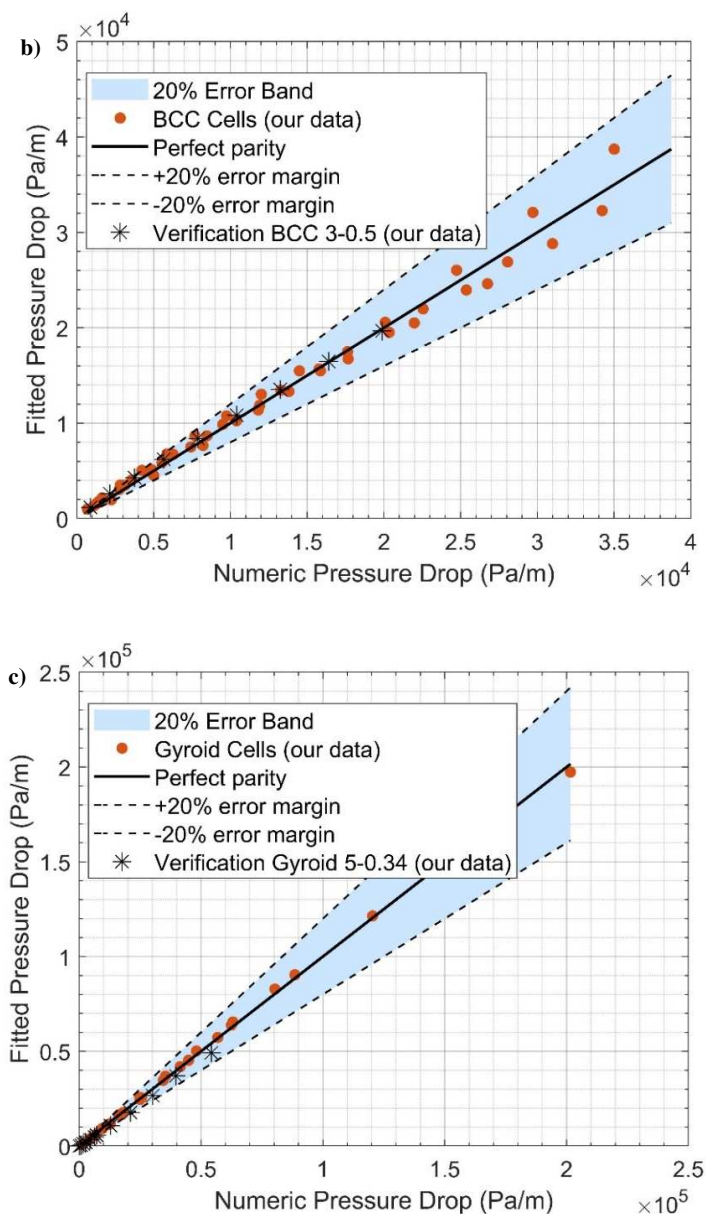


Figure 5-11: Parity plots comparing pressure drop obtained by the numeric investigation and correlation predictions for our selected POCS samples (a) Kelvin (b) BCC (c) Gyroid with the 20% error margin band. The star markers in each plot indicate the verification points used to check the proposed correlations

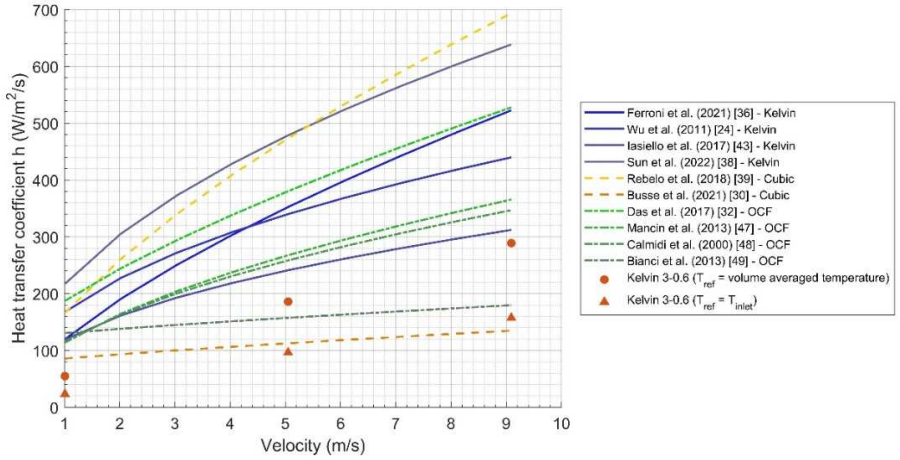


Figure 5-12: Comparison of our data with correlations found in the literature (Kelvin [12,14,23,30] Cubic [2,16] and OCF [6, 31-33]). The dot and triangle markers refer to the numerical results obtained using two different methodologies.

5.5. Conclusions

This chapter conducted an in-depth comparative analysis of three POCS: the widely recognized Kelvin cell, and the lesser-known BCC and gyroid lattice. Through a blend of numerical and experimental approaches, the study emphasized the design and fabrication using Laser Powder Bed Fusion, as well as the analysis of these structures using CFD simulations.

- 1) Regarding the manufacturability, various physico-morphological characterization techniques were utilized to determine geometric characteristics of 3D printed samples. The printed samples closely resembled their CAD counterparts, with an observed porosity deviating by a maximum of 15% less than the intended design values.
- 2) A CFD model was validated based on pressure drop experimental campaign and subsequently employed to conduct an in-depth comparison of POCS based on shared geometric features, specifically porosity and specific surface area. In terms of pressure drop, the BCC stands out as the superior structure. In contrast, the Kelvin cell registered the highest performance among all configurations from a heat transfer perspective. While the performance of the structures is relatively comparable, Gyroid configurations seem to offer superior momentum and heat transfer characteristics at lower velocities region whereas the BCC structure demonstrates superiority in the high-velocity range.
- 3) An Ergun-like correlation was formulated and validated for all three cell types, achieving a MAPE of less than 10%. When compared with existing literature correlations, our results demonstrated good alignment too, with a MAPE of less than 20%. Concerning heat transfer, the values forecasted in this research show a reasonable alignment with literature figures, though they tend to be on the lower spectrum.

This study advances our understanding of POCS thermohydraulic properties, offering insights for selecting cell types and also scaling up reactors or other continuous flow systems utilizing these structures, yet several areas remain unexplored. For example, a comprehensive analysis should also factor chemical reactions, moreover, many POCS designs have yet to be investigated, and cell orientation might have a significant impact at higher velocities, particularly in the gyroid lattice.

5.6. References

- [1] I. Kaur, P. Singh, Flow and Thermal Transport Through Unit Cell Topologies of Cubic and Octahedron Families, *International Journal of Heat and Mass Transfer* 158 (2020) 119784. <https://doi.org/10.1016/j.ijheatmasstransfer.2020.119784>.
- [2] C. Busse, H. Freund, W. Schwieger, Intensification of heat transfer in catalytic reactors by additively manufactured periodic open cellular structures (POCS), *Chemical Engineering and Processing - Process Intensification* 124 (2018) 199–214. <https://doi.org/10.1016/j.cep.2018.01.023>.
- [3] C. Ferroni, F.S. Franchi, M. Ambrosetti, M. Bracconi, G. Groppi, M. Maestri, E. Tronconi, Numerical and Experimental Investigation of Pressure Drop in Periodic Open Cellular Structures for Intensification of Catalytic Processes, *ACS Eng. Au* (2022) acsengineeringau.1c00034. <https://doi.org/10.1021/acsengineeringau.1c00034>.
- [4] Z. Cheng, R. Xu, P.-X. Jiang, Morphology, flow and heat transfer in triply periodic minimal surface based porous structures, *International Journal of Heat and Mass Transfer* 170 (2021) 120902. <https://doi.org/10.1016/j.ijheatmasstransfer.2021.120902>.
- [5] Z. Ahmed Qureshi, S. Addin Burhan Al-Omari, E. Elnajjar, O. Al-Ketan, R. Abu Al-Rub, Architected lattices embedded with phase change materials for thermal management of high-power electronics: A numerical study, *Applied Thermal Engineering* 219 (2023) 119420. <https://doi.org/10.1016/j.applthermaleng.2022.119420>.
- [6] Das, S., Transport through bidisperse porous media, PhD Thesis, TU Eindhoven, 2017.
- [7] S. Rambabu, K. Kartik Sriram, S. Chamarthy, P. Parthasarathy, V. Ratna kishore, A proposal for a correlation to calculate pressure drop in reticulated porous media with the help of numerical investigation of pressure drop in ideal & randomized reticulated structures, *Chemical Engineering Science* 237 (2021) 116518. <https://doi.org/10.1016/j.ces.2021.116518>.
- [8] F. Lucci, A. Della Torre, G. Montenegro, R. Kaufmann, P. Dimopoulos Eggenschwiler, Comparison of geometrical, momentum and mass transfer characteristics of real foams to Kelvin cell lattices for catalyst applications, *International Journal of Heat and Mass Transfer* 108 (2017) 341–350. <https://doi.org/10.1016/j.ijheatmasstransfer.2016.11.073>.
- [9] F. Lucci, A. Della Torre, G. Montenegro, P. Dimopoulos Eggenschwiler, On the catalytic performance of open cell structures versus honeycombs, *Chemical Engineering Journal* 264 (2015) 514–521. <https://doi.org/10.1016/j.cej.2014.11.080>.
- [10] M. Sun, M. Li, C. Hu, L. Yang, Y. Song, D. Tang, J. Zhao, Comparison of forced convective heat transfer between pillar and real foam structure under high Reynolds number, *Applied Thermal Engineering* 182 (2021) 116130. <https://doi.org/10.1016/j.applthermaleng.2020.116130>.
- [11] S. Meinicke, K. Dubil, T. Wetzel, B. Dietrich, Characterization of heat transfer in consolidated, highly porous media using a hybrid-scale CFD approach, *International Journal of Heat and Mass Transfer* 149 (2020) 119201. <https://doi.org/10.1016/j.ijheatmasstransfer.2019.119201>.
- [12] C. Ferroni, M. Bracconi, M. Ambrosetti, M. Maestri, G. Groppi, E. Tronconi, A Fundamental Investigation of Gas/Solid Heat and Mass Transfer in Structured Catalysts Based on Periodic

- Open Cellular Structures (POCS), *Ind. Eng. Chem. Res.* 60 (2021) 10522–10538. <https://doi.org/10.1021/acs.iecr.1c00215>.
- [13] C. Moon, H.D. Kim, K.C. Kim, Kelvin-cell-based metal foam heat exchanger with elliptical struts for low energy consumption, *Applied Thermal Engineering* 144 (2018) 540–550. <https://doi.org/10.1016/j.applthermaleng.2018.07.110>.
- [14] M. Sun, G. Yan, M. Ning, C. Hu, J. Zhao, F. Duan, D. Tang, Y. Song, Forced convection heat transfer: A comparison between open-cell metal foams and additive manufactured kelvin cells, *International Communications in Heat and Mass Transfer* 138 (2022) 106407. <https://doi.org/10.1016/j.icheatmasstransfer.2022.106407>.
- [15] M. Klumpp, A. Inayat, J. Schwerdtfeger, C. Körner, R.F. Singer, H. Freund, W. Schwieger, Periodic open cellular structures with ideal cubic cell geometry: Effect of porosity and cell orientation on pressure drop behavior, *Chemical Engineering Journal* 242 (2014) 364–378. <https://doi.org/10.1016/j.cej.2013.12.060>.
- [16] N.F.B. Rebelo, Pressure drop and heat transfer properties of cubic iso-reticular foams, *Chemical Engineering* (2018) 7.
- [17] M. Lämmermann, G. Horak, W. Schwieger, H. Freund, Periodic open cellular structures (POCS) for intensification of multiphase reactors: Liquid holdup and two-phase pressure drop, *Chemical Engineering and Processing - Process Intensification* 126 (2018) 178–189. <https://doi.org/10.1016/j.ccep.2018.02.027>.
- [18] G. Do, M. Geißelbrecht, W. Schwieger, H. Freund, Additive manufacturing of interpenetrating periodic open cellular structures (interPOCS) with in operando adjustable flow characteristics, *Chemical Engineering and Processing - Process Intensification* 148 (2020) 107786. <https://doi.org/10.1016/j.ccep.2019.107786>.
- [19] I.R. Woodward, L. Attia, P. Patel, C.A. Fromen, Scalable 3D printed lattices for pressure control in fluid applications, *AIChE Journal* 67 (2021) e17452. <https://doi.org/10.1002/aic.17452>.
- [20] A. Chaudhari, P. Ekade, S. Krishnan, Experimental investigation of heat transfer and fluid flow in octet-truss lattice geometry, *International Journal of Thermal Sciences* 143 (2019) 64–75. <https://doi.org/10.1016/j.ijthermalsci.2019.05.003>.
- [21] Y. Tang, H. Wang, C. Huang, Pore-scale numerical simulation of the heat transfer and fluid flow characteristics in metal foam under high Reynolds numbers based on tetrakaidecahedron model, *International Journal of Thermal Sciences* 184 (2023) 107903. <https://doi.org/10.1016/j.ijthermalsci.2022.107903>.
- [22] S. Xu, Z. Wu, H. Lu, L. Yang, Experimental Study of the Convective Heat Transfer and Local Thermal Equilibrium in Ceramic Foam, *Processes* 8 (2020) 1490. <https://doi.org/10.3390/pr8111490>.
- [23] Z. Wu, C. Caliot, G. Flamant, Z. Wang, Numerical simulation of convective heat transfer between air flow and ceramic foams to optimise volumetric solar air receiver performances, *International Journal of Heat and Mass Transfer* 54 (2011) 1527–1537. <https://doi.org/10.1016/j.ijheatmasstransfer.2010.11.037>.
- [24] M. Iasiello, N. Bianco, W.K.S. Chiu, V. Naso, Anisotropic convective heat transfer in open-cell metal foams: Assessment and correlations, *International Journal of Heat and Mass Transfer* 154 (2020) 119682. <https://doi.org/10.1016/j.ijheatmasstransfer.2020.119682>.
- [25] C. Italiano, M.A. Ashraf, L. Pino, C.W.M. Quintero, S. Specchia, A. Vita, Rh/CeO₂ Thin Catalytic Layer Deposition on Alumina Foams: Catalytic Performance and Controlling Regimes in Biogas Reforming Processes, *Catalysts* 8 (2018) 448. <https://doi.org/10.3390/catal8100448>.
- [26] M. Bracconi, M. Ambrosetti, O. Okafor, V. Sans, X. Zhang, X. Ou, C.P. Da Fonte, X. Fan, M. Maestri, G. Groppi, E. Tronconi, Investigation of pressure drop in 3D replicated open-cell foams: Coupling CFD with experimental data on additively manufactured foams, *Chemical Engineering Journal* 377 (2019) 120123. <https://doi.org/10.1016/j.cej.2018.10.060>.

- [27] MATLAB R2019b: lsqcurvefit (Version R2019b) [Computer software]. Natick, MA: The MathWorks Inc. Available, (2023). <https://fr.mathworks.com/help/optim/ug/lsqcurvefit.html>.
- [28] Z. Li, Y. Nie, B. Liu, Z. Kuai, M. Zhao, F. Liu, Mechanical properties of AlSi10Mg lattice structures fabricated by selective laser melting, *Materials & Design* 192 (2020) 108709. <https://doi.org/10.1016/j.matdes.2020.108709>.
- [29] C. Yan, L. Hao, A. Hussein, D. Raymont, Evaluations of cellular lattice structures manufactured using selective laser melting, *International Journal of Machine Tools and Manufacture* 62 (2012) 32–38. <https://doi.org/10.1016/j.ijmachtools.2012.06.002>.
- [30] M. Iasiello, S. Cunsolo, N. Bianco, W.K.S. Chiu, V. Naso, Developing thermal flow in open-cell foams, *International Journal of Thermal Sciences* 111 (2017) 129–137. <https://doi.org/10.1016/j.ijthermalsci.2016.08.013>.
- [31] S. Mancin, C. Zilio, A. Diani, L. Rossetto, Air forced convection through metal foams: Experimental results and modeling, *International Journal of Heat and Mass Transfer* 62 (2013) 112–123. <https://doi.org/10.1016/j.ijheatmasstransfer.2013.02.050>.
- [32] V.V. Calmidi, R.L. Mahajan, Forced Convection in High Porosity Metal Foams, *Journal of Heat Transfer* 122 (2000) 557–565. <https://doi.org/10.1115/1.1287793>.
- [33] E. Bianchi, T. Heidig, C.G. Visconti, G. Groppi, H. Freund, E. Tronconi, Heat transfer properties of metal foam supports for structured catalysts: Wall heat transfer coefficient, *Catalysis Today* 216 (2013) 121–134. <https://doi.org/10.1016/j.cattod.2013.06.019>.
- [34] S. Yagi, N. Wakao, Heat and mass transfer from wall to fluid in packed beds, *AIChE Journal* 5 (1) (1959) 79–85.

Appendix C

C1. Physical setting details

Table C1: Recap of physical settings for pressure drop simulations

Name	Value
Operating temperature	25 °C
Operating pressure	1 atm
Inlet velocity	{1,2,3, ..., 9} m. s ⁻¹
Fluid density	1,1452 kg. m ⁻³ [9]
Fluid viscosity	1,7805.10 ⁻⁵ Pl [9]

Table C2: Recap of physical settings for pressure drop simulations

Name	Symbol	Value
Inlet temperature	T_{in}	400 °C
Wall temperature	T_{wall}	450 °C
Operating pressure	P_{op}	1 atm
Inlet velocity	v_{in}	{1,2,3,4,5,6,7,8,9} m. s ⁻¹
Solid density	$\rho(\text{in625})$	8440 kg. m ⁻³

Solid specific heat	$C_p(\text{in625})$	Piecewise-linear, taken from [10] ($\sim 500 \text{ J} \cdot \text{kg}^{-1} \cdot \text{K}^{-1}$)
Solid thermal conductivity	$\lambda(\text{in625})$	Piecewise-linear, taken from [10] ($\sim 17 \text{ W} \cdot \text{m}^{-1} \cdot \text{K}^{-1}$)
Fluid density	$\rho(\text{N}_2)$	Computed (Fluent “incompressible-ideal-gas”)
Fluid specific heat	$C_p(\text{N}_2)$	Variable (Fluent “nasa-9-piecewise-polynomial”) ($\sim 1100 \text{ J} \cdot \text{kg}^{-1} \cdot \text{K}^{-1}$)
Fluid thermal conductivity	$\lambda(\text{N}_2)$	Piecewise-linear, taken from [9] ($\sim 0,05 \text{ W} \cdot \text{m}^{-1} \cdot \text{K}^{-1}$)
Fluid viscosity	$\mu(\text{N}_2)$	Computed (Fluent “kinetic-theory”)

C2. Mesh convergence analysis

A mesh convergence analysis was carried out aiming at obtaining pressure drop results independent of the grid refinement in the numerical investigation. For each of the three different types of structure, we made a meshing convergence study. Five meshes were tested for Kelvin and BCC structures, and four for Gyroid. For each of them, we made simulations corresponding to the nine flow speeds from 1 to 9 $\text{m} \cdot \text{s}^{-1}$. We then measured the pressure drop obtained and compared them to the value achieved with the finest mesh. Results are shown on **Figure C1**, on which each point represents the average error of the nine speeds. Considering the results of the convergence study, for each structure we retained the meshes with about 4,5M cells, as they allow about 1% error and good computation time. **Table C3** gives the typical settings we used to generate meshes with this number of cells. We used these parameters for all the other structures, including those for thermal simulations.

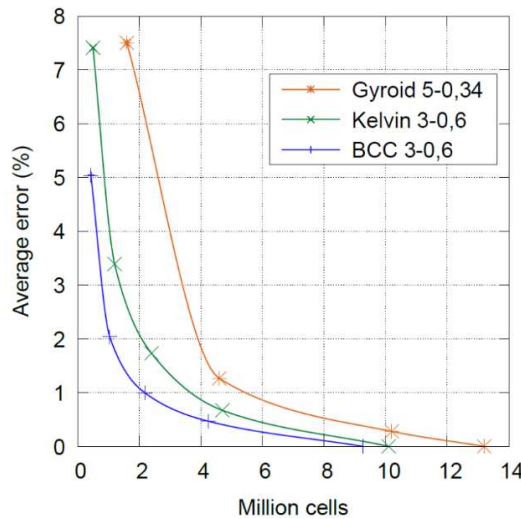


Figure C1: Mesh sensitivity

Table C3: Typical mesh generation settings

Setting	Value
Surface local sizing	0.05 mm on POCS surface
General minimum surface size	0.1 mm
Maximum surface size	0.4 mm
Surface growth rate	1.2
Boundary smooth transition	Layers: 3, Transition ratio: 0,272, Growth rate: 1,2
Maximum cell length	0.4 mm
Volume growth rate	1.2

C3. Ansys Fluent Solver setting

Table C4: Ansys Fluent Solver settings

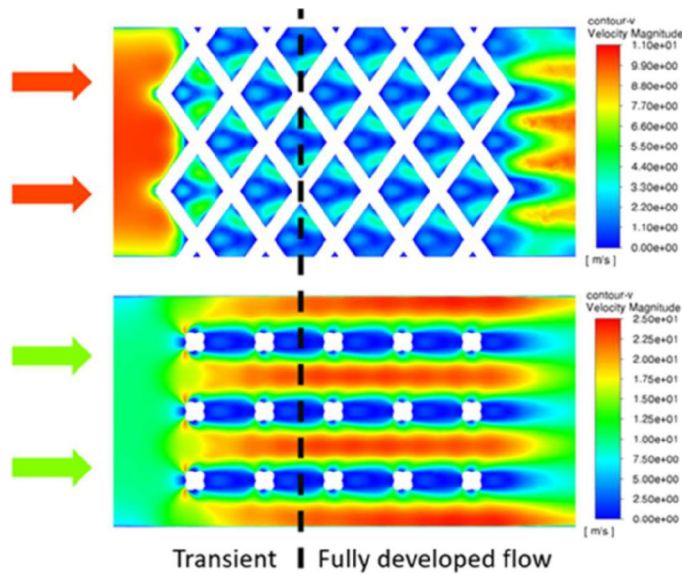
Setting	Value
Time	Steady-state
Solver type	Pressure-based
Pressure-velocity scheme	Coupled
Gradient discretization	Least squares cell based
Spatial discretization	Second order (upwind)
Pseudo-time method	Global time step
Viscous model	k- ϵ realizable, with scalable wall functions
Maximum tolerated continuity residual (with all other residuals lower)	10^{-4}

C4. Analysis of Flow Development

To investigate the effects of the POCS inlet and outlet on pressure drop, fresh simulations were conducted using the BCC 3-0.6 geometry. Considering the phenomenon's non-linear nature, the study included simulations on both a standard-length sample (15 mm) and a 1.4-times elongated sample (21 mm), with airflows set at 1 and 9 m/s. The actual values for the elongated sample were then compared to the extrapolated values from the standard sample, which were adjusted by the 1.4 factor. The results are presented in Table 8 below: As the gap is only 1% between elongated sample and proportional value from standard sample, inlet and outlet effects can be considered as negligible. A length of 15 mm is found sufficient for achieving a fully developed flow. Specifically, at an inlet speed of 9 m/s (the maximum speed, at which the flow requires the longest distance to fully develop), the velocity field exhibits periodic behavior in accordance with the geometry. As depicted in **Figure C2**, for two adjacent cutting planes with an inlet speed of 9 m/s, the velocity field is consistently repeated from the second cell in the flow direction, confirming that the flow stabilizes after about 6 mm. This observation underscores the establishment of a fully developed flow pattern.

Table C5: Effect of POCS sample length on pressure drop

Vin (m/s)	Pressure drop $\Delta P/L$ (Pa/m)			Relative gap (Proportional – Real values)
	Standard sample length (15 mm)	Extrapolated value for elongated sample (* 1.4 factor)	Real value for elongated sample (* 1.4 factor)	
1	1 115	1 561	1 564	0.2 %
9	26 749	37 448	36 976	1.3 %

**Figure C2:** Analysis of Flow Development on BCC 3-0.6 for two adjacent cutting planes

C5. Turbulence model justification

For flow through homogeneous porous media, for very low fluid velocity, the pressure drop is only balanced by the viscous shear stress at the solid surfaces (Darcy regime). When the Reynolds number is gradually increased, in the Forchheimer regime, the inertial forces related to the local acceleration of the fluid particles starts contributing and the total pressure drop contains both viscous and inertial contributions. The exact limiting value of the Reynolds number for flow transition from Darcy regime to Forchheimer regime depends on the structure of the porous medium. The study of Das et al. (2017) [6] offers insight into the transition Reynolds number, using DNS on a Kelvin cell study, as depicted in **Figure C3**. In our operating condition, we predominantly observe the Forchheimer regime, suggesting that both laminar and RANS simulation could be suitable alternatives. In our study the choice is made to resort to RANS simulation to cover the full velocity range.

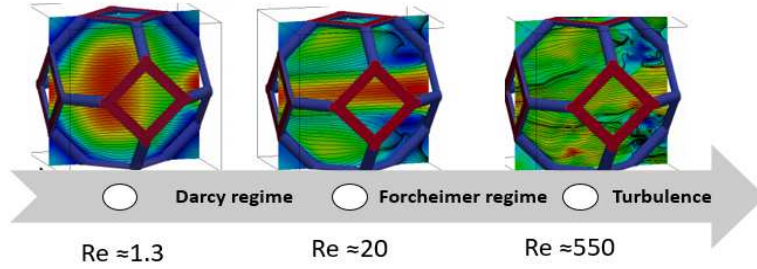


Figure C3: Description of the hydrodynamic regimes based on an equivalent sphere diameter as a characteristic length scale adapted from Das et al. (2017) [6]

C6. Comparison with packed beds

To provide context for the thermo-hydraulic performance of the 3D-printed structures, a comparative analysis was conducted using empirical correlations for conventional packed beds. The results from this analysis are presented in **Table C6**, allowing direct comparison with **Figure C4**, which reports the CFD simulation data from this study on POCS (Periodic Open-Cell Structures). In **Table C6**, the volumetric heat transfer coefficient (h_v) was calculated using two correlations [6, 34]:

$$Nu_{Yagi \& Wakao} = \begin{cases} 0.6 Pr^{1/3} Re^{1/2}, & 1 \leq Re \leq 40 \\ 0.2 Pr^{1/3} Re^{0.8}, & 40 \leq Re \leq 20000 \end{cases} \quad \text{Eq. C2}$$

$$Nu_{Das \text{ et al.}} = 1.351 + 0.1124 Re^{0.878} Pr^{1/3} \quad \text{Eq. C3}$$

Where Nu is the Nusselt number $h d_p / k_f$, Pr is the Prandtl number $\mu C_p / k_f$ and Re is the Reynolds number $\rho v d_p / \mu$. Additionally, the pressure drop ($\Delta P/L$) was determined using the Ergun equation:

$$\frac{\Delta P}{L} = \frac{150 (1-\epsilon)^2}{\epsilon^3} \frac{\mu v}{d_p^2} + \frac{1.75 (1-\epsilon)}{\epsilon^3} \frac{\rho v^2}{d_p} \quad \text{Eq. C2}$$

For these calculations, the fluid properties of nitrogen at 427 °C and 1 atm were used: dynamic viscosity: $\mu=3.2837 \times 10^{-5}$ Pa·s, density $\rho=0.48739$ kg/m³, thermal conductivity $k=0.050314$ W/m/K, and specific heat capacity $C_p=1098.1$ J/kg/K. The analysis was performed for spherical particles of 1 mm, 10 mm, and 20 mm diameters, assuming a porosity (ϵ) of 0.48. The specific surface area (SSA) was determined using the following relationship:

$$SSA = \frac{6(1-\epsilon)}{d_p} \quad \text{Eq. C4}$$

The results in **Table C6** show the trade-off between heat transfer and pressure drop in packed beds: smaller particles exhibit higher volumetric heat transfer coefficients due to their greater specific surface area. However, this enhancement comes at the cost of increased pressure drop, which becomes particularly pronounced at smaller particle sizes. By comparing these correlations with our

CFD results in **Figure C4**, it is observed that—under the chosen assumptions and correlations—the volumetric heat transfer coefficient is higher for the POCS structures studied in this work than for conventional packed beds at a given pressure drop. Further reducing pellet size (<5 mm) increases the volumetric heat transfer coefficient beyond that of POCS but at the cost of higher pressure drop.

Table C6: Pressure drop and volumetric heat transfer coefficient for three pellet diameters based on literature correlations

Velocity (m/s)	d_p (mm)	SSA (m ²)	Re	$\Delta P/L$ (Pa/m)	h_v (kW m ⁻³ K ⁻¹) Yagi & Wakao (1959) [34]	h_v (kW m ⁻³ K ⁻¹) Das et al. (2017) [6]
1	5	624	74	1.28*10 ³	35.00	36.00
4	5	624	296	1.48*10 ⁴	107.00	102.00
9	5	624	667	6.93*10 ⁴	205.00	200.00
1	10	312	148	521	15.30	14.80
4	10	312	593	6.9*10 ³	46.50	45.13
9	10	312	1.34*10 ³	3.36*10 ⁴	89.10	82.80
1	20	156	296	230	6.68	6.38
4	20	156	1.19*10 ³	3.33*10 ³	20.26	20.29
9	20	156	2.67*10 ³	1.65*10 ⁴	38.70	40.80

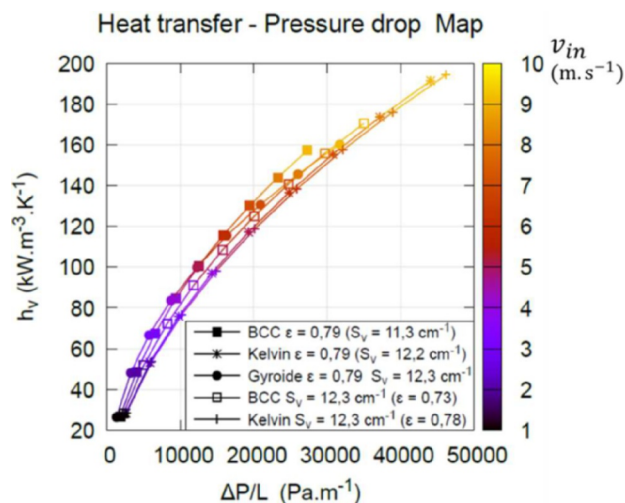


Figure C4: Heat transfer vs. pressure drop, reproduced from **Figure 5.10**, highlighting the inlet velocity used in the simulations

Chapter 6 | Ammonia synthesis using POCS membrane reactor: influence of cell types

Abstract

Ammonia has emerged as a promising hydrogen carrier due to its high hydrogen content and carbon-free composition. However, its production is still dominated by the energy-intensive Haber-Bosch process. This has prompted ongoing research into more sustainable production methods, including the development of new catalysts and integrated reactor designs with enhanced heat and mass transfer processes. This chapter* investigates external mass transfer in Periodic Open Cellular Structure (POCS) reactors during ammonia synthesis, both as standalone systems and integrated with a selective membrane. Laboratory-scale experiments were combined with Computational Fluid Dynamics (CFD) modeling to systematically assess different POCS topologies and evaluate membrane reactor performance. A dip/spin coating method was optimized to deposit Ru-based catalytic layers onto IN625 POCS produced via Selective Laser Melting (SLM), including BCC, gyroid, and Kelvin cell types. While homogeneous coatings were achieved for all structures, clogging issues were noted for the Kelvin cell, suggesting it may be less suitable for maintaining cell geometry during coating. Catalytic activity assessments showed consistency with literature values for Ru-based catalysts. CFD simulations of different POCS geometries indicated that cell type does not significantly influence catalytic activity under the chosen conditions. The impact of membrane permeance on reactor performance was assessed, revealing improvements in both conversion and recovery. However, these benefits reached a plateau due to the limited rate of ammonia production compared to extraction, as well as the effects of concentration polarization, particularly on the permeate side. A plug flow-based engineering model was found to inaccurately predict system behavior beyond a permeance of $0.05 \text{ mol} \cdot \text{s}^{-1} \cdot \text{m}^{-2} \cdot \text{bar}^{-1}$, highlighting the need for correction factors for non-ideal conditions. Future work should explore sensitivity analyses involving permeation parameters and evaluate structure-independent performance when POCS are interfaced with membranes.

* This chapter is based on the following paper : S. Richard, D. Tasso, M. Rajana, A. Saker, A. Ramirez Santos, C. Makhloufi, N. Meynet, B. Hary, S. Nardone, G. Marino, M. Thomas, H. Brahim, C. Italiano, A. Vita, F. Gallucci, Comparison of thermo-hydraulic performance among different 3D printed periodic open cellular structures, Chemical Engineering Journal, vol. 47, no. 21, pp. 11385–11401, 2024

6.1. Introduction

Chapter 5 examined Periodic Open Cellular Structures (POCS) from a thermohydraulic perspective. Building on that foundation, the current chapter delves into the catalytic activation of POCS, as introduced in **Chapter 2** (page 32), with a focus on ammonia synthesis. It further highlights the potential of membrane reactors in overcoming the thermodynamic barriers of this process. Conventional reactors employing iron-based catalysts typically achieve ammonia concentrations of approximately 20–25% under demanding operating conditions of 150–250 bar and 380–520 °C. From a catalytic perspective, the primary challenge lies in the cleavage of the high-energy nitrogen (N_2) bond, which requires 945 kJ/mol—a rate-determining step in the reaction mechanism. Supported ruthenium (Ru)-based catalysts are a key area of research due to their higher catalytic activity at lower temperatures and pressures compared to iron (Fe)-based catalysts. However, their high cost and susceptibility to hydrogen poisoning present challenges. Current studies focus on enhancing active site exposure and mitigating hydrogen poisoning by using specific supports and promoters. Notable examples include Ru/CeScSi [1], Ru/CeO₂ [2], Ru/MgOCeO₂, Ru/Pr₂O₃, and other lanthanides [3], as well as transition metal oxide supports like SrTa₂O₇ [4]. Huang et al. (2020) [4] demonstrated that Ru supported on Sr₂Ta₂O₇ with a cesium (Cs) promoter achieved more than a threefold increase in catalytic activity, with promoter effectiveness ranked as Cs > Rb > K > Ba. In addition, research is exploring catalysts with a better activity-to-cost ratio, such as the Co/10Mg–Nd catalyst, which achieved twice the ammonia formation rate compared to commercial Fe catalysts, as reported by Ronduda et al. (2023) [5].

At the mesoscale, Computational Fluid Dynamics (CFD) is a powerful tool for analyzing transport phenomena in membrane reactors, particularly the influence of geometry [6–9]. As shown in the previous chapter, CFD complements experiments by providing detailed visualizations and quantitative insights into fluid-solid interactions, enabling systematic parametric studies. Numerous studies have successfully employed CFD to investigate external mass transfer in POCS reactors. These studies often compare different POCS cell types [10–11], benchmark them against conventional supports [11], or introduce variations to the basic POCS design to create anisotropy [12–13]. For example, Ferroni et al. (2021) [14] compared Kelvin and Diamond cell POCS for mass transfer under similar specific surface areas. They found that Diamond cells performed better at lower velocities ($v=5$ m/s), while both Kelvin and Diamond cells showed similar performance at higher velocities ($v=25$ m/s). Their findings also suggest that these POCS structures could outperform state-of-the-art honeycomb substrates in mass transfer at higher flow rates, though it remains unclear if the comparisons were conducted under equivalent specific surface areas. Kaur et al. (2020) [15] observed that among various unit cell geometries, the Octet structure exhibited the highest volumetric Nusselt number, followed by the Kelvin, Cube, and Face-Diagonal Cubic (which includes an additional diagonal strut on each face) structures, particularly at low velocities (0.5–3 m/s) under comparable porosity conditions. In all four topologies, the primary mechanism for heat transfer enhancement at low velocities was stagnation-type flow. Papetti et al. (2018) [12] conducted a numerical and experimental study on mass transfer in open-cell lattice structures with different cell shapes (1 and 15 m/s). They found that POCS had better transport properties compared to honeycomb monoliths, with Kelvin and tilted cubic cells achieving higher mass transfer rates than

simple cubic cells. In our previous work [11] with velocity in between 1 and 10 m/s corresponding to Reynolds number between 30 and 400 calculated using the strut thickness as characteristic length we observed that the Kelvin cell distinctly stands out as the best choice from the heat transfer viewpoint nonetheless from while considering the tradeoff with pressure the gyroid cell emerged as the best position with the kelvin cell on the last closely followed by the BCC whether on similar porosity or on similar specific surface area. The difference among structure was particularly low under the lowest velocity. Balzarotti et al. (2021) [17] experimentally studied wash coated cubic cells. Based on these results, POCSs were effectively activated by depositing Pd/CeO₂ catalyst by slurry coating, using a dip-coating/spin-coating mixed procedure for CO oxidations reactions Their results indicated that, under similar specific surface areas, POCS could outperformed honeycomb structures.

Despite the potential of Periodic Open-Cell Structures (POCS) to enhance mass and heat transfer, limited research has explored their interaction with selective membranes. This chapter explores the interaction of Periodic Open-Cell Structures (POCS) with selective membranes during ammonia synthesis, focusing on external mass transfer both in standalone reactors and integrated with ammonia-selective membranes (cf. **Figure 6-1**). A dip/spin coating method was optimized to deposit ruthenium (Ru) catalytic layers onto IN625 POCS produced via Selective Laser Melting (SLM), with kinetic activity tests conducted to validate the modeling approach. CFD modeling was further utilized to investigate the effects of POCS characteristics—such as porosity, cell type, and flow conditions—on reactor performance, as well as the impact of membrane integration and its permeance under representative operating conditions.

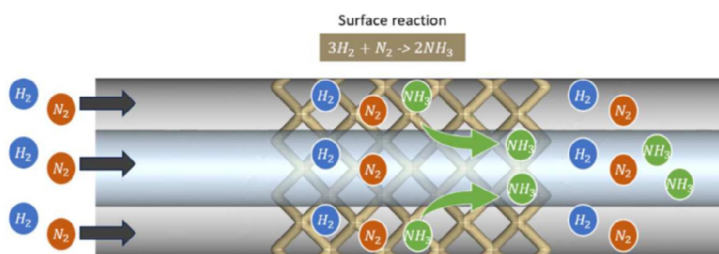


Figure 6-1: Sketch of a POCS Membrane Reactor for ammonia synthesis

6.2. Experimental set up

6.2.1. Manufacturing of the structures

As detailed in the previous chapter nickel alloy POCS samples with different cell types (e.g., body-centered cubic, Kelvin, and gyroid; see **Figure 5-1** in **Chapter 5**) were fabricated using an SLM280 LPBF machine at ENGIE Laborelec based on CAD designs. The cylindrical samples were 10 mm in diameter and 15 mm in height. The printed samples closely matched their CAD models, with porosity deviations of no more than 15% from the intended design. **Table 6-1**

summarizes the design parameters: strut diameter, cell length, porosity, and specific surface area relevant to this work. The notation for POCS samples used in this study starts with the cell type, followed by numbers indicating the cell and strut size in millimeters. **Figure 6-2** showcase some of the sample that were printed. (the smaller one are used in the tests in this study and longer versions designed for future tests with membrane reactors).

Table 6-1: Geometrical features of the CAD design cell parameters printed relevant to this study
The structured are denominated by the cell type followed by the size of the cell and the strut size.

Cell type	Cell length d_c [mm]	Strut diameter d_s [mm]	Theoretical Porosity %	Theoretical Specific surface area [cm ²]
BCC 3-0.4	3	0.4	0.91	8.1
BCC 3-0.75	3	0.75	0.73	12.3
Kelvin 3-0.61	3	0.61	0.78	12.3
Gyroid 5-0.34	5	0.34	0.79	12.3

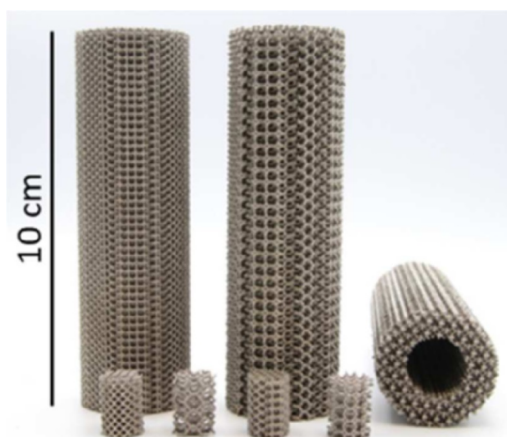


Figure 6-2: Image of POCS samples: smaller one used in the tests in this study and longer versions designed for future tests with membrane reactor experiments

6.2.2. POCS activation

A Ru-based catalysts* was coated on POCS supports by CNR using a dip/spin coating technique. The slurry preparation was optimized with a dispersion medium consisting of hydrolyzed Polyvinyl Alcohol (PVA) and bi-distilled Glycerol (GLY) in distilled water, combined with ball-

* Confidential catalyst: the exact composition is not detailed

milled catalyst the composition is reported in **Table 6-2**. The slurry's rheology, critical for achieving a stable and uniform coating, was characterized using a rotational rheometer (Modular Compact Rheometer MCR 92, Anton Paar GmbH, Graz, Austria). as shown in **Figure 6-3**, the slurry formulation, exhibiting a shear-thinning curve. At lower shear rates, the viscosity decreases significantly, characteristic of shear-thinning behavior, which is essential for ensuring good flowability and coating homogeneity. At higher shear rates, the slurry transitions to a Newtonian-like behavior, where the viscosity stabilizes. This behavior is crucial for the spinning step (1000 s^{-1}) in the coating procedure, as it ensures uniform application during high-shear conditions. The optimized slurry was then applied to a pretreated metallic structure, calcined at 900°C , through a combined dip and spin coating process. This process involved a 10-second immersion, followed by the removal of excess liquid using a commercial spin-coater (SPIN 150 SPS Europe). Parameters such as rotation speed and duration were finely tuned to achieve the desired material loading. Multiple dip-and-spin cycles were used to achieve catalyst loadings ranging from 0.242 g to 0.26 g/cm^3 as represented with the loading curves in **Figure 6-4** for BCC (3-0.6), BCC (3-0.4), Kelvin (3-0.6) and Gyroid (5-0.34) cells. Gravimetric analysis was conducted after each flash drying step and following the final calcination to monitor weight evolution and assess the washcoat load. Due to a lack of proper instrumentation for non-destructive cutting of the metal structure, washcoat thickness was estimated from the specific load for each sample. The catalytic loading (C_{load}), defined as the mass of catalyst deposited per unit surface area of the POCS, was calculated as $0.17 \text{ mg}_{\text{cat}}/\text{cm}^2_{\text{POCS}}$ and will be used as a conversion factor for translating volumetric reaction rates into surface reaction rates during subsequent numerical analyses.

A Keyence VHX-7000 digital optical microscope, featuring a fully integrated head with stage shift technology and 4K mode for high-resolution imaging, was used for morphological characterization. Detailed images of the POCS were captured using VHX-E20 (20–100x, high-resolution, low magnification) and VHX-E100 (100–500x, high-resolution, medium magnification) lenses. The adhesion of the deposited layers was assessed via an accelerated stress test in an ultrasound bath, showing that thermal treatment were crucial for mechanical stability, with a weight loss of about 1.3 wt% for Ni-alloy Kelvin structures.

Table 6-2: Slurry composition

Powder catalyst	Glycerol	PVA	Water	Slurry density (g/dm^3)
22.4 (%)	42.5 (%)	1.5 (%)	33.6 (%)	1.4

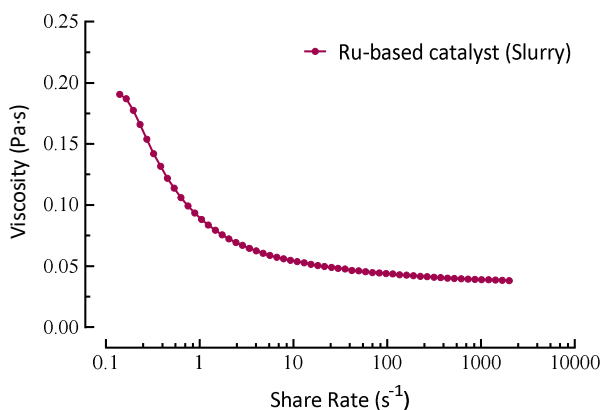


Figure 6-3: Rheological behavior of slurry formulation (shear thinning curve)

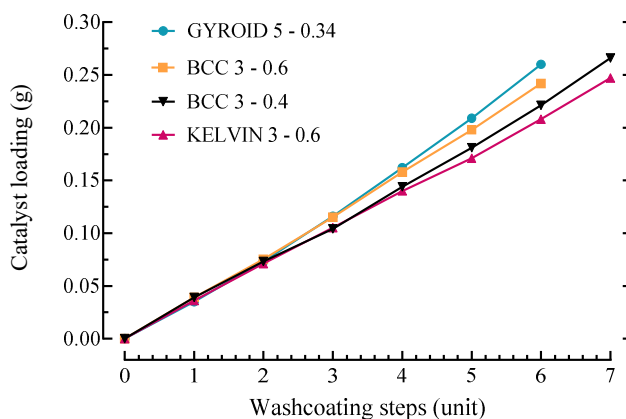


Figure 6-4: Example of catalyst loading steps on Gyroid, BCC and kelvin POCSs

6.2.3. Kinetic tests

Tests of the catalytic activity of the ammonia synthesis reaction were conducted at CNR. A steam of 72% hydrogen, 24% nitrogen and 4% helium was flowed into a fixed bed reactor, at WSV (Weight Space Velocity) from 13 654 to 43 725 $\text{Ncm}^3 \cdot \text{g}_{\text{cat}}^{-1} \cdot \text{h}^{-1}$ (i.e. flowrate about 180 $\text{cm}^3 \cdot \text{min}^{-1}$), pressure from 20 to 30 bar, and temperature from 350 to 550°C. The ammonia formation rate ($\text{mol} \cdot \text{h}^{-1} \cdot \text{g}_{\text{cat}}^{-1}$) was calculated from the NH_3 content in the reaction products. The effluent gases were taken at regular intervals and were analyzed by gas chromatography, using a GC-MS (Agilent GC 7890A) composed of three parallel columns (Hayesep Q, HP PLOT Q and Molesive 45/60) connected to a thermal conductivity detector (TCD) using Ar as carrier gas. Before

catalytic experiments, the reactor was reduced in situ by a flow of 75% hydrogen and 25% nitrogen, at 500 °C and 30 bar for 6 hours.

6.3. Numerical investigation

6.3.1. CFD modelling

To investigate the impact of morphological features and flow conditions on external mass transport rates in POCS with and without selective membranes, CFD simulations were conducted using ANSYS Fluent (version 2024 R1). Two geometrical domains were modeled: one replicating the experimental setup for chemical reaction validation, and the other representing a segment of a small-scale membrane reactor. These models, which are detailed in **Figure 6-5** along with dimensions and boundary conditions, solve fully coupled equations for momentum, mass transfer, and energy under laminar flow conditions.

For the “validation” domain, the POCS sample simulated had the same geometry as the ones tested by the CNR: a cylinder of 10 mm diameter and 15 mm length. 170 mm of free flow were added upstream from the POCS, to avoid counter-current diffusion at the inlet (which disturbs imposed boundary conditions). Temperature ranged from 350 to 600 °C, with inlet velocities range of $4.01 \cdot 10^{-3}$ to $5.76 \cdot 10^{-3}$ mm. s⁻¹ (i.e. constant normal flux of 3 Ncm. s⁻¹), and outlet pressure was maintained at 20 bar. Simulation conditions included a flow with 72% H₂, 24% N₂ and 4% He (volume fractions) to replicate experimental settings.

For the “membrane reactor” domain, a similar domain was simulated: a 10 mm diameter and 15 mm long cylinder, enclosing a 4 mm diameter central membrane. As previously, 170 mm of free flow upstream from the POCS, and a 0.2 mm gap between POCS and membrane are added. Indeed, in a real reactor, the junction would not be perfect, particularly because printed POCS surface is not ideal. This small gap between solid struts and membrane would be more than enough for molecules to travel to membrane. Temperature was set at 450 °C (to reach maximum hydrogen conversion), and pressure at 20 bar. Inlet flow had a velocity of 5.06 mm. s⁻¹ in the main part (comprising POCS sample), and 29 mm. s⁻¹ inside the membrane, allowing the same flux of 3 Ncm. s⁻¹ in both parts, with 75% H₂ and 25% N₂ (volume fractions).

For both domains, the model employs a zero-dimensional approach, treating the reacting layer as infinitesimally thin and neglecting potential irregularities such as cracks and cavities in the washcoat. The porous surface is modeled as both a source of product and a sink of reactants. The external cylinder had a no-slip condition, a zero heat flux before and after POCS, and temperature equal to the inlet around the POCS sample. The POCS surface's temperature was then governed by heat fluxes and materials properties with Inconel's characteristics based on a conjugate heat transfer approach.

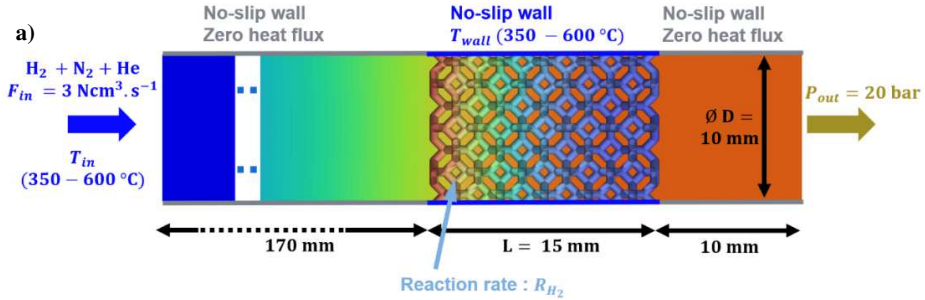
To conserve computational resources, only an eighth of the domain was modeled. A symmetry boundary condition was applied to the cutting planes. Ammonia produced permeates through a

porous membrane, with a selectivity of 50 compared to nitrogen and 10 compared to hydrogen [18]. The mass fluxes through the membrane were modeled by the following equation :

$$J_i = \mathcal{P}_i \cdot (P_i^{ret} - P_i^{perm}) \quad [\text{mol} \cdot \text{m}^{-2} \cdot \text{s}^{-1}] \quad \text{Eq. 6.1}$$

With \mathcal{P}_i the permeance of the membrane towards species i ($\frac{\mathcal{P}_{\text{NH}_3}}{\mathcal{P}_{\text{N}_2}} = 50$; $\frac{\mathcal{P}_{\text{NH}_3}}{\mathcal{P}_{\text{H}_2}} = 10$); P_i^{ret} and P_i^{perm} the partial pressure of species i inside retentate (POCS domain) and permeate (membrane cylinder).

From the numeric viewpoint, the chosen meshes comprise approximately 1 million cells, encompassing both the fluid and solid domains. CFD calculations are performed to model pure laminar flow regime through a POCS structure on which an ammonia synthesis reaction is taking place. Gradient computations were handled using the Least Square Cell-Based discretization scheme, while the Second Order Upwind scheme was adopted for the discretization of transport properties, including momentum, energy, and turbulence variables. The "coupled" algorithm was chosen for pressure-velocity coupling, ensuring a stable and rapid convergence in this steady-state analysis. Convergence was deemed achieved when the residuals fell below 10^{-4} and physical quantities (such as hydrogen conversion, outlet temperature, mole fractions...) became stable with computation iterations. Further details are given in **Appendix D1&D2**.



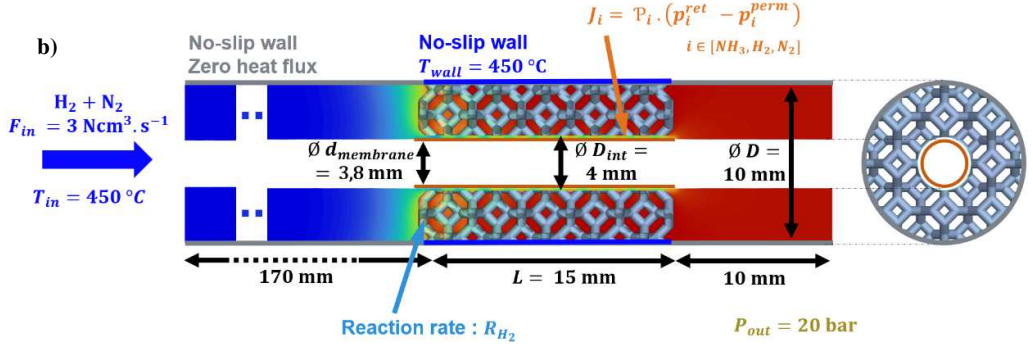
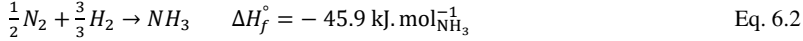


Figure 6-5: Implemented boundary conditions and physical setup applied. (a) Traditional reactor mirroring the experimental one used to validate the chemistry (b) membrane reactor, side (left) and front (right) views

6.3.2. Kinetic rate law

The synthesis of ammonia from H_2 and N_2 , is recapped in Eq. 6.2, it is mildly exothermic and thermodynamically favored at low temperatures. However, due to the temperature dependence of chemical kinetics, the highest conversion rates occur at intermediate temperatures. Furthermore, according to Le Châtelier's principle, the reaction is favored at high pressures due to the reduction in the number of gas molecules (cf. **Chapter 2**, page 43).



As in previous chapters a mathematical expression for the intrinsic rate of ammonia synthesis is required. One expression for this rate was established by Rossetti et al. (2006) [19] and is reported in Eq. 6.3-6.4 together with the parameters mentioned by Tripodi et al. (2018) [20].

$$R'_{H_2} = k_1 \frac{\left(p_{N_2}^{0.5} \left(\frac{p_{H_2}^{0.375}}{p_{NH_3}^{0.25}} \right) - \frac{1}{K_{eq}} \left(\frac{p_{NH_3}^{0.75}}{p_{H_2}^{1.125}} \right) \right)}{1 + K_{H_2} p_{H_2}^{0.3} + K_{NH_3} p_{NH_3}^{0.2}} [\text{kmol} \cdot \text{s}^{-1} \cdot \text{kg}_{\text{cat}}^{-1}] \quad \text{Eq. 6.3}$$

$$\leftrightarrow R'_{H_2} = \frac{4.2e5 \cdot e^{-\frac{1.2e4}{T}} \left(\frac{p_{N_2}^{0.5} \cdot p_{H_2}^{0.375}}{p_{NH_3}^{0.25} \cdot p_{H_2}^{1.125}} \cdot K_{eq} \right)}{1 + e^{\left(-6.8 + \frac{4.5e3}{T} \right)} \cdot p_{H_2}^{0.3} + e^{\left(-4.2 + \frac{3.5e3}{T} \right)} \cdot p_{NH_3}^{0.2}} [\text{kmol} \cdot \text{s}^{-1} \cdot \text{kg}_{\text{catalyst}}^{-1}] \quad \text{Eq. 6.4}$$

With the equilibrium constant as defined in Eq. 6.5. It has units of $[\text{bar}^{-1}]$ as determined through a dimensional analysis.

$$K_{eq} = 10^{2.7 + \frac{2.0e3}{T} - 2.7 \log_{10}(T) - (5.5e-5) \cdot T + (1.8e-7) \cdot T^2} \quad \text{Eq. 6.5}$$

To convert this expression to a surface rate law, reaction rate is multiplied by the loading of the catalyst, C_{load} :

$$R_{H_2} = R'_{H_2} \cdot C_{\text{load}} = \frac{\text{mol}}{\text{kg}_{\text{cat}} \cdot \text{s}} \cdot \frac{\text{kg}_{\text{cat}}}{\text{m}^2} = \frac{\text{mol}}{\text{m}^2 \cdot \text{s}} \quad \text{Eq. 6.6}$$

This factor allows to convert R_{H_2} from $[\text{kmol} \cdot \text{s}^{-1} \cdot \text{kg}_{\text{catalyst}}^{-1}]$ to $[\text{kmol} \cdot \text{s}^{-1} \cdot \text{m}^{-2}]$ as required for CFD simulations. It is assessed thanks to CNR test bench data: $C_{load} = 0.17 \text{ kg}_{\text{cat}} \cdot \text{m}^{-2}$. However, as the catalyst used in this work is not exactly the same as the one used by Tripodi et al. (2018) [20], a second coefficient was added, $C_{fitting}$, to fit CFD kinetics with CNR results. The reaction rate $R_{H_2} = C_{fitting} C_{load} \cdot R'_{H_2}$ was then used to perform CFD simulations, and $C_{fitting}$ was iteratively adjusted so that predicted H_2 conversion get closer to the experimental one. Finally, $C_{fitting} \cdot C_{load}$ was taken as $0.03 \text{ kg} \cdot \text{m}^{-2}$, and the CFD reaction rate could be written :

$$R_{H_2} = \frac{8.4e4 \cdot e^{-\frac{1.2e4}{T}} \left(\frac{p_{N_2}^{0.5} p_{H_2}^{0.375}}{p_{NH_3}^{0.25}} \frac{p_{NH_3}^{0.75}}{p_{H_2}^{1.125}} \cdot k_{eq} \right)}{1 + e^{(-6.8 + \frac{4.5e3}{T})} p_{H_2}^{0.3} + e^{(-4.2 + \frac{3.5e3}{T})} p_{NH_3}^{0.2}} [\text{kmol} \cdot \text{s}^{-1} \cdot \text{m}^{-2}] \quad \text{Eq. 6.7}$$

6.3.2. Performance index

Several metrics are used to evaluate the performances of the membrane reactor. Hydrogen conversion X_{NH_3} is defined as the ratio of H_2 consumption rate to the H_2 flow rate at the reactor inlet. Ammonia recovery factor (ARF) measures the amount of NH_3 crossing the membrane, relative to the total NH_3 produced. Both are defined in Eq. 6.8-6.9 and Eq. 6.10 respectively. Additionally, the degree of concentration polarization is assessed with the Coefficient of Concentration Polarization (CPC) as per Eq. 6.11, which is the ratio of average NH_3 concentration at the membrane surface to that at the external wall. A CPC of one would indicate radial diffusion limitations, whereas lower values would suggest more efficient radial diffusion. More details on this coefficient are given in **Appendix D3**. Furthermore, gas hourly space velocity (GHSV) is calculated as the inlet flow rate relative to the reactor volume, influencing metrics like conversion and ammonia recovery.

$$X_{H_2}^{TR} = \frac{F_{H_2, \text{in}}^{\text{Ret}} - F_{H_2, \text{out}}^{\text{Ret}}}{F_{H_2, \text{in}}^{\text{Ret}}} \quad \text{Eq. 6.8}$$

$$X_{N_2}^{MR} = \frac{F_{N_2, \text{in}}^{\text{Ret}} - F_{N_2, \text{out}}^{\text{Ret}} + F_{N_2, \text{tmb}}}{F_{N_2, \text{in}}^{\text{Ret}} + F_{N_2, \text{tmb}}} \quad \text{Eq. 6.9}$$

With:

$$F_{N_2, \text{tmb}} = F_{N_2, \text{in}}^{\text{perm}} - F_{N_2, \text{out}}^{\text{perm}} \quad N_2 \text{ transmembrane flow}$$

$$F_{N_2, \text{tmb}}^* = 0 \text{ if } F_{N_2, \text{tmb}} \leq 0 \text{ Reactant loss}$$

$$F_{N_2, \text{tmb}}^* = F_{N_2, \text{tmb}} \text{ if } F_{N_2, \text{tmb}} \geq 0 \text{ Reactant Co - feeding}$$

$$ARF = \frac{F_{NH_3, \text{out}}^{\text{Perm}}}{F_{NH_3, \text{out}}^{\text{Ret}} + F_{NH_3, \text{out}}^{\text{Perm}}} \quad \text{Eq. 6.10}$$

$$CPC = 1 - \frac{\frac{p_{NH_3}^{\text{surface-membrane, ext}}}{p_{NH_3}^{\text{surface-wall, ext}}} - \frac{p_{NH_3}^{\text{surface-membrane, int}}}{p_{NH_3}^{\text{surface-membrane, int}}}}{\frac{p_{NH_3}^{\text{surface-wall, ext}}}{p_{NH_3}^{\text{surface-membrane, int}}} - \frac{p_{NH_3}^{\text{surface-membrane, int}}}{p_{NH_3}^{\text{surface-membrane, int}}}} \quad \text{Eq. 6.11}$$

In chemical engineering, the Péclet number (as per Eq. 6.12) is a dimensionless number that helps quantify the relative effects of convection and diffusion in a flow system.

$$Pe = \frac{uL}{D}$$

Eq. 6.12



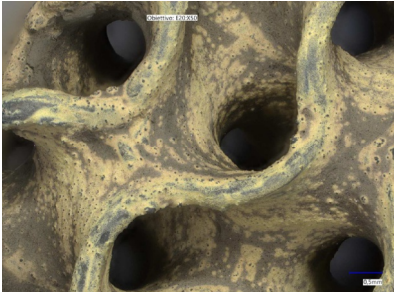
Where u refers to the fluid velocity, L the characteristic length taken as the cell size, and D the diffusion coefficient.

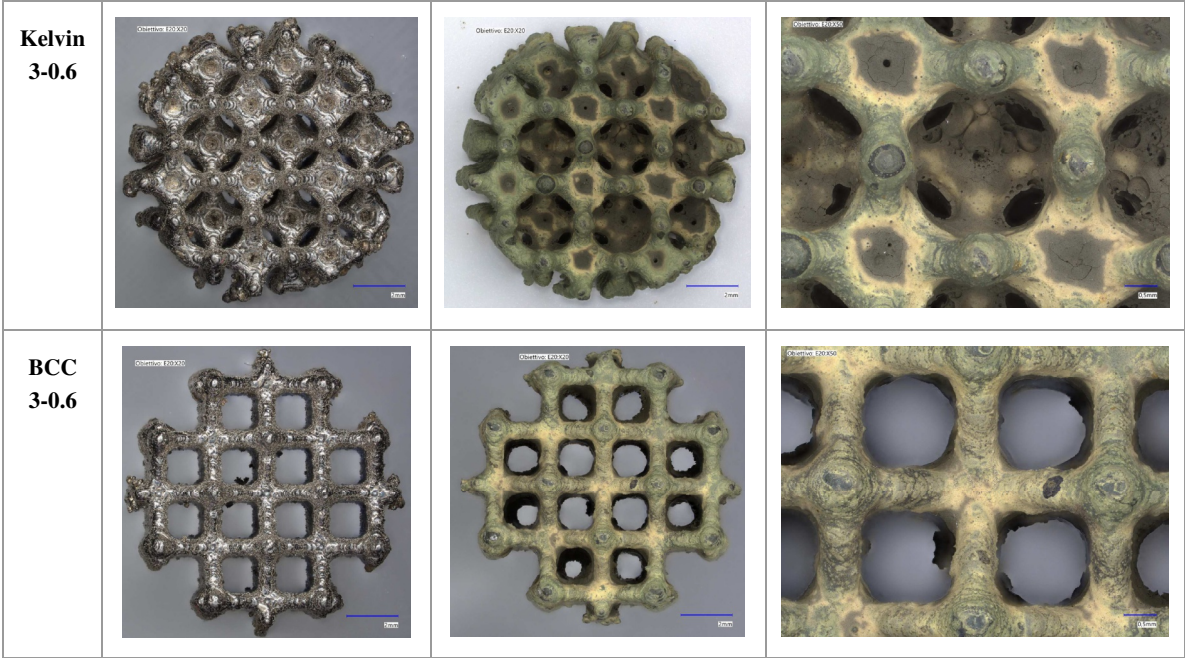
6.4. Results

6.4.1. Coating analysis

The homogeneity of the catalytic layer was characterized using an optical microscope. **Table 6-3** presents an example of the structural and morphological features of both bare Ni-alloy supports and coated supports prepared with the optimized dip/spin coating method. Overall, a homogeneous washcoat, giving the structures a brownish appearance, was observed across all samples, with no uncoated areas. These results demonstrate the reproducibility and effectiveness of the dip/spin coating method for preparing structured catalysts, regardless of the geometry of the support or the catalytic powders used. However, partial occlusion was observed in the Kelvin cell, particularly in the small square windows.

Table 6-3: Optical microscope images of Bare and coated POCS

	Bare	Washcoated (WC) calcinated	Washcoated (WC) calcinated
Gyroid 5-0.34			



6.4.2. Kinetic tests and model validation

The catalytic performance of the structured catalyst BCC 3-0.4 in ammonia synthesis was evaluated across a temperature range of 350–600 °C. Activity started to become noticeable around 300 °C, with a significant increase observed at 350 °C and 400 °C (the highest temperature tested). Thus, 300 °C can be considered the light-off temperature for ammonia synthesis on the Ru catalysts tested in this study. Hydrogen conversion increased with temperature from 350 °C to 450 °C, driven by the improvement in chemical kinetics, and then began to decrease from 450 °C to 600 °C due to reaching equilibrium of the exothermic reaction. This pattern indicates that hydrogen conversion peaks around 450–500 °C. As illustrated in **Figure 6-6**, the model accurately captures the behavior of the chemical reaction, with hydrogen conversion following the experimental trend—rising from 350 °C to 450 °C and then declining beyond 450 °C. For all six simulated temperatures, the CFD values for flowrate and reactant conversion are either within the experimental range or stay below a 13% error margin (except for ammonia flow at low temperatures). Therefore, the model is successfully validated and is ready to provide insights into the effects of morphological features and flow conditions on external mass transport rates in POCS, with or without selective membranes.

The ammonia synthesis rate is significantly influenced by factors such as Ru particle size, type of promoter, reaction conditions, and carbon support type. As shown in **Figure 6-7**, when compared with other catalysts from the literature, all catalysts exhibited little to no activity below 300 °C, irrespective of their type. The activity of Ru catalysts increased significantly at temperatures above 350 °C.

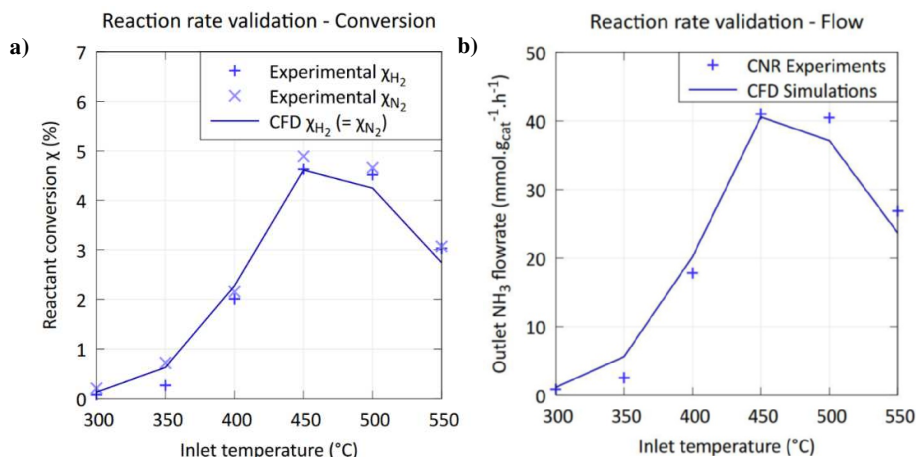


Figure 6-6: Fitting of reaction rate model based on Kelvin 3-0.6. The points are the experimental data, the line correspond to the numeric results (a) Conversion (b) Ammonia production. For reference the equilibrium N_2 conversion at 20 bar is: 23% at 350 °C, 7.7 % at 450 °C, 4.6% at 500 °C and 2.9 % at 550 °C

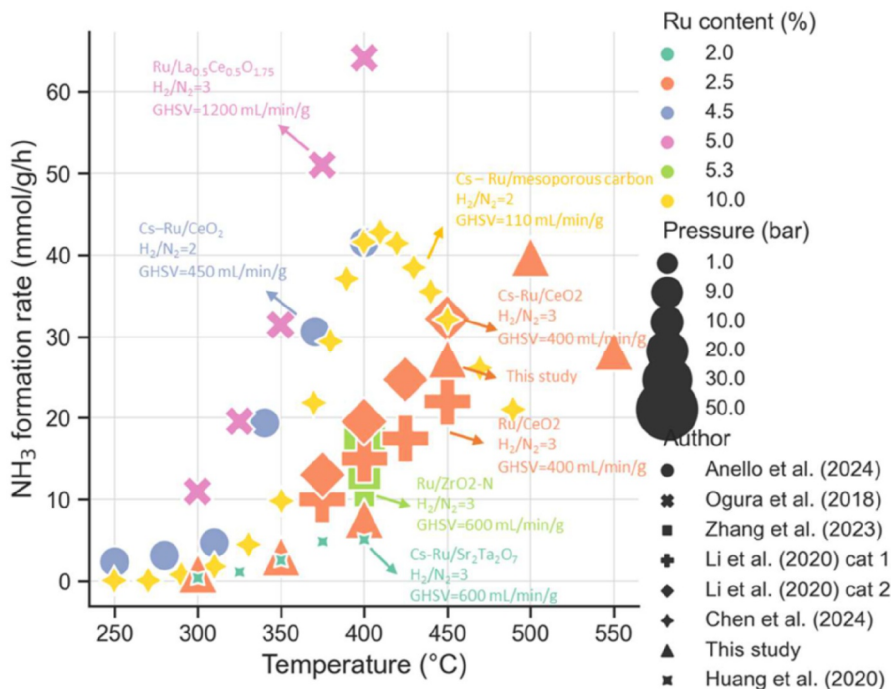


Figure 6-7: Comparison of catalytic activities of different Ru-based catalysts for ammonia formation rate in literature [4, 21-25]

6.4.3. Influence of POCS cell types

Given the reliability of the kinetic implementation into the CFD model, the influence of POCS cell type on reactor performance was assessed through simulations using three different geometries: BCC 3-0.75, Kelvin 3-0.61, and Gyroid 5-0.34. All geometries shared the same specific surface area of 12.3 cm^{-1} , ensuring an identical area of contact between the reactants and catalyst. The simulations were performed using the cylindrical domain depicted in **Figure 6-5.a**, consistent with the one used for kinetic validation. **Figure 6-8** illustrates the evolution of H_2 conversion for the three structures. The results indicate that conversion is effectively equal among the three geometries, with a maximum deviation of 1% (observed between BCC 3-0.75 and Gyroid 5-0.34), for both fluid inlet velocities of 0.005 and $0.05 \text{ m}\cdot\text{s}^{-1}$. This outcome may seem surprising, given the significant geometric differences between the structures, which would be expected to induce distinct flow patterns. However, the similarity in conversion can be attributed to the low velocities used in the simulation, where mass transfer is predominantly controlled by diffusion rather than convection. This conclusion is supported by the Peclet number calculation, which yields a value of $Pe = \frac{3e-3 \cdot 5e-3}{2.9e-5} = 0.5 < 1$. Here, a typical length of $3 \times 10^{-3} \text{ m}$ (cell size), a velocity of $5 \times 10^{-3} \text{ m}\cdot\text{s}^{-1}$, and a mass diffusivity of $2.9 \times 10^{-5} \text{ m}^2\cdot\text{s}^{-1}$ (provided by ANSYS Fluent) were used. With $Pe < 1$, diffusion is the dominant mode of mass transfer, meaning that the kinetic performance is largely governed by the area of contact between the reactants and catalyst, which is identical across the three structures and results in similar conversion levels. In term of experimental results as shown in **Figure 6-9** comparing the three different cell type. It can be observed an 18% difference in H_2 conversion between BCC 3-0.4 and Kelvin 3-0.4 at 450°C and GHSV of $\approx 9000 \text{ h}^{-1}$, with Gyroid 5-0.34 achieving intermediate results. This discrepancy is likely due to the 16% variation in specific surface area between these structures.

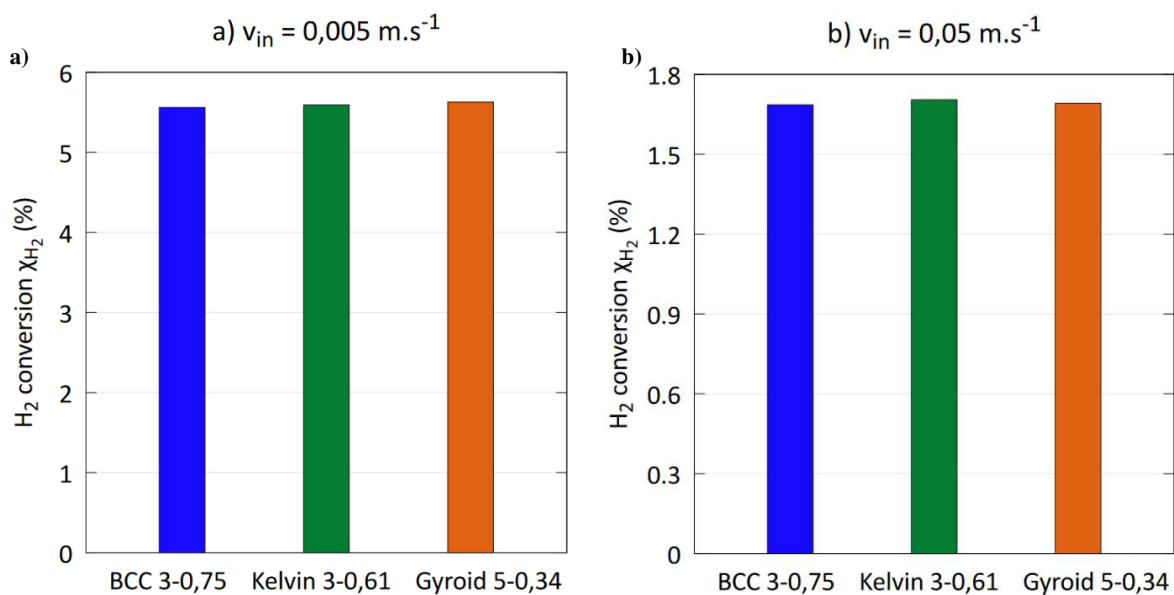


Figure 6-8 : Catalytic performances of three different POCS cells with the same specific surface area, and two different inlet fluid velocity: a) $v_{in} = 0.005 \text{ m.s}^{-1}$ b) $v_{in} = 0.05 \text{ m.s}^{-1}$ at $T=450^\circ\text{C}$ and $P=20 \text{ bar}$

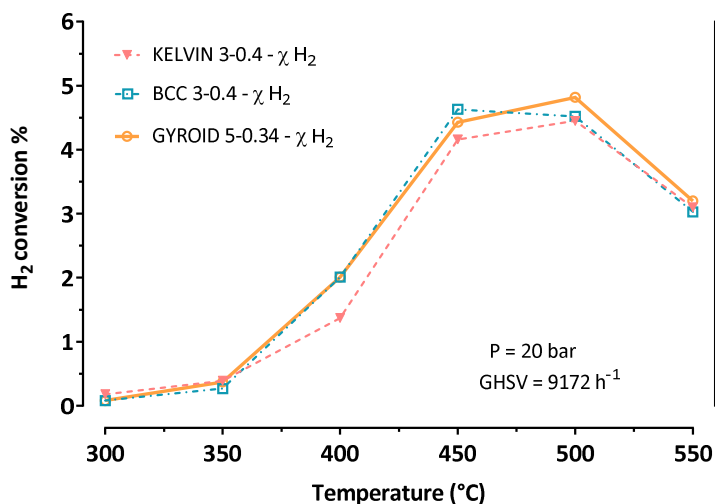


Figure 6-9: Experimental comparison of the catalytic performances of GYROID 5-0.34, BCC 3-0.4 and KELVIN 5-0.34

6.4.4. Membrane reactor

The impact of membrane integration on hydrogen conversion & ammonia recovery was assessed through CFD simulations of the sample depicted in **Figure 6-10**, using the BCC 3-0.4 cell with varying membrane permeance values. Initially, a permeance of $P = 0 \text{ mol.s}^{-1}.\text{m}^{-2}.\text{bar}^{-1}$ was used as a reference, representing reactor operation without any membrane effect. The permeance was then increased to values of $\{0.01, 0.05, 0.25\} \text{ mol.s}^{-1}.\text{m}^{-2}.\text{bar}^{-1}$, with $0.05 \text{ mol.s}^{-1}.\text{m}^{-2}.\text{bar}^{-1}$ being the typical membrane permeance expected for the AMBHER project. The effect of membrane activation is evident, as hydrogen conversion increased from 4.7% to 5.48% when the membrane was activated from $P = 0$ to $0.01 \text{ mol.s}^{-1}.\text{m}^{-2}.\text{bar}^{-1}$. Additionally, the Ammonia Recovery Factor (ARF) and Concentration Polarization Coefficient (CPC) jumped from 0 (as expected for zero permeance, which fully traps ammonia in the retentate) to 21.4% and 0.02%, respectively. These trends are consistent throughout the entire range of simulations: an increase in membrane permeance results in higher hydrogen conversion, ammonia recovery, and concentration polarization, which aligns with expected behavior. However, it is noteworthy that the increase in conversion and ammonia recovery is not linear and tends to diminish at higher permeance values. Beyond $P = 0.05 \text{ mol.s}^{-1}.\text{m}^{-2}.\text{bar}^{-1}$, the system becomes primarily limited by ammonia production. Ammonia mole fraction streamline plots for various permeance values are presented in **Figure 6-11**. At low permeation values, the concentration spreads uniformly across the structure, with minimal external film boundary layer. As the permeance value increases, concentration boundary layers become more distinct, forming sharp gradients along the membrane surface, particularly on the permeate side.

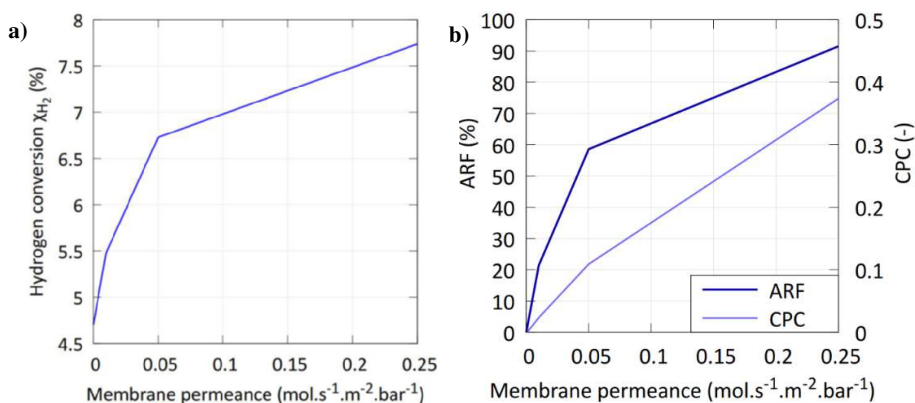


Figure 6-10: Effect of membrane permeance on ammonia synthesis. (a) Left: hydrogen conversion, (b) Right: Ammonia Recovery Factor and Concentration Polarization Coefficient

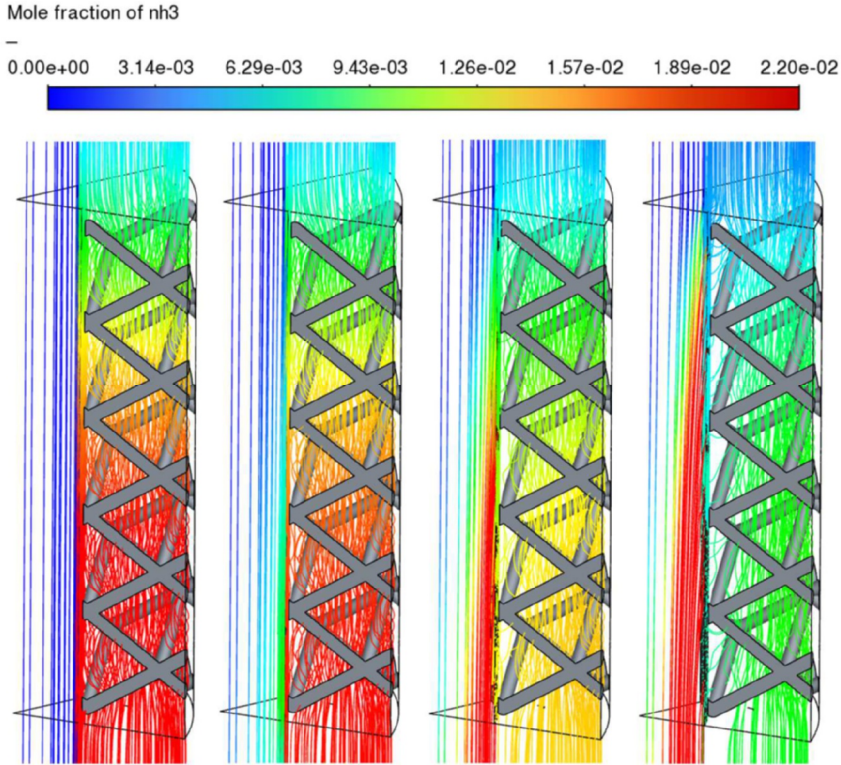


Figure 6-11: Visualization of ammonia repartition inside BCC 3-0.4 membrane reactor. From left to right: $P = 0$; 0.01 ; 0.05 ; $0.25 \text{ mol. s}^{-1} \cdot \text{m}^{-2} \cdot \text{bar}^{-1}$. On each of the four pictures, membrane is located at the left end of the POCS structure, where the ammonia mole fraction sharply changes ($T=450 \text{ }^{\circ}\text{C}$; $P_{\text{ret}}=20 \text{ bar}$, $P_{\text{perm}}=1 \text{ bar}$, $\text{GHSV}=9167 \text{ h}^{-1}$, $\text{SW}=1$; $\frac{P_{\text{NH}_3}}{P_{\text{N}_2}} = 50$; $\frac{P_{\text{NH}_3}}{P_{\text{H}_2}} =$

10)

6.4.5. Comparison with plug flow

Since the impact of cell type may not play a decisive role (at least without the membrane) under our chosen operating conditions, and concentration polarization remains relatively small up to a permeance value of $0.05 \text{ mol. s}^{-1} \cdot \text{m}^{-2} \cdot \text{bar}^{-1}$, it was decided to compare the results from the CFD model with those obtained from a 1D engineering membrane reactor model. A 1D model, used for system-scale analysis in previous work [26] is adjusted with the kinetic expression (cf. Eq. 6.6) is based on an ideal plug flow assumption. It involves no radial gradients, no axial mixing, and no back-mixing along the flow direction—meaning each fluid element moves downstream without dispersion while maintaining its "plug" shape, with instantaneous reaction assumed within each plug. As shown in **Figure 6-12**, the engineering model fails to accurately predict system behavior beyond a permeance of $0.05 \text{ mol. s}^{-1} \cdot \text{m}^{-2} \cdot \text{bar}^{-1}$. To simplify the modeling of a membrane reactor, a reduction factor or correlation should be used to correct deviations from the plug flow hypothesis.

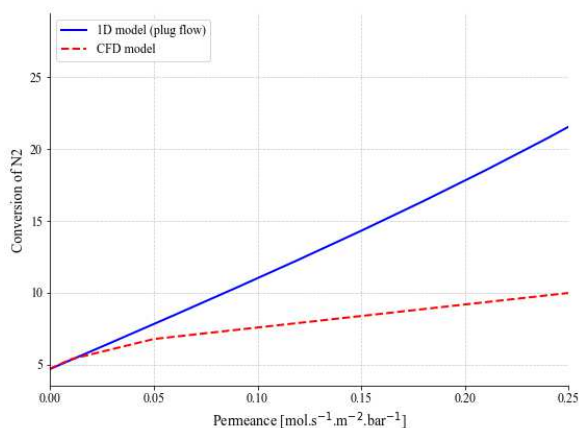


Figure 6-12: Comparison between CFD and engineering model for a BCC cell type ($T=450\text{ }^{\circ}\text{C}$; $P_{\text{ret}}=20\text{ bar}$, $P_{\text{perm}}=1\text{ bar}$, $\text{GHSV}=9167\text{ h}^{-1}$, $\text{SW}=1$)

6.5. Conclusion

This chapter aims to understand external mass transfer in POCS reactors during ammonia synthesis, both as standalone systems and when integrated with a vertical selective membrane. To achieve this, laboratory-scale experiments were combined with Computational Fluid Dynamics (CFD) modeling to systematically assess different POCS topologies and evaluate membrane reactor performance.

- A dip/spin coating method was first optimized to deposit a Ru-based catalytic layer onto IN625 POCS produced via Selective Laser Melting (SLM) for various cell types: BCC, gyroid, and Kelvin. While homogeneous and stable coating layers were successfully deposited on all cell types, the Kelvin cell experienced partial clogging issues in the small square windows.
- The catalytic activity for ammonia synthesis at different temperatures was investigated. The activity of the coated POCS was consistent with other Ru- based catalysts reported in the literature.
- Based on an existing kinetic model, a numerical CFD model was first validated and then used to compare the effects of external mass transfer across different POCS supports (gyroid, Kelvin, and BCC) with similar specific surface areas. The results showed no significant differences, indicating that the type of POCS support does not influence catalytic activity under the chosen process conditions.
- The impact of the driving force across the membrane was evaluated within a representative membrane reactor domain containing a BCC cell. As expected, increasing the permeance improved performance (in terms of conversion and recovery), though not linearly, as a

plateau-like trend was observed, likely due to insufficient ammonia production relative to its removal and a strong concentration polarization observed especially on the permeate side.

- An engineering model based on the plug flow assumption fails to predict system behavior accurately beyond a permeance of $0.05 \text{ mol}\cdot\text{s}^{-1}\cdot\text{m}^{-2}\cdot\text{bar}^{-1}$, suggesting the need for a correction factor to account for deviations from ideal plug flow conditions.

Further work could include sensitivity analysis regarding permeation parameters, such as selectivity towards hydrogen, nitrogen, pressure drop and sweep to feed gas flowrate ratio. Additionally, the structure-independent performance should also be checked when the POCS is interfaced with a membrane.

6.6. References

- [1] C. Croisé, K. Alabd, A. Villesuzanne, F. Can, X. Courtois, E. Gaudin, S. Tencé, N. Bion, Role of hydride ion within Ru/LaScSi and Ru/CeTiGe catalysts for NH_3 synthesis: A combination of DFT and experimental nitrogen isotopic exchange studies, *Catalysis Communications* 179 (2023) 106689. <https://doi.org/10.1016/j.catcom.2023.106689>.
- [2] R. Javaid, T. Nanba, Effect of reaction conditions and surface characteristics of Ru/CeO₂ on catalytic performance for ammonia synthesis as a clean fuel, *International Journal of Hydrogen Energy* 46 (2021) 18107–18115. <https://doi.org/10.1016/j.ijhydene.2020.07.222>.
- [3] S. Miyahara, K. Sato, Y. Kawano, K. Imamura, Y. Ogura, K. Tsujimaru, K. Nagaoka, Ammonia synthesis over lanthanoid oxide-supported ruthenium catalysts, *Catalysis Today* 376 (2021) 36–40. <https://doi.org/10.1016/j.cattod.2020.08.031>.
- [4] J. Huang, M. Yuan, X. Li, Y. Wang, M. Li, J. Li, Z. You, Inhibited hydrogen poisoning for enhanced activity of promoters-Ru/Sr₂Ta₂O₇ nanowires for ammonia synthesis, *Journal of Catalysis* 389 (2020) 556–565. <https://doi.org/10.1016/j.jcat.2020.06.037>.
- [5] H. Ronduda, M. Zybert, A. Dzielulska, W. Patkowski, K. Sobczak, A. Ostrowski, W. Raróg-Pilecka, Ammonia synthesis over lanthanoid oxide-supported ruthenium catalysts, *Catalysis Today* 376 (2021) 36–40. <https://doi.org/10.1016/j.cattod.2020.08.031>.
- [6] R.J.W. Voncken, I. Roghair, M. van Sint Annaland, A numerical study on concentration polarization in 3D cylindrical fluidized beds with vertically immersed membranes, *Chemical Engineering Science* 205 (2019) 299–318. <https://doi.org/10.1016/j.ces.2019.05.010>.
- [7] R. Ma, B. Castro-Dominguez, A.G. Dixon, Y.H. Ma, Scalability of multitube membrane modules for hydrogen separation: Technical considerations, issues and solutions, *Journal of Membrane Science* 564 (2018) 887–896. <https://doi.org/10.1016/j.memsci.2018.08.003>.
- [8] H. Choi, S.H. Kim, J. Bae, S.P.R. Katikaneni, A. Jamal, A. Harale, S.N. Paglieri, J.H. Lee, CFD analysis and scale up of a baffled membrane reactor for hydrogen production by steam methane reforming, *Computers & Chemical Engineering* 165 (2022) 107912. <https://doi.org/10.1016/j.compchemeng.2022.107912>.
- [9] A. Caravella, L. Melone, Y. Sun, A. Brunetti, E. Drioli, G. Barbieri, Concentration polarization distribution along Pd-based membrane reactors: A modelling approach applied to Water-Gas Shift, *International Journal of Hydrogen Energy* 41 (2016) 2660–2670. <https://doi.org/10.1016/j.ijhydene.2015.12.141>.
- [10] F. Lucci, A. Della Torre, G. Montenegro, R. Kaufmann, P. Dimopoulos Eggenschwiler, Comparison of geometrical, momentum and mass transfer characteristics of real foams to

- Kelvin cell lattices for catalyst applications, *International Journal of Heat and Mass Transfer* 108 (2017) 341–350. <https://doi.org/10.1016/j.ijheatmasstransfer.2016.11.073>.
- [11] S. Richard, D. Tasso, M. Rajana, A. Saker, A. Ramirez Santos, C. Makhloufi, N. Meynet, B. Hary, S. Nardone, G. Marino, M. Thomas, C. Italiano, A. Vita, F. Gallucci, Comparison of thermo-hydraulic performance among different 3D printed periodic open cellular structures, *Chemical Engineering Journal* 492 (2024) <https://doi.org/10.1016/j.cej.2024.152005>.
 - [12] V. Papetti, P. Dimopoulos Eggenschwiler, A. Della Torre, F. Lucci, A. Ortona, G. Montenegro, Additive Manufactured open cell polyhedral structures as substrates for automotive catalysts, *International Journal of Heat and Mass Transfer* 126 (2018) 1035–1047. <https://doi.org/10.1016/j.ijheatmasstransfer.2018.06.061>.
 - [13] M. Bracconi, M. Ambrosetti, M. Maestri, G. Groppi, E. Tronconi, Analysis of the effective thermal conductivity of isotropic and anisotropic Periodic Open Cellular Structures for the intensification of catalytic processes, *Chemical Engineering and Processing - Process Intensification* 158 (2020) 108169. <https://doi.org/10.1016/j.cep.2020.108169>.
 - [14] C. Ferroni, M. Bracconi, M. Ambrosetti, M. Maestri, G. Groppi, E. Tronconi, A Fundamental Investigation of Gas/Solid Heat and Mass Transfer in Structured Catalysts Based on Periodic Open Cellular Structures (POCS), *Ind. Eng. Chem. Res.* 60 (2021) 10522–10538. <https://doi.org/10.1021/acs.iecr.1c00215>.
 - [15] I. Kaur, P. Singh, Flow and Thermal Transport Through Unit Cell Topologies of Cubic and Octahedron Families, *International Journal of Heat and Mass Transfer* 158 (2020) 119784. <https://doi.org/10.1016/j.ijheatmasstransfer.2020.119784>.
 - [16] Das, S., Transport through bidisperse porous media, TU eindhoven, 2017.
 - [17] R. Balzarotti, M. Ambrosetti, M. Arnesano, A. Anglani, G. Groppi, E. Tronconi, Periodic open cellular structures (POCS) as enhanced catalyst supports: Optimization of the coating procedure and analysis of mass transport, *Applied Catalysis B: Environmental* 283 (2021) 119651. <https://doi.org/10.1016/j.apcatb.2020.119651>.
 - [18] J.L. Viviente, Ammonia and MOF Based Hydrogen storage for euRoPE, (2022).
 - [19] I. Rossetti, N. Pernicone, F. Ferrero, L. Forni, Kinetic study of Ammonia Synthesis on a Promoted Ru/C Catalyst, *Ind. Eng. Chem. Res.* 45 (2006) 4150–4155.
 - [20] A. Tripodi, M. Compagnoni, E. Bahadori, I. Rossetti, Process simulation of ammonia synthesis over optimized Ru/C catalyst and multibed Fe + Ru configurations, *Journal of Industrial and Engineering Chemistry* 66 (2018) 176–186. <https://doi.org/10.1016/j.jiec.2018.05.027>.
 - [21] G. Anello, G. De Luna, G. De Felice, A. Saker, L. Di Felice, F. Gallucci, Development of ruthenium-based catalysts for ammonia synthesis via polyol reduction method, *International Journal of Hydrogen Energy* 86 (2024) 922–930. <https://doi.org/10.1016/j.ijhydene.2024.08.408>.
 - [22] Y. Ogura, K. Sato, S. Miyahara, Y. Kawano, T. Toriyama, T. Yamamoto, S. Matsumura, S. Hosokawa, K. Nagaoka, Efficient ammonia synthesis over a Ru/La_{0.5}Ce_{0.5}O_{1.75} catalyst pre-reduced at high temperature, *Chem. Sci.* 9 (2018) 2230–2237. <https://doi.org/10.1039/C7SC05343F>.
 - [23] C. Zhang, S. Shi, B. Fang, J. Ni, J. Lin, X. Wang, B. Lin, L. Jiang, Zirconia prepared from UIO-66 as a support of Ru catalyst for ammonia synthesis, *Chinese Chemical Letters* 34 (2023) 107237. <https://doi.org/10.1016/j.cclet.2022.02.042>.
 - [24] W. Li, P. Liu, R. Niu, J. Li, S. Wang, Influence of CeO₂ supports prepared with different precipitants over Ru/CeO₂ catalysts for ammonia synthesis, *Solid State Sciences* 99 (2020) 105983. <https://doi.org/10.1016/j.solidstatesciences.2019.105983>.
 - [25] S.-Y. Chen, L.-Y. Wang, K.-C. Chen, C.-H. Yeh, W.-C. Hsiao, H.-Y. Chen, M. Nishi, M. Keller, C.-L. Chang, C.-N. Liao, T. Mochizuki, H.-Y.T. Chen, H.-H. Chou, C.-M. Yang, Ammonia synthesis over cesium-promoted mesoporous-carbon-supported ruthenium catalysts: Impact of graphitization degree of the carbon support, *Applied Catalysis B: Environment and Energy* 346 (2024) 123725. <https://doi.org/10.1016/j.apcatb.2024.123725>.

- [26] S. Richard, V. Verde, N. Kezibri, C. Makhloufi, A. Saker, I. Gargiulo, F. Gallucci, Power-to-ammonia synthesis process with membrane reactors: Techno- economic study, International Journal of Hydrogen Energy 73 (2024) 462–474. <https://doi.org/10.1016/j.ijhydene.2024.06.041>.
- [27] INCONEL 625 TECHNICAL DATA, (n.d.). <https://www.hightempmetals.com/techdata/hitempInconel625data.php> (accessed November 10, 2024).
- [28] National Institute of Standards and Technologies, NIST chemistry WebBook, (n.d.). <https://webbook.nist.gov/chemistry/form-ser/> (accessed November 10, 2024).
- [29] Fogler, H. S. (2016). Elements of chemical reaction engineering (5th ed.). Prentice Hall.
- [30] S. Poto, H. Van Den Bogaard, F. Gallucci, M. Fernanda Neira d'Angelo, Evaluation of the relevant mass and heat transfer phenomena in a packed bed membrane reactor for the direct conversion of CO₂ to dimethyl ether, Fuel 350 (2023) 128783. <https://doi.org/10.1016/j.fuel.2023.128783>.

Appendix D

D1: Physical setting details

Table D1: Recap of physical settings for numerical simulations

Name	Symbol	Value
Inlet temperature	T_{in}	400 – 600 °C
Wall temperature	T_{wall}	400 – 600 °C
Operating pressure	P_{op}	1 atm (“validation” domain) 10 atm (membrane reactor)
Inlet velocity	v_{in}	0,001 – 0,1 m.s ⁻¹
Solid density	$\rho(\text{in625})$	8440 kg.m ⁻³
Solid specific heat	$C_p(\text{in625})$	Piecewise-linear, taken from (~500 J.kg ⁻¹ .K ⁻¹) [27]
Solid thermal conductivity	$\lambda(\text{in625})$	Piecewise-linear, taken from (~17 W.m ⁻¹ .K ⁻¹) [27]
Fluid density	$\rho(\text{N}_2, \text{H}_2, \text{NH}_3)$	Computed (Fluent “incompressible-ideal-gas”)
Fluid specific heat	$C_p(\text{N}_2, \text{H}_2, \text{NH}_3)$	Variable (Fluent “nasa-9-piecewise-polynomial”)
Fluid thermal conductivity	$\lambda(\text{N}_2, \text{H}_2, \text{NH}_3)$	Piecewise-linear for each fluid, taken from [28]
Fluid viscosity	$\mu(\text{N}_2, \text{H}_2, \text{NH}_3)$	Computed (Fluent “kinetic-theory”)

D2: Ansys Fluent solver details

Table D2: Recap of physical settings for numerical simulations

Setting	Value
Time	Steady-state
Solver type	Pressure-based

Pressure-velocity scheme	Coupled
Gradient discretization	Least squares cell based
Spatial discretization	Second order (upwind)
Pseudo-time method	Global time step
Viscous model	Laminar
Maximum tolerated continuity residual (with all other residuals lower)	10^{-4}

D3: Concentration polarization coefficient

The degree of concentration polarization is assessed with the Coefficient of Concentration Polarization (CPC) as per Eq. D1, which is the ratio of average NH_3 concentration at the membrane surface to that at the external wall. $CPC \in [0; 1]$ (close to 1 means limitation by diffusion inside reactor, close to 0 means limitation by diffusion through membrane) This coefficient helps define the discrepancy between the ideal permeation driving force and the actual driving force, though it is challenging to measure experimentally, making simulation methods essential for its evaluation

$$CPC = 1 - \frac{p_{\text{NH}_3}^{\text{surface-membrane,ext}} - p_{\text{NH}_3}^{\text{surface-membrane,int}}}{p_{\text{NH}_3}^{\text{surface-wall,ext}} - p_{\text{NH}_3}^{\text{surface-membrane,int}}} \quad \text{Eq. D1}$$

$$CPC = 1 - \frac{\text{"real driving force "}}{\text{"driving force without concentration polarization"}} \quad \text{Eq. D2}$$

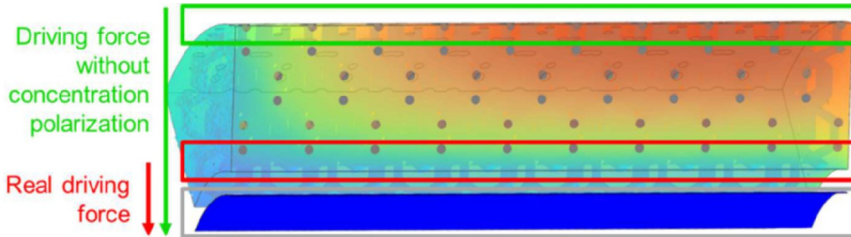
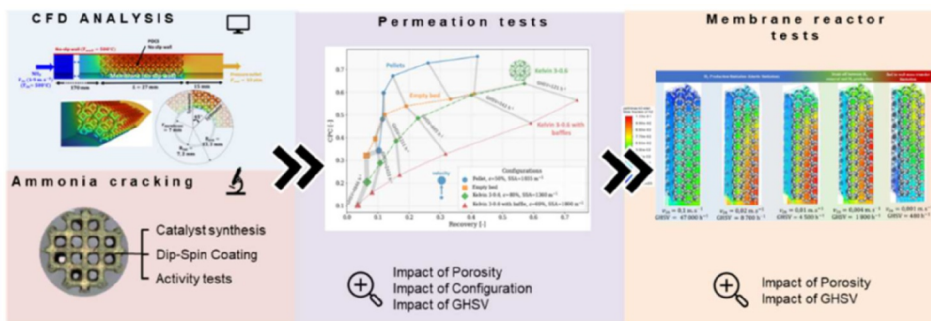


Figure D1: Visualization of the CPC calculation

Chapter 7 | Ammonia cracking using membrane reactors: towards the utilization of POCS to improve external mass transfer

Abstract

This chapter* investigates how operating conditions and design factors impact external mass transfer in Porous Open Cellular Structures (POCS) interfaced with Pd-based membranes. To achieve this, a dip/spin coating method was optimized to deposit Ru based catalytic layer onto nickel alloy POCS produced via Selective Laser Melting (SLM), and kinetic activity was tested providing validation basis for CFD modelling activities. Virtual permeation tests highlighted the influence of packing type and porosity, revealing that the Kelvin 3-0.6 with baffles performed best at a Gas Hourly Space Velocity (GHSV) below 1211 hr^{-1} , achieving higher hydrogen recovery and minimized concentration polarization. At higher GHSV, baffles improved the Concentration Polarization Coefficient (CPC) but resulted in slightly lower hydrogen recovery compared to baffle-free configurations. The study of ammonia decomposition in a Kelvin cell POCS membrane reactor, revealed that optimizing POCS membrane reactors requires balancing hydrogen production kinetics with the extraction driving force. Hydrogen production increased with GHSV, peaking at 1850 hr^{-1} before declining due to non-permeating gas accumulation, and a similar trade-off was observed with porosity, where optimal performance occurred at 0.8 porosity before kinetic limitations caused hydrogen recovery to decline. Overall, optimizing POCS membrane reactors involves a balance of hydrogen production and extraction, and the integration of baffles has the potential further boost performance. Certainly, POCS could yield economic benefits by protecting the membrane and reducing mass transfer limitations, requiring less membrane area for a given separation.



* This chapter is based on the following paper: S. Richard, D. Tasso, M. Rajana, A. Saker, A. Ramirez Santos, C. Makhoulfi, N. Meynet, B. Hary, S. Nardone, G. Marino, M. Thomas, C. Italiano, A. Vita, F. Gallucci, Comparison of thermo-hydraulic performance among different 3D printed periodic open cellular structures, Submitted to Chemical Engineering Journal

7.1. Introduction

Building on the previous chapters, which explored Periodic Open Cellular Structures (POCS), **Chapter 6** focused on comparing their thermohydraulic performance, while **Chapter 7** examined the role of mass transfer in ammonia synthesis, both in standalone reactors and those integrated with selective membranes. This final chapter shifts focus to the reverse reaction: ammonia cracking on coated POCS coupled with a palladium membrane. It further highlights the impact of operating conditions and POCS modifications, such as the addition of baffles, in reducing concentration polarization, a significant challenge for such membranes, as discussed in **Chapter 2** (page 41).

As in previous chapters, Computational Fluid Dynamics (CFD) simulations are deployed as a systematic tool to study transport phenomena. While an extensive literature review on this topic is no longer necessary (cf. page 151 & page 178), key studies offer valuable insights into leveraging CFD to reduce polarization effects and scale up membrane systems from single-tube to multi-tube configurations [1-4]. For instance, Voncken et al. (2019)[1] addressed challenges related to scalability, highlighting that the interaction of polarization zones in a multi-membrane module becomes more significant at smaller inter-membrane distances under fluidization conditions. Choi et al. (2022) [3] demonstrated the potential of incorporating baffles in a membrane reactor for methane reforming to enhance performance. Additionally, Ma et al. (2018) [2] explored the variation of radial mass transfer limitations, noting significant membrane tube-to-tube differences in a multi-tube module, particularly severe under low flow rates.

This chapter aims to provide insights into how operational conditions and design parameters influence external mass transfer in POCS interfaced with hydrogen-selective Pd-based membranes during hydrogen separation and ammonia decomposition in a membrane reactor, as illustrated in **Figure 7-1**. To achieve this, a dip/spin coating method was optimized to deposit Ru-based catalytic layers onto IN625 POCS produced via Selective Laser Melting (SLM), and kinetic activity was tested provided validation basis for the subsequent modelling activities. CFD modeling was used to examine the effects of POCS features (e.g., porosity, cell type) and flow conditions on external mass transfer validated on the mentioned experimental work. The findings of this study could influence future designs of POCS membrane reactors.

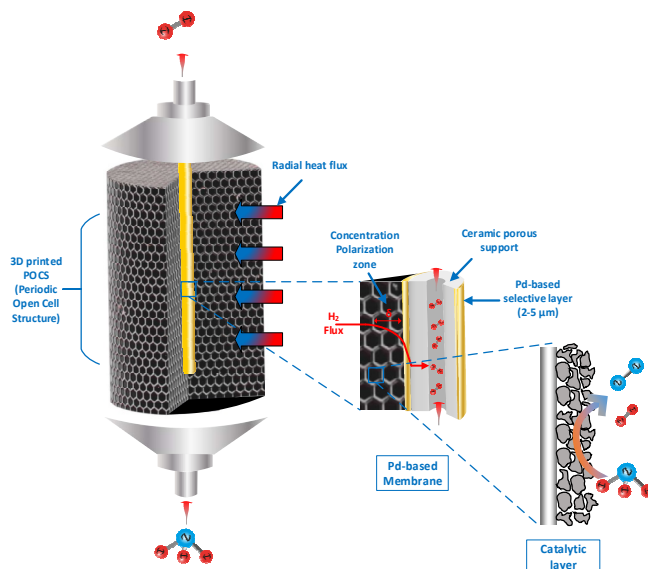


Figure 7-1: Sketch of a POCS Membrane Reactor studied for on-site hydrogen production from ammonia cracking. Reactants are introduced from the bottom and move upward, with hydrogen collected inside the membrane as permeate, while other chemical components form the retentate

7.2. Experimental set-up

7.2.1. Manufacturing of the structures

As detailed in the previous chapter nickel alloy POCS samples with different cell types (e.g., body-centered cubic, Kelvin, and gyroid; see **Figure 5-1** in **Chapter 5**) were fabricated using an SLM280 LPBF machine at ENGIE Laborelec based on CAD designs. The cylindrical samples were 10 mm in diameter and 15 mm in height. The printed samples closely matched their CAD models, with porosity deviations of no more than 15% from the intended design. The **Table 7-1** summarizes the design parameters: strut diameter, cell length, porosity, and specific surface area relevant to this work. The notation for the POCS samples remains consistent with the previous chapter, starting with the cell type geometry, followed by numbers indicating the cell size and strut size in millimeters, respectively.

Table 7-1: Geometrical features of the CAD design cell parameters printed relevant to this study. The POCS structures are denominated by the cell type followed by the size of the cell and the strut size

Cell type	Cell length, d_c [mm]	Strut diameter, d_s [mm]	Theoretical Porosity, ϵ %	Theoretical specific surface area, SSA [cm ⁻¹]
BCC 3-0.4	3	0.4	0.91	8.1
BCC 3-0.75	3	0.75	0.73	12.3
Kelvin 3-0.6	3	0.6	0.79	12.16

Kelvin 3-0.61	3	0.61	0.79	12.3
----------------------	---	------	------	------

7.2.2. Catalyst synthesis and POCS activation

The catalytic activation of the nickel alloy POCS samples by CNR-ITAE follows a multi-step process. It involves catalyst powder preparation, ball milling, optimizing slurry preparation, and applying the slurry to the pretreated metallic structure using a dip and spin coating method. Following Doh et al. (2017) [6], the solid oxide catalyst powder, $\text{Sr}_{0.84}\text{Y}_{0.16}\text{Ti}_{0.92}\text{Ru}_{0.08}\text{O}_{3-\delta}$, is synthesized via a modified Pechini method, a sol-gel technique producing fine, highly dispersed catalyst powders with abundant active sites [7]. This method involves dissolving metal salts in a solution, adding citric acid as a chelating agent to form a metal complex, and reacting it with ethylene glycol to form a solid resin. This solid is then ground and sieved through a 250 μm diameter sieve to ensure uniform composition and size. After drying and calcining, the resin transforms into a homogeneous metal oxide powder with a Ru content of 4 wt.%. The reference for the product used, along with detailed preparation steps, can be found in **Appendices E1 and E2**. The powder's physicochemical properties were analyzed using nitrogen physisorption, X-ray diffraction, H_2 chemisorption, and temperature-programmed reduction, with the results provided in **Appendix E3**.

The slurry preparation is optimized using a dispersion medium of hydrolyzed polyvinyl alcohol (PVA) and bi-distilled glycerol in distilled water, incorporating ball-milled catalyst and boehmite alumina powders (Disperal P2®, SASOL™) for enhanced dispersion. Disperal in water is also used to improve the adhesion of the washcoat. The slurry's rheology, critical for achieving a stable and uniform coating, is characterized with a rotational rheometer (Modular Compact Rheometer MCR 92, Anton Paar GmbH, Graz, Austria). A shear thinning behaviors was found with a viscosity value between 0.08 and 0.07 Pa s in the typical shear range for the spin-coating applications (1000 - 2000 s^{-1}), in this range the slurry assume a Newtonian behavior (see **Figure 7-2.B**). The optimized slurry is then applied to a pretreated metallic structure (Kelvin 3-0.6), calcined at 900 °C, using a combined dip and spin coating process. This process involves immersing the structure for 10 seconds, followed by removal of excess liquid with a commercial spin-coater (SPIN 150 SPS Europe), where parameters such as rotation speed and duration are carefully adjusted to achieve the desired material loading. A picture of the spin coater is shown in **Figure 7-2.C**. The coating process involves multiple dips and spins to achieve a catalyst load of 0.16 g/cm^3 (0.19 g) as shown in **Figure 7-2.D**.

Gravimetric analysis is performed after each flash drying step and the final calcination to monitor weight changes and assess the washcoat load. The final washcoat load is determined by the weight difference between the bare and coated POCS. The washcoat thickness (s_{coating}) is estimated from the specific load as per Eq 7.1, as precise instrumentation to cut the metallic structure were lacking.

$$\text{mass of catalyst}[\text{kg}] = \rho_{\text{cat}} \left[\frac{\text{kg}}{\text{m}^3_{\text{coating}}} \right] * \frac{\text{Volume of catalyst} [\text{m}^3_{\text{coating}}]}{\text{SSA} [\text{m}^{-1}] * V_{\text{reactor}} [\text{m}^3] * s_{\text{coating}} [\text{m}]}$$

$$\leftrightarrow s_{\text{coating}} = \frac{\text{mass of catalyst}[\text{kg}]}{\rho_{\text{cat}} \left[\frac{\text{kg}}{\text{m}^3_{\text{coating}}} \right] * \text{SSA} [\text{m}^{-1}] * V_{\text{reactor}} [\text{m}^3]}$$

Eq. 7.1

$$\leftrightarrow S_{coating} = \frac{0.19 \cdot 10^{-3} [kg]}{2044 \left[\frac{kg}{m^3_{coating}} \right] \cdot 1210 [m^{-1}] \cdot 1.17 \cdot 10^{-6} [m^3]} = 65 \mu m$$

The main physico-chemical features of the synthesized powders are reported in **Table 7-2**. As a first approximation, the catalytic loading C_{load} was calculated from these tests, defined as the mass of catalyst deposited per unit surface area of the POCS. This parameter will serve as factor in converting volumetric reaction rates into surface reaction rates in the numerical investigation. The adherence of the coating layer was assessed by measuring the weight loss after ultrasonic treatment in a petroleum ether bath for 30 minutes. The coated POCSs underwent ultrasonic treatment at 45 kHz and 130 W using the USC 900D ultrasonic bath, followed by drying at 120 °C for 1 hour. Mechanical stability, reflected in the weight loss relative to the loaded layer, ranged from 0.86 wt% for BCC structures to 7.3 wt% for Kelvin structures. A Keyence VHX-7000 digital optical microscope characterized by a fully integrated head that use a stage shift technology and 4K mode for high resolution imaging was also used for morphological measurements. Detailed images of the POCS were taken with VHX-E20 (High-Resolution, Low Magnification Objective Lens 20 -100X) and VHX-E100 lenses (High-Resolution, Medium Magnification Objective Lens 100-500x).

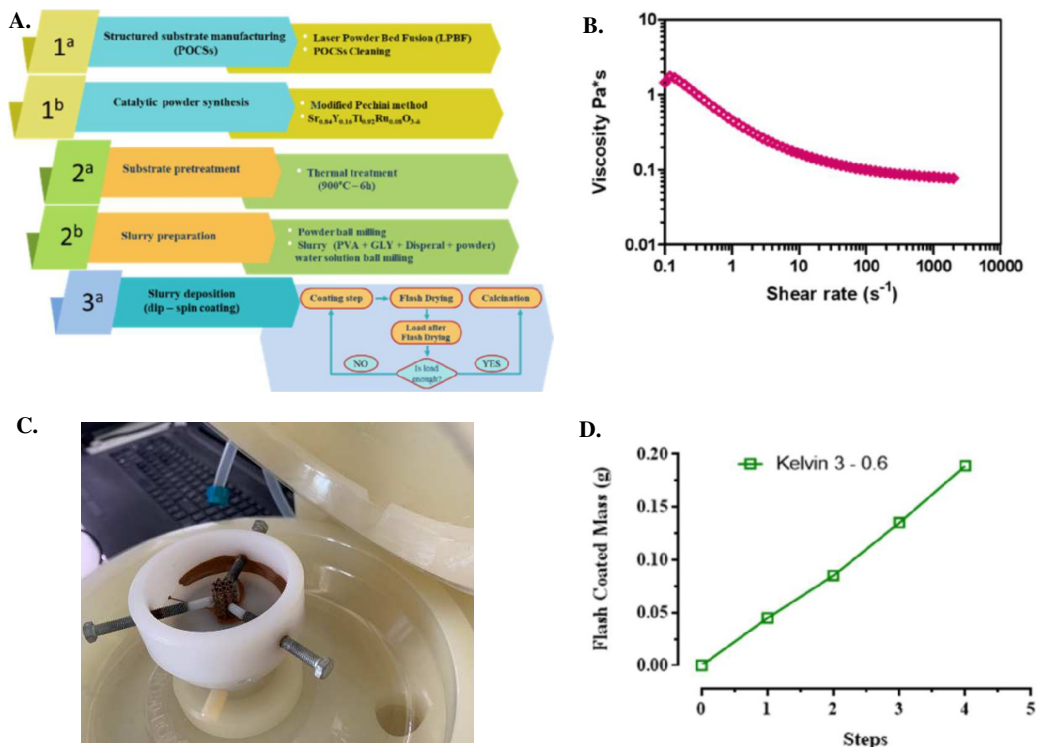


Figure 7-2: (A) Summary of main steps involved in the preparation of the coated POCS (B) Slurry's rheology (C) Spin coating step (D) Loading curve

Table 7-2: Geometrical characteristic of the Kelvin 3-0.6 POCS (*Assumed **Calculated ***Measured)

Catalyst Composition (wt%)	Ru(4.3%), Ti(23.43%), Y(7.57%), Sr(39.16%), O(25.54%)
$\rho_{\text{dense}} \left(\frac{\text{kg}_{\text{cat}}}{\text{m}^3_{\text{cat}}} \right) **$	2921
$\epsilon_{\text{coating}} \left(\frac{\text{m}^3_{\text{void}}}{\text{m}^3_{\text{coating}}} \right) *$	0.3
$\rho_{\text{cat}} \left(\frac{\text{kg}_{\text{cat}}}{\text{m}^3_{\text{coating}}} \right) **$	2044
$\rho_{\text{bed}} \left(\frac{\text{kg}_{\text{cat}}}{\text{m}^3_{\text{bed}}} \right) **$	429
Mass of catalyst (g)***	0.19
Thickness of the coating, s_{cat} (μm) calculated from Eq 7.1 **	65
Loading $\left(\frac{\text{mg}}{\text{cm}^2_{\text{POCS}}} \right) **$	13.2
Loading, $C_{\text{load}} \left(\frac{\text{mg}}{\text{cm}^3_{\text{reactor}}} \right) **$	0.16

7.2.3. Kinetic tests

Tests of the catalytic activity of the ammonia decomposition reaction were conducted by flowing a stream of 50.1% ammonia to a fixed reactor, at WSV of 95 mL·min⁻¹ (WSV 30000 cm³·g_{cat}⁻¹·h⁻¹). The catalyst was reduced at a temperature of 600 °C for 1h. The ammonia conversion and the hydrogen formation rate values in the reaction at temperature range of 400-600 °C and 1 atm total pressure. The effluent gases were taken at regular intervals and were analyzed by a Gas Chromatography(Agilent 7890A) equipped of three parallel columns (Hayesep Q, HP PLOT Q and Molesive 45/60) connected to a thermal conductivity detector (TCD) using Ar as carrier gas.

7.3. Numerical investigation

7.3.1. CFD modelling

To examine the effects of morphological features and flow conditions on external mass transport rates in Periodic Open Cellular Structures (POCS) interfaced with palladium selective membranes, CFD simulations were conducted using Comsol™ (version 6.0) for permeation tests and Ansys Fluent™ (version 2023 R1) for reactor simulations. Three geometrical domains were modeled, as shown in **Figure 7-3**, each with specific dimensions and boundary conditions. The first domain (**Figure 7-3.A**) focused on virtual permeation tests, isolating permeation effects from chemical reactions. The second domain (**Figure 7-3.B**) simulated the experimental setup for validating chemical reactions, while the third (**Figure 7-3.C**) represented a segment of a membrane reactor. In the first domain, isothermal conditions were applied. In contrast, the second and third

domains employed fully coupled equations for momentum, mass transfer, and energy under laminar flow conditions.

For the “permeation” domain, a 21 mm active length and a 0.5 mm spacing were implemented to avoid scratching the sensitive palladium layer, with a total active membrane area of 63 mm². As shown in the Figure, this domain was used to test the impact of baffles on the hydrogen permeation (The first baffle in direct contact with the membrane to simulate potential membrane support). Hydrogen permeation through the palladium-silver (Pd-Ag) plated ceramic membrane was simulated, assuming infinite selectivity for hydrogen. As in the previous **chapters 3 and 4**, that dealt with similar membranes, the hydrogen flux across the membrane was simulated using the Richardson equation, as presented in Eq. 7.2, ignoring the ceramic support's impact. Additionally, mass transfer limitations on the permeate side are considered negligible, since on the permeate side only virtually pure H₂ is present.

$$J_{H_2} = \frac{Pe}{\delta} (p_{H_2,ret}^n - p_{H_2,perm}^n) \left[\frac{mol}{s \cdot m^2} \right] \quad \text{Eq. 7.2}$$

Where Pe represents the permeability of the membrane, δ denotes the thickness of the selective layer membrane, $p_{H_2,ret}$ and $p_{H_2,perm}$ represent the hydrogen partial pressure on the retentate and permeate sides, respectively, and n represents the exponential factor that indicates the rate-limiting step of the mechanism by which hydrogen crosses the selective palladium layer. In the case of ideal conditions where there is thermodynamic equilibrium between the hydrogen atoms dissolved at the membrane surface and the hydrogen concentration in the gas phase, the pressure exponent n is equal to 0.5. In this scenario, Richardson equation (Eq 7.2) takes the form of Sieverts' law ($n=0.5$), suggesting that the diffusion of hydrogen atoms through the bulk of Pd is the limiting step in the hydrogen permeation mechanism. The membrane permeability Pe can be expressed using an Arrhenius-type correlation, as described in Eq.7.3.

$$Pe = Pe_{0,H_2} e^{-\frac{E_a}{RT}} \quad \text{Eq. 7.3}$$

where Pe_{0,H_2} represents the pre-exponential factor, E_a is the activation energy, R denotes the universal gas constant, and T represents the temperature. The permeation parameters were sourced from Fernandez et al. (2015) [8], closely aligned with other similar membrane studies [9].

For the "validation" domain, the geometry consisted of a cylindrical POCS structure, 15 mm in length and 10 mm in diameter. A free-flow domain of 170 mm upstream was added to prevent inlet diffusion phenomena, with a 10 mm downstream extension. Inlet velocities varied from 0.01 to 1 m/s, and the temperature ranged from 400 °C to 600 °C, while the outlet pressure was maintained at atmospheric conditions. The cylinder's exterior had a no-slip boundary condition, and its temperature matched the inlet. The surface temperature of the POCS was determined by heat fluxes and material properties, using Inconel characteristics in a conjugate heat transfer approach. A 50% ammonia flow was applied to replicate experimental conditions. The catalyst model employs a zero-dimensional approach, treating the reacting layer as infinitesimally thin and neglecting potential irregularities such as cracks and cavities in the washcoat. Here, the porous surface is modeled as both a source of product and a sink of reactants.

For the "membrane reactor" domain, a realistic portion of a membrane reactor was employed, featuring a POCS cylinder that is 27 mm long and 26.6 mm in external diameter, enclosing a central membrane with a diameter of 14 mm. Similar to previous models, 170 mm of free flow was added upstream from the POCS. In addition a 0.2 mm gap was introduced between the POCS and the membrane to account for this gap is required in order to avoid damaging the membrane during the insertion in the POCS. In addition, a 0.2 mm gap was introduced between the POCS and the membrane to prevent damage to the membrane during its insertion into the POCS for real application. Potentially even bigger gap would be required. In addition, a 0.2 mm gap was introduced between the POCS and the membrane to prevent damage to the membrane during its insertion into the POCS for real-world applications. In practice, an even larger gap might be necessary to accommodate further imperfections in the POCS or variations during the assembly process, ensuring the membrane remains undamaged. To optimize computational resources, only one-eighth of the domain was modeled, with symmetry boundary conditions applied to two selectively chosen cutting planes. Indeed, Kelvin and BCC structures are inherently symmetric onto these planes (as shown on **Figure 7-3.C**), and the whole domain can be defined by the symmetrical replication of this eight of the structure. Pure ammonia (NH_3) was introduced at the bottom inlet of the reactor, with a no-slip boundary condition applied to the surrounding walls of the reactor bed and both ends of the membrane. The hydrogen generated within the reactor permeated through a palladium-silver (Pd-Ag) plated ceramic membrane, which was assumed to be infinitely selective for hydrogen, allowing only pure hydrogen to pass to the permeate side. The hydrogen flux across each membrane was simulated using Eq.7.2.

From the numeric viewpoint, the chosen meshes comprise approximately 400000 cells for the permeation domain approximately 1 million cells for "validation" domain, and around 8 million for membrane reactor simulations, encompassing both the fluid and solid domains. CFD calculation are performed to model pure laminar flow regime through a POCS structure on which an ammonia cracking reaction is taking place. Gradient computations were handled using the Least Square Cell-Based discretization scheme, while the Second Order Upwind scheme was adopted for the discretization of transport properties, including momentum, energy, and turbulence variables. The "coupled" algorithm was chosen for pressure-velocity coupling, ensuring a stable and rapid convergence in this steady-state analysis. Convergence was deemed achieved when the residuals fell below 10^{-4} . A more comprehensive overview of the computational methods, encompassing domain, grid generation, and mesh independence analysis, is presented in **Appendices E and F**.

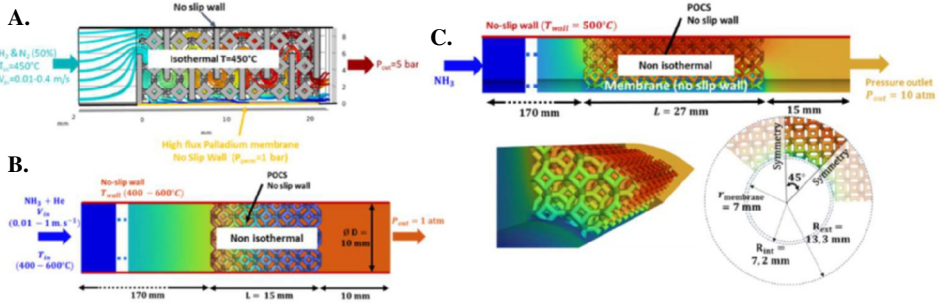
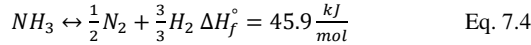


Figure 7-3: Implemented boundary conditions and physical setup applied (A) Virtual permeation domain set up (B) Traditional reactor mirroring the experimental one used to validate the chemistry (C) Representative (scaled up) portion of a Pd-membrane reactor

7.3.2. Kinetic rate law

A mathematical expression for the intrinsic rate of ammonia decomposition is essential for numerical simulations. However, a widely accepted reaction rate expression for ammonia decomposition is yet to be established. The stoichiometric decomposition of ammonia into H_2 and N_2 , as shown in Eq. 7.4, is mildly endothermic and thermodynamically favored at high temperatures. According to Le Châtelier's principle, the reaction is also favored at low pressure due to molar expansion during decomposition (cf. **Chapter 2**, page 43).



In line with the previous chapters (**Chapters 3 and 4**) and studies on ammonia cracking [10-11], a Temkin-Pyzhev-like power laws, as outlined in Eq. 7.5, was used to match the experimental conversion. This model, while relatively straightforward, has been found to predict empirical data by fitting the reaction order β , Activation energy E_{act} , and the pre-exponential factor k_0 .

$$R'_{NH_3} = k_0 e^{-E_0/RT} \left(\frac{p_{NH_3}^2}{p_{H_2}^3} \right)^\beta \quad \text{Eq. 7.5}$$

The kinetic parameters were determined through a nonlinear least squares method using a Nelder-Mead solver based on the simplex algorithm. This was conducted alongside solving a simple plug flow mass balance for a tubular reactor. Although Nelder-Mead does not guarantee convergence to the optimal solution and may converge to a sub-optimal solution, several successive optimization starting from the initial convergence point were performed to yield a better estimation. The effectiveness of this correlation was assessed using the Mean Absolute Percentage Error (MAPE) offering a percentage-based evaluation of prediction errors as per Eq. 7.6.

$$MAPE = \frac{100}{N} \sum_{i=1}^N \left| \frac{X_{obs,i} - X_{fit,i}}{X_{obs,i}} \right| \quad \text{Eq. 7.6}$$

where $X_{obs,i}$ and $X_{fit,i}$ represent the ammonia conversions obtained from experimental measurements and the model, respectively.

To convert this expression to a surface rate law, as demonstrated in the previous chapter, it is multiplied by the catalyst loading C_{load} as per Eq. 7.7.

$$R_{NH_3} = R'_{NH_3} * C_{load} = \frac{mol}{kg_{cat}s} * \frac{kg_{cat}}{m^2} = \frac{mol}{m^2s} \quad \text{Eq. 7.7}$$

7.3.3. Performance index

Several metrics are used to evaluate the performance of the membrane reactor, including ammonia conversion (X_{NH_3}), defined as the ratio of NH_3 consumption rate to the NH_3 flow rate at the reactor inlet, and the hydrogen recovery factor (HRF), which measures the amount of pure H_2 separated by the membrane relative to the total H_2 produced based on reaction stoichiometry. Both metrics are defined in Eqs. 7.8 and 7.9, respectively. However, HRF alone does not provide a comprehensive understanding of potential mass transfer limitations within the reactor, as a low HRF may result from either low membrane permeance or poor gas-phase mass transfer. Therefore, the degree of concentration polarization is evaluated using the Concentration Polarization Coefficient (CPC) [4], as defined in Eq. 7.10. CPC represents the ratio of the average H_2 concentration at the membrane surface to that at the wall (cf. page 198). Additionally, gas hourly space velocity (GHSV) is calculated as the NH_3 flow rate relative to the reactor volume.

$$X_{NH_3} = \frac{F_{NH_3,in}^{Ret} - F_{NH_3,out}^{Ret}}{F_{NH_3,in}^{Ret}} \quad \text{Eq. 7.8}$$

$$HRF_{NH_3} = \frac{F_{H_2,out}^{Per}}{F_{H_2,in}^{Ret}} * 100 \quad \text{Eq. 7.9}$$

$$CPC = 1 - \frac{driving\ force_{real}}{driving\ force_{ideal}} = 1 - \frac{(p_{H_2}^{surface-membrane})^{0.5} - (p_{H_2}^{permeate})^{0.5}}{(p_{H_2}^{surface-wall.ext})^{0.5} - (p_{H_2}^{permeate})^{0.5}} \quad \text{Eq. 7.10}$$

$$Recovered\ hydrogen\ flow = \int_{A_p} F_{H_2,out} dA_p \quad \text{Eq. 7.11}$$

In those equations $F_{i,in}$ and $F_{i,out}$ are the species molar flowrates at the inlet and outlets of the reactor, respectively. $p_{H_2}^{surface-membrane}$ & $p_{H_2}^{surface-wall.ext}$ designate a surface average of hydrogen partial pressure over the membrane and opposite external wall respectively.

7.4. Results

7.4.1. POCS coating characterization

A photograph of the Kelvin 3-0.6 structure before and after coating is presented in **Figure 7-4**, where a uniform washcoat layer is visible. The structures generally retained their original morphology, featuring hexagonal and square windows, with the smaller square windows being more prone to clogging. The catalytic coating imparted a brownish hue to the structures. Visual inspection revealed that additional material tends to accumulate at the strut intersections or nodes, particularly at the nodes of cubic windows. This accumulation is similar to what has been reported in the

literature for cubic cells and is also observed in honeycomb structures at the edges of the channels [12].

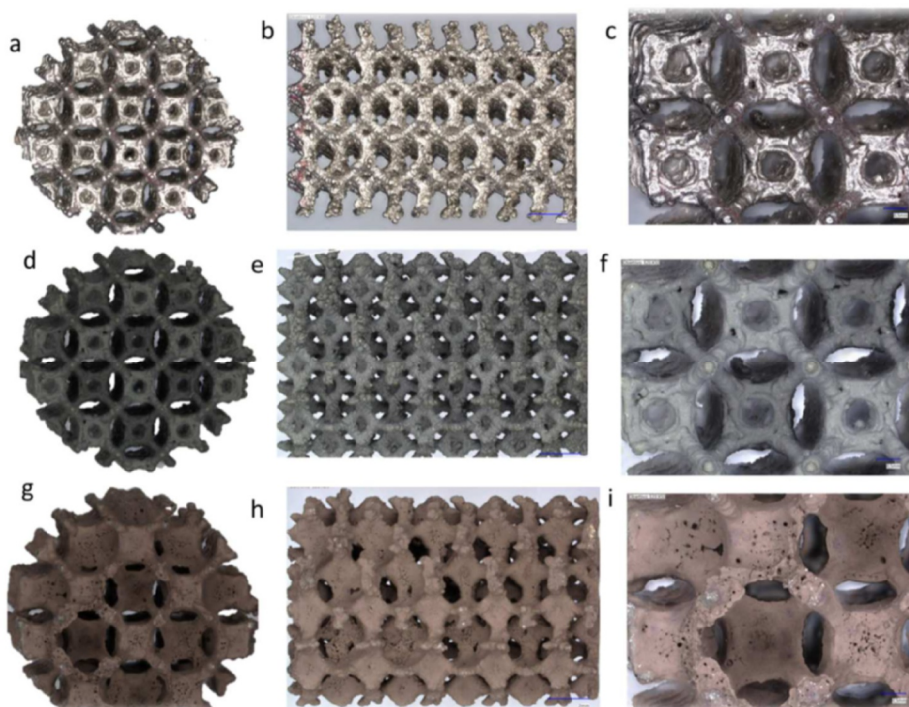


Figure 7-4: Optical microscopic images of (a-c) Fresh kelvin, (d-f) After 900 °C 6h, (g-i) After washcoating

7.4.2. Kinetic tests and model validation

The catalytic performance of the structured catalyst Kelvin 3-0.6 in ammonia decomposition was evaluated over a temperature range of 400-600 °C. Ammonia conversion increased with temperature, peaking between 500 °C and 600 °C, which is consistent with the endothermic nature of the reaction and its approach to equilibrium, as shown in **Figure 7-5**. However, it is important to note that the catalytic performance experienced a slight reduction during the washcoating process, likely due to changes in the properties of the catalytic materials. For instance, binders may block micropores in the perovskite, and the drying and calcination steps could further affect the coating... These aspects would need further investigation.

The kinetic law parameters derived from Eq. 7.5 were fitted and are shown in the table inset of **Figure 7-5**. The experimental and simulated results showed good agreement, with deviations

within $\pm 10\%$. This model is now capable of providing valuable insights into how morphological features and flow conditions influence external mass transport rates in POCS, both with and without selective membranes.

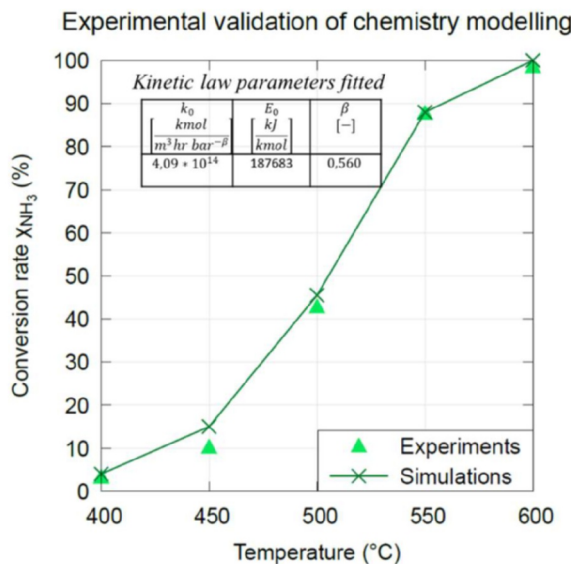


Figure 7-5: Fitting of reaction rate model based on Kelvin 3-0.6. The points are the experimental data, the line correspond to the numeric results. Under those conditions the equilibrium conversion is 100%

7.4.3. Permeation tests

Virtual permeation tests were first conducted at $T = 500^\circ\text{C}$, $P_{\text{ret}} = 5$ bar, and $P_{\text{perm}} = 0.1$ bar to assess the influence of configuration type (Kelvin cell, Kelvin cell with baffle, BCC, empty bed, and pellet), porosity, and superficial velocity on permeation, measured by hydrogen recovery factor and the coefficient of concentration polarization (CPC). **Figure 7-6** qualitatively illustrates that hydrogen is significantly depleted near the membrane, especially at low superficial velocities. Higher flow rates reduce this depletion but come at the cost of lower hydrogen recovery due to shorter diffusion times and reduced membrane contact. The extent of hydrogen depletion varies depending on the packing type. **Figure 7-7.A** further examines the impact of configuration type, showing that the Kelvin 3-0.6 with baffles performs the best at GHSV values below 1211 hr^{-1} . This configuration maximizes hydrogen recovery while minimizing concentration polarization. At low superficial velocities, the performance hierarchy is: Kelvin 3-0.6 with baffles > Kelvin 3-0.6 (without baffles) > empty bed > pellet bed. However, at higher GHSV values, the baffles, while still reducing CPC, slightly decrease hydrogen recovery compared to the configuration without baffles. This is likely due to the need to slow down fluid flow for longer membrane contact time at higher velocities. **Figure 7-7.B** illustrates the effect of porosity on the Kelvin cell type, showing that above

GHSV 605 hr^{-1} , lower porosity offers the best balance between CPC and hydrogen recovery. In contrast, below 605 hr^{-1} , higher porosity performs better, as it accelerates fluid flow and reduces stagnation at lower flow rates, while lower porosity helps slow the fluid and increase membrane contact time at higher flow rates, promoting cross-flow. Lastly, **Figure 7-7.C** compares the Kelvin 3-0.6 with BCC cells, showing that the Kelvin cell offers a superior trade-off between performance and geometric attributes such as porosity and specific surface area. In contrast, the BCC cell maintains consistent behavior across conditions, with no switch in trend, which can be explained by its more linear streamline pattern, as noted in previous publications [5].

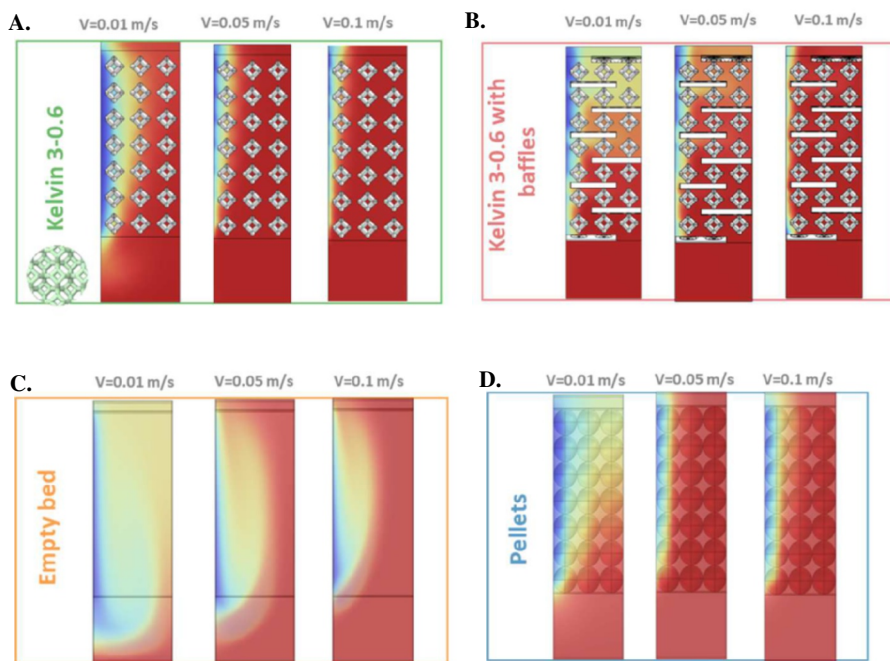


Figure 7-6: Qualitative visualization of the hydrogen molar fraction in baffled (A) Kelvin 3-0.6 (B) Kelvin 3-0.6 with baffles (C) Empty bed (D) Pellets bed

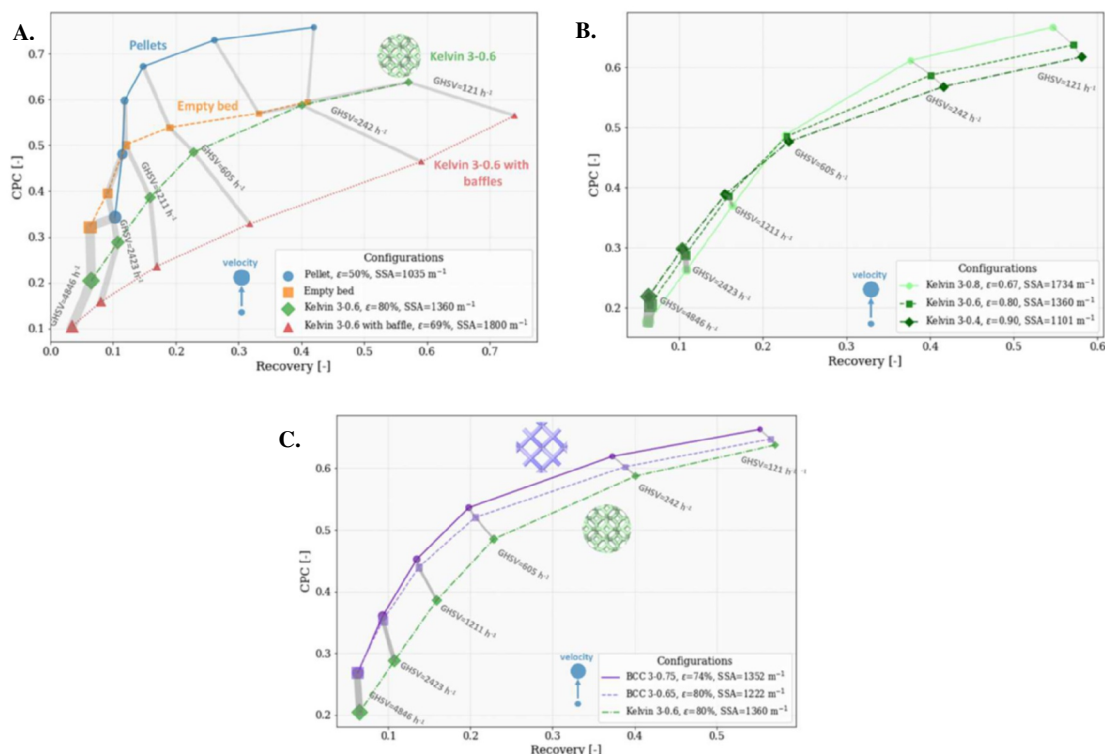


Figure 7-7: Influence of the packing type on the permeation performance under $T=500\text{ }^{\circ}\text{C}$, $P_{\text{ret}}=5\text{ bar}$, and $P_{\text{perm}}=0.1\text{ bar}$ and 50% H_2 inlet: (A) comparison across several configurations .comparison of performance between pellets, Kelvin 3-0.6, empty bed and (B) Impact of porosity on the Kelvin cell type (C) Impact of cell type comparison between BCC and Kelvin cells under similar geometric attributes

7.4.4. Influence of GHSV on MR performance

Under reaction conditions using the Kelvin 3-0.6 as a reference ($T_{\text{in}} = 500\text{ }^{\circ}\text{C}$, $P_{\text{ret}} = 10\text{ bar}$, $P_{\text{perm}} = 0.1\text{ bar}$), **Figure 7-8** illustrates the impact of Gas Hourly Space Velocity (GHSV) on hydrogen production and key performance indicators: NH_3 conversion, Hydrogen Recovery Factor (HRF), and Concentration Polarization Coefficient (CPC). As shown in **Figure 7-8.A** initially, HRF, conversion, and CPC decline sharply as GHSV increases up to 1850 hr^{-1} . Beyond this point, the decrease in HRF and conversion slows, while CPC stabilizes near a plateau. **Figure 7-8.B** shows that although total hydrogen production increases almost linearly with GHSV, the reactor's H_2 productivity (hydrogen permeation through the membrane) peaks at 1850 hr^{-1} and then declines. This pattern reflects the dominant effect of concentration polarization at low GHSV ($<1850\text{ hr}^{-1}$), where non-permeating gases accumulate near the membrane, reducing hydrogen concentration and extraction rates. At $\text{GHSV} = 1850\text{ hr}^{-1}$, an optimal balance between hydrogen production and extraction is reached. At higher GHSV, flow becomes more uniform, reducing concentration

polarization but lowering conversion, leading to decreased overall hydrogen flux. This trend aligns with studies by Sitar et al. (2022) [13] and Chen et al. (2023) [14], which found similar behaviors at different temperatures and GHSVs, as well as Cerrillo et al. (2021) [15], who observed peak performance in a similar GHSV range. **Figure 7-9** shows the contour plots of hydrogen concentration at various GHSV levels, outlining different permeation regimes. Ultimately, the reactor's geometry and operating conditions must be carefully tuned, depending on the catalyst and membrane performance, to avoid conversion-limited or permeation-limited regimes. This balance is especially important when the hydrogen-rich retentate is needed to fuel endothermic reactions, emphasizing the necessity of aligning hydrogen production with its removal.

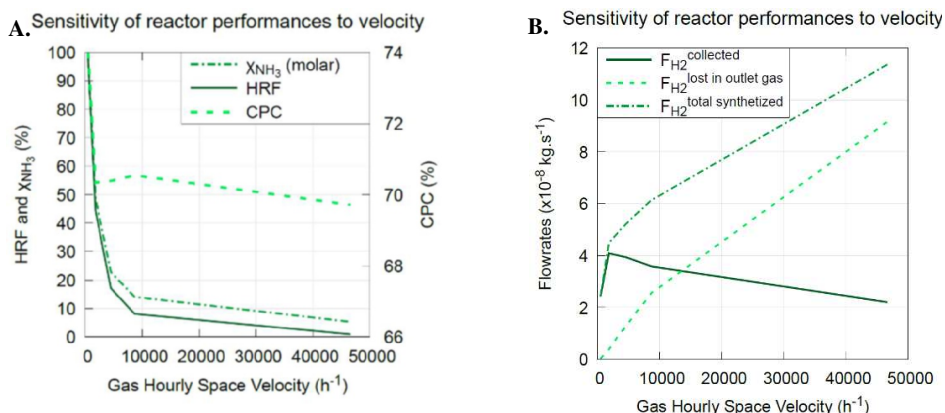


Figure 7-8: Effect of GHSV on the ammonia decomposition using membrane reactor. (A) Ammonia conversion, (B) hydrogen recovery and recovered H_2 flow rate $T_{\text{in}}=500^\circ\text{C}$, $P_{\text{ret}}=10$ bar, $P_{\text{perm}}=0.1$ bar

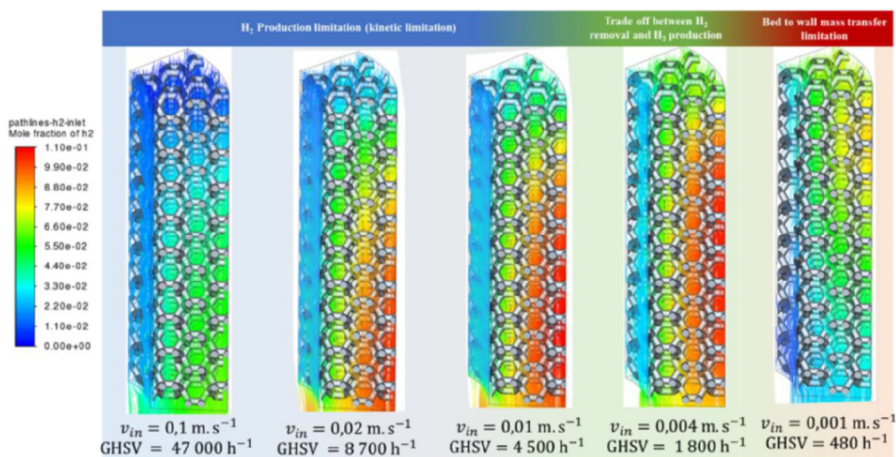


Figure 7-9: Contour plot of H₂ mole fraction for different GHSV using Kelvin 3-0.6 on a representative portion of a membrane reactor

7.4.5. Impact of porosity on MR performance

Keeping the Kelvin cell as a reference under operating conditions of $\text{GHSV}=4500 \text{ hr}^{-1}$, $T_{\text{in}}=500 \text{ }^{\circ}\text{C}$, $P_{\text{ret}}=10 \text{ bar}$, and $P_{\text{perm}}=0.1 \text{ bar}$, **Figure 7-10.A** and **B** illustrate how POCS porosity impacts hydrogen production and performance metrics. As porosity increases, NH_3 conversion declines due to a reduced specific surface area, resulting in lower total hydrogen production and retentate hydrogen content. Interestingly, both the hydrogen recovery factor and permeate hydrogen initially rise with porosity, reaching a peak around 0.8 before decreasing. This behavior indicates that at lower porosities, the process is limited by concentration polarization. Under those operating conditions, a porosity of approximately 0.8 achieves an optimal balance between hydrogen production and extraction, maximizing recovery. Beyond this point, hydrogen production becomes kinetically constrained by insufficient hydrogen partial pressure, limiting further recovery. Therefore, optimal membrane reactor operation requires balancing the kinetics of hydrogen production from ammonia decomposition with the driving force for hydrogen extraction, tailored to specific operating conditions. These observations are visually substantiated in **Figure 7-11**, which shows the H₂ fraction streamlines for each porosity value investigated, along with the corresponding operational regimes. The streamlines clearly demonstrate how changes in porosity affect hydrogen distribution.

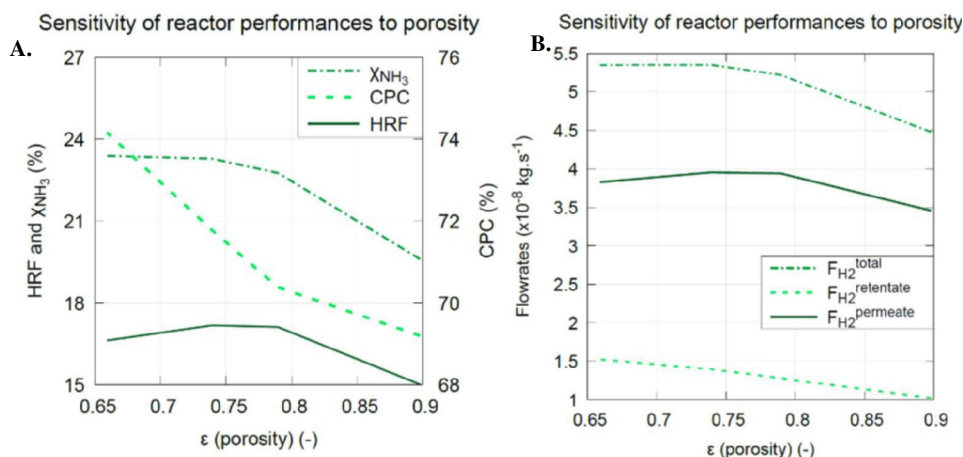


Figure 7-10: Performance indicators (A) NH_3 conversion and hydrogen recovery (B) Hydrogen productivity for different porosity values of the KC lattice obtained at $T_{in}=500^\circ\text{C}$, $P_{ret}=10\text{ bar}$, $P_{perm}=0.1\text{ bar}$

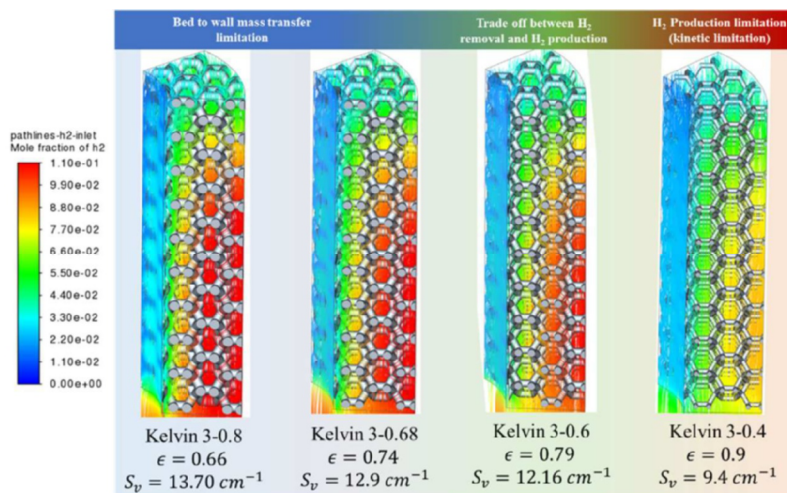


Figure 7-11: Streamlines of the fluid velocity field analysis at different porosity ($v_{in}=0.01\text{ m/s}$, $GHSV=4500 \text{ h}^{-1}$) on a representative portion of a membrane reactor

7.5. Conclusion

This chapter aimed at offering initial insights into the influence of operational conditions and design parameters on external mass transfer in POCS integrated with hydrogen-selective Pd-based membranes, specifically during standalone hydrogen separation and ammonia decomposition within

a membrane reactor. By integrating experimental results, with numerical simulations, we assess how these factors affect catalytic performance and separation performance.

- A dip/spin coating method was optimized to deposit a Ru-based catalytic layer onto IN625 POCS, produced via Selective Laser Melting (SLM). The coating of the Kelvin cell was successful but a loss of catalytic activity was noted compared to the pellet catalyst with similar catalytic loading which need further investigation.
- Virtual permeation tests evaluated highlighting the effects of packing type and porosity. In particular, The Kelvin 3-0.6 with baffles delivers the best performance below a GHSV of 1211 hr^{-1} , achieving higher hydrogen recovery and minimizing the degree of concentration polarization. The performance order at low superficial velocities, Kelvin 3-0.6 with baffles > Kelvin 3-0.6 (without baffles) > empty bed > pellet bed. At higher GHSV, baffles still show better CPC but slightly lower hydrogen recovery (i.e. hydrogen extraction) compared to the configuration without baffles. In addition comparing Kelvin and BCC cells, it was shown that the Kelvin cell provides a better permeation performance.
- The impact of GHSV on the membrane reactor equipped with Kelvin cell 3-0.6 was studied: hydrogen production increases with GHSV, but reactor productivity peaks at 1850 hr^{-1} before declining. At $\text{GHSV} < 1850 \text{ hr}^{-1}$, non-permeating gases accumulate near the membrane, reducing hydrogen extraction. At $\text{GHSV} = 1850 \text{ hr}^{-1}$, hydrogen production and extraction are balanced. Beyond this point, increasing GHSV reduces concentration polarization but decreases conversion, leading to lower hydrogen flux.
- A similar trade-off was observed with increasing POCS porosity in the Kelvin cell type, where hydrogen recovery and permeation initially improve, peaking at a porosity of 0.8, but further increases lead to a decline in total hydrogen production due to kinetic limitations, highlighting the importance of balancing hydrogen production and extraction in membrane reactors.

Optimizing the performance of a POCS membrane reactor requires carefully balancing hydrogen production kinetics with the extraction driving force, along with selecting the right POCS structure. POCS not only protect the fragile membrane by preventing direct contact but also enhance flow patterns and reduce mass transfer limitations, especially at low GHSV where these challenges are most significant. The easy integration of baffles has the potential to further amplifies their potential. Overall, the implementation of POCS could lead to economic savings by both protecting the membrane and reducing mass transfer limitations (i.e. less membrane area required for a given separation).

7.6. References

- [1] R.J.W. Voncken, I. Roghair, M. van Sint Annaland, A numerical study on concentration polarization in 3D cylindrical fluidized beds with vertically immersed membranes, *Chemical Engineering Science* 205 (2019) 299–318. <https://doi.org/10.1016/j.ces.2019.05.010>.
- [2] R. Ma, B. Castro-Dominguez, A.G. Dixon, Y.H. Ma, Scalability of multitube membrane modules for hydrogen separation: Technical considerations, issues and solutions, *Journal of Membrane Science* 564 (2018) 887–896. <https://doi.org/10.1016/j.memsci.2018.08.003>.
- [3] H. Choi, S.H. Kim, J. Bae, S.P.R. Katikaneni, A. Jamal, A. Harale, S.N. Paglieri, J.H. Lee, CFD analysis and scale up of a baffled membrane reactor for hydrogen production by steam methane reforming, *Computers & Chemical Engineering* 165 (2022) 107912. <https://doi.org/10.1016/j.compchemeng.2022.107912>.
- [4] A. Caravella, L. Melone, Y. Sun, A. Brunetti, E. Drioli, G. Barbieri, Concentration polarization distribution along Pd-based membrane reactors: A modelling approach applied to Water-Gas Shift, *International Journal of Hydrogen Energy* 41 (2016) 2660–2670. <https://doi.org/10.1016/j.ijhydene.2015.12.141>.
- [5] S. Richard, D. Tasso, M. Rajana, A. Saker, A. Ramirez Santos, C. Makhoulfi, N. Meynet, B. Hary, S. Nardone, G. Marino, M. Thomas, C. Italiano, A. Vita, F. Gallucci, Comparison of thermo-hydraulic performance among different 3D printed periodic open cellular structures, *Chemical Engineering Journal* 492 (2024) 152005. <https://doi.org/10.1016/j.cej.2024.152005>.
- [6] H. Doh, H.Y. Kim, G.H. Kim, Influence of Cation Substitutions Based on ABO₃ Perovskite Materials, Sr_{1-x}YxTi_{1-y}RuyO_{3-δ}, on Ammonia Dehydrogenation, *ACS Sustainable Chemistry & Engineering* (2017) 9370–9379.
- [7] S. Soisuwan, J. Panpranot, D.L. Trimm, P. Praserttham, A study of alumina–zirconia mixed oxides prepared by the modified Pechini method as Co catalyst supports in CO hydrogenation, *Applied Catalysis A: General* 303 (2006) 268–272. <https://doi.org/10.1016/j.apcata.2006.02.011>.
- [8] E. Fernandez, A. Helmi, K. Coenen, J. Melendez, J.L. Viviente, D.A. Pacheco Tanaka, M. van Sint Annaland, F. Gallucci, Development of thin Pd–Ag supported membranes for fluidized bed membrane reactors including WGS related gases, *International Journal of Hydrogen Energy* 40 (2015) 3506–3519. <https://doi.org/10.1016/j.ijhydene.2014.08.074>.
- [9] N. de Nooijer, F. Gallucci, E. Pellizzari, J. Melendez, D.A. Pacheco Tanaka, G. Manzolini, M. van Sint Annaland, On concentration polarisation in a fluidized bed membrane reactor for biogas steam reforming: Modelling and experimental validation, *Chemical Engineering Journal* 348 (2018) 232–243. <https://doi.org/10.1016/j.cej.2018.04.205>.
- [10] A. Di Carlo, L. Vecchione, Z. Del Prete, Ammonia decomposition over commercial Ru/Al₂O₃ catalyst: An experimental evaluation at different operative pressures and temperatures, *International Journal of Hydrogen Energy* 39 (2014) 808–814. <https://doi.org/10.1016/j.ijhydene.2013.10.110>.
- [11] S. Chiuta, R.C. Everson, R.C. Everson, H.W.J.P. Neomagus, H.W.J.P. Neomagus, D.G. Bessarabov, Ammonia Decomposition for Decentralized Hydrogen Production in Microchannel Reactors: Experiments and CFD Simulations, in: M. Sankir, N.D. Sankir (Eds.), *Hydrogen Production Technologies*, John Wiley & Sons, Inc., Hoboken, NJ, USA, 2017: pp. 77–111. <https://doi.org/10.1002/9781119283676.ch2>.
- [12] C. Busse, H. Freund, W. Schwieger, Periodic open cellular structures (POCS) as catalyst support for intensified heat transport in the partial oxidation of methanol to formaldehyde, *Chemical Engineering Journal* 489 (2024) 151139. <https://doi.org/10.1016/j.cej.2024.151139>.
- [13] R. Sitar, J. Shah, Z. Zhang, H. Wikoff, J.D. Way, C.A. Wolden, Compact ammonia reforming at low temperature using catalytic membrane reactors, *Journal of Membrane Science* 644 (2022) 120147. <https://doi.org/10.1016/j.memsci.2021.120147>.
- [14] W.-H. Chen, W.-S. Chou, R.-Y. Chein, A.T. Hoang, J.C. Juan, Multiple-objective optimization on ammonia decomposition using membrane reactor, *International Journal of*

- Hydrogen Energy (2023) S0360319923023339.
<https://doi.org/10.1016/j.ijhydene.2023.05.081>.
- [15] J.L. Cerrillo, N. Morlanés, S.R. Kulkarni, N. Realpe, A. Ramírez, S.P. Katikaneni, S.N. Paglieri, K. Lee, A. Harale, B. Solami, A. Jamal, S. Mani Sarathy, P. Castaño, J. Gascon, High purity, self-sustained, pressurized hydrogen production from ammonia in a catalytic membrane reactor, *Chemical Engineering Journal* (2021) 134310.
<https://doi.org/10.1016/j.cej.2021.134310>.

Appendix E

E1: Chemical product utilized

The following chemicals were used in the experiments, all as received without further purification: Titanium(IV) isopropoxide ($\text{Ti}(\text{OC}_3\text{H}_7)_4$) from Aldrich (USA), Ruthenium chloride hydrate ($\text{RuCl}_3 \cdot x\text{H}_2\text{O}$) from Merck (Germany), Strontium nitrate ($\text{Sr}(\text{NO}_3)_2$) from Sigma-Aldrich (Germany), Yttrium nitrate hexahydrate ($\text{Y}(\text{NO}_3)_3 \cdot 6\text{H}_2\text{O}$) from Sigma-Aldrich (USA), Ethylene glycol from Carlo Erba, and Citric acid from Merck (Germany).

E2: Catalyst Powder preparation

The perovskite material $\text{Sr}_{0.84}\text{Y}_{0.16}\text{Ti}_{0.92}\text{Ru}_{0.08}\text{O}_{3-\delta}$ was synthesized using a modified Pechini method, as described by Doh et al. [52]. First, 13.0 g of Titanium(IV) isopropoxide was added to 85.2 g of ethylene glycol with stirring in a beaker. Once combined, 43.9 g of citric acid was added to the mixture, which was stirred until a clear solution was formed. Separately, 0.8 g of ruthenium chloride hydrate was dissolved in 100 mL of deionized water and added to the yellowish solution. Afterward, 8.8 g of strontium nitrate and 2.9 g of yttrium nitrate were incorporated into the solution, continuing to stir until all salts were fully dissolved. The solution was then heated to 80 °C for 100 minutes while stirring, followed by storage at 110 °C for 10 hours, producing a gel with a honey-like consistency. This gel was subsequently heated to 300 °C at a rate of 5 °C/min for 2 hours to form a solid. The solid was then ground and sieved through a 250 μm sieve to ensure uniform composition and size. Finally, the powders were calcined at 650 °C for 10 hours with a heating rate of 2.5 °C/min to yield the desired $\text{Sr}_{0.84}\text{Y}_{0.16}\text{Ti}_{0.92}\text{Ru}_{0.08}\text{O}_3$ perovskite material, resulting in approximately 8 g of final powder.

E2: Catalyst powder characterization

- **Instrument used**

Physicochemical characterizations were performed to identify the various properties of the synthesized perovskite material. X-ray diffraction (XRD) patterns were recorded using a Bruker D8 advance diffractometer with Cu K α radiation ($\lambda = 1.5406 \text{ \AA}$, filtered). The diffraction data were collected over a 2θ range of 20 to 80° with a step size of 0.02°, and the results were compared with corresponding JCPDS files.

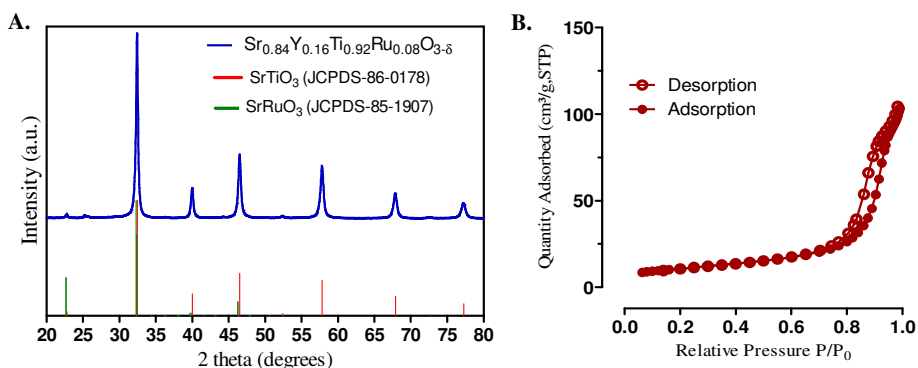
Nitrogen adsorption-desorption analysis was conducted at liquid nitrogen temperature (-196°C) using a Micromeritics ASAP 2020 instrument to determine the Brunauer-Emmett-Teller (BET) specific surface area and the Barrett-Joyner-Halenda (BJH) pore volume. Before measurement, the samples were degassed at 180°C under vacuum for 3 hours.

The reduction properties of the samples were evaluated by H_2 temperature-programmed reduction (H_2 -TPR) using a Micromeritics ChemiSorb 2750 instrument, equipped with a thermal conductivity detector (TCD). The samples were heated from room temperature to 1000°C at a rate of $10^{\circ}\text{C}/\text{min}$ in a 3% H_2/Ar gas mixture ($30\text{ SmL}/\text{min}$).

The XRD pattern of the synthesized perovskite (shown in Figure 1) was consistent with the SrTiO_3 perovskite structure, with additional peaks corresponding to SrRuO_3 . This confirmed the formation of the desired perovskite, with Y and Ru atoms successfully incorporated into the lattice, as no impurity peaks were detected.

• Analysis

The XRD pattern of the synthesized perovskite (shown in **Figure E1.A**) was consistent with the SrTiO_3 perovskite structure, with additional peaks corresponding to SrRuO_3 . This confirmed the formation of the desired perovskite, with Y and Ru atoms successfully incorporated into the lattice, as no impurity peaks were detected. Nitrogen adsorption-desorption isotherms (**Figure E1.B**) revealed a Type IV isotherm with hysteresis at high relative pressure, indicating the presence of mesopores. The hysteresis observed is due to the bottleneck effect, which delays desorption. H_2 -TPR analysis (**Figure E1.D**) identified two main reduction peaks at approximately 100°C and 462°C , along with some broader peaks. The initial reduction peaks around 76°C and 100°C are attributed to the reduction of RuO_x species to metallic Ru, while the higher temperature peak at 462°C is likely due to the reduction of surface Ru-TiO_3 species.



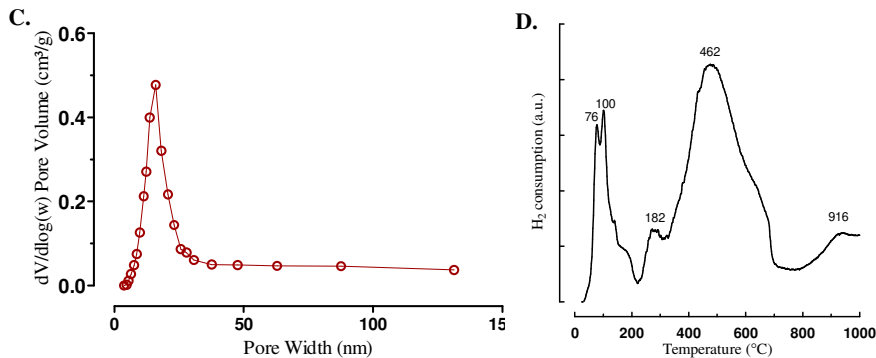


Figure E1: (A) XRD pattern of the prepared catalyst (B) The N₂ adsorption-desorption isotherm (C) desorption pore size distribution (D) H₂ – TPR profile

Table E1: Textural properties of Sr_{0.84}Y_{0.16}Ti_{0.92}Ru_{0.08}O_{3-δ}

Sample	S _{BET} (m ² /g)	Pore Volume (cm ³ /g)	Pore Diameter (nm)
Sr _{0.84} Y _{0.16} Ti _{0.92} Ru _{0.08} O _{3-δ}	38.9	0.17	16.6

E3: IN625 powder characterization

The IN625 powder was calcined at three different temperatures: 900°C, 1000°C, and 1100°C. The corresponding X-ray diffraction (XRD) patterns are shown in **Figure E2**. In the as-received IN625, peaks corresponding to Cr₂Ni₃ (or Ni₃Nb or Ni₃Al) were observed. After calcination at 900°C, additional peaks appeared, indicating partial oxidation, with the formation of CrMoO₃, Cr₂O₃, and NiO phases.

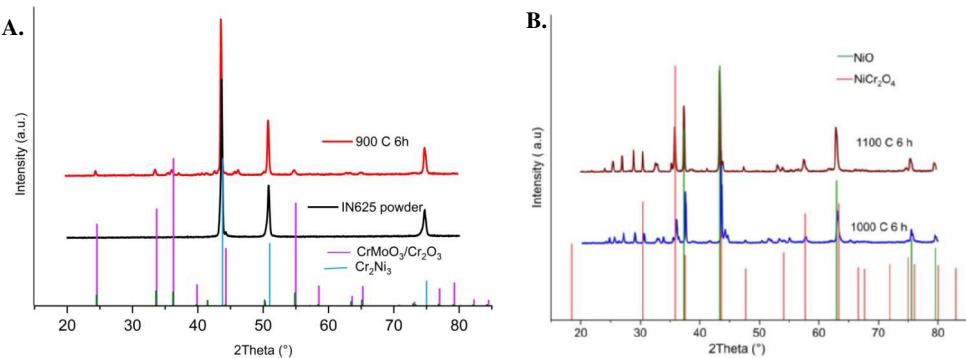


Figure E2: XRD pattern of (A) as received IN625 powder and powder after calcination at 900 °C, (B) powder after calcination at 1000 °C and 1100 °C

E4: Simulation physical setting details

Table E2: Recap of physical settings for numerical simulations

Name	Symbol	Value
Inlet temperature	T_{in}	400 – 600 °C
Wall temperature	T_{wall}	400 – 600 °C
Operating pressure	P_{op}	1 atm (“validation” domain) 10 atm (membrane reactor)
Inlet velocity	v_{in}	0,001 – 0,1 m.s ⁻¹
Solid density	$\rho(\text{in625})$	8440 kg.m ⁻³
Solid specific heat	$C_p(\text{in625})$	Piecewise-linear, taken from (~500 J.kg ⁻¹ .K ⁻¹)
Solid thermal conductivity	$\lambda(\text{in625})$	Piecewise-linear, taken from (~17 W.m ⁻¹ .K ⁻¹)
Fluid density	$\rho(\text{N}_2, \text{H}_2, \text{NH}_3)$	Computed (Fluent “incompressible-ideal-gas”)
Fluid specific heat	$C_p(\text{N}_2, \text{H}_2, \text{NH}_3)$	Variable (Fluent “nasa-9-piecewise-polynomial”)
Fluid thermal conductivity	$\lambda(\text{N}_2, \text{H}_2, \text{NH}_3)$	Piecewise-linear for each fluid, taken from (
Fluid viscosity	$\mu(\text{N}_2, \text{H}_2, \text{NH}_3)$	Computed (Fluent “kinetic-theory”)

E5: Ansys Fluent solver details

Table E3: Recap of physical settings for numerical simulations

Setting	Value
Time	Steady-state
Solver type	Pressure-based
Pressure-velocity scheme	Coupled
Gradient discretization	Least squares cell based
Spatial discretization	Second order (upwind)
Pseudo-time method	Global time step
Viscous model	Laminar
Maximum tolerated continuity residual (with all other residuals lower)	10 ⁻⁴

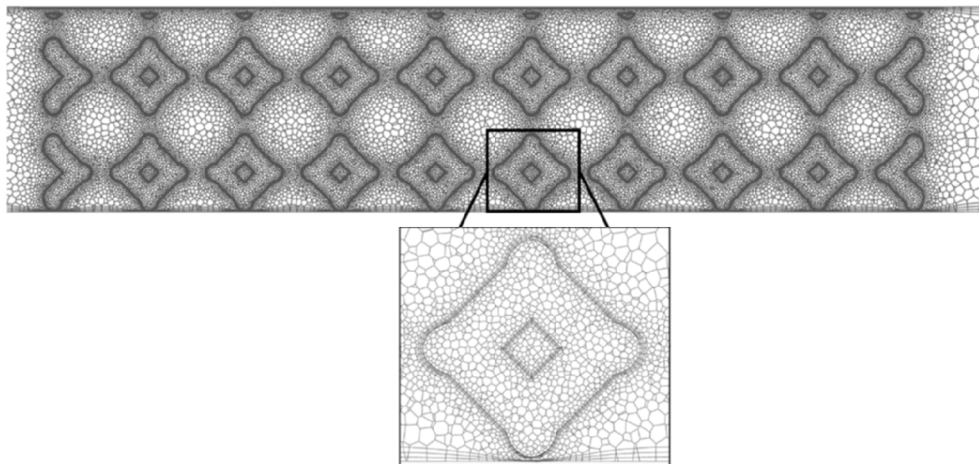
E6: Visualization of mesh

Figure E3: Mesh visualization for the realistic section of the membrane reactor

Chapter 8 | Power-to-ammonia synthesis process using membrane reactors: Techno-economic study

Abstract

This chapter* aims at investigating the potential of catalytic membrane reactors (CMRs) for ammonia production from renewable hydrogen at the process scale. To achieve this objective, computer-aided process simulation is deployed using Aspen plus v14 simulation tool. A 1D model is developed to describe the integration of a ruthenium catalyst into a CMR equipped with inorganic membranes that are selective to NH_3 over N_2 and H_2 . First, the CMR performance is studied across a broad spectrum of membrane properties and operating conditions. Subsequently, the CMR model is integrated into several Power-to-Ammonia (PtA) process layouts, which are optimized and techno-economically compared against a traditional PEM-based PtA production process, employing condensation for the purification stage. Key findings at the reactor level confirmed that beyond a selectivity threshold towards hydrogen of 10-20, both the degree of conversion and recovery tend to be generally independent of the membrane's selectivity. However, for producing pure ammonia permeate, highly selective membranes (>1000 towards H_2) depending on the pressure drop are found essential making this alternative elusive based on existing membranes. At the PtA level, results in terms of efficiency indicates that the use of membrane reactor increases the system efficiency by around ~8% with respect to reference case while ~15% enhancement is achieved with this process when using SOEC technology. When examining the final Levelized Cost of Ammonia (LCOA), incorporating a membrane reactor in conjunction with condensation separation results in a cost that nearly matches the reference case. Future research should focus on replacing the condensation process with a method of purification at lower pressures. This could potentially further improve efficiency and reduce the cost of the membrane reactor compared to the traditional one.

* This chapter is based on the following paper : S. Richard, V.Verde, N. Kezibri, C. Makhloufi, A. Saker, I. Gargiulo, F. Gallucci , Power-to-ammonia synthesis process with membrane reactors: Technoeconomic study, Int. J. Hydrogen Energy vol. 73, pp. 462–474, 2024

8.1. Introduction

This chapter returns to the macroscale to analyze the performance of a pellet-based membrane reactor at the system scale for ammonia synthesis. Readers are referred to **Chapter 7** for details on the catalytic aspects of this reaction and **Chapter 2** for broader insights into membrane reactors. As already mentioned, the study of catalytic membrane reactors for this reaction is still in its early stages. To our knowledge only Zhang et al. (2020) [1] contributed significantly by proposing a model for a fixed-bed membrane reactor and identifying the minimal membrane parameters needed for efficient operation. It was determined that to outperform conventional reactors, a membrane must possess an ammonia permeance over 100 GPU (i.e. $0.0034 \text{ mol m}^{-2} \text{ s}^{-1} \text{ bar}^{-1}$), as well as a selectivity of ammonia towards hydrogen and nitrogen of no less than 10. Several studies have been published on the use of both organic and inorganic membranes to separate NH_3 from H_2 and N_2 such as glassy polymer [2], silica [3], and ceramics [4] as shown in **Figure 8-1**. Nonetheless, these evaluations often occur under conditions that are considerably milder than the high temperature and pressure environments typical of ammonia synthesis. Despite not examining the implication of membrane reactors, multiple studies have evaluated the potential of the PtA process, emphasizing its efficiency and techno-economic considerations. These studies can generally be grouped into three categories [5-6]: 1) Macro-level analyses providing preliminary evaluations for policy makers, often comparing different energy sources or geographical locations [7-8]; 2) Dynamic PSE (Process System Engineering) studies which take into account the variability of renewable energy and the flexibility of plant operations, incorporating intermediate storage solutions like hydrogen buffers or batteries, usually with a focus on specific locations [5, 9-11]; 3) Steady-state PSE studies which are particularly valuable for comparing different process designs, but they have limitations in accurately projecting costs due to inherent assumptions about renewable energy variability [9, 12-16]. Assumptions typically include either dispatchable renewable energy power from the grid or complete system flexibility. As example of this latter category, Gomez et al. (2020) [13] evaluated an industrial-scale ammonia synthesis plant with a capacity of 140 tons per day, powered exclusively by the electrical grid. Their findings revealed a specific energy consumption of 17 MWh/ton, significantly higher than other estimates in literature. In a similar vein, Ishaq and Dincer (2020) [17], introduced a dual-reactor setup to explore the effects of pressure and temperature on ammonia production. Their system, using a PEM electrolyzer, achieved an energy efficiency of 61.1%. While Frattini et al. (2016) noted a 43.5% efficiency using AEC. Finally, Quintero-Masselski et al. (2020) [12] identified an optimal balance using a Ru catalyst, achieving a lower cost of ammonia (LCOA) at 766 €/ton and an energy efficiency of 57.2% while considering PEM electrolysis. In research focused on SOEC technology, Cinti et al. (2017) [18] documented an efficiency reaching up to 62%. Complementing this, Zhang et al. (2020) [19] conducted a comparative analysis of various ammonia production methods, finding that the power-to-ammonia (PtA) process achieved an impressive 74% energy efficiency. However, the PtA method was also the most expensive. This high expense is primarily attributed to the significant costs associated with electrolyzer stacks and electricity. Finally, Quintero-Masselski et al. (2020) [20] also evaluated zeolitic membranes as an alternative to condensation for ammonia

recovery in combination with a condensation stage. It was concluded that traditional condensation was a better option due to its cost-effectiveness (38% cheaper) and higher energy efficiency.

Despite clear advancements in PtA process research, the precise role and effectiveness of Catalytic Membrane Reactors (CMRs) within a complete architecture have not been established. This work aims to investigate the potentiality of catalytic membrane reactors (CMRs) for ammonia production from renewable hydrogen. Utilizing computer-aided process simulation, a one-dimensional CMR model is developed, validated, and investigated for a range of membrane properties and operational conditions. This model is then integrated into several PtA configurations, which are compared from a techno-economic perspective with a PEM-based PtA process.

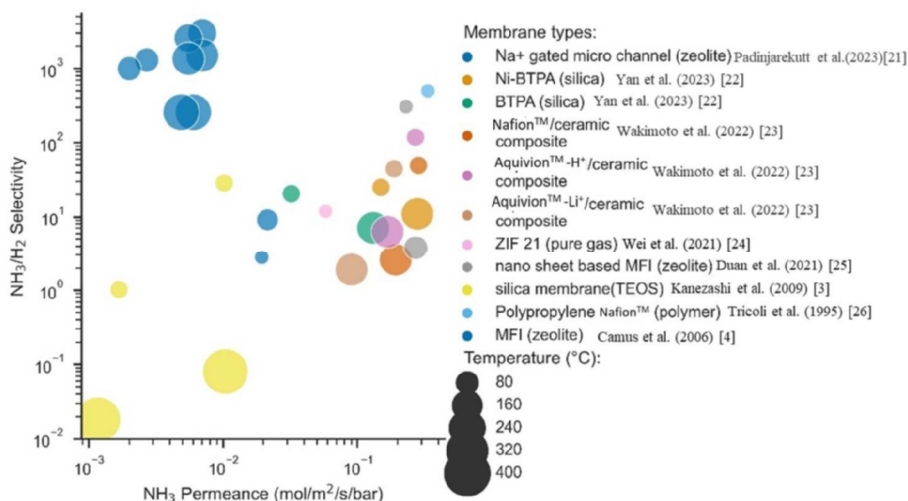


Figure 8-1: Example of selective membrane in the literature - The references are in the order of the legend. Padinjarekutt et al. (2023) [21]; Yan et al. (2023) [22]; Wakimoto et al. (2022) [23]; Wei et al. (2021) [24]; Duan et al. (2021) [25]; Kanezashi et al. (2009) [3]; Camus et al. (2006) [4]; Tricoli et al. (1995) [26].

8.2. Material and Method

In this chapter, the primary tool utilized is Aspen Plus™ v14. This software is notable for its accurate physical property descriptions, comprehensive models for various unit operations, and advanced numerical techniques capable of solving large systems of algebraic and differential equations. To model membrane reactors and SOEC stacks, Aspen Customized Modeler™ (ACM) is utilized, enabling straightforward integration with the Aspen Plus™ architecture as a customized component. In all simulations, the Peng-Robinson cubic equation of state is used both at the reactor and process level as used in similar work [27-28]. The steady state simulations performed allowed to derive the inputs for an optimization and techno-economic analysis as shown on **Figure 8-2**

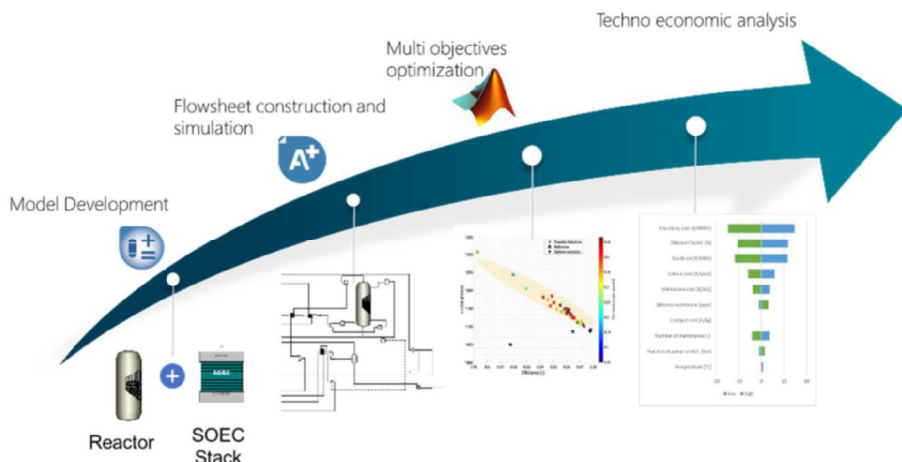


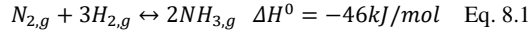
Figure 8-2: Methodology steps followed in this chapter

8.2.1. Membrane reactor modelling

In this study, a multi-tubular fixed bed membrane reactor is analyzed. This type of reactor is chosen for its ease of manufacturing, scalability from a single tube to multiple tubes and efficient heat exchange. The reactor is structured with an inner membrane tube and an outer shell hosting the catalyst, referred as the permeate and retentate sides. To enhance ammonia transfer, the study explores using a pressure gradient or a sweep gas of similar composition as the feed, which can be applied separately or together.

The study develops a simplified steady-state membrane model using a one-dimensional plug flow reactor approach. It includes mass and energy balances, the Ergun equation for pressure drop predictions, and assumes a unitary catalyst effectiveness factor, implying no internal diffusion limitations (a notable presumption for an industrial reactor in which intraparticle mass-transfer limits are likely to reduce the apparent catalyst activity). The model also neglects the effects of concentration polarization (permeate and retentate side) and potential mass transfer limitations in the membrane support. This is supported by Mourgues and Sanchez (2005) [29] investigated concentration polarization effects in hollow fiber membrane modules operating under co-current and counter-current configurations. Their model predicted that, in the system investigated, polarization effects become significant when the membrane permeance to the most permeable species exceeds 1000 GPU and the membrane material selectivity exceeds 100. But this topic is still far from being fully covered in the literature, although some few studies have addressed the question and there are sometimes contradiction [30]. For further discussion, the reader is referred to **Chapter 7**. The permeation is characterized by ammonia permeance and gas selectivities. These selectivities are evaluated by comparing the permeance of each gas to that of ammonia. Due to its larger kinetic diameter, nitrogen is arbitrarily attributed to a selectivity three times greater than hydrogen. Finally,

a mathematical expression for the ammonia synthesis reaction (Cf. Eq. 8.1) is crucial for the numerical simulations.



The kinetic rate expression as in **Chapter 7** is based on the work of Rossetti et al. (2006) [31] for a promoted Ru/C catalyst with a Ru content of 3.2 wt.%. This kinetic model has also been employed in studies cited as [14] and [12]. Details on assumptions, equations, and kinetic model parameters are reported in **Appendices F1 & F2**, with operating conditions and reactor design summarized in **Table 8-1**

Table 8-1: Membrane reactor modelling assumptions- The parameters with a subscript ⁿⁱ are relevant only when the non-isothermal reactor model case is studied

	Parameters	Unit	Value
Numeric	Numerical method	-	Euler method
	Number of points in the axial length discretization	-	300 with a refinement at the inlet
Reactor geometry	Membrane outer diameter	m	0.014
	Bed and membrane Length	m	3 (1.5 for section 8.3.2.)
	Inner Diameter of the tube	m	0.025
	Membranes volumetric coverage in the reactor	-	0.31
	Number of membranes/ Tube	-	1000-6000
	Diameter of spherical catalyst pellet	m	0.001
	Tube wall thickness ⁿⁱ	m	0.001
Parameters	NH ₃ Permeance	mol m ⁻² s ⁻¹ bar	∈[0.01-0.1]
	NH ₃ /H ₂ perm selectivity	-	∈[1-400]
	NH ₃ /N ₂ selectivity	-	H ₂ selectivity *3
	Bed porosity β	-	0.4
	Catalyst density	kg m _{bed} ⁻³	590 [27]
	Overall heat transfer coefficient through the membrane layer ⁿⁱ	Wm ⁻² K ⁻¹	2.4
	Overall heat transfer coefficient through the reactor tubes ⁿⁱ	Wm ⁻² K ⁻¹	200
	Reactor Inlet temperature ⁿⁱ	°C	360
Operating conditions	Sweep gas inlet temperature ⁿⁱ	°C	360
	Reactor temperature	°C	∈[320-400]
	Retentate Pressure	Bar	∈ [60-130]
	Wall temperature ⁿⁱ	°C	360
	N ₂ /H ₂ feed ratio	-	1.5

8.2.2. Plant layouts and general assumptions

Various PtA process configurations are investigated in this work, detailed in **Table 8-2** and differentiated by the type of electrolysis (PEM or SOEC), reactor types (TR or MR), and the employed purification method, primarily condensation except in the optimistic scenario for which membrane are consider as highly selective to ammonia. All comparisons are based on a similar hydrogen input of 85 kmol/hr and benchmarked against a PEM-based Power-to-Ammonia process.

Figure 8-3 depicts the system layouts that are being studied in this study. The "PEM-TR-Cond" benchmark process involves pressurizing nitrogen and hydrogen to 70 bar and mixing them with unreacted reactants, maintaining a hydrogen to nitrogen ratio of 1.5. This mixture is then heated to 360 °C before being introduced into the reactor. The reactor effluent requires cooling and

condensing the ammonia vapor phase for separation, which is more efficient at higher pressures and lower temperatures. For instance, the refrigeration temperature would be around 11.5 °C at 300 bar but -26.0 °C at 50 bar, as demonstrated in Tripodi et al. (2018) [27]. In our study, the reactor effluent is cooled to 30 °C with water and then refrigerated at -40 °C to separate the ammonia product from reactant gases. Unreacted gases are recycled after a 1% purge, and the liquid ammonia product is expanded and stored. Ammonia can be efficiently stored in large quantities at 1 bar and -33 °C in insulated tanks capable of holding up to 50000 tons [10]. However, this aspect falls outside the scope of our study's battery limits. This work intends to achieve 99.5% ammonia purity as in commercial or agricultural (C-grade) ammonia [32-34]. While discussion on fuel grade purity have not yet achieved a consensus, it is believed that this purity should be at or below the commercial purity [34].

In the "PEM-MR-Cond" setup, which includes a membrane reactor, the membranes' limited separation ability requires a condensation stage to attain the desired purity of ammonia. On the other hand, the "PEM-MR (ideal)" configuration is based on the assumption of using highly selective membranes, removing the necessity for a condensation step.

Finally, the study explores an alternative Power-to-Ammonia pathway using SOE for hydrogen generation. The SOEC in this study uses cathode-supported cell technology, with its model developed and validated by experimental data in [35]. Each stack is operated at near thermoneutral operation with a nominal temperature of 700 °C. Steam generated from high-grade demineralized water is sent to the cathode side of the stacks, where hydrogen is produced. Air is supplied to the anode side for thermal and safety reasons. At the system level, heat is recovered through heat exchangers on both the cathode and anode sides using outlet exhaust gases, while electrical heaters fine-tune the inlet gas temperatures. The hydrogen produced at the cathode side is then separated from water and compressed. Additional information regarding the model equations and assumptions can be found in **Appendix F3**.

From the modelling viewpoint of the ammonia synthesis loop, the condensation section is simplified to a single -40 °C equilibrium flash stage, aiding in estimating the overall cooling requirement. For simplicity, several black-box models are used considering only a specific energy consumption reported in literature. For Air Separation Unit (ASU) occurring typically by Pressure Swing Adsorption (PSA) or cryogenic air distillation, power consumption for the latter is typically in between 61 kWh/t_{N₂} to 160 kWh/t_{N₂} [6,19,36-38]. In the case of PEM electrolysis, an average specific energy consumption between 4 and 6 kWh/ Nm³ [6,12,39-40]. In our study a specific consumption of 4.2 kWh/ Nm³ (i.e. 46.7 kWh/kg) consistent to the values indicated by Schmidt et al. (2017) [40] and Rouwenhorst et al. (2019) [39]. Finally, considering the need for demineralized water in electrolysis, this study assumes a specific energy consumption of 4 kWh/m³ for reverse osmosis, within the typical range of 3.5-4.5 kWh/m³ [41]. Regarding other components, turbomachines (compressors and pumps) are modeled in Aspen Plus with assumed isentropic and mechanical efficiencies of 0.85 and 0.95, respectively, to determine outlet streams thermodynamic conditions and energy balance. Compressor intercoolers are set to maintain 25 °C, with a maximum pressure ratio of 3 per compression stage. Counter-current shell and tube heat exchangers are modeled using a shortcut method, and various design specifications were set to meet desired

constraints, such as the correct H_2/N_2 ratio. Further details on the flowsheet model are reported in **Appendix F4**, with main operating conditions and flowsheet assumptions summarized in **Table 8-3**.

Table 8-2: Recap of PtA processes investigated in the comparative analysis

Configuration	Electrolysis	Reactor	NH ₃ Separation
Option 1 PEM-TR-Cond.	PEM	TR	Condensation
Option 2 PEM-MR-Cond.	PEM	MR	Condensation
Option 3 PEM-MR (ideal)	PEM	MR (ideal)	-
Option 4 SOEC-MR-Cond.	SOEC	MR	Condensation

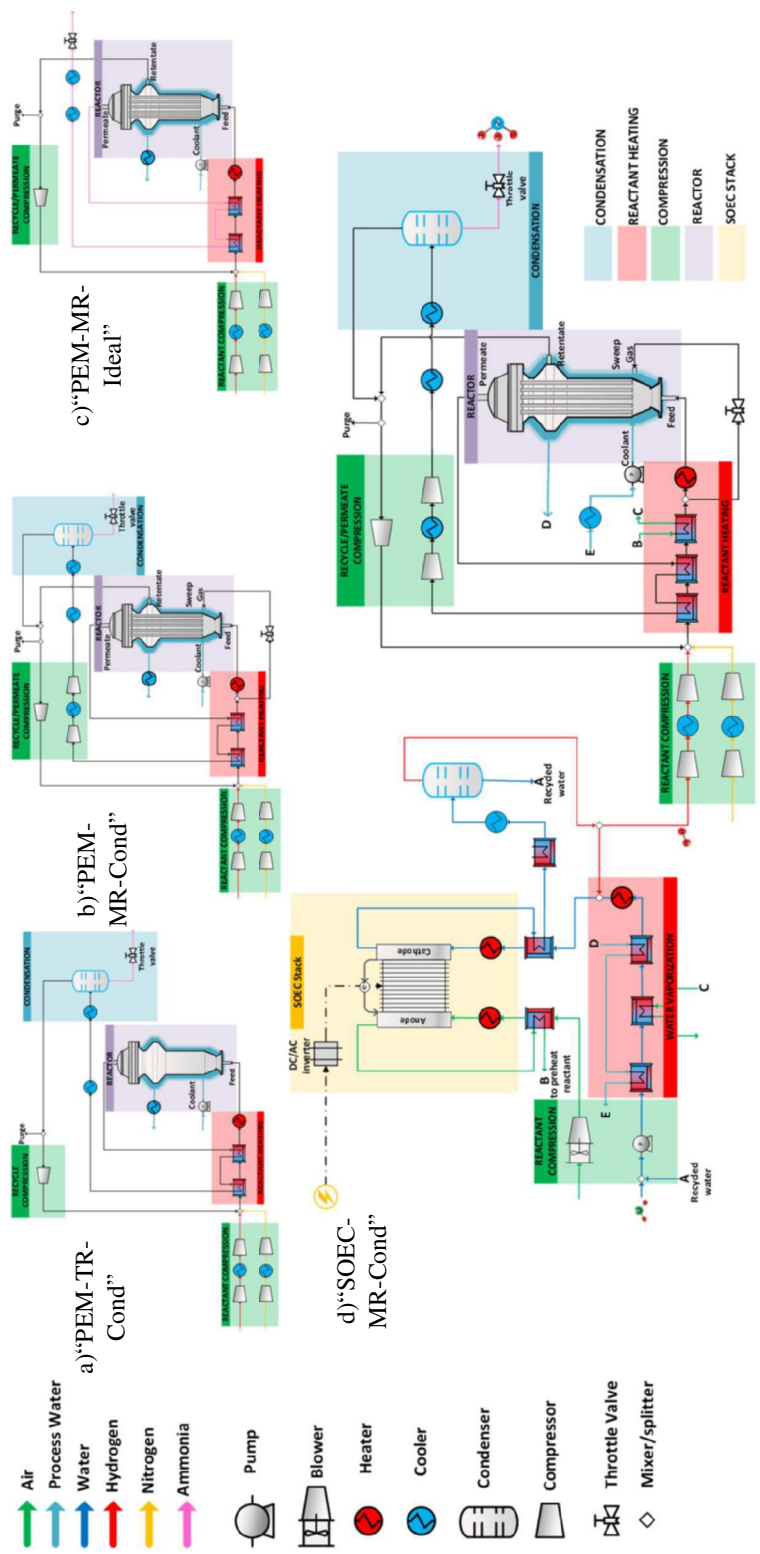


Figure 8-3: Proposed process configuration options compared in this study (a) Option 1: PEM-TR-Cond (b) Option 2: PEM-TR-Cond. (c) Option 3: PEM-MR (ideal) (d) Option 4: SOE-MR-Cond

Table 8-3: Recap of operating conditions and design parameters assumed in the base case scenario

Parameters	Unit	Value
Reactor operating conditions (base case)		
Reactor temperature	°C	360
Permeate & Retentate temperature inlet	°C	360
Pressure reaction side	Bar	70
Permeate pressure	Bar	70
H ₂ /N ₂	(mol/mol)	1.5
SW (sweep gas to feed molar flow ratio)	-	1
Heat exchangers		
Pressure drop in gas water heat exchanger (%)	Bar	0.1
Design Minimum ΔT in exchanger gas/liquid	°C	15
Minimum ΔT in exchanger gas/gas	°C	30
Heat transfer coefficient gas/gas	W/m ² /K	60
Heat transfer coefficient gas/liquid	W/m ² /K	70
Pump and compressors		
Pump isentropic efficiency/mechanical efficiency	%	70/90
Compressor/fan/blower isentropic efficiency	%	70/85
Vacuum pump isentropic efficiency/mechanical efficiency	%	70/85
Other units		
PEM specific consumption	kWh/Nm ³ _{H₂}	4.7 [39]
ASU specific consumption	kWh/t _{N₂}	119 [38]
Reverse Osmosis specific consumption	kWh/ m ³	4 [41]
General assumptions		
Purge fraction	%	1
Hydrogen produced by electrolysis	kmol/hr	85
SOEC stack		
Nominal Operating Temperature	°C	700 °C
Nominal Operating Current Density	A/cm ²	0.5
Operating Pressure	bar	1
Stack Pressure Drop	mbar	50
Single Cell voltage	V	1.29
Cell Power density	W/cm ²	0.645
Reactant Utilization	-	0.7

8.2.3. Performance indicators

The reactor's efficiency was assessed based on the conversion of N₂ as per Eq. 8.2 It is defined as the ratio of the nitrogen consumed by the synthesis reaction to the inlet nitrogen whilst taking into account the exchange of materials between the sweep gas and the reaction zone, including potential reactant loss or, conversely, the co-feeding of reactants (or the back permeation of reactants in the reaction zone) in adequation with similar work [42]. In addition two extra metrics are considered namely, the recovery of ammonia (Eq. 8.6) and the recovered ammonia flowrate (Eq. 8.7). Ammonia recovery is defined as the proportion of ammonia in the permeate relative to the total ammonia produced in the synthesis reaction. The recovered ammonia flowrate is simply the rate at which ammonia flows from the permeate side's outlet.

$$X_{N_2} = \frac{F_{N_2,in}^{Ret} - F_{N_2,out}^{Ret} + F_{N_2,tmb}}{F_{N_2,in}^{Ret} + F_{N_2,tmb}} \quad \text{Eq. 8.2}$$

$$F_{N_2,tmb} = F_{N_2,in}^{perm} - F_{N_2,out}^{perm} \quad N_2 \text{ transmembrane flow} \quad \text{Eq. 8.3}$$

$$F_{N_2,tmb}^* = 0 \text{ if } F_{N_2,tmb} \leq 0 \text{ Reactant loss} \quad \text{Eq. 8.4}$$

$$F_{N_2,tmb}^* = F_{N_2,tmb} \text{ if } F_{N_2,tmb} \geq 0 \text{ Reactant Co-feeding} \quad \text{Eq. 8.5}$$

$$Recovery_{NH_3} = \frac{F_{NH_3,out}^{Perm}}{F_{NH_3,out}^{Ret}} \quad \text{Eq. 8.6}$$

$$Recovered \text{ Ammonia flow} = \int_{A_p} F_{NH_3,out} dA_p \quad \text{Eq. 8.7}$$

In those equation $F_{i,in}$ and $F_{i,out}$ are the species molar flowrates at the inlet and outlets of the reactor, respectively. These metrics do not consider heat integration and auxiliaries' consumption of the overall plant. At the plant level, a PtA efficiency denoted (η_{PtA}) is defined in Eq. 8.8 as the ratio of the energy output associated to the produced ammonia by the total energy input required such as the electric consumptions of the system auxiliaries (i.e. compressors, pumps, control system).

$$\eta_{PtA} = \frac{F_{NH_3,produced} \times LHV_{NH_3}}{Energy \text{ consumption (fuel,electricity...)}} \quad \text{Eq. 8.8}$$

8.2.4. Cost estimates

An economic assessment is also conducted to evaluate and primarily contrast the cost of ammonia production using membrane reactors versus traditional reactors under varying operating conditions. In line with similar studies [43-46] and **Chapters 3** and **4**, a bottom-up approach is employed to determine the Total Plant Cost (TPC) as given in Eq 8.9 by dissecting the plant into its foundational equipment, and subsequently factoring installation, indirect, owner's, and contingency costs.

$$TPC = (\sum_i C_i) * (1 + \%_{TIC}) * (1 + \%_{IC}) * (1 + \%_{c\&oc}) \quad \text{Eq. 8.9}$$

The component prices are sourced from Turton et al. (2018) [47] and incorporate a correction factor for stainless steel material, which is necessary for ammonia due to its corrosive nature, are adjusted and updated using the CEPCI index method for considering price fluctuations like inflation, deflation. For this analysis, an index of 708 was used to adjust to the 2021 period which is one of the highest increase this index has seen (as shown **Appendix F5**). The TPC is converted in an annual operating cost using the Capital Charge Factor (CCF) as described in Eq. 8.10 as a function of the discount rate i and the plant lifetime n .

$$CCF = \sum_{j=1}^N \frac{1}{(1+i)^j} = \frac{i \times (1+i)^n}{(1+i)^n - 1} \quad \text{Eq. 8.10}$$

Subsequently, the levelized cost of ammonia (LCOA) is estimated following the established formula defined in Eq. 8.11. It is composed of the annualized TPC and the fixed and variable Operations and Maintenance denoted as $C_{O\&M,fix}$ and $C_{O\&M,var}$ which are determined by the expenses associated with consumables such as catalysts, reactants, water, and membranes, as well as maintenance, insurance, and labor costs, divided by the plant's productivity.

$$LCOA \left[\frac{\text{€}}{t} \right] = \frac{(TPC[\text{€}] * CCF[\%/year]) + C_{O\&M,fix}[\text{€}/year] + (C_{O\&M,var} \left[\frac{\text{€}}{year} \right] \times h_{eq})}{Production \ capacity \left[\frac{t}{year} \right] \times h_{eq} \left[\frac{h}{year} \right]} \quad \text{Eq. 8.11}$$

Labor costs, especially at a small scale, have a substantial impact on the final cost. The technique used to estimate operating labor requirements is also based on correlations from Turton et al. (2018)[47]. First, the operating labor requirement for chemical processing plants is evaluated by the following equation:

$$N_{OL} = (6.29 + 31.7P^2 + 0.23N_{np})^{0.5} \text{ Eq. 8.12}$$

where N_{OL} is the number of operators per shift, P is the number of processing steps involving the handling of particulate solids, such as transportation and distribution, particulate size control, and particulate removal, the value of P is zero in this study. N_{np} is the number of equipment, such as compressors, towers, heaters, exchangers. Then, the total number of operators can be estimated according to the following equation:

$$\text{Operating labor} = 4.5 \times N_{OL} \text{ Eq. 8.13}$$

The cost of operating labor can be calculated by operating labor multiplied by operator salary. The salary per operator is assumed to be 48600 €/year in this study. **Table 8-4** presents the key assumptions utilized for estimating the levelized costs in the base case scenario.

Table 8-4: Base case economic assumptions

O&M Fixed Cost	
Maintenance cost	0.02*TPC [44]
Insurance	0.025*TPC [44]
Operator salary	48k€/year
Calculated labor cost using Eq. 9 13	681352 €/year
O&M Variable	
Electricity cost	38 €/MWh
Cost of very low temperature refrigerant (-50°C)	14.12 \$/GJ [47]
Cost of Cooling tower water 30 °C-40 °C	0.378 \$/GJ [47]
Stack lifetime	91000 hr [38]
Catalyst cost Ruthenium	295 €/kg [14]
Catalyst lifetime	5 years[48]
Membrane lifetime	3 years [49]
General Assumptions	
Plant availability	0.65
Discount factor	8%
Operating lifetime	25 years[19]
Currency exchange rate	0.92 €/€
Calculated CCF using Eq. 9 10	0.0953
Component cost	
Membrane price	1950 €/m ² [49]
PEM cost	700 €/kWe
Hydrogen storage 200 bar cost	1050 \$/kg
H ₂ storage required	24 hr
Pressure swing adsorption cost	1315 €/kg/hr [38]
Battery cost	315 \$/KW [38]
TPC calculation	
% _{TIC}	80 [50]

% <i>IC</i>	14 [50]
% <i>C&OC</i>	16 [50]

8.2.5. Optimization

To compare the different process architectures, a multi-objective optimization was conducted using the Genetic Algorithm for Multi-Objective Optimization (MOGA) [51]. This approach aims to minimize costs while maximizing efficiency by varying design parameters (e.g., number of membranes) and operating conditions (e.g., pressures, temperatures, and flowrates). In the literature, trade-offs between these two key performance indicators (KPIs) [12,19] are commonly observed, making this approach particularly relevant. Due to the computational complexity of the flowsheet, involving seven solvers to resolve tear streams and design specifications in a sequential modular approach within Aspen Plus, the "MAXEVAL" parameter was capped at 100 evaluations to ensure computational feasibility. Despite this limitation, the approach enables the refinement of an initial heuristic guess.

8.3. Results and discussion

8.3.1. Model Validations

The modeling of catalytic reactors is heavily reliant on the accurate consideration of reaction kinetics, which can have a substantial impact on equipment size and cost. The kinetic model was validated using the results from Rossetti et al., (2006) [31]-a reference used by several authors in previous studies [14, 27]-using a packed bed reactor under specified flow rates and isothermal conditions. **Figure 8-4** illustrates the validation results for various residence times, showing the correct implementation of the kinetics model. Ammonia production peaks at a temperature determined by gas hourly space velocity (GHSV) and undergoes a transition from kinetic to equilibrium-limited regimes due to the reaction's exothermic nature. As already observed by Tripodi et al., (2018) [27] the Gillespie equilibrium correlation implemented in the kinetic model forecasts a lower ammonia equilibrium conversion compared to thermodynamic model predictions, calculated using Aspen Plus' 'RGibbs' reactor model (under those conditions).

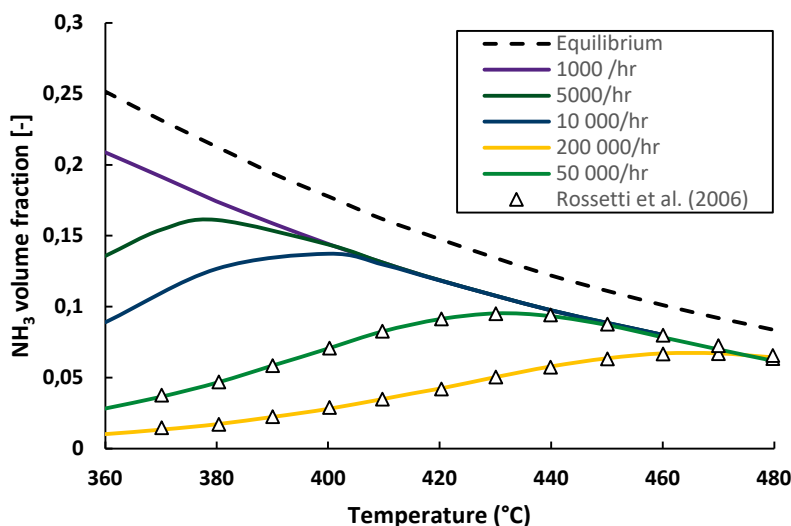


Figure 8-4: Validation of the kinetic model based on the work of Rossetti et al. (2006) [31] (triangle markers) based on an isothermal plug flow reactor model, across the full range of temperatures, and space velocities explored experimentally (GHSV=1000-200000 h⁻¹, T=360-480 °C, H₂/N₂=1.5, P=70 bar)

8.3.2. Sensitivity at the reactor level

In **Figure 8-5**, the influence of membrane properties, specifically NH₃-H₂ selectivity and permeance, on conversion is illustrated across various pressure drops and SW ratios. As anticipated, at the highest driving force (i.e. highest pressure drop and SW ratio in our case), the membrane reactor (MR) achieves conversions over 90% higher than those of the traditional reactor (TR), demonstrating the efficiency of the MR process. The plot also illustrates a significant increase in conversion with NH₃-H₂ selectivity up to a threshold at around 10-20, regardless of operating conditions. Beyond this threshold, enhancements in selectivity no longer impact conversion due to the establishment of an equilibrium between the reaction and permeation zones. Thus, it appears that the performance is mainly influenced by the ammonia permeance, eliminating the requirement for a highly selective membrane. These observations are consistent with findings from Zhang et al. (2021) [1] and Poto et al. (2020) study [42]. An exception can however be noticed when there is no pressure drop across the membrane, resulting in a reversed trend where higher conversions are achieved at the lowest selectivity. This condition nearly eliminates reactant loss, and in some cases, encourages co-feeding, and sometimes, promote the co-feeding, (i.e. to a net permeation of H₂ and N₂ from the permeation to the reaction zone, especially prevalent at higher sweep gas ratios). This phenomenon is clearly illustrated in **Figure 8-6**. As expected, the conversion rate demonstrates significant sensitivity to permeance, showing a diminishing effect at higher values. In **Figure 8-7**, hydrogen selectivity is kept constant at 20, while both permeance and GHSV are varied to study their impacts on several KPIs. As anticipated, a decline in conversion is observed in both MR and TR

configurations with higher GHSV, attributed to the reduced residence time. Conversely, an increase in total ammonia production is noted under these conditions. As for the recovered ammonia flow rate, it initially increases, reaching a peak at GHSV of 1100 h^{-1} , and then declines with further GHSV increments. At elevated GHSV, the membrane struggles to permeate the produced ammonia, resulting in a reduction in the recovered H_2 flowrate. Under these conditions, the process is limited by the mass transfer across the membrane.

Ending the investigation at the reactor stage, a theoretical case is examined to establish the lowest selectivity needed for ammonia over hydrogen, along with the essential permeance, to reach a 99% pure permeate without the need for further downstream processing. To accomplish this, a reactor operating without sweep gas is considered, which helps prevent dilution of the permeate, although it eliminates a source of driving force. This requires a higher pressure drop across the membrane which also put more mechanical stress on the membrane. In **Figure 8-8**, it seems that at least 60 bar across the membrane are required, albeit the selectivity threshold beyond 1000 are elusive based on existing materials. This makes mandatory an additional step by condensation.

All in all, this analysis just highlighted that for processes using a sweep gas of similar composition as the feed, highly selective membranes are not crucial, contrasting with scenarios needing pure ammonia permeate (where selective membranes are more critical). Additional sensitivity analyses are presented in **Appendices F6**. These analyses include an examination of the impacts of temperature changes, non-isothermal profiles, the effect of membrane coverage, and details on the transmembrane flows along the length of the reactor.

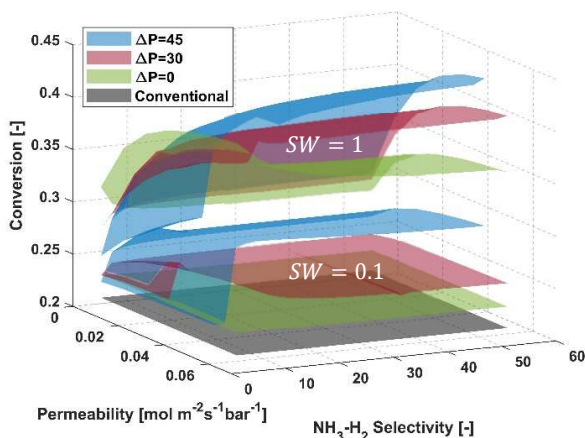


Figure 8-5: Conversion obtained with respect to membrane properties (GHSV= 500 h^{-1} , $T=360 \text{ }^{\circ}\text{C}$, H_2/N_2 ratio=1.5, $P_{\text{ref}}=70 \text{ bar}$) for various operating pressure drop and SW ratio. The selectivity of nitrogen is taken as three time the one of hydrogen and an isothermal model is used.

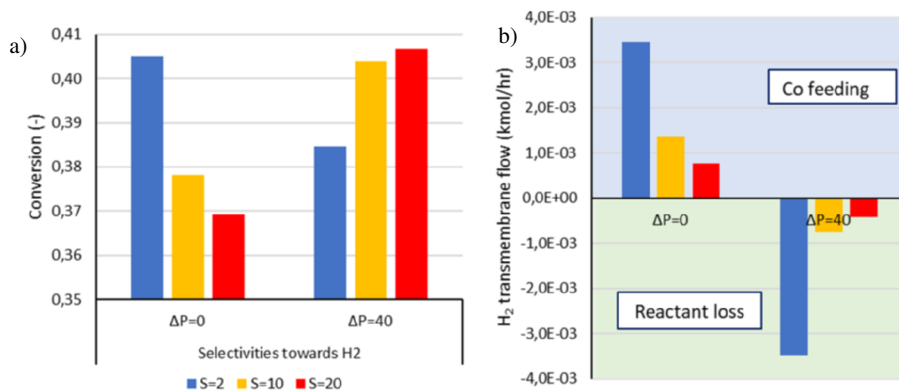


Figure 8-6: (a) Conversion obtained for three Selectivity NH₃-H₂ (2, 10 and 20) (b) Associated transmembrane H₂ flux (GHSV=500 h⁻¹, T=360 °C, P_{ret}=70 bar, H₂/N₂ ratio = 1.5, SW=1, NH₃ Permeance =0.5 mol m⁻²s⁻¹bar) The selectivity NH₃-N₂ is taken as three time the one of hydrogen and an isothermal model is used.

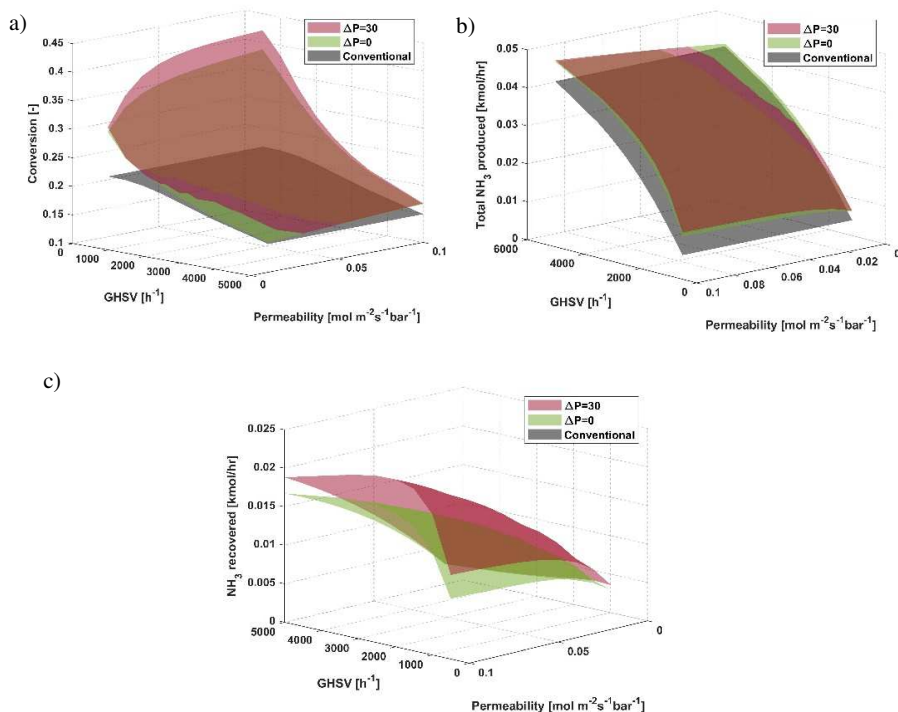


Figure 8-7: Impact of GHSV: (a) Conversion (b) Total NH₃ produced (c) Total NH₃ recovered (selectivity NH₃-H₂=20; T=360 °C, H₂/N₂ ratio = 1.5, SW=1, P_{ret}=70 bar) for various pressure drop across the membrane. The selectivity towards nitrogen is taken as three time the one of hydrogen and an Isothermal model is used.

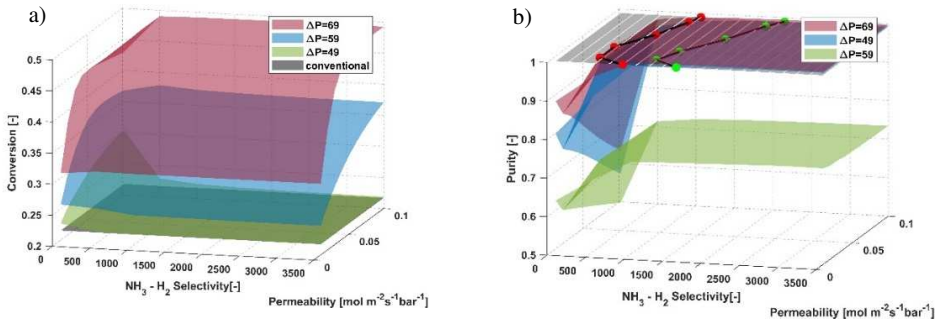
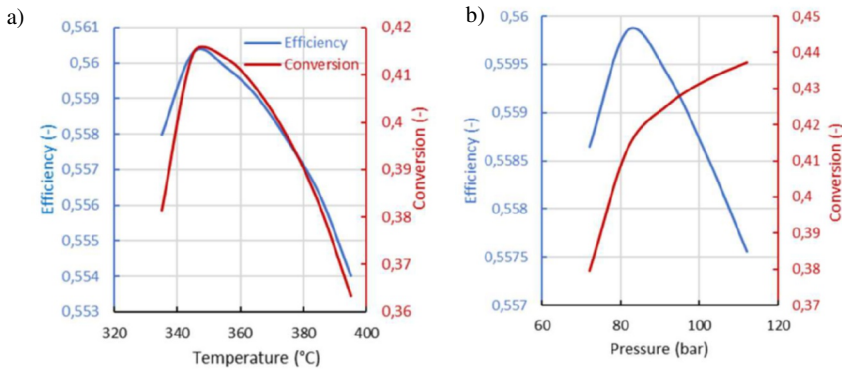


Figure 8-8: Selectivity required to reach targeted purity in the permeate stream of the membrane reactor (for this case no sweep gas is implemented) The selectivity towards nitrogen is taken as three time the one of hydrogen and an Isothermal model is used. (a) Conversion (b) Purity of the permeate stream

8.3.3. One way sensitivity analysis at the process level

A one-way sensitivity analysis is carried out at different operating conditions (reactor pressure and temperature and SW ratio) in **Figure 8-9**. Except for SW, the reactor temperature and pressure show a trade-off behaviour. Then the optimum should be accurately found depending on the layout considered and on the economic assumptions used in the analysis.



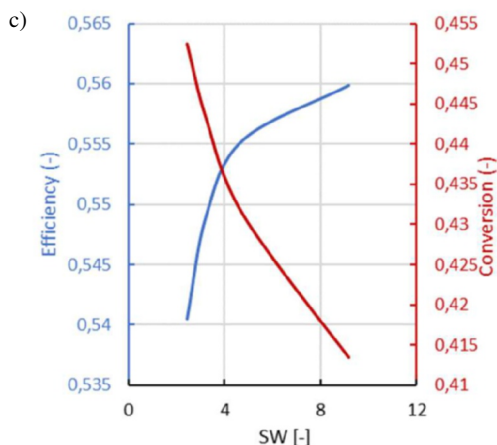


Figure 8-9: Sensitivity on (a) temperature, (b) retentate pressure, and (c) sweep gas ratio using PEM-MR-Cond system (Selectivity $\text{NH}_3\text{-H}_2=50$; $T=360\text{ }^\circ\text{C}$, H_2/N_2 ratio = 1.5, $\text{SW}=1$, $P_{\text{ret}}=81\text{ bar}$, $P_{\text{perm}}=15\text{ bar}$)

8.3.4. Optimization at the process level

The technology's performance is now evaluated at the process flowsheet level, considering both economic and energy factors. In order to help identify the best design and operating parameters for each process, stochastic optimization is used to try to reduce LCOA and maximize energy efficiency.

As global observations, the analysis reveals that both cost and efficiency metrics are reasonably similarly ranged, with energy efficiency between 51% and 59%, and the LCOA (from base case assumptions) 1050 to 1150 €/ton. **Figure 8-10** illustrates the trade-offs between cost and efficiency across the different configurations studied, specifically highlighting the feasible solutions obtained for the "PEM-MR-Condensation" setup. For this system, the optimization resulted in a reduced LCOA by 0.7% and increased energy efficiency by 3.9% compared to the initial population.

Table 8-5 details the variable limits used in the algorithms, summarizing their optimal values and the Key Performance Indicators (KPIs) achieved for each configuration. In terms of parameters bounds, the selectivity of ammonia over hydrogen was optimistically set between 1 and 400, but the algorithm didn't converge up to this upper limit, confirming the minimal impact of high selectivity values on KPIs. Unlike permeance, which consistently hit its upper limit. Finally, it was observed that the optimal GHSV values for Membrane Reactors (MRs) were significantly lower, about one-third, compared to those achieved with Traditional Reactors (TRs), indicating that operating MR systems at high space velocities is not a viable option.

Focusing on efficiency, using the "PEM-TR-Cond" system as a benchmark, the "PEM-MR-Cond" process shows an improvement of 8%, while the integration of the same process with SOE technology demonstrates a 16% improvement. **Figure 8-11.a** presents the distribution of specific energy consumption in kWh/kg_{NH₃}. In PEM-based systems, the electrolyzer is a major component, contributing approximately 85% of the specific energy requirement, while in SOEC systems, its contribution is about 63%. A notable observation is that the "PEM-MR-cond" system exhibits slightly lower energy consumption for water electrolysis due to its marginally higher ammonia production. Focusing on the benefits of the membrane reactor, the MR reactor significantly reduces cooling requirements by 70%, as only the permeate needs condensing, and it also cuts down the heating requirement by 50%. The study indicates that specific energy consumption ranges from 9.98 MWh/t_{NH₃} in the "PEM-MR-Cond" system to 8.45 MWh/t_{NH₃} in the "SOEC-MR-Condensation" system. These results align with existing literature; for instance, Quintero et al. (2022) [12] identified the optimal process with the lowest specific energy consumption in the optimal Ru case, at 10.67 kWh/kg_{NH₃}, considering PEM electrolysis. Cinti et al. (2017) [18] reported a specific energy consumption of 8.29 kWh/kg_{NH₃} for an "SOEC-TR-Cond" system and 14 kWh/kg_{NH₃} for an "AEC-TR-Cond" system.

Moreover, Haldor Topsoe has reported a new technology estimated to produce green ammonia at approximately 7.2 kWh/kg_{NH₃} [52]. Overall, these systems demonstrate respectable performance, albeit less energy-efficient compared to the best available current (fossil-based) technologies, such as a state-of-the-art, world-scale SMR-HB plant, which operates at roughly 27.4 GJ/t of NH₃ (7.61 kWh/kg_{NH₃}) [53].

Economically, **Figure 8-11.b** shows that under baseline assumptions, the LCOA for the MR process is nearly similar to the reference process, being about 2% higher, and increases by 10% when integrated with an SOEC system. Comparing with other studies, Osman et al. (2020) [28] reported an LCOA of approximately 653 €/t for a production scale of 1183 tons/day. Zhang et al. (2020) [19] found an LCOA of around 450 €/t for a production of about 130 tons/day, and Quintero et al. (2022) [12] estimated an LCOA of roughly 766 €/t for a production of 11.6 tons/day with hydrogen from PEM electrolysis. Nayak-Luke et al. (2018) [9] reported an LCOA near 1200 €/t using offshore wind for electricity. These comparisons, while valuable, are somewhat limited due to varying assumptions and methodologies in cost calculation. Overall, the reported values appear reasonable considering the small scale of the installation, though they are somewhat on the higher spectrum. In addition, for context, the price of "grey" ammonia was 250 euros per ton NH₃ in January 2021 and increased to

1500 euros per ton NH_3 by April 2022 in Western Europe [5]. The LCOA values identified in this study fall within this range.

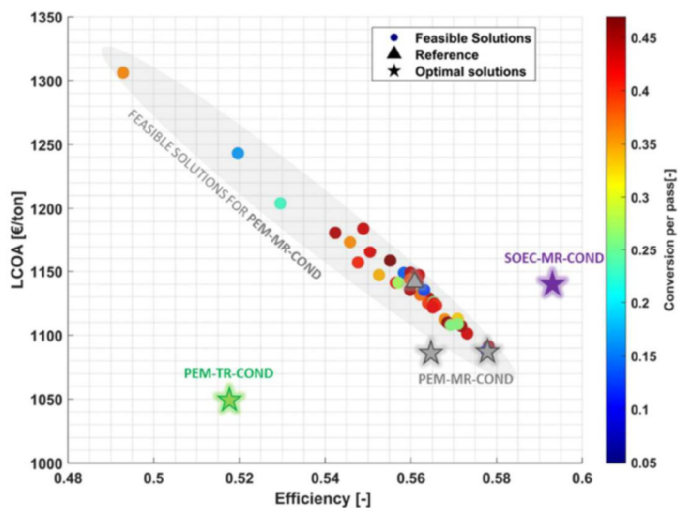
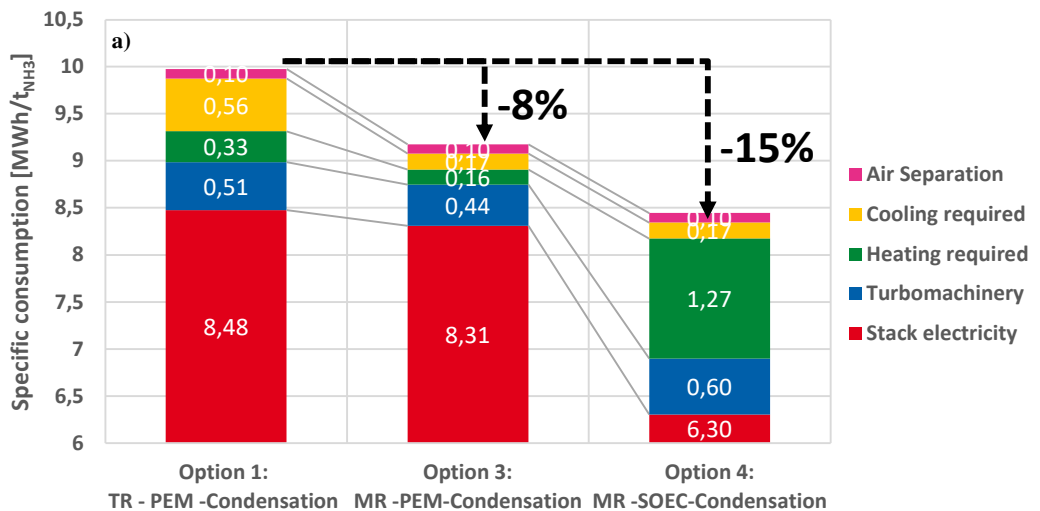


Figure 8-10: Trade-offs between the ammonia production cost and system energy efficiency & N_2 Conversion Effects. Red stars mark optimal solutions; colored dots indicate all feasible solutions. The triangle represents the initial population for the PEM-MR-COND systems, while stars denote optimal solutions for each configuration.

Table 8-5: Summary of the optimal operating conditions and design parameters and KPIs for each systems (Condensation temperature = -40 °C; Purge fraction=1%; fixed hydrogen inlet =85 kmol/hr)

<i>System</i>		<i>PEM-TR-COND</i>	<i>PEM-MR-COND</i>	<i>SOE-MR-COND</i>
<i>Electrolysis</i>		<i>PEM</i>	<i>PEM</i>	<i>SOE</i>
<i>Reactor</i>		<i>TR</i>	<i>MR</i>	<i>MR</i>
<i>Separation</i>		<i>Condensation</i>	<i>Condensation</i>	<i>Condensation</i>
Parameters and variables	Reactor temperature ∈ [350-410] (°C)	377	355	367
	Pressure ∈ [60-100] (bar)	77	81.66	87
	Number of membranes for MRs or tubes for the TR ∈ [1100-2300] (-)	1106	1942	2196
	SW ∈ [3-10] (-)	N/A	8.09	4.0
	Sweep gas pressure ∈ [3-25] (bar)	N/A	10.1	15.29
	Permeance ∈ [0.04-0.1] $\text{mol m}^{-2} \text{s}^{-1} \text{bar}$	N/A	0.1 (upper bound)	0.1 (upper bound)
	Selectivity $\text{NH}_3\text{-H}_2$ [-] ∈ [1-400]	N/A	360	360
Results	Efficiency [-]	0.517	0.57	0.59
	Specific consumptions [$\text{MWh/t}_{\text{NH}_3}$]	9.98	9.17	8.45
	GHSV (h^{-1})	2508	476	416
	Conversion per pass [-]	0.22	0.45	0.44
	Recovery per pass [-]	-	0.85	0.87
	NH_3 Production [t/days]	22.8	23.25	23.05
	LCOA [$\text{€}/\text{t}$]	1057	1070	1165



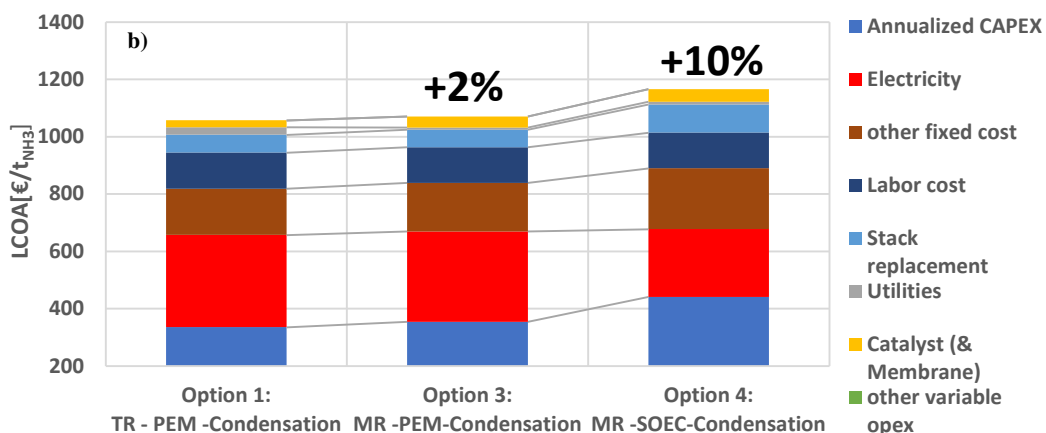


Figure 8-11: Breakdown of the (a) Specific energy consumption and (b) LCOA at optimal conditions under our baseline assumptions.

8.4. Conclusion

This study aimed to investigate the potentiality of catalytic membrane reactor (CMR) for ammonia production from renewable electricity. The assessment is carried out both at the reactor level and at the ammonia production plant level to outline the advantage of the innovative technology.

- A reactor model for ammonia production using a ruthenium catalyst-based CMR was developed, analyzing a range of membrane properties and operating conditions. It showed over 90% higher ammonia conversion compared to conventional reactors. This analysis confirmed that in processes employing a sweep gas akin to the feed, the necessity for highly selective membranes is diminished. Specifically, beyond a selectivity threshold towards hydrogen of 10-20, both the degree of conversion and recovery tend to be generally independent of the membrane's selectivity. However, for producing pure ammonia permeate, highly selective membranes (>1000 towards H₂) are found essential making this alternative elusive based on existing membranes.
- As this approach, however, does not fully consider energy losses related to creating driving force, recompression, and permeate purification, the technology's effectiveness was assessed at the PtA (Power-to-Ammonia) process level. The minimization of the LCOA (Levelized Cost of Ammonia) and the maximization of the energy efficiency allowed to obtain the optimal design and operating conditions for each process. The adoption of membrane reactor in this study, increased the system efficiency by around 8% with respect to reference cases (i.e. a PtA process using TR) while ~15 % enhancement is achieved with this process when using SOEC technology.

- Focusing on the economic results, considering our baseline assumptions and process architectures, the MR process showed a marginal 2% increase in cost over the reference process, and when incorporated with an SOEC (Solid Oxide Electrolysis Cell) system a 10 % increase in LCOA was observed.

These findings suggest that while membrane reactors are a promising technology for ammonia production at the unit operation level, their appeal diminishes when integrated into a traditional power-to-ammonia process when traditional condensation methods are used. Future research should focus on replacing the condensation process with a lower-pressure purification method to improve efficiency and reduce costs. Additionally, further refinement in the model of the membrane reactors would be needed to investigate aspects overlooked in this study, such as the estimation of concentration polarization and the impact of composition and temperature on permeation.

8.5. References

- [1] Z. Zhang, J.D. Way, C.A. Wolden, Design and operational considerations of catalytic membrane reactors for ammonia synthesis, *AIChE J* 67 (2021). <https://doi.org/10.1002/aic.17259>.
- [2] A. Bhowan, E.L. Cussler, Mechanism for selective ammonia transport through poly(vinylammonium thiocyanate) membranes, *J. Am. Chem. Soc.* 113 (1991) 742–749. <https://doi.org/10.1021/ja00003a002>.
- [3] M. Kanezashi, A. Yamamoto, T. Yoshioka, T. Tsuru, Characteristics of ammonia permeation through porous silica membranes, *AIChE J.* (2009) NA-NA. <https://doi.org/10.1002/aic.12059>.
- [4] O. Camus, S. Perera, B. Crittenden, Y.C. Van Delft, D.F. Meyer, P. P. A. C. Pex, I. Kumakiri, S. Miachon, J.-A. Dalmon, S. Tennison, P. Chanaud, E. Groensmit, W. Nobel, Ceramic membranes for ammonia recovery, *AIChE J.* 52 (2006) 2055–2065. <https://doi.org/10.1002/aic.10800>.
- [5] N. Champion, H. Nami, P.R. Swisher, P. Vang Hendriksen, M. Münster, Techno-economic assessment of green ammonia production with different wind and solar potentials, *Renewable and Sustainable Energy Reviews* 173 (2023) 113057. <https://doi.org/10.1016/j.rser.2022.113057>.
- [6] H. Bouaboula, M. Ouikhalfan, I. Saadoun, J. Chaouki, A. Zaabout, Y. Belmabkhout, Addressing sustainable energy intermittence for green ammonia production, *Energy Reports* 9 (2023) 4507–4517. <https://doi.org/10.1016/j.egy.2023.03.093>.
- [7] C. Fúnez Guerra, L. Reyes-Bozo, E. Vyhmeister, M. Jaén Caparrós, J.L. Salazar, C. Clemente-Jul, Technical-economic analysis for a green ammonia production plant in Chile and its subsequent transport to Japan, *Renewable Energy* 157 (2020) 404–414. <https://doi.org/10.1016/j.renene.2020.05.041>.
- [8] M. Fasihi, R. Weiss, J. Savolainen, C. Breyer, Global potential of green ammonia based on hybrid PV-wind power plants, *Applied Energy* 294 (2021) 116170. <https://doi.org/10.1016/j.apenergy.2020.116170>.
- [9] R. Nayak-Luke, R. Bañares-Alcántara, I. Wilkinson, “Green” Ammonia: Impact of Renewable Energy Intermittency on Plant Sizing and Levelized Cost of Ammonia, *Ind. Eng. Chem. Res.* 57 (2018) 14607–14616. <https://doi.org/10.1021/acs.iecr.8b02447>.
- [10] J. Armijo, C. Philibert, Flexible production of green hydrogen and ammonia from variable solar and wind energy: Case study of Chile and Argentina, *International Journal of Hydrogen Energy* 45 (2020) 1541–1558. <https://doi.org/10.1016/j.ijhydene.2019.11.028>.

- [11] R.M. Nayak-Luke, R. Bañares-Alcántara, Techno-economic viability of islanded green ammonia as a carbon-free energy vector and as a substitute for conventional production, *Energy Environ. Sci.* 13 (2020) 2957–2966. <https://doi.org/10.1039/D0EE01707H>.
- [12] C. Quintero-Masselski, J.-F. Portha, L. Falk, Conception and optimization of an ammonia synthesis superstructure for energy storage, *Chemical Engineering Research and Design* 177 (2022) 826–842. <https://doi.org/10.1016/j.cherd.2021.11.039>.
- [13] J.R. Gomez, J. Baca, F. Garzon, Techno-economic analysis and life cycle assessment for electrochemical ammonia production using proton conducting membrane, *International Journal of Hydrogen Energy* 45 (2020) 721–737. <https://doi.org/10.1016/j.ijhydene.2019.10.174>.
- [14] M. Yoshida, T. Ogawa, Y. Imamura, K.N. Ishihara, Economies of scale in ammonia synthesis loops embedded with iron- and ruthenium-based catalysts, *International Journal of Hydrogen Energy* 46 (2021) 28840–28854. <https://doi.org/10.1016/j.ijhydene.2020.12.081>.
- [15] B. Lin, T. Wiesner, M. Malmali, Performance of a Small-Scale Haber Process: A Techno-Economic Analysis, *ACS Sustainable Chem. Eng.* 8 (2020) 15517–15531. <https://doi.org/10.1021/acssuschemeng.0c04313>.
- [16] H. Ghiasirad, M. Khalili, F.K. Bahnamiri, P. Pakzad, A. Skorek-Osikowska, Techno-economic comparison of power-to-ammonia and biomass-to-Ammonia plants using electrolyzer, CO₂ capture and water-gas-shift membrane reactor, *Journal of the Taiwan Institute of Chemical Engineers* 151 (2023) 105097. <https://doi.org/10.1016/j.jtice.2023.105097>.
- [17] H. Ishaq, I. Dincer, Design and simulation of a new cascaded ammonia synthesis system driven by renewables, *Sustainable Energy Technologies and Assessments* 40 (2020) 100725. <https://doi.org/10.1016/j.seta.2020.100725>.
- [18] G. Cinti, D. Frattini, E. Jannelli, U. Desideri, G. Bidini, Coupling Solid Oxide Electrolyser (SOE) and ammonia production plant, *Applied Energy* 192 (2017) 466–476. <https://doi.org/10.1016/j.apenergy.2016.09.026>.
- [19] H. Zhang, L. Wang, J. Van herle, F. Maréchal, U. Desideri, Techno-economic comparison of green ammonia production processes, *Applied Energy* 259 (2020) 114135. <https://doi.org/10.1016/j.apenergy.2019.114135>.
- [20] C.S. QUINTERO-MASSIELSKI, Conception des procédés par optimisation de superstructure pour l'usine du futur (PRO-FUTUR), UNIVERSITÉ DE LORRAINE, 2022.
- [21] S. Padinjarekutt, H. Li, S. Ren, P. Ramesh, F. Zhou, S. Li, G. Belfort, M. Yu, Na⁺-gated nanochannel membrane for highly selective ammonia (NH₃) separation in the Haber-Bosch process, *Chemical Engineering Journal* 454 (2023) 139998. <https://doi.org/10.1016/j.cej.2022.139998>.
- [22] W.-W. Yan, U. Anggarini, H.-C. Bai, H. Nagasawa, M. Kanezashi, T. Tsuru, Enhanced NH₃ permeation of bis[3-(trimethoxysilyl)propyl] amine membranes via coordination with metals, *Journal of Membrane Science* 678 (2023) 121665. <https://doi.org/10.1016/j.memsci.2023.121665>.
- [23] K. Wakimoto, W.-W. Yan, N. Moriyama, H. Nagasawa, M. Kanezashi, T. Tsuru, Ammonia permeation of fluorinated sulfonic acid polymer/ceramic composite membranes, *Journal of Membrane Science* 658 (2022) 120718. <https://doi.org/10.1016/j.memsci.2022.120718>.
- [24] Q. Wei, J.M. Lucero, J.M. Crawford, J.D. Way, C.A. Wolden, M.A. Carreon, Ammonia separation from N₂ and H₂ over LTA zeolitic imidazolate framework membranes, *Journal of Membrane Science* 623 (2021) 119078. <https://doi.org/10.1016/j.memsci.2021.119078>.
- [25] X. Duan, D. Kim, K. Narasimharao, S. Al-Thabaiti, M. Tsapatsis, High-performance ammonia-selective MFI nanosheet membranes, *Chem. Commun.* 57 (2021) 580–582. <https://doi.org/10.1039/D0CC07217F>.
- [26] V. Tricoli, E.L. Cussler, Ammonia selective hollow fibers, *Journal of Membrane Science* 104 (1995) 19–26. [https://doi.org/10.1016/0376-7388\(94\)00208-G](https://doi.org/10.1016/0376-7388(94)00208-G).
- [27] A. Tripodi, M. Compagnoni, E. Bahadori, I. Rossetti, Process simulation of ammonia synthesis over optimized Ru/C catalyst and multibed Fe + Ru configurations, *Journal of*

- Industrial and Engineering Chemistry 66 (2018) 176–186. <https://doi.org/10.1016/j.jiec.2018.05.027>.
- [28] O. Osman, S. Sgouridis, A. Sleptchenko, Scaling the production of renewable ammonia: A techno-economic optimization applied in regions with high insolation, *Journal of Cleaner Production* 271 (2020) 121627. <https://doi.org/10.1016/j.jclepro.2020.121627>.
- [29] A. Mourgues, J. Sanchez, Theoretical analysis of concentration polarization in membrane modules for gas separation with feed inside the hollow-fibers, *Journal of Membrane Science* 252 (2005) 133–144. <https://doi.org/10.1016/j.memsci.2004.11.024>.
- [30] S. Poto, H. Van Den Bogaard, F. Gallucci, M. Fernanda Neira d'Angelo, Evaluation of the relevant mass and heat transfer phenomena in a packed bed membrane reactor for the direct conversion of CO₂ to dimethyl ether, *Fuel* 350 (2023) 128783. <https://doi.org/10.1016/j.fuel.2023.128783>.
- [31] I. Rossetti, N. Pernicone, F. Ferrero, L. Forni, Kinetic study of Ammonia Synthesis on a Promoted Ru/C Catalyst, *Ind. Eng. Chem. Res.* 45 (2006) 4150–4155.
- [32] J. Dorthe, A marine fuel standard for Ammonia - an engine designers perspective, (2020). <https://www.ammoniaenergy.org/wp-content/uploads/2020/12/Dorthe-Jacobsen.pdf> (accessed November 9, 2023).
- [33] J. Atchison, A Fuel Standard for Ammonia: panel wrap-up from the Ammonia Energy Conference 2020, *Ammonia Energy Association* (2020). <https://www.ammoniaenergy.org/articles/a-fuel-standard-for-ammonia-panel-wrap-up-from-the-ammonia-energy-conference-2020/> (accessed November 9, 2023).
- [34] D. Richardson, Ammonia Fuel Standard: Where do we go from here?, (2020). <https://www.ammoniaenergy.org/wp-content/uploads/2020/12/Dave-Richardson.pdf> (accessed November 10, 2020).
- [35] J. Tallgren, O. Himanen, M. Noponen, Experimental Characterization of Low Temperature Solid Oxide Cell Stack, *ECS Trans.* 78 (2017) 3103–3111. <https://doi.org/10.1149/07801.3103ecst>.
- [36] A.G. Dana, O. Elishav, A. Bardow, G.E. Shter, G.S. Grader, Nitrogen-Based Fuels: A Power-to-Fuel to Power analysis, *Angewandte Chemie* 55 (2016) 8769–9096.
- [37] Morgan, Techno-Economic Feasibility Study of Ammonia Plants Powered by Offshore Wind, (2021). <https://doi.org/10.7275/11KT-3F59>.
- [38] Z. Cesaro, M. Ives, R. Nayak-Luke, M. Mason, R. Bañares-Alcántara, Ammonia to power: Forecasting the leveled cost of electricity from green ammonia in large-scale power plants, *Applied Energy* 282 (2021) 116009. <https://doi.org/10.1016/j.apenergy.2020.116009>.
- [39] K.H.R. Rouwenhorst, A.G.J. Van Der Ham, G. Mul, S.R.A. Kersten, Islanded ammonia power systems: Technology review & conceptual process design, *Renewable and Sustainable Energy Reviews* 114 (2019) 109339. <https://doi.org/10.1016/j.rser.2019.109339>.
- [40] O. Schmidt, A. Gambhir, I. Staffell, A. Hawkes, J. Nelson, S. Few, Future cost and performance of water electrolysis: An expert elicitation study, *International Journal of Hydrogen Energy* 42 (2017) 30470–30492. <https://doi.org/10.1016/j.ijhydene.2017.10.045>.
- [41] J. Kim, K. Park, D.R. Yang, S. Hong, A comprehensive review of energy consumption of seawater reverse osmosis desalination plants, *Applied Energy* 254 (2019) 113652. <https://doi.org/10.1016/j.apenergy.2019.113652>.
- [42] S. Poto, F. Gallucci, M. Fernanda Neira d'Angelo, Direct conversion of CO₂ to dimethyl ether in a fixed bed membrane reactor: Influence of membrane properties and process conditions, *Fuel* 302 (2021) 121080. <https://doi.org/10.1016/j.fuel.2021.121080>.
- [43] S. Richard, A. Ramirez Santos, P. Olivier, F. Gallucci, Techno-economic analysis of ammonia cracking for large scale power generation, *International Journal of Hydrogen Energy* 71 (2024) 571–587. <https://doi.org/10.1016/j.ijhydene.2024.05.308>.
- [44] G. Di Marcobardardino, S. Foresti, M. Binotti, G. Manzolini, Potentiality of a biogas membrane reformer for decentralized hydrogen production, *Chemical Engineering and Processing - Process Intensification* 129 (2018) 131–141. <https://doi.org/10.1016/j.cep.2018.04.023>.

- [45] M. Ongis, G. Di Marcoberardino, G. Manzolini, F. Gallucci, M. Binotti, Membrane reactors for green hydrogen production from biogas and biomethane: A techno-economic assessment, *International Journal of Hydrogen Energy* (2023) S0360319923005700. <https://doi.org/10.1016/j.ijhydene.2023.01.310>.
- [46] S. Richard, A. Ramirez Santos, F. Gallucci, PEM gensets using membrane reactors technologies: An economic comparison among different e-fuels, *International Journal of Hydrogen Energy* (2023) S0360319923032913. <https://doi.org/10.1016/j.ijhydene.2023.06.312>.
- [47] R. Turton, ed., *Analysis, synthesis, and design of chemical processes*, 5th edition, Prentice Hall, Boston, 2018.
- [48] G. Di Marcoberardino, S. Foresti, M. Binotti, G. Manzolini, Potentiality of a biogas membrane reformer for decentralized hydrogen production, *Chemical Engineering and Processing - Process Intensification* 129 (2018) 131–141. <https://doi.org/10.1016/j.cep.2018.04.023>.
- [49] M. Nordio, S.A. Wassie, M. Van Sint Annaland, D.A. Pacheco Tanaka, J.L. Viviente Sole, F. Gallucci, Techno-economic evaluation on a hybrid technology for low hydrogen concentration separation and purification from natural gas grid, *International Journal of Hydrogen Energy* 46 (2021) 23417–23435. <https://doi.org/10.1016/j.ijhydene.2020.05.009>.
- [50] V. Spallina, D. Pandolfo, A. Battistella, M.C. Romano, M. Van Sint Annaland, F. Gallucci, Techno-economic assessment of membrane assisted fluidized bed reactors for pure H₂ production with CO₂ capture, *Energy Conversion and Management* 120 (2016) 257–273. <https://doi.org/10.1016/j.enconman.2016.04.073>.
- [51] MathWorks Inc., *Genetic Algorithm Function Documentation*, (2023). <https://fr.mathworks.com/discovery/genetic-algorithm.html>.
- [52] T. Brown, Green ammonia: Haldor Topsoe's solid oxide electrolyzer, *Ammonia Energy Association* (2019). <https://www.ammoniaenergy.org/articles/green-ammonia-haldor-topsoes-solid-oxide-electrolyzer/> (accessed November 25, 2023).
- [53] C. Smith, A.K. Hill, L. Torrente-Murciano, Current and future role of Haber–Bosch ammonia in a carbon-free energy landscape, *Environmental Science* (2020) 14.
- [54] H. Hamed, T. Brinkmann, Rigorous and Customizable 1D Simulation Framework for Membrane Reactors to, in *Principle, Enhance Synthetic Methanol Production*, *ACS Sustainable Chem. Eng.* 9 (2021) 7620–7629. <https://doi.org/10.1021/acsschemeng.1c01677>.
- [55] A.G. Dixon, Fixed bed catalytic reactor modelling-the radial heat transfer problem, *Can. J. Chem. Eng.* 90 (2012) 507–527. <https://doi.org/10.1002/cjce.21630>.
- [56] E. Tsotsas, H. Martin, Thermal conductivity of packed beds: A review, *Chemical Engineering and Processing: Process Intensification* 22 (1987) 19–37. [https://doi.org/10.1016/0255-2701\(87\)80025-9](https://doi.org/10.1016/0255-2701(87)80025-9).
- [57] S. Yagi, D. Kunii, Studies on effective thermal conductivities in packed beds, *AIChE Journal* 3 (1957) 373–381. <https://doi.org/10.1002/aic.690030317>.
- [58] C.T. Hsu, P. Cheng, K.W. Wong, Modified Zehner-Schlunder models for stagnant thermal conductivity of porous media, *International Journal of Heat and Mass Transfer* 37 (1994) 2751–2759. [https://doi.org/10.1016/0017-9310\(94\)90392-1](https://doi.org/10.1016/0017-9310(94)90392-1).
- [59] M. Defalco, L. Dipaola, L. Marrelli, Heat transfer and hydrogen permeability in modelling industrial membrane reactors for methane steam reforming, *International Journal of Hydrogen Energy* 32 (2007) 2902–2913. <https://doi.org/10.1016/j.ijhydene.2007.04.014>.
- [60] D. Taler, J. Taler, Simple heat transfer correlations for turbulent tube flow, *E3S Web Conf.* 13 (2017) 02008. <https://doi.org/10.1051/e3sconf/20171302008>.
- [61] F. Petipas, A. Brisse, C. Bouallou, Model-based behaviour of a high temperature electrolyser system operated at various loads, *Journal of Power Sources* 239 (2013) 584–595. <https://doi.org/10.1016/j.jpowsour.2013.03.027>.

- [62] J. Laurencin, D. Kane, G. Delette, J. Deseure, F. Lefebvre-Joud, Modelling of solid oxide steam electrolyser: Impact of the operating conditions on hydrogen production, *Journal of Power Sources* 196 (2011) 2080–2093. <https://doi.org/10.1016/j.jpowsour.2010.09.054>.
- [63] P. Costamagna, A. Selimovic, M. Del Borghi, G. Agnew, Electrochemical model of the integrated planar solid oxide fuel cell (IP-SOFC), *Chemical Engineering Journal* 102 (2004) 61–69. <https://doi.org/10.1016/j.cej.2004.02.005>.

Appendix F

These appendices bring further information on the conservation and constitutive equations used in the reactor model (Sections F1-F2), the model and validation of the Solid Oxide Electrolyzer Cell (SOEC) stack system (Section F3), and a glimpse into the Aspen Plus flowsheet architecture (“SOEC-MR-COND” case) (Section F4). Section F5 reports historical data for the Chemical Engineering Plant Cost Index (CEPCI). For interested readers, sections F6 also offer extra sensitivity analyses at the reactor level, examining the effects of membrane coverage, gas hourly space velocity (GHSV), reaction temperature, and non-isothermal behavior.

F1. 1D Reactor modelling equations

The model constructed in Aspen Custom Modeler relies on several key assumptions to simplify the analysis. Radial dispersion is considered negligible, enabling the use of 1D conservation equations, while diffusion effects are ignored due to their long characteristic times. Volumetric forces, such as gravity, and pressure drops on the permeation side or from friction on the membrane and shell are also deemed negligible. Only pressure drops caused by the fixed bed and permeation fluxes are included. The membrane material is assumed chemically inert with negligible diffusion time, implying instantaneous permeation. The catalyst affects pressure drop and reactions, but thermal inertia and other effects are ignored, with the gas phase assumed homogeneous. Additionally, the thermal inertia of the membranes and shell is considered negligible. Based on these assumptions, conservation equations for species, momentum, and energy are formulated. For momentum conservation on the retentate side, Ergun’s equation (Eq. F6) is used to model pressure drops in the fixed bed. For the permeate side, no momentum conservation equation is applied due to lower precision requirements and computational constraints; the pressure is instead assumed constant (Eq. F7). Regarding energy balance on the retentate side, the variation of kinetic energy is included to account for differences in molar masses. The energy balance equation (Eq. F4) also incorporates heat from reactions, radial heat transfer to the cooling system, and heat exchange between retentate and permeate, modeled as an isenthalpic process as suggested by Hamed et al. (2021) [54]. The global heat transfer coefficient U (Eq. F8) accounts for three heat transfer resistances: from the retentate zone to the shell, within the shell, and from the shell to the cooling medium. Proper modeling of heat exchange is critical due to the reaction’s temperature sensitivity. Heat transfer in a packed bed is complex, involving diffusion through the catalyst and gas. The model uses the Yagi and Kunii [57] correlation, recommended by Dixon et al. (2012) [55], for large reactors where the tube diameter greatly exceeds the catalyst diameter. This correlation estimates

the wall Nusselt number (Nu_w) as the sum of a stagnant term (Nu_{w0}) and a convective term. The stagnant term is computed using the Bauer and Schlünder [58] correlation, neglecting radiation effects. Heat transfer between permeate and retentate is assumed constant at 2.4 W/m²/K [59] for simplicity, as membranes typically have lower thermal conductivity than reactor shells. While this heat transfer is often negligible, its inclusion accounts for temperature variations in the permeate gas. For detailed modeling, the work of Taler et al. (2017) [60] is recommended. However, steady-state analysis for this case showed minimal temperature variations, allowing simplifications for computational efficiency.

Table F1: List of constitutive equations used in the reactor model

Material balance Retentate side	$\frac{dF_i^R}{dz} = -J_i \pi D_{mi} N_m + \frac{\pi}{4} (D_{si}^2 - N_m D_{mo}^2) \sum_{j=1}^3 \eta r_j \vartheta_{ij}$ Eq. F1
Material balance Permeate side	$\frac{dF_i^R}{dz} = +J_i \pi D_{mi} N_m$ Eq. F2
Permeation flux	$J_i = Perm_i * (P_i^{Ret} - P_i^{Perm})$ Eq. F3
Energy balance Retentate	$\frac{\partial F^R h^R}{\partial z} + \frac{\partial (F_{mass} e_c / \rho)}{\partial z} = \frac{\pi}{4} (D_{si}^2 - N_m D_{mo}^2) \sum_{j=1}^3 r_j (-\Delta H_{rj}(T^R)) - U \pi D_{si} (T^R - T_w) - \pi D_{mi} N_m (H_f \sum_{i=1}^6 J_{f,i} + H_r \sum_{i=1}^6 J_{r,i}) - U_m (T^R - T^P)$ Eq. F4
Energy Balance Permeate	$\frac{dT^P}{dz} = 0$ Eq. F5
Momentum balance Retentate	$\frac{\partial P^R}{\partial z} = - \left(\frac{150 \mu (1-\epsilon)^2 v_s}{\epsilon^3 d_p^2} + \frac{1.75 (1-\epsilon) \rho v_s^2}{\epsilon^3 d_p} \right)$ Eq. F6
Momentum balance Permeate	$\frac{\partial P^R}{\partial z} = 0$ Eq. F7
Overall heat transfer	$\frac{1}{U} = \frac{1}{h_i} + \frac{D_{si}}{2} * \frac{1}{k_w} * Ln \left(\frac{D_{so}}{D_{si}} \right)$ Eq. F8
Solid catalyst bed	$\frac{k_{e,r}}{k_f} = \frac{k_r^0}{k_f} + \frac{Pe_h^0}{Pe_{h,r}^\infty}$ Eq. F9
	$\frac{k_r^0}{k_f} = (1 - \sqrt{1 - \epsilon}) + \frac{2\sqrt{1-\epsilon}}{1-B\kappa^{-1}} \left[\frac{B(1-\kappa^{-1})}{(1-B\kappa^{-1})^2} \ln \left(\frac{\kappa}{B} \right) - \frac{B-1}{1-B\kappa^{-1}} + \frac{B+1}{2} \right]$ Eq. F10
	$B = C_f \left(\frac{1-\epsilon}{\epsilon} \right)^{1.11}; C_f = 1.25 \text{ (sphere)}, 2.5 \text{ (cylinder)} \text{ or } 2.5 \left(1 + \frac{d_i}{d_p} \right) \text{ (rings)}$ Eq. F11
	$k_p = 0.21 + 0.00015T$ Eq. F12
	$Pe_h^0 = \frac{u \rho_f c_{p,f} d_p^0}{k_f} = RePr$ Eq. F13
	$Pe_{h,r}^\infty = 8 \left[2 - \left(1 - \frac{2}{N} \right)^2 \right]$ Eq. F14
Near-wall region	$Nu_w = Nu_{w0} + \frac{1}{\frac{1}{Nu_w^*} + \frac{1}{0.054 Pr Re}}$ Eq. F15
	$N = \frac{d_t}{d_p}$ Eq. F16
	$Nu_w^* = 4 Re^{\frac{1}{2}} Pr^{0.33}$ Eq. F17
	$Nu_{w0} = \left(1.3 + \frac{5}{N} \right) \frac{k_r^0}{k_g}$ Eq. F18

F2. Reaction kinetic model

Similarly to **Chapter 6**, the kinetic rate law and parameters are derived from the work of Rossetti et al. [31], which appears to be the only study proposing modifications to the Temkin equation by introducing a term to account for the competitive adsorption between H_2 and N_2 on a Ru-based catalyst (Eq. F19).

$$\frac{dn}{d\tau} = k_1 \frac{\left(P_{N_2}^{0.5} \left(\frac{P_{H_2}^{0.375}}{P_{NH_3}^{0.25}} \right) - \frac{1}{K_{eq}} \left(\frac{P_{NH_3}^{0.75}}{P_{H_2}^{1.25}} \right) \right)}{1 + K_{H_2} P_{H_2}^{0.3} + K_{NH_3} P_{NH_3}^{0.2}} [kmol\ s^{-1} kg_{cat}^{-1}] \quad \text{Eq. F19}$$

Here P_i is the partial pressure of each component in the reaction zone, calculated as the product between the total pressure and the molar fractions.

With :

$$k_1 = 426000 * \exp \left(-23000 * \frac{4.184}{RT} \right)$$

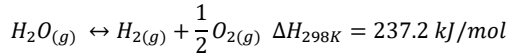
$$K_{H_2} = \exp \left(-\frac{56.9024}{R} + \frac{37656}{RT} \right)$$

$$K_{NH_3} = \exp \left(-\frac{34.7272}{R} + \frac{29228}{RT} \right)$$

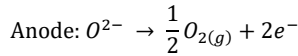
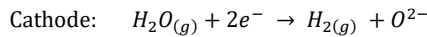
$$\log_{10} K_{eq} = -2.691122 \log_{10} T - 5.519265 * 10^{-5} T + 1.848863 * 10^{-7} T^2$$

F3. Stack modelling equations, operating conditions and validation

Solid Oxide electrolysis cell perform steam electrolysis which reaction stoichiometry is expressed as:



Half reactions at cathode and anode side are the following:



In Aspen Custom Modeler, a 0D lumped parameter model incorporating the Peng-Robinson equation of state was developed, predicated on assumptions including a consistent pressure drop across the stack, the use of average values for temperature, pressure, volume, and current to represent the entire unit accurately, and the negligible effect of mass diffusion on the anode side, attributed to the thinness of the electrode. The specific equations governing this model are outlined in **Table F2**. Model has been validated using data from [35]. **Table F3** summarizes the parameters fitted and assumed for this study.

Table F2:. SOEC stack model equations Ref. [61-63]

Type	Equation
Cell Potential	$V_{cell} = V_{rev} + \eta_{cath}^{act} + \eta_{anod}^{act} + \eta_{ohm} + \eta_{cath}^{conc}$ Eq. F20
Reversible Potential	$V_{rev} = \frac{\Delta \bar{g}_0}{z_e F} + \frac{RT}{z_e F} \ln \frac{p_{O_2}^{1/2} \cdot p_{H_2O}}{p_{H_2O}} \quad \text{Eq. F21}$ <p>Where:</p> $\Delta \bar{g}_0 = 244,800 - 49.18 \cdot T - 0.0072 \cdot T^2 \quad [61]$
Activation Overvoltage [62] [63]	<p>Where</p> $\eta_{a/c}^{act} = \frac{RT}{z_e F} \operatorname{arcsinh} \left(\frac{i}{2i_{0,a/c}} \right) \quad \text{Eq. F22}$ $i_{0,a} = B \cdot \left(\frac{p_{O_2}}{p_{ref}} \right)^r \cdot \exp \left(-\frac{E_{act,an}}{RT} \right) \left[\frac{A}{cm^2} \right]$ $i_{0,c} = A \cdot \left(\frac{p_{H_2}}{p_{ref}} \right)^m \cdot \left(\frac{p_{H_2O}}{p_{ref}} \right)^n \cdot \exp \left(-\frac{E_{act,cath}}{RT} \right) \left[\frac{A}{cm^2} \right]$
Ohmic Losses [63]	$\eta_{ohm} = i \left(\frac{\tau_{YSZ}}{\sigma_{YSZ}(T)} + R_{cc} \right) \quad \text{Eq. F23}$ <p>where</p> $\sigma_{YSZ}(T) = 20500 \cdot \exp \left(-\frac{9030}{T} \right) \cdot 0.01 \quad [ohm^{-1} cm^{-1}]$
Concentration Overvoltage	$\eta_c^{conc} = \frac{RT}{z_e F} \ln \prod_m \left(\frac{c_m}{c_{m,0}} \right)^{\nu} \quad \text{Eq. F24}$ <p>where</p> $c_{H_2}^* = c_{H_2,0} + \frac{i \cdot t_{cat}}{2 \cdot F \cdot D_{eff}}$ $c_{H_2O}^* = c_{H_2O,0} - \frac{i \cdot t_{cat}}{2 \cdot F \cdot D_{eff}}$ $D_{eff} = \frac{\epsilon}{\tau} \cdot \frac{1}{\frac{1}{D_{kn}} + \frac{1}{D_{1,2}}}$
Heat Balance	$C_{th} \cdot \frac{dT_{stack}}{dt} = \dot{n}_{in,an} \cdot h_{in,an} - \dot{n}_{out,an} \cdot h_{out,an} + \dot{n}_{in,an} \cdot h_{in,an} - \dot{n}_{out,an} \cdot h_{out,an} + W_{el} - \dot{Q}_{loss} \quad [61] \quad \text{Eq. F25}$ <p>where</p> $\dot{Q}_{loss} = -\frac{\lambda_{T_{cell}+T_{amb}}}{e_{insulation}} \cdot S_{unit} \cdot (T_{cell} - T_{amb})$

Table F3: Model Fitted and Fixed Parameters.

Fitted Model Parameters		
A		7.577e4
E_{act,cath}	<i>kJ/mol</i>	99.20
B		1.223e3
E_{act,an}	<i>kJ/mol</i>	86.49
r		-0.378
p		-0.851
n		0.563
R_{cc}	<i>Ohm · cm²</i>	0.211
Fixed Model Parameters [35]		
ΔP	<i>mbar</i>	50
A_{cell}	<i>cm²</i>	121
N_{cell}		60
N_{stack}		
t_{Cat}	<i>μm</i>	300
t_{YSZ}	<i>μm</i>	6

ϵ		0.4
τ		4
d_{pore}	μm	1
C_{th} [61]	J/K	98.86

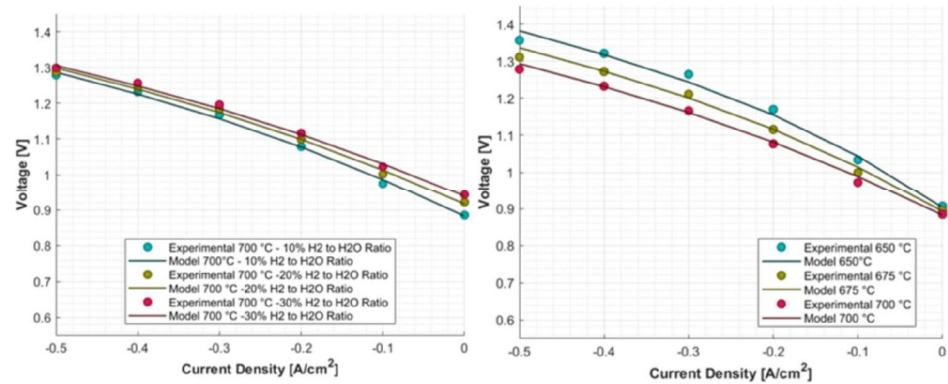


Figure F1: SOEC model validation. Cell voltage has been validated with a 15 cell short stack with the following conditions: 21.08 IN/min H₂O and 2.34 IN/min H₂ (10% Hydrogen to steam ratio) and 4 Air to steam ratio (right) – 63 IN Air inlet corresponding to 3 Air to steam ratio, 700 °C operating temperature.

F4. Top level Aspen Plus flowsheet

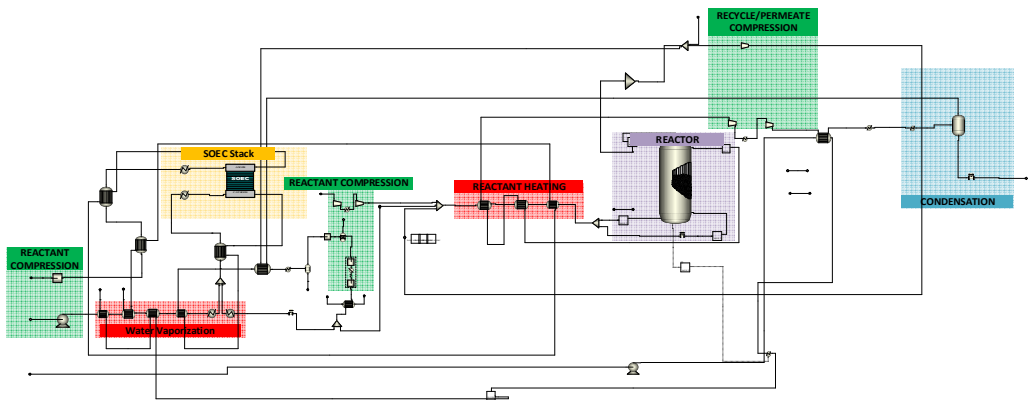


Figure F2: Aspen plus flowsheet of one of the configuration SOEC-MR-COND

F5. Chemical engineering plant index

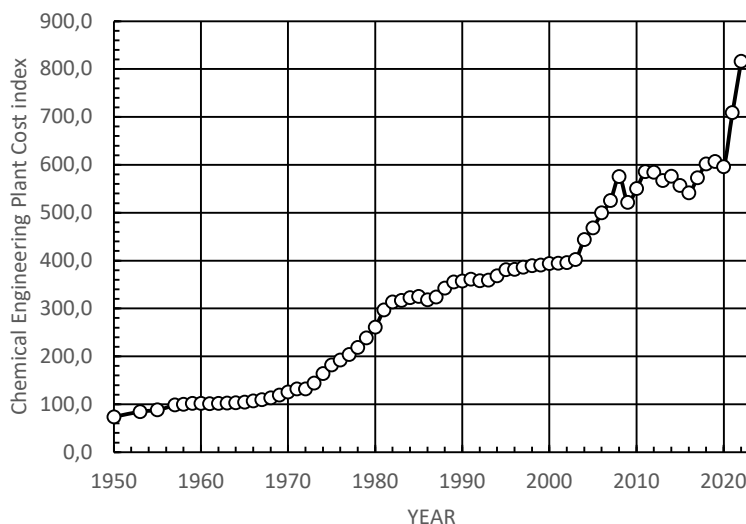


Figure F3: History values of the CEPCI

F6. Sensitivity analysis at the reactor level

Figure F4 illustrates the effects of varying membrane volumetric coverage on conversion rates, total ammonia (NH_3) production, and NH_3 recovery in the permeate, given the conditions (Selectivity $\text{H}_2\text{-NH}_3=20$; Temperature= 360°C ; H_2/N_2 ratio = 1.5, $\text{SW}=1$). It's observed that increased membrane coverage improves conversion efficiency but negatively affects both ammonia production and recovery rates. When permeance and coverage are low, the membrane reactor's performance closely aligns with that of a traditional reactor. **Figure F5** explores the influence of Gas Hourly Space Velocity (GHSV) on these parameters (Permeance= $0.05 \text{ mol m}^{-2}\text{s}^{-1}\text{bar}$; $T=360^\circ\text{C}$, H_2/N_2 ratio = 3, $\text{SW}=1$, $P_{\text{ret}}=70 \text{ bar}$), noting a decrease in conversion for both MR and TR as GHSV increases due to shorter gas residence times. However, total ammonia production increases under these conditions. The rate of ammonia recovery first rises, peaking at a GHSV of 1100 h^{-1} , before falling off as GHSV continues to climb, indicating a struggle in ammonia permeation through the membrane at high GHSVs, a trend that holds true across most selectivity values. In **Figure F6**, the impact of temperature is presented similarly on the conversion, total NH_3 production and NH_3 recovered (Selectivity $\text{H}_2\text{-NH}_3=20$; $T=360^\circ\text{C}$, H_2/N_2 ratio=3, $\text{SW}=1$, $\text{GHSV}=500 \text{ h}^{-1}$). The transition from kinetic to thermodynamic control threshold temperature can be noted at around 380°C . Finally, **Figure F7** showcases the non-isothermal profiles, highlighting how variations in the contributions of terms within the retentate energy balance affect the system. The term 'HomoRP' is introduced as a factor that multiplies the effectiveness of heat transfer across the membrane between the permeate and retentate, Similarly, 'HomoCooling' refers to the heat transfer from the reactor wall.

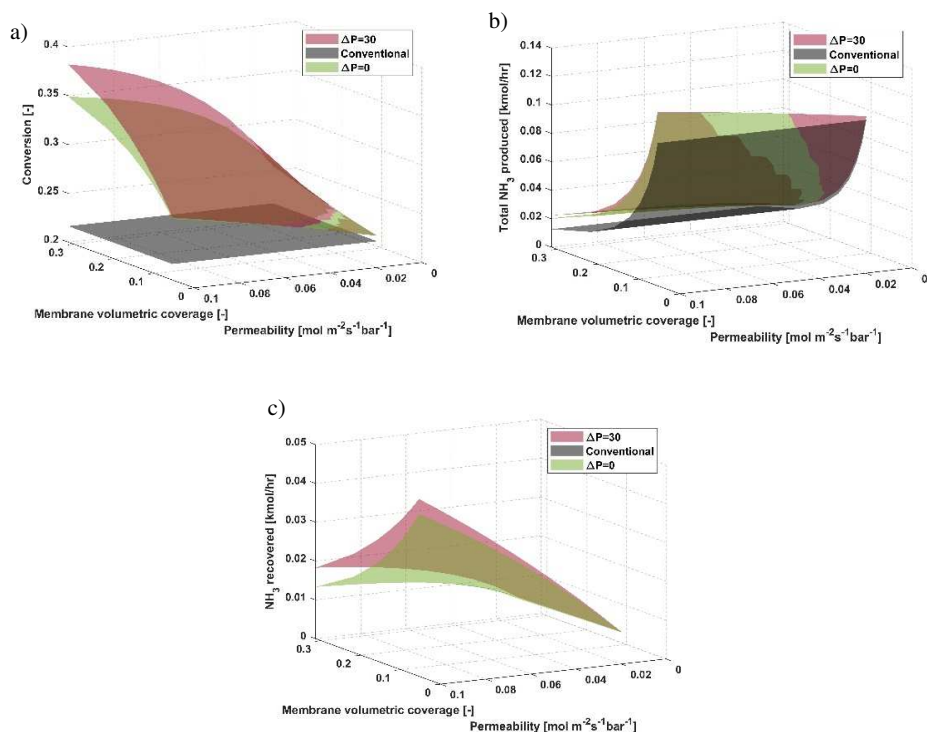
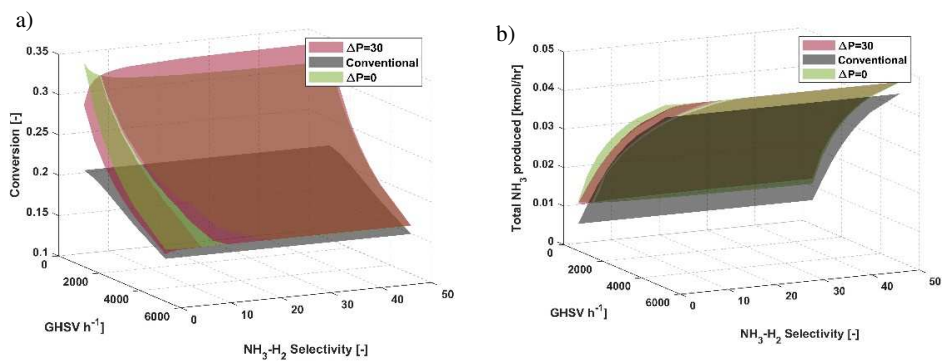


Figure F4: Impact of Membrane coverage (i.e. the ratio of membrane volume to reactor volume), (a) Conversion (b) Total NH_3 produced (c) Total NH_3 recovered (Selectivity $\text{NH}_3\text{-H}_2=20$; $T=360^\circ\text{C}$, H_2/N_2 ratio = 1.5, $\text{SW}=1$, $P_{\text{ref}}=70$ bar) for various pressure drop across the membrane ($\Delta P = 30$ bar and $\Delta P = 0$ bar) - The selectivity towards nitrogen is taken as three time the one of hydrogen (Isothermal model).



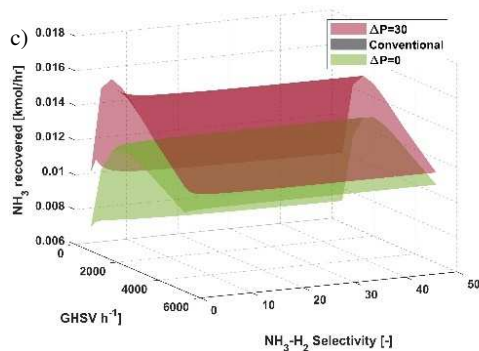


Figure F5: Impact of GHSV: (a) Conversion (b) Total NH_3 produced (c) Total NH_3 recovered (Permeance = 0.01; $T=360^\circ\text{C}$, H_2/N_2 ratio=1.5, $\text{SW}=1$, $P_{\text{rel}}=70$ bar) for various pressure drop across the membrane ($\Delta P = 30$ bar and $\Delta P = 0$ bar) - The selectivity towards nitrogen is taken as three time the one of hydrogen (Isothermal model).

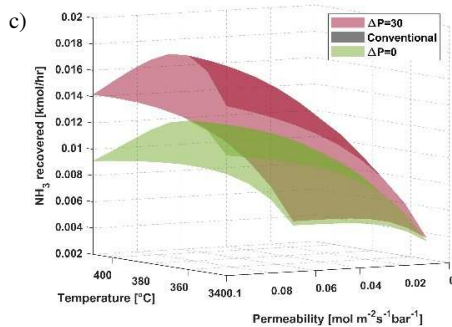
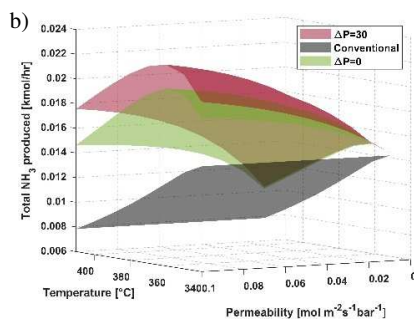
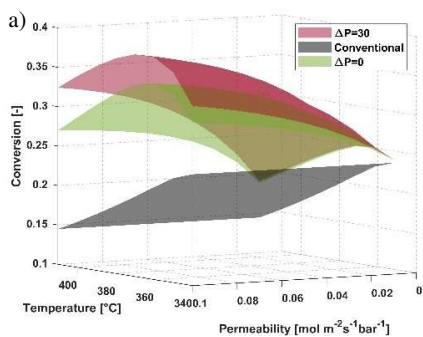
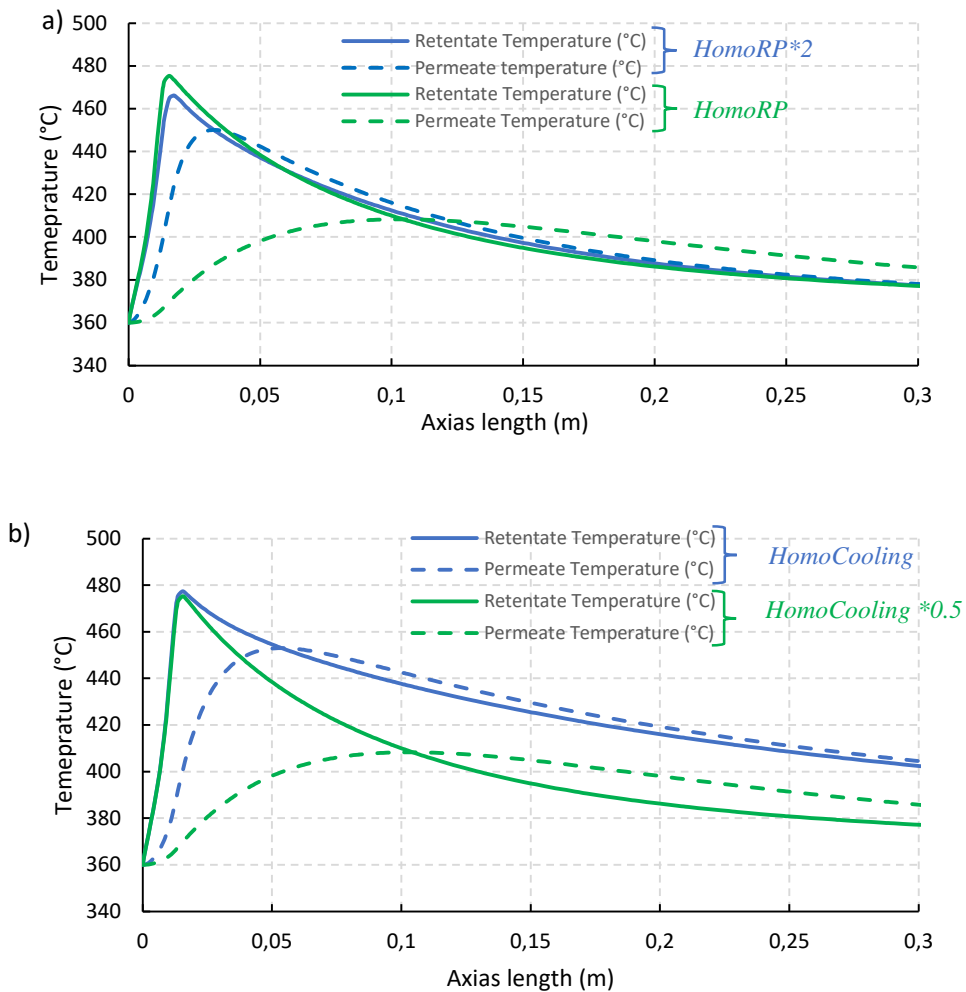


Figure F6: Impact of reaction temperature: (a) Conversion (b) Total NH_3 produced (c) Total NH_3 recovered (Selectivity $\text{NH}_3\text{-H}_2=20$; GHSV= 500 h^{-1} , H_2/N_2 ratio = 1.5, $\text{SW}=1$, $P_{\text{ret}}=70\text{ bar}$) for different pressure drop across the membrane ($\Delta P = 30\text{ bar}$ and $\Delta P = 0\text{ bar}$) - The selectivity towards nitrogen is taken as three time the one of hydrogen (Isothermal model).



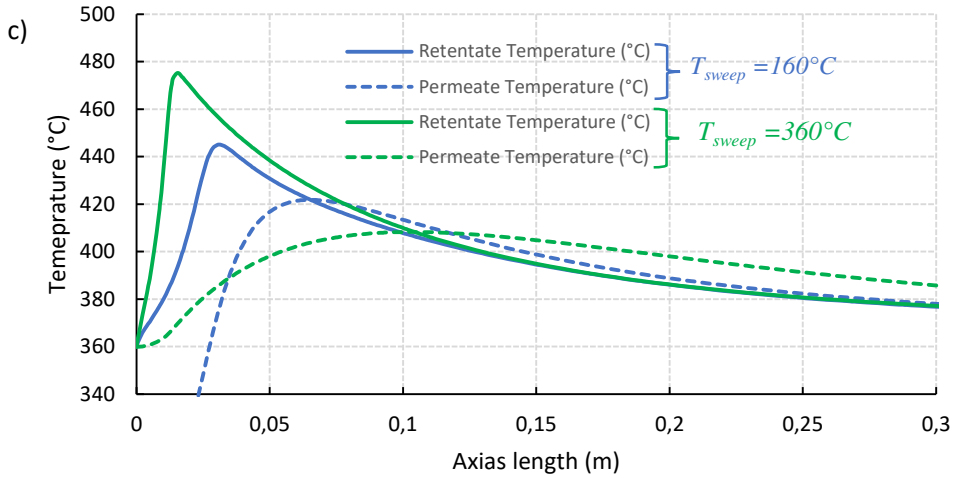


Figure F7: Variability of temperature profile effects due to alterations in the retentate heat transfer equation (Permeance= $0.05 \text{ mol m}^{-2} \text{ s}^{-1} \text{ bar}^{-1}$; Selectivity $\text{H}_2\text{-NH}_3=20$; Selectivity $\text{N}_2\text{-NH}_3=60$, $T=360^\circ\text{C}$, H_2/N_2 ratio = 1.5, $\text{SW}=1$, $\text{GHSV}=1000 \text{ h}^{-1}$); showing the first centimeter of the reactor

F7. Detail on the transmembrane flux

Figure F8 illustrates the transmembrane flow along the length of the reactor at two different pressure gradients across the membrane: $\Delta P=0 \text{ bar}$ and $\Delta P=30 \text{ bar}$. In this graph, the transmembrane flow $F_{i,tmb}$ is plotted for each species i under specific operating conditions, with the following convention:

$$\forall i \in \{\text{H}_2, \text{N}_2, \text{NH}_3\} :$$

- $F_{i,tmb} < 0$ indicate transfer from permeate to retentate
- $F_{i,tmb} > 0$ indicate transfer from retentate to permeate
- $F_{i,tmb} = 0$ indicate equilibrium between retentate and permeate

Regarding ammonia and hydrogen, it can be observed that the system moves toward an equilibrium of partial pressure between the retentate and permeate for each species. This equilibrium is achieved more quickly when the membrane has lower selectivity and when there is a higher pressure gradient across the membrane, promoting a high mass transfer rate between the two sides. For hydrogen, there is either reactant co-feeding or reactant loss at $\Delta P=0$ and $\Delta P=30$, respectively. For ammonia, product permeation occurs, and no back permeation is observed under these operating conditions. Regarding nitrogen, the situation is however further from equilibrium because excess nitrogen was used in the feed. Indeed, Ru is inhibited by H_2 , and thus, lower H_2/N_2 ratios are more advantageous for ammonia conversion compared to the stoichiometric ratio. The kinetic expression used considers the competitive adsorption between H_2 and N_2 on the Ru-based catalyst. Additionally, the membrane's selectivity for nitrogen is taken as three times that of hydrogen which reduces the transfer of this species compared to the other two.

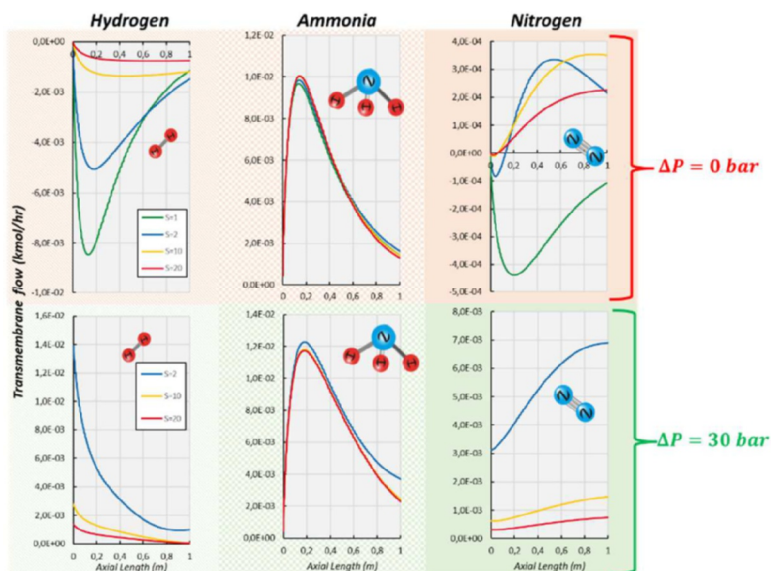


Figure 8-12: Detail on the species (N_2 , H_2 and NH_3) transmembrane flux for two different pressure drop applied across the membrane ($\text{GHSV}=500 \text{ h}^{-1}$, $T=360 \text{ }^\circ\text{C}$, H_2/N_2 ratio = 1.5, $P_{\text{ret}}=70 \text{ bar}$). The selectivity of nitrogen is taken as three time the one of hydrogen and an isothermal model is used.

Conclusion and Outlooks

This thesis investigated the application of membrane reactors (MRs) in Power-to-X from two main perspectives. First, at the mesoscale level, it examined the potential to integrate 3D-printed catalyst structures with selective membranes to enhance reactor performance. This approach was studied through experimental investigations supported by computational fluid dynamics modeling; Second, at the macroscale level, the thesis assessed the deployment of membrane reactors in Power-to-X environments, addressing questions like the selection of e-molecules or the choice of process configurations. Simplified 0D/1D phenomenological models were developed for key unit operations, including membrane reactors, electrolysis, and fuel cells, and were implemented within a process systems engineering (PSE) simulation tool. The main conclusions are presented chapter by chapter, followed by outlooks.

Conclusion

Chapter 2 provided a comprehensive review of recent advancements in membrane reactor design and applications for Power-to-X systems. Adopting a top-down approach, it examined shared design features such as membrane materials, heat management, and catalyst configurations, followed by a comparison of laboratory-scale demonstrations in various process environments. Innovations like additive manufacturing for optimizing porosity and shape, coupled with electric heating, were highlighted as solutions to heat and mass transfer challenges, enabling compact and flexible technologies suitable for Power-to-X applications. Laboratory studies reported significant conversion enhancements, including ~250% for methanol synthesis, ~200% for DME synthesis, ~175% for methane reforming, and up to ~30% for ammonia decomposition and methanol reforming, while also eliminating side reactions in cases like Fischer-Tropsch synthesis. However, differences in membrane properties, catalysts, and operating conditions, particularly in membrane area, space velocity, and driving forces, complicated direct performance comparisons across studies.

Chapters 3 and 4 examined the use of membrane reactors for power generation applications at the macroscale through process simulation. **Chapter 3** focused on the small-scale integration of MRs with proton exchange membrane (PEM) fuel cells, achieving up to 40 kWe gross power. Efficiency optimization reduced the levelized cost of hydrogen (LCOH) from 8.29 €/kg_{H2} in methanol systems to 6.12 €/kg_{H2} in ammonia systems and 5.43 €/kg_{H2} in methane systems, with corresponding fuel processor thermal efficiencies of 0.57, 0.92, and 0.77, respectively. At the genset level, costs decreased from 1400 €/MWh in methanol systems to 848 €/MWh and 665 €/MWh in electric and thermal ammonia systems, and 627 €/MWh in methane systems, with electric efficiencies ranging from 25% to 38%. Economically, methane was the most favorable option, while ammonia was the most efficient. However, high costs compared to traditional internal combustion engine (ICE) systems limited their adoption. Lowering PEMFC costs to under 2000 €/kW could have enabled economic competitiveness at scales of 150 kW, making industrial applications viable, assuming e-fuels could compete with fossil fuels. **Chapter 4** evaluated two ammonia-cracking technologies, membrane reactors and conventional Fired Tubular Reactors (FTRs), for co-firing ammonia and hydrogen in Combined Cycle Gas Turbine (CCGT) plants. Integrating MRs during

the cracking stage improved thermal efficiency by over 25% and reduced LCOH by ~10%, despite higher CAPEX. At the CCGT level, the levelized cost of electricity (LCOE) narrowed, driven primarily by ammonia costs, which constituted 80% of the total LCOE. Beyond costs, material scarcity posed significant challenges: revamping 1 GWe of CCGT capacity with MRs would have required ~0.11% of global palladium and 10% of global ruthenium production. Given the limited availability and high demand for these materials, along with geopolitical risks, this approach was deemed impractical. Future research was recommended to prioritize alternative membrane materials, such as carbon molecular sieves, and nickel-based catalysts to reduce reliance on scarce resources and enable broader adoption.

Chapters 5, 6, and 7 explored the potential of 3D-printed Periodic Open Cellular Structures (POCS) to enhance membrane reactor (MR) performance by improving mass transfer and thermohydraulic behavior. **Chapter 5** examined the thermohydraulic properties of Kelvin, BCC, and gyroid lattices, analyzing flow velocities from 1 to 10 m/s, corresponding to Reynolds numbers between 30 and 400 (based on strut thickness). These structures were successfully fabricated via Laser Powder Bed Fusion (LPBF), closely matching CAD designs with porosity deviations under 15%. CFD modeling, validated against pressure drop experiments, showed similar thermohydraulic performance across POCS, particularly at low velocities. The gyroid lattice performed better at low velocities, while the BCC structure excelled at higher velocities. Ergun-like correlations for each lattice achieved a Mean Absolute Percentage Error (MAPE) below 10%, with heat transfer predictions aligning with literature, though on the lower spectrum. By leveraging the analogy between heat and mass transport, these findings provide valuable insights into mass transfer behavior. At low velocities (Stokes flow regime), inertial effects were negligible, and heat transfer was primarily governed by conduction, dictated by thermal conductivity. Here, transport phenomena, including mass transfer, were largely influenced by wall friction, which depends on available surface area. Thus, for similar porosity and specific surface area, cell type variations had minimal impact. At higher velocities (Forchheimer regime), inertial forces contributed significantly to transport phenomena, typically following a quadratic velocity dependence (u^2 term). From a heat transfer perspective, the Kelvin cell exhibited the highest thermal performance, but when balancing heat transfer and pressure drop, the gyroid cell proved to be the optimal choice, outperforming both Kelvin and BCC cells. Flow visualization studies further revealed that the Kelvin cell exhibited a jet-like preferential flow path, the BCC cell maintained relatively straight streamlines, while the gyroid cell displayed a highly tortuous flow path, enhancing reactant dispersion and mitigating preferential flow paths, thereby improving external mass transfer performance at higher flow rates. **Chapter 6** investigated external mass transfer in POCS reactors during ammonia synthesis, with and without selective membranes. Ru-based catalytic layers were deposited on IN625 POCS using optimized dip/spin coating methods. While homogeneous coatings were achieved, Kelvin cells showed clogging issues, limiting their suitability. Laboratory tests confirmed catalytic activity consistent with literature values. CFD simulations indicated limited influence of cell geometry on catalytic activity but highlighted improvements in conversion and recovery with increased membrane permeance, up to a plateau caused by concentration polarization and production-extraction mismatches. A plug flow-based model inaccurately predicted behavior at permeances above $0.05 \text{ mol} \cdot \text{s}^{-1} \cdot \text{m}^{-2} \cdot \text{bar}^{-1}$, suggesting a need for correction factors. **Chapter 7** evaluated the

impact of operating conditions and design factors on POCS interfaced with Pd-based membranes. Optimized coating methods validated kinetic activity, and virtual permeation tests revealed that Kelvin 3-0.6 structures with baffles performed best at gas hourly space velocities (GHSV) below 1211 h^{-1} . At higher GHSV, baffles improved concentration polarization but slightly reduced hydrogen recovery. Ammonia decomposition studies showed that hydrogen production peaked at 1850 h^{-1} before declining due to non-permeating gas accumulation. Optimal performance was observed at 0.8 porosity, balancing production kinetics and extraction. Integration of baffles further enhanced performance by reducing mass transfer limitations, protecting the membrane, and potentially lowering the required membrane area.

Chapter 8 evaluated the cost and efficiency of power-to-fuel technologies under uniform assumptions, highlighting the advantages of innovative pathways, including membrane reactors (MRs) and solid oxide electrolysis cell (SOEC) integrations. The analysis aimed to investigate the potential of catalytic membrane reactors (CMRs) for ammonia production from renewable hydrogen at the process scale. To achieve this objective, computer-aided process simulation was deployed using the Aspen Plus v14 simulation tool. A 1D model was developed to describe the integration of a ruthenium catalyst into a CMR equipped with inorganic membranes that were selective to NH_3 over N_2 and H_2 . The CMR performance was first studied across a broad spectrum of membrane properties and operating conditions. Subsequently, the CMR model was integrated into several Power-to-Ammonia (PtA) process layouts, which were optimized and techno-economically compared against a traditional PEM-based PtA production process employing condensation for the purification stage. Key findings at the reactor level confirmed that beyond a selectivity threshold towards hydrogen of 10–20, both the degree of conversion and recovery tended to be generally independent of the membrane's selectivity. However, producing pure ammonia permeate required highly selective membranes (>1000 towards H_2), depending on the pressure drop, making this alternative elusive based on existing membranes. At the PtA level, results indicated that using a membrane reactor increased the system efficiency by approximately 8% compared to the reference case, while a ~15% enhancement was achieved when using SOEC technology. When examining the final Levelized Cost of Ammonia (LCOA), incorporating a membrane reactor in conjunction with condensation separation resulted in a cost that nearly matched the reference case. Future research was recommended to focus on replacing the condensation process with a purification method at lower pressures. This could potentially further improve efficiency and reduce the cost of the membrane reactor compared to traditional methods.

Outlooks

➤ Mesosopic CFD reactor modelling

At the mesoscale, 3D/2D models proved really useful in understanding and optimizing the impact of design on transport phenomena, offering valuable correlations and insights (e.g., pressure drop or concentration polarization) to inform macroscale models, as detailed in **Chapters 3, 5, 6,** and **7**. However, due to the high computational resource requirements, the most detailed pore-scale CFD analyses often necessitated scaling down membrane reactors to sizes smaller than their actual dimensions, as we did in **Chapter 6**. This was achieved by maintaining a comparable specific

membrane area and operating under similar gas hourly space velocity (GHSV) conditions. Nonetheless, this approach raises questions about the representativeness and scalability of the findings for larger systems. In miniaturized setups, diffusion plays a much larger role, and the velocity reaching the POCS is significantly lower than in full-scale reactors. To compare transport phenomena in POCS lattices within a computationally manageable domain, we would recommend to consider two key cases: (1) operating at a similar GHSV to the real reactor (i.e. the same volumetric flow rate relative to reactor size), as done in this study, and (2) operating at a similar Reynolds number for better representation of flow regimes (laminar vs. turbulent) and transport dynamics, such as mixing and heat/mass transfer. Finally, to further enhance model credibility, validation against experimental data is essential. This could be performed numerically on a real portion of a membrane reactor, as demonstrated in **Chapter 8**, ensuring that the flow regime remains consistent. A similar challenge actually exists in lab-scale membrane reactor experiments, typically conducted at very low GHSV, as highlighted in the literature review (**Chapter 2**). These conditions correspond to low Reynolds numbers ($\sim 2\text{--}20$, based on pellet diameter and nitrogen properties), confirming that flow falls within the creeping flow (Stokes) regime, where viscous forces dominate, convective transport is minimal, and diffusion-driven transport becomes the primary mechanism.

➤ Macroscopic system modelling

At the macroscale process level, flowsheet optimization in Aspen Plus (even using simplified 1D/0D models) faced significant challenges due to computational complexities, such as resolving tear streams and design specifications, and informatic difficulties, including code coupling and the steep learning curve of specialized tools like Aspen Custom Modeler™. In this PhD the sequential modular approach was used (by default) for solving the process flowsheet, where tear streams and recycle loops are solved iteratively until convergence. However, this iterative solving process can lead to long computation times for complex flowsheets. These challenges were further intensified by the use of tools like multi-objective optimization algorithms (cf. **Chapter 8**), which require additional coupling, increasing computational demands and limiting “true” optimization. To address these issues, two key recommendations can be proposed. First, adopting the equation-oriented approach, where all unit operation, material, and energy balance equations are solved simultaneously as a single system, would eliminate the need for iterative recycle stream resolution, improving computational efficiency. Second, the membrane reactor model used in these simulations should be simplified to enable fast computation while still capturing critical process limitations. While plug flow reactor assumptions (no axial mixing) while also neglecting intra-particle diffusion and fluid-particle mass transfer—are often reasonable, particularly at laboratory scale, concentration polarization can become a limiting factor depending on the system and operating conditions. Addressing this issue can be achieved through 2D and 3D modeling, which provides insights into the necessary reduction factors or enables the extrapolation of correlations across a broader range of operating conditions. Alternatively, metamodeling could transform these computationally expensive models into more efficient representations, maintaining key transport and reaction phenomena while significantly reducing computational burden. Implementing these strategies would enhance flowsheet optimization.

➤ POCS membrane reactor

The POCS membrane reactor technology, as presented in **Chapters 5 to 7**, offers potential but also some challenges as highlighted in the proposed SWOT analysis in **Figure 9-1**. Among the strengths, POCS offer superior membrane protection by addressing key issues compared to packed bed or fluidized bed reactors, as there is no direct contact between the catalyst and the membrane. Although POCS have reduced catalyst holdup relative to pellet beds—limiting the total available catalytic surface area and weight—their enhanced heat and mass transfer capabilities (e.g., reducing concentration polarization) make them a compelling alternative for demanding processes. Furthermore, POCS can be tailored to specific applications through design features such as porosity gradients or the addition of baffles. The use of 3D printing technology, particularly Laser Powder Bed Fusion (LPBF), ensures high reproducibility and precision, as evidenced by the ability to fabricate designs with only minor deviations from CAD models. Additionally, the development of effective catalytic coating methods further enhances the functionality of POCS. However, challenges persist. POCS have limited catalytic loading compared to packed bed reactors, and their multi-step fabrication process adds complexity, potentially increasing production costs. Long-term testing remains largely unexplored, raising questions about durability and reliability. Furthermore, few suppliers or laboratories currently possess the expertise needed for effective catalyst coating, which could hinder widespread adoption. POCS offer broad opportunities across a wide range of reactions, particularly in liquid-phase systems like low-temperature Fischer-Tropsch synthesis, where higher viscosity and diffusivity constraints could further enhance their advantages over packed beds. Additionally, integrating innovative features such as electric heating could improve performance, especially in small, compact reactors, making POCS an ideal choice for Power-to-X applications where flexibility is key. Beyond chemical reaction engineering, POCS also show promise in thermal applications, such as heat exchangers.

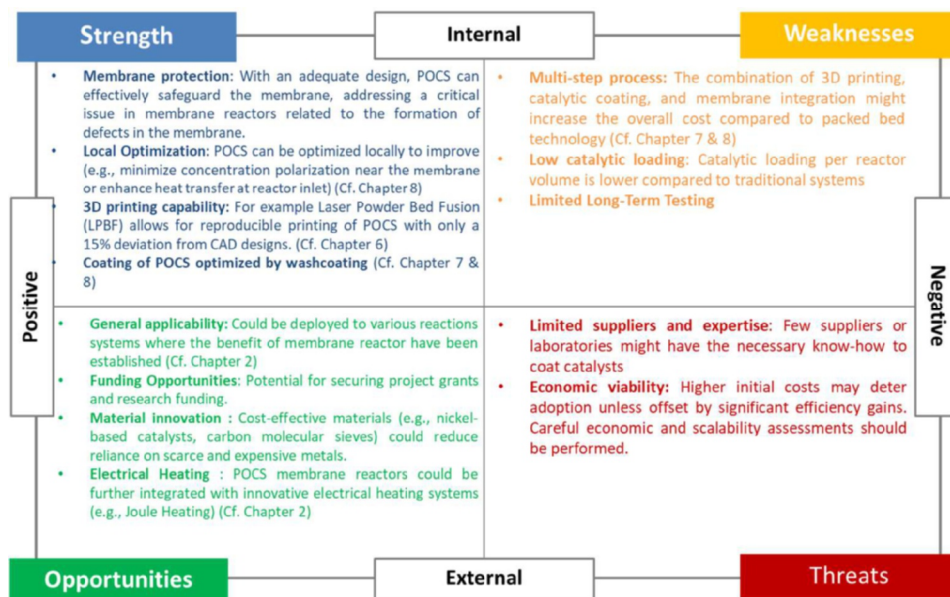


Figure 1: Strengths, Weaknesses, Opportunities, Threats (SWOT) about POCS membrane reactors

➤ **Power-to-X outlook**

To finish, it seems also important to reiterate some technical challenges associated with Power-to-X technologies. These include the intermittency of renewable energy, the energy-intensive nature of carbon capture, the difficulty of scaling up electrolyzers together with uncertainties in cost projections. Additionally, the reliance on scarce critical materials such as platinum, iridium, and palladium create supply chain risks¹. The high water demand for electrolysis also raises concerns, particularly in water-scarce regions. For specific e-molecules, such as ammonia, which is widely regarded as a promising e-molecule for its versatility as a commodity chemical, fuel, and hydrogen carrier, it is worth highlighting the environmental risks that remain poorly understood. For instance, studies suggest that if nitrogen emissions from ammonia are not tightly controlled, its large-scale use could disrupt the global nitrogen cycle. Alarmingly, releasing just 0.4% of ammonia's nitrogen as nitrous oxide (N₂O), a greenhouse gas with a global warming potential 265-298 times greater than that of CO₂, could negate the climate benefits of adopting ammonia². While resource scarcity, particularly for large-scale ammonia cracking, was briefly discussed in **Chapter 4**, these critical

¹ Clapp M. et al., Perspective on current and future iridium demand and iridium oxide catalyst for PEM water electrolysis. *Catalyst Today* 420 (2023)

² Wolfram P. et al, Using ammonia as a shipping fuel could disturb the nitrogen cycle , *Renewable and Sustainable Nature Energy* 7 (2022)

environmental and resource risks along with some technical challenges notably the intermittency operation of a PtX plant were largely overlooked in this PhD.

In addition to these challenges, there are concerns about the feasibility of achieving short-term defossilization targets by 2030 with e-fuels. Meeting these goals requires substantial energy input: a 10% share of e-kerosene for aviation would need approximately 1,500 TWh, while shipping would require an additional 600 TWh, bringing the total to 2,100 TWh³. Given the global efficiency ranging from ~16% to 48% (cf. **Appendix G**)—the actual electricity input required would be much higher. This means renewable electricity generation would need to be two to ten times greater than for direct electrification, ranging from 4,375 TWh to 13,125 TWh. Assuming a wind turbine capacity factor of 30-50% (meaning they generate power only 30-50% of the time on average), the total installed renewable capacity needed is summarized in **Table 1**. Electrolysis capacity requirements would also be of a similar magnitude, requiring a significant scale-up.

Table 1: Required renewable installed capacity (GW) for a 10% share of e-fuels in aviation and shipping (~2,100 TWh)

	Low capacity factor (30%)	High capacity factor (50 %)
Low Power-to- Power efficiency (16%)	4994	1665
High Power-to- Power efficiency (48%)	2997	999

Given the urgency of climate mitigation, e-fuels are unlikely to become cheap and abundant quickly enough to replace fossil fuels on a large scale. Over-reliance on this solution could be counterproductive, as it risks delaying decarbonization efforts. This underscores the need for strategic prioritization, even within hard-to-electrify sectors⁴. E-fuels should be only be reserved for applications where electrification is not feasible, such as aviation, shipping, and chemical feedstocks. In contrast, direct electrification is a far more efficient and cost-effective solution for sectors like light-duty vehicles and space and water heating in buildings. For instance, the cost of lithium-ion batteries has declined significantly—falling by a factor of 5.6 from 2013 to 2023 to reach 139 \$/kWh, with further reductions expected⁵—further strengthening the case for electrification. Therefore, in the near term, prioritizing direct electrification wherever possible remains the most effective approach to reducing emissions and maximizing the impact of renewable energy. In the

³ IEA, The Role of E-fuels in Decarbonising Transport, (2024).

⁴ F. Ueckerdt, C. Bauer, A. Dirnaichner, J. Everall, R. Sacchi, G. Luderer, Potential and risks of hydrogen-based e-fuels in climate change mitigation, Nat. Clim. Chang. 11 (2021) 384–393. <https://doi.org/10.1038/s41558-021-01032-7>.

⁵ BloombergNEF. Lithium-Ion Battery Pack Prices Hit Record Low of \$139/kWh; BloombergNEF, December 7, 2023. <https://about.bnef.com/blog/lithium-ion-battery-pack-prices-hit-record-low-of-139-kwh/>.

long term, advancements in electrolysis, flexible operation strategies, and global supply chain optimization may improve the competitiveness of e-fuels.

Appendix G: Energy and power densities

To evaluate the suitability of different energy vectors for onboard power plants (e.g., in shipping), three key criteria are considered: energy density of the storage system (per unit weight and volume), power density, and energy efficiency. For practical reasons, this appendix focuses on proton exchange membrane fuel cells (PEMFCs)—including a reforming step when necessary—and internal combustion engines (ICEs). The key assumptions for these technologies are derived from previous chapters and literature analysis and are summarized in **Table G1**. Additionally, both systems are compared with direct electrification using battery storage, which represents the primary competing alternative.

➤ Electrical efficiency of propulsion engines

Fuel cells offer a significant efficiency advantage over conventional internal combustion engine (ICE) generators by directly converting chemical energy into electricity through electrochemical reactions, eliminating the thermal and mechanical losses inherent in combustion engines. While ICEs typically operate at 25–45% efficiency, PEMFCs can reach up to 65% efficiency when using pure hydrogen. However, when operating with reformed fuels, overall PEMFC efficiency drops below 40% due to additional losses in reforming and purification (cf. **Chapter 3**). Efficiency is also influenced by part-load operation. ICEs experience significant efficiency losses at low loads, whereas PEMFCs can mitigate these losses through modular switch-off strategies [1]. This study assumes 40% efficiency for ICEs and 55% for PEMFCs, with reforming efficiencies of 92% for ammonia cracking, 57% for methanol reforming, and 72% for methane reforming, as detailed in **Chapter 3**. While batteries are limited in energy storage capacity, they offer a high round-trip efficiency of approximately 90%.

➤ Energy and Power densities

In onboard power plants, energy density and power density are critical design parameters that impact operational endurance, refueling intervals, and system responsiveness. Energy density (Wh/kg, Wh/L) determines how long a system can operate before refueling or recharging, while power density (W/kg, W/L) defines how quickly energy can be delivered. Energy density considerations vary by application. In weight-constrained sectors such as aviation, gravimetric energy density is a key factor, as battery size or tank volume directly limits range. In shipping, however, volumetric energy density becomes more critical, as fuel storage competes with cargo space. **Chapter 1** discusses energy density variations across fuels and storage systems, highlighting uncertainties due to tank design and insulation. Regarding power density, PEMFCs exhibit a wide range depending on whether they are optimized for mobility or stationary applications (cf. **Figure G1**). For example, PowerCell™ reports 1020 W/kg and 300 W/L at the system level, with stack-level densities exceeding 3000 W/kg and 3300 W/L. Modular system like the Nedstack™'s Gen 3, which separates fuel cell modules from the air supply, further enhances volumetric density. In this

study, PEMFCs are considered within the range of 250–1000 W/kg and 300–1000 W/L, while ICE engines operate at lower densities of 45–71 W/kg and 32–55 W/L. A relatively high upper bound for PEMFC power density is selected, consistent with van Biert et al. (2016) [1] to account for their modularity. When integrating a fuel reformer (e.g., ammonia cracker, methanol reformer) with a PEMFC, the reformer adds mass and volume without directly contributing to power output, reducing overall system power density. **Table G2** provides vendor data on reformer power densities, offering an order-of-magnitude idea. Ammonia reformers, leveraging membrane reactor technology, are expected to be the most compact, requiring fewer auxiliary components, while methanol and methane reformers require additional insulation. Estimated reformer power densities are 70–150 W/kg and 60–140 W/L for ammonia, with reductions of 20% for methanol and 40% for methane systems. The estimated reformer power densities and relative orders are rough approximations and should be taken with caution. Regarding Li-Ion batteries, a study [7] indicates that optimized electrodes can increase power density from 100 W/L to over 600 W/L at an energy density of 500 Wh/L. This finding supports our assumed power density ranges for lithium-ion batteries, where state-of-the-art (SoA) technology is considered within 150–450 W/kg & 150–450 W/L, while future perspectives could reach 200–600 W/kg & 200–600 W/L.

➤ Ragone charts

To systematically compare various onboard power plant configurations involving different propulsion engines and fuel combinations, effective power and energy densities are assessed using Ragone plots. Each option is characterized by the power density of its conversion engine, energy storage capacity, conversion efficiency, and the timescale over which power is delivered. The methodology follows van Biert et al. (2016) [1] and Diesveld and Maeyer (2020) [2], where effective power density (P_{eff}) and effective energy density (E_{eff}) are defined as functions of system parameters and operational timescale as expressed in Eq. G1 & G2.

$$P_{eff} = \frac{P}{1+t\frac{P}{\eta E}} \quad \text{Eq. G1}$$

$$E_{eff} = t P_{eff} = \frac{t P}{1+t\frac{P}{\eta E}} \quad \text{Eq. G2}$$

where P is the intrinsic power density of the conversion device, E is the energy density of the fuel storage, and η represents the conversion efficiency. As shown in Eq. G1, at short timescales ($t \rightarrow 0$), the system operates at nearly its peak power output ($P_{eff} \approx P$), while for long durations ($t \rightarrow \infty$), system's power output is no longer dictated by the power conversion device but is instead limited by the stored energy ($P_{eff} \approx \eta E/t$). Reversely in Eq. G2, the effective energy density E_{eff} approaches zero for very short operation times and asymptotically reaches the maximum storable energy ($E_{eff} \approx \eta E$) for long-duration applications. Two conversion efficiencies are distinguished, as defined in Eq. G3 & G4: local efficiency (fuel-to-power) and global efficiency (power-to-power), the former represents the efficiency of converting fuel energy into useful power at the conversion engine level, while the latter accounts for losses across the entire energy conversion chain, from fuel production and storage to final power delivery.

$$\eta_{local} = \eta_{power\ system} * \eta_{fuel\ processing} \quad \text{Eq. G3}$$

$$\eta_{global} = \eta_{fuel\ production} * \eta_{power\ system} * \eta_{fuel\ processing} \quad \text{Eq. G4}$$

To accurately account for the contribution of a fuel processor (e.g., ammonia cracker, methanol reformer) when integrated with a fuel cell, its mass and volume must be considered in the overall system design. The effective system power density is determined by the parallel combination of the fuel processor and the fuel cell as per Eq. G5

$$P = \left(\frac{1}{P_{power\ system}} + \frac{1}{P_{fuel\ processing}} \right)^{-1} \quad \text{Eq. G5}$$

Table G1: Base case assumptions [3]

LHV Efficiency (%) of the energy converter ($\eta_{power\ system}$)	
ICE (2 stroke)	~40[3]
PEM fuel cell	~55 (cf. chapter 3)
Electric Motor	~90
e-fuel production efficiency	
E-Diesel	37[3]
LH2	55[3]
E-Ammonia	54[3]
E-Methanol	46[3]
E-Methane	~50 [4] [5]
Efficiency (%) of reformer and ammonia crackers (assuming palladium membrane reactors) to produce hydrogen at ~1 bar ($\eta_{fuel\ processor}$)	
Ammonia cracker	92 (cf. chapter 3)
Methanol reformer	57 (cf. chapter 3)
Methane reformer	72 (cf. chapter 3)
Energy storage density, E (taken from Chapter 1, Figure 1-2)	
LH2	2.5 kWh/kg & 1.32 kWh/L
E-Ammonia	3.60 kWh/kg & 2.70 kWh/L
E-Methanol	4.03 kWh/kg & 3.83 kWh/L
E-Diesel	8.3 kWh/kg & 8.15 kWh/L
E-Methane	7.40 kWh/kg & 3.30 kWh/L
Li-Ion battery (state of the art)	0.17 kWh/kg & 0.3 kWh/L
Li-Ion battery (potential perspective)	0.235 kWh/kg & 0.500 kWh/L[6]
Power density, P of propulsion devices [W/kg] & [W/L]	
ICE engine	[45-71] W/kg & [32.5-55] W/L [1]
PEMFC	[250-1000] W/kg & [300-1550] W/kg [1]
Li-Ion battery (state of the art)	[150-450] W/kg & [150-450] W/L
Li-Ion battery (Perspective)	[200-600] W/kg & [200-600] W/L
Power density of cracker used in conjunction with PEMFC [W/kg] & [W/L]	
Ammonia cracker	150 W/kg & 140W/L
Methanol reformer	0.8* (150 W/kg & 140 W/L)
Methane reformer	0.6* (150 W/kg & 140 W/L)

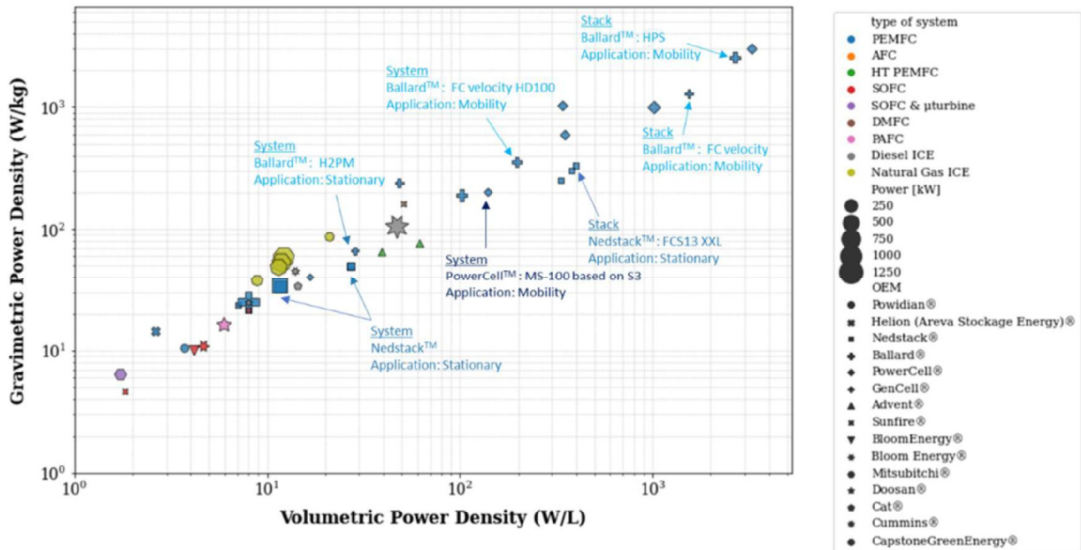


Figure G1: Gravimetric power density ($\text{W/kg}_{\text{system}}$) vs Volumetric power density ($\text{W/L}_{\text{system}}$) of systems currently available on the market (by consulting various OEM websites)

Table G2: OEM specifications of traditional fuel processors, with estimated power densities based on a PEMFC operating at 55% efficiency and a hydrogen lower heating value (LHV) of 33 kWh/kg

OEM	Fuel	Mass of the system (kg)	Volume of the system (m^3)	Hydrogen production rate (kg/hr)	Estimated electric power output (kW)	Estimated Power density (W/kg)	Estimated Power density (W/L)
RIX power™ M2H2-1800	Methanol	1455	3.2	10	183	~126	~57
e1-marine™ S series S130	Methanol	139	0.2	0.7	12.8	~92.3	~64
HyGear™	Methane	7300	NA	4.22	77.5	~11	NA

➤ Results and discussion

Figure G2 presents a comparative assessment of propulsion systems using Ragone plots, illustrating key trade-offs between power and energy density across different operational timescales. Technologies in the upper-right region achieve a balance of high power and energy density, while those in the top-left are optimized for short bursts of power, and those in the bottom-right excel in long-duration energy delivery. In gravimetric terms (**Figure G2.A**), diesel ICEs (blue) remain the most energy-dense option, making them ideal for long-range applications. PEMFC-based systems (red & orange), particularly those using methane, ammonia, and to a lesser extent LH_2 , are better suited for medium-range operations. Battery systems (green), despite their high efficiency, have low gravimetric energy density, limiting their use in long-haul shipping but making them effective for short, high-power applications (1–5 hours). Volumetric considerations (**Figure G2.B**) follow a

Conclusion and Outlook

similar trend, with diesel ICEs maintaining the highest energy density. However, PEMFC systems remain viable for medium-term operations ($\sim 10\text{--}15$ hours), and notably, LH_2 and ammonia PEMFCs can exceed diesel ICEs in power density. When factoring in global efficiency losses (**Figure G3**) from electrolysis and fuel synthesis, fuel-based pathways shift downward, with synthetic diesel and methanol particularly affected compared to battery solutions. **Figure G4** provides a sensitivity analysis on ammonia-based PEMFC, examining the impact of reduced cracker efficiency (dashed line) and lower cracker power density (dotted line). A drop in efficiency significantly reduces power output, shifting the curve downward, while a lower power density mainly limits peak power output with a smaller effect on energy storage. Efficiency losses have a greater impact, making the system less viable for high-power applications and emphasizing the importance of optimizing fuel processor efficiency and power output.

For an overview of efficiency metrics, **Table G3** summarizes both local and global efficiencies for comparison.

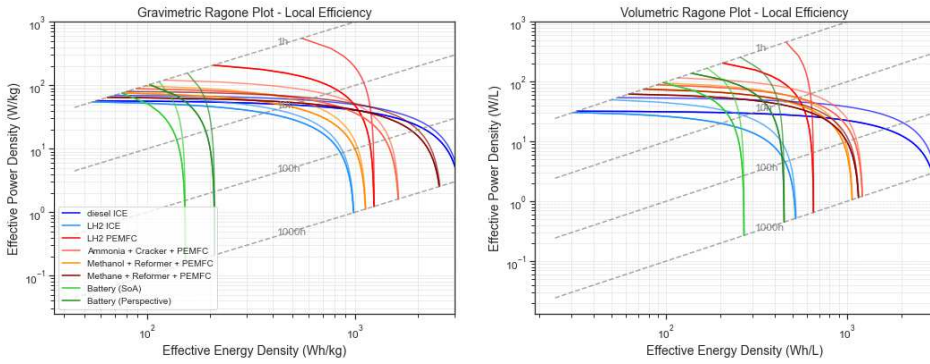


Figure G2: Gravimetric and Volumetric density of various combination considering η_{local}

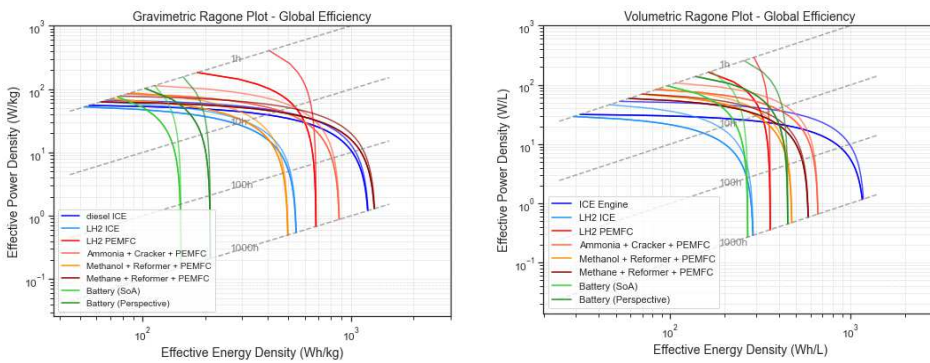


Figure G3: Gravimetric and Volumetric density of various combination considering η_{global} (i.e. considering the fuel production efficiency).

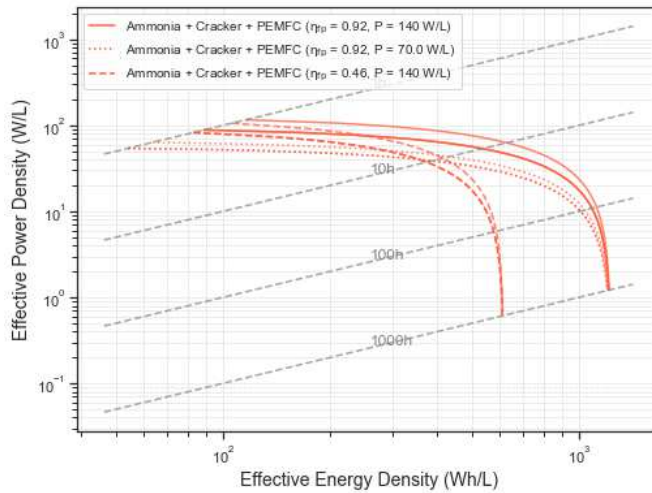


Figure G4: Impact of fuel processor efficiency and volumetric power density reduction (-50% from the reference case) on ammonia-based PEMFC power systems (volumetric basis)

Table G3: Table of local and global efficiencies for the different options assuming PEM electrolysis production

	Local system efficiency	Global efficiency
Diesel+ICE	0.4	0.14
LH2+ICE	0.4	0.22
LH2+PEMFC	0.49	0.27
Ammonia+ cracker+PEMFC	0.45	0.24
Methanol + reformer + PEMFC	0.28	0.12
Methane + reformer + PEMFC	0.36	0.18
Battery	0.81	0.81

➤ References

- [1] L. van Biert, M. Godjevac, K. Visser, P.V. Aravind, A review of fuel cell systems for maritime applications, *Journal of Power Sources* (2016) 20.
- [2] B. Diesveld, E. De Maeyer, Maritime fuel cell applications: A tool for conceptual decision making, *ISP 67* (2020) 57–77. <https://doi.org/10.3233/ISP-190275>.
- [3] A.D. Korberg, S. Brynolf, M. Grahn, I.R. Skov, Techno-economic assessment of advanced fuels and propulsion systems in future fossil-free ships, *Renewable and Sustainable Energy Reviews* 142 (2021) 110861. <https://doi.org/10.1016/j.rser.2021.110861>.
- [4] D. Bellotti, M. Rivarolo, L. Magistri, A comparative techno-economic and sensitivity analysis of Power-to-X processes from different energy sources, *Energy Conversion and Management* 260 (2022) 115565. <https://doi.org/10.1016/j.enconman.2022.115565>.

- [5] V. Dias, M. Pochet, F. Contino, H. Jeanmart, Energy and Economic Costs of Chemical Storage, *Front. Mech. Eng.* 6 (2020) 21. <https://doi.org/10.3389/fmech.2020.00021>.
- [6] R. Schmich, R. Wagner, G. Hörpel, T. Placke, M. Winter, Performance and cost of materials for lithium-based rechargeable automotive batteries, *Nat Energy* 3 (2018) 267–278. <https://doi.org/10.1038/s41560-018-0107-2>.
- [7] C. Cheng, R. Drummond, S.R. Duncan, P.S. Grant, Extending the energy-power balance of Li-ion batteries using graded electrodes with precise spatial control of local composition, *Journal of Power Sources* 542 (2022) 231758. <https://doi.org/10.1016/j.jpowsour.2022.231758>.

Research Outputs

The published (or intended to be) work associated to the thesis are recapped as follow:

Peer-reviewed publications

- **S. Richard**, P. Olivier, M. Jegoux, C. Makhloufi, F. Gallucci Membrane reactors technologies for e-fuel processing & production: Review, **Submitted to *Int. J. Hydrogen Energy***
- **S. Richard**, A. Ramirez Santos, F. Gallucci, PEM gensets using membrane reactors technologies: An economic comparison among different e-fuels *Int. J. Hydrogen Energy* vol. 50 part A, pp. 433-457, 2024
- **S. Richard**, A. Ramirez Santos, P. Olivier, F. Gallucci, Techno-economic analysis of ammonia cracking for large scale power generation, *Int. J. Hydrogen Energy* vol. 71, pp. 571-587, 2024
- **S. Richard**, D. Tasso, M. Rajana, A. Saker, A. Ramirez Santos, C. Makhloufi, N. Meynet, B. Hary, S. Nardone, G. Marino, M. Thomas, C. Italiano, A. Vita, F. Gallucci, Comparison of thermo-hydraulic performance among different 3D printed periodic open cellular structures, *Chemical Engineering Journal*, vol. 47, no. 21, pp. 11385-11401, 2024
- **S. Richard**, V. Verde, N. Kezibri, C. Makhloufi, A. Saker, I. Gargiulo, F. Gallucci, Power-to-ammonia synthesis process with membrane reactors: Technoeconomic study, *Int. J. Hydrogen Energy* vol. 73, pp. 462-474, 2024
- C. Italiano, G. Marino, M. Thomas, B. Hary, S. Nardone, **S. Richard**, A. Saker, D. Tasso, N. Meynet, P. Olivier, F. Gallucci, A. Vita, Carbon-free H₂ production from ammonia decomposition over 3D-printed Ni-alloy structures activated with Ru/Al₂O₃ catalyst, **Submitted to *Processes***
- **S. Richard**, D. Tasso, M. Rajana, A. Saker, N. Meynet, B. Hary, S. Nardone, G. Marino, M. Thomas, C. Italiano, A. Vita, F. Gallucci, Ammonia synthesis using POCS membrane reactor: influence of cell types and permeance, **Submitted to *Chemical Engineering Journal***
- I. Gargiulo, G. Anello, **S. Richard**, F. Gallucci, Modelling and simulation study of a packed bed membrane reactor for ammonia synthesis: assessing the role membrane permeance and operating conditions **Submitted to *Int. J. Hydrogen Energy***

Oral presentations

- **S. Richard** Power-to-ammonia using catalytic membrane reactors: influence of process conditions and membrane properties, *2nd Symposium on Ammonia Energy (2nd SAE)* held in Orléans, France, 2023
- **S. Richard**, Power-to-ammonia using catalytic membrane reactors, *16th International Conference on Catalyst in Membrane Reactors (ICCMR16)* held in Donostia-San Sebastián, Spain, 2023
- **S. Richard** Power-to-Maritime Fuel: A Techno-Economic Evaluation of Hydrogen Methanol, Ammonia and Diesel, *24th World Hydrogen Energy Conference (24th WHEC)* held in Tulum-Rivera Maya, México, 2024

Acknowledgments

I would like to thank my supervisor, Professor Fausto Gallucci at Eindhoven University of Technology for his constant support throughout the project, and Dr. Camel Makhoulfi, research engineer at ENGIE lab Crigen, who hired me for this PhD journey.

I am thankful to the Hydrogen Lab at ENGIE Lab CRIGEN for funding the PhD program and welcoming me into their team. I would like to extend a particular thanks to some of my (former) colleagues: Nouaamane Kezibri, Alvaro Ramirez Santos, Secil Torun, Stephane Hody, Assia Saker, Adeline Miquelot, Nicolas Meynet, Mathilde Jegoux, and Pierre Olivier who provided some support at various stages of my project, whether managerial, technical or through their editorial contributions to article / deliverable revisions.

I would like to thank my fellows PhD students in the Hydrogen Lab: Jean-Hugues Boilley, Vito Verde, Berenger Wegman, Nicola Benvenuti, and Emma Nguyen. It was always nice to have coffee breaks and share light-hearted moments with all of you. It was also nice to sometimes find common topics to collaborate on with some of you.

I would like to thank Damien Tasso; it was a pleasure working with you during your MSc project and later as you joined ENGIE.

On the Eindhoven side, I am thankful to Saskia and the PhD students there, Iolanda, Valentina, Gaetano, Huub and Daniël who welcomed me during my attempts to conduct experiments, even if things didn't go quite as planned with a design issue with the POCS (something that at least is not repeated in the Ambher project). Despite this, I appreciated the opportunity to do hands-on experimentations.

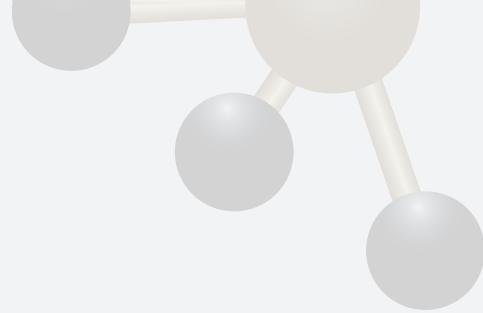
I would also like to thank the clarinet choir at Engie: Damien Tasso, Sławek Pietrasz, and Quentin Nouvelot, for the music and the conversations. I'll miss it and I think the chance of finding another one elsewhere aren't exactly high.

Finally and most importantly, I would like to thank the PhD committee for agreeing to evaluate the thesis: Prof. Dr. Ir. M. van Sint Annaland, Prof. Dr. Ir. J. van Der Schaaf, Dr. S. Soheil Mansouri Dr. M.F. Neira d'Angelo, Dr. V.S. Spallina, & Dr. Pierre Olivier.

Curriculum Vitae



Simon completed an MEng in Chemical Engineering from the University of Bath. During his studies, he conducted a research project on nitrous oxide (N_2O) emissions in oxidation ditch reactors, using CFD modeling under the supervision of Dr. Benedek Plosz. For his master's thesis, he designed a treatment plant for a small modular nuclear reactor, focusing on the degasification unit under the guidance of Dr. Alf Hill. Simon also undertook a year-long placement with EDF, addressing various challenges in cooling circuit systems: loss-of-coolant accidents simulation using CFD at EDF Energy's Modeling and Simulation Center (University of Manchester), make-up water oxygenation at EDF DI, and fouling phenomena in tertiary circuits at EDF R&D LNHE. These experiences motivated him to pursue a PhD, which he began in September 2020 at Eindhoven University of Technology in the Sustainable Process Engineering (SPE) group under the supervision of Prof. Dr. Fausto Gallucci. The PhD was funded by ENGIE Lab Crigen (H_2 lab), where he contributed to European projects such as Macbeth or Ambher.



Synthetic chemicals produced from green hydrogen and captured carbon dioxide for methanol and methane, or nitrogen for ammonia, can address renewable energy intermittency issues and provide fossil-free resources for hard-to-electrify sectors like transportation and distributed power generation. However, these reaction systems are typically limited by thermodynamic equilibrium, which constrains reactant conversion under relevant process conditions. Membrane reactors (MRs) have established as a significant contribution in process intensification allowing overcoming these limitations through the combination of reaction and product separation in a single device. In their most basic configuration, a MR involves a tubular vessel with vertically inserted membranes surrounded by a catalyst-packed bed. Reactants enter from the bottom and move upward, with the product collected inside the membrane as permeate, while other chemical components form the retentate. This thesis explores the use of the MR technology in the Power-to-X context from various perspectives, including process synthesis, techno-economic analysis and the potential of additive manufacturing to enhance the basic MR configuration along with experimental testing of the technology